ScuDo
Scuola di Dottorato ~ Doctoral School
WHAT YOU ARE, TAKES YOU FAR

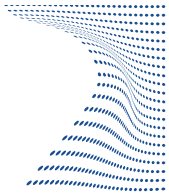

Doctoral Dissertation
Doctoral Program in Energy Engineering (XXXIVth cycle)

Methods for safety and stability analysis of nuclear systems

Nicolò Abrate
* * * * * *

Supervisors
Prof. Sandra Dulla
Prof. Nicola Pedroni

Doctoral Examination Committee:
Prof. Erez Gilad, *Referee*, Ben Gurion University of the Negev
Prof. Paolo Vinai, *Referee*, Chalmers University of Technology
Prof. Antonio Cammi, Politecnico di Milano
Prof. Edoardo Patelli, University of Strathclyde
Prof. Farzad Rahnema, Georgia Institute of Technology

Politecnico di Torino
2022

I hereby declare that, the contents and organisation of this dissertation constitute my own original work and does not compromise in any way the rights of third parties, including those relating to the security of personal data.

. . . . . .

Nicolò Abrate
Turin, 2022

Summary

This thesis has the double objective of proposing new methods, mainly concerning the safety and stability analyses of nuclear reactors, and, at the same time, of extending available techniques in order to be compliant with the industrial requirements concerning the adoption of qualified codes.

The development of new methods is mostly carried out in the first part of the thesis, where they are applied to simplified systems in order to better grasp their physico-mathematical features, but without loosing track of the real-life applications. In the first chapter, the classical P_N and S_N approximations are presented, in order to approach numerically the solution of the eigenvalue problems arising in neutron transport. After addressing some old-fashioned but still relevant questions concerning the angular parity order, the equivalence between odd and even angular orders and the possibility to accelerate numerically the angular convergence of these methods, some numerical benchmarks are carried out to check the implementation of these methods in an in-house Python package, called TEST, which is widely adopted in the course of the thesis.

Then, the classical eigenvalue formulations to the neutron transport equation are presented and discussed, focusing on their physico-mathematical peculiarities and on their eigenvalue spectra. Afterwards, a novel eigenvalue formulation, focused on neutron capture, is introduced and discussed as well. Finally, an example regarding the application of the eigenvalue spectrum for the optimal selection of the energy group for the energy collapsing is presented and discussed.

Exploiting the results of the eigenvalue formulation analysis, a possible application of the eigenfunctions associated to the various formulations are proposed as alternative weighting functions for the group collapsing procedure. The behaviour of the different weighting functions is assessed by comparing the main integral parameters obtained by multi- and few-group calculations. The major outcome of this analysis is that better alternatives to the eigenfunction associated to the classic multiplication eigenvalue exist, despite their performances depend on the calculation parameters.

Then, the first part of the thesis is concluded by proposing a generalisation of the standard eigenvalue formulations, with the final aim of deriving a new eigenvalue problem which allows to act on specific portions of the phase space and nuclides, for design-oriented applications. After discussing the main physico-mathematical aspects of this

formulation, relevant engineering problems like the determination of the critical boron concentration are evaluated using this new approach, showing its efficiency and its capability to find all the possible critical configurations for a given initial off-critical system. This last feature is particularly important for safety analyses, since it allows to explore the physical conditions that may lead a system to re-criticality. In the determination of the possible critical configurations of the system, emphasis is also put on the classical figure of merit used to assess the neutronic stability, i.e. the eigenvalue separation.

In the remaining chapters, more realistic systems are analysed, focusing on 2D and 3D models of some Gen-III+ and Gen-IV reactor concepts. This last part of the work mainly aims at proposing computationally efficient methods for the safety analyses of the neutronic behaviour of the core, trying to reduce as much as possible any intervention in the code. This goal is accomplished by means of Non-Intrusive Reduced-Order Modelling (NIROM) techniques, which permit a fair reduction of the computational time without any code modifications at the price of small approximations.

A non-intrusive reduced-order model (NIROM) is presented as an efficient way of reducing the computational cost of the original, high-fidelity models. Then, this model is applied to three different industrial application, with the goal of proving the NIROM effectiveness.

The first application deals with the spatial stability stability of the Gen-III+ core, with the aim of training an efficient NIROM to analyse the power tilt behaviour at the full-core level with respect to an input random perturbation. Due to core complexity and to the great number of free parameters, some extensions of the NIROM are devised, like proposing to use the Polynomial Chaos Method to compute the perturbed cross sections for the full-core diffusion calculation. Afterwards, the need for a new metric to evaluate the distance between the training data is highlighted, proposing a more accurate algorithm to accomplish this task. Finally, the NIROM performances are successfully tested, both in terms of memory and of computational time.

The second application concerns the parametric safety analysis of accidental transient scenarios in LFR. Also in this case, some of the NIROM steps are suitably modified and extended, in order to take into account the time-dependent behaviour of the model. Finally, the accuracy of the NIROM is proved by comparing its results with a validation dataset.

In order to show that the methods proposed have a wide applicability range also outside the nuclear field, this last application focuses on the safety analysis of accidental high-pressure gas releases in industrial, congested environments.

Finally, the last chapter focuses on the nuclear data uncertainty quantification, which is a relevant topic in the safety analysis of nuclear system. The chapter focuses both on methodological aspects and on the nuclear data uncertainty propagation for the lead fast reactor ALFRED design.

Acknowledgements

When I had to choose my university studies, I was coming from five years of classical studies at the high school, which are more theoretical and philosophical than practical. Therefore, I challenged my love for physics taking the courses of the Energy Engineering Bachelor program at Politecnico di Torino, with the final aim of taking the Nuclear Engineering program in the Master. Despite my long-term objective, my first three years at Politecnico were very tough and frustrating, and I was constantly asking myself why I did not choose Physics as my best friends did.

Luckily, at the end of the third year I was refunded for those hard times with the course "Fundamentals of Nuclear Engineering", given by Prof. Piero Ravetto. His teachings and his passion were the spark that gave me not only the motivation for the final rush in the Bachelor but also the ambition to undertake a PhD concerning the physics of nuclear reactors after the Master. Because of this reason, and for having been an inextinguishable source of motivations, inspirations and scientific ideas, he is the first person that I need to thank at the end of my studies. To me, he was like the latin poet Virgil was to the italian poet Dante.

Despite his importance (in a reactor physics sense, of course), Virgil guided Dante only in the first part of his journey, which would have not been completed without the guidance of Beatrice and Saint Bernard of Clairvaux. In full analogy with Dante's experience, my PhD journey has been accomplished thanks to the supervision of two guides, i.e. Prof. Sandra Dulla and Prof. Nicola Pedroni. They will always have my deepest gratitude for having believed in my qualities, for having trusted me in several occasions, for having given me responsibilities and for having taught me more than this PhD thesis could tell. Among the several virtues characterising my guides, Patience is certainly the one which better describes both of them in a single word. No one ever put pressure on me for anything, despite my despicable tendency of occupying all the time span I have at my disposal and to be constantly on the edge of the deadlines. They gave me time and a lot of freedom in my work, always providing their scientific and, above all, human support.

Moreover, I would like to thank all the other people who contributed to my journey, especially Prof. Andrea Carpignano for his support and for allowing me to take part to the SEADOG group activities, and Dr. Paolo Saracco, for sharing his scientific knowledge and his elegant equations.

Then, I would like to acknowledge all the past and present junior members of the NEMO and of the SEADOG research groups for having shared with me the burden of being a young researcher. The collaborative attitude of all these people is the proof that "*knowledge is the only good that grows when shared*" (H. Gadamer). A special thank goes to Antonio for his everlasting IT support and to Domenico and Giuseppe Francesco, the so-called "fellowship of the Hexagon". The three of us spent some hard times working on Liquid Metal Fast Reactors, but this experience was the origin of a sincere and beautiful friendship, which is another aspect of the PhD journey that goes beyond this manuscript.

Finally, I would like to thank my friends and my family for their endless support and understanding, especially for my very long *stealth mode* periods during the composition of this manuscript. The most special thank goes to my wife Francesca and to my one-year old daughter Beatrice, who constantly reminded me that, as a very wise woman once wrote on her desktop wallpaper, *"Life is elsewhere"*. This thesis is not certainly worth the time with you I had to sacrifice.

"I'm not living my life halfway. Even if for just a second, I want to burn bright as the sun...and after that, only white ashes remain." (Joe Yabuki, *Ashita no Joe*).

Contents

1 Introduction 1
- 1.1 Overview . . . 1
- 1.2 Motivations . . . 3
- 1.3 Aim of the work and outline of the thesis . . . 7

2 The P_N and S_N approximations of the neutron transport eigenvalue formulations 13
- 2.1 Introduction . . . 13
- 2.2 The neutron transport model in plane geometry . . . 15
- 2.3 Eigenvalue formulations in neutron transport . . . 17
  - 2.3.1 Design-oriented eigenvalue formulations . . . 19
- 2.4 Numerical framework for the solution of the neutron transport eigenvalue problems . . . 20
  - 2.4.1 The P_N equations . . . 22
  - 2.4.2 The S_N equations . . . 27
  - 2.4.3 The boundary conditions . . . 28
- 2.5 The P_N - S_{N+1} equivalence . . . 30
  - 2.5.1 Even-to-odd order reduction . . . 33
- 2.6 Numerical benchmark of the eigenvalue formulations to the P_N and S_N models . . . 36
  - 2.6.1 Numerical solvers for the solution of eigenvalue problems . . . 36
  - 2.6.2 Benchmark with the data available in the literature . . . 39
  - 2.6.3 The influence of boundary conditions and of the parity order on the angular convergence . . . 45
  - 2.6.4 Benchmark with the Monte Carlo approach using the Wynn-ε acceleration scheme . . . 53
- 2.7 Conclusions . . . 63

3 The spectrum of the neutron transport operator and its application to group collapsing 69
- 3.1 Introduction . . . 69
- 3.2 The multiplication eigenvalue . . . 71

3.3 The collision eigenvalue . . . 75
3.4 The time eigenvalue . . . 79
3.5 The density eigenvalue . . . 91
3.6 The capture eigenvalue . . . 99
3.7 The effect of energy group collapsing . . . 103
3.8 Conclusions . . . 110

4 Spectral formulations as alternative weighting functions for group collapsing 115
4.1 Introduction . . . 115
4.2 Transient simulation framework . . . 119
4.3 Homogeneous thermal system . . . 123
4.3.1 Sub-prompt positive reactivity insertion . . . 124
4.3.2 Super-prompt positive reactivity insertion . . . 126
4.3.3 Negative reactivity insertion . . . 128
4.3.4 Positive and negative reactivity insertions . . . 131
4.4 Homogeneous fast system . . . 135
4.4.1 Sub-prompt positive reactivity insertion . . . 136
4.4.2 Super-prompt positive reactivity insertion . . . 139
4.4.3 Negative reactivity insertion . . . 142
4.4.4 Positive and negative reactivity insertions . . . 143
4.5 Conclusions . . . 147

5 A generalised eigenvalue formulation for core-design applications 151
5.1 Introduction . . . 151
5.2 The theory of the ζ eigenvalue . . . 153
5.2.1 Implementation in the TEST code . . . 155
5.3 Determination of the moderation ratio for a homogeneous mixture of fuel and moderator . . . 156
5.4 Determination of the moderation ratio for a regular lattice . . . 158
5.5 Determination of the boron concentration for reactivity control . . . 168
5.6 Fissile concentration for reactivity control in the Molten Salt Fast Reactor 169
5.7 Determination of the coolant volume in a Lead Fast Reactor . . . 172
5.8 Determination of neutron absorbers for reactivity control . . . 174
5.9 Conclusions . . . 178

6 A non-intrusive, computationally efficient modelling framework for the safety analysis of complex systems 181
6.1 Introduction . . . 181
6.1.1 A non-intrusive POD-RBF model . . . 185
6.2 A non-intrusive reduced order model for the stability analysis of large thermal reactors . . . 197

6.2.1 Introduction . . . 197
6.2.2 Non-intrusive model reduction for the cell calculations . . . 204
6.2.3 Non-intrusive model reduction for the full-core calculations . . 216
6.2.4 Conclusions and future developments . . . 238
6.3 Application to the neutronic transient analysis of the ALFRED reactor . 241
6.3.1 Introduction . . . 241
6.3.2 Statement of the problem . . . 242
6.3.3 The time-dependent POD-RBF model . . . 243
6.3.4 Model training and validation . . . 245
6.3.5 Conclusions and future perspectives . . . 249
6.4 A robust and efficient NIROM for the safety analysis of accidental gas releases in congested plants . . . 251
6.4.1 Study case: accidental gas release in a congested environment . 255
6.4.2 Conclusions and future perspectives . . . 267

7 Generalized Perturbation Techniques for Uncertainty Quantification in Lead-Cooled Fast Reactors 277
7.1 Introduction . . . 277
7.2 Generalized perturbation methods for uncertainty quantification . . . 280
7.2.1 Evaluation of sensitivity coefficients . . . 281
7.2.2 Determination of the basis functions . . . 285
7.2.3 XGPT uncertainty quantification . . . 286
7.3 Application to the ALFRED reactor model . . . 287
7.3.1 Uncertainty quantification with GPT . . . 288
7.3.2 Comparison between XGPT and GPT results . . . 291
7.3.3 Multi-group constant distributions . . . 297
7.4 Conclusions . . . 298

8 Conclusions and future perspectives 305
8.1 Summary . . . 305
8.2 Conclusions and future perspective . . . 307

Chapter 1

Introduction

> It is, perhaps, the most remarkable book ever
> to come out [...]
> of which no Earthman had ever heard either.
> Not only is it a wholly remarkable book,
> it is also a highly successful one.
> [...] the Hitch Hiker's Guide [...]
> scores over the older, more pedestrian work in
> two important respects.
> First, it is slightly cheaper; and secondly it has
> the words DON'T PANIC inscribed in large
> friendly letters on its cover.
>
> The Hitchhiker's Guide to the Galaxy,
> Douglas Adams

1.1 Overview

The risk perception and, consequently, its public acceptability are probably the aspects which limited the most, during the last 40 years, the worldwide diffusion of nuclear power plants (NPP) as an effective, clean, reliable and carbon-free electricity source (Buongiorno, Parsons, and Petti, 2019). Despite they were featured by different initiating events, time evolution and consequences, all the three major accidents involving nuclear power plants, namely Three Mile Island (1979), Chernobyl (1986) and Fukushima Daiichi (2011), made evident the fact that, to avoid any accidental outbreak, safety has to be included *by design* when a new reactor concept is developed (Meshkati, 2007). In particular, Chernobyl pointed out both the dramatic rôle of human errors in the development of an accident and the difficulty of human intervention to restore the plant main functionalities in the presence of a severe accident, while Fukushima demonstrated that, in order to effectively certify the safety of a plant, the probabilistic

risk assessment should demonstrate that the nuclear installations are able to withstand also very unlikely yet still possible events, which are known as *beyond design basis accidents* (BDBA) (IAEA, 2020).

These lessons learnt brought up the need for innovative nuclear fission reactors that could meet these safety requirements and the ones concerning the fuel cycle sustainability, the long-life waste minimisation, the resistance to proliferation and the market competitiveness with the other energy sources. As an immediate, albeit partial, response to these necessities, it was first proposed to enhance the design of the most popular and reliable operating reactors, i.e. the Light Water Reactors (LWRs), including some passive safety features and improving their economic aspects. These reactor designs belongs to the so-called Generation-III+ (Gen-III+), which includes the Advanced-Passive 600 (AP-600), the Advanced-Passive 1000 (AP-1000) and the European Pressurised Reactor (EPR) (Marques, 2011).

For the long term, the ultimate response to these issue should come with the so-called Generation IV (Gen-IV) reactors, a set of evolutionary concepts heavily based on the passive safety principles. Among the most promising designs selected in the frame of the Generation IV International Forum (Locatelli, Mancini, and Todeschini, 2013), it is possible to mention, for example, the Lead Fast Reactor (LFR) and the Molten Salt Reactors (MSR).

Gen-III+ and Gen-IV reactors are nowadays featured by different technology readiness levels. Concerning the Gen-III+, the first AP1000, located in China, achieved criticality during the mid of 2018, while the first EPR unit entering commercial operations was the one of Taishan 1, in China, at the end of 2018[1]. The first unit to achieve criticality in Europe, after several delays, was the one in Olkiluoto, Finland, at the end of 2021[2]. Other units are still under construction in France (Flamanville) and United Kingdom (Hinkley Point). In spite of these construction delays, the Gen-III+ reactors are now a mature technology. Nevertheless, some design variations with respect to the traditional PWR concepts, like the larger core size, the adoption of a heavy stainless steel reflector and the reduction of the in-core equipment, make their operation more delicate in comparison to other LWRs (Sargeni, Burn, and Bruna, 2016). Therefore, there is a never-ending need for reliable and efficient calculation tools to assess their safe operation.

On the contrary, most of the Gen-IV systems are currently under different advancement stages of the design, and only a few of them are close to a maturity level sufficient for the construction of plant demonstrators (Kamide, Rodriguez, et al., 2021). Hence, the risk assessment for these reactors is currently at a preliminary stage, and mainly aims at guiding the design development and ensuring the inclusion of the safety aspects from the early design phases.

[1] https://world-nuclear-news.org/Articles/First-EPR-enters-commercial-operation

[2] https://www.world-nuclear-news.org/Articles/Europe-s-first-EPR-reaches-criticality

With respect to Gen-III+ reactors, which can benefit from the design and operational experience coming from the LWRs fleet, Gen-IV reactors are mostly first-of-a-kind systems, with very limited design and operational experience. Their unique features and working principles introduced the need for more sophisticated modelling and computational techniques for both the design and the licensing phases. For example, the inherent multiphysics features of these reactors put a larger emphasis on the multiphysics simulations, and the presence of uncommon nuclides requires the quantification of the nuclear data uncertainties on the reactor macroscopic parameters. Hence, the successful deployment of these revolutionary concepts requires the development of new experiments, methods, calculation tools, safety requirements and construction standards (Driscoll and Hejzlar, 2005).

Given these socio-economic-environmental aspects and the current nuclear industrial framework, it appears evident that both the operation of Gen-III+ reactors and the design, licensing and construction of Gen-IV reactors entail a keen effort towards the adoption of state-of-the-art methodologies to perform thorough safety assessments. One possibility to accomplish this goal could lie in the integration of practices pertaining to the safety and risk analysis into the different aspects of the reactor design and operation, like neutronics, thermo-hydraulics, fuel performance and system analysis. Due to the vastness of these disciplines, this Ph.D. thesis focuses mainly on the neutronic aspects and their rôle in the safety studies.

1.2 Motivations

Neutronics is, in a wide sense, a branch of physics dealing with the study of the neutrons distribution inside a system and their interactions with the medium composing the system. Thanks to their physical features, the behaviour of these sub-atomic particles can be effectively represented by the linear Boltzmann transport equation.

The neutron transport model in its general formulation, including delayed emissions from the fission products decay, consists in the following system of integro-differential

equations, coupled with appropriate boundary and initial conditions:

$$
\begin{cases}
\dfrac{1}{\mathrm{v}(E)}\dfrac{\partial\phi(\vec{r},E,\hat{\Omega},t)}{\partial t}+\vec{\nabla}\cdot\left(\vec{\Omega}\phi(\vec{r},E,\hat{\Omega},t)\right)+\Sigma_t(\vec{r},E)\phi(\vec{r},E,\hat{\Omega},t)= \\
+\displaystyle\int dE'\oint d\hat{\Omega}'\,\Sigma_s(\vec{r},E')\phi(\vec{r},E',\hat{\Omega}',t)f_s(\vec{r},E'\longrightarrow E,\vec{\Omega}\cdot\vec{\Omega}')+ \\
+(1-\beta)\dfrac{\chi_p(\vec{r},E)}{4\pi}\displaystyle\int dE'\oint d\vec{\Omega}'\,\nu\Sigma_f(\vec{r},E')\phi(\vec{r},E',\hat{\Omega}',t)+ \\
+\displaystyle\sum_{i=1}^{R}\dfrac{\chi_i(\vec{r},E)}{4\pi}\lambda_i C_i(\vec{r},t)+S_{ext}(\vec{r},E,\hat{\Omega},t) \\
\\
\dfrac{\partial C_i(\vec{r},t)}{\partial t}=\beta_i\displaystyle\int dE'\oint d\hat{\Omega}'\,\nu\Sigma_f(\vec{r},E')\phi(\vec{r},E',\hat{\Omega}',t)-\lambda_i C_i(\vec{r},t), \qquad i=1,\dots,R.
\end{cases}
\tag{1.1}
$$

where the symbols have their standard meaning, as it can be found in most of the nuclear reactor physics books (Weinberg and Wigner, 1958; Bussac and Reuss, 1985) and in chapter 2.

Equation (2.13) is featured by many levels of complexity, which may be roughly distinguished in *physico-mathematical* and *engineering* intricacies. The firsts are mainly related to its integro-differential nature, which has required the development of several solution techniques, both analytical and numerical. The second group of intricacies, strongly linked to the first one, is related to the practical application domain, which is usually a multi-scale system, e.g. a nuclear reactor. The way these two levels of complexity have been tackled during the years have profoundly influenced the development of nuclear reactor physics.

At the dawn of the nuclear history, these two aspects were tightly related. On one side, there was the need to understand the fundamental physical phenomena at the basis of the fission chain reaction. On the other, there was the technological competition to control the nuclear energy for military purposes. Enrico Fermi, who was the first to adopt a mathematical model to study the neutron balance, designed the Chicago Pile system tackling both physico-mathematical and engineering issues (Fermi, 1947). Thanks to the fundamental physical knowledge acquired with experiments and theory, he remarkably synthesised the complex phenomena related to fission and neutron slowing down in his famous *four factor formula*, which has been used for decades as a guidance for the design of thermal reactors.

In a somewhat similar way, Allan F. Henry exploited the physico-mathematical features of the transport equation to develop the quasi-static method for the solution of the time-dependent transport equation, inspired by the multi-scale time behaviour of the reactors that he observed in the experimental data (Henry, 1958). Some years later, Henry proposed to analyse an engineering problem, i.e. the flux tilts induced by localised perturbations like control rods adjustments or coolant flow perturbations, using

a modal expansion based on the so-called ω-modes (Henry, 1964). In this work, Henry wrote:

> *The capability of computing detailed transient behaviour in a reactor has increased considerably in recent years. To some extent this advance is associated with the greater capacity of digital computing equipment;*
>
> [...]
>
> *However, to a greater extent, the advance has resulted from an improved understanding of the heat transfer, pressure drop, fluid flow and neutron kinetic phenomena which interact in the course of a reactor transient. Of course, along with increased capability has come an obligation for responsible use.*

In a few lines concerning the status of the research at his time, Henry prophetically pointed out some aspects that are still crucial today. First, he recognised the fundamental rôle of the computational resources for acquiring the knowledge to understand, design and operate a reactor. Then, he placed an even greater value on the experimental works to understand the complex multi-scale, multi-physics phenomena occurring in a reactor. Finally, he warned that the greater is the power, the greater is the responsibility: computers are an irreplaceable aid to human activities, but they will hardly replace the human critical thinking and intuition.

According to the famous Moore's law (Moore, 1998), nowadays we dispose of a computational power that is roughly 50 million times the one of the 1970s. The existence of a huge, affordable and handy computational power enabled, in the last decades, the deployment of high-fidelity simulations, which seem to make some classic issues of reactor physics a blurred memory, completely disregarding Henry's "prophecy". In the frame of neutron transport, this is possible thanks to the Monte Carlo method (Metropolis and Ulam, 1949), which is a stochastic technique allowing the simulation of the neutron transport process in such an excruciating detailed way that the only limit to the accuracy achievable is, probably, the uncertainty in the basic nuclear data used to sample neutron interaction with matter. It is curious to notice that this method was conceived during the Manhattan projects, when the computational power was very far from being sufficient to run even very simple simulations (Metropolis, 1987). Nowadays, this approach fully exploits the massively parallel features of High Performance Computing (HPC), allowing, in principle, to solve even the most challenging problems in reactor physics with high precision (Faucher, Mancusi, and Zoia, 2018).

Analogous considerations cannot be easily extended to other fields of nuclear engineering like thermo-hydraulics and fuel performance, where there still are considerable knowledge gaps on fundamental phenomena. Therefore, we could claim that, concerning nuclear engineering, the existence of a high-fidelity methodology is an exclusive of neutronics.

Having a reference model is a blessing for several reasons, e.g., design of experiments or benchmarking, but this advantage should not be abused mainly for two reasons. First,

Monte Carlo does not necessarily ensure a better comprehension of the physics. Often, very detailed calculation provide too much detail, which may be difficult to interpret. On the contrary, simpler, approximated models (neutron diffusion, asymptotic theory, point kinetics...) can be much more effective to intuitively deliver the basic knowledge which can then be extended also to more complex, real-life scenarios. These considerations are indirectly safety-related, because they affect the education and training of designer and operators of the current and future NPP. Second, a high-fidelity modelling approach does not always fits the design and safety needs. The core-design is an iterative process, thus it should be based on fast calculation tools. The same applies to the preliminary safety studies used to support the design phase.

As regards the design licensing, both Probabilistic Risk Assessment (PRA) and Quantitative Risk Assessment (QRA) need to rely on a large amount of simulations and, thus, data, in order to identify with sufficient confidence which are the most safety-critical physical parameters and system components, and to suggest prevention and mitigation actions. High-fidelity simulations are very valuable for design verification and licensing studies, for example in the frame of the Best Estimate Plus Uncertainty (BEPU) approach (Bucalossi, Petruzzi, et al., 2010), which consists in the simulation of design basis accidents using qualified codes, accepted by the public authority, and providing an estimate of their overall uncertainties. Despite this approach has proven its effectiveness in the licensing phase, the use of best-estimate tools may not be adequate for design and preliminary safety studies, which requires accurate but fast running tools. In this respect, the use of simplified models could be accepted provided that a thorough evaluation of the epistemic and aleatory uncertainties is given.

Concerning operation, the plant monitoring should provide an exhaustive yet limited amount of information on the plant status, allowing the operators to understand what is actually going on in the system. Most of the times it is not possible to have direct access to all the main plant parameters, therefore the monitoring systems should be complemented by real-time simulators, like digital twins (Patterson, Taylor, and Bankhead, 2016). In this perspective, even if huge computational resources were available, high-fidelity modelling might not be the answer, for at least two reasons: it cannot provide information in real-time and it often produces unnecessary detail.

The relationship between the high-fidelity simulation, digital twins and reactor design and operation is nowadays a hot issue, and, as such, it was the *leit-motiv* of the international "Frédéric Joliot and Otto Hahn Summer School" 2021, "*High-fidelity Modelling and Simulation of Nuclear Reactors: Turning a Promise into Reality*". One of the issues brought up during the school live discussions between panelists and attendees, both coming from international industries, research centres and universities, was the current mismatch between the academic research and the industry needs. A significant amount of the academic efforts is focused on high-fidelity modelling, while the industry needs reliable but very efficient computational tools, even at the price of a slight overconservatism. In spite of some successful examples of high-fidelity modelling, like the CASL consortium (Cramer and Kropaczek, 2020), the digital twin of a full-scale, nuclear

plant actually does not currently exist.

Hence, despite the availability of huge computational resources with respect to Fermi's and Henry's times, the development of new methods and models is still of paramount importance, confirming that the warning given by Henry is valid even nowadays.

1.3 Aim of the work and outline of the thesis

The considerations made in the previous section highlight two current needs of rector physics, namely:

- the necessity of developing new methods for the fast and accurate analysis of innovative Gen-IV systems, with the final aim of incorporate safety since the early stages of design;
- the need for more efficient computational frameworks to support the core monitoring and, consequently, the safe and reliable operation of Gen-III/III+ systems.

Addressing the above issues effectively is extremely challenging from a practical point of view. As a matter of fact, only a few among the several codes available for reactor analysis are accepted by the licensing authority, after having passed a complex set of qualification steps, which aims at ensuring the quality of the calculation tools (Courtois, Bowell, and Seidel, 2010). Modifying existing codes to make them more efficient with the implementation of state-of-the-art methods would be unpractical for operating reactors, while could be feasible for Gen-IV reactors. On one side, the time scale for the deployment of the Gen-IV reactors would be probably compatible with the qualification procedure needed for the extended codes. On the other side, the peculiarities of such systems may require too invasive modifications that could make this solution unworthy, as new reactor concepts may also require new safety regulations, which may not be based on existing codes. An example of such situation is the EU Molten Salt Fast Reactor design, which has the peculiarity of having a fluid core: since the coolant and fuel coincides, the traditional severe accident definition consisting in the core melting do not have sense and cannot be considered (Gérardin, Uggenti, et al., 2019). Therefore, the development of new methods and codes is often the only possible approach for the deployment of these systems.

This thesis has the double objective of proposing new methods, mainly concerning the safety and stability analyses of nuclear reactors, and, at the same time, of extending available techniques in order to be compliant with the industrial requirements and constraints discussed previously.

The development of new methods is mostly carried out in the first part of the thesis, where they are applied to simplified systems in order to better grasp their physico-mathematical features, but without loosing track of the real-life applications. The methods presented in these chapters are all implemented *ex novo* in a Python package called TEST, which is adopted as a test-bench.

In chapter 2, the classical multi-group P_N and P_N approximations are presented, in order to approach numerically the solution of the eigenvalue problems arising in neutron transport. After addressing the old-fashioned question of the siginificativity of the P parity order, showing the equivalence between odd P orders and the succeeding P_{N+1} even orders, the numerical implementation of these methods is benchmarked with respect to some reference solutions, studying the effects of the boundary conditions on the angular convergence. Finally, convergence acceleration aspects are analysed, adopting the Wynn-ε scheme.

In chapter 3, the classical eigenvalue formulations to the neutron transport equation, i.e. the multiplication eigenvalue, the collision eigenvalue, the time eigenvalue and the density eigenvalue, are presented and discussed, focusing on their physico-mathematical peculiarities and analysing their eigenvalue spectra. In this chapter, a novel eigenvalue formulation, the capture eigenvalue, is introduced and discussed as well. Finally, an example regarding the application of the eigenvalue spectrum for the optimal selection of the energy group for the energy collapsing is presented and discussed.

In chapter 4, the eigenfunctions associated to the different eigenvalue formulations are proposed as alternative weighting functions for the group collapsing procedure. To assess the behaviour of the different weighting functions, some accidental transients are first performed in a multi-group framework and then some safety-critical integral parameters like the total power and the reactivity are compared with those obtained with the collapsed group constants.

In chapter 5, the standard eigenvalue formulations are generalised in order to derive a new eigenvalue problem which allows to act on specific portions of the phase space and nuclides, for design-oriented applications. After discussing the main physico-mathematical aspects of this formulation, relevant engineering problems like the determination of the critical moderation ratio, the critical boron concentration and the critical control rod density are evaluated using this new approach, showing its efficiency and its capability to find all the possible critical configurations for a given initial off-critical system. This last feature is particularly important for safety analyses, since it allows to explore the physical conditions that may lead a system to re-criticality. In the determination of the possible critical configurations of the system, emphasis is also put on the classical figure of merit used to assess the neutronic stability, i.e. the eigenvalue separation.

Then, in the remaining chapters, more realistic systems are analysed, focusing on 2D and 3D models of some Gen-III+ and Gen-IV reactor concepts. This last part of the work mainly aims at proposing computationally efficient methods for the safety analyses of the neutronic behaviour of the core, trying to reduce as much as possible any intervention in the code. This goal is accomplished by means of Non-Intrusive Reduced-Order Modelling (NIROM) techniques, which permit a fair reduction of the computational time without any code modifications at the price of small approximations.

In chapter chapter 6, after a brief literature overview, a non-intrusive reduced-order

model based on a combination of Proper Orthogonal Decomposition and Radial Basis Function techniques is presented as an efficient way of reducing the computational cost of the original, high-fidelity models. Then, this model is applied to three different industrial application, with the goal of proving the NIROM effectiveness.

The first application deals with the spatial stability stability of the Gen-III+ core, which is represented with a 2D model based on the UAM benchmark. The aim of this application is to develop an efficient NIROM to perform a sensitivity analysis of the flux and power tilt behaviour at the full-core level with respect to a random, localised perturbations. Due to core complexity and to the great number of free parameters, some extensions of the NIROM are devised. First, due to the tight relationship between the cell and the full-core models, the Polynomial Chaos Method is proposed as an efficient way of computing the perturbed cross sections, which are then employed in the full-core two-group diffusion calculation. Afterwards, some sampling strategies are proposed to perform the calculations needed for training the model, discussing their advantages and disadvantages. Then, the need for a new metric to evaluate the distance between the training data is highlighted, proposing an alternative, more accurate algorithm to accomplish this task. Finally, the NIROM performances are tested, both in terms of memory and of computational time.

The second application concerns the parametric safety analysis of accidental transient scenarios in LFR, which require accurate evaluations of the safety-critical parameters in different operational and accidental conditions. The case study considered for this application is the accidental insertion of a single control rod into the ALFRED reactor design, i.e. the european LFR demonstrator, which is described thoroughly with a 3D full-core model. Also in this case, some of the NIROM steps are suitably modified and extended, in order to take into account the time-dependent behaviour of the model. Finally, the accuracy of the NIROM is examined referring to some new, validation points.

In order to show that the methods proposed have a wide applicability range also outside the nuclear field, this last application presents another variation of the NIROM approach, which is applied to a novel two-step CFD simulation framework that has been recently proposed to efficiently model accidental high-pressure gas releases in industrial, congested environments. Exploiting the two-step nature of this approach, the chapter presents a methodology that combines statistical methods, namely the bootstrap and unscented transform, to efficiently estimate the uncertainty of the ROM in the safety-critical simulation output quantities of interest. This approach is then successfully applied to a test case involving a high pressure, accidental gas release in an off-shore oil&gas plant, to show its main features and to highlight its potential cross-disciplinary applications.

Then, chapter chapter 7 is focused on a very important aspect related to the safety analysis of nuclear system, i.e. the uncertainty quantification. More specifically, this chapter is devoted to perform an assessment of the main techniques used in the Monte Carlo framework to carry out the sensitivity and uncertainty analysis, focusing on the

propagation of the uncertainty from the raw nuclear data to some relevant neutronic output quantities. The uncertainty quantification is usually carried out with the legacy Generalised Perturbation Theory approach. However, the novel eXtended Generalised Perturbation Theory, which is a reduced-order modelling technique, has been recently proposed as a general improvement compared to GPT, and, thus, it has been implemented in the Monte Carlo code Serpent. After discussing the main differences between these two approaches, the chapter presents the application to an uncertainty quantification study on the lead-cooled fast reactor ALFRED design, performed with GPT and focused on the multi-group cross section generation. Afterwards, the two nuclides that most contribute to the overall uncertainties, i.e. Pu-239 and U-238, are considered to compare the GPT results to some XGPT calculations carried out with different multi-group energy structures. This analysis finally allows to draw some general conclusions concerning the propagation of the nuclear data uncertainty with methods based on Monte Carlo.

Finally, in chapter 8, some general conclusions on the thesis work and its possible impacts are drawn, and some future perspectives on extensions and applications of the methods presented in this work are given.

References

Bucalossi, A., A. Petruzzi, M. Kristof, and F. D'Auria (2010). "Comparison between Best-Estimate–Plus–Uncertainty Methods and Conservative Tools for Nuclear Power Plant Licensing". In: *Nuclear Technology* 172.1, pages 29–47 (cited on page 6).

Buongiorno, J., J. E. Parsons, and D. A. Petti (2019). "The future of nuclear energy in a carbon-constrained world". In: (cited on page 1).

Bussac, J. and P. Reuss (1985). "Traité de neutronique". Hermann, Paris (cited on page 4).

Courtois, P.-J., M. Bowell, and F. Seidel (2010). *Licensing of safety critical software for nuclear reactors. Common position of seven European nuclear regulators and authorised technical support organisations*. Technical report 2010:01. BEL V, BfS, Consejo de Seguridad Nuclear, ISTec, NII, SSM, STUK (cited on page 7).

Cramer, W. H. and D. J. Kropaczek (2020). *CASL Annual Report (FY2018)*. Technical report CASL-U-2020-1974-000. Oak Ridge National Lab.(ORNL), Oak Ridge, TN (U.S.A.) (cited on page 6).

Driscoll, M. J. and P. Hejzlar (2005). "Reactor physics challenges in Gen-IV reactor design". In: *Nuclear Engineering and Technology* 37.1, pages 1–10 (cited on page 3).

Faucher, M., D. Mancusi, and A. Zoia (2018). "New kinetic simulation capabilities for TRIPOLI-4®: methods and applications". In: *Annals of Nuclear Energy* 120, pages 74–88 (cited on page 5).

Fermi, E. (1947). "Elementary Theory of the Chain-reacting Pile". In: *Science* 105, pages 27–32 (cited on page 4).

Gérardin, D., A. C. Uggenti, S. Beils, A. Carpignano, S. Dulla, E. Merle, D. Heuer, A. Laureau, and M. Allibert (2019). "A methodology for the identification of the postulated initiating events of the Molten Salt Fast Reactor". In: *Nuclear Engineering and Technology* 51.4, pages 1024–1031 (cited on page 7).

Henry, A. F. (1958). "The Application of Reactor Kinetics to the Analysis of Experiments". In: *Nuclear Science and Engineering* 3, pages 52–70 (cited on page 4).

— (1964). "The application of inhour modes to the description of non-separable reactor transients". In: *Nuclear Science and Engineering* 20, pages 338–351 (cited on page 5).

IAEA (2020). *Implementation and Effectiveness of Actions Taken at Nuclear Power Plants following the Fukushima Daiichi Accident*. Technical report IAEA-TECDOC-1930. Vienna (cited on page 2).

Kamide, H., G. Rodriguez, P. Guiberteau, N. Kawasaki, B. Hatala, A. Alemberti, S. Bourg, Y. Huang, F. Serre, M. A. Fuetterer, et al. (2021). Technical report. Organisation for Economic Co-Operation and Development (cited on page 2).

Locatelli, G., M. Mancini, and N. Todeschini (2013). "Generation IV nuclear reactors: Current status and future prospects". In: *Energy Policy* 61, pages 1503–1520 (cited on page 2).

Marques, J. (2011). *Review of generation-III/III+ fission reactors* (cited on page 2).

Meshkati, N. (2007). "Lessons of the Chernobyl nuclear accident for sustainable energy generation: Creation of the safety culture in nuclear power plants around the world". In: *Energy Sources, Part A* 29.9, pages 807–815 (cited on page 1).

Metropolis, N. (1987). "The beginning of the Monte Carlo method". In: *Los Alamos Science Number 15: Special Issue on Stanislaw Ulam 1909 - 1984*. Edited by N. G. Cooper. Los Alamos National Laboratory, NM (U.S.A.) (cited on page 5).

Metropolis, N. and S. Ulam (1949). "The Monte Carlo method". In: *Journal of the American statistical association* 44.247, pages 335–341 (cited on page 5).

Moore, G. E. (1998). "Cramming More Components Onto Integrated Circuits". In: *Proceedings of the IEEE* 86, pages 82–85 (cited on page 5).

Patterson, E. A., R. J. Taylor, and M. Bankhead (2016). "A framework for an integrated nuclear digital environment". In: *Progress in Nuclear Energy* 87, pages 97–103 (cited on page 6).

Sargeni, A., K. Burn, and G. Bruna (2016). "The impact of heavy reflectors on power distribution perturbations in large PWR reactor cores". In: *Annals of Nuclear Energy* 94, pages 566–575 (cited on page 2).

Weinberg, A. M. and E. P. Wigner (1958). "The Physical Theory of Neutron Chain Reactors". University of Chicago Press, Chicago (cited on page 4).

Chapter 2

The P_N and S_N approximations of the neutron transport eigenvalue formulations

γνῶθι σεαυτόν (know thyself)

Temple of Apollo, Delphi

2.1 Introduction

The concepts of eigenvalue and eigenfunction of an operator are fundamental in a wide range of applications, from basic physics to statistics to engineering. Since their first appearance in the XIXth century, they have rapidly become so popular that they are now considered a standard tool of applied mathematics. As reported by Trefethen and Embree (2005), there are at least four main reasons behind the success of the eigenvalues and eigenfunctions:

1. the possibility to use them as a basis to solve partial differential equations, when variables can be separated
2. their use in sensitivity analysis, for example in connection to the physical phenomena of mechanical resonances
3. their connection to stability and asymptotic analyses, to determine the dominant response of a system to a perturbation
4. their ability to provide the *personality* of an operator by means of its spectrum.

Most of these aspects are particularly relevant in the framework of fission reactor physics. The first feature is used to approach analytically the solution of the transport equation (Case and Zweifel, 1967), while the second one is very useful to estimate the sensitivity of a system with respect to a certain input variation, in order to perform uncertainty quantification or design optimisation (Cacuci, Ronen, et al., 1982). Concerning the third feature, the concept of eigenvalue has played a fundamental rôle in the development of perturbation methods, which are widely employed for stability analysis (Gandini, 1978). All these applications implicitly rely on the fourth aspect, despite its only apparent theoretical nature.

In addition to these applications related to reactor physics, is is convenient to mention here also the fundamental importance of the eigenvalue analysis in the framework of statistics and, consequently, of machine learning, which heavily leans on the eigenvalue decomposition in order to reduce the data dimensionality to its essential content, so that the analysis of huge datasets can be handled more efficiently.

This chapter will focus on the different eigenvalue formulations available in the framework of the neutron transport equation, with a specific focus on its P_N and S_N approximations. A new eigenvalue formulation for control-oriented applications will be introduced. Some new perspectives on old-fashioned, open questions like the impact of the boundary conditions and of the P_N parity-order on the eigenvalue accuracy will be given, and a thorough numerical assessment will be provided for the solution of the different eigenvalue problems, comparing the results obtained by an *ad hoc* computational code with the data available in the literature. Finally, the outcomes of the numerical and theoretical study on the even-odd angular approximation will be exploited in a convergence acceleration scheme showing, for the first time, some new acceleration strategies, useful to obtain high-precision eigenvalues approaching some reference Monte Carlo calculations within their statistical range, minimising the computational model evaluation.

Most of the content of this chapter has been already published in two conference proceedings and in two peer-reviewed journal articles: the first one has been published on the special issue of Journal of Computational and Theoretical Transport dedicated to the International Conference on Transport Theory (ICTT) 2019, while the second one has been published on the special issue of Annals of Nuclear Energy dedicated to the memory of Massimo Salvatores,

- N. Abrate, M. Burrone, S. Dulla, P. Ravetto, P. Saracco, *"Study of the eigenvalue spectra of the neutron transport problem in P_N approximation"*, Proceedings of the Physor 2020 conference in EPJ Web of Conferences, **247**, 2020

- N. Abrate, M. Burrone, S. Dulla, P. Ravetto, P. Saracco, *"Eigenvalue formulations for the P_N approximation to the neutron transport equation"*, Journal of Computational and Theoretical Transport, **50**, 2020

- N. Abrate, S. Dulla, P. Ravetto, *"On some features of the eigenvalue problem for the*

P_N approximation of the neutron transport equation", Annals of Nuclear Energy, **163**, 2021

- N. Abrate, B.D. Ganapol, S. Dulla, P. Ravetto, P. Saracco, A. Zoia, *"Convergence acceleration aspects in the solution of the P_N neutron transport eigenvalue problem"*, Proceedings of the M&C conference 2021, Raleigh, NC, U.S.A., 2021

2.2 The neutron transport model in plane geometry

The neutron transport model, for the case of a one-dimensional cartesian system in the absence of an external source, is described by the following system of integro-differential equations,

$$\begin{cases} \dfrac{1}{\mathrm{v}(E)}\dfrac{\partial\phi(x,E,\mu,t)}{\partial t} + \mu\dfrac{\partial\phi(x,E,\mu,t)}{\partial x} + \Sigma_t(x,E)\phi(x,E,\mu,t) = \\ \quad \displaystyle\int_0^\infty dE' \int_{-1}^{1} d\mu' \Sigma_s(x,E')\phi(x,E',\mu',t) f_s(x,E'\longrightarrow E,\mu\mu') + \\ \quad (1-\beta)\dfrac{\chi_p(x,E)}{2}\displaystyle\int_0^\infty dE' \int_{-1}^{1} d\mu' \nu\Sigma_f(x,E')\phi(x,E',\mu',t) + \\ \quad \displaystyle\sum_{r=1}^{\mathrm{R}} \dfrac{\chi_{d,r}(x,E)}{2}\lambda_r C_r(x,t) \\ \\ \dfrac{\partial C_r(x,t)}{\partial t} = \beta_r \displaystyle\int_0^\infty dE' \int_{-1}^{1} d\mu' \nu\Sigma_f(x,E')\phi(x,E',\mu',t) - \lambda_r C_r(x,t), \\ \quad r = 1,\dots,R, \end{cases} \tag{2.1}$$

subject to appropriate initial and boundary conditions. The symbols have the usual meaning:

- $\mathrm{v}(E)$ is the neutron velocity, expressed in cm s^{-1};
- $\phi(x,E,\mu,t)$ is the angular neutron flux as a function of the spatial coordinate x, the particle energy E, the cosine of the flying direction μ and the time instant t. This quantity is expressed in cm^{-1} s^{-2} eV^{-1} rad^{-1};
- $\Sigma_t(x,E)$ is the total macroscopic cross section. It is useful to recall here that this quantity is given as the sum of total capture, total fission and total scattering interactions, respectively

$$\Sigma_t(x,E) = \Sigma_c(x,E) + \Sigma_f(x,E) + \Sigma_s(x,E). \tag{2.2}$$

  All macroscopic cross sections are expressed in cm^{-1};

- $f_s(x, E' \longrightarrow E, \mu\mu')$ is the scattering transfer function, which represents the probability density function that an incident neutron colliding with the medium is transferred from the phase space coordinates (E', μ') to (E, μ). It is expressed in eV^{-1} rad^{-1}.

- β is the total neutron delayed fraction, given as

$$\beta = \sum_{r=1}^{\text{R}} \beta_r, \tag{2.3}$$

  where β_r is the delayed fraction of the r^{th} of the R precursor families. These quantities are dimensionless;

- $\chi_p(x, E)$ is the prompt fission emission spectrum, while $\chi_{d,r}(x, E)$ is the delayed fission emission spectrum for the r^{th} family. Both spectra are expressed in eV^{-1}.

- $\nu\Sigma_f(x, E)$ is the neutron fission production macroscopic cross section, measured in cm^{-1};

- λ_r is the radioactive decay constant for the r^{th} precursor family, measured in s^{-1};

- $C_r(x, t)$ is the density of delayed neutron precursor, measured in cm^{-3}.

The following operators are now introduced in order to express this model in a more compact way:

- the streaming operator,

$$\hat{L} = \mu \frac{\partial}{\partial x} *; \tag{2.4}$$

- the removal by collision operator,

$$\hat{R} = \Sigma_t(x, E) *; \tag{2.5}$$

- the scattering operator,

$$\hat{S} = \int_0^\infty dE' \int_{-1}^1 d\mu' \, \Sigma_s(x, E') f_s(x, E' \longrightarrow E, \mu\mu') *; \tag{2.6}$$

- the prompt fission operator,

$$\hat{F}_p = (1 - \beta) \frac{\chi_p(x, E)}{2} \int_0^\infty dE' \int_{-1}^1 d\mu' \, \nu\Sigma_f(x, E') *; \tag{2.7}$$

- the delayed fission operator for the i^{th} delayed precursor family,

$$\hat{F}_{d,r} = \beta_r \frac{\chi_{d,r}(x,E)}{2} \int_0^\infty dE' \int_{-1}^1 d\mu' \, \nu\Sigma_f(x,E') * . \tag{2.8}$$

In addition to these definitions, other operators that will be adopted later in this chapter are introduced here. The first one is the total fission production operator, which is useful for a steady-state system, when the neutron population is in equilibrium with the precursors concentrations,

$$\hat{F} = \hat{F}_p + \sum_{r=1}^{\mathrm{R}} \hat{F}_{d,r}. \tag{2.9}$$

Recalling eq. (2.2) the other operators can be defined splitting the removal operator in (2.5) accordingly to the three sum reactions,

- total capture operator,

$$\hat{C} = \Sigma_c(x,E) *; \tag{2.10}$$

- total fission operator,

$$\hat{F}_T = \Sigma_f(x,E) *; \tag{2.11}$$

- total scattering operator,

$$\hat{S}_T = \Sigma_s(x,E) * . \tag{2.12}$$

These definitions allow the definition of a more compact form of equation (2.1),

$$\begin{cases} \dfrac{1}{\mathrm{v}} \dfrac{\partial \phi}{\partial t} + \hat{L}\phi + (\hat{C} + \hat{F}_T + \hat{S}_T)\phi = \hat{S}\phi + \hat{F}_p\phi + \displaystyle\sum_{r=1}^{\mathrm{R}} \lambda_r \epsilon_r \\ \dfrac{\partial \epsilon_r}{\partial t} = \hat{F}_{d,r}\phi - \lambda_r \epsilon_r \quad r = 1, \dots, R, \end{cases} \tag{2.13}$$

where the flux and precursors dependencies are omitted, for the sake of conciseness, and we have introduced the delayed emissivity ϵ_r as:

$$\epsilon_r(x,E,t) = \frac{\chi_{d,r}(x,E)}{2} C_r(x,t). \tag{2.14}$$

.

2.3 Eigenvalue formulations in neutron transport

The fundamental problem of reactor physics is to assess the existence of an asymptotic, bounded and non-negative solution of Eq. (2.13) for a given multiplying system. When such a system is able to reach a steady-state condition, it is said to be

self-sustaining or *critical*. From a physical perspective, maybe the most intuitive way of approaching criticality is to observe the free evolution of the system under examination, assuming the medium properties to be time-independent, at least on the evolution time scale.

It has been observed, both experimentally (Henry, 1964) and theoretically (Bell and Glasstone, 1970), that, under these hypotheses, the neutron flux can be factorised into a time exponential behaviour and a distribution in the phase space

$$\phi(x, E, \mu, t) = \varphi_\omega(x, E, \mu) e^{\omega t}, \tag{2.15}$$

independently on the initial conditions.

Substituting this physically intuitive factorisation, which is assumed to hold also for the precursors concentration C_i, into Eq. (2.13) yields the so-called *time* eigenvalue formulation of the transport equation,

$$\begin{cases} \dfrac{\omega}{\mathrm{v}}\varphi_\omega + \hat{L}\varphi_\omega + (\hat{C} + \hat{F}_T + \hat{S}_T)\varphi_\omega = \hat{S}\varphi_\omega + \hat{F}_p\varphi_\omega + \displaystyle\sum_{r=1}^{\mathrm{R}} \lambda_r \epsilon_r \\ \omega\epsilon_r = \hat{F}_{d,r}\varphi_\omega - \lambda_r\epsilon_r \quad i = r, \dots, R. \end{cases} \tag{2.16}$$

The solution of this eigenvalue problem, which could be obtained equivalently also taking the Laplace transform of Eq. (2.13), describes the time frequencies ω characterising the system free evolution. Therefore, the eigenstates associated to this problem are usually identified as the *natural modes* of the neutron transport operator. Since the Laplace transform is a common approach to tackle time-dependent problems in both physics and engineering, it is hard to assess who was the first to derive this eigenvalue problem in the reactor physics community. Regardless, Henry (1964) was the first to study the time eigenvalue and to highlight its value for different applications.

When the delayed neutrons contribution is neglected or absent, Eq. (2.16) can be simplified, removing the precursors balance equations,

$$\frac{\alpha}{\mathrm{v}}\varphi_\alpha + \hat{L}\varphi_\alpha + (\hat{C} + \hat{F}_T + \hat{S}_T)\varphi_\alpha = \hat{S}\varphi_\alpha + \hat{F}_p\varphi_\alpha, \tag{2.17}$$

where symbol ω is replaced by α in order to distinguish the two cases. This equation, usually known as α- or *prompt* time eigenvalue formulation, is valid for non-multiplying system as well, confirming that this formulation arises naturally when dealing with the time-dependent transport equation.

Since the time eigenvalue, say ω in this case, can be interpreted as a time frequency, its inverse is related to the system period, say T. When the system reaches a steady state, i.e. it is critical, its time period tends to become infinite, $T \longrightarrow \infty$. Therefore, to approach criticality, the dominant time eigenvalue, i.e. the one associated to the non-negative, non-trivial eigenstate, should tend to zero, $\omega_0 \longrightarrow 0$.

From another perspective, the criticality is achieved when the net number of neutrons does not change as time goes by, i.e. the loss and the production terms are the

same:

$$(\hat{L} + \hat{R} - \hat{S} - \hat{F})\phi = 0. \tag{2.18}$$

When Eq. (2.18) is satisfied, the neutron population self-sustains and a steady state equilibrium is reached. However, in practice, this condition is never fully achieved: even assuming that the equilibrium is reached at a certain time t, the fissile nuclides would be consumed by fissions at time t^+, changing the material properties of the system and, thus, its ability to sustain fission. From this perspective, operating a real reactor would seem barely impossible. In reality, the constraint expressed by Eq. (2.18) should be interpreted more weakly: in order to achieve and maintain criticality, it is sufficient that the control actions adopted, i.e. reactivity insertions, are faster than time scale of the reactor stable period, T.

Despite its natural definition and its elegance in connecting an idealised physico-mathematical condition with engineering aspects, the time eigenvalue is not appropriate for the design of a critical system. In this respect, Eq. (2.18) is useful in order to formulate design-oriented eigenvalue problems.

2.3.1 Design-oriented eigenvalue formulations

Among its peculiarities, eq. (2.18) is homogeneous. From a mathematical standpoint, this means that non-trivial steady-state distributions exist only as solutions of an eigenvalue problem, namely

$$\hat{A}\vec{\varphi}_{\xi,n} = \xi_n \hat{B}\vec{\varphi}_{\xi,n}, \tag{2.19}$$

where $\hat{A}$ and $\hat{B}$ are, in principle, any reasonable linear combination of the operators appearing in eq. (2.18), and $\{\xi_n, \vec{\varphi}_{\xi,n}\}$ is the n^{th} eigenpair, constituted by an eigenvalue ξ_n and an eigenfunction $\vec{\varphi}_{\xi,n}$, respectively. According to the geometric multiplicity of the eigenproblem $g(\xi)$, n ranges from 0 to $g(\xi) - 1$. To approach the criticality condition, several design-oriented eigenvalue formulations have been proposed.

Probably because of the peculiarity of the newly discovered fission phenomenon (Hanh and Strassmann, 1939), Fermi (1942) firstly introduced an eigenvalue, which he called *reproduction factor* k, in front of the total fission operator:

$$\hat{L}\varphi_{k,n} + (\hat{C} + \hat{F}_T + \hat{S}_T)\varphi_{k,n} - \hat{S}\varphi_{k,n} = \frac{1}{k_n}\hat{F}\varphi_{k,n}. \tag{2.20}$$

When the system is *sub-critical*, $k < 1$ in order to increase the neutron production by fission, while, when the system is *super-critical*, $k > 1$ in order to decrease the neutron production. Therefore, a system is critical when no modification of the fission operator is required, i.e. $k = 1$. To the author's knowledge, the second eigenvalue formulation proposed is due to Davison and Sykes (1957).They proposed to approach criticality introducing a *collision* eigenvalue to modify all the interactions leading to a neutron emission, i.e. scattering and fission,

$$\hat{L}\varphi_{\gamma,n} + \hat{R}\varphi_{\gamma,n} = \frac{1}{\gamma}\left(\hat{S} + \hat{F}\right)\varphi_{\gamma,n}. \tag{2.21}$$

The third design-oriented eigenvalue formulation present in the literature is due to Ronen, Shalitin, and Wagschal (1976). In this paper, they cleverly observe that, given a certain medium, it should be possible to attain criticality varying its density, introducing an eigenvalue acting on all the material properties of the system,

$$\hat{L}\varphi_{\delta,n} = \frac{1}{\delta}\left(\hat{S} + \hat{F} - \hat{R}\right)\varphi_{\delta,n}\varphi_{\delta,n}. \tag{2.22}$$

Due to its collocation in the transport equation, the action of this eigenvalue can be interpreted in different ways. The most intuitive one is probably the modification of the medium density, which introduces a "competition" between positive (fission, scattering) and negative (removal) contributions. Because of this aspect, this eigenvalue is usually known as *density* eigenvalue. However, multiplying the equation by δ, this eigenvalue can be interpreted as well as a *streaming* eigenvalue, which modifies the relationship between the angular current spatial derivative and the angular flux. In this case, the eigenvalue operates a re-scaling of the spatial coordinates, changing the free-flight kernel of the transport process.

In addition to these formulations, it is also possible to introduce an eigenvalue acting on the capture cross section. To the best of the author's knowledge, this eigenvalue formulation has never been proposed so far. The symbol proposed here to indicate this capture eigenvalue is taken from the ancient Greek translation of "capture", θηράω,

$$\left(\hat{L} + \hat{F}_T + \hat{S}_T - \hat{S} - \hat{F}\right)\varphi_{\theta,n} = \frac{1}{\theta}\hat{C}\varphi_{\theta,n}. \tag{2.23}$$

The eigenvalue problems presented so far can be obtained from a generalisation of eq. (2.13),

$$\begin{aligned}\varepsilon_\delta\hat{L}\phi(x,\mu,E) + \left(\varepsilon_\theta\hat{C} + \hat{F}_T + \hat{S}_T + \frac{\varepsilon_\alpha}{v}\right)\phi(x,\mu,E) = \\ \varepsilon_\gamma\left[\hat{S} + \varepsilon_k\left(\hat{F}_p + \sum_{r=1}^{R}\frac{\lambda_r}{\lambda_r + \varepsilon_\omega}\hat{F}_{d,r}\right)\right]\phi(x,\mu,E),\end{aligned} \tag{2.24}$$

where the values of the ε parameters are provided in table 2.1. The symbol ϕ is used to indicate the neutron angular flux for an arbitrary eigenvalue formulation. In the following, the symbol φ_x will be used to indicate the angular flux associated to a specific eigenvalue formulation x.

2.4 Numerical framework for the solution of the neutron transport eigenvalue problems

From a physico-mathematical perspective, all the formulations illustrated so far are useful to get a deeper insight of the criticality problem, suggesting different modifications to the physical parameters featuring the system. Moreover, the spectrum and

eigenvalue	critical value	ε_k	ε_α	ε_ω	ε_γ	ε_δ	ε_θ
k	1	$1/k$	0	0	1	1	0
α	0	1	α	0	1	1	0
ω	0	1	ω	ω	1	1	0
γ	1	1	0	0	$1/\gamma$	1	0
δ	1	1	0	0	1	δ	0
θ	1	1	0	0	1	1	$1/\theta$

Table 2.1: *The set of ε parameters to be used in eq. (2.24) to retrieve the different eigenvalue formulations.*

the eigenfunctions obtained solving the different eigenproblems can be extremely relevant for many applications. However, due to its complexity, the solution of the neutron transport equation (NTE) usually requires, in practice, the adoption of some approximations, even in this simple plain geometry case (see eq. (2.1)). The first approximation that is commonly introduced in the integro-differential form of the NTE concerns the dependence of the flux on the particle flying direction, which can be either expressed by means of a truncated series of Legendre polynomials, via the P_N method (Meghreblian and Holmes, 1960), or discretised, via the S_N method (Wick, 1943; Chandrasekhar, 1950). Then, these approximate transport models are further simplified, discretising their energy and space dependencies as well.

In order to study the theoretical, numerical, and engineering peculiarities of the solutions of these eigenvalue problems, the rest of this chapter will be devoted to present their numerical calculation framework, focusing on the development and verification of an *in-house* Python package, denoted in the following as TEST (Transport Equation Solver in Turin). This code allows first to assemble the spatially discretised operators of the multi-group NTE, which are then manipulated to construct the desired eigenvalue formulation. Finally, the code can be used to look for the whole spectrum or for only some of the dominant eigenpairs. Since its primary aim is the investigation of the basic physical, mathematical and engineering aspects related to these eigenvalue problems, much of the development effort concerned the treatment of the energy and angular models and the definition and solution of the eigenvalue problems, rather than the management of complex geometries. Therefore, the code can currently perform calculations only for multi-layered cartesian systems, which anyhow should provide a sufficiently faithful representation of the main physical features of a multiplying system.

2.4.1 The P_N equations

The P_N model in plane geometry can be retrieved assuming that the angular flux can be expanded as follows,

$$\phi(x,\mu,E) = \sum_{n=0}^{\infty} \frac{2n+1}{2} \phi_n(x,E) P_n(\mu), \tag{2.25}$$

where ϕ_n is the n-th flux moment, obtained projecting the angular flux on the n-th Legendre polynomial $P_n(\mu)$,

$$\phi_n(x,E) \equiv \int_{-1}^{1} d\mu\, P_n(\mu)\, \phi(x,\mu,E). \tag{2.26}$$

It is noteworthy to recall here that the first two flux moments have a strong physical meaning: the 0^{th} order moment represents the total flux, while the 1^{st} order moment is the neutron net current:

$$\phi_0(x,E) = \Phi(x,E) \equiv \int_{-1}^{1} d\mu\, P_0(\mu)\, \phi(x,\mu,E) = \int_{-1}^{1} d\mu\, \phi(x,\mu,E), \tag{2.27}$$

$$\phi_1(x,E) = J(x,E) \equiv \int_{-1}^{1} d\mu\, P_1(\mu)\, \phi(x,\mu,E) = \int_{-1}^{1} d\mu\, \mu\, \phi(x,\mu,E). \tag{2.28}$$

Substituting eq. (2.25) into the streaming and scattering terms yields,

$$\begin{aligned} \hat{L}\phi &= \mu \frac{\partial}{\partial x} \sum_{n=0}^{\infty} \frac{2n+1}{2} \phi_n(x,E) P_n(\mu) \\ &= \sum_{n=0}^{\infty} \frac{2n+1}{2} \frac{\partial \phi_n(x,E)}{\partial x} \frac{(n+1)P_{n+1}(\mu) + nP_{n-1}(\mu)}{2n+1} \end{aligned} \tag{2.29}$$

and

$$\hat{S}\phi = \int_0^{\infty} dE' \Sigma_s(x,E') \sum_{n=0}^{\infty} \frac{2n+1}{2} f_{s,n}(x,E' \longrightarrow E) \phi_n(x,E') P_n(\mu) \tag{2.30}$$

where $f_{s,n}$ is the n-th moment of the scattering function, defined as

$$f_{s,n} \equiv \int_{-1}^{1} d\mu\, P_n(\mu)\, f_s(x,E' \longrightarrow E,\mu). \tag{2.31}$$

Similarly, the time, removal and fission terms yield,

$$\hat{T}\phi = \frac{1}{\nu(E)} \frac{\partial}{\partial t} \sum_{n=0}^{\infty} \frac{2n+1}{2} \phi_n(x,E) P_n(\mu), \tag{2.32}$$

$$\hat{R}\phi = \Sigma_t(x,E) \frac{\partial}{\partial t} \sum_{n=0}^{\infty} \frac{2n+1}{2} \phi_n(x,E) P_n(\mu), \tag{2.33}$$

$$\hat{F}_p\phi = (1-\beta)\frac{\chi_p(x,E)}{2}\int_0^\infty dE'\,\nu\Sigma_f(x,E')\sum_{n=0}^{\infty}\frac{2n+1}{2}\phi_n(x,E')P_n(\mu), \tag{2.34}$$

and

$$\hat{F}_{d,r}\phi = \beta_r\frac{\chi_{d,r}(x,E)}{2}\int_0^\infty dE'\,\nu\Sigma_f(x,E')\sum_{n=0}^{\infty}\frac{2n+1}{2}\phi_n(x,E')P_n(\mu), \qquad r=1,\dots,R. \tag{2.35}$$

Projecting each term on $P_m(\mu)$, exploiting the orthogonality property and the recurrence relations of the Legendre polynomials (Abramowitz and Stegun, 1964), a set of coupled partial differential equations, known as $\mathrm{P_N}$ equations, can be finally obtained. Similarly to eq. (2.24), the general $\mathrm{P_N}$ eigenvalue problem yields,

$$\begin{aligned}&\varepsilon_\delta\left[\frac{n+1}{2n+1}\frac{\partial\phi_{n+1}(x,E)}{\partial x}+\frac{n}{2n+1}\frac{\partial\phi_{n-1}(x,E)}{\partial x}\right]+\left(\varepsilon_\theta\hat{C}+\hat{F}_T+\hat{S}_T+\frac{\varepsilon_\alpha}{\mathrm{v}}\right)\phi_n(x,E)=\\&\varepsilon_\gamma\left[\hat{S}_n+\varepsilon_k\left(\hat{F}_{p,n}+\sum_{r=1}^{\mathrm{R}}\frac{\lambda_r}{\lambda_r+\varepsilon_\omega}\hat{F}_{d,r,n}\right)\right]\phi_n(x,E),\quad n=0,\dots,\mathrm{N},\end{aligned} \tag{2.36}$$

where N is the truncation order chosen to approximate the expansion. The $\hat{S}_n$, $\hat{F}_{p,n}$ and $F_{d,r,n}$ operators are defined, respectively, as

$$\begin{aligned}\hat{S}_n &= \int_0^\infty dE'\Sigma_s(x,E')f_{s,n}(x,E'\longrightarrow E)\,*\\ \hat{F}_{p,n} &= (1-\beta)\frac{\chi_p(x,E)}{2}\int_0^\infty dE'\,\nu\Sigma_f(x,E')\delta_{n0}\,*\\ F_{d,r,n} &= \beta_r\frac{\chi_{d,r}(x,E)}{2}\int_0^\infty dE'\,\nu\Sigma_f(x,E')\delta_{n0}\,*, \qquad r=1,2,\dots,R,\end{aligned} \tag{2.37}$$

where δ_{n0} is the Kronecker symbol. It should be noticed that the definition of the $\hat{C}$, $\hat{S}_T$ and $\hat{F}_T$ operators has been omitted since it only amounts to change the reaction channel of the cross section appearing in eq. (2.33).

2.4.1.1 The multi-group approach for the energy discretisation

As mentioned, the next approximation level usually deals with the discretisation of the energy variable by means of the multi-group approach. A rigorous derivation of the multi-group equations would require the integration of the continuous-energy $\mathrm{P_N}$ model (eq. (2.36)). In this way, it would be possible to derive a set of equations featured by energy-integrated flux moments, but the the group-averaged cross sections, which preserves the reaction rates being weighted on the flux moments, would depend on the spherical harmonics order n as follows (Bell, Hansen, and Sandmeier, 1967),

$$\Sigma_{t,g,n}(x) = \frac{\displaystyle\int_{E_g}^{E_{g+1}} dE\,\Sigma_t(x,E)\,\phi_n(x,E)}{\displaystyle\int_{E_g}^{E_{g+1}} dE\,\phi_n(x,E)}, \tag{2.38}$$

$$\Sigma_{s,g'\to g,n}(x) = \frac{\displaystyle\int_{E_g}^{E_{g+1}} dE \int_{E'_g}^{E'_{g+1}} dE'\, \Sigma_s(x,E') f_n(E' \longrightarrow E)\, \phi_n(x,E')}{\displaystyle\int_{E_g}^{E_{g+1}} dE\, \phi_n(x,E)}, \tag{2.39}$$

except for the production by fission cross section, which would depend only on the total flux,

$$(\nu\Sigma_f)_{g,n}(x) = \frac{\displaystyle\int_{E_g}^{E_{g+1}} dE\, \nu(x,E)\Sigma_f(x,E)\, \phi_0(x,E)}{\displaystyle\int_{E_g}^{E_{g+1}} dE\, \phi_0(x,E)}. \tag{2.40}$$

As a first approximation, the angular dependence is often omitted, assuming that energy and angle are independent. This approach, known as P_N *inconsistent* (Bell and Glasstone, 1970), allows to express the continuous-energy cross sections as discrete values obtained preserving the reaction rates y over each energy bin $[E_g, E_{g+1}]$ by integration over the total flux,

$$\Sigma_{y,g}(x) = \frac{\displaystyle\int_{E_g}^{E_{g+1}} dE\, \Sigma_y(x,E)\, \Phi(x,E)}{\displaystyle\int_{E_g}^{E_{g+1}} dE\, \Phi(x,E)}. \tag{2.41}$$

Thus, the continuous-energy flux can be expressed as a G-dimensional vector, where G is the total number of groups selected,

$$\begin{aligned} \vec{\phi} &= \begin{bmatrix} \phi_1(x,\mu) \\ \dots \\ \phi_{\mathrm{G}}(x,\mu) \end{bmatrix} = \sum_{n=0}^{\mathrm{N}} \frac{2n+1}{2} \begin{bmatrix} \phi_{1,n}(x) \\ \dots \\ \phi_{2,n}(x) \end{bmatrix} P_n(\mu) = \\ &= \sum_{n=0}^{\mathrm{N}} \frac{2n+1}{2} \vec{\phi}_n(x) P_n(\mu). \end{aligned} \tag{2.42}$$

It is then possible to express the streaming and scattering terms as:

$$\hat{L}\vec{\phi} = \sum_{n=0}^{\mathrm{N}} \frac{2n+1}{2} \frac{d}{dx} \begin{bmatrix} \phi_{1,n}(x) \\ \dots \\ \phi_{2,n}(x) \end{bmatrix} \frac{(n+1)P_{n+1}(\mu) + nP_{n-1}(\mu)}{2n+1}, \tag{2.43}$$

$$\hat{S}\vec{\phi} = \sum_{n=0}^{\mathrm{N}} \frac{2n+1}{2} \begin{bmatrix} \Sigma_{s,1} f_{1\to 1,n} & \dots & 0 \\ \vdots & \ddots & \vdots \\ \Sigma_{s,1} f_{1\to \mathrm{G},n} & \dots & \Sigma_{s,\mathrm{G}} f_{\mathrm{G}\to \mathrm{G},n} \end{bmatrix} \begin{bmatrix} \phi_{1,n}(x) \\ \dots \\ \phi_{2,n}(x) \end{bmatrix} P_n(\mu), \tag{2.44}$$

where $f_{g' \to g,n}$ indicates the transfer from group g' to g. Similarly, the following matrix operators can be defined,

$$\hat{V}_{\mathrm{G}} = \begin{bmatrix} \frac{1}{\mathrm{v}_1} & \dots & 0 \\ \vdots & \ddots & \vdots \\ 0 & \dots & \frac{1}{\mathrm{v}_{\mathrm{G}}} \end{bmatrix} \tag{2.45a}$$

$$\hat{R}_{\mathrm{G}} = \begin{bmatrix} \Sigma_{t,1}(x) & \dots & 0 \\ \vdots & \ddots & \vdots \\ 0 & \dots & \Sigma_{t,\mathrm{G}}(x) \end{bmatrix} \tag{2.45b}$$

$$\hat{S}_{n,\mathrm{G}} = \begin{bmatrix} \Sigma_{s,1}(x) f_{1\to 1,n}(x) & \dots & 0 \\ \vdots & \ddots & \vdots \\ \Sigma_{s,1}(x) f_{1\to \mathrm{G},\mathrm{n}}(x) & \dots & \Sigma_{s,\mathrm{G}}(x) f_{\mathrm{G}\to \mathrm{G},\mathrm{n}}(x) \end{bmatrix} \tag{2.45c}$$

$$\hat{F}_{p,n,\mathrm{G}} = \begin{bmatrix} \nu_1 \Sigma_{f,1}(x) \chi_{p,1}(x) & \dots & \nu_G \Sigma_{f,\mathrm{G}}(x) \chi_{p,1}(x) \\ \vdots & \ddots & \vdots \\ \nu_1 \Sigma_{f,1}(x) \chi_{p,\mathrm{G}}(x) & \dots & \nu_G \Sigma_{f,\mathrm{G}}(x) \chi_{p,\mathrm{G}}(x) \end{bmatrix} (1-\beta)\delta_{n0} \tag{2.45d}$$

$$\hat{F}_{d,r,n,\mathrm{G}} = \begin{bmatrix} \nu_1 \Sigma_{f,1}(x) \chi_{r,1}(x) & \dots & \nu_G \Sigma_{f,\mathrm{G}}(x) \chi_{r,1}(x) \\ \vdots & \ddots & \vdots \\ \nu_1 \Sigma_{f,1}(x) \chi_{r,\mathrm{G}}(x) & \dots & \nu_G \Sigma_{f,\mathrm{G}}(x) \chi_{r,\mathrm{G}}(x) \end{bmatrix} \beta_r \delta_{n0}, \ r = 1, ..., R. \tag{2.45e}$$

Finally, the multi-group, $\mathrm{P_N}$ eigenvalue generalised equation yields

$$\begin{aligned} &\varepsilon_\delta \left[\frac{n+1}{2n+1} \frac{d\vec{\phi}_{n+1}(x)}{dx} + \frac{n}{2n+1} \frac{d\vec{\phi}_{n-1}(x)}{dx} \right] + \left(\varepsilon_\theta \hat{C}_G + \hat{F}_{0,\mathrm{G}} + \hat{S}_{0,\mathrm{G}} + \frac{\varepsilon_\alpha}{\mathrm{v}} \right) \vec{\phi}_n(x) = \\ &\varepsilon_\gamma \left[\hat{S}_{n,\mathrm{G}} + \varepsilon_k \left(\hat{F}_{p,n,\mathrm{G}} + \sum_{r=1}^{\mathrm{R}} \frac{\lambda_r}{\lambda_r + \varepsilon_\omega} \hat{F}_{d,r,n,\mathrm{G}} \right) \right] \vec{\phi}_n(x), \ n = 0, \dots, \mathrm{N}, \end{aligned} \tag{2.46}$$

where the ε parameters are provided in table 2.1. Also in this case, the definition of the $\hat{C}_G$, $\hat{S}_{0,\mathrm{G}}$ and $\hat{F}_{0,\mathrm{G}}$ operators requires to change the reaction channel of the cross section appearing in eq. (2.45b).

2.4.1.2 The finite difference scheme for the spatial discretisation

The final step to solve eq. (2.46) numerically is the identification of an appropriate spatial discretisation scheme and of an adequate spatial grid. Since the $\mathrm{P_N}$ equations are coupled through the previous and the succeeding adjacent moments, the choice of the grid needs special handling in order to avoid the so-called *checkerboard* instability, which is a well known numerical issue in the field of Computational Fluid-Dynamics (Ferziger and Peric, 1999). The standard way to avoid this issue is to rely on a *staggered*

spatial grid, like the one sketched in fig. 2.1: the integer nodes are associated to even equations, while the half-integer nodes are used for the odd equations. The same approach is presented also in Bell and Glasstone (1970) for the numerical solution of the P_1 model, although without any reference to the stability problem mentioned so far. As a confirmation to the instabilities arising from the use of a trivial co-located grid,

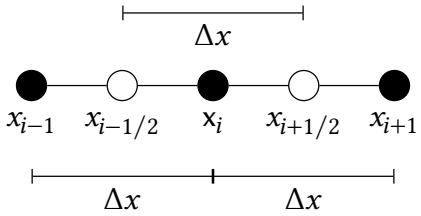

Figure 2.1: *Sketch of the staggered grid with mesh size Δx adopted for the spatial discretisation of the P_N equations.*

i.e. even and odd equations are discretised on the same meshes, the resulting discrete P_N equations are featured by a strong oscillating behaviour. A simple proof of the inconsistencies of the co-located central finite differences is the fact that the well-known equivalence between P_1 and the diffusion model does not hold: substituting the discretised equation for the 1st order moment, i.e. Fick's law, into the total flux equation yields a discretised Laplacian term that is not defined on the adjacent preceding and succeeding neighbours. Combining the P_1 equations for the one-speed, homogeneous case, the co-located grid would yield

$$-\frac{1}{3\Sigma_t}\frac{\Phi_{i-2}-2\Phi_i+\Phi_{i+2}}{2\Delta x^2}+(\Sigma_t-\Sigma_s)\Phi_i=\frac{\nu\Sigma_f}{k}\Phi_i \quad i=0,\dots,\mathrm{I}, \tag{2.47}$$

instead of

$$-\frac{1}{3\Sigma_t}\frac{\Phi_{i-1}-2\Phi_i+\Phi_{i+1}}{\Delta x^2}+(\Sigma_t-\Sigma_s)\Phi_i=\frac{\nu\Sigma_f}{k}\Phi_i \quad i=0,\dots,\mathrm{I}. \tag{2.48}$$

As an example, the k eigenvalue problem cast in a multi-group P_3 model, discretised via the central finite differences on a staggered mesh and featured by linearly anisotropic scattering, yields

$$\begin{cases} \dfrac{\vec{\varphi}_{k,1,i+\frac{1}{2}}-\vec{\varphi}_{k,1,i-\frac{1}{2}}}{x_{i+\frac{1}{2}}-x_{i-\frac{1}{2}}}+\hat{R}_{\mathrm{G,i}}\vec{\varphi}_{k,0,i}=\hat{S}_{0,\mathrm{G,i}}\vec{\varphi}_{k,0,i}+\dfrac{1}{k}\hat{F}_{0,\mathrm{G,i}}\vec{\varphi}_{k,0,i} \\ \dfrac{1}{3}\dfrac{\vec{\varphi}_{k,0,i+1}-\vec{\varphi}_{k,0,i}}{x_{i+1}-x_i}+\dfrac{2}{3}\dfrac{\vec{\varphi}_{k,2,i+1}-\vec{\varphi}_{k,2,i}}{x_{i+1}-x_i}+\hat{R}_{\mathrm{G,i}+\frac{1}{2}}\vec{\varphi}_{k,1,i+\frac{1}{2}}=\hat{S}_{1,\mathrm{G,i}+\frac{1}{2}}\vec{\varphi}_{k,1,i+\frac{1}{2}} \\ \dfrac{2}{5}\dfrac{\vec{\varphi}_{k,1,i+\frac{1}{2}}-\vec{\varphi}_{k,1,i-\frac{1}{2}}}{x_{i+\frac{1}{2}}-x_{i-\frac{1}{2}}}+\dfrac{3}{5}\dfrac{\vec{\varphi}_{k,3,i+\frac{1}{2}}-\vec{\varphi}_{k,3,i-\frac{1}{2}}}{x_{i+\frac{1}{2}}-x_{i-\frac{1}{2}}}+\hat{R}_{\mathrm{G,i}}\vec{\varphi}_{k,2,i}=0 \\ \dfrac{3}{7}\dfrac{\vec{\varphi}_{k,2,i+1}-\vec{\varphi}_{k,2,i}}{x_{i+1}-x_i}+\hat{R}_{\mathrm{G,i}+\frac{1}{2}}\vec{\varphi}_{k,3,i+\frac{1}{2}}=0, \quad i=0,\dots,\mathrm{I}. \end{cases} \tag{2.49}$$

2.4.2 The S_N equations

The S_N model can be obtained assuming that the neutron flying direction can be described by a set of *discrete ordinates* μ_j, with $j = 1, \dots, N$.

By expanding the scattering operator in series of Legendre polynomials $P_\ell(\mu)$ and by performing the integration over the angle with the Gauss-Legendre quadrature rule, which allows to integrate exactly polynomials with degree $\leqslant$ 2N-1 using a set of symmetric weights w_j,

$$\int_{-1}^{1} d\mu f(\mu) \approx \sum_{j=1}^{N} w_j f(\mu_j), \tag{2.50}$$

it is possible to get the S_N form of the streaming, prompt and delayed fission operators, respectively,

$$\hat{S}_{L,j}\vec{\phi}_\mu(x,E) = \int_0^\infty dE'\Sigma_s(x,E') \sum_{\ell=1}^{L} \frac{2\ell+1}{2} f_{\ell,j}(x,E\longrightarrow E')P_\ell(\mu_j) \sum_{n=1}^{N} w_n P_\ell(\mu_n)\phi(x,\mu_n,E), \tag{2.51}$$

$$\hat{F}_{p,j}\vec{\phi}_\mu(x,E) = (1-\beta)\frac{\chi_p(x,E)}{2} \int_0^\infty dE'\,\nu\Sigma_f(x,E') \sum_{n=1}^{N} w_n\phi(x,\mu_n,E), \tag{2.52}$$

and

$$\hat{F}_{d,r,j}\vec{\phi}_\mu(x,E) = \beta_r\frac{\chi_{d,r}(x,E)}{2} \int_0^\infty dE'\,\nu\Sigma_f(x,E') \sum_{n=1}^{N} w_n\phi(x,\mu_n,E), \tag{2.53}$$

where L in $\hat{S}_{L,j}$ indicates the scattering anisotropy order. It should be noticed that, because of the Gauss-Legendre scheme, which involves a sum over the discrete angular fluxes, these operators are applied to the column vector containing the flux along each discrete direction, $\vec{\phi}_\mu(x,E) = [\phi(x,\mu_1,E), \dots, \phi(x,\mu_N,E)]^T$, yielding the incoming flux in the j-th direction. Therefore, the S_N form of eq. (2.24) is

$$\begin{aligned} &\varepsilon_\delta\mu_j\frac{\partial\phi(x,\mu_j,E)}{\partial x} + \left(\varepsilon_\theta\hat{C} + \hat{F}_T + \hat{S}_T + \frac{\varepsilon_\alpha}{v}\right)\phi(x,\mu_j,E) = \\ &\varepsilon_\gamma\left[\hat{S}_j + \varepsilon_k\left(\hat{F}_{p,j} + \sum_{r=1}^{R}\frac{\lambda_r}{\lambda_r+\varepsilon_\omega}\hat{F}_{d,r,j}\right)\right]\vec{\phi}_\mu(x,E),\ j = 1,\dots,N. \end{aligned} \tag{2.54}$$

Also in this case, the practical solution of the S_N model requires the introduction of energy and spatial approximations. Since the application of the multi-group formalism yield the same group-wise operators appearing in eq. (2.45e), except for the angular terms, they will be omitted for the sake of brevity.

Concerning space, also in this case the central finite differences are applied as a second order approximation of the spatial derivative. Contrarily to the previous case, the same grid can be used for both positive and negative directions, although ensuring that the node order follows the streaming direction.

The k eigenvalue problem cast in a multi-group S_4 model, discretised via the central finite differences on a co-located mesh and featured by linearly anisotropic scattering, yields

$$\begin{cases} \mu_1 \dfrac{\vec{\varphi}_{k,1,i+1} - \vec{\varphi}_{k,1,i}}{x_{i+1} - x_i} + \hat{R}_{\mathrm{G,i+\frac{1}{2}}} \vec{\varphi}_{k,1,+1/2} = \hat{S}_{1,1,\mathrm{G,i+\frac{1}{2}}} \vec{\varphi}_{k,i+\frac{1}{2}} + \dfrac{1}{k} \hat{F}_{1,\mathrm{G,i+\frac{1}{2}}} \vec{\varphi}_{k,i+\frac{1}{2}} \\ \mu_2 \dfrac{\vec{\varphi}_{k,2,i+1} - \vec{\varphi}_{k,2,i}}{x_{i+1} - x_i} + \hat{R}_{\mathrm{G,i+\frac{1}{2}}} \vec{\varphi}_{k,2,i+\frac{1}{2}} = \hat{S}_{1,2,\mathrm{G,i+\frac{1}{2}}} \vec{\varphi}_{k,i+\frac{1}{2}} + \dfrac{1}{k} \hat{F}_{2,\mathrm{G,i+\frac{1}{2}}} \vec{\varphi}_{k,i+\frac{1}{2}} \\ -\mu_3 \dfrac{\vec{\varphi}_{k,3,i+1} - \vec{\varphi}_{k,3,i}}{x_{i+1} - x_i} + \hat{R}_{\mathrm{G,i+\frac{1}{2}}} \vec{\varphi}_{k,3,i+\frac{1}{2}} = \hat{S}_{1,3,\mathrm{G,i+\frac{1}{2}}} \vec{\varphi}_{k,i+\frac{1}{2}} + \dfrac{1}{k} \hat{F}_{3,\mathrm{G,i+\frac{1}{2}}} \vec{\varphi}_{k,i+\frac{1}{2}} \\ -\mu_4 \dfrac{\vec{\varphi}_{k,4,i+1} - \vec{\varphi}_{k,4,i}}{x_{i+1} - x_i} + \hat{R}_{\mathrm{G,i+\frac{1}{2}}} \vec{\varphi}_{k,4,i+\frac{1}{2}} = \hat{S}_{1,4,\mathrm{G,i+\frac{1}{2}}} \vec{\varphi}_{k,i+\frac{1}{2}} + \dfrac{1}{k} \hat{F}_{4,\mathrm{G,i+\frac{1}{2}}} \vec{\varphi}_{k,i+\frac{1}{2}} \\ i = 0, \dots, \mathrm{I}, \end{cases} \tag{2.55}$$

where the pedixes in the scattering operator have the meaning of anisotropicity order, emission direction, energy group and spatial node, respectively, while the vector $\vec{\varphi}_{k,i}$ is obtained stacking the group-wise fluxes in each flying directions. Since this set of algebraic equations is undetermined, the well-known diamond difference scheme (Lewis and Miller, 1984), which assumes a linear variation of the angular flux between two nodes, is introduced as an auxiliary relationship to close the system,

$$\vec{\varphi}_{k,j,i+\frac{1}{2}} = \frac{\vec{\varphi}_{k,j,i+1} + \vec{\varphi}_{k,j,i}}{2}. \tag{2.56}$$

It is noteworthy to mention that the solution of this edge-based numerical setup is more efficient than the usual centre-based S_N formulation, which yields a matrix with a denser sparsity pattern.

2.4.3 The boundary conditions

A common feature to both the P_N and the S_N methods is the fact that a finite number of degrees of freedom related to the flying direction is introduced in the system, making thus impossible to satisfy exactly the boundary conditions of the original transport model, which involves all the incoming directions. In the presence of vacuum, the exact boundary condition would be

$$\begin{cases} \phi(x = -\mathrm{H}, \mu > 0, \mathrm{E}) = 0 \ \forall \ \mu > 0 \\ \phi(x = +\mathrm{H}, \mu < 0, \mathrm{E}) = 0 \ \forall \ \mu < 0, \end{cases} \tag{2.57}$$

i.e. the angular flux should vanish for all the positive directions at a left boundary and for all the negative ones at a right boundary. Since the exact fulfillment of this condition is not mathematically possible, also the boundary conditions are approximated.

Mark (Mark, 1945a; b) was the first suggesting to make the angular flux to vanish in a specific set of directions. When these directions are taken as the roots μ_i of the even Legendre polynomial $P_N(\mu)$, i.e. they are symmetric with respect to zero, these boundary conditions turn out to be the most natural way to satisfy the vacuum condition in the S_N framework,

$$\begin{cases} \phi(x = -\mathrm{H}, +\mu_\mathrm{i}, \mathrm{E}) = 0, \;\; \mathrm{i} = 1, \dots, \frac{\mathrm{N}}{2} \\ \phi(x = +\mathrm{H}, -\mu_\mathrm{i}, \mathrm{E}) = 0, \;\; \mathrm{i} = 1, \dots, \frac{\mathrm{N}}{2}. \end{cases} \tag{2.58}$$

In the case of P_N equations, these conditions may not appear very intuitive. For example, the boundary condition for the left edge of the slab in a P_3 framework yield,

$$\begin{aligned} \phi(x = -\mathrm{H}, \mu_\mathrm{i}, \mathrm{E}) &= \sum_{n=0}^{\mathrm{N}=3} \frac{2n+1}{2} \phi_n(x, E) P_n(\mu_i) = \\ &= \frac{1}{2}\phi_0(x, E) + \frac{3}{2}\phi_1(x, E)P_1(\mu_i) + \frac{5}{2}\phi_2(x, E)P_2(\mu_i) \\ &+ \frac{7}{2}\phi_3(x, E)P_3(\mu_i) = 0 \quad i = 1, \dots, \frac{\mathrm{N}+1}{2}, \end{aligned} \tag{2.59}$$

which is a linear combination of the flux angular moments. Nevertheless, the use of Mark conditions can be more flexible than for the discrete ordinates model. In S_N, the directions for Mark conditions are determined by the choice of the quadrature scheme, typically Gauss-Legendre, while in P_N it is possible to select a different set. Because of their nice properties, the roots of Legendre polynomials are usually taken as well for the P_N approach. However, when an even value of N is used, one can could either compute the roots of $P_{N+1}(\mu)$, removing the zero solution, which is the direction parallel to the boundary surface, or the roots of $P_N(\mu)$. As it will be shown, the choice of the roots for even N can seriously affect the angular convergence. In the following, option A will indicate the roots of $P_{N+1}(\mu)$ excluding zero, while option B will indicate the roots of $P_N(\mu)$.

A more intuitive boundary condition for the P_N model was proposed by Marshak (Marshak, 1947). By substituting the flux angular expansion, eq. (2.25), into the exact boundary condition, eq. (2.57), projecting over the m-th odd Legendre polynomial and integrating over the incoming directions, the following involving the odd flux moments is obtained,

$$\begin{cases} \int_0^1 d\mu \phi(x = 0, \mu, E) P_m(\mu) = 0, \quad m = 1,3, \dots, \mathrm{N} \\ \int_{-1}^0 d\mu \phi(x = 0, \mu, E) P_m(\mu) = 0, \quad m = 1,3, \dots, \mathrm{N}. \end{cases} \tag{2.60}$$

When m=1, the Marshak formalism yields a zero incoming partial current, consistently with the exact boundary condition.

It should be remarked here that, in spite of their simplicity, both boundary conditions could yield negative values at the boundaries for some directions of the angular flux, especially for optically thin systems.

2.5 The P_N - S_{N+1} equivalence

The P_N and the S_N equations are certainly the most popular transport models used to solve the NTE in its integro-differential form. Despite it is possible to prove that they are equivalent under certain hypotheses, these methods have important differences.

The P_N approach is very elegant and has a rich physical meaning, since the equation for the 0^{th} order moment represents the neutron balance. When the system is truncated at N=1 and a steady state is assumed, the first moment equation provides Fick's law, which can be combined with the balance equation to yield the diffusion model, which is thus a first-order transport model. From a mathematical standpoint, the P_N equations are weakly coupled, as in each equation only the preceding and succeeding moments appear. Thanks to this structure, the resulting discretised operator is featured by a nice sparsity pattern, which can be exploited to solve the P_N system using direct methods (e.g., Gauss-Seidel) quite easily even for relatively large values of N. However, the implementation of the P_N method is rather involved: its complexity may become prohibitive for 2D or 3D geometries.

On the contrary, the S_N model derivation is more intuitive and its implementation is much easier even in presence of complex geometries. These are the main reasons that justify its implementation in the first computational codes for neutron transport (Lathrop and Carlson, 1964), despite the presence, in multi-dimensional systems, of the *ray-effect*, which is an unpleasant numerical effect inducing an artificial anisotropy in the angular flux (Lathrop, 1968) in the presence of absorbing media and localised sources. From a mathematical standpoint, the system of S_N equations is tightly coupled by the scattering and fission operators. Thus, the resulting sparsity pattern of the discretised S_N model is not suitable for an efficient solution via direct methods, making the use of an iterative, matrix-free procedure, known as *transport sweep*, more preferable for both memory consumption and computational burden (Lewis and Miller, 1984).

Despite these differences, for a one-dimensional system it is possible to prove that, selecting the discrete ordinates to coincide with the roots of the Legendre polynomials $P_N(\mu)$, the S_{N+1} approach is equivalent to the corresponding P_N model.

Exploiting the Gauss-Legendre (G-L) quadrature rule, it is possible to evaluate the projection of the S_N equations on the n-th Legendre polynomial,

$$\int_{-1}^{1} d\mu \, P_N(\mu) \, * \approx \sum_{j=1}^{N} w_j P_n(\mu_j) \, *, \tag{2.61}$$

where the symbol $*$ represents eq. (2.54). Thanks to this procedure, a set of P_N-like equations can be constructed for the flux angular moments approximated with G-L formula,

$$\phi_n(x,E) \equiv \int_{-1}^{1} d\mu \, P_N(\mu) \, \phi(x,\mu,E) \approx \sum_{j=1}^{N} w_j P_n(\mu_j) \phi(x,\mu_j,E) = \tilde{\phi}_n(x,E). \tag{2.62}$$

It is important to remark that, since the flux in the j-th direction is not a polynomial in general, the moment evaluation may not be computed exactly. Using eq. (2.62), it is possible to get the different P_N-equivalent operators:

- the streaming operator can be obtained using the Legendre polynomials recurrence formula $nP_{n-1}(\mu) + (n+1)P_{N+1}(\mu) = (2n+1)\mu P_n(\mu)$,

$$\begin{aligned}\sum_{j=1}^{N} w_j P_n(\mu_j)\left[\mu_j \frac{\partial \phi(x,\mu_j,E)}{\partial x}\right] &= \frac{\partial}{\partial x}\sum_{j=1}^{N} w_j \phi(x,\mu,E)\left[\frac{nP_{n-1}(\mu_j)+(n+1)P_{n+1}(\mu_j)}{2n+1}\right] \\ &= \frac{n}{2n+1}\frac{\partial \tilde{\phi}_{n-1}(x,E)}{\partial x} + \frac{n+1}{2n+1}\frac{\partial \tilde{\phi}_{n+1}(x,E)}{\partial x}.\end{aligned} \tag{2.63}$$

- the derivation of the time and "interaction" terms is straightforward,

$$\sum_{j=1}^{N} w_j P_n(\mu_j)\left[\frac{1}{v}\frac{\partial}{\partial t}\phi(x,\mu_j,E)\right] = \frac{1}{v}\frac{\partial}{\partial t}\tilde{\phi}_n(x,E), \tag{2.64}$$

$$\sum_{j=1}^{N} w_j P_n(\mu_j)\left[\Sigma_x(x,E)\phi(x,\mu_j,E)\right] = \Sigma_x(x,E)\tilde{\phi}_n(x,E), \tag{2.65}$$

  where x can indicate capture, total scattering or total fission.

- the scattering operator is obtained exploiting the orthogonality property of Legendre polynomials,

$$\begin{aligned}&\sum_{j=1}^{N} w_j P_n(\mu_j)\left[\int_0^\infty dE'\Sigma_s(x,E')\sum_{\ell=1}^{L}\frac{2\ell+1}{2}f_{\ell,j}(x,E\longrightarrow E')P_\ell(\mu_j)\sum_{m=1}^{N} w_m P_\ell(\mu_m)\phi(x,\mu_m,E)\right] = \\ &= \int_0^\infty dE'\Sigma_s(x,E')\sum_{\ell=1}^{L}\left[\sum_{j=1}^{N} w_j P_n(\mu_j)\frac{2\ell+1}{2}P_\ell(\mu_j)\right] f_{\ell,j}(x,E\longrightarrow E')\sum_{m=1}^{N} w_m P_\ell(\mu_m)\phi(x,\mu_m,E) = \\ &= \int_0^\infty dE'\Sigma_s(x,E')\delta_{n\ell} f_{\ell,j}(x,E\longrightarrow E')\sum_{m=1}^{N} w_m P_\ell(\mu_m)\phi(x,\mu_m,E) = \\ &= \int_0^\infty dE'\Sigma_s(x,E')\delta_{n\ell} f_{\ell,j}(x,E\longrightarrow E')\tilde{\phi}_l(x,E).\end{aligned} \tag{2.66}$$

- the prompt and delayed fission can be obtained using the fact that $P_0(\mu) \equiv 1$,

$$\begin{aligned}
&\sum_{j=1}^{N} w_j P_n(\mu_j) \left[(1-\beta) \frac{\chi_p(x,E)}{2} \int_0^\infty dE' \, \nu\Sigma_f(x,E') \sum_{n=1}^{N} w_n \phi(x,\mu_n,E) \right] = \\
&= (1-\beta) \frac{\chi_p(x,E)}{2} \int_0^\infty dE' \, \nu\Sigma_f(x,E') \tilde{\phi}_0(x,E) \sum_{j=1}^{N} w_j P_n(\mu_j) P_0(\mu_j) = \\
&= (1-\beta) \frac{\chi_p(x,E)}{2} \int_0^\infty dE' \, \nu\Sigma_f(x,E') \tilde{\phi}_0(x,E) \delta_{n0}
\end{aligned} \tag{2.67}$$

and

$$\begin{aligned}
&\sum_{j=1}^{N} w_j P_n(\mu_j) \left[\beta_r \frac{\chi_{d,r}(x,E)}{2} \int_0^\infty dE' \, \nu\Sigma_f(x,E') \sum_{n=1}^{N} w_n \phi(x,\mu_n,E) \right] = \\
&= \beta_r \frac{\chi_{d,r}(x,E)}{2} \int_0^\infty dE' \, \nu\Sigma_f(x,E') \sum_{j=1}^{N} w_j P_n(\mu_j) P_0(\mu_j) \sum_{n=1}^{N} w_n \phi(x,\mu_n,E) = \\
&= \beta_r \frac{\chi_{d,r}(x,E)}{2} \int_0^\infty dE' \, \nu\Sigma_f(x,E') \tilde{\phi}_0(x,E) \delta_{n0}.
\end{aligned} \tag{2.68}$$

Since the maximum degree that can be integrated exactly by the G-L scheme is 2N-2, and the anisotropy order L should be less or equal than N to have a non-vanishing integral in the scattering operator, the exact integration of eq. (2.54) can occur only if $n + \mathrm{L} = \mathrm{n} + \mathrm{N} \leqslant 2\mathrm{N} - 2$, thus implying that $n \leqslant \mathrm{N} - 1$. Since the $\mathrm{P_{N-1}}$ equations are defined for n ranging from 0 up to N-1, the projection of the $\mathrm{S_N}$ operators with the G-L scheme is exact. Moreover, since the discrete ordinates are taken as the roots of $P_N(\mu)$, the moment $\phi_N(x,E)$ vanishes,

$$\tilde{\phi}_N(x,E) = \sum_{j=1}^{N} w_j \phi(x,\mu_j,E) P_N(\mu_j) = 0, \tag{2.69}$$

meaning that the equations for $\tilde{\phi}_n(x,E)$ coincide with the ones for $\phi_n(x,E)$.

The formal equivalence of these methods is a fundamental result for many reasons. First, it links two different approaches, showing their mutual consistency. Moreover, since the two approaches lead to the same result, the choice of the method to be adopted could be made regardless of the computational accuracy, but according to other requirements, e.g., the memory consumption (in favour of the $\mathrm{S_N}$ method). Then, despite this equivalence is valid only for one-dimensional systems, it is helpful for the code verification and validation stages. Finally, the relationship between the two methods could be helpful to transfer physico-mathematical considerations pertaining to one model to the other.

2.5.1 Even-to-odd order reduction

In this last sense, the P_N-S_{N+1} equivalence is fundamental in order to understand the underpinning reasons for the historical disfavour towards the even (odd) P_N (S_{N+1}) approximations (Case and Zweifel, 1967; Faris, 2005). When an odd order S_{N+1} is chosen, one of the roots of $P_{N+1}(\mu)$ is always equal to zero. In this case, one of the equations appearing in the S_{N+1} system would be no more differential, as a consequence of the fact that the streaming along the direction μ=0, parallel to the boundaries, would not add further physical detail on the system boundaries (see fig. 2.2). Thanks to the P_N-S_{N+1} equivalence, the same consideration should hold for the even-order P_N as well, despite its less intuitive behaviour.

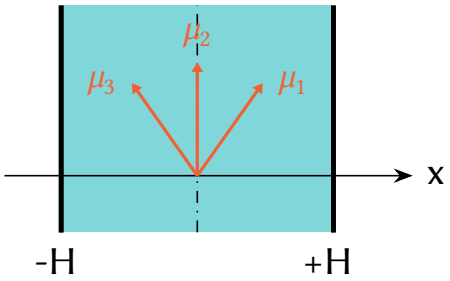

Figure 2.2: *Sketch of a one-dimensional slab with the three discrete directions featuring the* S_3 *model.*

Inspired by this physico-mathematical fact, a more formal investigation could be performed on this old fashion even-vs.-odd dispute, showing that an even P_N model can be always cast in a form similar to the preceding P_{N-1} model, which is odd, with modified coefficients.

This fact can be appreciated explicitly by simply analysing the P_2 case. Taking eq. (2.36) and omitting the angular flux space and energy dependencies,

$$\begin{cases} \varepsilon_\delta \dfrac{\partial \phi_1}{\partial x} + \hat{A}_0 \phi_0 = 0 \\ \varepsilon_\delta \left(\dfrac{2}{3} \dfrac{\partial \phi_2}{\partial x} + \dfrac{1}{3} \dfrac{\partial \phi_0}{\partial x} \right) + \hat{A}_1 \phi_1 = 0 \\ \varepsilon_\delta \dfrac{2}{5} \dfrac{\partial \phi_1}{\partial x} + \hat{A}_2 \phi_2 = 0 \end{cases} \tag{2.70}$$

where $\hat{A}_0$ and $\hat{A}_n$ for n = 1,2 are defined as follows,

$$\begin{aligned} \hat{A}_0 &= \varepsilon_\theta \hat{C} + \hat{F}_T + \hat{S}_T + \frac{\varepsilon_\alpha}{\mathrm{v}} - \varepsilon_\gamma \left[\hat{S}_0 + \varepsilon_k \left(\hat{F}_{p,0} + \sum_{r=1}^{\mathrm{R}} \frac{\lambda_r}{\lambda_r + \varepsilon_\omega} \hat{F}_{d,r,0} \right) \right] \\ \hat{A}_n &= \varepsilon_\theta \hat{C} + \hat{F}_T + \hat{S}_T + \frac{\varepsilon_\alpha}{\mathrm{v}} - \varepsilon_\gamma \hat{S}_n, \end{aligned} \tag{2.71}$$

it is possible to manipulate the system substituting the equation for ϕ_0 into the equation for ϕ_1 and then the equation for ϕ_2 into the equation for ϕ_1,

$$\begin{cases} \varepsilon_\delta \dfrac{\partial \phi_1}{\partial x} + \hat{A}_0 \phi_0 = 0 \\ \varepsilon_\delta \left(+ \dfrac{4}{15} \hat{A}_0^{-1} \hat{A}_2 + \dfrac{1}{3} \right) \dfrac{\partial \phi_0}{\partial x} + \hat{A}_1 \phi_1 = 0 \\ -\dfrac{2}{5} \hat{A}_0 \phi_0 + \hat{A}_2 \phi_2 = 0. \end{cases} \tag{2.72}$$

This system is equivalent to a set of P_1 equations, with the replacement

$$\frac{1}{3} \longrightarrow \frac{1}{3} + \frac{4}{15} \hat{A}_0^{-1} \hat{A}_2. \tag{2.73}$$

Since the P_1 equations can be cast into the diffusion model by defining

$$D_{P_1} = \frac{1}{3} \hat{A}_1^{-1}, \tag{2.74}$$

the same equivalence should hold for the P_2 case as well (Heizler and Ravetto, 2012). Indeed, this relationship is valid taking a different definition of the coefficient, namely

$$D' = \frac{1}{3} \hat{A}_1^{-1} + \frac{4}{15} \hat{A}_0^{-1} \hat{A}_2 \hat{A}_1^{-1} = D_{P_1} + D_{P_2}. \tag{2.75}$$

A similar procedure can be applied to the succeeding even-order case, P_4,

$$\begin{cases} \varepsilon_\delta \dfrac{\partial \phi_1}{\partial x} + \hat{A}_0 \phi_0 = 0 \\ \varepsilon_\delta \left(\dfrac{2}{3} \dfrac{\partial \phi_2}{\partial x} + \dfrac{1}{3} \dfrac{\partial \phi_0}{\partial x} \right) + \hat{A}_1 \phi_1 = 0 \\ \varepsilon_\delta \left(\dfrac{3}{5} \dfrac{\partial \phi_3}{\partial x} + \dfrac{2}{5} \dfrac{\partial \phi_1}{\partial x} \right) + \hat{A}_2 \phi_2 = 0 \\ \varepsilon_\delta \left(\dfrac{4}{7} \dfrac{\partial \phi_4}{\partial x} + \dfrac{3}{7} \dfrac{\partial \phi_2}{\partial x} \right) + \hat{A}_3 \phi_3 = 0 \\ \varepsilon_\delta \dfrac{4}{9} \dfrac{\partial \phi_3}{\partial x} + \hat{A}_4 \phi_4 = 0. \end{cases} \tag{2.76}$$

Similarly to the previous case, in order to reduce the P_4 system to an equivalent P_3 one the spatial gradient of ϕ_4 should disappear from the equation for ϕ_3. This objective can be achieved substituting the equation for ϕ_0 into the equation for ϕ_2 and then substitute this equation into the one for ϕ_4, obtaining

$$\phi_4 = -\frac{1}{\varepsilon_\delta} \frac{4}{9} \frac{\partial \phi_3}{\partial x} \hat{A}_4^{-1} = \frac{20}{27} \left(-\frac{2}{5} \hat{A}_0 \phi_0 + \hat{A}_2 \phi_2 \right) \hat{A}_4^{-1}. \tag{2.77}$$

As for P_2, the highest order even moment turns out to be a linear combination of the lower-order even moments. It is intuitive that, due to the structure of the P_N model, the

set of preceding equations for the even moments can be used recursively to express the odd-order spatial gradient as a function of the lower-order even moments.

However, contrarily to the previous case, the substitution of eq. (2.77) into the $n = 3$ equation is not sufficient to obtain the required P_3-like system, due to the appearance of ϕ_0,

$$\begin{cases} \varepsilon_\delta \dfrac{\partial \phi_1}{\partial x} + \hat{A}_0 \phi_0 = 0 \\ \varepsilon_\delta \left(\dfrac{2}{3} \dfrac{\partial \phi_2}{\partial x} + \dfrac{1}{3} \dfrac{\partial \phi_0}{\partial x} \right) + \hat{A}_1 \phi_1 = 0 \\ \varepsilon_\delta \left(\dfrac{3}{5} \dfrac{\partial \phi_3}{\partial x} + \dfrac{2}{5} \dfrac{\partial \phi_1}{\partial x} \right) + \hat{A}_2 \phi_2 = 0 \\ \varepsilon_\delta \dfrac{80}{189} \left(-\dfrac{2}{5} \hat{A}_0 \dfrac{\partial \phi_0}{\partial x} + \hat{A}_2 \dfrac{\partial \phi_2}{\partial x} \right) \hat{A}_4^{-1} + \varepsilon_\delta \dfrac{3}{7} \dfrac{\partial \phi_2}{\partial x} + \hat{A}_3 \phi_3 = 0. \end{cases} \tag{2.78}$$

To obtain the desired equivalent form, the gradient of ϕ_0 is first made explicit from the equation for $n = 1$,

$$\frac{\partial \phi_0}{\partial x} = -2 \frac{\partial \phi_2}{\partial x} - \frac{3}{\varepsilon_\delta} \hat{A}_1 \phi_1, \tag{2.79}$$

and then substituted into eq. (2.78),

$$\begin{cases} \varepsilon_\delta \dfrac{\partial \phi_1}{\partial x} + \hat{A}_0 \phi_0 = 0 \\ \varepsilon_\delta \left(\dfrac{2}{3} \dfrac{\partial \phi_2}{\partial x} + \dfrac{1}{3} \dfrac{\partial \phi_0}{\partial x} \right) + \hat{A}_1 \phi_1 = 0 \\ \varepsilon_\delta \left(\dfrac{3}{5} \dfrac{\partial \phi_3}{\partial x} + \dfrac{2}{5} \dfrac{\partial \phi_1}{\partial x} \right) + \hat{A}_2 \phi_2 = 0 \\ \varepsilon_\delta \left[\left(\dfrac{64}{189} \hat{A}_0 + \dfrac{80}{189} \hat{A}_2 \right) \hat{A}_4^{-1} + \dfrac{3}{7} \right] \dfrac{\partial \phi_2}{\partial x} + \dfrac{32}{63} \hat{A}_1 \hat{A}_4^{-1} \phi_1 + \hat{A}_3 \phi_3 = 0. \end{cases} \tag{2.80}$$

This operation introduces a term depending on ϕ_1, which should not be present in the equivalent P_3 system. At this point, it is convenient to introduce a new definition for the third order moment,

$$\phi_3' = \hat{A}_3 \phi_3 + \frac{32}{63} \hat{A}_1 \hat{A}_4^{-1} \phi_1. \tag{2.81}$$

Thanks to this definition, the coveted equivalent system is finally obtained, replacing ϕ_3 with ϕ_3' into the equation for $n = 3$ and adjusting equation $n = 2$ according to eq. (2.81),

$$\begin{cases} \varepsilon_\delta \dfrac{\partial \phi_1}{\partial x} + \hat{A}_0 \phi_0 = 0 \\ \varepsilon_\delta \left(\dfrac{2}{3} \dfrac{\partial \phi_2}{\partial x} + \dfrac{1}{3} \dfrac{\partial \phi_0}{\partial x} \right) + \hat{A}_1 \phi_1 = 0 \\ \varepsilon_\delta \left[\dfrac{3}{5} \dfrac{\partial \phi_3'}{\partial x} + \left(-\dfrac{32}{105} \hat{A}_1 \hat{A}_4^{-1} + \dfrac{2}{5} \right) \dfrac{\partial \phi_1}{\partial x} \right] + \hat{A}_2 \phi_2 = 0 \\ \varepsilon_\delta \left[\left(\dfrac{64}{189} \hat{A}_0 + \dfrac{80}{189} \hat{A}_2 \right) \hat{A}_4^{-1} + \dfrac{3}{7} \right] \dfrac{\partial \phi_2}{\partial x} + \phi_3' = 0. \end{cases} \tag{2.82}$$

These two examples are extremely useful to get some insight into the reduction process, providing fundamental information to develop a general reduction algorithm:

- the equation for the highest order even moment is algebraic, being a linear combination of lower order even moments. Consistently, the streaming eigenvalue placeholder ε_δ does not appear in this equation, confirming that the highest-order even moment is not related to the streaming phenomenon;
- a new definition of the odd-order moments may be required in order to obtain the equivalence;
- The equivalence with the P_{N-1} model, intended as obtaining a system with the same structure of the preceding odd-order, is accomplished by means of a change in the coefficients of the system.

When larger values of N are considered, the reduction process is more involved, since the new moment definition depends on the lower, odd-order moments. Despite these additional intricacies, it is possible to prove by induction that the same reduction mechanism applies also for arbitrary even values of N thanks to a similarity transformation based on the Gauss elimination method. This transformation corresponds to perform left and right matrix multiplications: the first are useful to remove the derivative terms terms from higher order rows, while the right multiplications are related to the new definition of the odd-order moment needed to close the process. It is noteworthy to remark here that, thanks to the weak coupling of the angular moments, which makes the P_N system lower triangular, this algorithm requires a finite number of steps. The formal details of this proof, mainly due to Dr. Paolo Saracco, are omitted here for the sake of brevity, as they can be found in Abrate, Dulla, et al. (2021).

2.6 Numerical benchmark of the eigenvalue formulations to the P_N and S_N models

In this section, the numerical implementation of the multi-group P_N and S_N models in the TEST code, based on a finite difference scheme in space, is benchmarked against some reference results pertaining to the different eigenvalue formulations presented in section 2.3.1. Most of these reference values are taken from the literature, but a comparison with semi-analytical and Monte Carlo calculations is presented as well in the following. It is important to point out that, due to the scarceness of numerical results concerning some eigenvalues, e.g., ω and δ, the numerical benchmark will be focused mainly on the eigenvalues available in the literature.

2.6.1 Numerical solvers for the solution of eigenvalue problems

The solution of eigenvalue problems for large matrices is often a very expensive operation, especially when the objective of the calculation is the full set of the eigenpairs, i.e. the eigenvectors and the associated eigenvalues. According to the application, one

is generally interested in the evaluation of only one (the fundamental) or a few relevant eigenpairs, e.g., for modal expansion methods (Gandini, 1978).

Historically, the most popular method employed to find the fundamental eigenpair for the k eigenvalue problem is the *power method*, which is an iterative algorithm with a very intuitive physical meaning (Saad, 1992). First, an initial neutron distribution is guessed. Then, the distribution of the next generation of neutrons is estimated solving a source-driven problem where the external source is defined applying the fission operator to the initial neutron generation. Then, the effective multiplication factor k is estimated, taking the ratio between the fission productions at different neutron generations. The procedure is stopped when a certain tolerance on the flux and on the eigenvalue is met. The convergence of this algorithm is ensured by multiplying the fission source at each n-th cycle by a factor $1/k_n$, thus forcing the system to be critical. The main advantages of this approach are its easiness of implementation, its natural physical interpretation and its ensured convergence. However, since the convergence of this algorithm scales with the dominance ratio (DR) of the matrix, i.e. the ratio between the first two eigenvalues, the power method can be extremely inefficient for loosely coupled cores, featured by large DRs. Moreover, this approach does not allow to retrieve eigenvalues other than the fundamental. In spite of its shortcomings, this is currently the most popular approach for the solution of the criticality eigenvalue problem both in deterministic (Rimpault, Plisson, et al., 2002) and stochastic codes (Nowak, Miao, et al., 2016).

To overcome this serious limitation, the so-called *filtered power method*, also known as *subtraction* or *elimination* method, has been proposed to extend the classical power method using a filtering technique based on the bi-orthogonality property between the direct and the adjoint eigenvectors (Vondy and Fowler, 1983). Nevertheless, being an extension of the power method, this method suffers from the same slow convergence in case of large DRs, especially for symmetrical system, featured by spectrum degeneracies (Tommasi, Maillot, and Rimpault, 2016). Moreover, since both the direct and the adjoint harmonics are evaluated, this approach is computationally demanding and, as a consequence of the filtering procedure, its implementation in commercial codes would require some non-negligible modifications, especially for discrete ordinates codes. In this case, the fix-up (Lewis and Miller, 1984) usually adopted to correct the negative values of the flux should be avoided because of the non-uniform sign of the the higher-harmonics. On top of these considerations, the use of the direct and adjoint lower-order eigenvectors to filter the higher-order components of the spectrum can introduce approximation errors in the solution that would in turn propagate this numerical noise through the whole calculation chain.

Several alternative methods have been proposed during the years, like the use of subspace iteration methods (Modak and Jain, 1996), or the adoption of boundary conditions to enhance the convergence breaking the spectrum degeneracies (Maillot, Tommasi, and Rimpault, 2016). Notwithstanding all these efforts, most of these techniques, including the power method, are tailored on the calculation of k, whose spectrum is by

far the simplest among the ones of the eigenvalue problems presented in sec. 2.3.1.

Specific alternative methods for determination of the time (Modak and A. Gupta, 2003; Singh, Degweker, et al., 2011) and collision (Modak, H. P. Gupta, and Jain, 1994) eigenvalue have also been proposed, albeit they are not very efficient.

Nowadays, the most efficient and robust algorithms to compute the leading eigenpairs of a general eigenvalue problem belong to the class of Krylov-Arnoldi method (Saad, 1992). The fundamental, basic idea of Krylov, a Russian naval engineer, was to keep all the vectors generated during the power method iterations, instead of discarding them at each iteration, in order to construct a subspace. It is interesting to notice that, in full analogy with the power method, this approach could be interpreted from a physical perspective as a neutron population that is able to reach its eigenstate faster because it retains the collective memory of all its preceding generations. In addition to the improved convergence, which scales non-linearly, the methods belonging to this family require little or no modification to existing codes, as they only need the vectors obtained applying the operator $\hat{A}$ to the initial guess $\vec{v}$ to construct the subspace $\hat{K}$,

$$\hat{K} = \{\vec{v}, \hat{A}\vec{v}, \hat{A}^2\vec{v}, \dots, \hat{A}^n\vec{v}\}. \tag{2.83}$$

Since this matrix-vector operation is embedded in the original code, the Krylov-Arnoldi techniques are non-intrusive, as they only require data exchange. Therefore, these methods are usually implemented in highly efficient numerical libraries and are wrapped around the existing code. Because of their recent popularity, these methods have been recently investigated for the solution of eigenvalue problems in the frame of reactor physics, showing excellent computational performances with respect to the traditional power methods (Zinzani, Demaziére, and Sunde, 2008; Abrate, Bruna, et al., 2019). The Krylov-based algorithms have also been successfully applied to other eigenvalue formulations (Carreño, Vidal-Ferrándiz, et al., 2017), due to the possibility to search for only some specific portions of the eigenvalue spectrum by means of the introduction of a shift (Saad, 1992).

All the eigenvalue calculations performed throughout this work are performed using either the ARPACK (ARnoldi PACKage) library (Lehoucq, Sorensen, and Yang, 1998) or the SLEPc/PETSc (Scalable Library for Eigenvalue Problem Computations and Portable, Extensible Toolkit for Scientific Computation) libraries (Balay, Abhyankar, et al., 2020; Hernandez, Roman, and Vidal, 2005), for which *ad hoc*, open-source Python wrappers are available in the *eigs* function of the Scipy package and in the *slepc4py* package, respectively. ARPACK is a set of numerical routines, initially written in Fortran77 but currently available also in other languages like C++, implementing the Implicit Restarted Arnoldi Method (Arnoldi, 1951), which is suitable for the solution of large, sparse matrices. With respect to ARPACK, the SLEPc and PETSc packages, written in Fortran, C and C++, are more modern and efficient, aiming at parallel and distributed computing applications. In addition, the SLEPc library offers a vast choice of Krylov subspace methods, including the Arnoldi methods as well.

2.6.2 Benchmark with the data available in the literature

The first numerical verifications aimed at verifying the spatial grid independence of the models for two slab thicknesses, 1 and 8 mfp, respectively, analysing the behaviour of the eigenvalues for some angular approximation orders. Tables 2.3 and 2.2 compare the fundamental c eigenvalue, which is related to γ through the following equation:

$$c\gamma = \frac{\Sigma_s + \nu\Sigma_f}{\Sigma_t}, \tag{2.84}$$

with the reference values taken from Modak, Sahni, and Paranjape (1995), where a variant of the sub-space iteration method is employed to compute the eigenvalues (Modak, H. P. Gupta, and Jain, 1994). In these tables, the calculations are performed for the two slab thicknesses employing the same set of one-group cross sections, namely $\Sigma_t = 1$, $\Sigma_s = 0.8$, $\Sigma_a = 0.2$ and $\nu\Sigma_f = 1$, expressed in mfp^{-1}. The P_N and S_{N+1} results computed by TEST show an increasing good agreement, up to 0.1 pcm for the finest mesh, with respect to the reference values, for both the slab thicknesses, suggesting that the boundary conditions are handling correctly the transport effects arising in the thinnest slab.

Table 2.2: *Convergence of the fundamental collision eigenvalue c_0 to the benchmark values (Modak, Sahni, and Paranjape, 1995) for increasing number of meshes for P_N and S_N approximations with Mark boundary conditions and isotropic scattering. The slab is assumed to be 8 mfp thick.*

spatial meshes	P_{63}	S_{64}	ref. S_{64}	P_{127}	S_{128}	ref. S_{128}
30	1.0364284	1.0364464	1.0364130	1.0364273	1.0364458	1.0364125
60	1.0364139	1.0364133	1.0364054	1.0364129	1.0364127	1.0364048
100	1.0364083	1.0364066	1.0364038	1.0364074	1.0364060	1.0364032

Table 2.3: *Convergence of the fundamental collision eigenvalue c_0 to the benchmark values (Modak, Sahni, and Paranjape, 1995) for increasing number of meshes for P_N and S_N approximations with Mark boundary conditions and isotropic scattering. The slab is assumed to be 1 mfp thick.*

spatial meshes	P_{127}	S_{128}	ref. S_{128}	P_{255}	S_{256}	ref. S_{256}
60	1.6154789	1.6154505	1.6154165	1.6154607	1.6154302	1.6153960
100	1.6154329	1.6154215	1.6154095	1.6154150	1.6154012	1.6153891
150	1.6154178	1.6154126	1.6154074	1.6153991	1.6153923	1.6153869

The presence of a certain discrepancy in the eigenvalues computed by solving the P_N and the S_{N+1} models with Mark boundary conditions seems in contrast with their formal equivalence, suggesting the presence of one or more inconsistencies in the numerical code implementation. However, it should be noticed that this equivalence does not hold anymore when the two models are discretised in space: the S_N model employs a co-located scheme, i.e. the same grid is employed for positive and negative directions, while the P_N model exploits a staggered scheme to avoid numerical instabilities. In such a case, it would not be possible to retrieve the staggered P_N equations starting from the co-located S_{N+1} equations coupled with the diamond difference scheme (and viceversa), due to the mismatch between the two grids. Therefore, also in light of the excellent agreement with the reference, this disagreement is likely due to this effect. Consistently, the difference between the fundamental eigenvalues estimated by the two models diminishes refining the mesh, and, thus, reducing the difference between the two grids. The break up of the P_N-S_{N+1} equivalence is even more important for the higher-order eigenvalues, which are associated to eigenfunctions featured by steeper spatial gradients.

For the same system, the k eigenvalue is computed for different angular approximation orders, with a fixed number of spatial meshes, equal to 200. Table 2.4 provides the fundamental eigenvalues computed with the P_N and S_{N+1} methods with Mark boundary conditions, while table 2.5 reports the P_N values with Marshak boundary conditions. Also in this case there is a good agreement between the values computed by TEST and the reference ones, within 1 pcm. Again, the accuracy seems unaffected by the value of the slab thickness. For the Marshak case, the agreement between the P_N and the reference S_{N+1} values is progressively better as the difference between the two models and the associated boundary conditions is reduced for increasing values of the angular order.

Table 2.4: *Convergence of the fundamental multiplication eigenvalue k_0 to the benchmark value at increasing orders of P_N and S_N approximation with Mark boundary conditions. Reference values are evaluated with S_{256} (Modak, Sahni, and Paranjape, 1995; Deo, Krishnani, and Modak, 2014), using vacuum boundary conditions as well. All calculations are performed using 200 meshes.*

N	1 mfp			8 mfp		
	P_N	S_{N+1}	ref. S_{N+1}	P_N	S_{N+1}	ref. S_{N+1}
3	1.129077	1.129073	1.129075	4.225108	4.225092	4.225105
7	1.209379	1.209376	1.209376	4.229059	4.229053	4.229065
15	1.223481	1.223481	1.223479	4.229825	4.229828	4.229840
31	1.225737	1.225738	1.225737	4.229997	4.230008	4.230020
255	1.226402	1.226408	1.226406	4.230050	4.230065	4.230078

Table 2.5: *Convergence of the fundamental multiplication eigenvalue k_0 to the benchmark value at increasing orders of* P_N *approximation with Marshak boundary conditions. Reference values are evaluated with* S_{256} *(Modak, Sahni, and Paranjape, 1995; Deo, Krishnani, and Modak, 2014), using vacuum boundary conditions as well. All calculations are performed using 200 meshes.*

N	1 mfp		8 mfp	
	P_N	ref. S_{N+1}	P_N	ref. S_{N+1}
3	1.171867	1.129075	4.228452	4.225105
7	1.219462	1.209376	4.229717	4.229065
15	1.225369	1.223479	4.229976	4.229840
31	1.226151	1.225737	4.230035	4.230020
255	1.226409	1.226406	4.230051	4.230078

Since one of the objectives of the TEST code is the study of the spectrum of the different eigenvalues, the analysis of the accuracy of the P_N and S_{N+1} models in the evaluation of the higher-order eigenvalues is of the utmost importance. Table 2.6 shows a comparison between the two models and the reference values computed by Modak, Sahni, and Paranjape (1995). The benchmark values are given with a limited number of significant digits, probably due to a loss of accuracy in the sub-space iteration eigenvalue solver. The results in the table shows an overall satisfactory agreement between the higher-order eigenvalues evaluated by the two models and the reference values, for both isotropic and linearly anisotropic scattering cases. It is interesting to notice that, except for the fundamental, the difference in the eigenvalues computed by the P_N and S_{N+1} models is progressively different, suggesting that, due to the spatial discretisation, the two operators are featured by different spectra.

In addition to k and γ (or its c variant), the other eigenvalue formulation widely present in the literature is the time eigenvalue. Table 2.7 provides a comparison between the α eigenvalues, in ms^{-1}, computed with TEST and the reference values, obtained either with a semi-analytical method (Dahl, Protopopescu, and Sjöstrand, 1983) or with S_8 calculations (Modak and A. Gupta, 2003) for the case of non-multiplying slabs featured by Σ_t=1 cm^{-1}, Σ_s=0.8 cm^{-1}, v=1 cm/s and different thicknesses. The agreement between the α eigenvalues computed by TEST and the available semi-analytical ones is very good, also for the higher-order eigenvalues. Also in this case it is possible to appreciate the difference, for large frequencies, in the eigenvalues of the P_N and S_{N+1} models due to the different discretisation approaches employed.

The paper by Modak and A. Gupta (2003) presents also a set of extremely useful results to verify the solution of the α eigenvalue for the case of a heterogeneous, 1 cm thick slab obtained alternating two materials. The first one is a perfect neutron diffuser, featured by Σ_t=Σ_s=10 cm^{-1}, while the second is a neutron absorber, featured by Σ_t=10 cm^{-1} and Σ_s=0.9 cm^{-1}. Table 2.8 presents the first four α eigenvalues for different slab

Table 2.6: *Higher-order k eigenvalues computed with* P_{63} *and* S_{64} *models imposing Mark boundary conditions and reference values (Modak, Sahni, and Paranjape, 1995) for the 1 mfp slab, assuming isotropic and linearly anisotropic scattering. All calculations are performed using 100 spatial meshes, consistently with the reference values provided.*

k mode	Isotropic scattering $\bar{\mu}_0 = 0$			Linearly anisotropic scattering $\bar{\mu}_0 = 0.375$		
	P_{255}	S_{256}	ref. S_{256}	P_{255}	S_{256}	ref. S_{256}
0	1.2263693	1.2263901	1.2264084	1.1784718	1.1785020	1.1785157
2	0.2321258	0.2319993	0.232083	0.2176900	0.2175786	0.217653
4	0.1216449	0.1213847	0.12153	0.1169190	0.1166776	0.11681
6	0.0821309	0.0817410	0.08195	0.0798521	0.0794824	0.07968
8	0.0619800	0.0614614	0.06174	0.0606479	0.0601502	0.06041
10	0.0497915	0.0491446	0.0495	0.0489191	0.0482937	0.0486

Table 2.7: *First four α eigenvalues, in* ms^{-1}*, evaluated with* P_{15}*,* S_{32}*,* P_{255} *and* P_{256} *approximations imposing Mark boundary conditions and 100 spatial meshes and compared to the reference* S_{16} *results by Modak and A. Gupta (2003). The semi-analytical results are taken from Dahl, Protopopescu, and Sjöstrand (1983).*

H [cm]	α mode	P_7	S_8	ref. S_8	P_{255}	S_{256}	semi-analyt.
5	0	−81.319	−81.322	−81.249	−81.102	−81.100	−81.093
	1	−343.777	−343.909	−345.348	−341.239	−341.333	−341.216
10	0	−25.385	−25.386	−25.378	−25.354	−25.353	−25.352
	1	−103.143	−103.195	−103.353	−102.984	−103.026	
	2	−238.497	−238.817	−238.123	−237.907	−238.195	−237.942
	3	−443.506	−444.723	−447.714	−439.598	−440.680	
	4	−889.535	−889.104	−887.349	−723.448	−726.527	−724.185
20	0	−7.186	−7.186	−7.185	−7.182	−7.181	−7.180
	1	−28.865	−28.881	−28.897	−28.847	−28.861	
	2	−65.407	−65.508	−65.449	−65.361	−65.457	−65.376
	3	−117.456	−117.804	−118.060	−117.360	−117.696	
	4	−185.973	−186.874	−186.414	−185.782	−186.659	−185.998
	5	−272.330	−274.309	−275.683	−271.927	−273.857	
	6	−378.684	−382.615	−380.843	−377.537	−381.334	−378.585
	7	−511.430	−519.273	−524.560	−504.906	−511.814	

arrangements, featured by an increasing heterogeneity level, from two to ten alternating layers. The results obtained by the TEST code are, once again, consistent with the reference ones, suggesting the code correct behaviour also for strong heterogeneous

media.

Table 2.8: *First four α eigenvalues, in ms^{-1}, for a heterogeneous slab evaluated with P_7 and S_8 models using 101 spatial meshes and Mark boundary conditions, compared to the reference results by Modak and A. Gupta (2003).*

layer width [mfp]	α mode	P_7	S_8	ref. S_8
5.0	0	−551.530	−551.528	−551.429
	1	−1708.303	−1709.011	−1711.49
	2	−2949.523	−2952.764	−2943.99
	3	−5231.261	−5244.641	−5282.34
2.5	0	−703.854	−703.803	−703.578
	1	−1450.967	−1451.376	−1453.15
	2	−3077.478	−3081.021	−3072.82
	3	−5218.135	−5231.336	−5269.25
1.0	0	−750.021	−749.926	−749.672
	1	−1557.749	−1558.165	−1560.62
	2	−2969.154	−2972.262	−2963.23
	3	−5138.743	−5151.476	−5187.72
0.5	0	−759.226	−759.151	−758.893
	1	−1568.920	−1569.365	−1571.89
	2	−2984.970	−2988.137	−2978.99
	3	−5167.054	−5179.958	−5217.64
0.1	0	−763.890	−763.901	−763.640
	1	−1573.858	−1574.380	−1576.95
	2	−2990.283	−2993.509	−2984.29
	3	−5172.618	−5185.563	−5223.82

In order to verify the capability of the numerical code to handle also the energy effects and to check the implementation of the density eigenvalue δ, the region-wise integral spectral ratio for the α, γ, δ and k eigenvalue have been benchmarked with the ones evaluated in Cacuci, Ronen, et al. (1982). In this paper, co-authored by Ronen, Shayer, Wagschal and Yeivin, who first formulated the density eigenvalue δ, the energy spectral effects arising from the solution of the eigenvalues mentioned above are examined, focusing on the spectrum-hardness hierarchy. In order to better understand the rôle of the eigenvalues in the neutron balance and, thus, on their energy behaviour, they examine the effects of a set of perturbations with different features on a reflected, thermal reactor.

Table 2.9 provides a selection of some cases presented in the paper. For all the cases,

Table 2.9: *Comparison for the spectral ratios of the various eigenvalue formulations for a two-group, reflected slab subjected to different perturbations. The reference values are taken from (Cacuci, Ronen, et al., 1982).*

perturbation	eigenvalue formulation	Integral spectral index					
		% rel. diff. in core			% rel. diff. in reflector		
		P_3	S_4	ref. S_4	P_3	S_4	ref. S_4
-10% reactor dimensions	α	2.43	2.43	2.41	−3.53	−3.53	−3.47
	γ	1.90	1.90	1.88	−4.29	−4.29	−4.24
	δ	0.00	0.00	0.00	0.00	0.00	0.00
	k	−0.89	−0.89	−0.90	−7.57	−7.57	−7.52
+10% reactor dimensions	α	−1.92	−1.91	−1.91	3.51	3.51	3.41
	γ	−1.51	−1.51	−1.50	4.69	4.70	4.14
	δ	0.00	0.00	0.00	0.00	0.00	0.00
	k	0.64	0.64	0.63	7.41	7.41	7.29
-10% reflector dimensions	α	−0.05	−0.05	−0.03	−6.57	−6.57	−6.32
	γ	−0.12	−0.12	−0.11	−6.69	−6.69	−6.44
	δ	−0.40	−0.40	−0.38	−6.02	−6.02	−5.78
	k	−0.54	−0.54	−0.52	−7.18	−7.18	−6.93
+10% reflector dimensions	α	0.04	0.04	0.06	6.43	6.43	6.54
	γ	0.11	0.11	0.12	6.55	6.55	6.66
	δ	0.37	0.37	0.38	5.86	5.86	5.99
	k	0.48	0.48	0.48	7.09	7.09	7.19

there is generally a good agreement between the P_3 and the S_4 models and the reference S_4 calculations, despite no information on the number of spatial meshes and on the numerical eigenvalue solver is available in the original article. Postponing any consideration on the eigenvalue energy spectra to the next chapter, it is worth noticing that, when the whole reactor dimensions are varied, the δ eigenvalue and, thus, the associated spectral index remains constant, being invariant under the geometrical scaling of the system. In addition to these numerical data, the benchmark also involves the analysis of the energy spectra hierarchies, which are depicted in 2.3 for a close-to-critical and an off-critical cases. As expected, the spectral indexes are basically the same when the system is close to criticality, while the ones for the super-critical case seem to match the original ones presented in Cacuci, Ronen, et al. (1982).

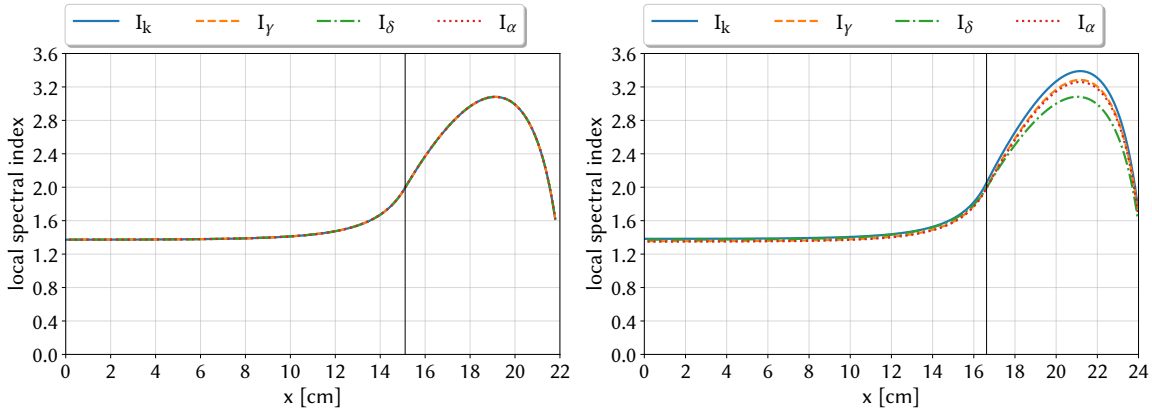

Figure 2.3: *Local spectral index for α, γ, δ and k eigenvalue problems for a close-to-critical (left) and a super-critical (right), computed with the P_3 model imposing Mark boundary conditions. The number of spatial meshes adopted in each reflector regions is 150, while 200 are employed in the core region. For the sake of brevity, only the positive half of the slab is showed.*

2.6.3 The influence of boundary conditions and of the parity order on the angular convergence

As mentioned previously, the transport calculations can be strongly affected by both the boundary conditions and the parity order adopted in the model. In order to shed some light on these aspects, from both the numerical and the physico-mathematical standpoints, and to provide some reference data to fill the gap in the literature, this section reports the eigenvalue calculations pertaining to a two-group homogeneous slab. To ensure the results reproducibility, table 2.10 provides the physical constants employed in the calculations, taken from the collection of critical problems available in Sood, Forster, and Parsons (2003). Since the reference deals with critical systems, assumed to be in equilibrium, the decay constants of the precursors and the physical delayed neutron fractions are not provided. Some physically reasonable data for the missing ones are provided in tables 2.10 and 2.11. For the sake of simplicity, the prompt and the delayed neutrons are assumed to have equal fission spectra.

The angular convergence trend of the fundamental α, γ, δ, θ, k and ω eigenvalues computed with the P_N and S_{N+1} models are showed in figures 2.4 and 2.5. These two sets of calculations are obtained imposing Mark boundary conditions and using 121 spatial meshes. With respect to the S_{N+1} case, fig. 2.4 shows two sets of bars for the even parity order, one for each possible set of discrete directions used in the Mark boundary conditions. As mentioned previously (see 2.4.3), option A stands for the non-zero roots of $P_{N+1}(\mu)$, while option B indicates the roots of $P_N(\mu)$. This double choice for the discrete directions is a peculiarity of the P_N model, as in the S_{N+1} case the incoming directions are enforced by the angular discretisation. By inspection of these figures, it is evident

ν_1	Σ_1	$\Sigma_{f,1}$	$\Sigma_{1\to1}$	$\Sigma_{1\to2}$	χ_1	v_1^{-1}
3.1	0.22080	0.09360	0.07920	0.04320	0.575	4.53849E-08
ν_2	Σ_2	$\Sigma_{f,2}$	$\Sigma_{2\to1}$	$\Sigma_{2\to2}$	χ_2	v_2^{-1}
2.93	0.33600	0.08544	0	0.23616	0.425	2.18142E-06

Table 2.10: *Two-group constants, taken from Sood, Forster, and Parsons (2003), for the two-group Pu-239 slab used as the case study presented in this section. The data have their usual dimensions, i.e. cross sections are given in cm^{-1}. The critical thickness for such system is approximately equal to to 3.5912040 cm (0.792938 mfp).*

i	λ_i $[s^{-1}]$	β_i $[-]$
1	0.0133826	$8.86440 \cdot 10^{-05}$
2	0.0308055	$6.75625 \cdot 10^{-04}$
3	0.1170030	$5.37368 \cdot 10^{-04}$
4	0.3066840	$1.22693 \cdot 10^{-03}$
5	0.8780670	$7.10462 \cdot 10^{-04}$
6	2.9378800	$2.50592 \cdot 10^{-04}$

Table 2.11: *Precursors decay constants and delayed neutron fraction for each family of precursors.*

that the even P_N/odd S_{N+1} overestimate the eigenvalues, while the odd P_N/even S_{N+1} do the opposite. Due to this behaviour, it can be concluded that, with this setup of the problem, the odd- and the even-order estimates of the eigenvalues envelop the asymptotic ($N\to\infty$) result. This feature is very important for at least two reasons:

(i) it provides a confidence range for the asymptotic value

(ii) it can be used to accelerate convergence.

Qualitatively, the same behaviour can be observed as well for one-group case, despite it is not reported here for the sake of conciseness (see Abrate, Burrone, et al., 2021).

A physical justification for this peculiarity can lie in the fact that the directions obtained solving the roots of odd-order $P_{N+1}(\mu)$ are more forward peaked than the ones obtained with the preceding even-order $P_N(\mu)$, as visible in table 2.12. Intuitively, the extrapolation distance associated to option A is associated to a larger value, which means that the leakages through the boundaries are reduced. This explanation is consistent with both the trend of the eigenvalues, which behave as the system was super-critical, and the lack of correlation between this phenomenon and the number of energy groups, as the vacuum boundary conditions are imposed group-wise. As a practical example,

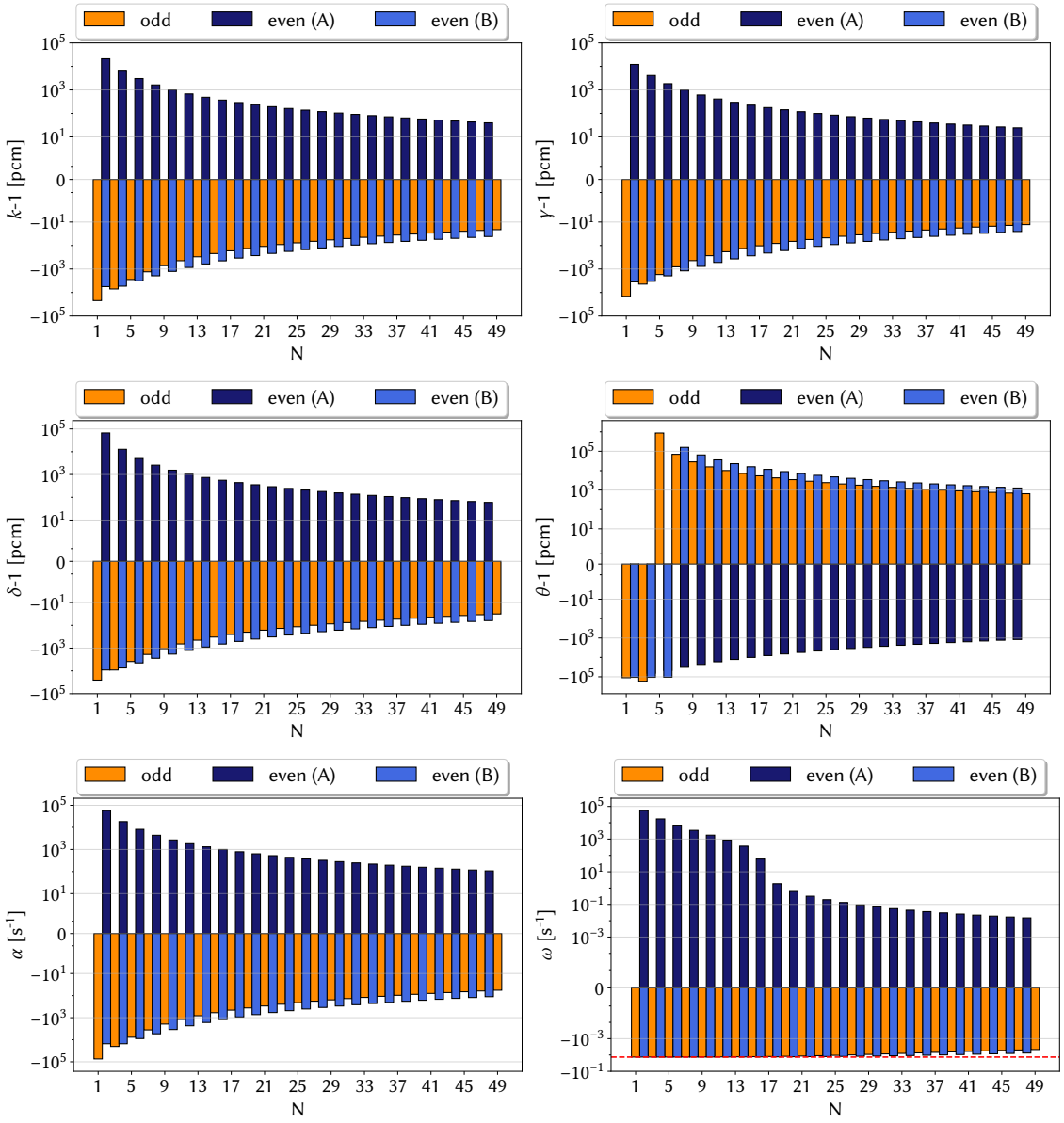

Figure 2.4: *Angular convergence trend for the fundamental values of k, γ, δ, θ, α and ω, computed with the* P_N *model imposing Mark boundary conditions.*

it is possible to look at the one-speed P_1 and P_2 models. Assuming a non-multiplying medium featured by isotropic scattering, the two models lead to the following equations, respectively:

$$\begin{cases} \dfrac{d\phi_1}{dx} + \Sigma\phi_0 = \Sigma_s\phi_0 \\ \dfrac{1}{3}\dfrac{d\phi_0}{dx} + \Sigma\phi_1 = 0, \end{cases} \tag{2.85}$$

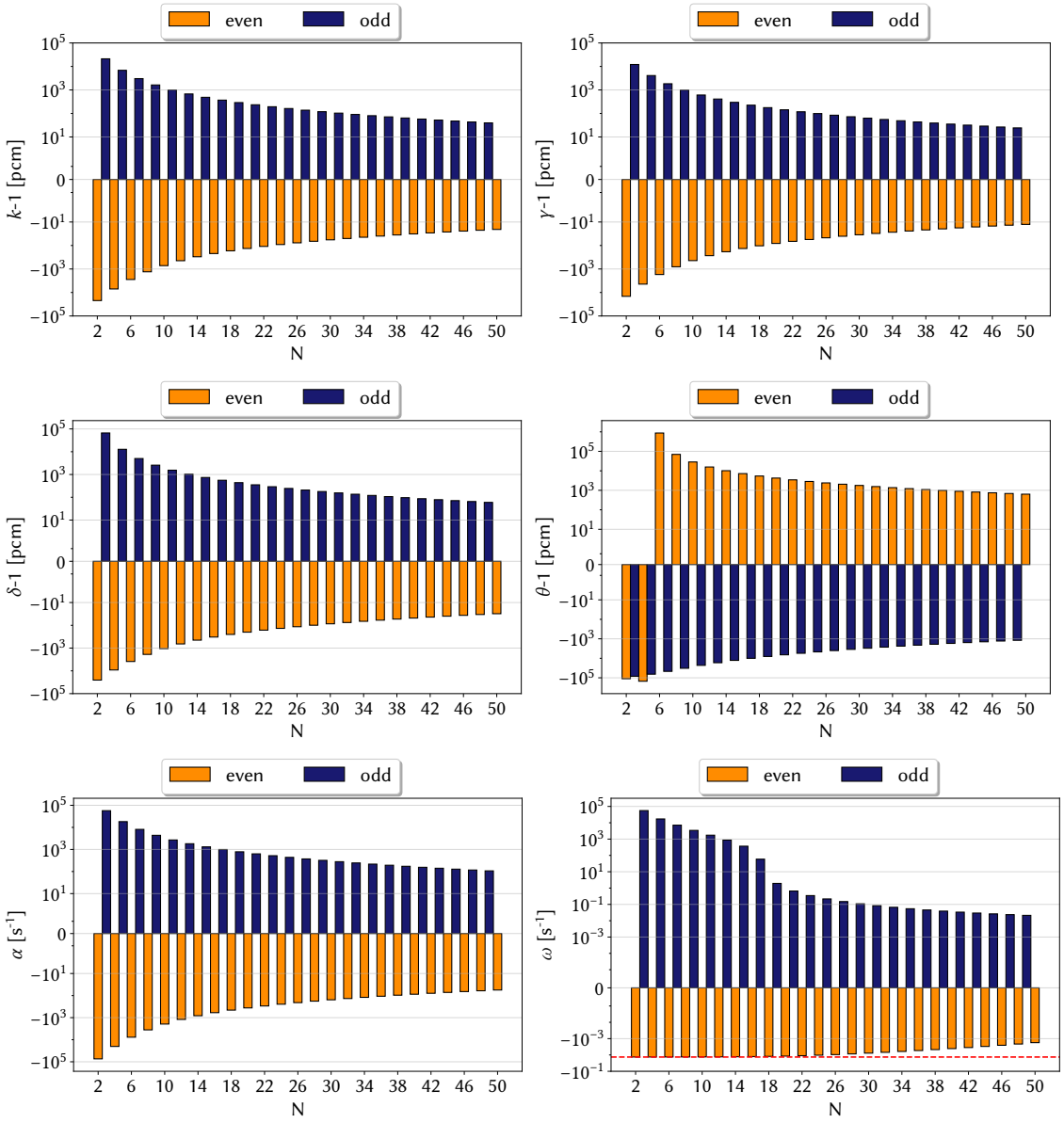

Figure 2.5: *Angular convergence trend for the fundamental values of k, γ, δ, θ, α and ω, computed with the* S_N *model imposing Mark boundary conditions.*

$$\begin{cases} \dfrac{d\phi_1}{dx} + \Sigma\phi_0 = \Sigma_s\phi_0 \\ \dfrac{2}{3}\dfrac{d\phi_0}{dx} + \Sigma\phi_1 + \dfrac{2}{3}\dfrac{d\phi_2}{dx} = 0 \\ \dfrac{2}{5}\dfrac{d\phi_1}{dx} + \Sigma\phi_2(x) = 0. \end{cases} \tag{2.86}$$

With a limited amount of algebra, the systems can be manipulated to make their equivalence to the diffusion theory explicit,

$$\begin{cases} \dfrac{d\phi_1}{dx} = -(\Sigma - \Sigma_s)\phi_0 = -\Sigma_a\phi_0 \\ \phi_1 = -\dfrac{1}{3\Sigma}\dfrac{d\phi_0}{dx} = -D_{P_1}\dfrac{d\phi_0}{dx}, \end{cases} \tag{2.87}$$

$$\begin{cases} \dfrac{d\phi_1}{dx} = -(\Sigma - \Sigma_s)\phi_0 = -\Sigma_a\phi_0 \\ \phi_1 = -\left(\dfrac{1}{3\Sigma} + \dfrac{4}{15}\dfrac{\Sigma_a}{\Sigma^2}\right)\dfrac{d\phi_0}{dx} = -(D_{P_1} + D_{P_2})\dfrac{d\phi_0}{dx} \\ \phi_2 = -\dfrac{2}{5\Sigma}\dfrac{d\phi_1}{dx} = +\dfrac{2}{5}\dfrac{\Sigma_a}{\Sigma}\phi_0, \end{cases} \tag{2.88}$$

where D_{P_1} and D_{P_2} are defined as in eqs. (2.74) and (2.75), respectively. For such models, the Mark boundary conditions imposed on the left boundary yields

$$\begin{aligned} \phi(x = 0, \mu_1) &= \sum_{n=0}^{1} \frac{2n+1}{2}\phi_n(x)P_N(\mu) = \\ &= \frac{1}{2}\phi_0(0) + \frac{3}{2}\mu_1\phi_1(0) = \\ &= \frac{1}{2}\phi_0(0) - \frac{3}{2}\mu_1 D_{P_1}\left.\frac{d\phi_0}{dx}\right|_{x=0} = 0, \end{aligned} \tag{2.89}$$

$$\begin{aligned} \phi(x = 0, \mu_{1,*}) &= \sum_{n=0}^{2} \frac{2n+1}{2}\phi_n(x)P_N(\mu) = \\ &= \frac{1}{2}\phi_0(0) + \frac{3}{2}\mu_{1,*}\phi_1(0) + \frac{5}{2}\frac{1}{2}(3\mu_1^{*2} - 1)\phi_2(0) \\ &= \frac{1}{2}\phi_0(0) - \frac{3}{2}\mu_{1,*}(D_{P_1} + D_{P_2})\left.\frac{d\phi_0}{dx}\right|_{x=0} \\ &+ \frac{5}{4}\frac{2}{5}\left(3\mu_{1,*}^2 - 1\right)\frac{\Sigma_a}{\Sigma}\phi_0(0) = 0, \end{aligned} \tag{2.90}$$

where μ_1 is the positive root of P_2 and $\mu_{1,*}$ can be either the positive root of P_3 ($\mu_{1,A}$) or the positive root of P_2 ($\mu_{1,B}$). Due to the roots symmetry, analogous equations can be retrieved with the negative roots for the right boundary.

The extrapolated distance is defined as the ratio between the total flux and its derivative, which yields

$$d_{P_1} = 3\mu_1 D_{P_1} = \frac{\mu_1}{\Sigma}, \tag{2.91}$$

$$d_{P_2} = \frac{\frac{3}{2}\mu_{1,*}(D_{P_1} + D_{P_2})}{\frac{1}{2}\left(1 + (3\mu_{1,*}^2 - 1)\frac{\Sigma_a}{\Sigma}\right)} = \frac{\frac{\mu_{1,*}}{\Sigma} + \frac{4}{5}\frac{\Sigma_a}{\Sigma^2}\mu_{1,*}}{1 + (3\mu_1^{*2} - 1)\frac{\Sigma_a}{\Sigma}}. \tag{2.92}$$

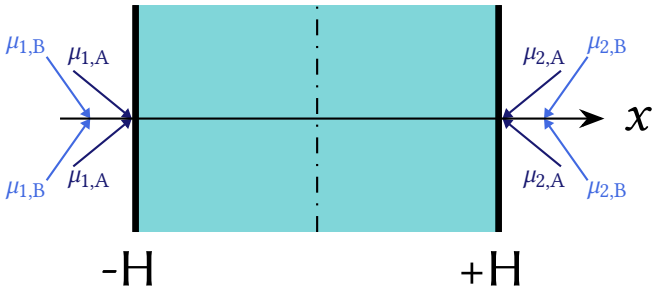

Figure 2.6: *Sketch of the one-dimensional slab and the different sets of discrete directions associated to the Mark boundary conditions applied to the* P_2 *model. The dark blue arrows, indicated as* μ_A*, are related to the roots of* $P_3(\mu)$*, while the light blue one, indicated as* μ_B*, are related to the non-zero roots of* $P_2(\mu)$*.*

Figure 2.6 provides a sketch of the incoming directions for options A and B, given with a slope such that the cosine of the angle between them and the x-axis is equal to μ_A and μ_B, respectively. In order to help the reader, the colours of the arrows also match with the colour of the histogram bars. Moreover, table 2.13 provides the trend of the extrapolated distance in relation to the approximation order and the chosen boundary condition option. Assuming to have a purely absorbing medium, the largest extrapolated distance is retrieved with option B. On the contrary, when a purely scattering medium is considered, option A provides the largest extrapolation distance, while option B provides the same distance as P_1. In an intermediate case, similar extrapolated distances are obtained using the two options for the even-order case. Therefore, eqs. (2.91) and (2.92) suggest that:

- the extrapolation distances are constant when P_1 and P_2 with option A are considered,
- d_{P_1} is always smaller than d_{P_2} with the same option.

To conclude, these observations induce to conclude that the eigenvalue convergence trend may be case-dependent when the even-order P_N exploits μ_B, while, when μ_A are used as incoming directions, the eigenvalue sequences estimated by an even approximation should converge always from the opposite side of the odd-order sequences. Similar considerations could be drawn for the S_N model, which is featured by the same behaviour. It is useful to remark here that, for this model, the incoming directions used to prescribed the Mark boundary conditions are the same set used to discretise the flying direction, i.e. the roots of $P_N(\mu)$, with even N.

In the case the roots of the even-order Legendre polynomial $P_N(\mu)$ are considered (option B), the eigenvalues are less accurate than the ones computed with the previous P_N order, yielding almost always to higher errors, with the exception of P_2 with respect to P_1. This fact may help reconsidering P_2 as a viable alternative to P_1.

N			
2	0.57735		
3	0.77459		
4	0.33998	0.86114	
5	0.53847	0.90618	
6	0.23862	0.66121	0.93247
7	0.40585	0.74153	0.94911

Table 2.12: *Positive roots for some Legendre polynomials $P_N(\mu)$ (Abramowitz and Stegun, 1964).*

cm^{-1}		P_1	P_2 (A)	P_2 (B)
Σ_a=0	d	0.57735	0.77460	1.03923
	D	0.33333	0.60000	0.60000
	d/L	0.99999	1.00000	1.34164
Σ_a=0.5	d	0.57735	0.77460	0.80829
	D	0.33333	0.46667	0.46667
	d/L	0.70710	0.80179	0.83666
Σ_a=1	d	0.57735	0.77460	0.57735
	D	0.33333	0.33333	0.33333
	d/L	0	0	0

Table 2.13: *Extrapolated distance d, expressed in cm^{-1}, diffusion coefficient D, expressed in cm^{-1}, and extrapolated distance to diffusion length L ratio, for P_1 and P_2 with options A and B for a medium with $\Sigma = 1$ cm^{-1}.*

Among the various eigenvalues, it should be noted the peculiar behaviour of θ and ω. The first one exhibits a quite irregular trend for small values of N, which can be explained looking at the nature of the capture eigenvalue. For N<5, due to the poor transport approximation, the system appears to be so sub-critical that negative values of θ arise. The physical interpretation of this situation is that the capture operator should introduce neutrons instead of removing them from the system. When the P_N model becomes sufficiently accurate, the trend becomes similar to the other eigenvalues, except for an opposite sign in the residual. Also this aspect can be justified by means of a physical consideration: when the system is slightly super-critical, the capture eigenvalue suggests to increase the capture cross sections ($\theta > 1$). On the contrary, the multiplication/collision/density eigenvalues suggest to decrease the fission production/collision production/density ($k > 1/\gamma > 1/\delta > 1$) of the system.

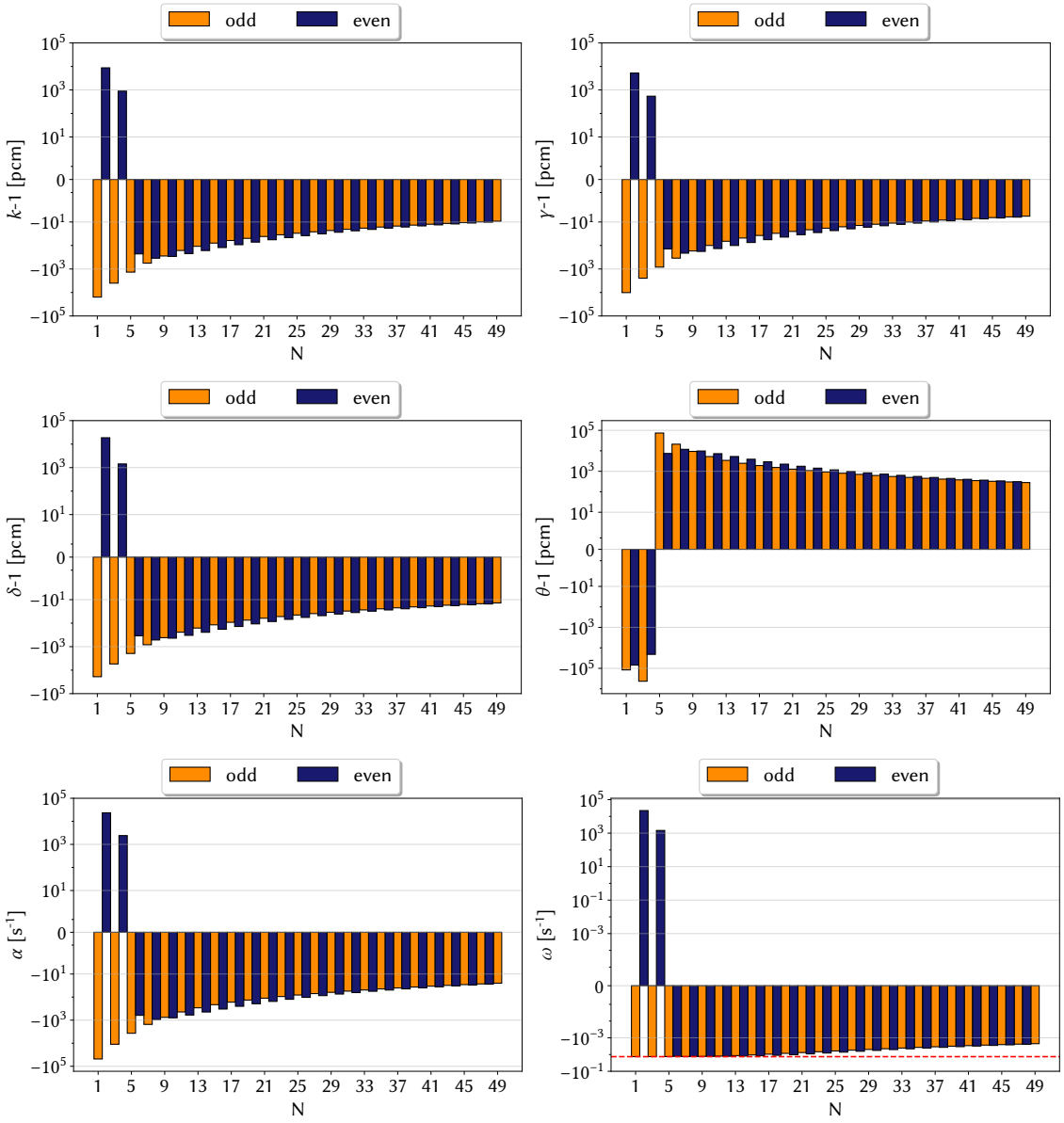

Figure 2.7: *Angular convergence trend for the fundamental values of k, γ, δ, θ, α and ω, computed with the* P_N *model imposing Marshak boundary conditions.*

Concerning the delayed time eigenvalue ω, the residual is strongly asymmetric, especially for negative values. Also this aspect has a physical justification, related to the existence of clusters of eigenvalues, associated to the delayed neutron precursors, which push the fundamental eigenvalue on the right of $-\lambda_1$, i.e. the smallest decay constant with opposite sign (Sanchez, Tomatis, et al., 2017; Sanchez and Tomatis, 2019). To highlight this constant, a dashed red line is showed on the graphs for ω. The main features

of each eigenvalue formulations, especially the newly introduced capture eigenvalue, will be analysed in more detail in chapter 3.

At last, fig. 2.7 provides the convergence trend in the case Marshak boundary conditions are used in the P_N model. In this case, a regular convergence pattern can be observed only for N>5. From this value onward, both even- and odd-order approximations underestimate the eigenvalues with respect to the reference. For N<5, it is worth noticing that, contrarily to the historical disfavour for the even-approximations (Davison and Sykes, 1957; Case and Zweifel, 1967), the first four even order approximations provide better results than the previous odd-order calculation.

N	k [-]	γ [-]	δ [-]	θ [-]	α s^{-1}	ω $^{-1}$
201	0.9999757396	0.9999851980	0.9999636225	1.0007381602	-6.5566304223	-6.243417E-04
202	0.9999798359	0.9999876973	0.9999697648	1.0006134436	-5.4495411470	-5.207699E-04
401	0.9999781586	0.9999866739	0.9999672495	1.0006645059	-5.9028576703	-5.632693E-04
402	0.9999804984	0.9999881015	0.9999707578	1.0005932757	-5.2704980078	-5.039507E-04
601	0.9999786556	0.9999869772	0.9999679947	1.0006493741	-5.7685302820	-5.506890E-04
602	0.9999799800	0.9999877852	0.9999699804	1.0006090570	-5.4106092928	-5.171149E-04
801	0.9999788751	0.9999871111	0.9999683238	1.0006192907	-5.7092086649	-5.451298E-04
802	0.9999796438	0.9999875801	0.9999694764	1.0006426917	-5.5014640514	-5.256448E-04
1001	0.9999789882	0.9999871801	0.9999684934	1.0006392488	-5.6786445762	-5.422648E-04

Table 2.14: *Values of fundamental k, γ, δ, θ α and ω for various P_N orders and Marshak boundary conditions using 121 spatial meshes.*

To complement the analysis on the angular convergence trend, and to fill a gap in the data available in the literature, tables 2.15 and 2.14 provides the eigenvalues estimated computed with the P_N approach imposing Mark and Marshak boundary conditions and using relatively high approximation orders. These tables allow to appreciate the same convergence trend shown in figs. 2.4-2.7 for large values of N. Up to P_{202}, when using Mark boundary conditions, option A, k, γ and δ are still larger than the reference, while, from P_{401} onward, both options A and B underestimate the reference, suggesting that there is a certain order for which the error is minimum. A similar behaviour occurs also for θ, α and ω, although the latter keeps always the same sign. This trend is probably due to the limited accuracy in the slab critical thickness, which is given in Sood, Forster, and Parsons (2003) with only 5 significant digits. Finally, it is possible to appreciate that, due to the presence of the delayed neutron precursors, ω approaches zero more rapidly than the prompt time eigenvalue α.

2.6.4 Benchmark with the Monte Carlo approach using the Wynn-ε acceleration scheme

In this section, the possibility of accelerating the convergence of the P_N numerical model using the Wynn-ε (W-ε) is investigated, exploiting the observations made about

N	BC	k [-]	γ [-]	δ [-]	θ [-]	α s^{-1}	ω s^{-1}
201		0.9999678725	0.9999803980	0.9999518269	1.0009777748	-8.6828282535	-8.211782E-04
202	A	1.0000077738	1.0000047430	1.0000116573	0.9997637126	2.1009131707	2.057052E-04
	B	0.9999622839	0.9999769882	0.9999434487	1.0009841499	-10.1932439604	-9.593605E-04
401		0.9999755828	0.9999851023	0.9999633873	1.0007429337	-6.5990034889	-6.282912E-04
402	A	0.9999879542	0.9999926505	0.9999819373	1.0003663695	-3.2554890613	-3.133042E-04
	B	0.9999758138	0.9999852433	0.9999637337	1.0005520931	-6.5365820922	-6.224728E-04
601		0.9999772297	0.9999861072	0.9999658567	1.0006927865	-6.1538958367	-5.867509E-04
602	A	0.9999835466	0.9999899613	0.9999753284	1.0005004937	-4.4466753337	-4.263066E-04
	B	0.9999777461	0.9999864223	0.9999666310	1.0004873488	-6.0143364578	-5.737018E-04
801		0.9999779404	0.9999865408	0.9999669223	1.0006711487	-5.9618235960	-5.687884E-04
802	A	0.9999817887	0.9999888887	0.9999726924	1.0005540003	-4.9217874910	-4.711359E-04
	B	0.9999783105	0.9999867666	0.9999674772	1.0004686704	-5.8618085744	-5.594263E-04
1001		0.9999783238	0.9999867747	0.9999674972	1.0006594767	-5.8582115034	-5.590894E-04

Table 2.15: *Values of fundamental k, γ, δ, θ, α and ω for some large* P_N *orders and Mark boundary conditions using 121 spatial meshes.*

the angular convergence behaviour with respect to the boundary conditions and to the parity order. The W-ε acceleration scheme belongs to the family of the so-called Shanks accelerations (Shanks, 1955), extremely powerful non-linear techniques to estimate the asymptotic limit/anti-limit of a numerical convergent/non-convergent sequence A_m more efficiently than a brute-force, consecutive approach. The sequence to be accelerated can be constituted by the successive truncated sums of series, by the iterative approximations to the roots of a function or by the solutions of a differential equation via numerical discretisation (Hamming, 1986), as the application presented in this section. In this last case, it is well-known that, due to the numerical discretization and to the iterative solution algorithm, the final elements of the sequence will be affected by both residual errors and by round-off errors. Convergence acceleration is helpful to "clean" the solution from these errors, acting as a constructive sensitivity study on the error arising from a certain numerical procedure. Contrarily to standard sensitivity studies, which only provide general information, the sequence acceleration should introduce a systematic correction in the solution, thus improving its convergence.

Following the basic idea behind the Padé approximant (m, n), which yields the best approximation of a certain function as the ratio of an m-th degree polynomial to an n-th degree polynomial, Shanks proposed to apply the following non-linear transformation in order to enhance the convergence properties of a slowly convergent sequence S_m,

$$\hat{S}A_m = \frac{A_{m+1}A_{m-1} - A_m^2}{A_{m+1} - 2A_m + A_{m-1}}. \tag{2.93}$$

Iterative applications of the Shanks operator $\hat{\mathcal{S}}^R A_m = \hat{\mathcal{S}}\hat{\mathcal{S}} \dots \hat{\mathcal{S}} A_m$ increasingly speed up the convergence, at the price of the calculation of the ratio of two determinants,

$$\hat{\mathcal{S}}^R A_m = \frac{\begin{vmatrix} A_{m-R} & \cdots & A_{m-1} & A_m \\ \Delta A_{m-R} & \cdots & \Delta A_{m-1} & \Delta A_m \\ \Delta A_{m-R+1} & \cdots & \Delta A_m & \Delta A_{m+1} \\ \vdots & & \vdots & \vdots \\ \Delta A_{m-1} & \cdots & \Delta A_{m+R-2} & \Delta A_{m+R-1} \end{vmatrix}}{\begin{vmatrix} 1 & \cdots & 1 & 1 \\ \Delta A_{m-R} & \cdots & \Delta A_{m-1} & \Delta A_m \\ \Delta A_{m-R+1} & \cdots & \Delta A_m & \Delta A_{m+1} \\ \vdots & & \vdots & \vdots \\ \Delta A_{m-1} & \cdots & \Delta A_{m+R-2} & \Delta A_{m+R-1} \end{vmatrix}}, \tag{2.94}$$

where $\Delta A_m = A_{m+1} - A_m$ (Graves-Morris, Roberts, and Salam, 2000).

Thanks to Wynn (1956), the R-th Shanks transformation can be computed very efficiently exploiting the following recursive formula,

$$\varepsilon_{r+1}^{(m)} = \varepsilon_{r-1}^{(m+1)} + \frac{1}{\varepsilon_r^{(m+1)} - \varepsilon_r^{(m)}} \qquad r = 0, \dots, 2R-1, \tag{2.95}$$

with $\varepsilon_{-1}^{(m)}$=0. Figure 2.8 provides a graphical sketch reproducing the behaviour of the W-ε algorithm. The first column corresponds to the M elements constituting the sequence, while the following columns are the elements of the transformed sequence. Since $\varepsilon_{2R}^{(m)} = \varepsilon_{2R}(A_m)$ is equivalent to $\hat{\mathcal{S}}^R A_m$, the last entry of each odd column is, progressively, the result of the Shanks transformation, which yields a better and better approximation to the limit of the sequence, until $\varepsilon_{2R}^{(m)} = \hat{\mathcal{S}}^R A_m$. One of the most remarkable features of this algorithm is that there is no constraint on the sequence index, i.e. irregular strides can be used. Moreover, thanks to the structure of Wynn's scheme, the approximation limit can be updated on-the-fly as more elements of the sequence are provided. However, since the asymptotic value of the sequence is not known *a priori* and there is a lack of a thorough theory on convergence acceleration Sidi, 2003, reference results are needed to actually verify that the convergence acceleration work for a specific application, despite the W-ε scheme is considered the best all-purpose acceleration tool currently available (Graves-Morris, Roberts, and Salam, 2000).

In this specific application, the elements of the sequence are the solutions of a discretised eigenvalue problem, k in this specific case, $A_m = \hat{L}_m^{-1}\hat{F}_m\vec{\phi}_m = k_{\text{eff},m}$, for $m = 0, \dots, M$. Since the P_N model depends both on the angular convergence order N and on the number of spatial points N_x, a fully converged solution should involve a sequence depending on these two parameters, namely $k_{\text{eff,N,N}_x}$. To the best of the author's knowledge, this is the first application of its kind in the field of numerical neutron transport. Therefore, to check the effectiveness of the whole procedure, the accelerated values are compared

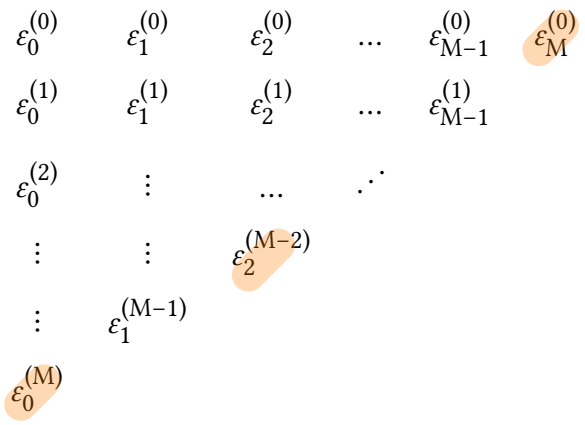

Figure 2.8: *Sketch of the Wynn-ε acceleration scheme based on eq. 2.95.*

to the outcome of a Monte Carlo simulation, which is usually taken as a numerical reference within its statistical uncertainty range. The choice of the k eigenvalue is closely related to the use of Monte Carlo and to a couple of other reasons:

1. concerning the solution of the eigenvalue problem by means of Krylov methods, k, together with γ, is featured by the largest convergence rate among the ones described so far. This reduces the computational burden for very large values of N and N_x;

2. k is the most popular eigenvalue, so studying the possibility to achieve high-precision values by means of the W-ε scheme is of great interest from a practical point of view;

3. k can be obtained quite easily with standard Monte Carlo codes, while the other formulations are rather uncommon and require *ad hoc* implementations. As an example, the α eigenvalue can be estimated using a recently developed algorithm involving the iterative solution of a k-eigenvalue problem (Zoia, Brun, and Malvagi, 2014; Vitali, 2020).

ν [-]	Σ_t [cm^{-1}]	Σ_f [cm^{-1}]	$\Sigma_{s,0}$ [cm^{-1}]	$\Sigma_{s,1}$ [cm^{-1}]	$\Sigma_{s,2}$ [cm^{-1}]
2.5	1	0.266667	0.7333333	0.2	0.075

Table 2.16: *One-group constants for a slab with critical thickness equal to 1.54064 cm, taken from Sood, Forster, and Parsons (2003).*

The convergence acceleration involves a quite large number of P_N calculations, with N ranging from 1 through 1000 for each of the seven spatial discretizations adopted

(N_x=10, 20, 40, 80, 160, 320, 640). These calculations are performed for the one- and two-group instances of the same critical slab, made of Pu-239, imposing both Marshak and Mark (A and B) boundary conditions. The group constants featuring the slab are taken again from Sood, Forster, and Parsons (2003) and reported in tables 2.10 and 2.16.

One of the challenges of this novel application of the W-ε algorithm is the definition of a suitable acceleration strategy that takes into account both the discretisation-related indexes of the k sequence. Since the scheme is non-linear, multiple acceleration strategies can be devised. The most intuitive are probably to accelerate along N and then N_x, or vice-versa. Alternatively, the acceleration could be performed along the diagonal of the dataset, combining the two indexes. An example of the dataset is displayed in table 2.17. The accelerations presented in this sections are all performed using the open-source *mpmath* Python package (Johansson et al., 2013) and verified against a Fortran77 code written by Prof. B. D. Ganapol (Ganapol, 2013).

Table 2.17: *Example of the dataset constructed to test the W-ε scheme, for the one-group case imposing Mark A boundary condition.*

N \ N_x	10	20	...	320	640
1	0.82077525	0.82136798	...	0.82153805	0.82153851
2	1.12788208	1.12838748	...	1.12853252	1.12853291
...	...	...	...	...	...
999	0.99782830	0.99937270	...	1.00001709	1.00002071
1000	0.99783010	0.99937445	...	1.00001848	1.00002180

Before performing the double accelerations, it is worth to compare the convergence history of the original and the accelerated sequences for the angle parameter. Figures

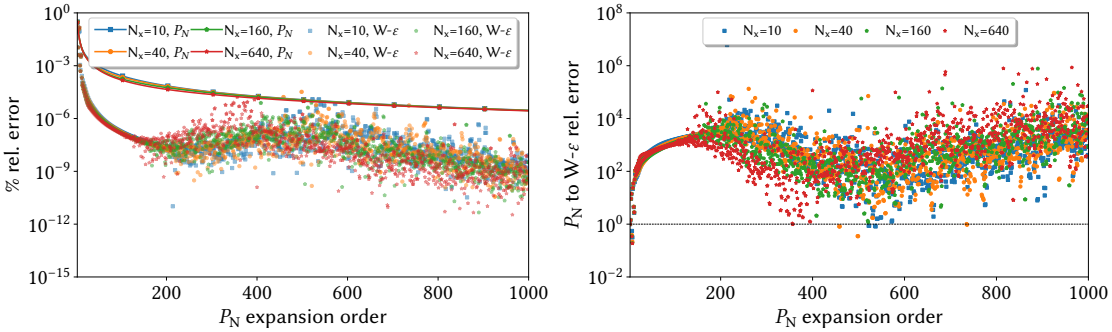

Figure 2.9: *Relative difference between two successive iterates for the original (solid) and accelerated (scatter) sequences on the left, original-to-accelerated sequences ratio on the right, for the two-group case imposing Mark A boundary conditions.*

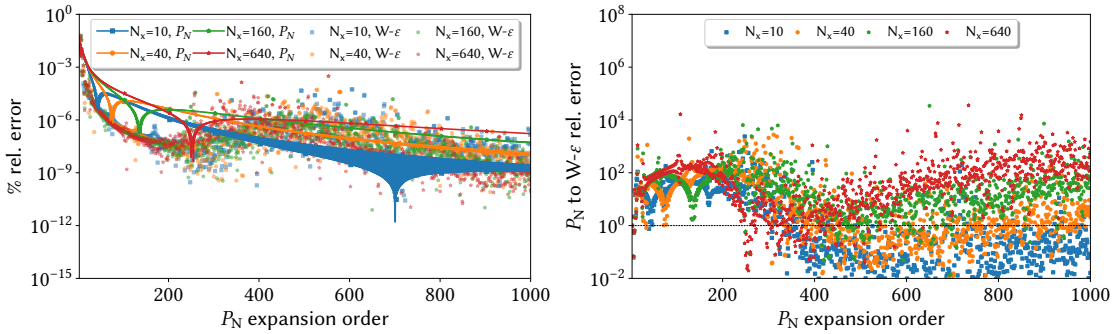

Figure 2.10: *Relative difference between two successive iterates for the original (solid) and accelerated (scatter) sequences on the left, original-to-accelerated sequences ratio on the right, for the two-group case imposing Mark B boundary conditions.*

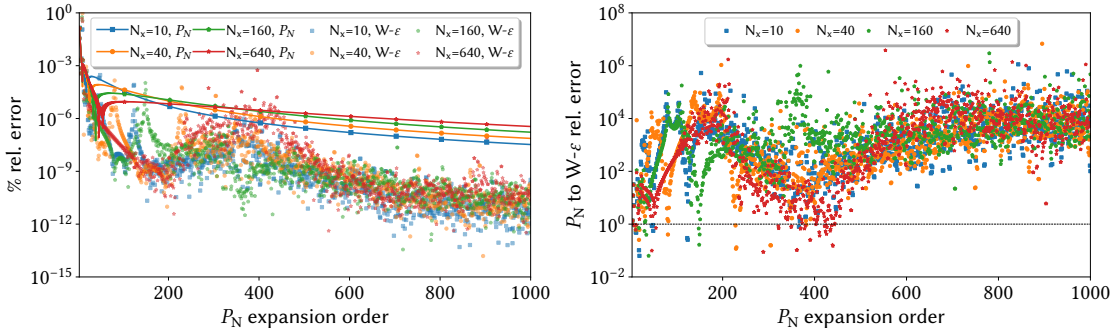

Figure 2.11: *Relative difference between two successive iterates for the original (solid) and accelerated (scatter) sequences on the left, original-to-accelerated sequences ratio on the right, for the two-group case imposing Marshak boundary conditions.*

2.9 to 2.11 provide useful information on the convergence acceleration process, considering the different boundary condition options. To this aim, the dataset is accelerated using moving windows that span 10 elements each, advancing one term at a time, e.g., $\{k_{\text{eff},1}, \ldots, k_{\text{eff},10}\}$ for the first window, $\{k_{\text{eff},2}, \ldots, k_{\text{eff},11}\}$ for the second one, and so on. This approach allows to distinguish the less precise, early elements from the more precise, following ones, aiming at reducing the numerical noise. The left graphs represent the relative residual r between two consecutive elements of the non-accelerated (solid line) and accelerated (coloured dots) sequences for every spatial discretizations case,

$$r_{i+1} = \frac{k_{\text{eff,i+1}} - k_{\text{eff,i}}}{k_{\text{eff,i+1}}} 100, \tag{2.96}$$

while the graphs on the right show the convergence gain (CG), defined as the ratio between the residual of the non-accelerated sequence and the residual of the accelerated one, $r_{\text{P}_\text{N}}/r_{W-\varepsilon}$. This last quantity is an important figure of merit to appreciate the effect of the convergence acceleration, which occurs when this ratio is larger than 1.

When Mark A boundary conditions are imposed, the residual for the original sequence, r_{P_N}, presents a quite smooth behaviour, with an unnoticeable difference concerning the spatial discretisation, while the W-ε residual initially exhibits a strong decay, below N=200, and then a significant spreading, probably due to the effect of the truncation error. Nevertheless, the effect of the W-ε acceleration can be appreciated *ictu oculi* looking at the CG, which yields values of $r_{W-\varepsilon}$ several orders of magnitude lower than the corresponding r_{P_N} ones. On the contrary, when Mark B boundary conditions are chosen, the acceleration is not very effective, especially for the sequences featured by the smallest number of meshes. The missing acceleration can be related to the oscillating behaviour featuring the original sequences for N_x=10, 40. These oscillations are progressively damped when the spatial mesh is refined. In this case, convergence acceleration is possible, as showed by the points for N_x=640 represented in right graph of fig. 2.10. Similar oscillations are present as well in the Marshak case, despite in a rather reduced fashion. For this last case, acceleration seems almost always effective, except for some tens of points falling below the dashed, black line delimiting the region with CG>1. Similar comments could be made also for the convergence histories and gains of the one-group case, which are omitted here for the sake of brevity. These observations are fully consistent with the angular convergence behaviour depicted in figs. 2.4-2.7, thus confirming the useful features observed for the Mark A boundary conditions with respect to the other two possibilities.

N_x	P_{1000}	W-ε(N)	W-ε(N_x)	W-ε(N, N_x)	W-ε(N_x, N)
10	0.99783010	0.99782900	0.99783010	0.99782900	0.99782900
20	0.99937445	0.99937338	0.99937445	0.99937338	0.99937338
40	0.99982891	0.99982786	1.00001840	1.00001737	1.00001737
80	0.99996565	0.99996462	1.00002451	1.00002349	1.00002349
160	1.00000653	1.00000554	1.00002401	1.00002304	1.00002305
320	1.00001848	1.00001760	1.00004181	1.00002140	1.00002698
640	1.00002180	1.00002112	1.00002257	1.00002257	1.00002237
diag. W-ε			1.0000224		
Monte Carlo			1.000022(3)		

Table 2.18: *Original (N=1000) and accelerated (N=1, … , 1000) sequences for the one-group problem, obtained imposing Mark A boundary conditions. The Monte Carlo result is provided with a confidence interval of 2σ, to be interpreted as ±3 on the last significant digit.*

Tables 2.18 to 2.22 provide a summary of the different acceleration strategies adopted to approach the Monte Carlo reference values, kindly provided by Dr. A. Zoia. The first column of each table provides the sequence for the best angular approximation, while the second and the third provide the results of the single W-ε accelerations, along N

N_x	P_{1000}	W-ε(N)	W-ε(N_x)	W-ε(N, N_x)	W-ε(N_x, N)
10	0.99813885	0.99813705	0.99813885	0.99813705	0.99813705
20	0.99947502	0.99947326	0.99947502	0.99947326	0.99947326
40	0.99984927	0.99984754	0.99999488	0.99999318	0.99999318
80	0.99995775	0.99995607	1.00000203	1.00000040	1.00000040
160	0.99998917	0.99998765	1.00000198	1.00000060	1.00000062
320	0.99999800	0.99999674	1.00000203	1.00000050	1.00000051
640	1.00000036	0.99999933	1.00000108	1.00000034	1.00000012
diag. W-ε			1.00000036		
Monte Carlo			1.0000003(3)		

Table 2.19: *Original (N=1000) and accelerated (N=1, … , 1000) sequences for the two-group problem, obtained imposing Mark A boundary conditions. The Monte Carlo result is provided with a confidence interval of 2σ, to be interpreted as ±3 on the last significant digit.*

and N_x, respectively. Finally, the last two columns stand for the double acceleration cases. As expected, due to the W-ε non-linearity, the acceleration order (N and then N_x or viceversa) has some impact on the final results, but only on the last three digits out of 8. This behaviour seems to suggest that the acceleration algorithm is robust, as it is only slightly dependent on the order of the discretisation indexes. The tables also report the extrapolated value obtained using a diagonal acceleration strategy, which has the considerable advantage of using a sequence of only 7 elements instead of 7000. The agreement between the double N-N_x acceleration and the reference Monte Carlo (MC) calculation is excellent, up to $2 \cdot 10^{-2}$ of pcm. This result is even more astounding considering that, in the original 7x1000 dataset obtained with Marshak boundary conditions, only 14 values are above 1, suggesting that the algorithm is really able to extrapolate the asymptotic result. The same occurs if the acceleration is performed diagonally. For this last case, a sensitivity analysis involving the selection of the diagonals is reported in table 2.20. The diagonal extrapolations yield very similar values, despite the different boundary conditions and the selection of different parity orders (only odd, even-odd and only even), suggesting once again the robustness of the method for this kind of application.

The different results are clearly summarised in figures 2.12 and 2.13, where the extrapolated values for the different sequences and acceleration strategies are compared to the Monte Carlo reference, given with its confidence interval. First, it is worth noticing that every case considered yields a value falling within the statistical uncertainty of the MC value, given as a 2σ confidence interval and represented by the shaded area. The first group of values on the left of each graph is the best P_N estimate, with N=1000 and N_x=640. The diagonal acceleration, displayed in the second group of fig. 2.12 and in the

N	15	31	63	125	249	499	999
Mark A, one-group				1.00002244			
Mark B, one-group				1.00002242			
Marshak, one-group				1.00002243			
Mark A, two-group				1.00000022			
Mark B, two-group				1.00000022			
Marshak, two-group				1.00000025			
N	14	31	62	125	250	501	1000
Mark A, one-group				1.00002251			
Marshak, one-group				1.00002250			
Mark B, one-group				1.00002244			
Mark A, two-group				1.00000036			
Mark B, two-group				1.00000016			
Marshak, two-group				1.00000021			
N	14	30	62	124	250	500	1000
Mark A, one-group				1.00002254			
Mark B, one-group				1.00002242			
Marshak, one-group				1.00002241			
Mark A, two-group				1.00000012			
Mark B, two-group				1.00000018			
Marshak, two-group				1.00000023			

Table 2.20: *Extrapolated values obtained through a diagonal acceleration involving increasing values of N (reported in the table) and N_x (10, 20, 40, 80, 160, 320, 640) and different boundary conditions. The one-group MC reference is 1.000022(3), while the two-group case is 1.0000003(3).*

last three groups of fig. 2.13 proves to be very effective, pushing the values on the expected value of the Monte Carlo calculation, despite the different boundary conditions. Figure 2.12 is very informative on the effect of the different non-diagonal acceleration strategies. When the extrapolation is performed along N, the effects due to the different boundary conditions disappear, leaving a bias with respect to the reference, related to the spatial discretisation. Similarly, when the acceleration involves the spatial discretisation for the N=1000 case, the values move towards the reference, but a bias due to both the boundary conditions and the P_N truncation is visible. At last, when the double W-ε acceleration is performed, most of the eigenvalues cluster around the Monte Carlo reference.

Comment on the use of W-ε to estimate the discretisation errors accelerating the

N_x	P_{1000}	W-ε(N)	W-ε(N_x)	W-ε(N, N_x)	W-ε(N_x, N)
10	0.99782891	0.99782890	0.99782891	0.99782890	0.99782890
20	0.99937330	0.99937329	0.99937330	0.99937329	0.99937329
40	0.99982780	0.99982776	1.00001733	1.00001727	1.00001728
80	0.99996461	0.99996453	1.00002352	1.00002340	1.00002339
160	1.00000561	1.00000545	1.00002318	1.00002296	1.00002296
320	1.00001771	1.00001740	1.00002693	1.00002496	1.00002308
640	1.00002111	1.00002104	1.00002084	1.00002257	1.00002171
diag. W-ε			1.0000224		
Monte Carlo			1.000022(3)		

Table 2.21: *Original (N=1000) and accelerated (N=1, … , 1000) sequences for the one-group problem, obtained imposing Marshak boundary conditions. The Monte Carlo result is provided with a confidence interval of 2σ, to be interpreted as ±3 on the last significant digit.*

N_x	P_{1000}	W-ε(N)	W-ε(N_x)	W-ε(N, N_x)	W-ε(N_x, N)
10	0.99813691	0.99813689	0.99813691	0.99813689	0.99813689
20	0.99947314	0.99947310	0.99947314	0.99947310	0.99947310
40	0.99984749	0.99984739	0.99999318	0.99999303	0.99999303
80	0.99995615	0.99995593	1.00000059	1.00000026	1.00000026
160	0.99998781	0.99998749	1.00000084	1.00000043	1.00000055
320	0.99999681	0.99999664	1.00000067	1.00000038	1.00000040
640	0.99999923	0.99999920	0.99999990	1.00000047	1.00000013
diag. W-ε			1.00000021		
Monte Carlo			1.0000003(3)		

Table 2.22: *Original (N=1000) and accelerated (N=1, … , 1000) sequences for the two-group problem, obtained imposing Marshak boundary conditions. The Monte Carlo result is provided with a confidence interval of 2σ, to be interpreted as ±3 on the last significant digit.*

other indexes, citing paper SIMMER-FRENETIC as an example of WE for this purpose. The diagonal seems the best but partial accelerations can be useful for code qualification

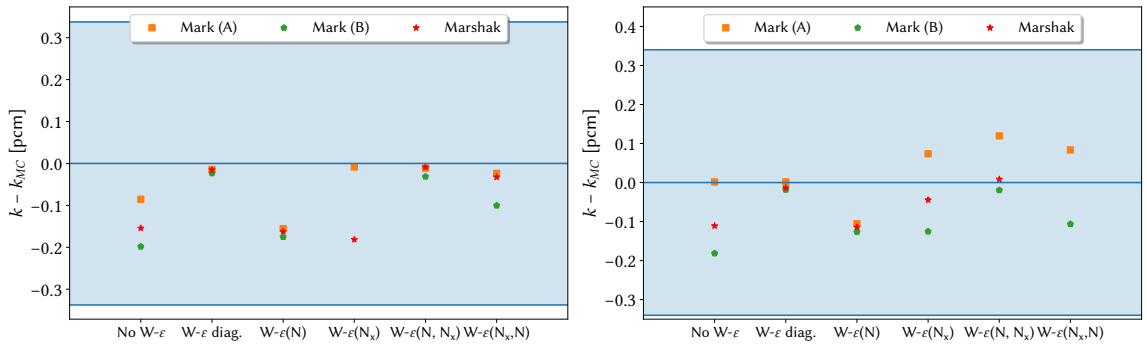

Figure 2.12: *Differences between the k_{eff} values and the Monte Carlo reference for the one- (left) and two-group (right) slab, with N ranging from 1 to 1000. The shaded area indicates the confidence interval of the Monte Carlo calculation.*

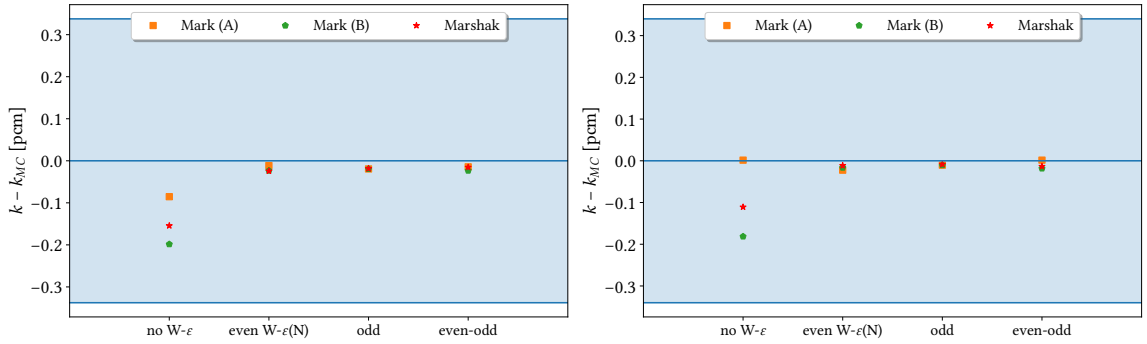

Figure 2.13: *Differences between the k_{eff} values and the Monte Carlo reference for the one- (left) and two-group (right) slab, with N ranging from 1 to 1000. The shaded area indicates the confidence interval of the Monte Carlo calculation.*

2.7 Conclusions

This chapter presented the numerical framework, based on the P_N and S_N multi-group models, used to solve the eigenvalue problem formulations arising in neuron transport. After proving the equivalence between the odd P_N equation and the succeeding even order P_{N+1}, the code numerical implementation is verified with several benchmark values taken from the available literature on the topic. Then, the impact of the boundary conditions and of the parity order on the angular convergence of the fundamental eigenvalues was assessed. In this case, it was interesting to show that, with a proper selection of the boundary conditions, it is possible to realise even and odd sequences that converge to the asymptotic value from two opposite directions. This interesting feature is thus exploited to study the possibility to accelerate the eigenvalue sequences, which suffers from the energy and spatial modelling error, to the asymptotic values. In this case, the Wynn-ε scheme is employed, showing its applications to

estimate the numerical errors.

References

Abramowitz, M. and I. A. Stegun (1964). "Handbook of Mathematical Functions with Formulas, Graphs, and Mathematical Tables". New York: Dover (cited on pages 23, 51).

Abrate, N., G. Bruna, S. Dulla, and P. Ravetto (2019). "Assessment of numerical methods for the evaluation of higher-order harmonics in diffusion theory". In: *Annals of Nuclear Energy* 128, pages 455–470 (cited on page 38).

Abrate, N., M. Burrone, S. Dulla, P. Ravetto, and P. Saracco (2021). "Eigenvalue Formulations for the P_N Approximation to the Neutron Transport Equation". In: *Journal of Computational and Theoretical Transport* 50, pages 407–429 (cited on page 46).

Abrate, N., S. Dulla, P. Ravetto, and P. Saracco (2021). "On some features of the eigenvalue problem for the P_N approximation of the neutron transport equation". In: *Annals of Nuclear Energy* 163, pages 108–477 (cited on page 36).

Arnoldi, W. E. (1951). "The principle of minimized iterations in the solution of the matrix eigenvalue problem". In: *Quarterly of Applied Mathematics* IX, pages 17–29 (cited on page 38).

Balay, S., S. Abhyankar, M. F. Adams, J. Brown, P. Brune, K. Buschelman, L. Dalcin, A. Dener, V. Eijkhout, W. D. Gropp, D. Karpeyev, D. Kaushikand, M. G. Knepley, D. A. Mayand, L. C. McInnes, R. T. Mills, T. Munson, K. Rupp, P. Sanan, B. F. Smith, S. Zampini, and H. Zhang (2020). *PETSc Users Manual*. Technical report ANL-95/11 - Revision 3.13. Argonne National Laboratory, Cass Ave, Lemont, IL (U.S.A.) (cited on page 38).

Bell, G. I. and S. Glasstone (1970). "Nuclear Reactor Theory". Van Nostrand Reinhold (cited on pages 18, 24, 26).

Bell, G. I., G. E. Hansen, and H. A. Sandmeier (1967). "Multitable Treatments of Anisotropic Scattering in SN Multigroup Transport Calculations". In: *Nuclear Science and Engineering* 28.3, pages 376–383 (cited on page 23).

Cacuci, D. G., Y. Ronen, Z. Shayer, J. J. Wagschal, and Y. Yeivin (1982). "Eigenvalue-dependent neutron energy spectra: definitions, analyses, and applications". In: *Nuclear Science and Engineering* 81, pages 432–442 (cited on pages 14, 43–44).

Carreño, A., A. Vidal-Ferrándiz, D. Ginestar, and G. Verdú (2017). "Spatial modes for the neutron diffusion equation and their computation". In: *Annals of Nuclear Energy* 110, pages 1010–1022 (cited on page 38).

Case, K. M. and P. L. Zweifel (1967). "Linear Transport Theory". Addison-Wesley, Reading (cited on pages 14, 33, 53).

Chandrasekhar, S. (1950). "Radiative transfer". London: Oxford University Press (cited on page 21).

Dahl, E. B., V. Protopopescu, and N. G. Sjöstrand (1983). "On the relation between decay constants and critical parameters in monoenergetic neutron transport". In: *Nuclear Science and Engineering* 83, pages 374–379 (cited on pages 41–42).

Davison, B. and J. B. Sykes (1957). "Neutron transport theory". Oxford: Clarendon Press (cited on pages 19, 53).

Deo, K., P. D. Krishnani, and R. S. Modak (2014). *Development of one-dimensional neutron transport theory code based on method of characteristics*. Technical report BARC/2014/E/015. Bhabha Atomic Research Centre, Mumbai (cited on pages 40–41).

Faris, G. W. (2005). "P_N approximation for frequency-domain measurements in scattering media". In: *Applied Optics* 44, pages 2058–2071 (cited on page 33).

Fermi, E. (1942). Technical report CP-283 (Chicago Project Report). Chicago University, Metallurgical Laboratory, Chicago, IL (cited on page 19).

Ferziger, J. H. and M. Peric (1999). "Computational methods for fluid dynamics". Springer, Berlin (cited on page 25).

Ganapol, B. (2013). "What Is Convergence Acceleration Anyway?" In: *Integral Methods in Science and Engineering*. Edited by C. Constanda, B. Bodmann, and H. Velho. New York: Birkhäuser (cited on page 57).

Gandini, A. (1978). "Higher order time-dependent generalized perturbation theory". In: *Nuclear Science and Engineering* 67, pages 91–106 (cited on pages 14, 37).

Graves-Morris, P. R., D. E. Roberts, and A. Salam (2000). "Epsilon algorithm and related topics". In: *Journal of Computational and Applied Mathematics* 122, pages 51–80 (cited on page 55).

Hamming, R. W. (1986). "Numerical Methods for Scientists and Engineers". Dover Publications, Inc. (cited on page 54).

Hanh, O. and F. Strassmann (1939). "Über den nachweis und das verhalten der bei der bestrahlung des urans mittels neutronen entstehenden erdalkalimetalle". In: *Naturwissenschaften* 27, pages 11–15 (cited on page 19).

Heizler, S. I. and P. Ravetto (2012). "SP_2 - asymptotic P_1 equivalence". In: *Transport Theory and Statistical Physics* 41, pages 304–324 (cited on page 34).

Henry, A. F. (1964). "The application of inhour modes to the description of non-separable reactor transients". In: *Nuclear Science and Engineering* 20, pages 338–351 (cited on page 18).

Hernandez, V., J. E. Roman, and V. Vidal (2005). "SLEPc: a scalable and flexible toolkit for the solution of eigenvalue problems". In: *ACM Transactions on Mathematical Software* 31, pages 351–362 (cited on page 38).

Johansson, F. et al. (2013). *mpmath: a Python library for arbitrary-precision floating-point arithmetic (version 1.2.0)* (cited on page 57).

Lathrop, K. D. (1968). "Ray effects in discrete ordinates equations". In: *Nuclear Science and Engineering* 32, pages 357–369 (cited on page 30).

Lathrop, K. D. and B. G. Carlson (1964). *Discrete ordinates angular quadrature of the neutron transport equation*. Technical report LA-3186. Los Alamos National Laboratory (LANL), Los Alamos, NM (U.S.A.) (cited on page 30).

Lehoucq, R., D. Sorensen, and C. Yang (1998). "ARPACK USERS GUIDE: solution of large scale eigenvalue problems by implicitly restarted Arnoldi methods". SIAM, Philadelphia (cited on page 38).

Lewis, E. E. and W. F. Miller (1984). "Computational methods of neutron transport". New York: Wiley (cited on pages 28, 30, 37).

Maillot, M., J. Tommasi, and G. Rimpault (2016). "Calculation of higher-order fluxes in symmetric cores—II: implementation". In: *Nuclear Science and Engineering* 184, pages 190–207 (cited on page 37).

Mark, C. (1945a). *The spherical harmonics method, method II - application to problems with plane and spherical symmetry*. CRT-338(Rev.) - AECL-490. Atomic Energy of Canada Ltd. Chalk River Project, Chalk River, Ontario (Canada) (cited on page 29).

— (1945b). *The spherical harmonics method, Part I - General development of the theory*. CRT-340(Rev.) - AECL-491. Atomic Energy of Canada Ltd. Chalk River Project, Chalk River, Ontario (Canada) (cited on page 29).

Marshak, R. E. (1947). "Note on the spherical harmonics method as applied to the Milne problem for a sphere". In: *Physical Review* 71, pages 443–446 (cited on page 29).

Meghreblian, R. V. and D. K. Holmes (1960). "Reactor Analysis". McGraw-Hill, New York (cited on page 21).

Modak, R. S. and A. Gupta (2003). "A simple scheme for the direct evaluation of time-eigenvalues of neutron transport equation". In: *Annals of Nuclear Energy* 30, pages 211–222 (cited on pages 38, 41–43).

Modak, R. S., H. P. Gupta, and V. K. Jain (1994). "A scheme for the evaluation of γ-modes of a neutron diffusion equation". In: *Annals of Nuclear Energy* 21, pages 195–199 (cited on pages 38–39).

Modak, R. S. and V. K. Jain (1996). "Sub-Space iteration scheme for the evaluation of λ-modes of finite-differenced multi-group neutron diffusion equations". In: *Annals of Nuclear Energy* 23, pages 229–237 (cited on page 37).

Modak, R. S., D. C. Sahni, and S. D. Paranjape (1995). "Evaluation of higher k-eigenvalues of the neutron transport equation by S_N method". In: *Annals of Nuclear Energy* 22, pages 359–366 (cited on pages 39–42).

Nowak, M., J. Miao, E. Dumonteil, B. Forget, A. Onillon, K. S. Smith, and A. Zoia (2016). "Monte Carlo power iteration: entropy and spatial correlations". In: *Annals of Nuclear Energy* 94, pages 856–868 (cited on page 37).

Rimpault, G., D. Plisson, J. Tommasi, R. Jacqmin, and J. Rieunier (2002). "The ERANOS code and data system for fast reactor neutronic analyses". In: *International Conference on Physics of Reactors, PHYSOR 2002, Seoul, South Korea*, pages 1134–1143 (cited on page 37).

Ronen, Y., D. Shalitin, and J. J. Wagschal (1976). In: Transactions of the American Nuclear Society.24, page 474 (cited on page 20).

Saad, Y. (1992). "Numerical methods for large eigenvalue problems". Manchester University Press (cited on pages 37–38).

Sanchez, R. and D. Tomatis (2019). "Analysis of α modes in multigroup transport". In: *International Conference on Mathematics and Computational Methods Applied to Nuclear Science and Engineering, M&C 2019, Portland, OR (U.S.A.)* Pages 1134–1143 (cited on page 52).

Sanchez, R., D. Tomatis, I. Zmijarevic, and H. G. Joo (2017). "Analysis of alpha modes in multigroup diffusion". In: *Nuclear Engineering and Technology* 49, pages 1259–1268 (cited on page 52).

Shanks, D. (1955). "Nonlinear Transformations of Divergent and Slowly Convergent Sequences". In: *Journal of Mathematics and Physics* 34, pages 1–42 (cited on page 54).

Sidi, A. (2003). "Practical Extrapolation Methods". Cambridge University Press (cited on page 55).

Singh, K. P., S. B. Degweker, R. S. Modak, and K. Singh (2011). "Iterative method for obtaining the prompt and delayed alpha-modes of the diffusion equation". In: *Annals of Nuclear Energy* 38, pages 1996–2004 (cited on page 38).

Sood, A., R. A. Forster, and D. K. Parsons (2003). "Analytical benchmark test set for criticality code verification". In: *Progress in Nuclear Energy* 42, pages 55–106 (cited on pages 45–46, 53, 56–57).

Tommasi, J., M. Maillot, and G. Rimpault (2016). "Calculation of higher-order fluxes in symmetric cores—I: theory". In: *Nuclear Science and Engineering* 184, pages 174–189 (cited on page 37).

Trefethen, L. N. and M. Embree (2005). "Spectra and pseudospectra:the behavior of non-normal matrices and operators". Princeton University Press (cited on page 13).

Vitali, V. (2020). "Monte Carlo analysis of heterogeneity and core decoupling effects on reactor kinetics: Application to the EOLE critical facility". PhD thesis. Université Paris-Saclay (cited on page 56).

Vondy, D. R. and T. B. Fowler (1983). "Solving the uncommon nuclear reactor Core neutronics problems". In: *Nuclear Science and Engineering* 83, pages 100–111 (cited on page 37).

Wick, G. (1943). "über ebene diffusionsprobleme". In: *Zeitschrift für Physik* 121, pages 702–718 (cited on page 21).

Wynn, P. (1956). "On a device for computing the $e_m(S_n)$ transformation". In: *Mathematical Tables and Other Aids to Computation* 10, pages 91–96 (cited on page 55).

Zinzani, F., C. Demaziére, and C. Sunde (2008). "Calculation of the eigenfunctions of the two-group neutron diffusion equation and application to modal decomposition of BWR instabilities". In: *Annals of Nuclear Energy* 35, pages 2109–2125 (cited on page 38).

Zoia, A., E. Brun, and F. Malvagi (2014). "Alpha eigenvalue calculations with TRIPOLI-4". In: *Annals of Nuclear Energy* 63, pages 276–284 (cited on page 56).

Chapter 3

The spectrum of the neutron transport operator and its application to group collapsing

> Perfection. That's what it's about. It's those moments. When you can feel the perfection of creation. The beauty of physics, you know, the wonder of mathematics. The elation of action and reaction, and that is the kind of perfection that I want to be connected to.
>
> Samuel T. Anders, Battlestar Galactica

3.1 Introduction

As mentioned in chapter 2, the eigenvalue analysis is a fundamental, well established tool in reactor physics. In addition to its classic applications, involving criticality approach, sensitivity analysis, modal expansion and perturbation theory, the solution of the eigenvalue problems described previously can be extremely valuable also for other purposes, e.g.,

1. showing the intimate behaviour of the transport operator through its eigenvalue spectrum
2. weighting the multi-group constants and the kinetic parameters
3. providing information concerning the stability of a system.

Despite their importance and huge potentialities, the adoption of the different eigenvalue formulations for these applications is rather scarce in the literature, except for the well known k and α formulations. Studies of the spectrum behaviour for these two eigenvalues can be found, for example, in Saracco, Dulla, and Ravetto, 2012, Sanchez, Tomatis, et al., 2017 and Dulla, Ravetto, and Saracco, 2018 for a diffusion theory framework, and in Sanchez and Tomatis, 2019 and McClarren, 2019 for a transport theory framework. Regarding the multi-group collapsing, the only alternative to k, which is the usual eigenvalue formulation used for this purpose despite it may provide poor results for off-critical systems, was proposed by Dugan, Zmijarevic, and Sanchez, 2016. In this work, the adoption of the fundamental α and ω modes as weighting functions is proposed, to account for the dynamic behaviour of the system when it is off-critical. Similarly to these two applications, the multiplication and time eigenvalues are the only formulations discussed in the literature for the spectral stability analysis of a multiplying system (Beckner and Rydin, 1975; Vitali, 2020; Pázsit and Dykin, 2018).

In this chapter, the different eigenvalue formulations addressed in chapter 2 will be investigated numerically, in order to highlight their peculiarities and to characterise them for the applications previously mentioned, possibly filling a gap in the literature on their possible uses. This chapter will present the different eigenvalue formulations more in detail, focusing on their spectral behaviour according to the numerical and modelling approximations to the neutron transport equation. The knowledge of the full spectrum of a certain eigenvalue formulation is usually not needed for most applications, which exploit only the dominant eigenpairs. However, analysing the eigenvalue spectrum allows to draw some useful indications for driving the eigenvalue solver towards the most interesting portions of the spectrum. Moreover, as it will be discussed in the chapter, the eigenvalue spectrum, being intimately related to the approximated transport operator, can provide a very rich information on the physics of the transport process.

As for chapter 2, part of the content of this chapter has been already published in a conference proceedings and in two peer-reviewed journal articles: the first one has been published on the special issue of Journal of Computational and Theoretical Transport dedicated to the International Conference on Transport Theory (ICTT) 2019, while the second one has been published on the special issue of Annals of Nuclear Energy dedicated to the memory of Massimo Salvatores,

- N. Abrate, M. Burrone, S. Dulla, P. Ravetto, P. Saracco, *"Study of the eigenvalue spectra of the neutron transport problem in P_N approximation"*, Proceedings of the PHYSOR 2020 conference, Cambridge (U.K.), in *EPJ Web of Conferences*, **247**, 2020

- N. Abrate, M. Burrone, S. Dulla, P. Ravetto, P. Saracco, *"Eigenvalue formulations for the P_N approximation to the neutron transport equation"*, Journal of Computational and Theoretical Transport, **50**, 2020

- N. Abrate, S. Dulla, P. Ravetto, *"On some features of the eigenvalue problem for the*

P_N approximation of the neutron transport equation", Annals of Nuclear Energy, **163**, 2021

3.2 The multiplication eigenvalue

As discussed in chapter 2, Fermi first approached criticality introducing an eigenvalue called *reproduction factor k* (Fermi, 1942) with the aim of controlling the recently discovered fission reaction (Hanh and Strassmann, 1939),

$$\hat{L}\varphi_{k,n} + (\hat{C} + \hat{F}_0 + \hat{S}_0)\varphi_{k,n} - \hat{S}\varphi_{k,n} = \frac{1}{k_n}\hat{F}\varphi_{k,n}. \tag{3.1}$$

When the system is *sub-critical*, the eigenvalue $k_0 < 1$ modifies the neutron production by fission increasing it, while, when the system is *super-critical*, $k > 1$ reduces the neutron production. The differences induced on the neutron distribution can be understood on physical basis: for example, remembering that neutrons emitted by fissions are fast, in the sub-critical case the increase in fission production will result in hardening of the energy spectrum characterising the system, while in the super-critical case the spectrum would soften. The criticality condition is satisfied when no modification of the fission operator is required, i.e. $k_0 = 1$. Since the reproduction factor depends on both the system geometry and composition, Fermi focused at first on the material properties of the reactor, which yields the reproduction factor of an infinite system, k_∞, via the four factor formula. Once the composition is such that $k_\infty > 1$, the critical size of the system can be estimated with the six factor formula, which accounts also for boundary effects.

The physical meaning of the reproduction factor, which is commonly known as *effective multiplication factor*, is straightforward. Integrating (3.1) over the phase space and isolating k_n, it is possible to get

$$k_n = \frac{\langle \hat{F}\varphi_{k,n} \rangle}{\langle (\hat{L} + \hat{R} - \hat{S})\varphi_{k,n} \rangle}, \tag{3.2}$$

which is the ratio between the number of neutrons produced by fission and the number of neutron losses. In addition to its physically meaningful interpretation, which is related also to other disciplines dealing with multiplying systems like epidemiology and demography (Adam, 2020; Shryock and Siegel, 1980), the reason that probably contributed the most to make the k-eigenvalue the main way of addressing criticality lies in the fact that its always yields a solution, provided that the system is multiplying. This property can be justified by a physical observation: whatever the configuration of a system is, as long as it contains a certain amount of fissile material, it is always possible to achieve criticality by adjusting its multiplying properties.

The fact that k_{eff} is the fundamental eigenvalue is also extremely convenient from a numerical point of view, as most algorithms for the solution of eigenvalue problems,

e.g., the power method described in chapter 2, are very efficient in computing the eigenvalues at the extremities of the spectrum.

Table 3.1: *Energy group structures employed in the following sections.*

group boundary [MeV]	CASMO-2	CASMO-4	CASMO-7
2.00×10^{1}	x	x	x
8.21×10^{-1}		x	x
5.53×10^{-3}		x	x
4.00×10^{-6}			x
6.25×10^{-7}	x	x	x
1.40×10^{-7}			x
5.80×10^{-8}			x
1.00×10^{-11}	x	x	x

These two physico-mathematical features can be appreciated looking at the k-spectrum in fig. 3.1 where the different numerical approximations to the neutron transport model, discussed in chapter 2, are employed. Figure 3.1a represents the spectra computed for a two-group, P_3 model using an increasing numbers of spatial meshes, fig. 3.1b shows the spectra obtained for a P_3 model discretised with 25 spatial meshes adopting different energy grid structures, while fig. 3.1c provides the spectra for increasing angular approximation orders, using the CASMO-4 grid for a system discretised with 25 spatial meshes. The details on the energy structures employed in these calculations are reported in table 3.1. Unless differently specified, the cross sections are collapsed on the CASMO energy grids starting from a set of cross sections scored on the CASMO-70 with the Serpent-2 Monte Carlo code (Leppänen, Pusa, et al., 2015).

The influence of the various numerical approximations on the spectrum, in this case, is rather predictable: more refined approximations introduce new degrees of freedom in the discretised operator, thus more eigenvalues appear, accumulating after some dominant, discrete eigenvalues. It is useful to recall here that the CASMO energy structures are nested, i.e. each grid contains the preceding one and additional groups, thus ensuring a consistent comparison among different energy group grids. Finally, fig. 3.1d provides a comparison between the P_1 and the S_2, which are formally equivalent only when no space discretisation occurs. As already stated in chapter 2, the discrepancy between the two sets of eigenvalues increases for the higher-order eigenvalue, associated to higher spatial frequencies.

Figure 3.2 provides an example of the spectrum behaviour when the system criticality and heterogeneity levels change. As one could reasonably expect from the previous physico-mathematical considerations, the three spectra in fig. 3.2a maintain the same shape and order, but they are shifted towards 0 or 1 according to the values of the fundamental, represented by the three stars. It is important to notice that the eigenvalues

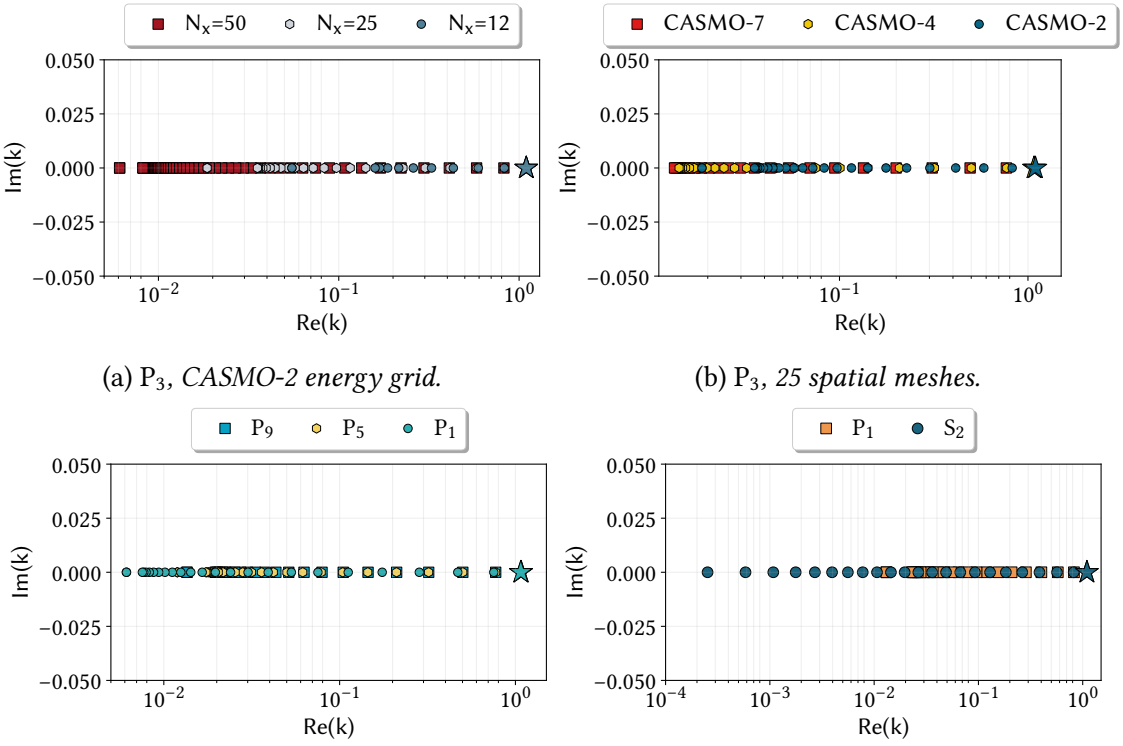

(a) P_3, *CASMO-2 energy grid.*

(b) P_3, *25 spatial meshes.*

(c) *CASMO-4 energy grid, 25 meshes.*

(d) *25 meshes and CASMO-2 energy grid.*

Figure 3.1: *k-spectrum for a homogeneous, isotropic, fissile slab, imposing Mark boundary conditions. The stars represent the fundamental eigenvalues.*

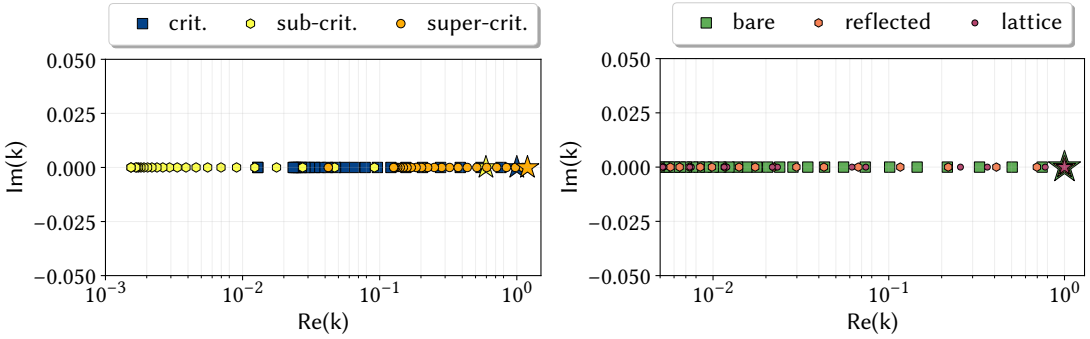

(a) *P_1, 25 meshes, Mark boundary conditions, CASMO-2 energy grid.*

(b) *P_3, 125 meshes, Mark boundary conditions, CASMO-7 energy grid.*

Figure 3.2: *k-spectrum for a homogeneous, isotropic slab featured by different thicknesses (left) and for a linearly anisotropic slab featured by different levels of heterogeneity (right). The stars represent the fundamental eigenvalues.*

for the sub-critical case are more separated with respect to the other two cases, when the values seem to shrink. Concerning fig. 3.2b, three slabs with equal thickness but different compositions and material arrangement have been considered, to appreciate the impact of the system heterogeneity on the spectrum shape: in the "bare" case, the slab is filled with the same fissile material used above, in the "reflected" case there are 30 cm of fuel surrounded, at both sides, by water, while in the "lattice" case there are alternating 10 cm thick layers of water and fuel. Except for a different separation between the eigenvalue, which is a fundamental parameter to assess the spatial stability of a multiplying system and that will be discussed in chapter 5, it is not possible to appreciate any substantial difference due to the presence of different media.

The spectra depicted in these figures are useful to show that the k-spectrum has three well established features:

- the spectrum is always real, consistently with the fact that it is always possible to attain criticality changing ν, provided that there is fissile material inside the system;
- the fundamental eigenvalue, i.e. the one associated to the eigenfunction with a uniform sign, is always the largest positive real value;
- the spectrum shape is rather insensitive to both the system features (energy spectrum, spatial heterogeneities, criticality level) and the transport approximations (number of groups, angular detail, spatial mesh), despite its pattern may shrink or inflate according to the system physical features, as it will be point out later in the chapter.

Due to its intuitiveness and to its nice properties, the k-eigenvalue formulation is the most popular one for a set of reactor physics applications ranging from multi-group collapsing to core-design. Nevertheless, despite its popularity, this spectral formulation has two main drawbacks, which are too often ignored:

- let us assume that an off-critical system is given. Since $k \neq 1$, it is known that something has to change to achieve criticality. As mentioned, k acts on the fission operator, so it changes the fission parameters. Since the fission cross sections must be consistent with the other data, i.e. eq. (2.2) must hold, k can be interpreted as a scaling factor acting on the number of neutrons emitted by fission, ν: the system can achieve criticality when $\nu \longrightarrow \nu/k_{\text{eff}}$. However, it is not possible to change ν, in practice, without actually changing the fuel composition itself and, thus, its fission cross section. As a consequence, in practical situations, the reactor physicist can only adjust the reactivity changing the system geometrical dimensions or relying on the control systems, e.g. the control rods. In this sense, the k eigenvalue does not provide any quantitative information that could guide the action of the controller;

- the fundamental k-eigenfunction $\varphi_{k,0}$ may be strongly inaccurate to describe the neutron spatial and energy distribution of the system, unless the system is close to criticality. The evaluation of the reproduction factor characterising a multiplying system, defined as the ratio between the populations of two successive generations $g-1$ and g, with Λ defined as the effective neutron generation time,

$$k^{(g)} = \frac{\left\langle \frac{\phi(x,E,\mu,t=g\Lambda)}{\mathrm{v(E)}} \right\rangle}{\left\langle \frac{\phi(x,E,\mu,t=(g-1)\Lambda)}{\mathrm{v(E)}} \right\rangle}, \tag{3.3}$$

  always makes sense, both in steady-state, where it would be unitary, and in transient conditions. However, the actual population distribution associated to $k^{(g)}$ for a system far from criticality could be extremely different from the one computed solving the k-eigenvalue problem, as this would provide the steady-state distribution for a system that is actually time-dependent, as brilliantly explained in Cullen, Little, et al. (2003).

3.3 The collision eigenvalue

To the author's knowledge, the second eigenvalue formulation proposed in the frame of the neutron transport equation can be found in Davison and Sykes, 1957. In this book, it is proposed to approach criticality extending the multiplication process to include all collisions leading to a neutron emission, i.e. scattering and fission,

$$\hat{L}\varphi_{\gamma,n} + \hat{R}\varphi_{\gamma,n} = \frac{1}{\gamma}\left(\hat{S}+\hat{F}\right)\varphi_{\gamma,n}. \tag{3.4}$$

Due to its position in the transport equation, this eigenvalue has some similarities to the k formulation. Also in this case, the physical meaning of the fundamental eigenvalue γ_0 is straightforward. Integrating (3.4) over the phase space and isolating γ_0 yields,

$$\gamma_n = \frac{\langle(\hat{F}+\hat{S})\varphi_{\gamma,n}\rangle}{\langle(\hat{L}+\hat{R})\varphi_{\gamma,n}\rangle}, \tag{3.5}$$

which is closely related to the number of secondaries per collision. Thanks to this equation, it should be evident that the system is critical when $\gamma = 1$, i.e. the number of neutrons emitted per collision is equal to the number of neutrons lost, while it is larger/lower than the unity when the system is super-critical/sub-critical.

Since it acts also on the fission term, the γ spectrum inherits the property of existence of a real, positive eigenvalue from the k formulation, provided that the system is multiplying. However, the inclusion of the scattering operator enriches the physical content of the spectrum, as visible *ictu oculi* from figures 3.3 and 3.4. Since γ acts also

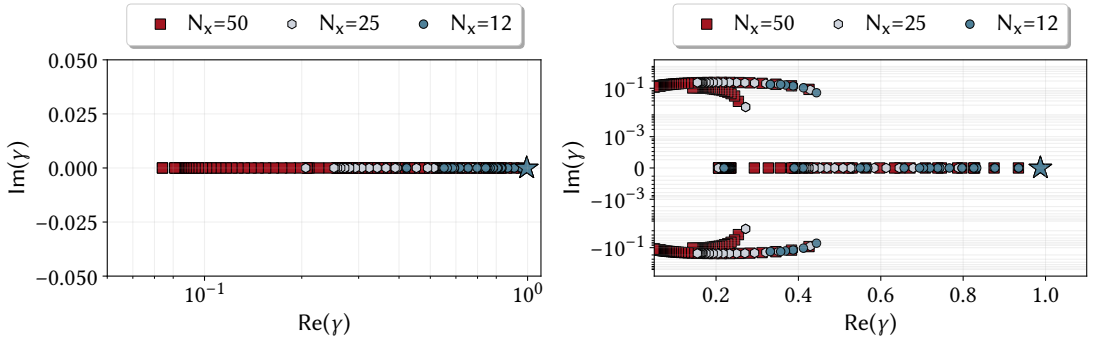

(a) P_3, *CASMO-2 energy grid, isotropic scattering.*

(b) P_3, *CASMO-2 energy grid, anisotropic scattering.*

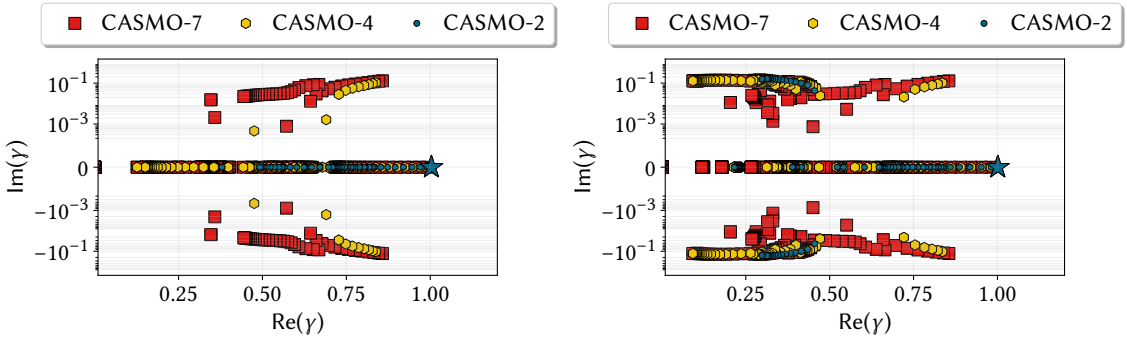

(c) P_3, *25 spatial meshes, isotropic scattering.*

(d) P_3, *25 spatial meshes, anisotropic scattering.*

Figure 3.3: *γ-spectrum for a homogeneous, isotropic, fissile slab, imposing Mark boundary conditions. The stars represent the fundamental eigenvalues.*

on the scattering, the spectrum appears to be very sensitive to both the energy and the angular aspects of the transport process, contrarily to what occurs for the k case, where these variables do not affect the shape of the spectrum. Figure 3.3 shows the influence of the number of spatial meshes and energy groups on the spectrum, for the isotropic and linearly anisotropic scattering orders. As for k, increasing the number of degrees of freedom has the general effect of introducing more eigenvalues. However, contrarily to k, the linear anisotropy and the adoption of finer energy discretisations introduce some complex eigenvalues, which are related to the higher-order effects induced by the scattering phenomenon. As long as the collisions are simply described by an isotropic, two-group model, the γ spectrum is very close to the k one, but when the physical detail increases, the spectrum becomes complex.

It is interesting to observe how these additional complexities are still preserved when coarser models are employed, confirming the consistency of the numerical scheme adopted. For example, the two branches in fig. 3.3b associated to N_x=50 (red squares) are represented by a branch and a discrete point when the number of spatial meshes is halved (grey hexagons) and by a single branch when the number of meshes is reduced

to 12 (blue dots). A similar comment can be made concerning the group structures. In this case, the complex branches collapse consistently with the group collapsing.

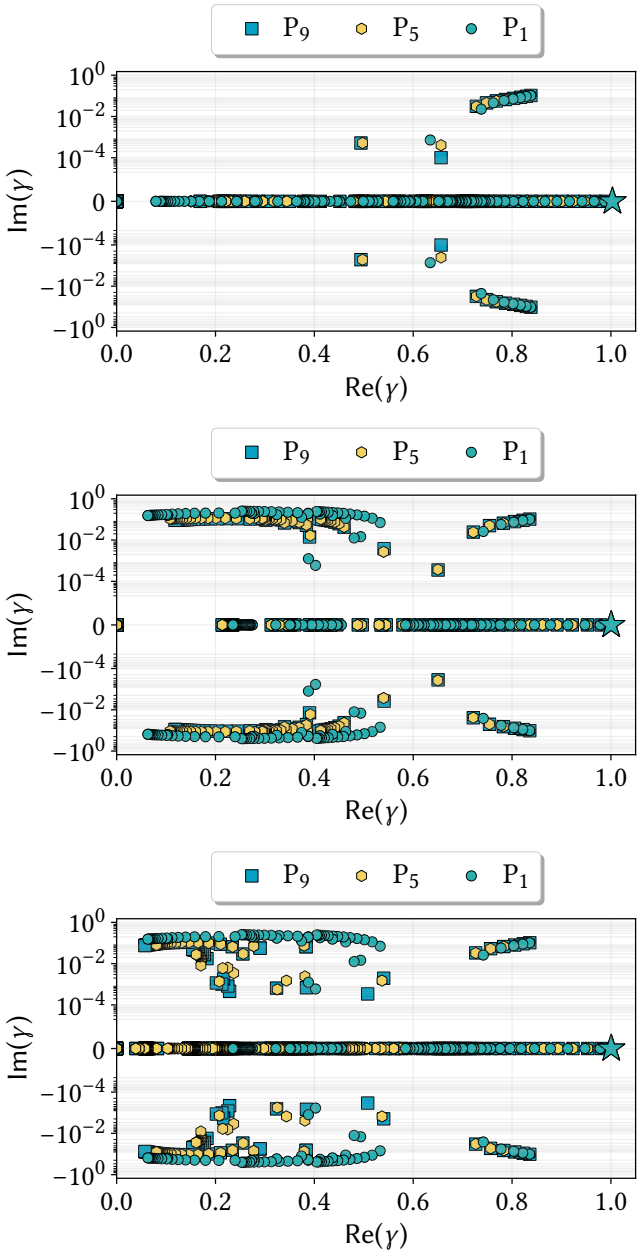

Figure 3.4: *γ-spectrum for a homogeneous, fissile slab, imposing Mark boundary conditions and using 25 meshes, with isotropic (top), linearly anisotropic (centre) and quadratically anisotropic (bottom) scattering orders. The cross sections are collapsed on the CASMO-4 energy grid. The stars represent the fundamental eigenvalues.*

An analogous behaviour can be observed as well in fig. 3.4, where more and more accurate transport models are adopted to treat different anisotropy levels. When the scattering is assumed to be isotropic or linearly anisotropic, the adoption of progressively better angular models does not have a significant impact on the spectrum: most of the changes in the spectrum shape are due to the introduction of the linear anisotropy. However, when a quadratic scattering is assumed, the P_5 and the P_9 spectra shows additional clusters of complex eigenvalues, located around $\mathrm{Re}(\gamma)$=[0.2, 0.4], with respect to the spectrum computed with the P_1 model, which is not able to take into account the additional anisotropy scattering order.

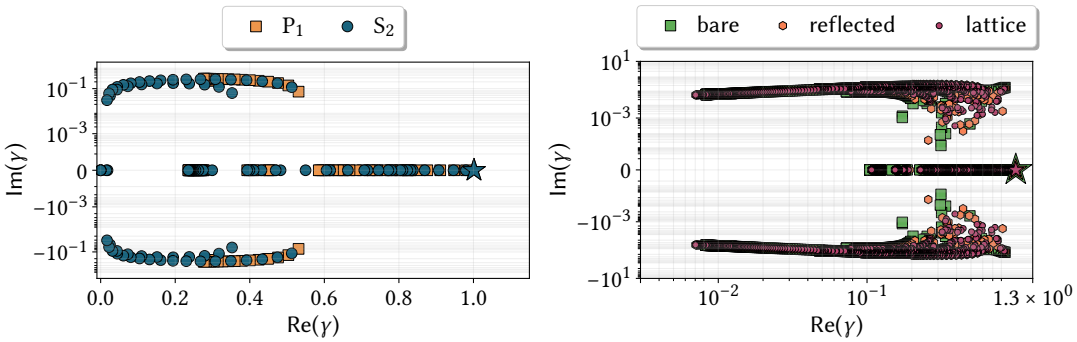

(a) *25 meshes, CASMO-2 energy grid* (b) *P_3, 125 meshes, CASMO-7 energy grid.*

Figure 3.5: *γ-spectrum of a homogeneous, fissile slab featured by linearly anisotropic scattering (left) and for a linearly anisotropic slab featured by different levels of heterogeneity (right). The stars represent the fundamental eigenvalues.*

Similar considerations on the anisotropy effect hold also for the S_N model. Figure 3.5 provides a comparison between the spectra of the P_1 and the S_2 models, which are very similar except for the high frequency eigenvalues, and an example of the behaviour of the spectra in the presence of spatial heterogeneity. In this case, despite some slight differences in the complex branches, it is not possible to notice specific effects induced by the number of layers of different materials.

Regarding the influence of the criticality level, reported in fig. 3.6, the γ spectrum behaves similarly to the k case, i.e. the eigenvalues tend to be more dispersed when the system is sub-critical.

The analysis of the γ spectrum in different cases allows to observe some general features:

- the spectrum is featured by complex eigenvalues, associated to higher-order energy and angular effects;
- the fundamental eigenvalue always lies at the right of the spectrum, assuming the largest real value, provided that $\tilde{F} \neq 0$;

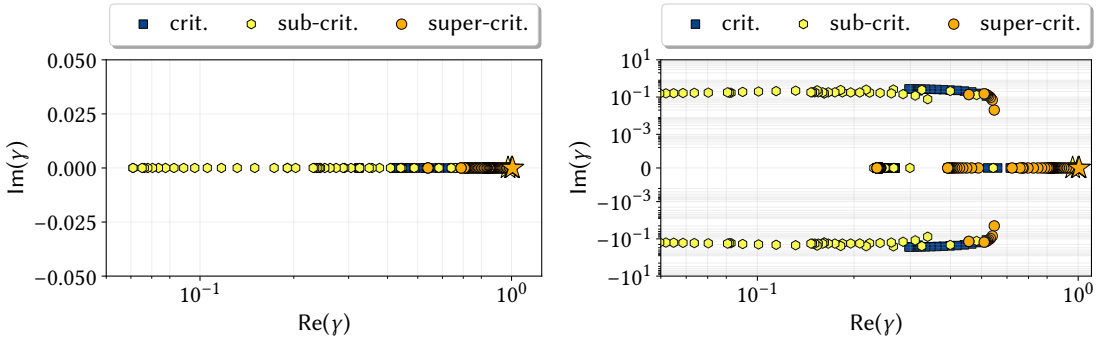

Figure 3.6: *γ-spectrum for a homogeneous, fissile slab with different thicknesses, imposing Mark boundary conditions and using 25 meshes, with isotropic (left) and linearly anisotropic (right) scattering orders. The cross sections are collapsed on the CASMO-2 energy grid. The stars represent the fundamental eigenvalues.*

- the fundamental eigenvalue appears to be by far less sensitive than k_0 to the criticality level. This aspect can be a drawback from the point of view of the calculation accuracy, as the tolerance on this parameter should be lower than the usual pcm scale (Ronen, Shvarts, and Wagschal, 1976), but is can be also an advantage as the energy spectrum deformation should be minimised with respect to the k case.

Since it is not possible to simultaneously change the fission and the scattering cross sections, this eigenvalue is not adequate for design-oriented applications. Moreover, the low sensitivity to the criticality level makes this eigenvalue unattractive for the approach to criticality. Nevertheless, as suggested in (Cacuci, Ronen, et al., 1982), the γ formulation may be of interest as weighting function for the few-group collapsing, since, acting simultaneously on both scattering and fission, it does not alter their energy spectrum ratio, contrarily to what occurs when k is introduced. Hence, criticality is attained by means of a rescaling of the total number of particles emitted by collisions, minimising the energy spectrum shift.

3.4 The time eigenvalue

The third eigenvalue formulation proposed in the history of reactor physics is the so-called *time* eigenvalue, which is also the most employed one after the multiplication eigenvalue. Firstly introduced by Henry, 1964, this formulation has recently attracted more attention due to its strong relationship with the time evolution of an off-critical system (Zoia, Brun, and Malvagi, 2014; Vitali, 2020), which could be of interest in order to obtain better few-group constants for dynamic calculations (Dugan, Zmijarevic, and Sanchez, 2016). The time eigenvalue is also the only natural spectral formulation of the transport equation, being associated to its Laplace transform. This is the reason why the time eigenfunctions are often referred to as the *natural* modes.

According to the time scale considered and to the assumptions made, two formulations of the time eigenvalue are currently possible. The most general one, proposed by Henry and already introduced in chapter 2, yields

$$\begin{aligned}\hat{L}\varphi_{\mu,n} + \left(\hat{R} + \frac{\omega_n}{\mathrm{v}(E)}\right)\varphi_{\mu,n} &= \hat{S}\phi + \hat{F}_p\varphi_{\mu,n} + \sum_{i=1}^{\mathrm{R}} \frac{\lambda_i}{\mu_n + \lambda_i}\hat{F}_i\varphi_{\mu,n},\\ \hat{L}\varphi_{\mu,n} + \left(\hat{R} + \omega_n\hat{T}\right)\varphi_{\mu,n} &= \hat{S}\varphi_{\mu,n} + \hat{F}_p\varphi_{\mu,n} + \sum_{i=1}^{\mathrm{R}} \frac{\lambda_i}{\mu_n + \lambda_i}\hat{F}_i\varphi_{\mu,n}.\end{aligned} \tag{3.6}$$

This non-linear spectral form is equivalent to the one obtained from the full transport model coupled with the precursors concentration (see eq. (2.1)). In this last case, the formulation would be defined by R + 1 equations, but it would be linear in ω. All the calculations presented in this work are obtained exploiting the linear form of the ω formulation.

When the delayed neutron contributions are neglected, the α eigenvalue, i.e. *prompt time eigenvalue*, would be obtained,

$$\hat{L}\varphi_{\alpha,n} + \left(\hat{R} + \alpha_n\hat{T}\right)\varphi_{\alpha,n} = \hat{S}\varphi_{\alpha,n} + \hat{F}\varphi_{\alpha,n}, \tag{3.7}$$

where the total fission operator $\hat{F}$ is considered. From a physical standpoint, this means that the delayed neutrons energy is accounted for, but they are assumed to be emitted with the prompt ones.

The hypothesis at the basis of these formulations is that the neutron flux (and the precursor concentrations as well, in the case of ω) is separable in time and described by an exponential decay,

$$\phi(x, E, \vec{\mu}, t) = \varphi_{\alpha,n}(x, E, \vec{\mu})e^{\alpha_n t}. \tag{3.8}$$

This equation allows to highlight the physical meaning of the time eigenvalues, which are the time frequencies characterising the free evolution of the system. As such, these quantities, also known as *natural frequencies*, are physical observables (Chentre, Saracco, et al., 2019), contrarily to the other eigenvalue formulations addressed in this chapter. The time eigenvalue has been a hot issue of reactor physics for decades, as it can be noticed from the wide literature concerning both its theoretical (Dahl, Protopopescu, and Sjöstrand, 1983; Sahni and Sjöstrand, 1990; Sahni, D. C. and Sjöstrand, N. G. and Garis, N. S., 1995; Dulla, Ravetto, and Saracco, 2018) and practical (Cacuci, Ronen, et al., 1982; Singh, Degweker, et al., 2011; Dugan, Zmijarevic, and Sanchez, 2016; McClarren, 2019) aspects.

The most peculiar feature of this spectral form is that its spectrum is featured by a continuous and a discrete parts, located on the left and on the right, respectively, of the so-called Corngold limit, defined as $min(\mathrm{v}(E)\Sigma_t(E))$ (Corngold, 1969; Corngold, 1975). Another well known aspect characterising the time spectrum when the delayed neutrons are considered is the presence of clusters of discrete eigenvalues, which are

usually known as *delayed frequencies*. As proved by Henry, 1958, these discrete eigenvalues tend to accumulate at the right of $-\lambda_i$, i.e. the opposite of the decay constant of the i-th neutron precursors family, $\forall i = 1, \dots, \mathrm{R}$. The phenomenon of the eigenpair clustering, tightly related to the nature of the inhour equation (Sanchez and Tomatis, 2019), is explained by the presence of eigenstates featured by very similar fluxes but different precursors spatial concentrations. This peculiarity has often suggested that each eigenstate, i.e. flux and R precursors concentrations, belonging to a cluster is equally important to provide some physically significant information for the description of the system dynamics. However, as found by Ravetto, 1974, only one eigenstate, associated to $\omega + \lambda_1 > 0$, has a uniform sign, while the other ω modes in the cluster are featured by fluxes with uniform sign but by precursors concentration C_i with non-uniform sign, when $\omega + \lambda_i < 0$.

Since clustering is an issue for any eigenvalue algorithm aiming at retrieving only the most significant eigenvalues, this feature is extremely important to provide a shift to enable the convergence of the numerical solver. In this respect, fig. 3.7 provides a useful comparison between the α and the ω spectra. Concerning the prompt spectrum on the left, the fundamental eigenvalue is clearly positive, meaning that the flux amplitude diverges as time goes by. Except for this point, the spectrum is composed by negative, larger frequencies, which are related to rapidly vanishing flux modes. When the delayed neutrons are taken into account, the overall system dynamics becomes slower, as visible looking at the magnitude of the time frequencies. This phenomenon depends on the typical time scale characterising the delayed neutrons emission, which are represented by the clusters of eigenvalue around -10^3 and -10^{-1}.

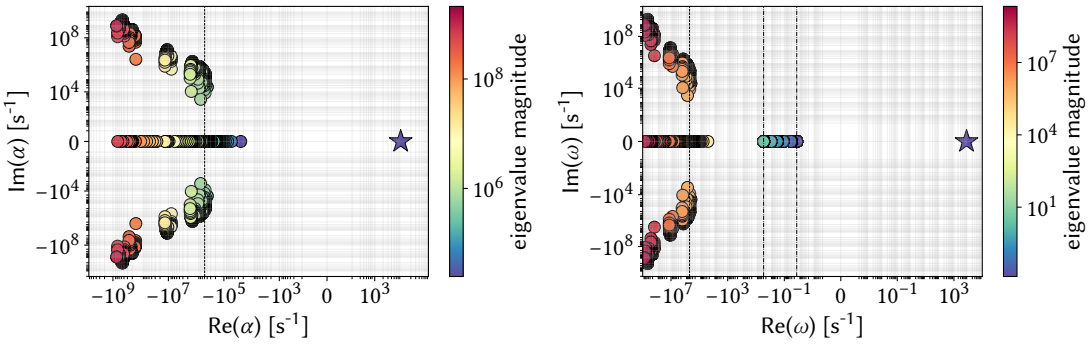

Figure 3.7: *Prompt (left) and delayed (right) spectra for a homogeneous, isotropic, fissile slab, computed with a P_3 model defined on 25 spatial and imposing Mark boundary conditions. The stars represent the fundamental eigenvalues, while the dashed black lines around -10^7 s indicates the Corngold limit.*

Due to its collocation in the transport equation, the term $\alpha/\mathrm{v}(E)$ is often referred to as *time absorption*, although a more appropriate name should be *time capture*, as it does

not modify the fission cross section,

$$\Sigma_{\alpha,c}(E) = \frac{\alpha}{\mathrm{v}(E)}. \tag{3.9}$$

This time capture cross section can be physically interpreted as a virtual capture reaction featured by a $1/\mathrm{v}(E)$ spectrum (Bell and Glasstone, 1970, chapter 1). For critical systems, the fundamental eigenvalue α_0 vanishes: no time capture is needed to reach the equilibrium. When the system is off-critical, there are two possibilities:

- for super-critical systems, there is a positive reactivity, which hardens the energy spectrum yielding a positive value of α. Consequently, the fictitious time capture is positive ($\alpha_0 > 0$) (Ronen, Shalitin, et al., 1977). In this case, the neutron energy spectrum is hardened, since $\Sigma_{\alpha,c}(E)$ is larger at lower energies;
- for sub-critical systems, the time capture is negative ($\alpha_0 < 0$). In this case, the neutron energy spectrum is softened, since $\Sigma_{\alpha,c}(E)$ is lower at lower energies;

The action of the $\Sigma_{\alpha,c}(E)$ virtual cross section has two important detrimental effects from the numerical point of view:

- some numerical instabilities may arise when the total removal term $\Sigma_t + \alpha/\mathrm{v}$ is negative or close to zero;
- the search for the fundamental eigenvalue may not be straightforward, as it can be either positive or zero or negative.

In spite of these intricacies, the time eigenproblem conveys a lot of physical information. First of all, as written above, it is the only natural eigenvalue formulation, opposed to the other formulations that are somewhat artificial. Then, the fundamental eigenvalue is the inverse of the reactor stable period, while the associated mode describes the asymptotic population distribution. The same considerations apply to the case of ω as well, with the additional complications related to eigenvalue clustering.

Figure 3.8 shows the influence of the number of spatial meshes on the prompt and delayed spectra, for a P_3 model employing a set of cross sections collapsed on the CASMO-2 grid. As expected, the spatial mesh refinement enriches locally the spectrum, but does not affect its pattern. However, when the number of energy groups increases, both the spectra exhibit additional features, as clearly visible from fig. 3.9. The number of branches and their disposition in the Gauss-Argand plane are remarkably related to the energy group boundaries adopted to collapse the cross sections. To fully appreciate this relationship, it is useful to observe that the CASMO-4 and the CASMO-7 grids, reported in table 3.1, share the same fast ($2.00 \times 10^{1} - 5.53 \times 10^{-3}$ MeV) and epithermal (8.21×10^{-1} –MeV) groups, while the CASMO-4 and the CASMO-2 grid are featured by the same thermal group ($6.25 \times 10^{-7} - 1.00 \times 10^{-11}$ MeV). As a consequence, the branches associated to these common energy groups are perfectly overlapped. The association

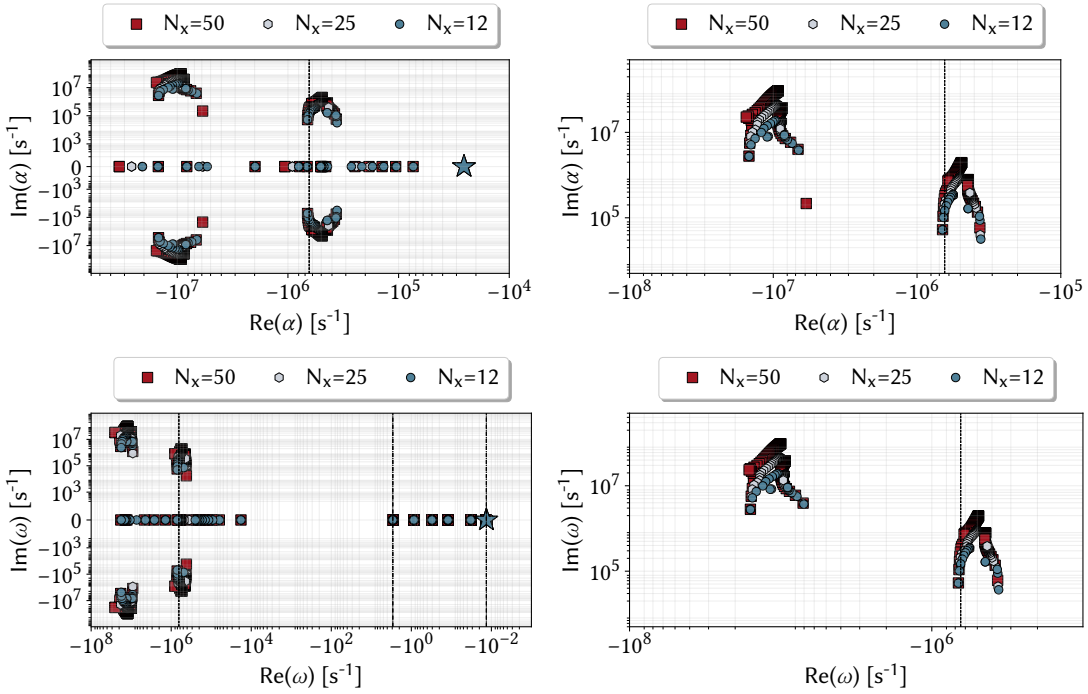

Figure 3.8: *Prompt (top) and delayed (bottom) spectra for a homogeneous, isotropic, fissile slab, using a* P_3 *model with cross sections collapsed on the CASMO-2 structure and Mark boundary conditions. The stars represent the fundamental eigenvalues, while the dashed black lines represent the Corngold limit (around* -10^6*) and* $-\lambda_R$ *and* $-\lambda_1$ *(around* -10 *and* -10^{-2}*). The full spectra are displayed on the left, while a zoom of each spectra is reported on the right.*

of each branch to the corresponding energy group is possible on a physical basis: the higher the neutron velocity in a group, v_g, the faster the dynamics associated to that group. Therefore, the fast groups will trigger large negative frequencies, while the thermal groups will be associated to smaller negative frequencies. Heuristically, it is possible to relate these branches to the neutron mean collision time in each group, defined as

$$\ell_{g,coll} = \frac{1}{v_g \Sigma_{g,t}}. \tag{3.10}$$

In light of this definition, it is possible to give a new interpretation to the Corngold limit (CL), which turns out to be

$$\mathrm{CL} = -\min(v_g \Sigma_{g,t}) = -\min(\ell^{-1}_{g,coll}), \tag{3.11}$$

i.e. the opposite of the smallest collision frequency. As visible from the graphs on the right of fig. 3.9, which is an enlargement of the graphs on the left, each branch gathers around the collision frequency of the corresponding group. This behaviour is confirmed

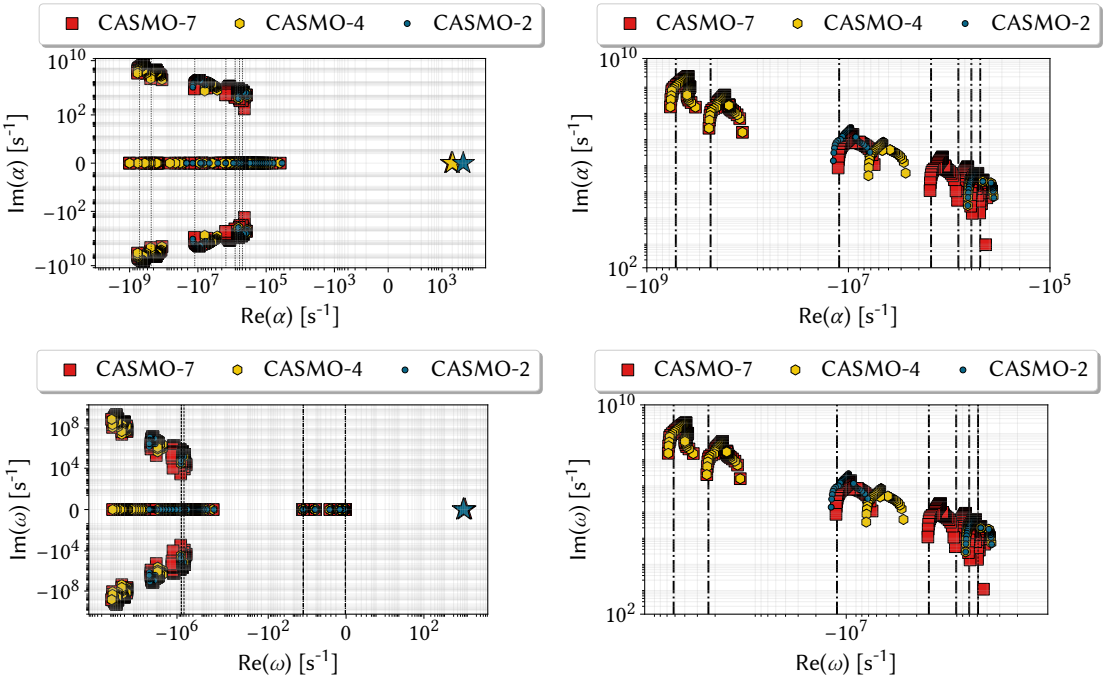

Figure 3.9: *Prompt (top) and delayed (bottom) spectrum for a homogeneous, linearly anisotropic, fissile slab, whose cross sections are collapsed according to the energy structures indicated. The calculation is carried out with a* P_3 *model using 25 meshes and Mark boundary conditions. The stars represent the fundamental eigenvalues, while the dashed black lines indicate the mean collision time for the CASMO-7 grid. The full spectra are displayed on the left, while a zoom of each spectra is reported on the right.*

also for the case of a fast, homogeneous system, whose spectrum is reported in fig. 3.10. In this case, two different energy grid structures, specified in table 3.2 are used to further highlight the rôle of the group structure choice on the complex branch disposition.

The time spectrum shape is also strongly influenced by the angular approximation order, as visible from fig. 3.11. In analogy to what already observed in Abrate, Burrone, et al., 2021 and Abrate, Dulla, et al., 2021, it is possible to distinguish, more or less clearly according to the number of spatial meshes and energy groups and on a linearly scaled graph, N+1 (N) wing-shaped batches of eigenvalue per energy group, where N is the odd (even) order of the P_N (S_N) model employed to approximate the spectrum. As showed in Abrate, Burrone, et al., 2021, new branches appear only when the succeeding odd/even order for the P_N/S_N model is employed, while the even/odd approximation orders only induce some distortions of the spectrum shape.

The symmetrical disposition with respect to the real axis is due to the symmetry of the roots of the Legendre polynomial $P_N(\mu)$, which are employed in both models.

The mutual disposition of these wing-shaped branches also depends on the interaction channel between the neutrons and the diffusing medium. Figure 3.12 shows the

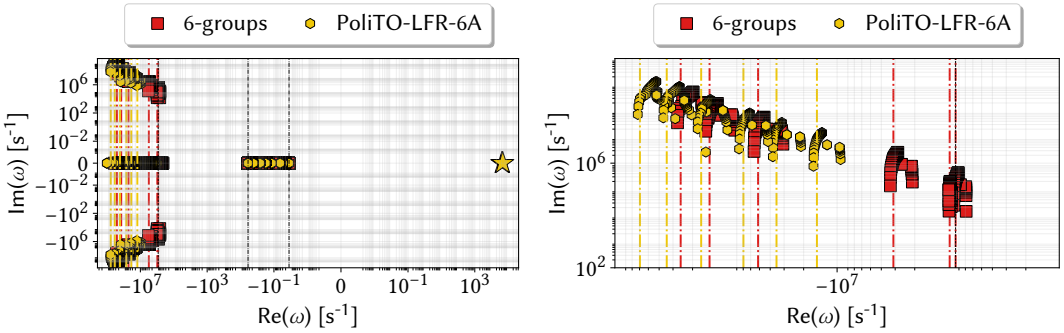

Figure 3.10: *Time spectrum with delayed neutrons of a homogeneous, linearly anisotropic, fissile slab, computed using a* P_3 *model with 25 meshes and Mark boundary conditions and collapsing the cross sections according to the energy structures indicated. The stars represent the fundamental eigenvalues, while the dashed lines indicate the mean collision time for the two grid structures. The full spectrum is displayed on the left, while a zoom is reported on the right.*

Table 3.2: *Energy group structures employed for the fast energy spectrum calculations.*

group boundary [MeV]	6-groups	PoliTO-LFR-6A
2.000000×10^{1}	x	x
2.231300×10^{0}		x
4.978710×10^{-1}		x
1.831564×10^{-1}	x	
2.478752×10^{-2}	x	x
5.530840×10^{-3}		x
2.260329×10^{-5}	x	
7.485180×10^{-4}		x
5.400000×10^{-7}	x	
1.000000×10^{-7}	x	
1.000000×10^{-11}	x	x

time spectrum for the one-group P_7 and S_8 models for a non-multiplying medium featured by different values of secondaries per collision $c = \Sigma_s/\Sigma_t$. In the P_7 case, each angular batch is independent for $c = 0$, due to the absence of scattering. When scattering is triggered, there is an evident repulsion and crossing between the branches, due to the collision-riven angular redistribution. In a multi-group case, the same physical justification can be adopted for each group.

Concerning the S_8 model, it is possible to qualitatively observe the same behaviour, with some notable exceptions. First, in the case of purely absorbing medium, $c = 0$, the

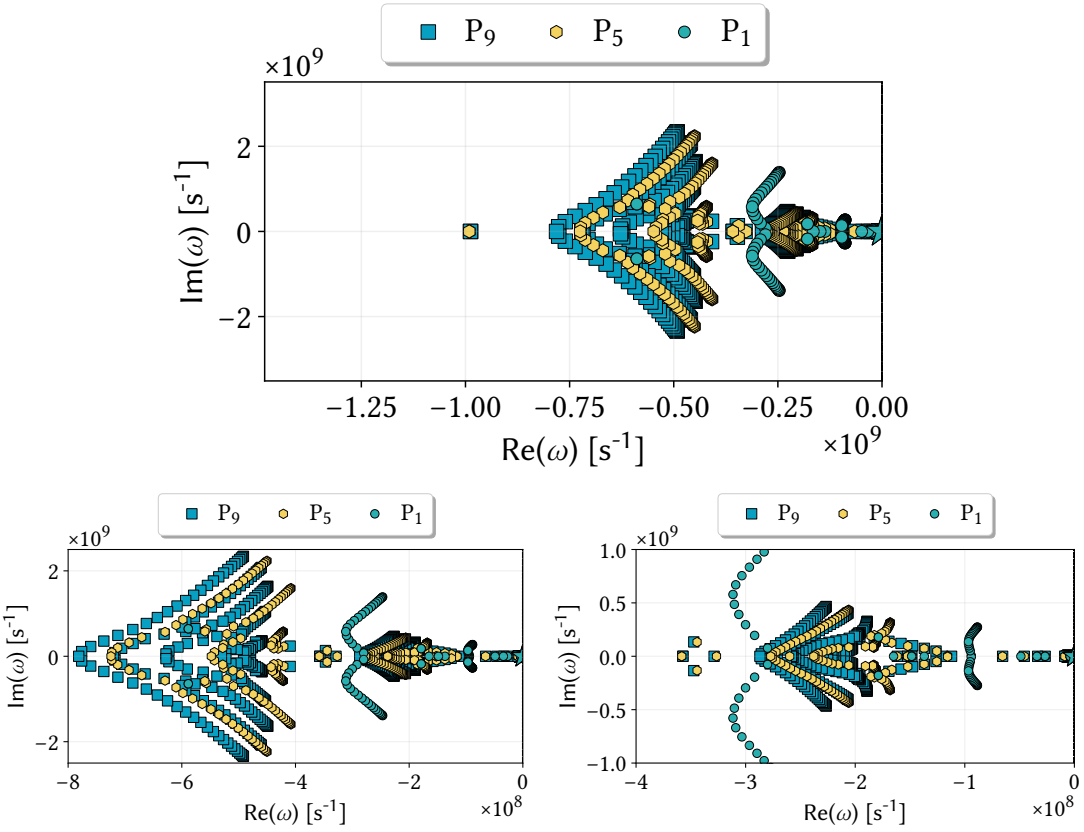

Figure 3.11: *Time spectrum with delayed neutrons of a homogeneous, isotropic, fissile slab, computed collapsing the cross sections on the CASMO-4 structure, using 25 meshes and imposing Mark boundary conditions. The stars represent the fundamental eigenvalues. The top graph shows the full spectrum, while the bottom ones show two enlargements.*

α spectrum degenerates in five points, and no fundamental mode can be distinguished. This peculiar behaviour is a consequence of the inherent structure of the S_N model, in which each direction is independent in the case of a purely absorbing medium, contrarily to the set of coupled equations for the flux angular moments in the P_N model. The five degeneracy points should be interpreted as one degeneracy per each N/2 = 4 direction, due to the symmetry of the quadrature weights, plus one degeneracy associated to the Mark (vacuum) boundary conditions. In this case, it is not possible to identify a fundamental eigenvalue. When c increases, the spectrum assumes a shape similar to the P_7 case, but with the wing-shaped batches pointing towards $-\infty$. The difference between the P_N and S_N spectra cannot be ascribed only to the differences in the numerical setup described in chapter 2, but are rather due to the fact that this is a limit cases in which neither fission nor external source are present. In case fission is introduced, the two angular models provide very similar time spectra, as visible in fig. 3.13 for the S_2-P_1 case.

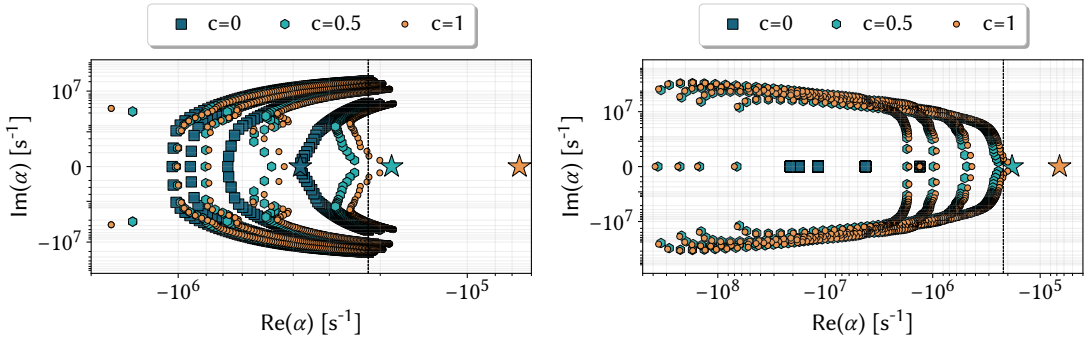

Figure 3.12: *Prompt spectrum of a homogeneous, isotropic slab, computed with one-group P_7 (left) and S_8 (right) models using 100 meshes and imposing Mark boundary conditions. The stars represent the fundamental eigenvalues. For the sake of readability, the ordinate axes of the graphs are linear in the interval* $[-5 \times 10^5, 5 \times 10^5]$.

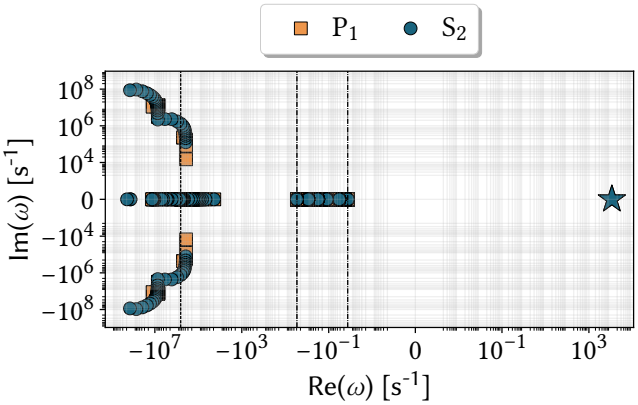

Figure 3.13: *Time spectrum with delayed neutrons for a homogeneous, isotropic, fissile slab discretised with 25 meshes and described with a set of cross sections collapsed on the CASMO-2 grid.*

To complete the discussion on the impact of the angular approximation on the spectrum shape, it is important to remember that, in time-dependent situations, the diffusion model is not equivalent anymore to the P_1 system, which can be cast into the so-called telegrapher's equation form,

$$\frac{3D}{v^2}\frac{\partial^2\phi_0}{\partial t^2} + \frac{3D\Sigma_a + 1}{v}\frac{\partial\phi_0}{\partial t} = D\frac{d^2\phi_0}{dx^2} - \Sigma_a\phi_0 + \nu\Sigma_f\phi_0, \tag{3.12}$$

where the terms have their usual meaning (see chapter 2) and the dependencies of the flux has been omitted. Figure 3.14 shows the prompt spectra computed with diffusion, P_1 and P_3 with two energy structures, the CASMO-40 and the CASMO-4. In the first case, the diffusion spectrum is completely real, while in the second case, due to the

larger number of groups, complex eigenvalues appear, consistently with what observed in Sanchez, Tomatis, et al., 2017.

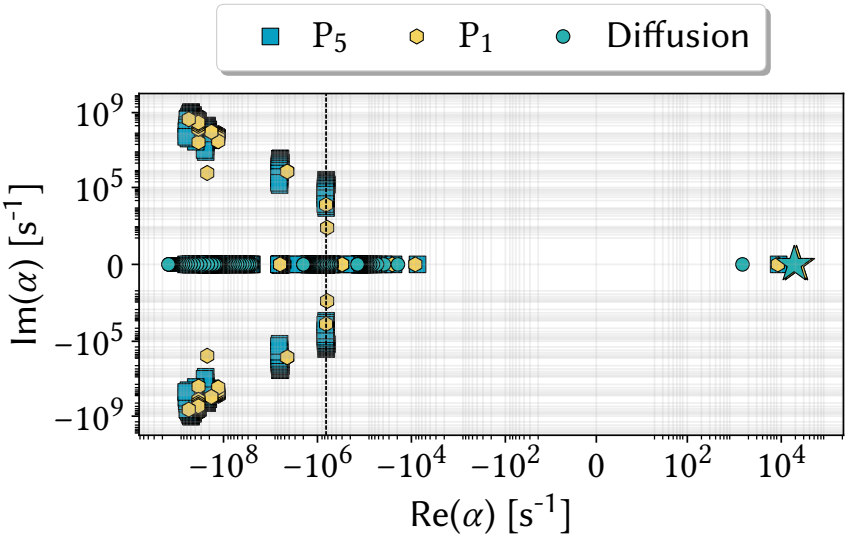

(a) *Model parameters: CASMO-4 energy grid, 25 meshes.*

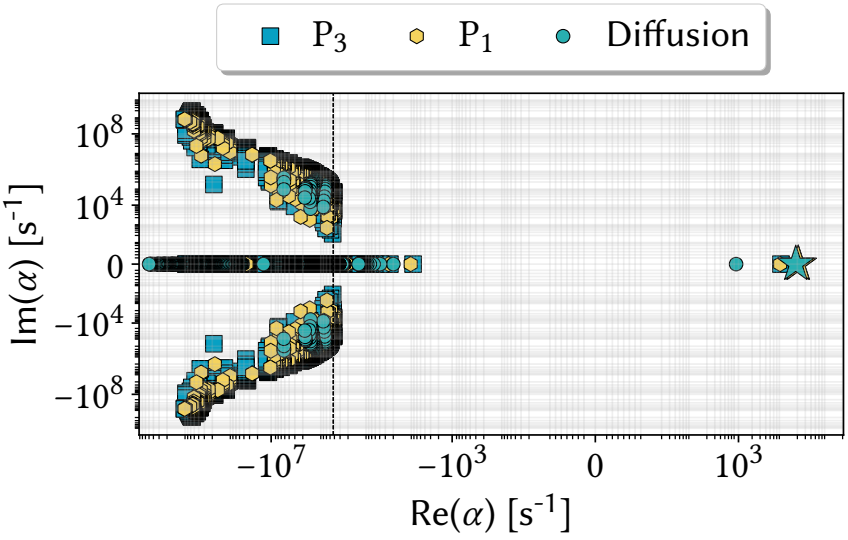

(b) *Model parameters: CASMO-40 energy grid, 25 meshes.*

Figure 3.14: *Prompt spectrum for a homogeneous, isotropic, fissile slab, whose cross sections are collapsed on the CASMO-4 (top) and CASMO-40 (bottom) structures. The calculation is carried out using 25 meshes and imposing Mark boundary conditions. The stars represent the fundamental eigenvalues, while the dashed black lines indicate the Corngold limit.*

Since most of the reactor concepts are strongly heterogeneous, it is extremely interesting to observe the spectrum deformation according to the heterogeneity of the

system, keeping the total number of degrees of freedom fixed as done for the other spectral formulations. Figure 3.15 shows some details of the time spectrum, considering the rôle of delayed neutrons, for the three configurations discussed previously: a bare reactor made of fissile material, a reactor composed by an inner fissile core and surrounded by a water reflector and a lattice alternating layers of water and fissile material. The time spectra are computed for a one-group, P_7 model, with the purpose of highlighting the angular behaviour in presence of heterogeneity, and for a two-group, P_3 model, aiming at evaluating the energy effects. The shape of the spectra associated to the bare reactor is consistent with the previous considerations: the number of complex branches scales as N+1, where N is the odd P_N order, and, an angular batch per group is located near the opposite of the smallest group-wise collision frequency. When the heterogeneity appears, as one could expect on a physical ground, the time spectrum pattern becomes more intricate, due to the interplay between spatial, angular and energy effects. Concerning the one-group case, it is possible to observe, on the right of fig. 3.15a, 8 branches (despite some small overlapping) per each imaginary half-plane for both the heterogeneous arrangements, in contrast with the 4 per each half-plane for the homogeneous reactor. Since both configurations are featured by different numbers of layers but by the same number of different materials, i.e. water and fuel, it could be concluded that the number of complex branches is proportional to the second parameter, while the number of layers seems to affect only the branch disposition and their separation, consistently with what observed for the case observed in fig. 3.12. At a first glance, the fact that the angular branches are sensitive to the material properties could sound unphysical, as the streaming of neutrons does not depend on the medium properties, $\hat{L}\phi = \vec{\nabla} \cdot (\vec{\Omega}\phi)$. Hence, this phenomena most likely origins from a spatial-angular effect, in analogy to the spatial-energy coupling that features the heterogeneous media (Weinberg and Wigner, 1958) and that can be observed in fig. 3.15b, where two details of the spectrum around $-\ell^{-1}_{1,coll}$ (fast) and $-\ell^{-1}_{2,coll}$ (thermal) are provided. The spectrum for the homogeneous system behaves as discussed previously, i.e. the branches are located around $-\ell^{-1}_{1,coll}$ and $-\ell^{-1}_{2,coll}$ and maintain a very similar shape. On the contrary, the fast and the thermal branches featuring the heterogeneous media exhibits different shapes, as a consequence of the involved interaction between spatial, angular and energy effects.

The influence of the criticality level on the time spectra can be appreciated looking at fig. 3.16, where the prompt (top) and delayed (bottom) spectra computed with 25 meshes and the P_1 model collapsing the cross sections on the CASMO-4 grid are reported for the same fissile slab featured by isotropic and linearly anisotropic scattering. The striking difference between the α and ω formulations is the fact that, in the case of a sub-critical system, the fundamental eigenvalue is bounded by $-\lambda_1$ when the delayed neutrons are taken into account. This feature is consistent with the physical expectations, and is of paramount importance to direct the numerical search for the fundamental delayed eigenvalue in practical cases. Despite this lower limit, the fundamental eigenvalue exhibits a large sensitivity to the criticality level in both formulations, being

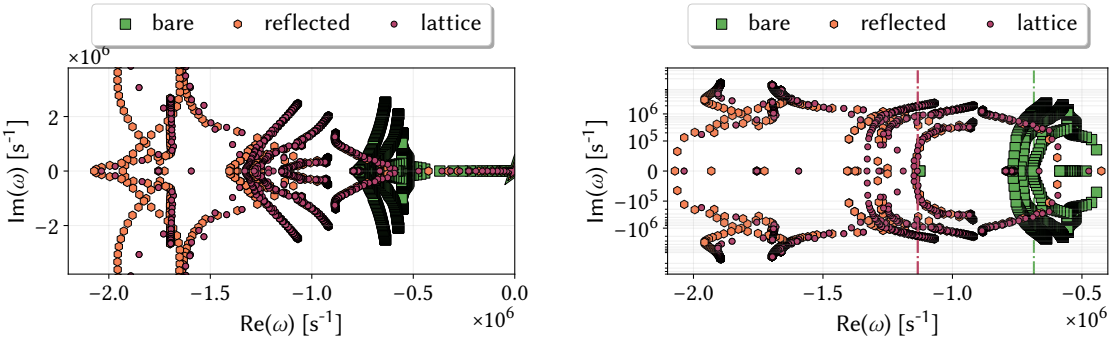

(a) *Time spectrum (left) computed with a one-group P_7 model, discretised with 121 meshes and a detail of the same spectrum (right) for $Re(\omega) = [-2 \times 10^6, -5 \times 10^5]$.*

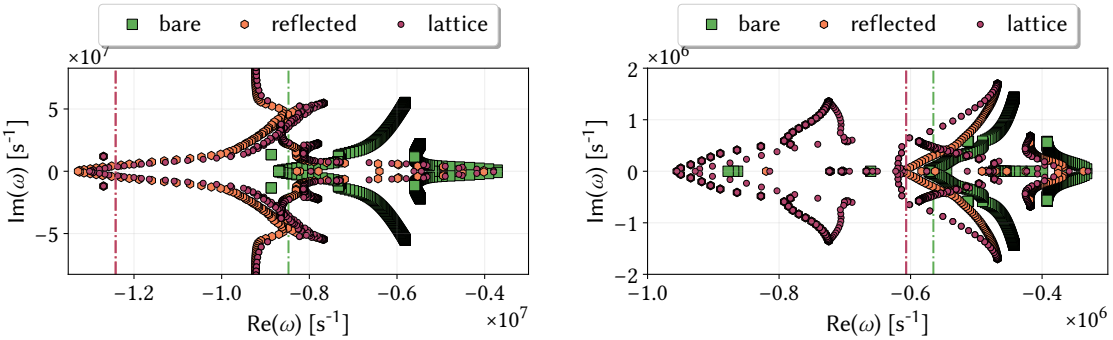

(b) *Details on the fast (left) and thermal (right) frequencies featuring the time spectrum computed with a two-group (CASMO-2) P_3 model.*

Figure 3.15: *Details of the time spectrum with delayed neutrons for a linearly anisotropic slab featured by different levels of heterogeneity.*

a time frequency.

Concerning the fast dynamics region, beyond the Corngold limit, the spectra do not show differences that can be appreciated *ictu oculi*, due to the departure from criticality. Nevertheless, it is worth observing that, when the system is super-critical and the scattering is isotropic, the frequencies associated to the thermal groups are purely real. Considering this fact and the different spectra commented above, it is likely that there is some intricate connection, whose investigation is left as a future development, between the criticality offset, the scattering anisotropy order and the angular and energy approximations.

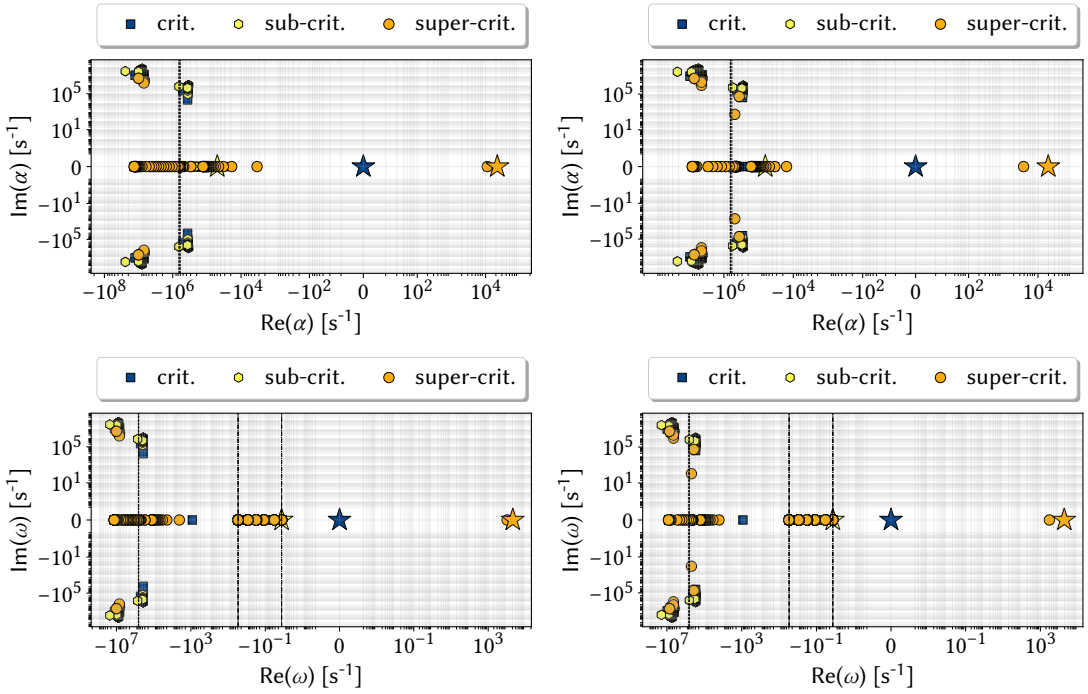

Figure 3.16: *Prompt (top) and delayed (bottom) spectra for isotropic (left) and linearly anisotropic (right) scattering for a homogeneous, isotropic, fissile slab. The calculations are carried out using 25 meshes, imposing Mark boundary conditions and collapsing the cross sections on the CASMO-4 grid. The stars represent the fundamental eigenvalues, while the dashed black line indicates the Corngold limit.*

3.5 The density eigenvalue

Except for the time eigenvalue, the other two eigenvalue formulations addressed so far act on some specific reaction channels, i.e. fission production and neutron emission. Despite the advantages of these formulations, as it has been previously pointed out, it not possible to practically modify these interactions without affecting also the other cross sections. Probably inspired by the desire of avoiding this drawback, Ronen, Shalitin, and Wagschal, 1976 introduced the so-called *density* eigenvalue,

$$\hat{L}\varphi_{\delta,n} = \frac{1}{\delta}\left(\hat{S} + \hat{F} - \hat{R}\right)\varphi_{\delta,n}, \tag{3.13}$$

which can be interpreted as the ratio between the net number of particles emitted in the system and the number of particles leaking out of the system,

$$\delta = \frac{\langle(\hat{S} + \hat{F} - \hat{R})\varphi_{\delta,n}\rangle}{\langle\hat{L}\varphi_{\delta,n}\rangle}. \tag{3.14}$$

This eigenvalue lends itself to two physical interpretations. First, it can be seen as a tuning parameter acting on the competition between neutron production and removal terms, whose density is varied by the same amount, i.e. δ itself. From a different perspective, it can be interpreted as a *streaming* eigenvalue, changing the relationship between the angular flux and the angular current ($\hat{\Omega}\phi$). In this case, δ turns out to be a scaling parameter acting on the geometrical size of the system. Referring to the integral form of the NTE, it is possible to verify that the eigenvalue acts on the free-flight kernel of the transport process (Barbarino, Dulla, and Ravetto, 2013).

As observed in the literature available about this formulation (Velarde, Ahnert, and Aragonés, 1978; Perel, Wagchal, and Yeivin, 1999), a consequence of this property is the fact that, when the geometry of the system is scaled by a certain factor β, the δ eigenvalue spectrum is scaled by the same factor, and the flux energy spectrum does not change. This feature appears to be a considerable advantage with respect to the other spectral formulations previously discussed, which introduce some distortions in the energy spectrum. In contrast with k and γ, δ acts simultaneously on all the energy-dependent cross sections, so it does not affect their mutual relationship. However, with respect to what it can be found in the literature, this equivalence condition actually verifies only under a specific assumption, namely that, when each geometrical coordinate is scaled with a factor β,

$$\vec{r} = \begin{pmatrix} x \\ y \\ z \end{pmatrix} \longrightarrow \vec{\mathcal{R}} = \beta\vec{r} = \begin{pmatrix} \beta x \\ \beta y \\ \beta z \end{pmatrix}, \tag{3.15}$$

the divergence of the current scales accordingly,

$$\begin{aligned} \nabla \cdot (\vec{\Omega}\phi(\vec{r}, E, \vec{\Omega})) \longrightarrow & \beta \nabla \cdot (\vec{\Omega}\phi(\vec{\mathcal{R}}, E, \vec{\Omega})) = \\ & = \beta(\vec{\Omega} \cdot \nabla\phi(\vec{\mathcal{R}}, E, \vec{\Omega}) + \phi(\vec{\mathcal{R}}, E, \vec{\Omega})\nabla \cdot \vec{\Omega}). \end{aligned} \tag{3.16}$$

It can be easily shown that this condition is satisfied whenever $\nabla \cdot \vec{\Omega} = 0$, as for a cartesian set of coordinate,

$$\begin{aligned} \nabla \cdot (\vec{\Omega}\phi(\vec{r}, E, \vec{\Omega})) = \Omega \cdot \nabla\phi(\vec{r}, E, \vec{\Omega}) = \\ = \sqrt{1-\mu^2}cos\varphi \frac{\partial\phi(\vec{r}, E, \vec{\Omega})}{\partial x} + \sqrt{1-\mu^2}sin\varphi \frac{\partial\phi(\vec{r}, E, \vec{\Omega})}{\partial y} + \mu \frac{\partial\phi(\vec{r}, E, \vec{\Omega})}{\partial z}, \end{aligned} \tag{3.17}$$

where μ is the cosine of the polar angle θ and φ is, in this specific formula, the azimuthal angle. In this case, it is easy to verify that, when the coordinates are rescaled by a constant factor β,

$$\begin{cases} \mathrm{x} = \beta x \longrightarrow \partial\mathrm{x} = \beta\partial x \\ \mathrm{y} = \beta y \longrightarrow \partial\mathrm{y} = \beta\partial y \\ \mathrm{z} = \beta z \longrightarrow \partial\mathrm{z} = \beta\partial y, \end{cases} \tag{3.18}$$

the streaming term for the scaled geometry becomes

$$\begin{aligned}\nabla\cdot(\vec{\Omega}\phi(\vec{r},E,\vec{\Omega}))\longrightarrow &= \beta\sqrt{1-\mu^2}cos\varphi\frac{\partial\phi(\vec{\mathcal{R}},E,\vec{\Omega})}{\partial \mathrm{x}}+\beta\sqrt{1-\mu^2}sin\varphi\frac{\partial\phi(\vec{r},E,\vec{\Omega})}{\partial \mathrm{y}}\\ &+\beta\mu\frac{\partial\phi(\vec{r},E,\vec{\Omega})}{\beta\partial z}=\\ &=\beta\Omega\cdot\nabla\vec{\phi}(\vec{\mathcal{R}},E,\vec{\Omega}).\end{aligned}\tag{3.19}$$

When the reference frame is not fixed in space, as for curvilinear geometries (Bell and Glasstone, 1970), the condition expressed in eq. (3.16) should be examined case by case. For spherical and cylindrical frames, it is possible to prove that this condition still holds. Assuming a symmetrical sphere with radius scaled as $\mathrm{r}=\beta r$, it is possible to get

$$\begin{aligned}\nabla\cdot(\vec{\Omega}\phi(\vec{r},E,\vec{\Omega}))\longrightarrow&\beta\nabla\cdot(\vec{\Omega}\phi(\vec{\mathcal{R}},E,\vec{\Omega}))=\\ &=\beta\mu\frac{\partial\phi(\vec{\mathcal{R}},E,\vec{\Omega})}{\partial \mathrm{r}}+\beta\frac{1-\mu^2}{\mathrm{r}}\frac{\partial\phi(\vec{\mathcal{R}},E,\vec{\Omega})}{\partial\mu},\end{aligned}\tag{3.20}$$

while, for a cylinder whose radius and height are scaled by the same factor,

$$\begin{aligned}\nabla\cdot(\vec{\Omega}\phi(\vec{r},E,\vec{\Omega}))\longrightarrow&\beta\nabla\cdot(\vec{\Omega}\phi(\vec{\mathcal{R}},E,\vec{\Omega}))=\\ &=\beta\mu\frac{\partial\phi(\vec{\mathcal{R}},E,\vec{\Omega})}{\partial \mathrm{z}}+\beta\frac{\sqrt{1-\mu^2}}{\mathrm{r}}sin\varphi\left(\frac{\partial\phi(\vec{\mathcal{R}},E,\vec{\Omega})}{\partial\mu}-\beta\frac{\partial\phi(\vec{\mathcal{R}},E,\vec{\Omega})}{\partial\mu}\right)\\ &+\beta\sqrt{1-\mu^2}cos\varphi\frac{\partial\phi(\vec{\mathcal{R}},E,\vec{\Omega})}{\partial \mathrm{r}}.\end{aligned}\tag{3.21}$$

For more complex geometries, a useful generalisation of the scattering term can be found in Pomraning, 1989.

Exploiting this scaling, it is easy to show that, when $\beta=\delta$, the scaled system is critical, as δ cancels out in eq. (3.13). This fact further confirms that δ can be interpreted as the streaming eigenvalue: given a certain material composition, criticality is attained changing the volume of the system, thus its surface-to-volume ratio and, thus, the leakage contribution. Of course, this operation is not always possible, since the effective multiplication constant of the infinite system, k_∞, which is a material parameter featuring the system, should be larger than unity. This condition can be deduced from elementary criticality theory: considering a homogeneous, one-speed slab with zero-flux vacuum boundary condition, for which the identity $\nabla^2\varphi_\delta(x)=-B^2\varphi_\delta(x)$ holds, it is possible to get

$$\delta=\frac{\sqrt{k_\infty-1}}{LB},\tag{3.22}$$

which yields a real and positive eigenvalue if and only if $k_\infty>1$. This simple example poses the interesting question of how to interpret the fact that $\delta\longrightarrow\infty$ when $B\longrightarrow 0$,

which is verified when the slab thickness H tends to infinity. Since criticality is attained by changing the leakage contribution in the balance equation, it is not possible to derive a criticality condition for the infinite medium, where no leakage occurs by definition. From another perspective, the streaming operator becomes singular, so eq. (3.13) can be satisfied only in the limit $\delta \longrightarrow \infty$. The same result can be obtained also more rigorously taking the limit for $\beta \longrightarrow \infty$, when condition eq. (3.16) is verified. Despite its clear relationship with the streaming operator, which manifests in the geometry scaling under specific hypotheses, δ will be addressed in the following as the density eigenvalue, in order to be consistent with the literature and to be as general as possible.

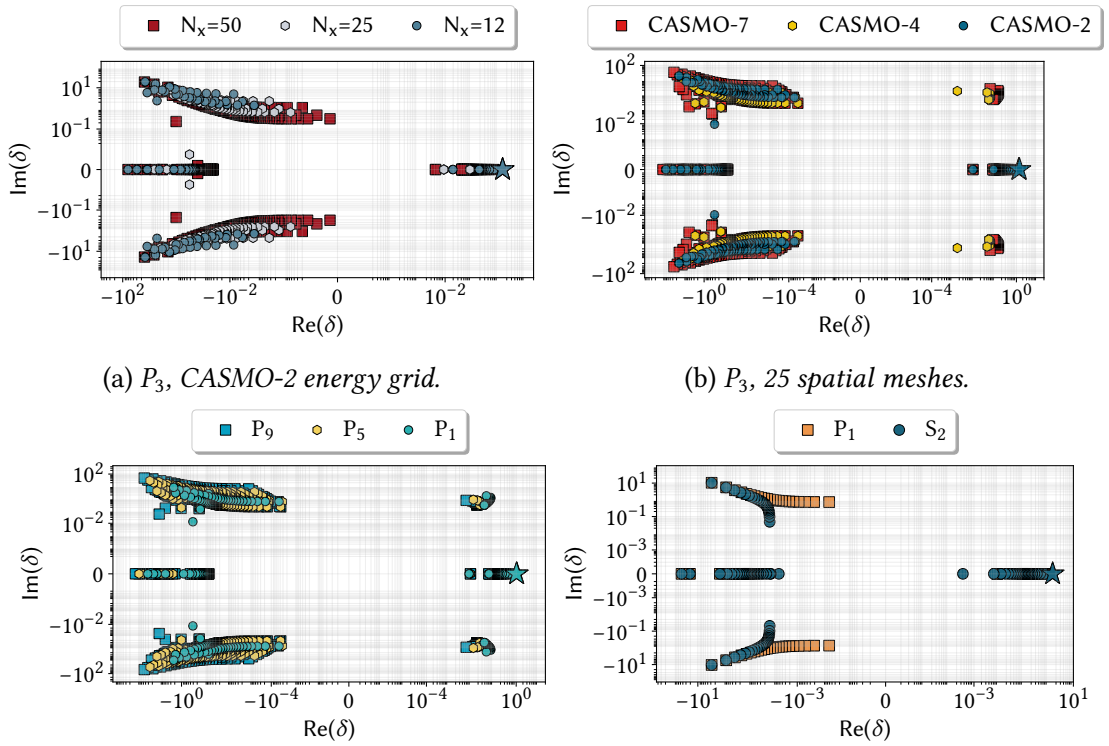

(a) P_3, *CASMO-2 energy grid.*

(b) P_3, *25 spatial meshes.*

(c) *CASMO-4 energy grid, 25 meshes.*

(d) *25 meshes and CASMO-2 energy grid.*

Figure 3.17: *δ-spectrum for a homogeneous, isotropic, fissile slab, imposing Mark boundary conditions. The stars represent the fundamental eigenvalues.*

Figure 3.17 provides an idea of the behaviour of the δ eigenvalues on the complex plane for different numerical discretisations, assuming the usual one-dimensional cartesian system. Observing the figures, it is not easy to individuate an intuitive, clear relationship between the spectrum shape and the number of spatial meshes, the energy group structures and the angular approximation, also due to the difficulty in giving a physical interpretation to the higher-order eigenvalues. Nevertheless, it is possible to make some general comments. First, the additional degrees of freedom available with

finer numerical approximations mainly affect the complex branches. Then, it is possible to appreciate a strong interplay between directional and energetic effects. As an example of such intricacy, it should be noticed that, in fig. 3.18, the spectrum computed with P_1 and the CASMO-4 grid is featured by two branches of complex conjugate values when $\mathrm{Re}(\delta) > 0$, while the spectrum for the same system solved with P_3 and the CASMO-4 grid does not show any complex conjugate branch in the half-plane $\mathrm{Re}(\delta) > 0$. In this last case, these branches can be found in the $\mathrm{Re}(\delta) < 0$ half-plane. Despite this complexity, it is possible to notice that the number of complex branches is proportional to the number of groups and to the angular approximation order. For example, two complex conjugate branches appear in the P_1, CASMO-2 case while six complex conjugate branches are present for the P_3, CASMO-2 case, while six branches can be appreciated for the P_1, CASMO-4 case and twelve batches can be observed for the P_3, CASMO-4 case. Despite this clear proportionality, it is not possible to observe a striking relationship like for the time spectrum.

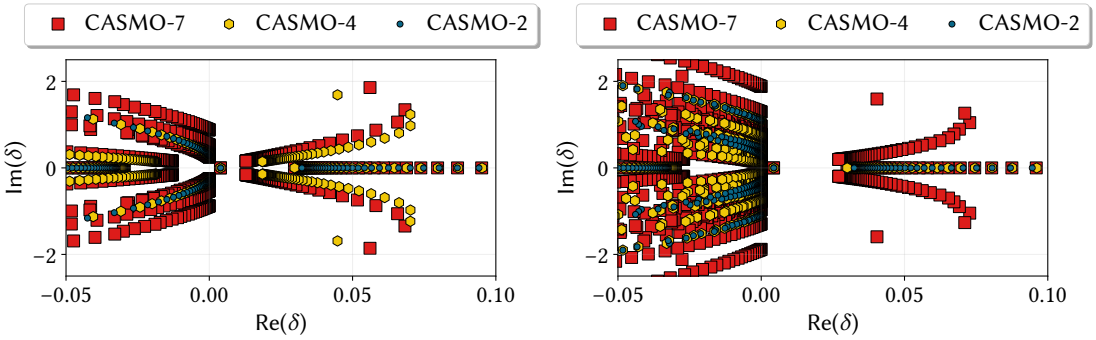

(a) P_1. (b) P_3.

Figure 3.18: *δ-spectrum for a homogeneous, isotropic, fissile slab, imposing Mark boundary conditions and using 50 meshes. The stars represent the fundamental eigenvalues.*

Then, it is possible to see some complex structures also for the simplest case studies, employing the CASMO-2 energy grid and the P_1 model, like in fig. 3.17d. In this case, it is interesting to observe that, differently from the other formulations, there is a significant difference related to the angular model employed. This increased sensitivity is probably due to the different approach, i.e. projection against discretisation, at the basis of the P_N and S_N methods, respectively, to approximate the streaming term, whose eigenvalue is δ itself.

Another general feature of the δ spectrum is the presence of negative, real eigenvalues associated to spatially oscillating solutions. Their existence can be probably explained by the fact that, in virtue of the competition between the production and the removal terms, some critical systems could be obtained switching the signs of these terms and introducing negative neutrons.

Finally, it is interesting to highlight the fact that, when even-order (odd-order) P_N

(S_N) approximations are used to evaluate the spectrum, a set of extremely large eigenvalues (~ 10^{15}) appears. The spawning of such eigenvalues can be explained recalling that, when such parity order is employed, the streaming operator becomes singular, as discussed in section 2.5.1. From a physical point of view, it is possible to justify the existence of such eigenvalues exploiting the S_N formalism. When N is odd, the following equation could be written for the streaming direction $\mu_{N/2+1} = 0$, parallel to the slab boundaries,

$$\mu_{N/2+1} \frac{\partial \phi(x, \mu_{N/2+1})}{\partial x} = -\frac{1}{\delta} \Sigma \phi(x, \mu_{N/2+1}) = 0. \tag{3.23}$$

Since Σ and ϕ are non-zero, eq. (3.23) holds only in the limit case $\delta \longrightarrow \infty$.

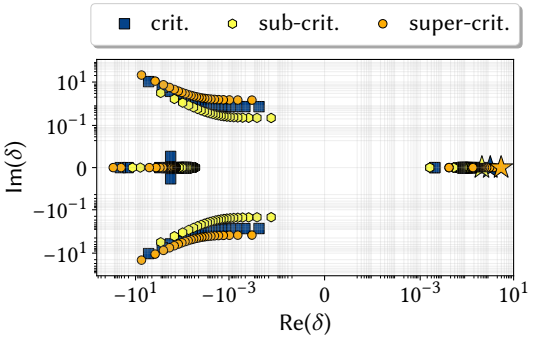

Figure 3.19: *δ-spectrum for a homogeneous, fissile slab with different thicknesses, computed with a P_1 model using data collapsed on the CASMO-2 grid and 25 meshes, imposing Mark boundary conditions. The stars represent the fundamental eigenvalues.*

Concerning the sensitivity of the spectrum to the offset from criticality, it is possible to observe, looking at section 3.3.5, that the overall shape is not distorted by this parameter, despite the fundamental eigenvalue exhibits a significant variation according to the distance from criticality, as also observed in Ronen, Shalitin, and Wagschal, 1976. However, with respect to the k and γ cases, it is not always possible to justify the existence of a positive, real eigenvalue, especially in the case of a heterogeneous medium. In this last case, it may be possible that criticality is attained with a negative value of δ, which could artificially exchange the rôle of production and removal among the different regions of the system in case the multiplicativity was not sufficient to sustain the chain reaction. This behaviour could be regarded as an unpleasant issue concerning δ, but it should be interpreted as a consequence of the additional physical constraints considered in the search for criticality.

Finally, section 3.3.5 shows the effect of the spatial heterogeneity on the spectrum shape. In this case, despite some additional complex values, related to the use of more energy groups and common to each arrangement, it is not possible to appreciate evident deformations of the spectrum due to the number of layers or to their composition. Nevertheless, the detail of the right portion of the complex spectrum, depicted in the

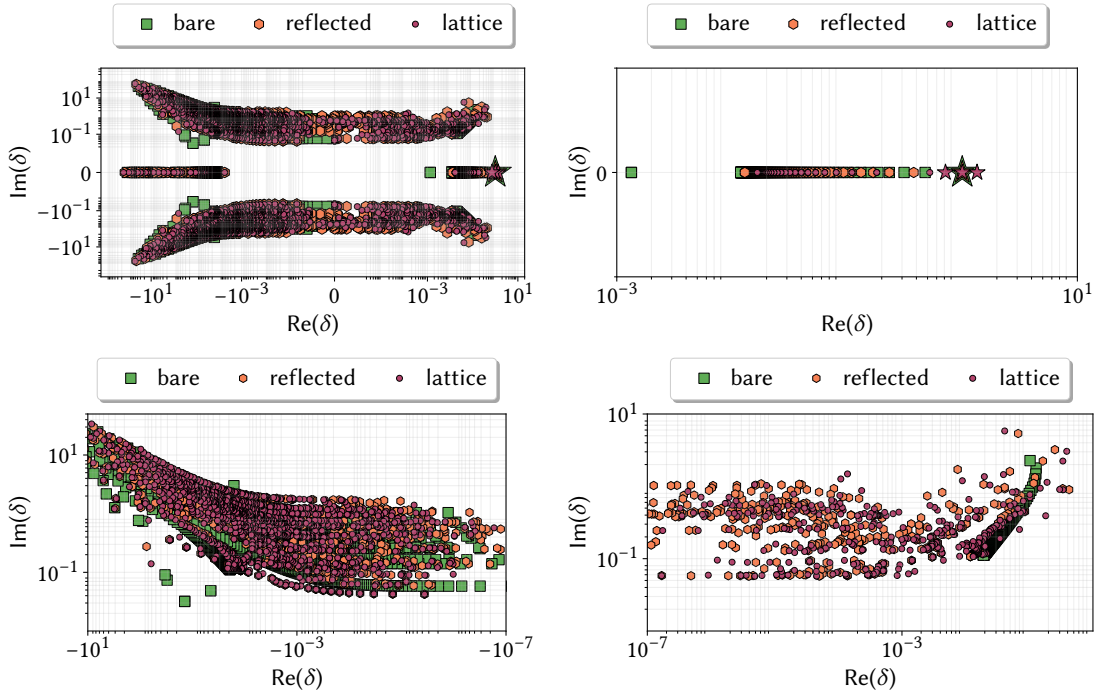

Figure 3.20: *δ-spectrum (top) for different slabs featured by different material arrangements, computed with a P_3 model using data collapsed on the CASMO-7 grid and 121 meshes, imposing Mark boundary conditions, and zoom on the negative (left) and positive (right) half-planes. The stars represent the fundamental eigenvalues.*

bottom-right of the same figure, suggests that the heterogeneity has an impact on the eigenvalues distribution, which appear to be more dispersed than in the homogeneous case, although it is not easy to identify a clear pattern. Moreover, for the lattice case, more than one fundamental eigenvalue appears, each associated to an eigenfunction with uniform sign. These fluxes, reported in section 3.3.5, are very similar in space but with a different energy spectrum. The appearance of these multiple fundamental eigenpair is related to the fact that δ acts on all the cross sections of all the materials. This simultaneous modification means that there is a competition between different terms and different spatial regions. For example, the slowing down occurring in water competes with the its absorption. Thus, more than one configurations are possible,

The analysis of the δ spectrum in different cases allows to observe some general features:

- the spectrum is featured by complex eigenvalues, associated to higher-order effects, with a strong coupling between energy and direction;
- the fundamental eigenvalue usually lies at the right of the spectrum, assuming the largest real value, but this may not hold in general, especially for heterogeneous

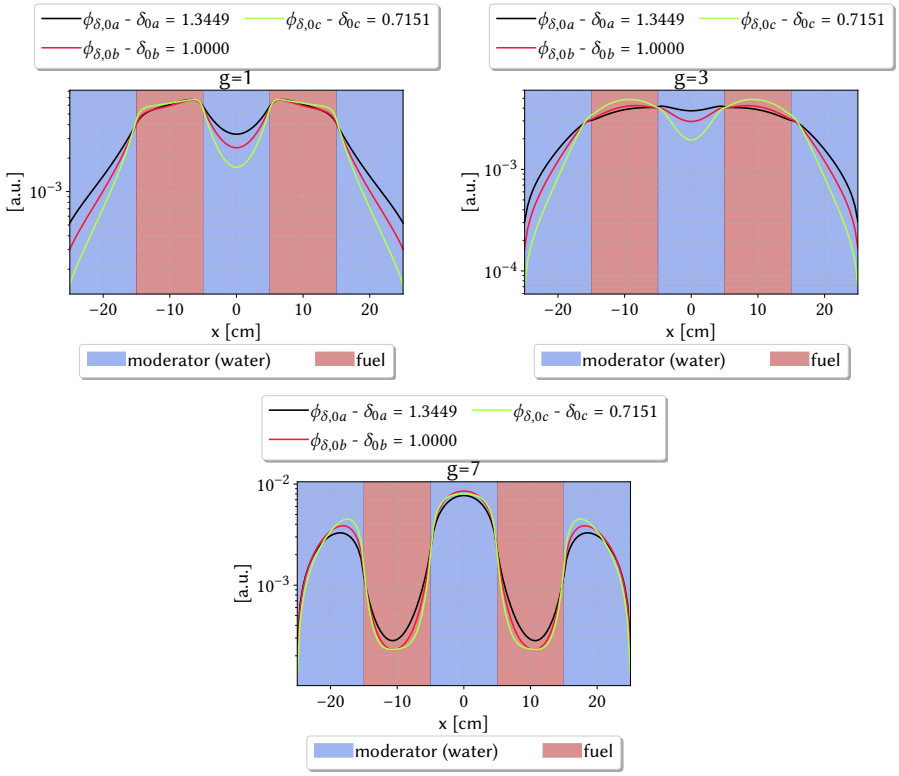

Figure 3.21: .

media;

- the fundamental eigenvalue appears to be more sensitive than k_0 and γ_0 to the criticality level;
- the fundamental eigenfunction is a solution common to each system featured by a geometrical similarity transformation;
- the energy spectrum is not affected by the eigenvalue, which can be seen as modifying the nuclides densities or the boundary leakages.
- the δ formulation could be applied as well in a diffusion model, but at the price of solving a non-linear eigenvalue problem, since the diffusion coefficient would depend on δ itself.
- more than one configurations is possible for heterogeneous systems.

3.6 The capture eigenvalue

Inspired by the fact that k and γ act on specific reaction channels, an eigenvalue acting on neutron capture, indicated with θ, can be introduced as well,

$$\left(\hat{L} + \hat{F}_0 + \hat{S}_0 - \hat{S} - \hat{F}\right) \varphi_{\theta,n} = \frac{1}{\theta_n} \hat{C} \varphi_{\theta,n}. \tag{3.24}$$

As mentioned in chapter 2, to the author's knowledge, this is the first time that this formulation is addressed. Integrating (3.24) over the phase space and isolating θ_0 is useful to give a physical interpretation to this eigenvalue,

$$\theta_n = \frac{\langle \hat{C} \varphi_{\theta,n} \rangle}{\langle (\hat{L} + \hat{S}_0 + \hat{F}_0 - \hat{F} - \hat{S}) \varphi_{\theta,n} \rangle}, \tag{3.25}$$

which expresses the number of neutrons that have to be captured to maintain criticality per neutron that is present inside the system. Since the attention is focused on capture, which is a loss term, the behaviour of this eigenvalue with respect to criticality is reversed: a super-critical system requires to increase capture, so $\theta < 1$, while a sub-critical system requires the system to reduce capture, so $\theta > 1$. In this last case, it is also possible that, for a significant level of sub-criticality, θ becomes negative. In such a case, the criticality could be attained only substituting the removal with a production term, similarly to what occurs for the δ case. This situation, which seems rather unphysical, should be considered as the counter-part of adjusting $\nu\Sigma_f$ with k and $\nu\Sigma_f + \Sigma_s$ with γ: it is always possible to reach criticality adjusting these parameters, with k and γ ranging from 0 to $+\infty$, provided that the system is able to emit neutrons. However, if the number of neutrons emitted cannot be adjusted, the only way to compensate this lack of particles is to introduce them by mean of a negative capture. Despite this fact may sound misleading, this property may be very useful for the design of a reactor, because, in this specific situation, the designer could be immediately aware that it is necessary to increase the multiplication properties of the system. The same situation handled with the k (or γ) eigenvalue would not provide a one-way suggestion, since a value of k (or γ) smaller than 1 could be interpreted ambiguously as the need for either more fissile material or reduced leakages or reduced parasitic captures. Therefore, due to its tight connection with the capture reactions, this eigenvalue could be useful for the design of specific components of a reactor, e.g., control rods and breeding blankets.

As for the δ eigenvalue, it is not trivial to give a clear, physical interpretation to the θ higher-order eigenvalues. Nevertheless, the spectrum behaviour is clearly sensitive to the physical model employed to solve the NTE. Figure 3.22 provides an overview of the spectrum behaviour, considering the same approximations used for the previous analyses. Similar considerations to the ones made for the time and density eigenvalue can be drawn, with an important difference: the θ fundamental eigenvalue may not lie at the real axis extremity, as clearly visible in figs. 3.22c and 3.22e. In this specific case,

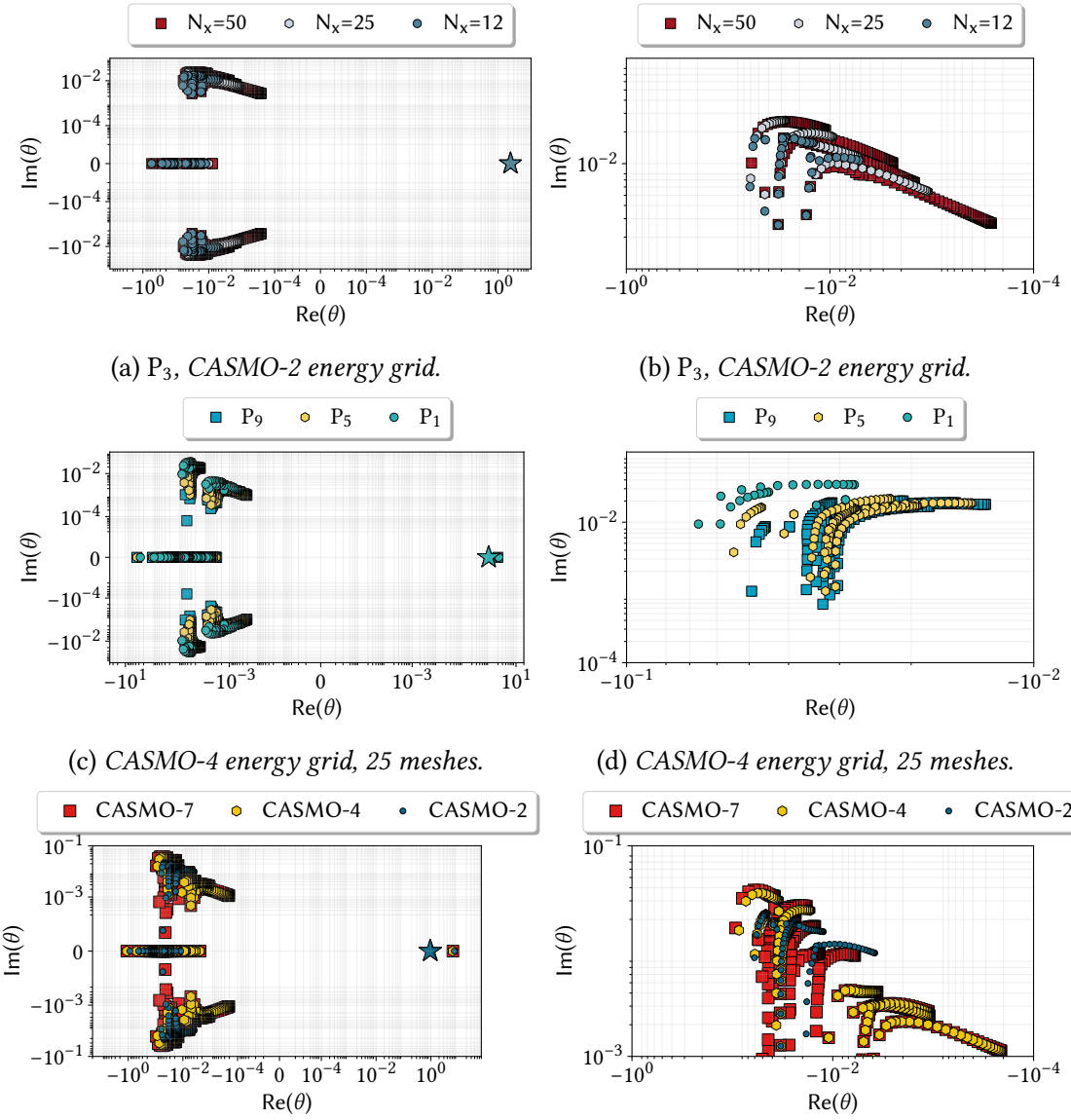

(a) P_3, *CASMO-2 energy grid.*

(b) P_3, *CASMO-2 energy grid.*

(c) *CASMO-4 energy grid, 25 meshes.*

(d) *CASMO-4 energy grid, 25 meshes.*

(e) P_3, *25 spatial meshes.*

(f) P_3, *25 spatial meshes.*

Figure 3.22: *θ-spectrum for a homogeneous, isotropic, fissile slab, imposing Mark boundary conditions. The stars represent the fundamental eigenvalues.*

the eigenvalue on the right of the fundamental is associated to the first-order harmonic, i.e. the flux featured by one sign change.

Figure 3.23 shows a detail of the spectrum, in linear scale, for the P_1 and P_3 approximations as a function of different energy grid structures. Also in this case, it is possible to appreciate a relationship between the number of complex branches, the number of groups and the angular approximation order: for each group, (N + 1)/2 branches with

positive imaginary part and (N + 1)/2 branches with negative imaginary part can be individuated.

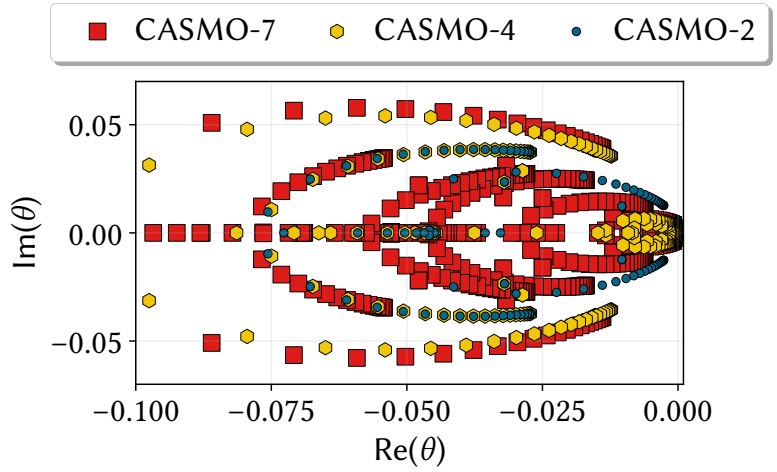

(a) P_1, *30 spatial meshes.*

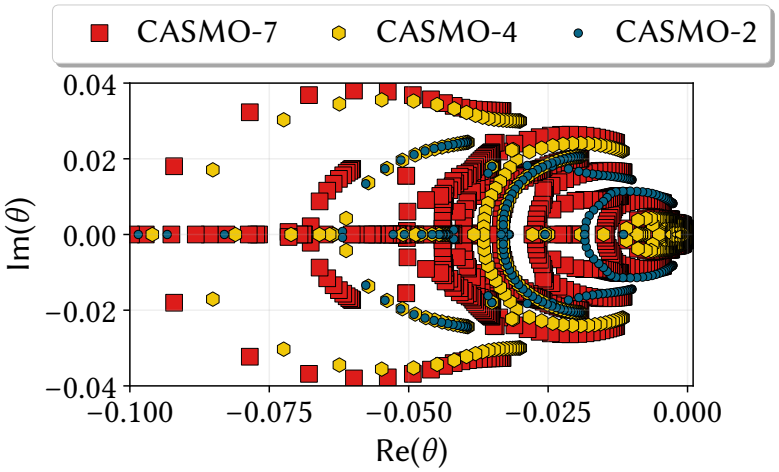

(b) P_3, *30 spatial meshes.*

Figure 3.23: *θ-spectrum for a homogeneous, isotropic, fissile slab, imposing Mark boundary conditions. The stars represent the fundamental eigenvalues. Graphs on the right represent a zoom of the spectra depicted on the left.*

As regards the impact of the angular model, the spectra yielded by the P_N and S_N models are very close, as visible from fig. 3.25a.

Figure section 3.3.6 shows some details of the spectrum for the different heterogeneous arrangements studied for the other eigenvalues. With respect to the homogeneous case, which is featured by N+1 oval-shaped branches per each energy group,

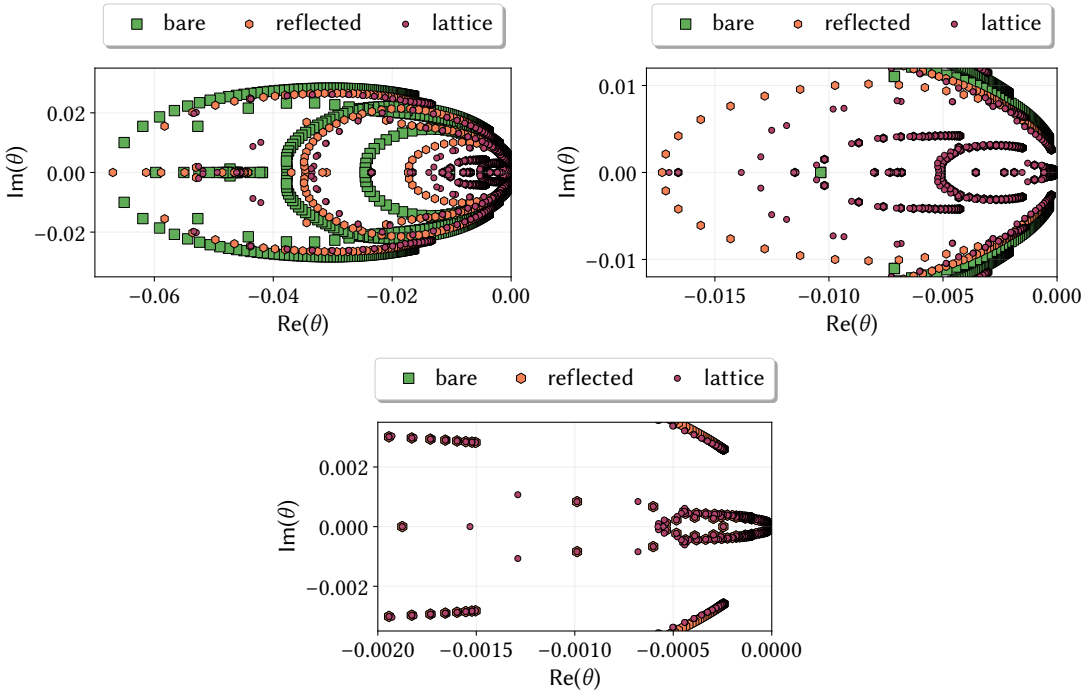

Figure 3.24: *Details of the θ-spectrum for slabs featured by different heterogeneous arrangements, computed with the P_3 model with 121 meshes and Mark boundary conditions. The cross sections are collapsed on the CASMO-2 energy grid. The stars represent the fundamental eigenvalues.*

the introduction of the heterogeneity alters the shape of the spectrum, which is characterised by additional branches, visible in the region $\mathrm{Re}(\theta) = [-0.02, 0]$. As for the previous eigenvalues, the number of branches seems proportional to the number of different materials composing the system, two in this case, while their disposition in the complex plane is related to the specific arrangement of the system.

Concerning the effect of the departure from criticality, it is possible to see in fig. 3.25b that there is a strong sensitivity of the real eigenvalues with respect to this parameter, as already discussed above.

The analysis of the newly proposed capture eigenvalue allows to draw some general conclusions, which may be useful for its application:

- the fundamental may not be positive. Even if it was, it may not be the larger positive eigenvalue;
- when the criticality cannot be attained with the available fissile material, the fundamental becomes negative;
- the spectrum is very sensitive to the departure from criticality;

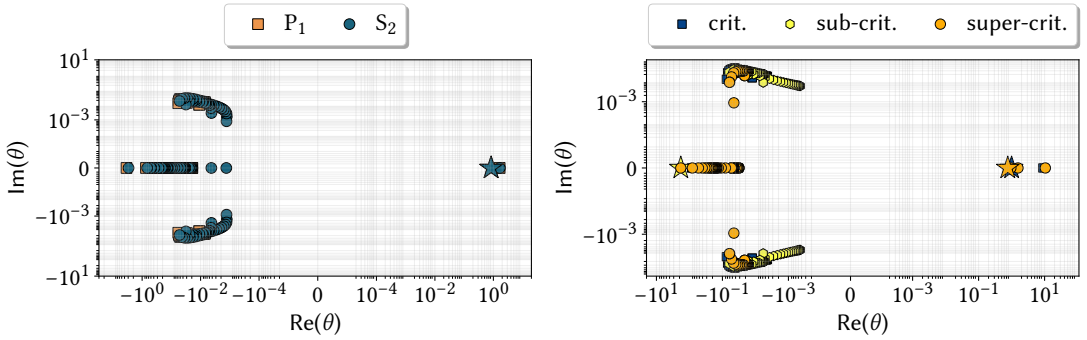

(a) (b)

Figure 3.25: *θ-spectrum for a homogeneous, linearly anisotropic, fissile slab, computed with the P_1 model with 25 meshes and Mark boundary conditions. The cross sections are collapsed on the CASMO-2 energy grid. The stars represent the fundamental eigenvalues.*

- since the eigenvalue acts on the overall capture cross section of the system, it is not possible to establish *a priori* the impact on the energy spectrum, especially for heterogeneous systems: in some cases, e.g., in presence of boron, the capture could harden the energy spectrum, removing thermal neutrons, while in other it may soften the energy spectrum, e.g., in presence of fertile material that could remove fast neutrons.

3.7 The effect of energy group collapsing

As highlighted throughout the chapter, the eigenvalue spectra associated to the different NTE formulations is tightly connected both to the physics of the transport process and to the modelling and numerical approximations used to solve the problem. Except for the k and γ eigenvalues in case of isotropic scattering, the shape of the spectrum of the different formulations is strongly sensitive to the modelling approximations, like the number of groups and directions chosen to discretize the equation.

In light of these observations, it is interesting to observe the effect of group collapsing on the shape of the eigenvalue spectrum, since it could disclose some aspects of the collapsing procedure that could be exploited to improve the choice of the group structure, which is still an open issue of reactor physics, as will also be pointed out in chapter 4.

In order to get some qualitative information, the spectrum of the time eigenvalue formulation is analysed in the following for a homogeneous slab, filled first with a mixture of water and enriched uranium, and then with a mixture of uranium and plutonium, in order to highlight both the impact of the energy spectrum on the eigenvalue distribution and the influence of the group structures chosen for the collapsing. The thickness of the thermal slab is 37.8 cm, while the thickness of the second one is 74.6 cm. In both

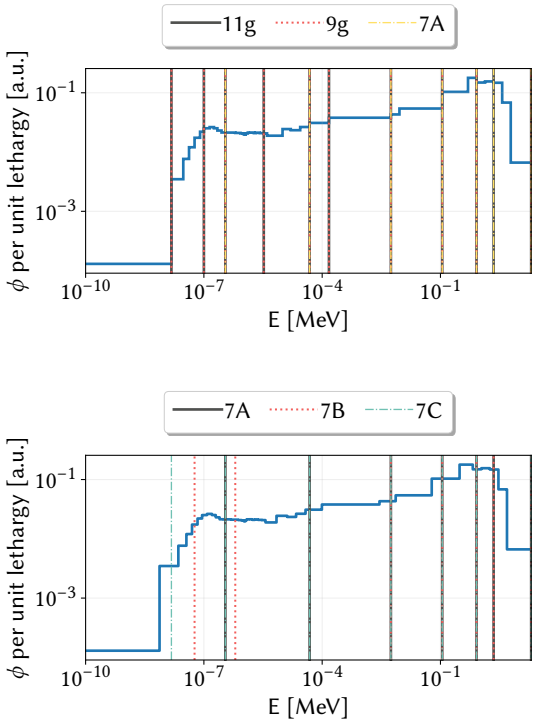

Figure 3.26: *Flux per unit lethargy computed with a P_1 model using CASMO-40 group structure for a thermal system. The vertical lines represent some coarse-group grids used to collapse the cross sections.*

cases, the slab is featured by linearly anisotropic scattering.

Figure 3.26 shows the α-flux per unit lethargy scored on the CASMO-40 grid for the thermal slab case, and the few-group structures used to perform the group collapsing, whose specifications can be found in table 3.3.

At first, the spectrum is collapsed using the grid with 11 groups. Then, some groups are removed from this grid, in order to collapse over 10 and 7 groups, respectively. Observing table 3.3, it is possible to notice that the 10-group grid is obtained collapsing the first two fast groups of the 11-group grid, while the 7-group structure is obtained collapsing some epithermal groups where the flux is almost constant and the three thermal groups with the lowest energy. The best option among the two turns out to be the 7-group grid, which yields $\alpha_{0,7g}$ =564s^{-1} against $\alpha_{0,11g}$ =524s^{-1}, while the 10–group structure, despite three additional groups, provides $\alpha_{0,7g}$ =770s^{-1}. The fundamental eigenvalue α_0 computed with the CASMO-40 grid is equal to 244s^{-1}.

Figure 3.27 shows the impact on the spectrum shape due to the loss of degrees of freedom caused by the collapsing procedure. Exploiting the physical meaning of the α_n frequencies, it is possible to notice the presence of two batches of eigenvalues, one in

Table 3.3: *Energy group structures employed to assess the impact of group collapsing on the eigenvalue spectrum.*

group boundary [MeV]	11g	10g	7A	7B	7C
2.00000×10^{1}	x	x	x	x	x
2.31000×10^{0}	x		x	x	
8.21000×10^{-1}	x	x	x	x	x
1.11000×10^{-1}	x	x	x	x	x
5.53000×10^{-3}	x	x	x	x	x
1.48728×10^{-4}	x	x			
4.80520×10^{-5}	x	x	x		x
4.00000×10^{-6}					
3.30000×10^{-6}	x	x			
6.25000×10^{-7}				x	
1.00000×10^{-7}	x	x			
1.40000×10^{-7}					
3.50000×10^{-7}	x	x	x		x
5.80000×10^{-8}				x	
1.50000×10^{-8}	x	x			
1.00000×10^{-9}					x
1.00000×10^{-11}	x	x	x	x	x

the interval $[-1 \times 10^{9}, -1 \times 10^{8}]\,\mathrm{s}^{-1}$ and the other in $[-1 \times 10^{7}, -1 \times 10^{5}]\,\mathrm{s}^{-1}$, respectively. This net subdivision is a consequence of the thermal energy spectrum featuring the system, which is historically known to be adequately described by a two-group model. As already observed previously, the branches of the collapsed spectrum are located according to the opposite of their group-wise collision frequency. Thanks to the detail of the spectrum reported on the bottom of the figure, is possible to notice that there are four branches of the 10-group spectrum that are very close to each other, due to the presence of many thermal groups in this grid, but only two branches are located in the fast region. On the contrary, the 7-group grid, featured by less degrees of freedom, allows to span different frequencies, providing an overall better representation of the original spectrum and, thus, of the fundamental eigenvalue. This behaviour is consistent with the common practice of dividing the energy grid with into uniform lethargy bins (Bell and Glasstone, 1970).

Similarly, fig. 3.28 provides the time spectra computed for different 7-group structures. Again, the best results are provided by the cases that allow to cover more uniformly the frequencies, i.e. A ($\alpha_0 = 564.3\,\mathrm{s}^{-1}$) and B ($\alpha_0 = 540.3\,\mathrm{s}^{-1}$), while the worst case, C ($\alpha_0 = 2309.3\,\mathrm{s}^{-1}$), is featured by two thermal groups, providing unnecessary detail, and only one fast group. The bottom part of fig. 3.28 shows the comparison between

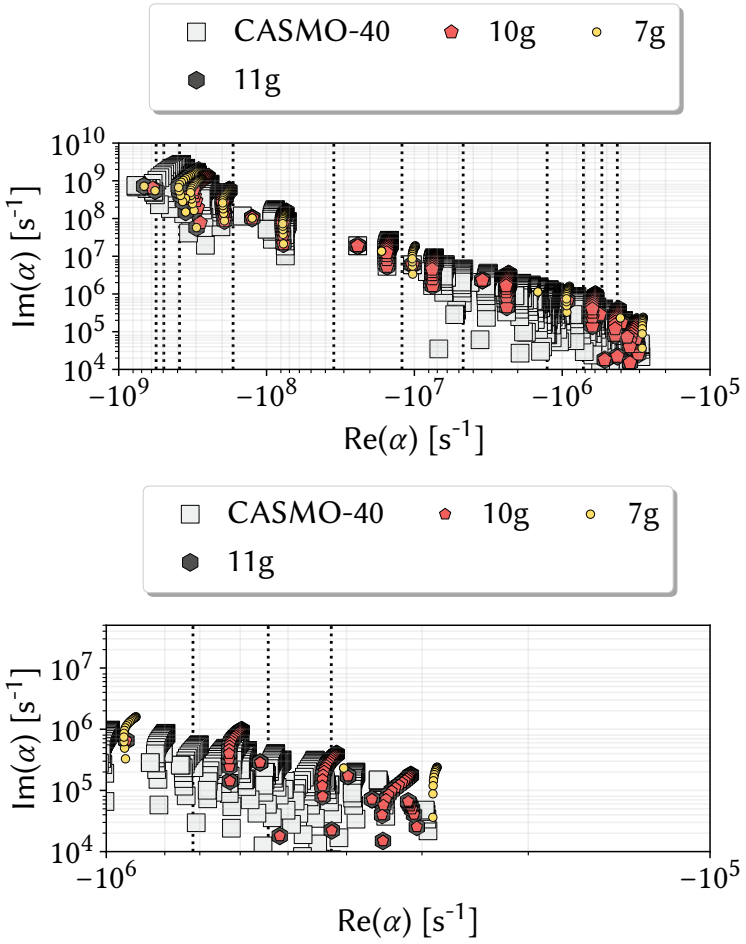

Figure 3.27: *Time spectrum computed for a homogeneous, fissile slab using the P_1 model and different group structures for the cross section collapsing.*

the A and C cases, which are identical except for one group: in the A case, an energy group is employed in the fast region, while in the C case it is used to cover the thermal region, where the flux variation is reduced with respect to the one in the fastest groups. As clearly visible in the figure, the complex branches associated to the thermal groups, indicated by the round markers, appears to be overlapped around $3 \times 10^{-5}\,\mathrm{s}^{-1}$, suggesting that the information associated to the additional thermal group is redundant, while the corresponding branches in the fast region for the C case, indicated by the hexagonal markers, are more separated. Considering that the first three eigenvalues of the discrete spectrum, reported in table 3.4, are much more accurate when computed using the 7A grid rather than using the 7C grid, it could be concluded that, in this case, the fast group is more important to correctly reproduce the behaviour of the reference model. Hence, due to the observations made so far regarding the behaviour of the time frequencies with respect to the group structure employed for collapsing, it is reasonable

to conclude that these features are tightly connected.

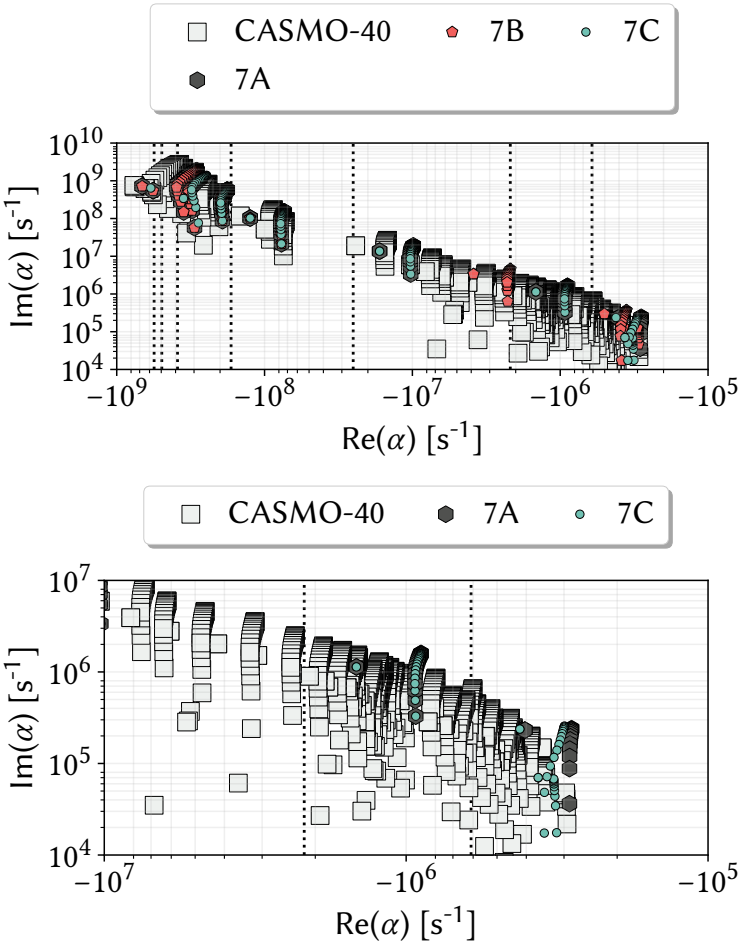

Figure 3.28: *Time spectrum computed for a homogeneous, fissile slab using the P_1 model and different group structures for the cross section collapsing.*

eigenvalue [s^{-1}]	CASMO-40	7A	7B	7C
α_0	244.5	564.3	540.3	2309.3
α_1	−42 957.4	−44 200.7	−43 529.7	−38 055.44
α_2	−73 107.8	−75 572.6	−74 282.6	−67 741.1

Table 3.4: *First three time eigenvalues computed collapsing the data for the thermal slab case with different group structures.*

The same relationship can be appreciated also for the slab featured by a fast spectrum, depicted in fig. 3.29. In this case, three 10-group structures with the same group

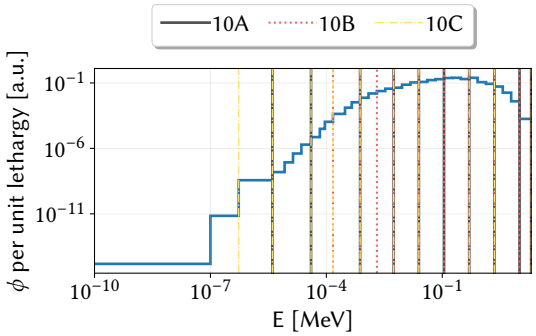

Figure 3.29: *Flux per unit lethargy computed with a P_1 model using ECCO-33 group structure for a fast system. The vertical lines represent some coarse-group grids used to collapse the cross sections.*

boundaries except few ones, reported in table 3.6, are used to perform the cross sections collapsing, starting from the reference ones scored on the ECCO-33 grid. The first grid, 10A, presents an intermediate cut-off boundary for the thermal group with respect to the cases B and C, where the thermal group is at lower and higher energies, respectively.

Contrarily to the thermal case, the time spectrum in fig. 3.30 does not show a clear subdivision in batches of the "continuous" portion of the spectrum, but it is worth noticing that the largest frequencies fall around $7 \times 10^{-5}\,s^{-1}$ instead of $2 \times 10^{-5}\,s^{-1}$, which is the largest frequency characterising the thermal system. These features of the time spectrum suggest that the thermal group is less relevant than in the thermal spectrum case, but still important enough to be considered for the definition of the collapsing structure. Table 3.6 helps to confirm this fact. The case that best matches the three time frequencies is the 10A, which is featured by a rather uniform subdivision in lethargy. When the thermal region is collapsed with some epithermal energies, as in case B, the fundamental eigenvalue is still quite accurate, but the higher-order harmonics, which are crucial to determine the behaviour of the system (Beckner and Rydin, 1975), are associated to quite different frequencies with respect to the reference ones. As a consequence of the lack of thermal groups, the spectrum computed with this grid does not present any complex branch around the frequencies characterising the thermal region. On the contrary, case C, which includes a thermal group at the price of a wider fast group, yields a fundamental frequency that is quite far from the reference, but higher-order frequencies that are close to the reference. This last case seems to suggest that, if a modal expansion was used to study the system evolution, the initial instants of the transient could be accurate. As for the thermal slab, the presence of a superfluous thermal group is made evident by the reduced separation between the complex branches associated to these groups.

In this section, the relationship between the time spectrum for a collapsed system

Table 3.5: *Energy group structures employed to assess the impact of group collapsing on the eigenvalue spectrum for the fast slab.*

group boundary [MeV]	10A	10B	10C
2.000000×10^{1}	x	x	x
1.000000×10^{1}	x	x	
2.231020×10^{1}	x	x	x
4.978707×10^{-1}	x	x	x
1.110900×10^{-1}	x	x	
2.478752×10^{-2}	x	x	x
5.530844×10^{-3}	x	x	x
2.034684×10^{-3}		x	
7.485183×10^{-4}			x
1.486254×10^{-4}			x
7.485183×10^{-4}	x	x	
1.486254×10^{-4}		x	
4.016900×10^{-5}	x		x
4.000000×10^{-6}	x		x
5.400000×10^{-7}			x
1.000000×10^{-11}	x	x	x

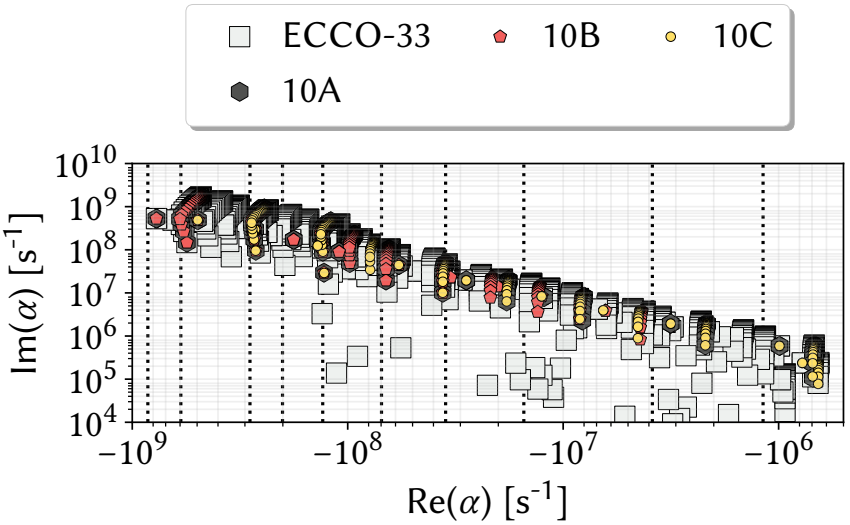

Figure 3.30: *Time spectrum computed for a homogeneous, fissile slab using the P_1 model and different group structures for the cross section collapsing.*

eigenvalue $[s^{-1}]$	ECCO-33	10A	10B	10C
α_0	5094.4	8950.1	8929.9	17 467.2
α_1	−193 382.2	−193 629.2	−889 079.9	−194 341.1
α_2	−201 054.8	−201 269.2	−905 034.3	−202 012.0

Table 3.6: *First three time eigenvalues computed collapsing the data for the fast slab case with different group structures.*

and the group structure used to perform the collapsing has been analysed, highlighting that the both the discrete and the continuous parts of the spectrum can be used to assess whether the group structure is adequate to provide a sufficiently accurate approximation of the reference one. In light of these observations, it could be interesting, as a future perspective, to exploit the spectrum as a driver for feature-selection algorithms (Liu, 2010) like genetic algorithms, which have been successfully employed for the optimal selection of the group boundaries in the recent years (Massone, Gabrielli, and Rineiski, 2017). In this application, the accuracy between the region-wise, few-group flux and the associated k_{eff} and the reference quantities is used to guide the optimisation process. Despite its intuitiveness, this approach may be difficult and expensive to apply in case the target of the optimisation process involves a time-dependent problem. In this case, it could be worth to employ the time spectrum as a concise indicator of the temporal, spatial, angular and energetic behaviour of the system, to drive the group selection process more rigorously. For this application, some operator transformations like the Givens rotation of the QR factorisation (Saad, 1992) could be employed to compute the eigenvalues without the need for evaluating the associated eigenvectors, reducing both the computational time and the memory consumption.

3.8 Conclusions

In this chapter, the different eigenvalue formulations to the neutron transport equation available in the literature, i.e. the time, the multiplication, the collision and the density eigenvalues, and a newly introduced capture eigenvalue, introduced here for the first time, have been presented, discussing thoroughly both their advantages and their disadvantages. The attention has been focused mainly on the behaviour of the different eigenvalue spectra according to the spatial, angular and energetic models employed and to the spatial heterogeneity. For instance, the concept of Corngold limit has been extended to the case of multi-group systems, showing heuristically that the group-wise fast, complex conjugate frequencies are bounded by the opposite of the group-wise collision frequency.

The analysis of the spectrum, led using the TEST code, has been extremely useful to highlight the tight connection between the spectra and the approximation used to solve

the neutron transport equation and to draw some important, practical conclusions to drive the eigenvalue solver towards the fundamental eigenpair according to the spectral formulation employed. Finally, a possible application of the spectrum as a concise figure of merit for the optimal selection of the group boundaries has been suggested as a future perspective.

References

Abrate, N., M. Burrone, S. Dulla, P. Ravetto, and P. Saracco (2021). "Eigenvalue Formulations for the P_N Approximation to the Neutron Transport Equation". In: *Journal of Computational and Theoretical Transport* 50, pages 407–429 (cited on page 84).

Abrate, N., S. Dulla, P. Ravetto, and P. Saracco (2021). "On some features of the eigenvalue problem for the P_N approximation of the neutron transport equation". In: *Annals of Nuclear Energy* 163, pages 108–477 (cited on page 84).

Adam, D. (2020). "A guide to R–the pandemic's misunderstood metric". In: *Nature* 583, pages 346–349 (cited on page 71).

Barbarino, A., S. Dulla, and P. Ravetto (2013). In: *Integral methods in science and engineering*. Edited by C. Constanda, B. Bodmann, and H. Velho. New York: Birkhäuser (cited on page 92).

Beckner, W. D. and R. A. Rydin (1975). "A higher order relationship between static power tilts and eigenvalue separation in nuclear reactors". In: *Nuclear Science and Engineering* 56, pages 131–141 (cited on pages 70, 108).

Bell, G. I. and S. Glasstone (1970). "Nuclear Reactor Theory". Van Nostrand Reinhold (cited on pages 82, 93, 105).

Cacuci, D. G., Y. Ronen, Z. Shayer, J. J. Wagschal, and Y. Yeivin (1982). "Eigenvalue-dependent neutron energy spectra: definitions, analyses, and applications". In: *Nuclear Science and Engineering* 81, pages 432–442 (cited on pages 79–80).

Chentre, N., P. Saracco, S. Dulla, and P. Ravetto (2019). "On the prompt time eigenvalue estimation for subcritical multiplying systems". In: *Annals of Nuclear Energy* 132, pages 172–180 (cited on page 80).

Corngold, N. (1975). "Quasi-exponential decay of neutron fields". In: *Advances in Nuclear Science and Technology*. Edited by E. J. Henley and J. Lewins. Academic Press, pages 1–46 (cited on page 80).

Corngold, N. (1969). "Some recent results in the theory of the transport of thermal". In: *SIAM-AMS Proceedings*. Volume 1. American Mathematical Society, page 79 (cited on page 80).

Cullen, D. E., R. C. Little, R. Procassini, and C. Clouse (2003). *Static and Dynamic Criticality: Are They Different?* Technical report UCRL-TR-201506 TRN: US0406611. Lawrence Livermore National Lab. (LLNL), Livermore, CA (U.S.A.) (cited on page 75).

Dahl, E. B., V. Protopopescu, and N. G. Sjöstrand (1983). "On the relation between decay constants and critical parameters in monoenergetic neutron transport". In: *Nuclear Science and Engineering* 83, pages 374–379 (cited on page 80).

Davison, B. and J. B. Sykes (1957). "Neutron transport theory". Oxford: Clarendon Press (cited on page 75).

Dugan, K., I. Zmijarevic, and R. Sanchez (2016). "Cross-Section Homogenization for Reactivity-Induced Transient Calculations". In: *Journal of Computational and Theoretical Transport* 45.6, pages 425–441 (cited on pages 70, 79–80).

Dulla, S., P. Ravetto, and P. Saracco (2018). "The time eigenvalue spectrum for nuclear reactors in multi-group diffusion theory". In: *European Physical Journal Plus* 133, pages 1–24 (cited on pages 70, 80).

Fermi, E. (1942). Technical report CP-283 (Chicago Project Report). Chicago University, Metallurgical Laboratory, Chicago, IL (cited on page 71).

Hanh, O. and F. Strassmann (1939). "Über den nachweis und das verhalten der bei der bestrahlung des urans mittels neutronen entstehenden erdalkalimetalle". In: *Naturwissenschaften* 27, pages 11–15 (cited on page 71).

Henry, A. F. (1958). "The Application of Reactor Kinetics to the Analysis of Experiments". In: *Nuclear Science and Engineering* 3, pages 52–70 (cited on page 81).

— (1964). "The application of inhour modes to the description of non-separable reactor transients". In: *Nuclear Science and Engineering* 20, pages 338–351 (cited on page 79).

Leppänen, J., M. Pusa, T. Viitanen, V. Valtavirta, and T. Kaltiaisenaho (2015). "The Serpent Monte Carlo code: Status, development and applications in 2013". In: *Annals of Nuclear Energy* 82, pages 142–150 (cited on page 72).

Liu, H. (2010). "Feature Selection". In: *Encyclopedia of Machine Learning*. Edited by C. Sammut and G. I. Webb. Boston, MA: Springer US, pages 402–406 (cited on page 110).

Massone, M., F. Gabrielli, and A. Rineiski (2017). "A genetic algorithm for multigroup energy structure search". In: *Annals of Nuclear Energy* 105, pages 369–387 (cited on page 110).

McClarren, R. G. (2019). "Calculating Time Eigenvalues of the Neutron Transport Equation with Dynamic Mode Decomposition". In: *Nuclear Science and Engineering* 193.8, pages 854–867 (cited on pages 70, 80).

Pázsit, I. and V. Dykin (2018). "The role of the eigenvalue separation in reactor dynamics and neutron noise theory". In: *Journal of Nuclear Science and Technology* 55, pages 484–495 (cited on page 70).

Perel, R. L., J. J. Wagchal, and Y. Yeivin (1999). "One group transport calculations revisited". In: *Conference of the Nuclear Societies in Israel, Dead Sea, Israel*, pages 33–36 (cited on page 92).

Pomraning, G. C. (1989). In: *Nuclear Science and Engineering* 101.4, pages 330–340 (cited on page 93).

Ravetto, P. (1974). "Metodi analitici per la dinamica spaziale di sistemi non omogenei". Master's thesis. Politecnico di Torino (cited on page 81).

Ronen, Y., D. Shalitin, D. Shvarts, J. J. Wagschal, and Y. Yeivin (1977). "The Reactivity Dependence of Neutron Energy Spectra". In: *Nuclear Science and Engineering* 62, pages 180–181 (cited on page 82).

Ronen, Y., D. Shalitin, and J. J. Wagschal (1976). In: Transactions of the American Nuclear Society.24, page 474 (cited on pages 91, 96).

Ronen, Y., D. Shvarts, and J. J. Wagschal (1976). "A comparison of some eigenvalues in reactor theory". In: *Nuclear Science and Engineering* 60, pages 97–101 (cited on page 79).

Saad, Y. (1992). "Numerical methods for large eigenvalue problems". Manchester University Press (cited on page 110).

Sahni, D. C. and N. G. Sjöstrand (1990). "Criticality and time eigenvalues in one-speed neutron transport". In: *Progress in Nuclear Energy* 23, pages 241–289 (cited on page 80).

Sahni, D. C. and Sjöstrand, N. G. and Garis, N. S. (1995). "Spectrum of one-speed Neutron transport operator with reflective boundary conditions in slab geometry". In: *Transport Theory and Statistical Physics* 24, pages 629–656 (cited on page 80).

Sanchez, R. and D. Tomatis (2019). "Analysis of α modes in multigroup transport". In: *International Conference on Mathematics and Computational Methods Applied to Nuclear Science and Engineering, M&C 2019, Portland, OR (U.S.A.)* Pages 1134–1143 (cited on pages 70, 81).

Sanchez, R., D. Tomatis, I. Zmijarevic, and H. G. Joo (2017). "Analysis of alpha modes in multigroup diffusion". In: *Nuclear Engineering and Technology* 49, pages 1259–1268 (cited on pages 70, 88).

Saracco, P., S. Dulla, and P. Ravetto (2012). "On the spectrum of the multigroup diffusion equations". In: *Progress in Nuclear Energy* 59, pages 86–95 (cited on page 70).

Shryock, H. S. and J. S. Siegel (1980). "The methods and materials of demography". Volume 2. Department of Commerce, Bureau of the Census (cited on page 71).

Singh, K. P., S. B. Degweker, R. S. Modak, and K. Singh (2011). "Iterative method for obtaining the prompt and delayed alpha-modes of the diffusion equation". In: *Annals of Nuclear Energy* 38, pages 1996–2004 (cited on page 80).

Velarde, G., C. Ahnert, and J. M. Aragonés (1978). "Analysis of the eigenvalue equations in k, λ, γ, and α applied to some fast- and thermal-neutron systems". In: *Nuclear Science and Engineering* 66, pages 284–294 (cited on page 92).

Vitali, V. (2020). "Monte Carlo analysis of heterogeneity and core decoupling effects on reactor kinetics: Application to the EOLE critical facility". PhD thesis. Université Paris-Saclay (cited on pages 70, 79).

Weinberg, A. M. and E. P. Wigner (1958). "The Physical Theory of Neutron Chain Reactors". University of Chicago Press, Chicago (cited on page 89).

Zoia, A., E. Brun, and F. Malvagi (2014). "Alpha eigenvalue calculations with TRIPOLI-4". In: *Annals of Nuclear Energy* 63, pages 276–284 (cited on page 79).

Chapter 4

Spectral formulations as alternative weighting functions for group collapsing

Then all the colors will bleed into one,
Bleed into one

I still haven't found what I'm looking for, U2

4.1 Introduction

The generation of a set of effective cross sections to perform deterministic, few-group, full-core calculations using either diffusion (Nallo, Abrate, et al., 2020) or some low-order transport models like the SP_N approach (Gelbard, 1968; Cervi, Lorenzi, et al., 2019) is definitively one of the most challenging and exciting problems in reactor physics. The rigorous definition of the multi-group cross section for a certain interaction y can be obtained by integrating the continuous-energy transport equation over a general energy interval $[E_g, E_{g+1}]$ and by imposing the preservation of the reaction rate, namely

$$\Sigma_{y,g}(\vec{r},\Omega) = \frac{\int_{E_g}^{E_{g+1}} dE\, \Sigma_y(\vec{r},E)\, \phi(\vec{r},E,\Omega)}{\int_{E_g}^{E_{g+1}} dE\, \phi(\vec{r},E,\Omega)}, \quad g = 1,\dots,G, \tag{4.1}$$

where the symbols have their usual notation. As pointed out in the classic book by Bell and Glasstone, 1970, it can be noticed that the integration over the energy helps to reduce the number of degrees of freedom of the system, which is the ultimate goal of this

approximation, but at the price of an additional angular dependence for the effective cross sections. As observed in chapter 2, this further complexity is often neglected, assuming the separability between energy and angle. In this case, considering also the spatial homogenisation over a certain volume V_i, eq. (4.1) yields

$$\overline{\Sigma}_{y,g,i} = \frac{\int_{V_i} d\vec{r} \int_{E_g}^{E_{g+1}} dE\, \Sigma_y(\vec{r}, E)\, \psi(\vec{r}, E)}{\int_{V_i} d\vec{r} \int_{E_g}^{E_{g+1}} dE\, \psi(\vec{r}, E)}, \quad g = 1, \dots, \mathrm{G},\ \mathrm{i} = 1, \dots, \mathrm{I}, \tag{4.2}$$

where $\psi(\vec{r}, E)$ is a suitable weighting function, which, neglecting the angular effects, is usually identified as the total flux $\Phi(\vec{r}, E)$ for a simplified geometrical configuration of the system under investigation. In order to yield an optimal set of collapsed data, the calculation of the weighting function is usually performed with a very detailed transport calculation, using an accurate angular model and a fine-group structure. A standard example for this computational framework is the full-core calculation route followed for Light Water Reactors (LWRs), which is usually composed by three steps (Cacuci, 2010): first, a set of self-shielded cross sections are computed starting from the point-wise libraries at the pin level, then the cross sections are further collapsed over a fine-group structure at the assembly level and, finally, these data are condensed over few groups in order to carry out coarse-mesh calculations at the full-core level.

Despite its apparent simplicity, eq. (4.2) hides a series of different complexities, which can be summarised as:

- the choice of an adequate number of energy groups G;
- the choice of the group boundaries $[E_1, \dots, E_g, \dots, E_{\mathrm{G}}]$;
- the choice of the regions $[V_1, \dots, V_i, \dots, V_{\mathrm{I}}]$ for the spatial homogenisation;
- the cross section dependence on some physical and operational parameters such as the burn-up level, the offset to criticality (e.g., related to the control rod position), the thermodynamic conditions of the medium;
- the loss of accuracy derived from the assumption of energy and angle separability;
- the choice and the the calculation of the weighting function $\psi(\vec{r}, E)$.

Due to the involved relationship between the point-wise cross sections, the system physical parameters, and the different modelling and numerical approximations, it is extremely difficult to individuate a reliable, case-independent strategy for the cross section generation that could be applied to any reactor concept. Hence, the calculation of the effective cross section $\overline{\Sigma}_{y,g,i}$ is today often considered more an art rather than a rigorous operation, especially for systems that cannot be described adequately by a two-group approach.

Because of these intricacies and of the intrinsic uncertainties of this procedure, some strategies have been proposed, aiming at reducing the computational burden of the cross section generation and, at the same time, at minimising the modelling error.

One possibility is to avoid *in toto* the need for collapsing and homogenisation at the assembly level, as it has been proposed in the CASL project, where neutronics calculations are perform at a pin-level calculations with an intermediate number of groups, 51 in this case (Kulesza, Franceschini, et al., 2016; Cramer and Kropaczek, 2020). This approach has proved to be adequate in a high-fidelity, multi-physics modelling framework, but it cannot be practically employed for design- and safety-oriented applications, especially when transient scenarios are considered. Therefore, more sophisticated methods have been proposed to minimise the impact of the effective cross sections generation on the final calculation accuracy.

Massone, Gabrielli, and Rineiski, 2017 have proposed to employ a genetic algorithm for a clever selection of the group boundaries based on some constraints on the accuracy between some relevant quantities obtained with few- and multi-group calculations, e.g. the multiplication factor and the flux. Exploiting the advantages of the heuristic nature of the genetic algorithm, it is possible to deliver automatically a group structure that fits the needs of a specific reactor configuration, minimising the approximation error.

As regards the spatial homogenisation at the assembly level, different sophisticated techniques have been suggested during the years. Smith, 1986 introduced the concept of *assembly discontinuity factor*, outlining the so-called General Equivalence Theory, while in Rahnema, 1989; Rahnema and Nichita, 1997; Rahnema and McKinley, 2002 it is showed that taking into account the leakage effects on the energy spectrum can improve significantly the quality of the nodal calculations. In this spirit, Gamarino, Dall'Osso, et al., 2018 have recently suggested to exploit a rehomogenisation method that takes into account the energy spectrum shift between the infinite medium, used to generate the data, and the current conditions of the system, in order to enhance the nodal calculations accuracy. Concerning the choice of the weighting function used to perform the collapsing and homogenisation, it is a standard practice to assume the separation between angular and energy dependencies. Under this hypothesis, the total flux is usually the preferable choice in order to preserve the reaction rates.

For a time-dependent problem, the weighting function would depend on time, so eq. (4.2) would be

$$\overline{\Sigma}_{y,g,i}(t) = \frac{\displaystyle\int_{V_i} d\vec{r} \int_{E_g}^{E_{g+1}} dE\, \Sigma_y(\vec{r}, E, t)\, \psi(\vec{r}, E, t)}{\displaystyle\int_{V_i} d\vec{r} \int_{E_g}^{E_{g+1}} dE\, \psi(\vec{r}, E, t)}, \quad g = 1, \dots, \mathrm{G},\ \mathrm{i} = 1, \dots, \mathrm{I}. \tag{4.3}$$

In analogy to what occurs in eq. (4.1), also in this case the resulting effective cross section depends on time. This dependence would still be valid even in case the continuous-group cross section would be time-independent, due to the temporal variation of the

weighting function. On top of the additional memory requirements associated to their adoption, the calculation of time-dependent cross sections would be extremely computationally demanding. Therefore, the weighting is usually accomplished with the flux obtained by a static, k-based criticality calculation, $\varphi_k(\vec{r}, E)$, for a set of different operating conditions in order to be as close as possible to the time-dependent system.

As one could expect, this approximation yields very poor results when the system is heavily off-critical, because

- the static calculation does not consider the time effects, like the accumulation term $1/\mathrm{v}(E)\partial/\partial t *$ and the action of the delayed neutrons;
- the k eigenvalue distorts the energy spectrum of the physical, time-dependent system.

In this respect, as pointed out in Dugan, Zmijarevic, and Sanchez, 2016; Dugan, Sanchez, and Zmijarevic, 2018, a good alternative could be the adoption of the time eigenfunctions $\varphi_\alpha(\vec{r}, E)$ and $\varphi_\omega(\vec{r}, E)$. The advantage of this approach is the fact that it is possible to convey the information of the free time evolution of the system through the weighting procedure, with a computational burden similar to the one of the static calculations, despite some additional numerical difficulties that pertain to these spectral formulations and that have been addressed, for instance, in section 3.3.4 and in Mancusi and Zoia, 2018.

In Dugan, Zmijarevic, and Sanchez, 2016, the fundamental time mode is proposed as an alternative weighting function for collapsing a set of 281-group cross sections into different few-group structures, with the goal of simulating a power excursion, due to an accidental reduction of the capture cross section, in an infinite medium. In this paper, a simplified lumped-parameters thermal model is coupled with the neutron transport equation to take into account the feedback effects. This paper shows that, as expected on a physical ground, the cross sections collapsed with the time eigenfunction allows to improve the overall accuracy of the results, especially for super-prompt critical transients.

Due to the encouraging results of this paper and to some gaps in the literature concerning this kind of analysis, this section will focus on assessing the advantages coming from the adoption of the different eigenfunctions associated to the spectral forms of the NTE as weighting functions for the few-group collapsing. To this aim, this section reports some time-dependent calculations performed first with intermediate group structures and then with few-group structures, collapsing the data using the eigenfunctions of the different formulations discussed in this chapter.

4.2 Transient simulation framework

In order to be as much general as possible, the analysis will involve different energy spectra (fast vs. thermal) and reactivity insertion levels (sub-prompt critical vs. super-prompt critical), but it will not deal with spatial heterogeneity. Usually, the presence of the spatial heterogeneity induces strong space-energy effects, thus the collapsing procedure is often combined with a spatial homogenisation. However, as discussed in the previous chapters, the most relevant differences in the fundamental eigenfunctions computed with the various eigenvalue formulations are more related to their energy spectrum rather than to their spatial shapes, which are very similar. Thus, this chapter focuses only on homogeneous systems, leaving the analysis of the heterogeneity effects and of the homogenisation as a future development.

The transient simulations are performed with the neutronic module of the multi-physics code FRENETIC, developed in the last ten years at Politecnico di Torino by former PhD students (Bonifetto, 2014; Caron, 2017). This module, written in Fortran, implements a nodal diffusion solver and a wide variety of efficient methods for the reactor kinetics, like the Improved Quasi-Static method and the Predictor-Corrector Quasi-Static (PCQS) method (Caron, Dulla, and Ravetto, 2016). All the transient calculations presented in this chapter are carried out exploiting the PCQS method, coupled with an adaptive time-step selection for the solution of the shape and the amplitude functions.

The main purpose of FRENETIC is the simulation of 3D systems featured by closed, hexagonal fuel assemblies, but the code allows to consider simplified geometries as well, like 2D hexagonal systems and 1D cartesian systems. In this case, the choice of the geometry arrangement is driven by the need of ensuring a consistent exchange of information between the TEST code and FRENETIC. The first code is employed to compute the eigenfunctions and to use them as weighting functions for the multi-group data condensation, while the second is used to solve the time-dependent problems. The choice of a one-dimensional geometry also forces to neglect the effects of the thermal feedback, since FRENETIC currently supports coupled neutronics/thermo-hydraulics simulations only for 3D systems. Thus, also this aspect is left as a future work.

In spite of the apparent simplicity of the problem, the generation of the FRENETIC input is not a smooth operation, due to the low flexibility offered by the Fortran language and to fact that the management of the few-group data needed for the transient calculations is quite an error-prone operation. Since all the scenarios start from a steady state, critical configuration, the driver of the transients is a perturbation in the set of the multi-group cross sections. Therefore, FRENETIC requests a configuration file where the set of group constants for each material region is specified for each *configuration time* $\mathcal{T}$. When the set of group constants changes between two configuration times $\mathcal{T}^{(n)}$ and $\mathcal{T}^{(n+1)}$, the code linearly interpolates the data. To avoid the manual intervention of the user and to ensure the reproducibility of the calculations, an external Python wrapper, named *coreutils*, has been developed as a high-level interface for the generation of the FRENETIC input.

Exploiting these codes, the calculation route described in the following was pursued for each scenario presented in this chapter:

1. The input for the neutronic module of FRENETIC is generated with the *coreutils* package;
2. The reference transient simulations are carried out with the set of group constants collapsed on the intermediate group structure;
3. The intermediate group constants are used to solve the time, collision, multiplication, density and capture eigenvalue problems at each configuration time $\mathcal{T}$, using TEST;
4. The cross sections featuring each time configuration are collapsed with the eigenfunctions computed at the previous step. Also the collapsing process is performed in TEST;
5. As done in Dugan, Zmijarevic, and Sanchez, 2016, the condensed fission cross section is normalised to ensure that the system is initially critical at the round-off precision. This correction factor, $1/k_{\text{eff,few-group}}$, computed by solving the static k eigenvalue problem in FRENETIC for the few-group system, allows to avoid that the condensation errors produces slightly off-critical systems, ensuring that all the cases analysed in this chapter start from the same initial condition;
6. The transient calculations with the few-group constants are carried out in FRENETIC, leaving all the numerical settings used in the reference simulation unaltered;
7. The evolution of the main neutronic integral parameters computed in the two cases, i.e. the effective neutron lifetime $\Lambda(t)$, the effective delayed neutron fraction $\beta_{\text{eff}}(t)$, the reactivity $\rho(t)$ and the total power $P(t)$, is compared.

In order to ensure the full consistency between the two codes, the eigenfunctions, except for the time ones, are computed with the P_1 model and Marshak boundary conditions, exploiting the equivalence between diffusion and P_1. This choice makes the solution of the δ formulation smoother, since the diffusion model would yield a non-linear eigenproblem, as pointed out in chapter 3.

Concerning the time eigenvalue, due to the inherent difference between transient diffusion and P_1 equations, both models are used to determine the eigenfunctions. With respect to the previous chapters, where both α and ω were considered, here only the last formulation will be adopted, in order to properly account for the spectral effects due to the prompt and delayed contributions. Since there are $R + 1$ fundamental modes, where R is the number of delayed neutron precursors families, a question concerning how to actually define the weighting function may arise. Recalling the literature evidences (Sanchez, Tomatis, et al., 2017; Henry, 1964), confirmed also in chapter 2 and chapter 3,

the ω-modes are featured by R delayed modes and one prompt mode. The delayed cluster actually represents the fundamental eigenstate of the system defined by the relationship between the neutron and the precursors populations, while the prompt mode represents the prompt eigenstate of the system, before the contribution of the delayed emissions becomes relevant. As mentioned, the cluster is characterised by a set of fluxes that are very close to each other and by a set of precursors concentration that can assume negative values. The flux shapes in the cluster are in general very close but, in this case, they are the same, at numerical precision, because the delayed fission emission spectrum evaluated by Serpent 2 is the same for each of the R families.

As opposed to Dugan, Zmijarevic, and Sanchez, 2016, who consider some linear combinations of the delayed and prompt modes as a weighting function, here only the flux of the fundamental eigenstate, which is associated to the stable period of the system and positive on the whole phase space, and the prompt mode are adopted as weighting functions. The reason for this choice is that, to define a physically meaningful linear combination, the flux at the beginning of each configuration interval must be known, namely

$$\phi(x, E, \mathcal{T}^{(n)}) = \sum_{m=1}^{M} a_m \varphi_{\omega,\mathcal{T}^{(n)},m}(x, E), \tag{4.4}$$

where $\varphi_{\omega,\mathcal{T}^{(n)},m}$ indicates the m-th mode computed with the set of group constants featuring the system at time $\mathcal{T}^{(n)}$ and M spans from 1 up to R + 1. The flux at each core configuration is generally not known *a priori*, except for the initial condition, i.e. $t = t_0 = \mathcal{T}^{(0)}$. As highlighted previously in this chapter, in real-life applications we usually aim at collapsing the data for some reactor configuration without solving the multi-group transient, but rather solving a static problem. Thus, in this logic, the linear combination of ω-modes is not considered in this work.

In addition to these precautions, it is also assumed that the scattering is isotropic. This hypothesis allows to ensure the full consistency between the multi-group constants generated by Serpent, which adopts the so-called out-scattering approximation for the evaluation of the diffusion coefficient (Leppänen, Pusa, and Fridman, 2016),

$$\begin{aligned} D_g &= \frac{1}{3}\left[\overline{\Sigma}_{t,g} - \frac{\displaystyle\int_{E_{g-1}}^{E_g} dE \int_{E_{g-1}}^{E_g} dE' \Sigma_s(x, E') f_1(x, E' \longrightarrow E) \phi_1(x, E')}{\displaystyle\int_{E_{g-1}}^{E_g} dE \phi_1(x, E)}\right]^{-1} \\ &\approx \frac{1}{3}\left[\overline{\Sigma}_{t,g} - \frac{\displaystyle\int_{E_{g-1}}^{E_g} dE \int_{E_{g-1}}^{E_g} dE' \Sigma_s(x, E) f_1(x, E \longrightarrow E') \phi_1(x, E)}{\displaystyle\int_{E_{g-1}}^{E_g} dE \phi_1(x, E)}\right]^{-1} \\ &= \frac{1}{3(\overline{\Sigma}_{t,g} - \overline{\Sigma}_{s1,g})}. \end{aligned} \tag{4.5}$$

Due to this approximation, the first-order scattering moment used in the P_1 model would not be fully consistent with the diffusion coefficient estimated by Serpent, because of the small discrepancy introduced by this approximation. Therefore, assuming the scattering isotropicity, the diffusion coefficient can be simply defined as follows,

$$D_g = \frac{1}{3\overline{\Sigma}_{t,g}}. \tag{4.6}$$

Some benchmark calculations revealed that, thanks to this assumption, the difference between TEST and the static module of FRENETIC amounts to some pcm in the worst case.

The collapsing process, performed in TEST, is applied to all the group constants used in the reference calculations, following the usual definitions (Bell and Glasstone, 1970) of group constants,

$$\begin{aligned}
\frac{1}{\mathrm{v}_g}\int_{E_{g-1}}^{E_g} dE\,\varphi_\xi(E) &= \int_{E_{g-1}}^{E_g} dE\,\frac{1}{\mathrm{v}(E)}\varphi_\xi(E)\\
D_g\int_{E_{g-1}}^{E_g} dE\,\varphi_\xi(E) &= \int_{E_{g-1}}^{E_g} dE\frac{1}{3\Sigma_t(E)}\varphi_\xi(E)\\
\Sigma_{y,g}\int_{E_{g-1}}^{E_g} dE\,\varphi_\xi(E) &= \int_{E_{g-1}}^{E_g} dE\,\Sigma_y(E)\varphi_\xi(E)\\
\nu_g\int_{E_{g-1}}^{E_g} dE\,\Sigma_f(E)\varphi_\xi(E) &= \int_{E_{g-1}}^{E_g} dE\,\nu(E)\Sigma_f(E)\varphi_\xi(E)\\
E_{f,g}\int_{E_{g-1}}^{E_g} dE\,\Sigma_f(E)\varphi_\xi(E) &= \int_{E_{g-1}}^{E_g} dE\,E_{f,g}(E)\Sigma_f(E)\varphi_\xi(E)\\
\chi_{z,g} &= \int_{E_{g-1}}^{E_g}\chi_z(E)dE,
\end{aligned} \tag{4.7}$$

where ξ indicates the eigenvalue formulation used for the condensation, y may indicate either capture or scattering or fission and z refers to kind of fission emission spectra, which can be either delayed or prompt. These relations allows to preserve the number of neutrons, the reaction rates, the number of neutrons emitted by fission and the overall fission energy. It should be noticed that, with respect to eq. (4.2), the space dependence is dropped due to the space-energy separation for a homogeneous medium (Weinberg and Wigner, 1958; Dulla and Ravetto, 2020). This allows to weight the diffusion coefficient on the flux spectrum rather than on the spectrum of its spatial gradient.

Before moving on, it is important to make some considerations concerning the fourth step of the workflow presented above, i.e. the condensation of the group constants at the beginning of each configuration interval. Since the multi-group cross sections and diffusion coefficients are interpolated between two succeeding configuration times $\mathcal{T}^{(n)}$ and $\mathcal{T}^{(n+1)}$, the collapsing could be performed either with the eigenfunctions of

the configuration at $\mathcal{T}^{(n)}$ or with the eigenfunctions of the configuration at $\mathcal{T}^{(n+1)}$. In analogy with the nomenclature used for the time discretisation schemes, these two possibilities could be addressed respectively as *implicit* and *explicit*.

The implicit collapsing, in principle, should provide better results, because, in this way, the multi-to-few group condensation would be carried out with the energy spectrum featuring the future state of the system, $\mathcal{T}^{(n+1)}$. However, this approach could not be applied in practice if the thermal feedback was taken into account, because the temperature field is usually not known at time $t = \mathcal{T}^{(n+1)}$. On the contrary, in the explicit collapsing case, the temperature field is known at $t = \mathcal{T}^{(n)}$, meaning that the thermal feedback evaluation is consistent with the flux spectrum. Since one of the aims of the group collapsing is reducing the number of degrees of freedom of the problem to allow its time-dependent, multiphysics solution, only the explicit collapsing will be considered in the following.

Concerning the tuning of the numerical parameters of the PCQM used for the solution of the transients, a sensitivity study related to the most challenging transient scenario showed that choosing the maximum time step allowed for the adaptive time step selection during the reactivity update ($\Delta t_{\rho,\max}$) equal to 1×10^{-5} s and the maximum time step allowed for the adaptive shape update ($\Delta t_{\varphi,\max}$) equal to 1×10^{-3} s provides results which are independent on the time steps, as visible from fig. 4.1.

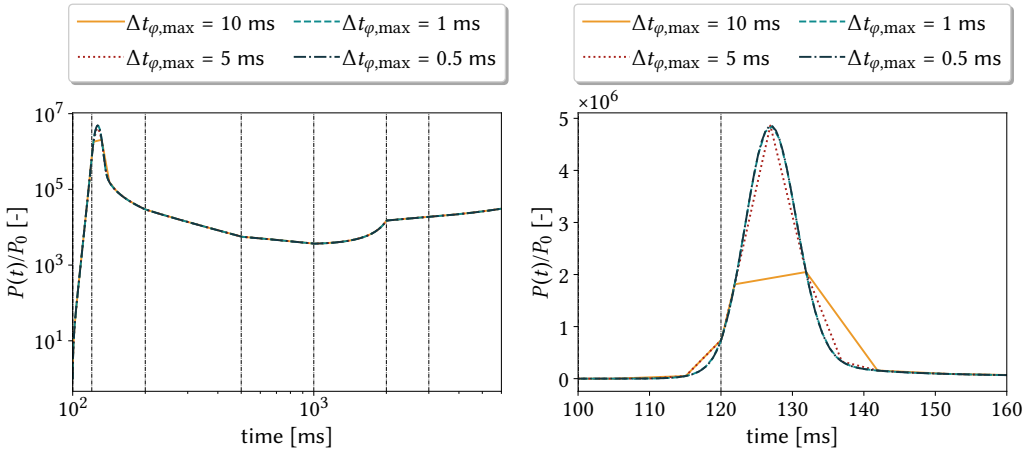

Figure 4.1: *Sensitivity of the total power evolution with respect to the maximum time step allowed for the shape update, with* $\Delta t_{\rho,\max} = 1 \times 10^{-5}$ s.

4.3 Homogeneous thermal system

In this section, a homogeneous slab featured by a thermal energy spectrum is considered. The system, whose thickness is set to 250 cm, is filled with the same mixture of

UOx and water fissile isotopes which is used in chapter 3. The multi-group cross sections employed in the reference transient calculation are collapsed on the CASMO-25 structure with the Serpent 2 Monte Carlo code and then used as input for FRENETIC, which discretises the slab in 60 uniformly spaced nodes. A graph of the energy spectrum and of the group-grid used for the collapsing is provided in fig. 4.2.

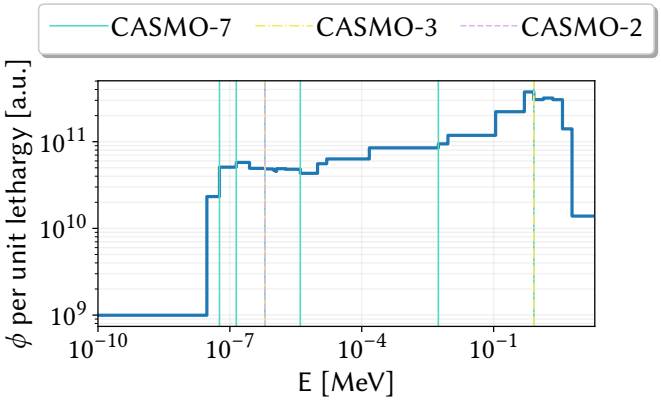

Figure 4.2: *Flux energy spectrum of the initially critical system scored on the CASMO-25 grid and group structures used to perform the collapsing.*

4.3.1 Sub-prompt positive reactivity insertion

The first transient scenario analysed is the insertion of a sub-prompt reactivity in the critical system, obtained reducing the capture cross section on the whole energy axis by the same amount, -0.75 %, at $t = 10 + 10^{-9}$ ms, in order to simulate the reactivity insertion step.

Figure 4.3 shows the time evolution of the total power and of the total concentration of the precursors for the given reactivity profile. After an initial sharp increase, the power evolution is soon softened by the delayed neutrons emissions. Since there is no thermal feedback, and the cross section set does not change anymore after 10 ms, the flux shape is expected to behave asymptotically as the fundamental ω-mode, which is associated, in this specific case, to a positive time frequency.

For each configuration interval, i.e. the time interval between two configuration changes, the set of fundamental eigenfunctions is evaluated using TEST, except for the initial condition, since the system is critical and all the eigenfunctions are supposed to be identical. Figure 4.4 shows the relative error between the time-averaged energy spectrum, computed by FRENETIC, and the corresponding energy spectrum of the different eigenfunctions. In order to draw a consistent comparison between the two spectra, the relative percentage error is computed between the time-average of the FRENETIC

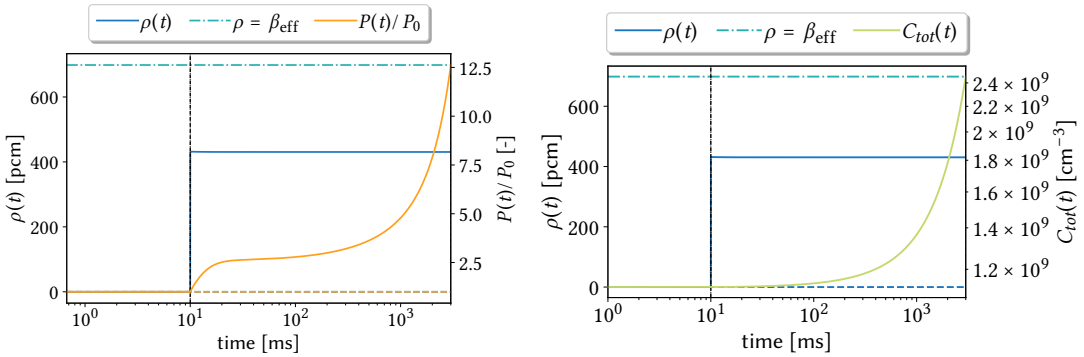

Figure 4.3: *Evolution of the total power and total precursors concentration in the case of a sub-prompt reactivity insertion (ρ = 431.2 pcm).*

spectrum in each time configuration interval and the spectrum of the generic ξ eigenfunction for the reactor configuration at $t = \mathcal{T}^{(n)}$, namely

$$\epsilon(E)\% = \frac{\int_{\mathcal{T}^{(n)}}^{\mathcal{T}^{(n+1)}} dt \left[\Psi_{FRE}(E,t) - \Psi_{TEST,\xi,\mathcal{T}^{(n)}}(E)\right]}{\int_{\mathcal{T}^{(n)}}^{\mathcal{T}^{(n+1)}} dt \Psi_{FRE}(E,t)} * 100. \tag{4.8}$$

As clearly visible from fig. 4.4, the eigenfunction with the closest spectrum are the fundamental ω ones, consistently with the fact that the asymptotic period for this configuration, $\tau = 1/\omega_0$ =2235 ms, is slightly shorter than the transient simulation time. A part from the excellent agreement for the time eigenfunction case, it is interesting to notice that the spectra which are the closest to the time-averaged spectrum of the system are the γ and the δ ones, while the worst one is the k mode, which is usually employed for the condensation process.

Concerning the performances of the few-group data condensed with the different eigenfunctions, some relevant information can be obtained by inspection of fig. 4.5. The figure allows to observe the instantaneous ratio between the few-group to the multi-group total power, according to the type of eigenfunction adopted. When the data are condensed from 25 to 7 groups, the best weighting functions turn out to be the time and the multiplication ones. On the contrary, when the data are collapsed in a two-group structure, the best option seems to be the capture eigenfunction, while the worst one is represented by the multiplication eigenfunction. In both cases, the collision eigenfunction seem to provide a good accuracy with respect to the other weighting functions. In addition to this observation, it is possible to notice that, when two groups are used instead of seven, the few-group results are reasonably less accurate and the differences between the various cases are more evident.

A quantitative and more thorough information concerning the error on the main integral parameters featuring the transient is given for these two few-group cases in

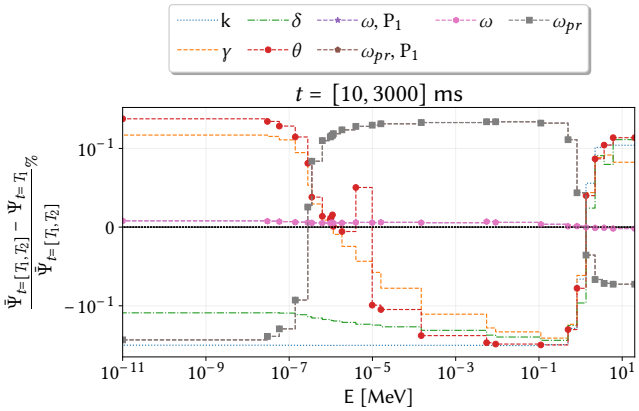

Figure 4.4: *Group-wise, relative error between the time-averaged spectrum computed by FRENETIC and the spectrum of the different eigenvalue formulations as a function of the incident neutron energy.*

tables 4.1 and 4.2, where the relative L_2 distance between the reference multi-group quantity $y_{\mathrm{MG}}(t)$ and the approximated few-group one $y_{\mathrm{FG}}(t)$ duration is provided for the whole transient duration, namely,

$$\epsilon\% = \frac{||y_{\mathrm{MG}}(t) - y_{\mathrm{FG}}(t)||_2}{||y_{\mathrm{MG}}(t)||_2} * 100. \tag{4.9}$$

In both cases, it is interesting to notice that the sensitivity of the effective neutron lifetime Λ with respect to the weighting function chosen for the group condensation is very small, while the sensitivity of the effective delayed neutron fraction β_{eff} is negligible. On the contrary, both the reactivity and the total power are very sensitive to the choice of the weighting function. Looking at the values of the relative errors it is possible to appreciate that, in both cases, the γ collapsing ranks among the best three, while the performances of the other eigenfunctions seem to be dependent on the energy structure adopted for the collapsing. In the CASMO-7 case, the fundamental time eigenfunctions allow to get the closest results to the reference, while in the CASMO-2 case the most accurate matching is achieved with the capture eigenfunction θ.

4.3.2 Super-prompt positive reactivity insertion

When a super-prompt ($\rho > \beta_{\mathrm{eff}}$) critical reactivity is inserted, decreasing the capture cross section by 1.5%, the system is featured by a faster dynamics, since the system is super-critical considering only the prompt neutrons. As a consequence of the very fast power growth, it is not possible to appreciate the characteristic prompt jump in the first time instants of fig. 4.6.

Due to its very short asymptotic period, $\tau = 1/\omega_0 = 5.85$ ms, also in this case the time-averaged energy spectrum is very close to the one of the fundamental ω mode,

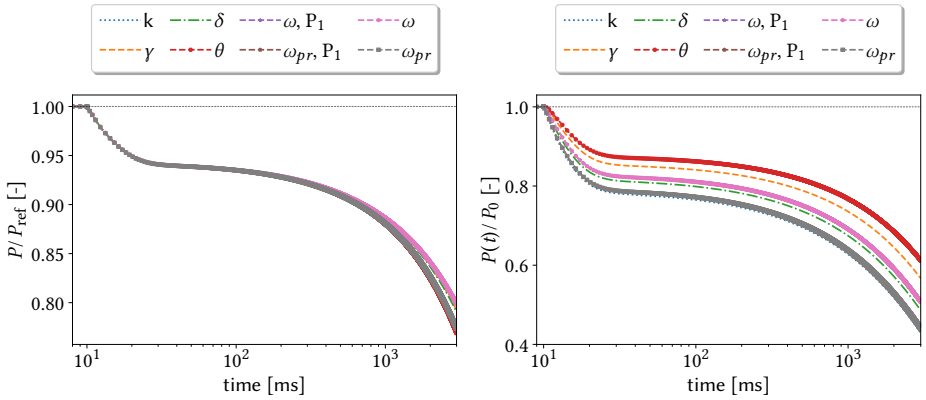

Figure 4.5: *Evolution of the ratio between the total power computed in the few-group cases (CASMO-7 on the left, CASMO-2 on the right) and the total power in the reference case.*

Table 4.1: *% relative error for the whole transient between the reference CASMO-25 calculation and the few-group calculations using the various eigenfunction to collapse on the CASMO-2 grid for some relevant integral parameters: ρ is the reactivity, Λ is the effective neutron lifetime, β_{eff} is the effective delayed neutron fraction and P is the total thermal power.*

	k	γ	δ	θ	ω, P_1	ω_{pr}, P_1	ω	ω_{pr}
ρ	723.76	340.85	543.75	245.97	485.27	683.30	485.27	683.29
Λ	298.00	297.82	298.28	297.10	299.49	302.97	299.49	302.97
β_{eff}	275.55	275.55	275.55	275.55	275.55	275.55	275.55	275.55
P	2361.23	1727.84	2091.01	1531.62	1993.45	2304.32	1993.45	2304.31

followed by the γ spectrum, as visible in fig. 4.7.

Despite this very good agreement in the energy spectra, the ratio between the reference power and the ones computed in the few-group transients shows that, despite some noticeable differences among the weighting spectra, the error between the reference calculation and the collapsed ones is quite large. This discrepancy should be mostly due to the approximation error related to the group averaging and its propagation through time. Due to the fast dynamics, even a small difference between the initial power profiles can cause larger and larger deviations as time goes by. In practical situations, this diverging behaviour does not occur, because of the negative thermal feedback, which stabilises the power evolution. Despite this transient seems practically meaningless, its study is important to highlight the strong biases induced by the group collapsing in the transient evolution.

A clear example of the rôle played by the group choice can be found in fig. 4.8. When the collapsing is carried out with the CASMO-7 groups, the best profile is obtained with

Table 4.2: *% relative error for the whole transient between the reference CASMO-25 calculation and the few-group calculations using the various eigenfunction to collapse on the CASMO-7 grid for some relevant integral parameters: ρ is the reactivity, Λ is the effective neutron lifetime, β_{eff} is the effective delayed neutron fraction and P is the total thermal power.*

	k	γ	δ	θ	ω, P_1	ω_{pr}, P_1	ω	ω_{pr}
ρ	162.76	166.42	168.08	189.79	159.93	184.87	159.93	184.87
Λ	43.63	43.67	43.63	43.77	43.93	44.33	43.93	44.33
β_{eff}	53.80	53.80	53.80	53.80	53.80	53.80	53.80	53.80
P	777.62	787.92	792.54	851.41	769.59	838.39	769.59	838.39

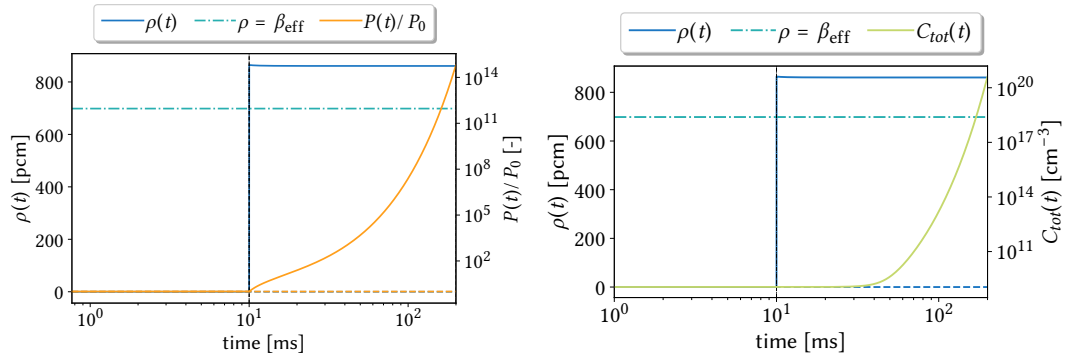

Figure 4.6: *Evolution of the total power and total precursors concentration in the case of a super-prompt positive reactivity insertion (ρ = 862.4 pcm).*

the asymptotic ω mode, consistently with what observed in fig. 4.7. However, when the CASMO-2 grid is employed, i.e. the classical two-group model with the cut-off at 0.625 eV, the profile obtained with the ω weighting is not the best one anymore. The largest contribution to this discrepancy, which seems to contradict the excellent agreement between the spectra in fig. 4.7, is mostly due to the fact that the spectral effects due to the delayed neutrons are not distinguishable from the prompt one when a two-group model is adopted.

Tables 4.3 and 4.4 show the relative error for the evolution of the main neutronic integral parameters. As for the sub-prompt positive reactivity insertion, Λ and β_{eff} are not very sensitive to the collapsing function, while ρ and P are featured by a much lower sensitivity than in the previous case.

4.3.3 Negative reactivity insertion

In this section, a shut-down transient is examined, increasing the capture cross section of the medium by 0.8%, which corresponds to a negative reactivity insertion around

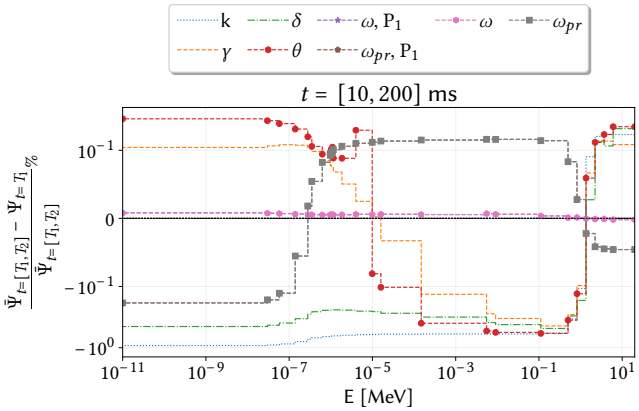

Figure 4.7: *Group-wise, relative error between the time-averaged spectrum computed by FRENETIC and the spectrum of the different eigenvalue formulations as a function of the incident neutron energy.*

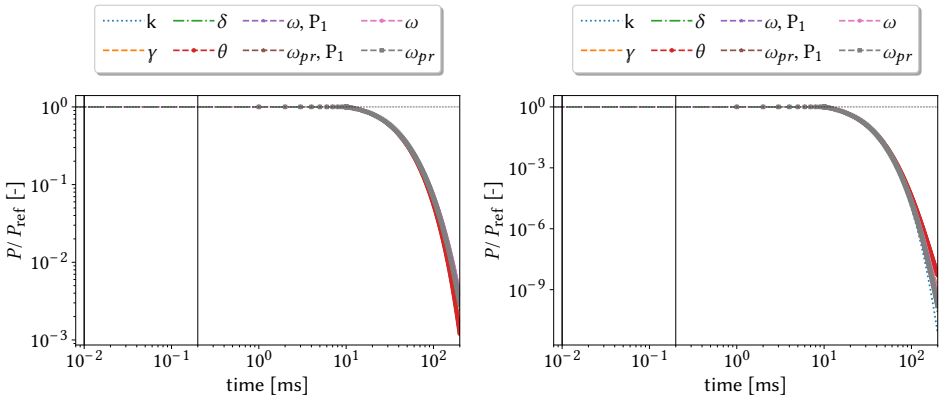

Figure 4.8: *Evolution of the ratio between the total power computed in the few-group cases (CASMO-7 on the left, CASMO-2 on the right) and the total power in the reference case.*

-460 pcm. For this system, the reactor period, $\tau = 1/\omega_0 = 79365$ ms, is much longer than the total transient duration, equal to 3000 ms, since $\omega_0 = -0.01211\,\mathrm{s}^{-1}$ is lower-bounded by the opposite of the smallest precursors decay constant, $-\lambda_1 = -0.0124667\,\mathrm{s}^{-1}$. Nevertheless, since the shapes in the cluster are equal within machine precision due to the fact that they share the same delayed emission spectrum, the time-average spectrum is still very close to the asymptotic ω mode, as for the previous cases.

Figure 4.11 shows the time-dependent ratio between the power computed in the reference transient and the power computed with different group structures for each eigenfunction. Also in this case, it is interesting to observe how the group choice strongly affects the error behaviour for the different eigenvalue formulations. For all

Table 4.3: *% relative error for the whole transient between the reference CASMO-25 calculation and the few-group calculations using the various eigenfunction to collapse on the CASMO-2 grid for some relevant integral parameters: ρ is the reactivity, Λ is the effective neutron lifetime, β_{eff} is the effective delayed neutron fraction and P is the total thermal power.*

	k	γ	δ	θ	ω, P_1	ω_{pr}, P_1	ω	ω_{pr}
ρ	188.65	144.79	167.22	135.25	153.68	160.62	153.68	160.62
Λ	79.77	79.77	79.86	79.61	79.92	80.18	79.92	80.18
β_{eff}	73.50	73.50	73.50	73.50	73.50	73.50	73.50	73.50
P	1326.30	1324.99	1325.71	1324.63	1325.29	1325.51	1325.29	1325.51

Table 4.4: *% relative error for the whole transient between the reference CASMO-25 calculation and the few-group calculations using the various eigenfunction to collapse on the CASMO-7 grid for some relevant integral parameters: ρ is the reactivity, Λ is the effective neutron lifetime, β_{eff} is the effective delayed neutron fraction and P is the total thermal power.*

	k	γ	δ	θ	ω, P_1	ω_{pr}, P_1	ω	ω_{pr}
ρ	42.46	43.33	43.77	49.05	39.99	41.85	39.99	41.85
Λ	11.68	11.69	11.67	11.73	11.76	11.82	11.76	11.82
β_{eff}	14.35	14.35	14.35	14.35	14.35	14.35	14.35	14.35
P	1179.40	1180.80	1181.50	1188.93	1175.02	1178.33	1175.02	1178.33

the few-group grids, all the collapsed transients exhibit the same behaviour immediately after the reactivity insertion, which occurs at 10 ms, but each case is featured by a progressively larger error as the group structure becomes coarser. Then, around 100 ms, the effect of the delayed neutron precursors becomes more relevant and the profiles behave quite differently. When the prompt ω mode is used to perform the collapsing, the resulting system tends to underestimate the reference power with a rate related to the grid structure. Despite it seems the best option when a two-group model is used, this choice clearly gets worst and worst as time goes by.

On the contrary, the γ and the θ collapsed systems are featured by a slower error increase in time, suggesting that they are the best weighting functions for this kind of transient. The energy-dependent relative error reported in fig. 4.7 seems to confirm this behaviour, except for the case with the ω collapsing, which does not always yield the best results. A possible explanation of this behaviour is the fact that, since the system is not yet in the asymptotic state during the time evolution, performing the collapsing with the fundamental time mode introduces a larger error in the non-asymptotic part of the transient.

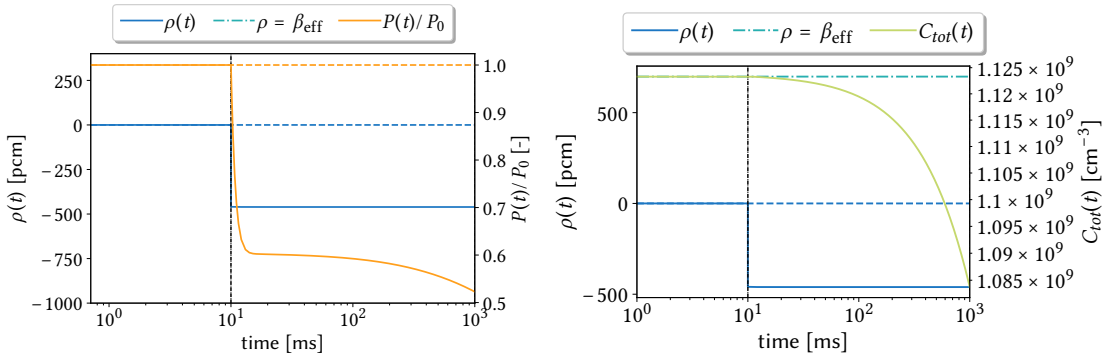

Figure 4.9: *Evolution of the main integral parameters in the case of negative reactivity insertion ($\rho = -460$ pcm).*

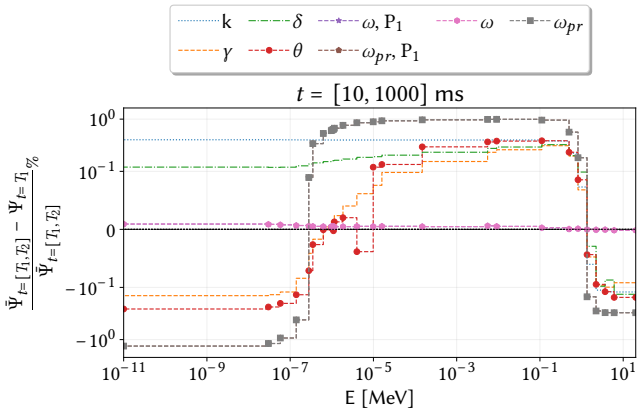

Figure 4.10: *Group-wise, relative error between the time-averaged spectrum computed by FRENETIC and the spectrum of the different eigenvalue formulations as a function of the incident neutron energy.*

As for the previous cases, tables 4.5 and 4.6 provide a more precise quantification of the errors associated to the different collapsing strategies. Also in this case both Λ and β_{eff} have a negligible sensitivity to the choice weighting function, while the reactivity and the power strongly depend on it. As mentioned previously in this section, in order to assess the quality of the various condensation schemes it is important to have a look also on the time-dependent behaviour of the error. For this reason, the prompt time mode is not the best solution despite the relative error is the lowest one. Again, one of the most accurate transient is the one using the γ mode to perform the collapsing.

4.3.4 Positive and negative reactivity insertions

Figure 4.12 shows the power and the precursors total concentration in response to a more sophisticated reactivity profile, that is composed by step and non-linear time

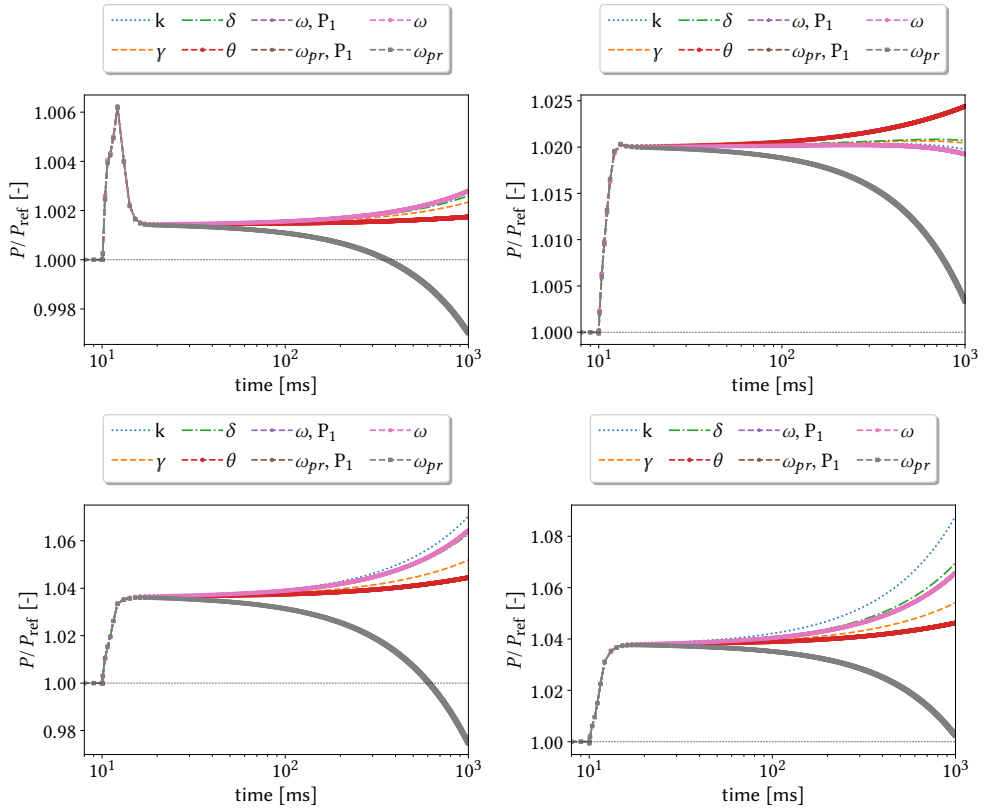

Figure 4.11: *Evolution of the ratio between the total power computed in the few-group cases (CASMO-18 on top-left, CASMO-7 on top-right, CASMO-3 on bottom-left and CASMO-2 on bottom-right) and the total power in the reference case.*

Table 4.5: *% relative error for the whole transient between the reference CASMO-25 calculation and the few-group calculations using the various eigenfunction to collapse on the CASMO-2 grid for some relevant integral parameters: ρ is the reactivity, Λ is the effective neutron lifetime, β_{eff} is the effective delayed neutron fraction and P is the total thermal power.*

	k	γ	δ	θ	ω, P$_1$	ω_{pr}, P$_1$	ω	ω_{pr}
ρ	293.34	173.33	228.45	146.03	214.58	91.82	214.58	91.81
Λ	171.47	171.49	171.37	171.68	171.02	175.10	171.02	175.10
β_{eff}	159.59	159.59	159.59	159.59	159.59	159.59	159.59	159.59
P	201.08	146.31	171.28	133.86	165.02	73.22	165.02	73.22

variations. At first, the capture cross section of the critical system gets perturbed by -1.28 % and the system becomes super-prompt critical for 20 ms. Then, the positive reactivity is compensated by a linear increase of the perturbed capture cross section by

Table 4.6: *% relative error for the whole transient between the reference CASMO-25 calculation and the few-group calculations using the various eigenfunction to collapse on the CASMO-18 grid for some relevant integral parameters: ρ is the reactivity, Λ is the effective neutron lifetime, β_{eff} is the effective delayed neutron fraction and P is the total thermal power.*

	k	γ	δ	θ	ω, P_1	ω_{pr}, P_1	ω	ω_{pr}
ρ	4.87	3.38	4.44	1.03	5.22	18.58	5.22	18.58
Λ	0.24	0.24	0.24	0.26	0.19	0.47	0.19	0.47
β_{eff}	10.49	10.49	10.49	10.49	10.49	10.49	10.49	10.49
P	6.72	6.12	6.54	5.18	6.86	4.70	6.86	4.70

a factor 0.8% between t =30 ms and t =110 ms. This system is then perturbed again linearly in time in such a way that the capture cross section at t =110 ms is increased by 2% at t =410 ms. Finally, at t =1000 ms the new capture cross section is decreased linearly in time in order to obtain a decrease of -2.2 % at t =2000 ms. The simulation is then arrested at 3000 ms.

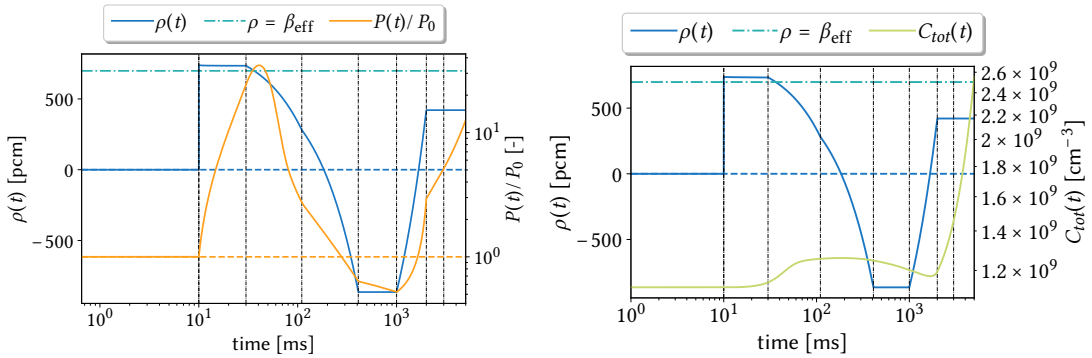

Figure 4.12: *Evolution of the total power and total precursors concentration in the case of super- and sub-prompt positive and negative reactivity insertions.*

Figure 4.7 provides the relative error between the time-averaged energy spectra obtained by solving the time-dependent diffusion equation and the energy spectra of the various eigenfunctions used in the condensation, for the most relevant time intervals. For all intervals, except the one for $t \in [110, 410]$ ms, the k spectrum is definitively the worst one, while the spectra featured by the smaller error are the prompt and delayed ω mode and the γ and θ modes. The instantaneous ratio between the few-group and the reference power, displayed in fig. 4.14 for the CASMO-7 and the CASMO-3 grids, behaves consistently, except for the θ eigenfunction when the CASMO-7 grid is used. A more detailed information on the error behaviour of the main integral parameters is reported in tables 4.7 and 4.8. Also for this more complex transient, the same comments

made for the previous cases hold: only the power and the reactivity are very sensitive to the weighting function choice, and the γ collapsing always ranks among the best two options for both the CASMO-3 and CASMO-7 cases.

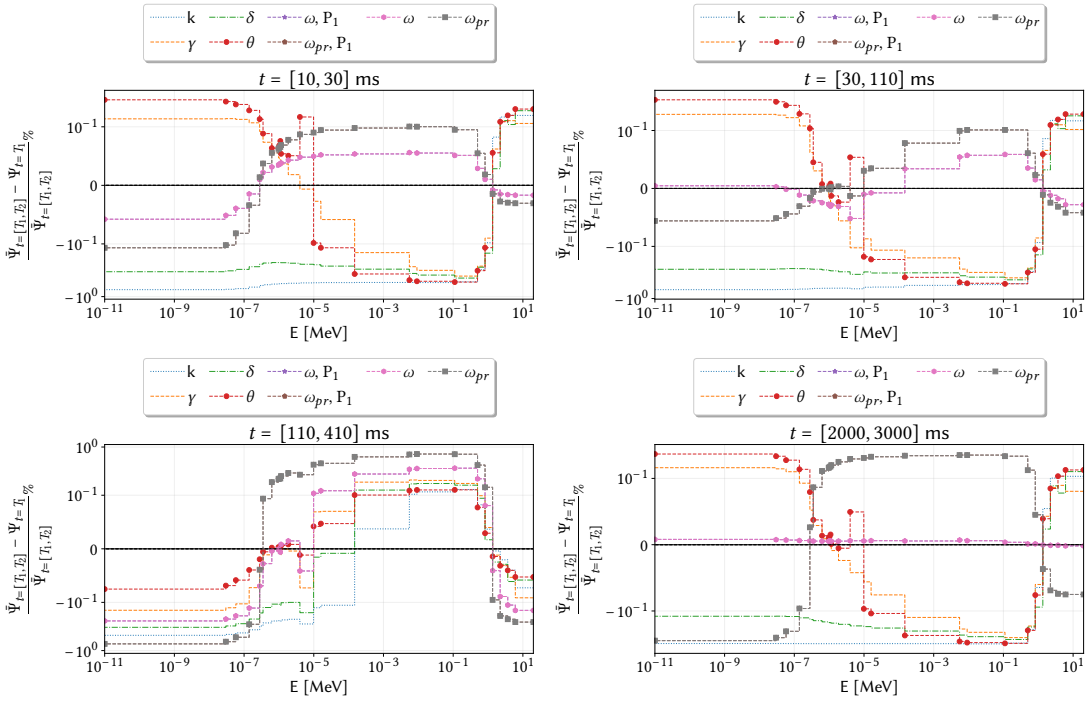

Figure 4.13: *Group-wise, relative error between the time-averaged spectrum computed by FRENETIC and the spectrum of the different eigenvalue formulations as a function of the incident neutron energy.*

Table 4.7: *% relative error for the whole transient between the reference CASMO-25 calculation and the few-group calculations using the various eigenfunction to collapse on the CASMO-7 grid for some relevant integral parameters: ρ is the reactivity, Λ is the effective neutron lifetime, β_{eff} is the effective delayed neutron fraction and P is the total thermal power.*

	k	γ	δ	θ	ω, P_1	ω_{pr}, P_1	ω	ω_{pr}
ρ	443.55	338.02	451.26	281.01	428.62	11931.31	428.63	11931.04
Λ	56.44	56.46	56.39	56.50	56.63	58.92	56.63	58.92
β_{eff}	69.55	69.55	69.55	69.55	69.55	69.55	69.55	69.55
P	1173.46	1203.80	1217.19	1383.55	1141.82	1329.16	1141.82	1329.16

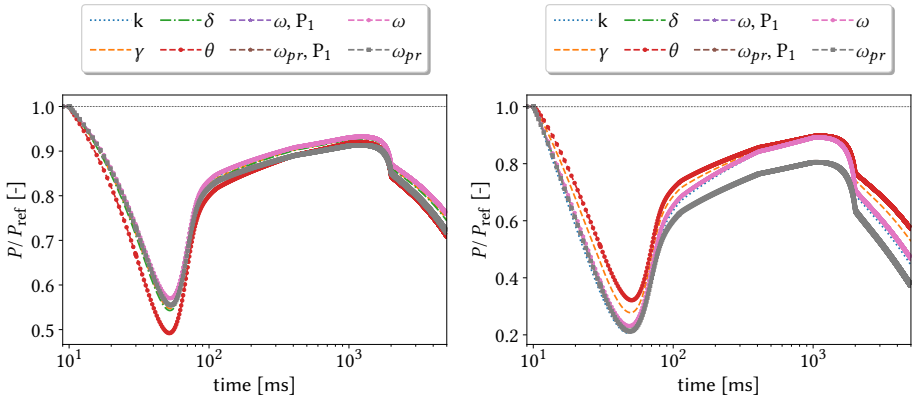

Figure 4.14: *Evolution of the ratio between the total power computed in the few-group cases (CASMO-7 on the left, CASMO-3 on the right) and the total power in the reference case.*

Table 4.8: *% relative error for the whole transient between the reference CASMO-25 calculation and the few-group calculations using the various eigenfunction to collapse on the CASMO-3 grid for some relevant integral parameters: ρ is the reactivity, Λ is the effective neutron lifetime, β_{eff} is the effective delayed neutron fraction and P is the total thermal power.*

	k	γ	δ	θ	ω, P_1	ω_{pr}, P_1	ω	ω_{pr}
ρ	1241.72	709.94	1212.69	557.87	1009.46	67814.07	1009.46	67812.01
Λ	444.48	443.95	444.36	443.66	444.58	452.85	444.58	452.85
β_{eff}	69.52	69.52	69.52	69.52	69.52	69.52	69.52	69.52
P	2635.34	2233.27	2519.29	2027.05	2518.40	3068.71	2518.41	3068.70

4.4 Homogeneous fast system

The second set of cases involves a homogeneous slab featured by a fast energy spectrum. The system, whose thickness is set to 200 cm, is filled with the same mixture of MOx which is used in the inner fuel assemblies of the LEADER version of the ALFRED reactor (Grasso, Petrovich, et al., 2014). The multi-group cross sections employed in the reference transient calculation are collapsed on the ECCO-33 structure with the Serpent 2 Monte Carlo code (Leppänen, Pusa, et al., 2015) and then used as input for FRENETIC, which approximates the slab using 40 nodes. A graph of the energy spectrum and of the group-grid used for the collapsing is provided in fig. 4.15.

In the following, the same types of transients analysed for the thermal system are presented and discussed, in order to make a consistent comparison between the two systems and to favour some general conclusions.

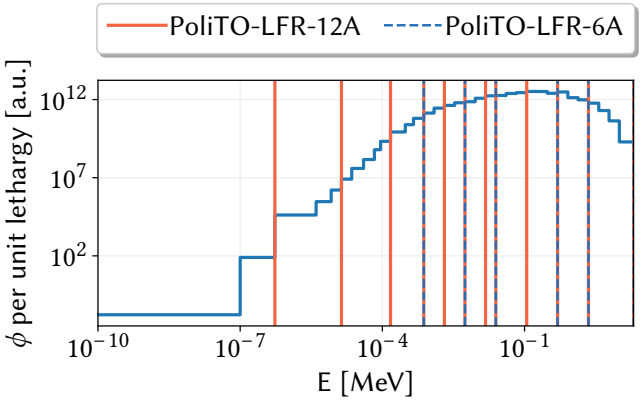

Figure 4.15: *Flux energy spectrum of the initially critical system scored on the ECCO-33 grid and group structures used to perform the collapsing.*

4.4.1 Sub-prompt positive reactivity insertion

In this section, a sub-prompt super-critical transient is triggered perturbing the capture cross section by -0.75 %, at $t = 10 + 10^{-9}$ ms, again with the purpose of reproducing the step reactivity insertion.

Figure 4.16 shows the total power and total precursors concentration evolution in response to the step insertion of reactivity. After the prompt jump, which is sharper than the one featuring the thermal case because of the faster dynamics featuring the fast system (Λ_{therm} ≈$9.6 \times 10^{-6}\,\text{s}^{-1}$ against Λ_{fast} ≈$4.4 \times 10^{-7}\,\text{s}^{-1}$), the power evolution slows down thanks to the delayed neutrons emissions, which are less effective than in the thermal system case ($\beta_{\text{eff,therm}} \approx 698$ pcm against $\beta_{\text{eff,fast}} \approx 309$ pcm).

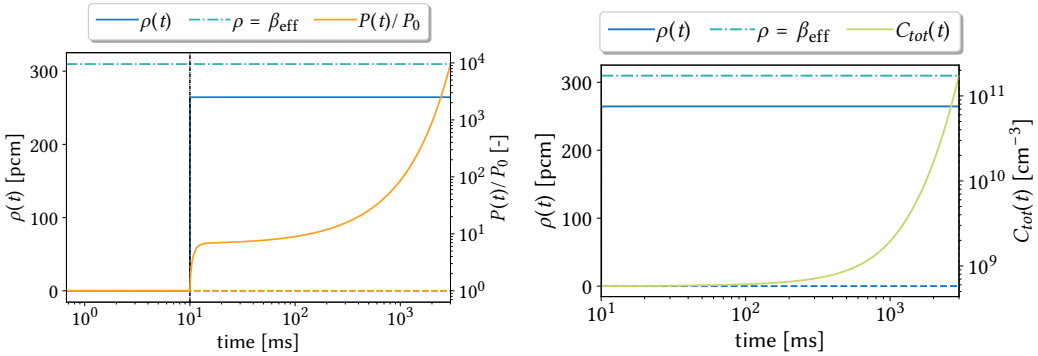

Figure 4.16: *Evolution of the total power and total precursors concentration in the case of a sub-prompt reactivity insertion (ρ = 431.2 pcm).*

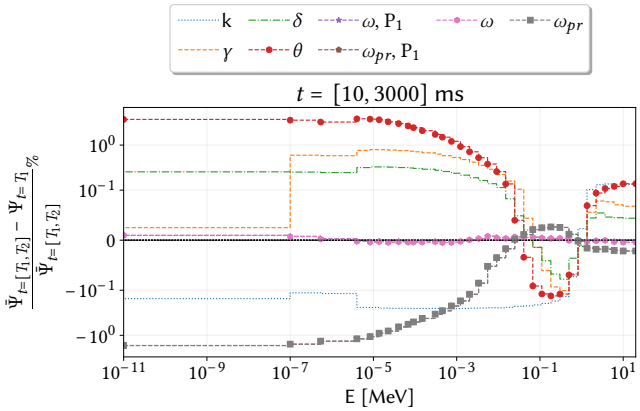

Figure 4.17: *Group-wise, relative error between the time-averaged spectrum computed by FRENETIC and the spectrum of the different eigenvalue formulations as a function of the incident neutron energy.*

In analogy with the corresponding thermal case, the flux shape behaves asymptotically as the fundamental ω-mode, the asymptotic period of the system is much shorter than the one featuring the analogous thermal system, $\tau_{\text{fast}} \approx 405\,\text{ms}$ against $\tau_{\text{therm}} \approx 2235\,\text{ms}$. This aspect is made evident by fig. 4.17, which shows the usual relative error between the various energy spectra with respect to the reference one. It is interesting to observe that, in this case, the γ and the δ spectra are the most accurate one in representing the time-averaged spectrum, after the ω mode.

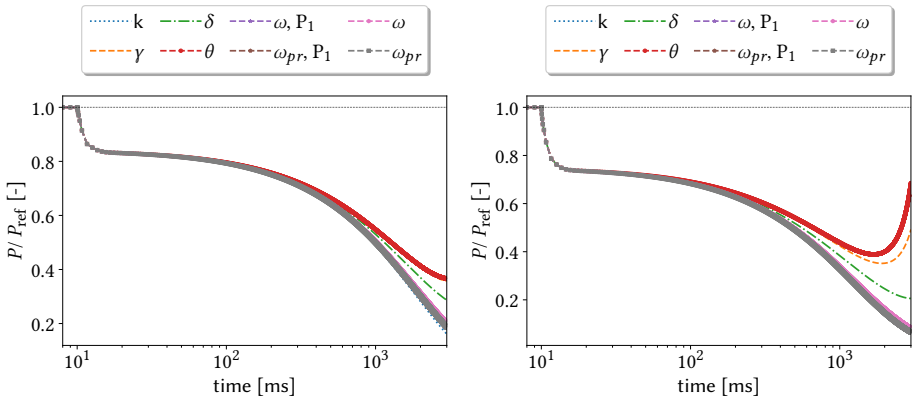

Figure 4.18: *Evolution of the ratio between the total power computed in the few-group cases (PoliTO-LFR-12A on the left, PoliTO-LFR-6A on the right) and the total power in the reference case.*

However, fig. 4.18 shows that, concerning the ratio between the few-group power and the reference one, the θ and the γ collapsing seem to provide more accurate results with respect to the other eigenfunctions, especially with respect to ω. This is probably

due to the fact that, despite the asymptotic spectrum basically corresponds to the fundamental time mode, using this spectrum to perform the few-group collapsing may not be necessarily adequate to produce good results before the asymptotic state is reached, i.e. for t approximately smaller than 405 ms. As a matter of fact, the curves have a similar trend up to t around 200 ms, but then they start to diverge. In light of these considerations, it may be reasonably assumed that the θ- and γ-collapsed few-group data may not be as accurate as ω in reproducing the asymptotic energy spectrum, but they are more accurate in yielding the overall system dynamics, including the instants before the asymptotic period.

Table 4.9: *% relative error for the whole transient between the reference ECCO-33 calculation and the few-group calculations using the various eigenfunction to collapse on the PoliTO-LFR-12A grid for some relevant integral parameters: ρ is the reactivity, Λ is the effective neutron lifetime, β_{eff} is the effective delayed neutron fraction and P is the total thermal power.*

	k	γ	δ	θ	ω, P_1	ω_{pr}, P_1	ω	ω_{pr}
ρ	23.55	73.55	50.26	76.50	15.19	11.94	15.17	11.93
Λ	132.19	131.80	131.76	132.01	131.72	131.67	131.72	131.67
β_{eff}	169.44	169.44	169.44	169.44	169.44	169.44	169.44	169.44
P	3385.67	2807.02	2988.39	2782.07	3234.19	3294.05	3234.34	3293.98

Tables 4.9 and 4.10 report the L_2-error norm for the whole transient duration for the most relevant integral parameters. As for the thermal system, also in this case it is possible to notice that the parameters which are most sensitive to the weighting function used in the collapsing are the reactivity and the power. The results of these tables confirm the trends observed in fig. 4.18, but they show that, quite interestingly, the γ-collapsing provides a better power evolution than the one obtained with the k-collapsing although ρ computed in this last case is more accurate. Since these quantities are related, in the quasi-static method, through the equations for the amplitude function $A(t)$,

$$\begin{cases} \dfrac{dA(t)}{dt} = \dfrac{\rho(t) - \beta_{\text{eff}}(t)}{\Lambda(t)} A(t) + \displaystyle\sum_{i=1}^{\text{R}} \lambda_i c_i(t) \\ \dfrac{dc_i(t)}{dt} = \dfrac{\beta_{\text{eff}}(t)}{\Lambda(t)} A(t) - \lambda_i c_i(t) \;\; i = 1, \ldots, \text{R}, \end{cases} \tag{4.10}$$

it appears that, for the same value of β_{eff}, a better estimate of Λ is more advisable than a better estimate on the reactivity to obtain an overall better estimate of the power.

Table 4.10: *% relative error for the whole transient between the reference ECCO-33 calculation and the few-group calculations using the various eigenfunction to collapse on the PoliTO-LFR-6A grid for some relevant integral parameters: ρ is the reactivity, Λ is the effective neutron lifetime, β_{eff} is the effective delayed neutron fraction and P is the total thermal power.*

	k	γ	δ	θ	ω, P_1	ω_{pr}, P_1	ω	ω_{pr}
ρ	123.72	171.01	92.57	198.84	77.62	106.41	77.67	106.37
Λ	366.15	365.53	365.59	365.92	365.65	365.59	365.65	365.59
β_{eff}	220.23	220.23	220.23	220.23	220.23	220.23	220.23	220.23
P	4129.74	3110.48	3638.93	2864.24	4005.79	4091.07	4006.00	4090.97

4.4.2 Super-prompt positive reactivity insertion

With a super-prompt ($\rho > \beta_{\text{eff}}$) critical reactivity insertion, the dynamics of the system gets faster, diverging rapidly. With respect to the thermal case, the system is only slightly super-prompt critical, thus it is possible to appreciate the characteristic prompt jump in the first time instants of fig. 4.19. Due to its very short asymptotic period,

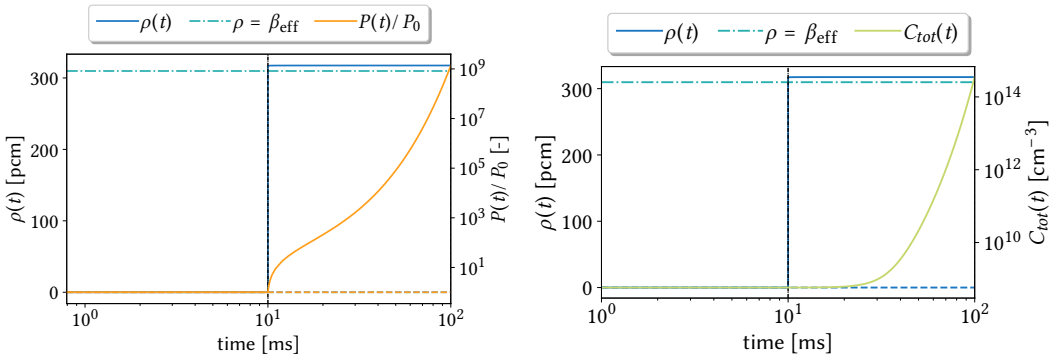

Figure 4.19: *Evolution of the total power and total precursors concentration in the case of a super-prompt positive reactivity insertion (ρ = 310.8 pcm) pcm).*

$\tau = 1/\omega_0 = 4.437$ ms, as visible in fig. 4.20, also in this case the time-averaged energy spectrum is very close to the one of the fundamental ω mode, except in the low energy groups, where the flux is very low. The second most accurate spectrum is the δ one. By inspection of the figure, it is clear that the spectra that fail the most in reproducing the time-averaged spectrum are the k and the θ one.

Nevertheless, the cross section collapsed with the θ spectrum seem to provide the best results, compared to the power computed with the ECCO-33 grid. It is interesting to notice that, when the cross sections are collapsed with the six-group grid, the ratio between the collapsed and the reference power reaches a minimum for the θ and γ cases.

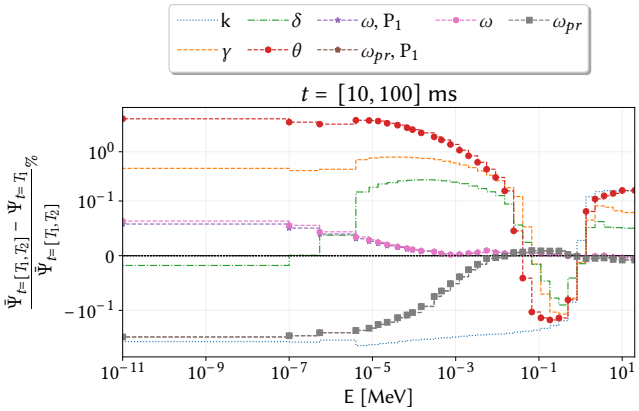

Figure 4.20: *Group-wise, relative error between the time-averaged spectrum computed by FRENETIC and the spectrum of the different eigenvalue formulations as a function of the incident neutron energy.*

From a physical point of view, both systems have reached their transient asymptotic state, which means that their shape in the phase space should not change anymore, and that the only varying quantity is the amplitude, which in this case should increase exponentially. Therefore, the fact that the ratio has a minimum is very likely due some numerical effect.

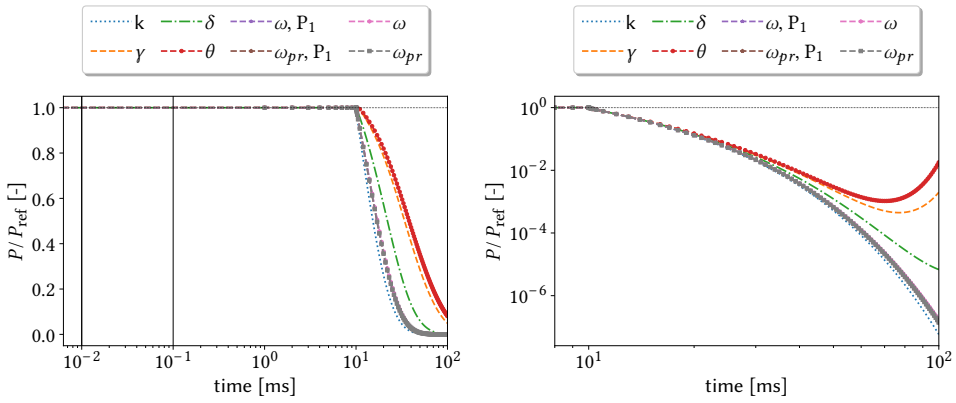

Figure 4.21: *Evolution of the ratio between the total power computed in the few-group cases (PoliTO-LFR-12A on the left, PoliTO-LFR-6A on the right) and the total power in the reference case.*

Concerning the overall trend of the ratio, also in this case it should be considered that, due to the fast dynamics and due to its monotonic behaviour, even a small difference between the initial power profiles can diverge after a few ms. This fact suggests that a future development of this analysis should consider the effects of the thermal feedback, which should dampen not only the power evolution, but, probably also the

numerical error between reference and collapsed calculations.

Table 4.11: *% relative error for the whole transient between the reference ECCO-33 calculation and the few-group calculations using the various eigenfunction to collapse on the PoliTO-LFR-6A grid for some relevant integral parameters: ρ is the reactivity, Λ is the effective neutron lifetime, β_{eff} is the effective delayed neutron fraction and P is the total thermal power.*

	k	γ	δ	θ	ω, P_1	ω_{pr}, P_1	ω	ω_{pr}
ρ	22.54	31.14	17.69	36.02	14.27	14.98	14.26	14.99
Λ	70.35	70.21	70.23	70.28	70.25	70.25	70.25	70.25
P	918.34	914.03	915.99	912.02	917.53	917.63	917.53	917.63
β_{eff}	42.29	42.29	42.29	42.29	42.29	42.29	42.29	42.29

Tables 4.11 and 4.12 provide the usual integral parameters as a function of the group structure used for the collapsing (six- and twelve-group, respectively) and of the eigenfunction used as weight. In the first table, it is possible to appreciate the higher accuracy of the reactivity collapsed with the time eigenfunction, while the differences in the power relative error are so tiny that it is hard to assess the notice the effect of the collapsing function. Concerning the adoption of the PoliTO-LFR-12A group grid, it can be noticed that the best reactivity is provided collapsing with k, which, however, is featured by the largest error in the power. For this last parameter, the best cases are the ones obtained with θ and γ, due to the fact that the error decreases after the minimum is reached. Once again, the effective delayed neutron fraction and the effective lifetime are not influenced at all by the collapsing choice, but only by the group structure selection.

Table 4.12: *% relative error for the whole transient between the reference ECCO-33 calculation and the few-group calculations using the various eigenfunction to collapse on the PoliTO-LFR-12A grid for some relevant integral parameters: ρ is the reactivity, Λ is the effective neutron lifetime, β_{eff} is the effective delayed neutron fraction and P is the total thermal power.*

	k	γ	δ	θ	ω, P_1	ω_{pr}, P_1	ω	ω_{pr}
ρ	4.25	25.08	17.58	26.04	5.80	5.09	5.81	5.09
Λ	25.43	25.23	25.22	25.32	25.21	25.21	25.21	25.21
P	898.15	687.75	829.56	642.17	881.15	882.76	881.14	882.78
β_{eff}	32.54	32.54	32.54	32.54	32.54	32.54	32.54	32.54

4.4.3 Negative reactivity insertion

Mirroring the corresponding section for the thermal system, in the following a typical shut-down transient is analysed, perturbing the capture cross section of the medium to get a negative reactivity insertion around -250 pcm, which is almost the half of the reactivity drop featuring the thermal case (-460 pcm). The corresponding reactor period is, again, much longer than the overall transient duration, $\tau = 1/\omega_0 = 82569$ ms, because of the delayed effects. As for the thermal case, the asymptotic ω mode reproduces very well the time-averaged spectrum, since the delayed neutrons have the same emission spectrum, which implies that their shapes in the delayed cluster are equal within machine precision.

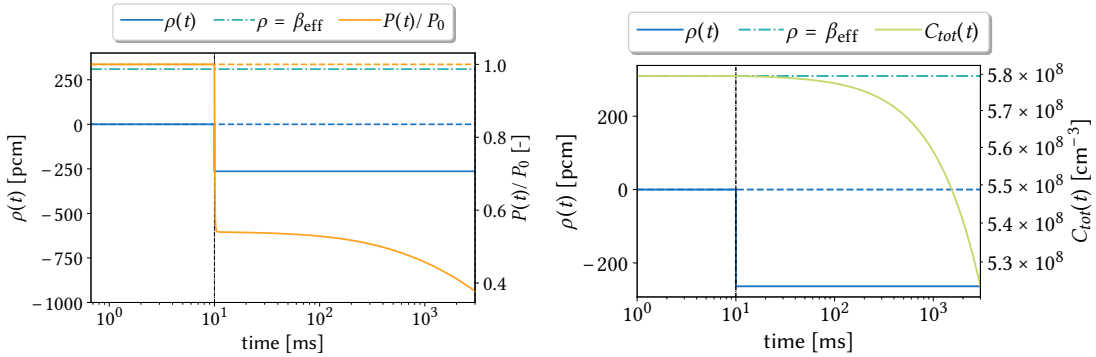

Figure 4.22: *Evolution of the main integral parameters in the case of negative reactivity insertion ($\rho = -250$ pcm).*

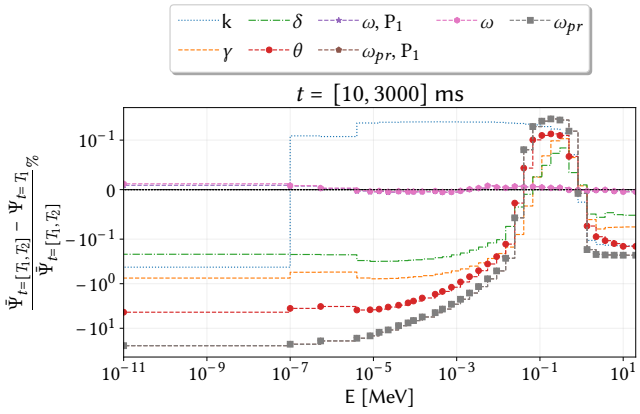

Figure 4.23: *Group-wise, relative error between the time-averaged spectrum computed by FRENETIC and the spectrum of the different eigenvalue formulations as a function of the incident neutron energy.*

The usual time-dependent figure of merit, depicted in fig. 4.24, has a similar behaviour to the corresponding thermal case, except for the fact that, in this case, the fundamental time mode provides the best error trend. Compared to the other cases, this one exhibits an almost steady error evolution and, thus, seems the best in reproducing the reference result during the overall transient duration.

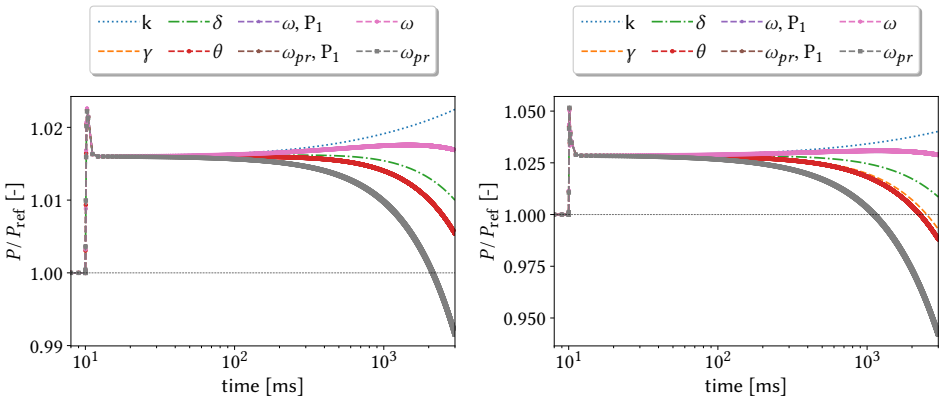

Figure 4.24: *Evolution of the ratio between the total power computed in the few-group cases (CASMO-18 on top-left, PoliTO-LFR-12A on top-right, PoliTO-LFR-6A on bottom-left and CASMO-2 on bottom-right) and the total power in the reference case.*

However, an inspection of the relative error on the integral parameters in table 4.13 would suggest that, concerning the power, the best options for the collapsing are θ and γ for the six-group case and ω_{pr}, θ and γ for the twelve-group case. This "wrong" suggestion is clearly a consequence of the fact that, during the transient evolution, the ratio between the few-group and the reference power tends to unity and, then, goes below it. If the transient was longer, the integral error would certainly change in favour of the ω case. This suggests that a future analysis should consider also some "local" definition of the relative error, maybe evaluating it in some fixed instants of the transient.

4.4.4 Positive and negative reactivity insertions

Figure 4.25 shows the response of the power and of the precursors concentration to a complex reactivity evolution, obtained with step and non-linear variations. At first, the capture cross section of the critical system gets perturbed by -0.9 % to induce a super-prompt critical transient for 20 ms. Then, the positive reactivity is compensated by a linear increase of the perturbed capture cross section by a factor 0.8% between t =30 ms and t =110 ms. Afterwards, a linear perturbation in time occurs, such that the capture cross section at t =110 ms is increased by 2% at t =410 ms. The last variation is obtained decreasing linearly the new capture cross section in order to obtain a decrease of -2.2 % at t =2000 ms. The simulation is stopped at 3000 ms.

Table 4.13: *% relative error for the whole transient between the reference ECCO-33 calculation and the few-group calculations using the various eigenfunction to collapse on the PoliTO-LFR-6A grid for some relevant integral parameters: ρ is the reactivity, Λ is the effective neutron lifetime, β_{eff} is the effective delayed neutron fraction and P is the total thermal power.*

	k	γ	δ	θ	ω, P_1	ω_{pr}, P_1	ω	ω_{pr}
ρ	123.41	170.66	92.44	197.49	76.58	477.48	76.63	477.45
Λ	370.57	371.18	371.11	370.83	371.03	370.32	371.03	370.32
P	195.22	91.34	116.61	87.51	164.98	155.39	165.02	155.37
β_{eff}	220.23	220.23	220.23	220.23	220.23	220.23	220.23	220.23

Table 4.14: *% relative error for the whole transient between the reference ECCO-33 calculation and the few-group calculations using the various eigenfunction to collapse on the PoliTO-LFR-12A grid for some relevant integral parameters: ρ is the reactivity, Λ is the effective neutron lifetime, β_{eff} is the effective delayed neutron fraction and P is the total thermal power.*

	k	γ	δ	θ	ω, P_1	ω_{pr}, P_1	ω	ω_{pr}
ρ	24.24	73.09	50.01	75.56	15.66	154.91	15.64	154.90
Λ	132.59	132.96	132.99	132.78	133.01	132.42	133.01	132.42
P	109.25	67.64	77.07	66.70	94.37	48.59	94.38	48.59
β_{eff}	169.44	169.44	169.44	169.44	169.44	169.44	169.44	169.44

Due to the complex reactivity evolution, the relative error between the time-averaged energy spectra and the energy spectra of the various eigenfunctions is reported in fig. 4.20 for the most relevant time intervals. For all these intervals, except the one for $t \in [110, 410]$ ms, the ω spectrum is the most accurate one, followed by the prompt time spectrum when the time interval duration is not too long. Concerning the static eigenfunctions, δ seems the most accurate one in most of the different time intervals, with a relative error slightly larger than the one featuring ω, while θ is almost always the worst one.

Notwithstanding these relative error trends, fig. 4.27 clearly shows that, with respect to the thermal case, the performance of the various collapsing eigenfunctions are much more sensitive to the choice of the few-group grid. Specifically, in the six-group case, the θ eigenfunction seems even the best option for the cross section generation. In the case with twelve groups, the best case is the δ one, consistently with the observations on the relative error of the energy spectrum.

Compared to the previous case, the relative error on the power, visible in tables 4.15 and 4.16, is completely consistent with the trend observed in fig. 4.27. Concerning the

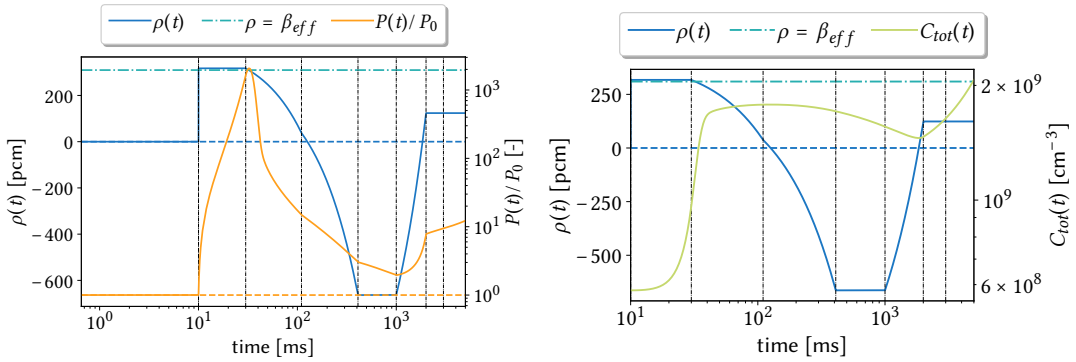

Figure 4.25: *Evolution of the total power and total precursors concentration in the case of super- and sub-prompt positive and negative reactivity insertions.*

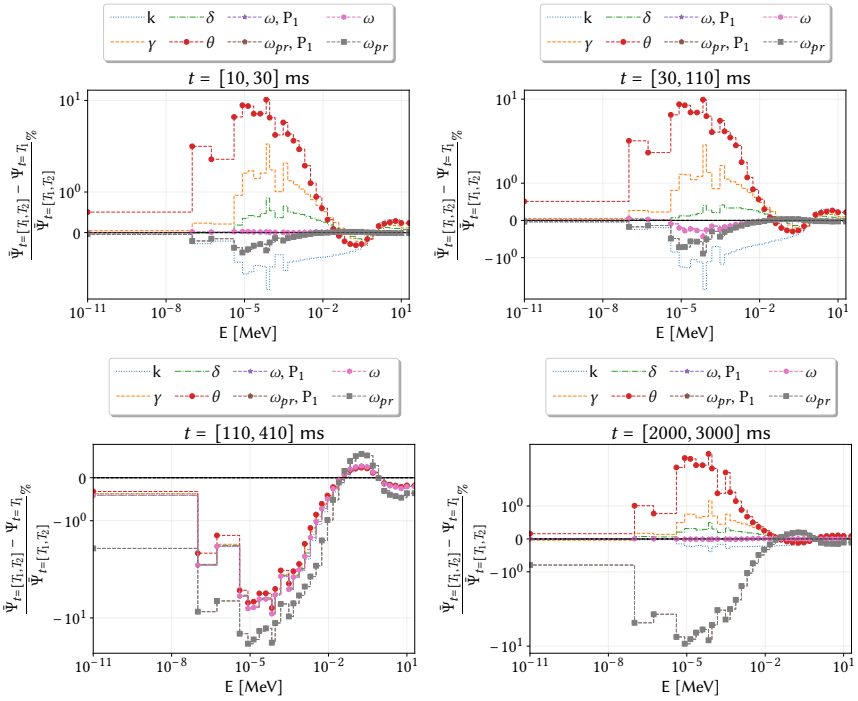

Figure 4.26: *Group-wise, relative error between the time-averaged spectrum computed by FRENETIC and the spectrum of the different eigenvalue formulations as a function of the incident neutron energy.*

reactivity, the most accurate values are obtained with the fundamental time eigenmode with both energy grids.

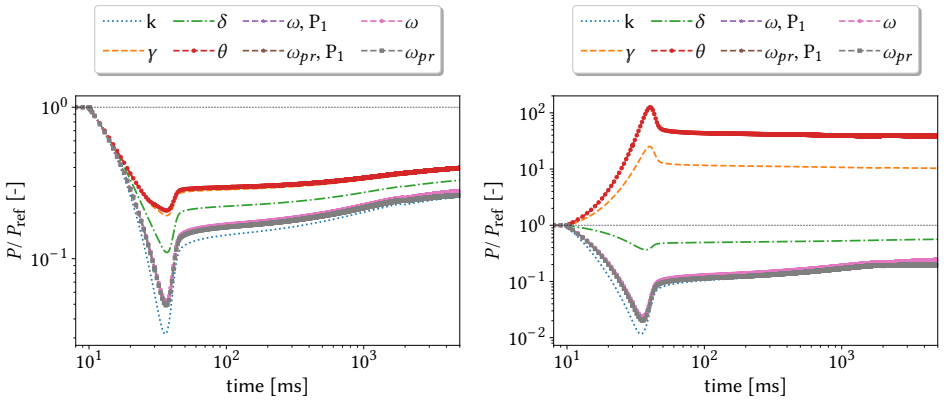

Figure 4.27: *Evolution of the ratio between the total power computed in the few-group cases (PoliTO-LFR-12A on the left, PoliTO-LFR-6A on the right) and the total power in the reference case.*

Table 4.15: *% relative error for the whole transient between the reference ECCO-33 calculation and the few-group calculations using the various eigenfunction to collapse on the PoliTO-LFR-6A grid for some relevant integral parameters: ρ is the reactivity, Λ is the effective neutron lifetime, β_{eff} is the effective delayed neutron fraction and P is the total thermal power.*

	k	γ	δ	θ	ω, P_1	ω_{pr}, P_1	ω	ω_{pr}
ρ	36.70	187.64	136.11	190.38	45.67	5045.21	45.63	5044.66
Λ	171.18	171.45	171.47	171.33	171.47	170.44	171.47	170.44
P	5483.67	4559.65	4968.87	4490.10	5321.41	5399.57	5321.37	5399.70
β_{eff}	218.99	218.99	218.99	218.99	218.99	218.99	218.99	218.99

Table 4.16: *% relative error for the whole transient between the reference ECCO-33 calculation and the few-group calculations using the various eigenfunction to collapse on the PoliTO-LFR-12A grid for some relevant integral parameters: ρ is the reactivity, Λ is the effective neutron lifetime, β_{eff} is the effective delayed neutron fraction and P is the total thermal power.*

	k	γ	δ	θ	ω, P_1	ω_{pr}, P_1	ω	ω_{pr}
ρ	170.14	467.81	272.24	525.50	61.16	18048.22	61.25	18045.64
Λ	476.91	477.35	477.29	477.11	477.22	475.98	477.22	475.98
P	5749.29	67907.89	3229.64	272479.40	5584.67	5782.53	5584.55	5782.73
β_{eff}	284.64	284.64	284.64	284.64	284.64	284.64	284.64	284.64

4.5 Conclusions

In this chapter, one of the current open issues in reactor physics, i.e. the cross section group-collapsing, has been addressed from the point of view of the weighting spectrum used to perform the integration over the energy range. In particular, the use of the fundamental eigenfunctions associated to the different eigenvalue formulations arising in neutron transport is investigated as an alternative to the usual choice of considering the k-eigenvalue spectrum.

Due to the problem complexity and to the large number of parameters affecting the group constant generation, the analysis was carried out performing some numerical experiments for a simplified system, i.e. a homogeneous slab, for which the calculation of the various eigenfunctions is possible using the TEST code. The choice of neglecting any heterogeneity effect allowed to focus on the energy effects related to the system spectrum, to the choice of the weighting function and to the energy group structure used for the cross sections and diffusion coefficient condensation.

For the sake of generality, several calculations were carried out, analysing different basic transient scenarios, featured by positive and negative reactivity insertions, considering both a thermal and a fast spectrum. In order to be consistent in the examination of the various scenarios, each reactivity modification involved the modification of the group-wise capture cross section of the system. The choice for this kind of perturbation is that is allows to mimic the behaviour of a control rod, which is usually the reactivity driver in an operating reactor.

The analysis showed that it is actually very difficult to foresee the performances of each weighting eigenfunction only relying on physical considerations, because of the appearance of numerical error compensations in the condensation scheme that depend on the type of the reactivity insertion, on the few-group grid, on the type of the eigenfunction and, of course, on the system energy spectrum.

Nevertheless, it is possible to conclude that, in most of the cases, the k eigenfunction, which is the one traditionally employed in the group constant generation process, is certainly the one yielding the worst results, especially when the system is far from criticality. In this respect, the best option for the condensation procedure seems to be γ energy spectrum. Actually, other eigenfunctions like the ω and the θ ones may provide slightly more accurate results than the ones produced with the γ condensation, but the evaluation of these eigenfunctions is always much more computationally expensive. On top of that, the performances of γ can found a justification on a physical ground, since, among the static eigenvalue formulations presented in the thesis, it is the one which distorts the less the energy spectrum of the system.

From this perspective, the low relative error obtained with the θ collapsing may be explained by the fact that both the nature of the perturbation and the θ eigenvalue definition involve the capture cross section. In order to shed some light on this aspect, the reactivity should be driven by the change of other parameters, for example the fission cross section or the density of the system, which are strongly related to k and δ,

respectively.

In order to draw some more general conclusions, other numerical experiments should be envisaged in the future. In addition to the analysis of the influence of the kind of perturbation triggering the reactivity insertion, the spatial and energy effects related to the presence of heterogeneities in the system should be definitively taken into account. Finally, the thermal feedback should be introduced, especially for the analysis of heavily off-criticality.

References

Bell, G. I. and S. Glasstone (1970). "Nuclear Reactor Theory". Van Nostrand Reinhold (cited on pages 115, 122).

Bonifetto, R. (2014). "Computational thermal-hydraulic modeling for nuclear fusion and fission applications". PhD thesis. Politecnico di Torino (cited on page 119).

Cacuci, D. G. (2010). "Handbook of Nuclear Engineering: Vol. 1: Nuclear Engineering Fundamentals; Vol. 2: Reactor Design; Vol. 3: Reactor Analysis; Vol. 4: Reactors of Generations III and IV; Vol. 5: Fuel Cycles, Decommissioning, Waste Disposal and Safeguards". Volume 1. Springer Science & Business Media (cited on page 116).

Caron, D. (2017). "Neutronics methods for the multiphysics analysis of nuclear fission systems". PhD thesis. Politecnico di Torino (cited on page 119).

Caron, D., S. Dulla, and P. Ravetto (2016). "New aspects in the implementation of the quasi-static method for the solution of neutron diffusion problems in the framework of a nodal method". In: *Annals of Nuclear Energy* 87, pages 34–48 (cited on page 119).

Cervi, E., S. Lorenzi, A. Cammi, and L. Luzzi (2019). "Development of an SP_3 neutron transport solver for the analysis of the Molten Salt Fast Reactor". In: *Nuclear Engineering and Design* 346, pages 209–219 (cited on page 115).

Cramer, W. H. and D. J. Kropaczek (2020). *CASL Annual Report (FY2018)*. Technical report CASL-U-2020-1974-000. Oak Ridge National Lab.(ORNL), Oak Ridge, TN (U.S.A.) (cited on page 117).

Dugan, K., R. Sanchez, and I. Zmijarevic (2018). "Cross section homogenization for transient calculations in a spatially heterogeneous geometry". In: *Annals of Nuclear Energy* 116, pages 439–447 (cited on page 118).

Dugan, K., I. Zmijarevic, and R. Sanchez (2016). "Cross-Section Homogenization for Reactivity-Induced Transient Calculations". In: *Journal of Computational and Theoretical Transport* 45.6, pages 425–441 (cited on pages 118, 120–121).

Dulla, S. and P. Ravetto (2020). "A re-visitation of space asymptotic theory in neutron transport". In: *European Physical Journal Plus* 135, page 347 (cited on page 122).

Gamarino, M., A. Dall'Osso, D. Lathouwers, and J. L. Kloosterman (2018). "Rehomogenization of nodal cross sections via modal synthesis of neutron spectrum changes". In: *Nuclear Science and Engineering* 190.1, pages 1–30 (cited on page 117).

Gelbard, E. M. (1968). New York: Gordon & Breach (cited on page 115).

Grasso, G., C. Petrovich, D. Mattioli, C. Artioli, P. Sciora, D. Gugiu, G. Bandini, E. Bubelis, and K. Mikityuk (2014). "The core design of ALFRED, a demonstrator for the European lead-cooled reactors". In: *Nuclear Engineering and Design* 278, pages 287–301 (cited on page 135).

Henry, A. F. (1964). "The application of inhour modes to the description of non-separable reactor transients". In: *Nuclear Science and Engineering* 20, pages 338–351 (cited on page 120).

Kulesza, J. A., F. Franceschini, T. M. Evans, and J. C. Gehin (2016). "Overview of the consortium for the advanced simulation of light water reactors (CASL)". In: *EPJ web of conferences*. Volume 106. EDP Sciences, page 03002 (cited on page 117).

Leppänen, J., M. Pusa, T. Viitanen, V. Valtavirta, and T. Kaltiaisenaho (2015). "The Serpent Monte Carlo code: Status, development and applications in 2013". In: *Annals of Nuclear Energy* 82, pages 142–150 (cited on page 135).

Leppänen, J., M. Pusa, and E. Fridman (2016). In: *Annals of Nuclear Energy* 96, pages 126–136 (cited on page 121).

Mancusi, D. and A. Zoia (2018). "Chaos in eigenvalue search methods". In: *Annals of Nuclear Energy* 112, pages 354–363 (cited on page 118).

Massone, M., F. Gabrielli, and A. Rineiski (2017). "A genetic algorithm for multigroup energy structure search". In: *Annals of Nuclear Energy* 105, pages 369–387 (cited on page 117).

Nallo, G. F., N. Abrate, S. Dulla, P. Ravetto, and D. Valerio (2020). "Neutronic benchmark of the FRENETIC code for the multiphysics analysis of lead fast reactors". In: *The European Physical Journal Plus* 135, page 238 (cited on page 115).

Rahnema, F. (1989). "Boundary Condition Perturbation Theory for Use in Spatial Homogenization Methods". In: *Nuclear Science and Engineering* 102.2, pages 183–190 (cited on page 117).

Rahnema, F. and E. M. Nichita (1997). "Leakage corrected spatial (assembly) homogenization technique". In: *Annals of Nuclear Energy* 24.6, pages 477–488 (cited on page 117).

Rahnema, F. and M. S. McKinley (2002). "High-order cross-section homogenization method". In: *Annals of Nuclear Energy* 29.7, pages 875–899 (cited on page 117).

Sanchez, R., D. Tomatis, I. Zmijarevic, and H. G. Joo (2017). "Analysis of alpha modes in multigroup diffusion". In: *Nuclear Engineering and Technology* 49, pages 1259–1268 (cited on page 120).

Smith, K. (1986). "Assembly homogenization techniques for light water reactor analysis". In: *Progress in Nuclear Energy* 17.3, pages 303–335 (cited on page 117).

Weinberg, A. M. and E. P. Wigner (1958). "The Physical Theory of Neutron Chain Reactors". University of Chicago Press, Chicago (cited on page 122).

Chapter 5

A generalised eigenvalue formulation for core-design applications

> I stand upon my desk to remind myself that we should constantly look at things in a different way. See, the world looks very different from up here… Just when you think you know something, you have to look at it in another way. Even if it may seem silly, or wrong, you must try.
>
> Prof. John Keating, Dead Poets Society

5.1 Introduction

In chapter 3, the various eigenvalue formulations available in the literature have been examined, highlighting their potential application as design-oriented tools. From the designer perspective, all of these spectral forms of the NTE share the issue of showing unsatisfactory adherence to the physical constraints that are practically encountered when the design is actually carried out. Exploiting the features of the eigenvalue problem formulations in neutron transport theory, and aiming at improving the core-design phase, a new eigenvalue formalism is thus introduced and some of its potentialities are discussed in this chapter, analysing some relevant problems of reactor physics.

As mentioned in the previous chapters, the design of the core of a nuclear fission reactor has been traditionally carried out focusing on the k eigenvalue. According to the

value of k_{eff}, i.e. the fundamental eigenvalue k_0, the designer can immediately understand how far the system is from criticality. Assuming that a certain system is featured by $k > 1$, the designer guesses that the multiplication properties of the core should decrease, either changing its geometrical features to increase leakage or changing its material properties, e.g. increasing parasitic capture or decreasing fission, but no precise indication on *what* has to change can be obtained. Most of the times, the other design constraints can guide this selection. For example, the fuel pins should have a minimum surface-to-volume ratio for thermo-hydraulics requirements, so the criticality could be attained, in this case, acting only on the material composition. However, the quantitative information provided by k is not sufficient to practically achieve criticality. As discussed in chapter 3, k can be interpreted as a correction factor for the total fission production, so it can be viewed as a correction either for Σ_f or for ν. In the first case, changing the total fission cross section would imply to change the absorption and the total cross sections as well, while changing ν is not possible unless acting on the mixture of fissile materials, which implies to change the cross sections of the medium. At this point, it should be clear that the quantitative information delivered by k does not provide a *physically consistent* indication for the design. The same could be argued also for the γ and the θ cases.

On the contrary, the other design-oriented formulation, i.e. the density eigenvalue δ, provides a correction factor for the medium density, so it acts simultaneously on all the cross sections. In principle, this information is physically consistent, but it may not be useful from a practical point of view, as it is not always possible to act on the atomic density of a certain material. Moreover, the same correction factor should be applied to each nuclide composing the medium, meaning that this formulation does not allow to handle specific regions, e.g. the fuel pins or the control rods.

This chapter presents an innovative formulation of the density eigenvalue, based on a generalised eigenvalue formulation, which overcomes the issues of the traditional δ formulation in order to be applicable for design-oriented applications. In the next section, this new eigenvalue formulation will be derived starting from a generalisation of the neutron transport eigenvalue problem, while in the rest of the chapter some relevant problems in reactor physics will be analysed in light of this new formulation, in order to show its advantages with respect to the legacy calculation approach.

Part of the content of this chapter has been already published as a conference proceedings for the Physor 2022 conference,

- N. Abrate, S. Dulla, P. Ravetto, P. Saracco, *"Formulation of the Density Eigenvalue Problem in Neutron Transport for Relevant Engineering Applications"*, Proceedings of the PHYSOR 2022 conference, Pittsbutgh, PA (U.S.A.), 2022.

Part of the content of this chapter was also presented, after a preliminary selection, at the European Nuclear Education Network (ENEN) PhD event 2022, hosted during the FISA2022-EURADWASTE'22 conference, where I was awarded with the ENEN Prize 2022 *ex aequo* with other two PhD students.

5.2 The theory of the ζ eigenvalue

Except for the time eigenvalues, which naturally arise from the Laplace transform of the NTE, all the other design-oriented formulations discussed so far are simply derived introducing an eigenvalue in front of the operator of interest. Recalling here the definition of eigenvalue problem at the basis of the design-oriented formulations, given in eq. (2.19),

$$\hat{A}\vec{\varphi}_{\xi,n} = \xi_n \hat{B}\vec{\varphi}_{\xi,n}, \tag{5.1}$$

it is evident that the eigenvalue ξ_n turns out to be a tuning parameter that is used to force the system to reach the criticality condition. In this case, this parameter acts on the operator $\hat{B}$ and, consequently, on the phase space where this operator is defined. For example, in case ξ was k, this parameter would act only on those regions of the phase space where $\chi(x,E)\nu(x,E')\Sigma_f(x,E') \neq 0$, i.e. only on the fissile nuclides in the active regions and only on the fission energy range.

As such, it would be still valid, from both a mathematical and a physical point of views, to introduce the eigenvalue to act on a more specific portion of the phase space. Let's assume, for example, that the objective of the design is to determine which is the amount of captures that a cluster of control rods should ensure in order to compensate the excess of reactivity for a fresh fuelled, thermal reactor. In this case, due to the spectrum of the system, we could assume that our control rods are made of a thermal absorber, like cadmium. Since the control rods are localised in a specific position in the core, it is possible to introduce the θ eigenvalue as follows,

$$\left(\hat{L} + \hat{F}_0 + \hat{S}_0 - \hat{S} - \hat{F}\right)\varphi_{\theta_n} = \frac{1}{\theta_n(\vec{r},E)}\hat{C}\varphi_{\theta_n}, \tag{5.2}$$

where the dependence of the eigenvalue with respect to the spatial and energy variable should be interpreted as

$$\theta_n(\vec{r},E) = \begin{cases} \theta_n & \forall \vec{r} \in \mathcal{V}_{CR}, \forall E \in [E_{min}, E_{max}] \\ 1 & \text{otherwise.} \end{cases} \tag{5.3}$$

The symbol $\mathcal{V}_{CR}$ indicates the volume of the control rods, while $[E_{min}, E_{max}]$ indicates the thermal range for the capture cross section of the cadmium.

With respect to the formulation given in chapters 2 and 3, this alternative form of θ allows to estimate the capture reaction rate needed to achieve criticality for a specific region, without affecting the other ones. However, from a practical point of view, this form is still unsatisfactory, as it includes also other nuclides in addition to cadmium, e.g., the structural materials composing the rods. Therefore, to achieve the maximum level of flexibility, the eigenvalue formulation should be generalised in order to act only on the nuclides of interest.

In this case, the quantitative information obtained by solving the θ eigenvalue problem would be a correction factor $1/\theta_{\text{eff}}$ for the capture cross section of cadmium, $\Sigma_{c,Cd}(E) =$

$N_{Cd}\sigma_{c,Cd}(E)$. Since it is not possible to change $\sigma_{c,Cd}(E)$, which is an intrinsic property of cadmium, the correction factor should be interpreted as a scaling factor for its atomic density N_{Cd}. However, if the cadmium concentration was re-scaled, also the other cross sections of cadmium, like the scattering one, would change. Hence, in light of this consideration, the only physically meaningful eigenvalue turns out to be the density eigenvalue, which is the only one able to provide scaling factors consistent with the physics. In order to distinguish this generalised eigenvalue from the classic one, hereafter this eigenvalue will be addressed as ζ.

Considering a system defined in a limited spatial domain $\mathcal{V}$, filled by a mixture of M nuclides, each characterised by a local atomic density $N_m(\vec{r})$, $m = 1, \dots, \mathrm{M}$, the generalised eigenvalue problem ζ for a specific isotope, identified as $m^\star$ and located in a region $\mathcal{V}_{m^\star}$, would yield

$$\begin{aligned}
&\vec{\Omega}\cdot\nabla\phi(\vec{r},E,\vec{\Omega}) + \sum_{\substack{m=1\\m\neq m^\star}}^{\mathrm{M}}\left[N_m(\vec{r})\sigma_{t,m}(E)\right]\phi(\vec{r},E,\vec{\Omega}) + \frac{1}{\zeta}\left[N_{m^\star}(\vec{r})\sigma_{t,m^\star}(E)\right]\phi(\vec{r},E,\vec{\Omega}) = \\
&\sum_{\substack{m=1\\m\neq m^\star}}^{\mathrm{M}}\int dE'\oint d\vec{\Omega}'\left[N_m(\vec{r})\sigma_{s,m}(E')\right]f_{s,m}(\vec{r},E'\longrightarrow E,\vec{\Omega}'\cdot\vec{\Omega})\phi(\vec{r},E',\vec{\Omega}') + \\
&\frac{1}{\zeta}\int dE'\oint d\vec{\Omega}'\left[N_{m^\star}(\vec{r})\sigma_{s,m^\star}(E')\right]f_{s,m^\star}(\vec{r},E'\longrightarrow E,\vec{\Omega}'\cdot\vec{\Omega})\phi(\vec{r},E',\vec{\Omega}') + \\
&\sum_{\substack{m=1\\m\neq m^\star}}^{\mathrm{M}}\int dE'\oint d\vec{\Omega}'\left[N_m(\vec{r})\nu_m(E')\sigma_{f,m}(E')\right]\frac{\chi_m(E)}{4\pi}\phi(\vec{r},E',\vec{\Omega}') + \\
&\frac{1}{\zeta}\int dE'\oint d\vec{\Omega}'\left[N_{m^\star}(\vec{r})\nu_{m^\star}(E')\sigma_{f,m^\star}(E')\right]\frac{\chi_{m^\star}(E)}{4\pi}\phi(\vec{r},E',\vec{\Omega}'),
\end{aligned} \tag{5.4}$$

for $\vec{r}\in\mathcal{V}_{m*}$, while, for $\vec{r}\notin\mathcal{V}_{m*}$,

$$\begin{aligned}
&\vec{\Omega}\cdot\nabla\phi(\vec{r},E,\vec{\Omega}) + \sum_{m=1}^{\mathrm{M}}\left[N_m(\vec{r})\sigma_{T,m}(E)\right]\phi(\vec{r},E,\vec{\Omega}) = \\
&\sum_{m=1}^{\mathrm{M}}\int dE'\oint d\vec{\Omega}'\left[N_m(\vec{r})\sigma_{s,m}(E')\right]f_{s,m}(\vec{r},E'\longrightarrow E,\vec{\Omega}'\cdot\vec{\Omega})\phi(\vec{r},E',\vec{\Omega}') + \\
&\sum_{m=1}^{\mathrm{M}}\int dE'\oint d\vec{\Omega}'\left[N_m(\vec{r})\nu_m(E')\sigma_{f,m}(E')\right]\frac{\chi_m(E)}{4\pi}\phi(\vec{r},E',\vec{\Omega}'),
\end{aligned} \tag{5.5}$$

imposing the continuity of the angular flux on any internal interface. It should be noticed that it is not required that the zone $\mathcal{V}_{m*}$ is simply connected, meaning that the same eigenvalue can be applied also to different zones in the reactor at the same time.

Eqs. 5.4-5.5 constitutes a general eigenvalue problem that allows to estimate the effect of a specific nuclide and its positioning within the reactor on the total neutron balance in a completely self-consistent way. In general, the eigenvalue ζ could be defined to filter a more specific volume in phase space, as for the example of cadmium,

thus including the possibility to select a specific energy window and a specific reaction channel. In this sense, each eigenvalue formulation discussed so far can be interpreted as a particular case of the ζ model:

- k is restricted to the phase space region featured by $\Sigma_f(\vec{r}, E) \neq 0$;
- γ is applied to each phase space region and nuclide featured by a particle emission;
- θ filters the specific capture reaction, extending to the whole phase space and to each nuclide;
- δ is defined over the whole phase space and applies to each nuclide.

Due to its generality, it is extremely difficult to provide a formal proof concerning the existence and uniqueness of an eigenfunction with uniform sign over the phase space. Since ζ includes also the other formulations, the same considerations made in chapter 3 hold under some hypotheses. If ζ was cast into a k form, it would be always possible to assess the existence and uniqueness of a fundamental eigenpair. On the contrary, if ζ was cast as θ, the existence of a positive eigenvalue would not be guaranteed. Despite this lack of formal evidences could seem a bit disappointing, it is not an issue from a practical standpoint. In the framework of the core design, the designer is aware that, in the design process, different possibilities may arise: the lack of a fundamental solution would simply mean that it is not possible to obtain a steady state system acting on that particular isotope and region of the phase space, while, if one or more fundamental eigenpair exist, this would mean that the problem can be solved.

The following sections present a set of relevant applications of this new eigenvalue problem, showing in more detail these different possibilities.

5.2.1 Implementation in the TEST code

Exploiting the built-in classes already implemented in TEST to handle the various eigenvalue formulations presented in chapter 2, an *ad hoc* sub-class was defined to properly handle the ζ formulation and its action on specific nuclides and/or portions of the phase space. Aiming at maximising the code flexibility, the full set of matrix operators appearing in eq. (2.13) are first assembled for the initially off-critical system. Then, the formulation is built acting on the different operators, according to a user-defined object that represents the volume of the phase space and the nuclides on which ζ should operate. If the nuclide of interest does not exist in the starting off-critical system, e.g., the boron to be diluted in water, its few-group cross sections are read and the set of the matrix operators are defined accordingly in order to yield eq. (5.4). Because of the additional implementation complexities that may arise, TEST does not currently support matrix-free, iterative solution of eq. (5.4), like the transport-sweep algorithm.

5.3 Determination of the moderation ratio for a homogeneous mixture of fuel and moderator

One of the classical problems of reactor physics is the determination of the critical moderator-to-fuel ratio in a thermal reactor. Due to the competition between the neutron slowing down and the parasitic captures that both occur in the moderator, it is usually possible to find two critical moderation ratios N_m/N_f, where N_m and N_f are the atomic density of the moderator and of the fuel material, respectively (Weinberg and Wigner, 1958). A typical example of the behaviour of the effective multiplication constant for a thermal system moderated by light water can be found in fig. 5.1, which has been constructed iteratively changing N_m, for a fixed value of N_f. In case the lowest value of N_m is selected, the critical structure is said to be *under-moderated*, while, in case the largest one is employed, the system is said to be *over-moderated*. The existence of a maximum in this curve induces the designer to choose the under-moderated configuration, because of its better behaviour in presence of instabilities. There are at least two physical justifications for this choice. From a purely neutronic point of view, this configuration is more spatially coupled, so it is less sensitive to localised perturbations. Consequently, the under-moderated arrangement is featured by a larger eigenvalue separation (ES), which is a well established figure of merit to assess the spatial stability of a reactor (Beckner and Rydin, 1975; Vitali, 2020). From a thermo-hydraulics point of view, an increase of the average temperature of the system would cause a larger variation in the density of the moderator, meaning that the moderation ratio of the system would decrease and that, consequently, the multiplication factor of the system would increase, destabilising the system.

Table 5.1: *Critical moderation ratios N_m/N_f to achieve criticality for a slab thick 170 cm filled with a homogeneous mixture of fissile material and light water, computed with the ζ formulation and with an iterative procedure.*

ζ formulation		iterative approach	
N_m/N_f	k_{eff}	N_m/N_f	k_{eff}
0.09096	1.00000	[0.09060, 0.09132]	[0.99918, 1.00082]
20.01752	1.00000	[19.98347, 20.14059]	[1.00074, 0.99734]

Figure 5.1 shows the k_{eff} behaviour for a slab, thick 140 cm and filled with a homogeneous mixture of fissile material and light water, as a function of the moderation ratio. Following the common practice, the critical moderation ratios, i.e. the red dots in the figure, are determined increasing iteratively the moderator density, using 1000 uniformly-spaced values. Therefore, each dot in the Figure corresponds to the solution of a k-eigenvalue problem cast in the two-group P_1 model.

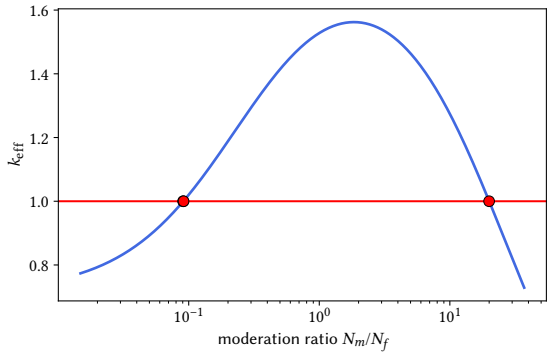

Figure 5.1: *Effective multiplication factor as a function of the moderation ratio for a two-group homogeneous system of thickness 140 cm and filled with a mixture of uranium oxide enriched at 3% and light water.*

Both solutions can be obtained "exactly", without iterations, introducing the ζ eigenvalue in front of the moderator density. Table 5.1 provides the density correction factors needed to attain criticality computed with the two methods. For the iterative approach, the range including the critical values is reported. The presence of two critical configurations is reflected by the existence of two fundamental eigenfunctions, both featured by a uniform sign across the domain. These modes are showed in fig. 5.2 with the first- and second-order harmonics. By inspection, it is easy to notice that the solution associated to the larger value of ζ, i.e. the one requiring the largest moderator density reduction, is associated with a harder spectrum, featured by a spectral index roughly equal to 0.6, than the second arrangement, featured by a spectral index about 71. Figure 5.3 represents the full ζ eigenvalue spectrum. Thanks to the detail on the right of the figure, it is possible to appreciate the existence of two batches of eigenvalues around the stars, which represents, as usual, the fundamental eigenvalues. The largest value represents the under-moderated configuration, while the other star represents the over-moderated one. These figures are very informative. First, it is extremely interesting to notice that the eigenvalue separation ES in the first batch is much larger than the second one, where the eigenvalue are very close to each other. Then, it is possible to notice that the over-moderated fundamental is the lowest values in its batches, meaning that its ES is negative.

This fact, which can be appreciated also looking at the eigenvalues reported in the legend of fig. 5.2, is consistent with the known relationship between ES and the core spatial decoupling degree, and would have an important implication: the designer could look only for the dominant eigenpair, avoiding the determination of the full spectrum. However, this peculiarity depends on the system initial configuration. When the starting off-critical configuration is featured by a larger moderation ratio, closer to the critical over-moderated configuration, the situation is reversed, i.e. the largest ζ

corresponds to the over-moderated solution. Since the ζ spectrum behaviour is case-dependent, computing only the dominant eigenvalue could be risky. This observation seems to suggest that, in order to find all the physically meaningful solutions and to choose the best one, the complete spectrum should be estimated. In case this would not be affordable, a smart computational strategy for the reduction of the computational burden could be to use a low-order transport model (e.g. with fewer energy groups and less angular detail) to look for the approximated fundamental eigenvalues, which then could be used in the well known shift-and-invert procedure to enhance the eigenvalue solver convergence towards more precise estimates of the eigenvalues (Saad, 1992). Alternatively, if some basic knowledge of the various possible critical arrangements was available, the calculation could be made more efficient starting from a configuration close to the desired one.

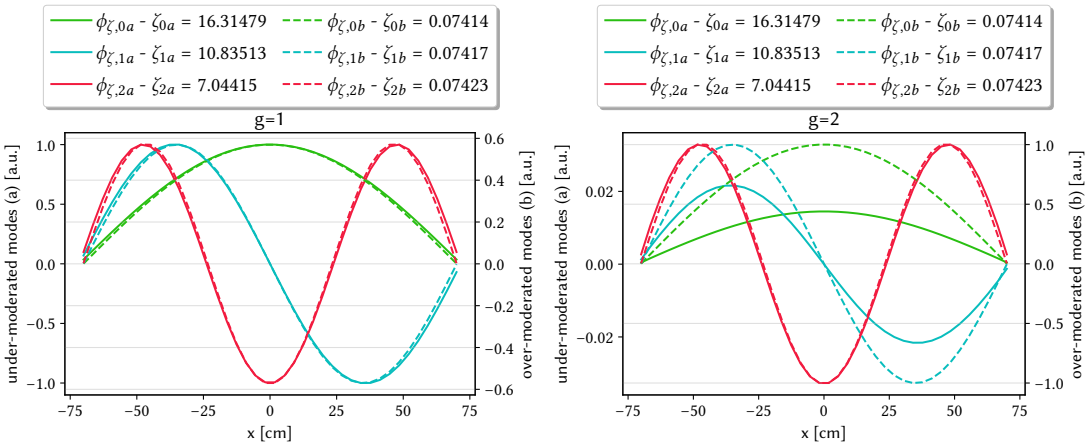

Figure 5.2: *Higher-order, two-group ζ modes for a homogeneous mixture of light water and fissile material. The spectral index ϕ_1/ϕ_2 of the systems is equal to 70.3 and 0.6 for the under- and over-moderated cases, respectively.*

5.4 Determination of the moderation ratio for a regular lattice

Due to its great flexibility, ζ can be used to deal with more complex problems, for example the determination of the moderation ratio for a heterogeneous arrangement of fuel and moderator layers, surrounded by a reflector. In this case, the iterative search of the critical moderation ratio is more expensive, due to the larger number of spatial nodes needed to resolve the spatial gradients. Of course, the design is usually carried out using smart, non-linear root-finding algorithms, like the Newton-Raphson method

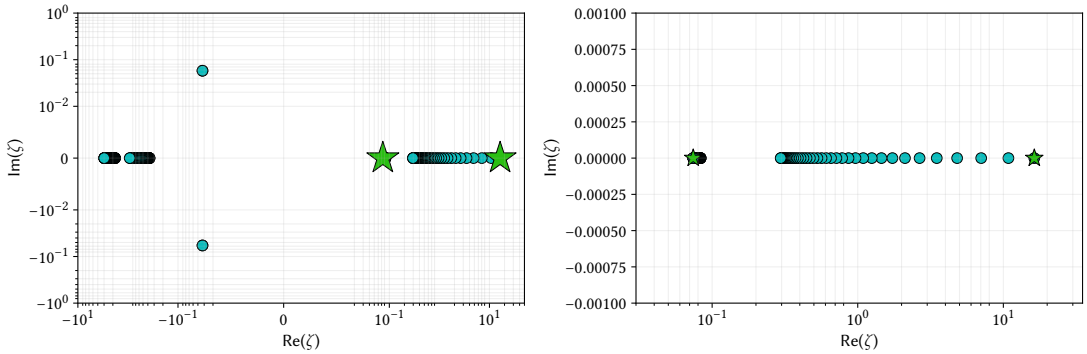

Figure 5.3: *ζ eigenvalue spectrum for a homogeneous mixture of light water and fissile material. The stars are the eigenvalues associated to positive modes.*

(Quarteroni, Sacco, and Saleri, 2010), to minimise the number of static calculations required. However, the presence of more solutions, like in this case, can have a detrimental effect on such techniques, limiting their effectiveness. As visible from fig. 5.4, which has been again obtained iteratively, three critical configurations could be devised for a lattice composed by 17 sheets, 3 cm thick and composed of uranium oxide (UOx) enriched at 3%, and 16 sheets of water 3 cm thick, surrounded at both sides by 20 cm of water used as a reflector. It is important to remark here that, despite the curve seems to approach a fourth zero around $N_m/N_f = 10^2$, it was not possible to found a solution to the static, k problem around these values of N_m, due to the ill conditioning of the moderator cross sections, which assume very large, unphysical values.

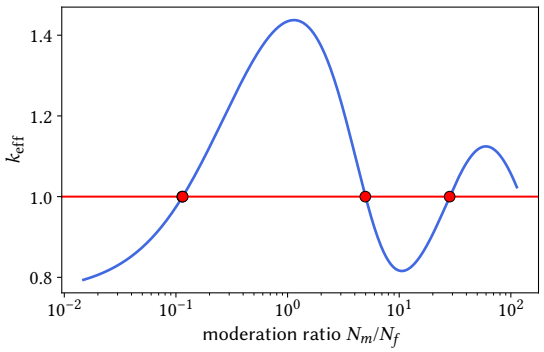

Figure 5.4: *Effective multiplication factor as a function of the moderation ratio for a two-group heterogeneous system composed of alternating layers of fuel and moderator.*

In this case it is possible to determine three possible critical eigenstate, casting the

ζ eigenvalue problem as follows,

$$\begin{cases} \mu\dfrac{\partial\phi(x,E,\mu)}{\partial x} + \dfrac{1}{\zeta}N_m\sigma_{t,m}(E)\phi(x,E,\mu) = \\ \dfrac{1}{\zeta}\displaystyle\int_0^\infty dE'\int_{-1}^1 d\mu' N_m\sigma_{s,m}(E')f_{s,m}(E'\longrightarrow E,\mu')\phi(x,E',\mu') \qquad x\in\mathcal{X}_m, \\ \\ \mu\dfrac{\partial\phi(x,E,\mu)}{\partial x} + \Sigma_t(x,E)\phi(x,E,\mu) = \\ \displaystyle\int_0^\infty dE'\int_{-1}^1 d\mu'\Sigma_s(x,E')f_s(x,E'\longrightarrow E,\mu')\phi(x,E',\mu') + \qquad x\notin\mathcal{X}_m, \\ \displaystyle\int_0^\infty dE'\int_{-1}^1 d\mu'\,\nu_m(x,E')\Sigma_{f,m}(x,E')\frac{\chi(x,E)}{2}\phi(x,E',\mu') \end{cases} \tag{5.6}$$

where $\mathcal{X}_m$ is defined as $\{[x_1,x_2],\cup[\ldots]\cup[x_i,x_{i+1}]\}$. In the first equation, the eigenvalue acts only on the nuclide density N_m featuring the homogeneous water sheets, while in the second one the cross sections are expressed as space-dependent functions since they refer to the reflector and to the fuel regions.

Eq. 5.6 makes possible, also in this case, to determine the three scaling factors $1/\zeta$ for the moderator density identified by the iterative procedure used to draw the curve in fig. 5.4. In order to distinguish the eigenvalues belonging to the fundamental set, i.e. the eigenvalues associated to eigenfunctions with uniform sign over the phase space, they will be indicated in the following as ζ_0 $*$, where $*$ is replaced by a letter. In this specific case, the largest eigenvalue in the fundamental set will be indicated as ζ_{0a}, while the smallest fundamental eigenvalue will be indicated as ζ_{0c}.

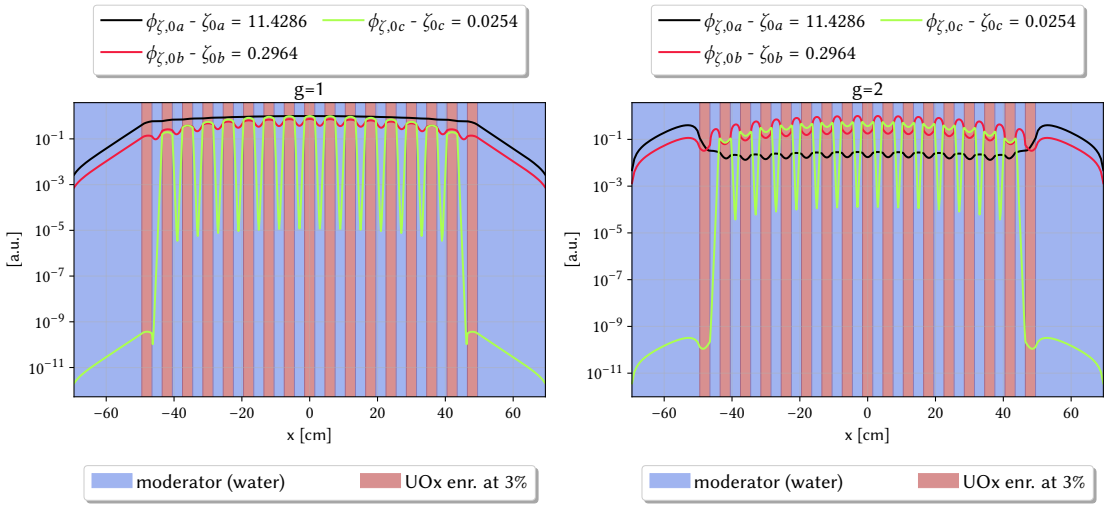

Figure 5.5: *Fundamental two-group ζ modes for the heterogeneous arrangement of light water and fissile material.*

The thermal and fast fluxes associated to these configurations are represented on

top of the lattice geometry in fig. 5.5. These eigenfunctions correspond to the critical neutron distribution in the phase space, provided that the moderator density was modified by a factor $1/\zeta_0^*$. The black curve, associated to the largest fundamental eigenvalue, i.e. to the under-moderated solution, presents smaller spatial gradients in the core, consistently with the larger degree of spatial coupling, while the red curve, associated to the over-moderated solution ζ_{0b}, shows significant oscillations in both the fast and the thermal fluxes. These local oscillations in the fluxes are due to the stronger interplay between slowing down and fission for larger moderator densities: the moderation is a sink for the fast population and a source for the thermal one, while the fission produces fast neutrons and removes thermal ones. This mechanism is exacerbated when the moderator density is further increased adopting the scaling factor $1/\zeta_{0c}$. Similar considerations hold also for the spatial behaviour of the first harmonic, represented in fig. 5.6. In this case, only the *a* and the *b* modes are showed in order to make the figure cleared.

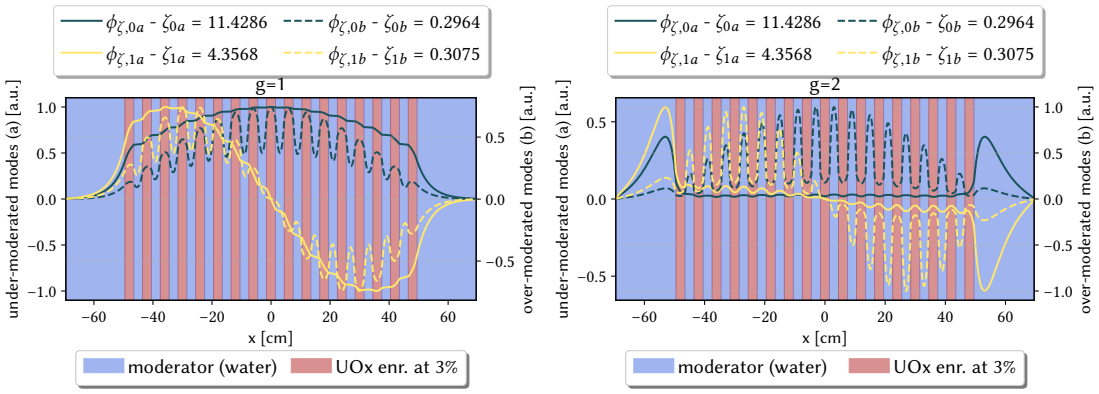

Figure 5.6: *Fundamental two-group ζ modes for the heterogeneous arrangement of light water and fissile material.*

As for the homogeneous case, the eigenvalue spectrum for ζ, in fig. 5.7, presents batches of eigenvalues near the fundamental ones. The first batch is well separated, while the other two batches, related to the over-moderated configurations, are less and less separated, as visible in the right part of the figure.

The fact that the largest fundamental eigenvalue, ζ_{0a}, is featured by the largest dominance ratio ζ_{0a}/ζ_{1a} is a very nice feature of the ζ formulation. From a numerical point of view, the convergence speed of the numerical algorithms for the solution of the eigenvalue problems is always somehow proportional to the dominance ratio, especially for the legacy power method. Thus, if the system was closer to the desired configuration, the convergence should be enhanced, avoiding the risk of finding one of the other possible critical arrangements.

As pointed out in this chapter, one of the advantages of ζ is that the consistency of the cross sections of the system is guaranteed by acting only on the atomic density

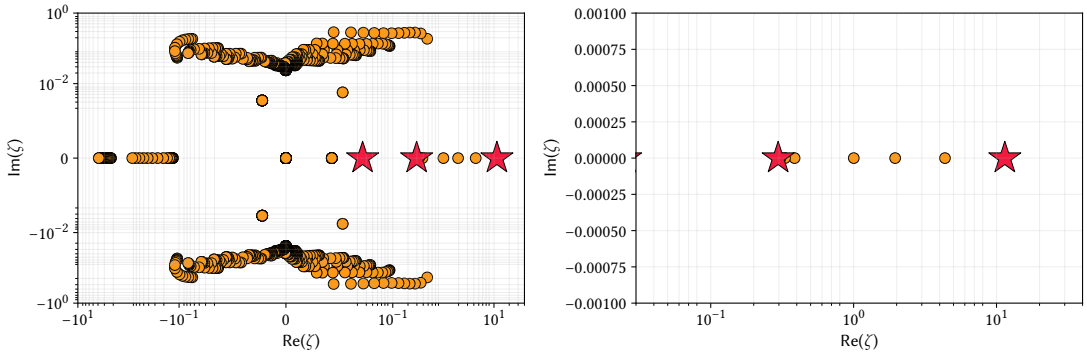

Figure 5.7: *ζ eigenvalue spectrum for the heterogeneous arrangement of light water and fissile material. The stars are the eigenvalues associated to positive modes.*

of one or more nuclides. Notwithstanding this inherent advantage, it is not always possible to practically act on the atomic density. According to the medium considered, the atomic density could be interpreted macroscopically as a chemical concentration or as a physical density. In the first case, the range of variation for the isotope atomic density is determined by the solubility of the solute into the solvent. This situation is often encountered in nuclear engineering, for example when the boric acid H_3BO_3 is dissolved in water to control the reactivity in PWRs or when some fissile nuclides like ^{233}U or ^{239}Pu are added to a molten salt reactor. In these cases, the solubility range is usually wide enough to allow a fine regulation of the atomic concentration that is useful in most situations (Cacuci, 2010). Hence, the scaling factor $1/\zeta$ could be effectively achieved.

On the contrary, when the atomic density corresponds to the physical density, as in the case of the moderator choice, the designer is not free to change N, which is a physical property of the medium that depends on its thermodynamic conditions. From this perspective, ζ seems to provide a quantitative information that is not practically achievable, as for the other eigenvalue formulations. However, under some rather mild assumptions, it is possible to prove that $1/\zeta$ can be interpreted as a scaling factor for the geometrical volumes containing the isotope under investigation, in analogy to what occurs with the δ formulation, for which ζ is a generalisation.

Recalling eq. (3.16), which shows that scaling the geometry by a factor β, $\vec{\mathcal{R}} = \beta\vec{r}$, scales the density eigenvalue by the same factor, it is possible to prove quite easily that also (5.6) behaves similarly for a one-dimensional cartesian system, provided that the scaling is applied only to the geometrical volume where ζ is actually operating. In particular, by choosing $\beta = 1/\zeta_{\text{eff}}$, i.e. $\mathrm{x} = 1/\zeta_{\text{eff}}x$ and $\mathcal{Z}_m = 1/\zeta_{\text{eff}}\mathcal{X}_m$, it is possible to

obtain a critical system,

$$\begin{cases} \mu \dfrac{\partial \phi(\mathrm{x}, E, \mu)}{\zeta_{\mathrm{eff}} \partial \mathrm{x}} + \dfrac{1}{\zeta_{\mathrm{eff}}} N_m \sigma_{t,m}(E) \phi(\mathrm{x}, E, \mu) = \\ \dfrac{1}{\zeta_{\mathrm{eff}}} \displaystyle\int_0^\infty dE' \int_{-1}^{1} d\mu' N_m \sigma_{s,m}(E') f_{s,m}(E' \rightarrow E, \mu') \phi(\mathrm{x}, E', \mu') \qquad \mathrm{x} \in \mathcal{Z}_m, \\ \\ \mu \dfrac{\partial \phi(x, E, \mu)}{\partial x} + \Sigma_t(x, E) \phi(x, E, \mu) = \\ \displaystyle\int_0^\infty dE' \int_{-1}^{1} d\mu' \Sigma_s(x, E') f_s(x, E' \rightarrow E, \mu') \phi(x, E', \mu') + \qquad x \notin \mathcal{Z}_m. \\ \displaystyle\int_0^\infty dE' \int_{-1}^{1} d\mu' \nu_m(x, E') \Sigma_{f,m}(x, E') \frac{\chi(x, E)}{2} \phi(x, E', \mu') \end{cases} \tag{5.7}$$

as the $1/\zeta_{\mathrm{eff}}$ terms cancel out. As for the δ eigenvalue, the physical consistency of this local volume scaling can be justified intuitively referring to the fact that the microscopic cross sections are not altered by this procedure, which only affects the streaming term.

This relationship cannot be extended in a straightforward manner also to more complex 2D and 3D systems, due to the fact that scaling a certain region would imply a modification also to the surface-to-volume ratio of the surrounding regions. Due to these intricacies, it is likely that this property holds only for some very specific cases, for example when ζ is formulated in a δ fashion, i.e. it acts on all the regions of the system. Hence, further analyses are left for a future development of this work.

In addition to these assumptions, ζ should act on all the isotopes contained in the phase space volume $\mathcal{V}_{m*}$. It is easy to prove that, in case ζ is introduced in front of a specific isotope m^* inside the selected phase space volume $\mathcal{V}_{m^*}$, scaling the geometrical volume would not be equivalent to change the density of that specific nuclide, since the factor $1/\zeta_{\mathrm{eff}}$ would operate on the volume containing also the other nuclides $m \neq m^*$. Therefore, ζ_{eff} can be interpreted either as a density scaling factor with constant geometry (always) or as a geometrical volume scaling factor for constant density and cross sections (under some assumptions). Despite the volume is scaled only in some non-simply connected zones of the system, the consistency of the system of equations is ensured by enforcing the continuity of the angular flux at the interfaces.

In the following, an example involving the estimation of the geometrical scaling is provided for a sub-critical (k_{eff}=0.92070) lattice composed by 17 fuel sheets, each 1 cm thick and made of 3% enriched UOx, and 16 water sheets, each 0.2 cm thick, surrounded by a 4 cm thick water reflector on both sides. Solving the ζ eigenvalue problem for the moderator provides two correction factors, namely $1/\zeta_{0a} = 1.54392$ and $1/\zeta_{0b} = 37.76805$. Figure 5.8 provides a graphical sketch of the critical configurations obtained adjusting the moderator volume inside the lattice according to the two values of ζ, while fig. 5.9 shows the off-critical system and the under-moderated configuration on the same scale. As expected, the under-moderated design, obtained with a slight increase of the moderator thickness between each couple of fuel sheets, is more compact than

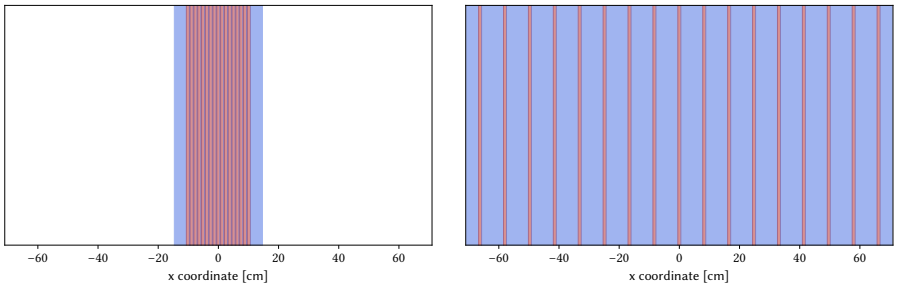

Figure 5.8: *Under-moderated critical lattice (left) and over-moderated critical lattice (right) designed using the ζ eigenvalue.*

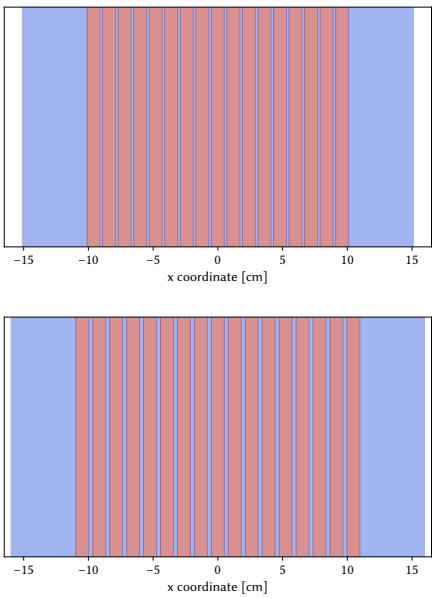

Figure 5.9: *Initial off-critical lattice (top) and under-moderated critical lattice.*

the other one, proving once again its better spatial stability. The spatial distribution of the thermal and fast critical fluxes for the two cases, visible in fig. 5.10, further confirms this observation: the under-moderated case, on the left, is featured by a rather smooth profile, similar to what occurs in a homogeneous system, while the over-moderated case presents local spikes in both groups.

As mentioned previously, the decoupling degree of a system can be inferred in a more rigorous way from the eigenvalue separation (ES) or from the dominance ratio (DR) of the system under design. An intuitive relationship between of the ES and the system stability can be found in the framework of the Generalised Perturbation Theory, which was mainly developed during the '80s by Gandini (Gandini, 1978; Gandini, 1981; Gandini, 1987). Following the basic idea at the basis of other well known expansion

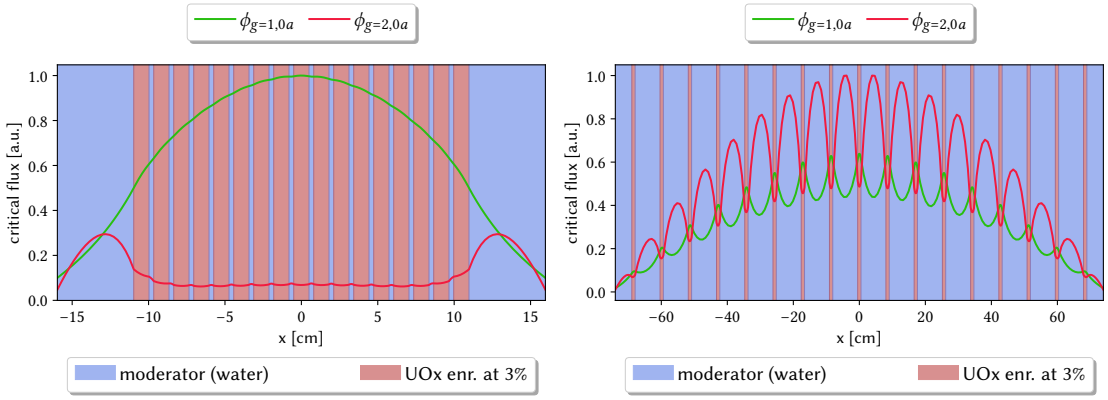

Figure 5.10: *Fast and thermal fluxes for the under- (left) and over-moderated (right) design solutions.*

methods like the Helmholtz one, he proposed to exploit the higher-order eigenfunctions of a reference, unperturbed configuration, namely

$$(\hat{A} - \xi_0 \hat{B})\vec{\varphi}_0 = 0, \tag{5.8}$$

as a basis for the estimation of the approximated eigenpair of a perturbed system,

$$(\hat{A}' - \xi' \hat{B}')\vec{\varphi}' = 0, \tag{5.9}$$

avoiding to solve directly the full perturbed eigenproblem. The perturbed operators can be assumed as the unperturbed operators with the addition of a small perturbation, explicitly $\hat{A}' = \hat{A}' + \delta\hat{A}'$, $\hat{B}' = \hat{B}' + \delta\hat{B}'$. According to the GPT approach, the perturbed eigenvalue and eigenfunction can be expressed as infinite series, reading

$$\xi' = \xi^{(0)} + \xi^{(1)} + \ldots + \xi^{(\infty)} = \xi^{(0)} + \sum_{n=1}^{\infty} \xi^{(n)} = \eta_0 + \sum_{n=1}^{\infty} \xi^{(n)}, \tag{5.10}$$

and

$$\phi' = \vec{\phi}^{(0)} + \vec{\phi}^{(1)} + \ldots + \vec{\phi}^{(\infty)} = \vec{\phi}^{(0)} + \sum_{n=1}^{\infty} \vec{\phi}^{(n)} = \vec{\varphi}_0 + \sum_{n=1}^{\infty} \vec{\phi}^{(n)}, \tag{5.11}$$

where the first term for the two series, η_0 and $\vec{\varphi}_0$, are the fundamental eigenvalue and eigenfunction of the reference system, while $\xi^{(i)}$ and $\vec{\phi}^{(i)}$ are the i-th order perturbations for the eigenvalue and flux, respectively. Substituting equations (5.10) and (5.11) into the perturbed eigenproblem (5.9) and equating the terms of the same order, the following

recursive set of equations can be obtained:

$$\begin{cases} (\hat{A} - \eta_0 \hat{B})\vec{\varphi}_0 = 0 \\ (\hat{A} - \eta_0 \hat{B})\vec{\phi}^{(1)} = -(\delta\hat{A} - \eta_0 \delta\hat{B})\vec{\varphi}_0 + \xi^{(1)}\hat{B}\vec{\varphi}_0 \\ \dots \\ (\hat{A} - \eta_0 \hat{B})\vec{\phi}^{(n)} = -(\delta\hat{A} - \eta_0 \delta\hat{B})\vec{\phi}^{(n-1)} + \sum_{k=1}^{n-1} \xi^{(k)}\hat{B}\vec{\phi}^{(n-k)} + \sum_{k=1}^{n-1} \xi^{(k)}\delta\hat{B}\vec{\phi}^{(n-k-1)} + \xi^{(n)}\hat{B}\vec{\varphi}_0. \end{cases} \tag{5.12}$$

The direct solution of such system can be avoided by means of projections on the adjoint eigenfunctions $\vec{\varphi}_i^+$ of the following equation:

$$(\hat{A} - \eta_i \hat{B})\vec{\varphi}_i = 0. \tag{5.13}$$

Exploiting the so-called Standard Method proposed in Gandini, 1978, it is assumed that the n-th order flux perturbation $\vec{\phi}^{(n)}$ can be explicitly estimated as linear combinations of the harmonics of the unperturbed eigenvalue problem, $\vec{\varphi}_i$, as

$$\vec{\phi}^{(n)} = \sum_{i=0}^{\infty} a_i^{(n)} \vec{\varphi}_i, \tag{5.14}$$

where $a_i^{(n)}$ are unknown expansion coefficients to be determined. Exploiting the bi-orthogonality property between direct and adjoint harmonics and isolating the i-th order perturbation terms, the quantities $\xi^{(i)}$ and $a_i^{(n)}$ can be estimated as:

$$\xi^{(n)} = \frac{\langle \vec{\varphi}_0^+ | | (\delta\hat{A} - \xi^{(0)}\delta\hat{B})\vec{\phi}^{(n-1)} \rangle - \sum_{k=1}^{n-1} \langle \vec{\varphi}_0^+ | | \xi^{(k)}\hat{B}\vec{\phi}^{(n-k)} \rangle - \sum_{k=1}^{n-1} \langle \vec{\varphi}_0^+ | | \xi^{(k)}\delta\hat{B}\vec{\phi}^{(n-k-1)} \rangle}{\langle \vec{\varphi}_0^+ | | \hat{B}\vec{\varphi}_0 \rangle}, \tag{5.15}$$

$$a_m^{(n)} = \frac{1}{(\eta_m - \eta_0)\langle \vec{\varphi}_m^+ | | \hat{B}\vec{\varphi}_m \rangle} \left[\sum_{k=1}^{n-1} \left[\xi^{(k)} a_m^{(n-k)} \langle \vec{\varphi}_m^+ | | \hat{B}\vec{\varphi}_m \rangle + \sum_{i=0}^{\infty} \xi^{(k)} a_i^{(n-k-1)} \langle \vec{\varphi}_m^+ | | \delta\hat{B}\vec{\varphi}_i \rangle \right] + \right.$$
$$\left. - \sum_{i=0}^{\infty} a_i^{(n-1)} \langle \vec{\varphi}_m^+ | | (\delta\hat{A} - \xi^{(0)}\delta\hat{B})\vec{\varphi}_i \rangle \right]. \tag{5.16}$$

By inspection of the equation for $a_m^{(n)}$, it is possible to notice that the magnitude of the coefficient is inversely proportional to the distance between the fundamental eigenvalue and the higher-order eigenvalues of the reference system, $\{\eta_1, \eta_2, \dots, \eta_m\}$. When $m = 0$, the singularity is avoided imposing that all the values $a_0^{(n)}$ satisfy an arbitrary condition, consistently with the homogeneous nature of the perturbed eigenvalue problem. A common practice consist in fixing the fission rate of the perturbed system to be

equal to the reference one, i.e. $\langle 1||*\rangle \hat{F}\vec{\varphi}_0 = \langle 1||*\rangle \hat{F}'\vec{\phi}'$. When $m > 0$, the magnitude of the perturbation coefficient, so the perturbation term itself, is inversely proportional to $1/(\eta_m - \eta_0)$, i.e. the eigenvalue separation ES. With the appropriate definitions, the generic eq. (5.8) can be cast into the different eigenvalue formulation discussed in chapter 2. For example, the k eigenproblem would be obtained imposing $\hat{A} = \hat{L}$, $\hat{B} = \hat{F}$ and $\eta_n = 1/k_n$, which implies that

$$\frac{1}{\mathrm{ES_k}} = \frac{1}{\left(\dfrac{1}{k_m} - \dfrac{1}{k_0}\right)} = \frac{1}{(\eta_m - \eta_0)}. \tag{5.17}$$

Therefore, the inverse proportionality between the ES and the intensity of the perturbation term $a_m^{(n)}$ is independent on the eigenvalue formulation adopted, meaning that, in principle, the ES associated to each spectral formulation can be useful to assess the stability of a multiplying system. It is important to remark here that the ES may not be a very informative figure of merit *per se*, but it becomes a powerful indicator when it is computed for different system configurations. In this respect, the ES is a valuable criterion to guide the neutronic design of a reactor (Shirakata, Sanda, and Nakashima, 1999). In this specific case, it is interesting to compare the values of the ES computed with different eigenvalue formulations for the possible design solutions determined by the ζ problem. To this aim, these figures of merit and the related dominance ratios, defined as $\mathrm{DR} = \eta_1/\eta_0$, are reported in table 5.2.

Table 5.2: *Critical moderation ratios N_m/N_f to achieve criticality for a slab thick 170 cm filled with a homogeneous mixture of fissile material and light water, computed with the ζ formulation and with an iterative procedure.*

	$\zeta_{0a} = 0.74697$		$\zeta_{0b} = 0.02748$	
eig.	ES	DR	ES	DR
α	-2.09226×10^{7}	-3.24026×10^{-12}	-2.78505×10^{6}	-8.80089×10^{-10}
γ	1.43712×10^{-2}	1.01437	3.77510×10^{-4}	1.00038
δ	1.41445	2.41445	-2.32373×10^{-1}	7.67627×10^{-1}
k	8.59768×10^{-1}	1.85977	3.83623×10^{-2}	1.03836
θ	−9.60989	−8.60989	-6.01560×10^{-2}	9.39844×10^{-1}

As it could be expected, the critical solution featured by the largest value of ζ presents the largest eigenvalue separation for the different eigenvalue formulations, despite some significant variations. The prompt time eigenvalue yields the largest eigenvalue separation, while the collision eigenvalue γ yields the smallest one. The other formulations falls between these two. The capture eigenvalue θ yields a negative ES, since the fundamental eigenvalue is smaller than the one associated to the first harmonic, as visible in

fig. 3.22a. It is interesting to notice that δ presents two fundamental harmonics in addition to the critical one. This peculiarity, discussed in chapter 2, makes ambiguous to evaluate the ES. In this case, the distance between the fundamental critical eigenvalue ($\delta = 1$) and the first harmonic is evaluated.

When the design solution is over-moderated, all the eigenvalues exhibit a reduction of their distance from the first harmonic, meaning that the system is more spatially decoupled, i.e. it is more sensitive to the localised perturbation than to the neutron leakages. The eigenvalue formulations featured by the largest variation from one case to the other are the capture eigenvalue, the collision eigenvalue and the density eigenvalue, suggesting that it is worth investigating their capability of delivering information about the system stability in alternative to the ES computed referring to k.

5.5 Determination of the boron concentration for reactivity control

Another fundamental problem in the operation of PWRs is the search for the critical boron concentration to be diluted in the water to control the reactivity during normal conditions. Even in this case, the common approach to determine this parameter is resorting to iterations. Exploiting the generalised density eigenvalue, it is possible to avoid iterations, by looking for the fundamental ζ eigenvalue. Assuming that the moderator surrounding the fuel sheets can be modelled as a homogeneous material, the ζ eigenvalue problem can be cast as follows,

$$\begin{cases} \mu\dfrac{\partial\phi(x,E,\mu)}{\partial x} + \dfrac{1}{\zeta}N_a\sigma_{t,a}(E)\phi(x,E,\mu) + N_m\sigma_{t,m}(E)\phi(x,E,\mu) = \\ \displaystyle\int_0^\infty dE' \int_{-1}^{1} d\mu' N_m\sigma_{s,m}(E')f_{s,m}(E'\longrightarrow E,\mu')\phi(x,E',\mu')+ \\ \dfrac{1}{\zeta}\displaystyle\int_0^\infty dE' \int_{-1}^{1} d\mu' N_a\sigma_{s,a}(E')f_{s,a}(E'\longrightarrow E,\mu')\phi(x,E',\mu') \qquad x\in\mathcal{X}_a, \\ \\ \mu\dfrac{\partial\phi(x,E,\mu)}{\partial x} + \Sigma_t(x,E)\phi(x,E,\mu) = \\ \displaystyle\int_0^\infty dE' \int_{-1}^{1} d\mu' \Sigma_s(x,E')f_s(x,E'\longrightarrow E,\mu')\phi(x,E',\mu') + \qquad x\notin\mathcal{X}_a, \\ \displaystyle\int_0^\infty dE' \int_{-1}^{1} d\mu' \nu_m(x,E')\Sigma_{f,m}(x,E')\frac{\chi(x,E)}{2}\phi(x,E',\mu') \end{cases} \tag{5.18}$$

where N_a indicates the absorber atomic density, N_m indicates the moderator absorber atomic density and $\mathcal{X}_m$ is defined as $\{[x_1,x_2],\cup[...]\cup[x_i,x_{i+1}]\}$. This equation is then cast in a two-group, P_1 model assuming linearly anisotropic scattering, using the group constants computed with Serpent 2.

Figure 5.11 (left) shows the two-group, off-critical flux ($k_{\text{eff}} = 1.02420$), computed with the k eigenvalue problem, for a super-critical system with no boron in water and the two-group eigenfunction that corresponds to the critical flux in case some boron with density multiplied by $1/\zeta$ is added to the water inside the coolant layers. The geometrical representation refers to the critical case. As expected on a physical ground, the addition of a thermal absorber to the coolant has an impact on the energy spectrum of the system, which is featured by a slight spectrum hardening.

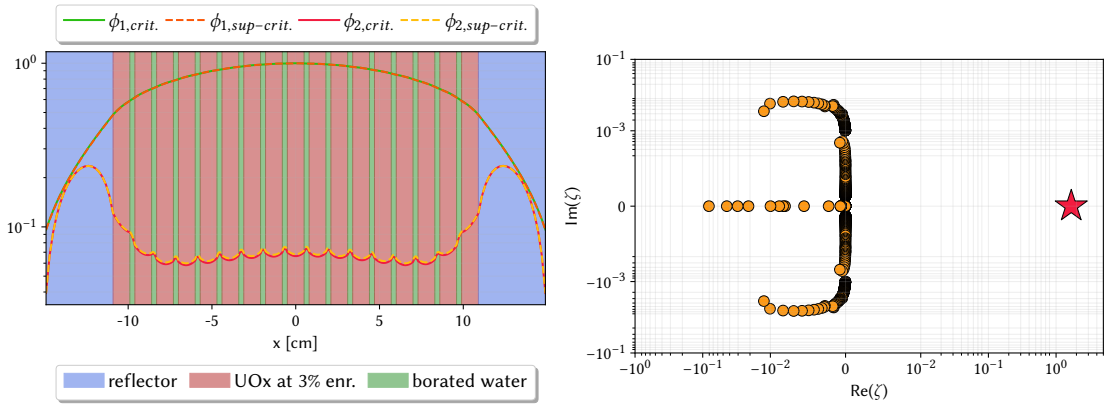

Figure 5.11: *Two-group fundamental off-critical (k) and critical (ζ) modes for a heterogeneous arrangement of fuel and borated water sheets, surrounded by a light water reflector (left) and eigenvalue spectrum (right).*

Figure 5.11 (right) shows the full ζ spectrum. Since the phase space where the eigenvalue is defined comprises only a neutron poison, there is only one possible critical configuration, associated to the fundamental eigenvalue, while most of the spectrum degenerates around zero. This behaviour can be justified on a physical ground. When the moderator density is changed, it is possible to identify more critical solutions, due to the competition between absorption and scattering of the moderator. On the contrary, the absorber influences the reactivity of the system monotonically, thus only one configuration can be devised.

5.6 Fissile concentration for reactivity control in the Molten Salt Fast Reactor

Similarly to the case concerning the determination of the critical boron concentration, the ζ spectrum appears to have a unique solution when the objective of the analysis is the determination of the critical concentration for a fissile material.

Solving this problem efficiently is very important in several situations. For example, one could be interested in estimating which is the minimum fissile enrichment needed to sustain criticality for a given fuel composition, e.g., mixed oxides (MOx) of uranium

and plutonium coming from reprocessed spent fuel. Alternatively, the same problem would be relevant for the evaluation of the fissile inventory needed to operate a fluid core system, like the Molten Salt Fast Reactor (MSFR) design, conceived in the European Union funded projects EVOL, SAMOFAR and SAMOSAFER. One of the advantages of using a fluid core would be the continuous adjustment of criticality acting on its composition, through the injection of fresh fuel and the extraction and reprocessing of the fuel containing the fission products. From this perspective, the ζ formulation could be extremely valuable, as it could be employed to estimate the fissile concentration needed in different operating configurations of the system.

Having this application in mind, in the following the generalised eigenvalue formulation will be applied to determine the critical concentration of ^{233}U to be diluted in the core of the MSFR (Allibert, Gérardin, et al., 2017), starting from an initial sub-critical configuration ($k_{\text{eff}} = 0.98072$),

$$
\begin{cases}
\mu\dfrac{\partial\phi(x,E,\mu)}{\partial x} + \dfrac{1}{\zeta}N_f\sigma_{t,f}(E)\phi(x,E,\mu) + N_s\sigma_{t,s}(E)\phi(x,E,\mu) = \\
\displaystyle\int_0^\infty dE' \int_{-1}^{1} d\mu' N_s\sigma_{s,s}(E')f_{s,m}(E'\longrightarrow E,\mu')\phi(x,E',\mu') + \\
\dfrac{1}{\zeta}\displaystyle\int_0^\infty dE' \int_{-1}^{1} d\mu' N_f\sigma_{s,f}(E')f_{s,f}(E'\longrightarrow E,\mu')\phi(x,E',\mu') + \\
\displaystyle\int_0^\infty dE' \int_{-1}^{1} d\mu' \nu_s(x,E')\Sigma_{f,s}(x,E')\frac{\chi(x,E)}{2}\phi(x,E',\mu') + \\
\displaystyle\int_0^\infty dE' \frac{1}{\zeta}\int_{-1}^{1} d\mu' \nu_f(x,E')\Sigma_{f,f}(x,E')\frac{\chi(x,E)}{2}\phi(x,E',\mu') \qquad x\in\mathcal{X}_f, \\
\\
\mu\dfrac{\partial\phi(x,E,\mu)}{\partial x} + \Sigma_t(x,E)\phi(x,E,\mu) = \\
\displaystyle\int_0^\infty dE' \int_{-1}^{1} d\mu' \Sigma_s(x,E')f_s(x,E'\longrightarrow E,\mu')\phi(x,E',\mu') + \qquad x\notin\mathcal{X}_f, \\
\displaystyle\int_0^\infty dE' \int_{-1}^{1} d\mu' \nu_n(x,E')\Sigma_{f,n}(x,E')\frac{\chi(x,E)}{2}\phi(x,E',\mu')
\end{cases}
\tag{5.19}
$$

where N_f indicates the fissile atomic density, N_s indicates the atomic density of the FLiTh salt, N_n indicates the nuclides constituting the liquid breeding blanket and $\mathcal{X}_f$ is defined as $[-H, H]$, where H is the half-thickness of the core region. This equation is then cast in a 30-group structure matching the ECCO-33 grid except for the last three thermal groups, which are collapsed to avoid statistical issues in the effective group constant generation performed in Serpent 2.

The eigenvalue spectrum for this case, shown in fig. 5.12, supports the hypotheses made for the boron case: in the absence of competing phenomena, only one configuration can yield a critical system, like in the presence of a fissile isotope, which is directly proportional to the reactivity. In contrast with the boron case, here it is possible to observe more than one real and positive eigenvalue, associated to higher-order spatial harmonics.

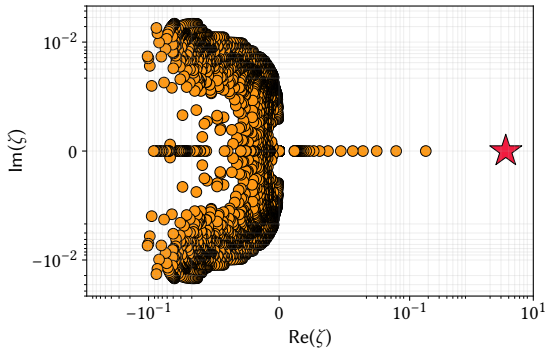

Figure 5.12: *Eigenvalue spectrum computed for the MSFR case.*

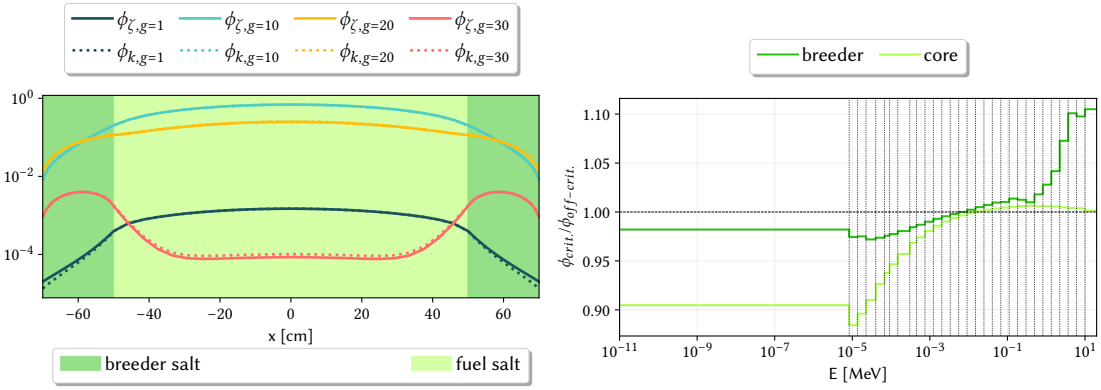

Figure 5.13: *Critical (ζ) modes obtained diluting N_f/ζ moles of ^{233}U in the molten salt fast reactor (left) and the off-to-critical ratio for the energy spectrum (right).*

Figure 5.13 provides, on the right, the spatial behaviour of the group-wise, critical fluxes, while, on the left, the ratio between the critical energy spectrum, obtained adjusting the ^{233}U concentration of $1/\zeta_{\text{eff}}$, and the off-critical one is shown for both the regions composing the core. This last graph helps to appreciate the fact that, for a given set of multi-group constants, the ζ formulation takes automatically into account the spectral effects induced by the change in the system composition or volume. In this case, the intermediate group structure allows to get a deeper insight the spectral variations occurring after the fissile concentration adjustment. The addition of 10.79 mg cm^{-3} of ^{233}U to the FLiTh salt has a relatively small impact on the overall energy spectrum. By inspection of this graph, it is possible to appreciate a reduction in the thermal spectrum, consistently with the fact that the fission cross section of ^{233}U is maximum in the thermal region, and, conversely, a slight increase in the fast spectrum, caused by the additional fast neutrons emitted by fissions. The other large spectral variation involves the blanket: since it is composed only by FLiTh, which can do fission only at high energy (see fig. 5.14), the flux spectrum increases as a consequence of the larger fraction

of fast neutrons diffusing from the core to the blanket.

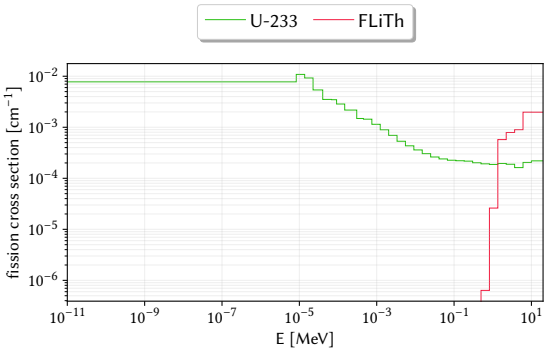

Figure 5.14: *Fission cross section collapsed on the 30-group grid based on the ECCO-33 structure.*

The graphs in fig. 5.13 allows to conclude that the ζ formulation allows to naturally take into account the spectral and spatial effects occurring as a consequence of the density (or volume) adjustments. Henceforth, in addition to the modelling and numerical errors, the only physical approximations induced by the adoption of the ζ approach are due to the fact that the self-shielding of the input multi-group cross sections are computed *a priori*, without taking into account the additional self-shielding effects induced by the $1/\zeta$ correction in the density or in the volume of the selected region. The most natural way to tackle this issue would be to perform a ζ calculation for a configuration close to the studied one during the multi-group cross section calculation stage, similarly to what is usually done for standard k calculations. In this way, most of the spatial and the energy self-shielding effects on the flux would be automatically accounted for, thus ensuring that the small spectral adjustments induced by the solution of the ζ problem for the coveted configuration do not affect significantly the accuracy of the self-shielded cross sections. Since both the cases involving the search for the critical boron concentration and the search for the critical fissile concentration are loosely off-critical, they do not induce sharp variations in the flux spectrum, suggesting that this approach should be adequate. Nonetheless, since this is the first application of the ζ eigenvalue problem and since TEST does not currently support too fine group calculations, this aspect will not be addressed in more detail in the following.

5.7 Determination of the coolant volume in a Lead Fast Reactor

Similarly to what discussed in section 5.5.4, this section presents the solution of the ζ eigenvalue problem for the case of a lattice composed by fuel sheets made of MOx of minor actinides (MAs) and cooled by liquid lead. As for the MSFR, also this

system is featured by a fast spectrum. Due to the absence of a moderator, the MOx fuel is usually highly enriched (≈ 20%), thus allowing to achieve higher power densities and more compact core arrangements with respect to light water reactors. Since ^{208}Pb, which constitutes roughly half of the natural lead, is stable, the average capture cross section of lead is very small and, thus, adequate for the neutron economy of the system. Moreover, due to its relatively heavy nucleus, neutrons are not significantly slowed down by scattering interactions, thus making lead one of the best coolant options for MOx-fuelled, fast-spectrum reactors. The fact that there is not a dominant phenomenon between capture and slowing down allows the existence of more than one possible critical configurations.

Given a sub-critical ($k_{\text{eff}} = 0.96298$) lattice featured by 14 MOx sheets, each 1.5 cm thick, surrounded by sheets of lead, each 1 cm thick, the ζ approach allows to identify two different configurations. This system has been analysed employing a P_1, collapsing the cross sections on the six-group PoliTO-LFR-6A structure, reported in table 3.2 and casting the eigenproblem as in eq. (5.6), *mutatis mutandis*. Similarly to what occurs for a light water lattice, one solution is featured by a slight adjustment in the coolant volume, while the other is featured by a substantially larger volume fraction. The dominant mode, associated to the largest ζ, allows to realise a critical arrangement with ES= 1.01922, while the other solution yields a more decoupled critical structure, featured by ES= 0.12770. Interestingly, fig. 5.15 shows *ictu oculi* that there are no other positive, real eigenvalues except the fundamental ones, implying that there are no higher-order real harmonics.

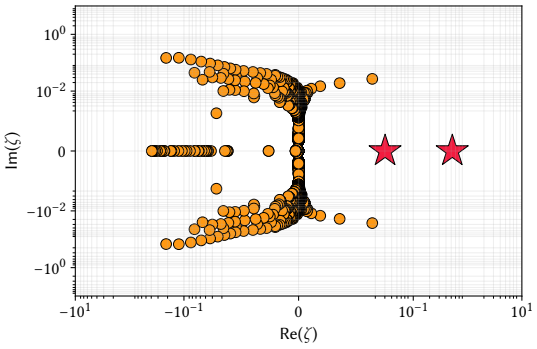

Figure 5.15: *Eigenvalue spectrum for the MOx-lead lattice.*

Figure 5.16 provides the six-group spectrum of the two critical configurations (left) and the ratio between each of the two critical spectra and the starting, sub-critical one (right). The first configuration slightly perturbs the spectrum, because of the reduced increase in volume of lead ($V'_{\text{Pb}} = 1/\zeta_{0a} V = 1.913V$), while the other ($V'_{\text{Pb}} = 1/\zeta_{0b} V = 33.02V$) strongly soften the spectrum, increasing the thermal population roughly by a factor 30. Of course, the preferable solution among the two is the first one since, in addition to its better neutronic stability, it allows to minimise the volume of lead,

reducing both the weight of the reactor and its size. Nevertheless, being aware that criticality could be reached also for a larger coolant-to-fuel volume ratio is certainly very important for the safety assessment of the reactor.

The flux spatial distribution in the lattice is shown in fig. 5.17 for some selected groups. The solution for the configuration that requires the minimum lead volume is featured by a spatial trend that is very close to the one featuring a homogeneous system, while the solution associated to the more decoupled configuration exhibits strong variations passing from the fuel to the coolant sheets, similarly to what occurs for a moderated system.

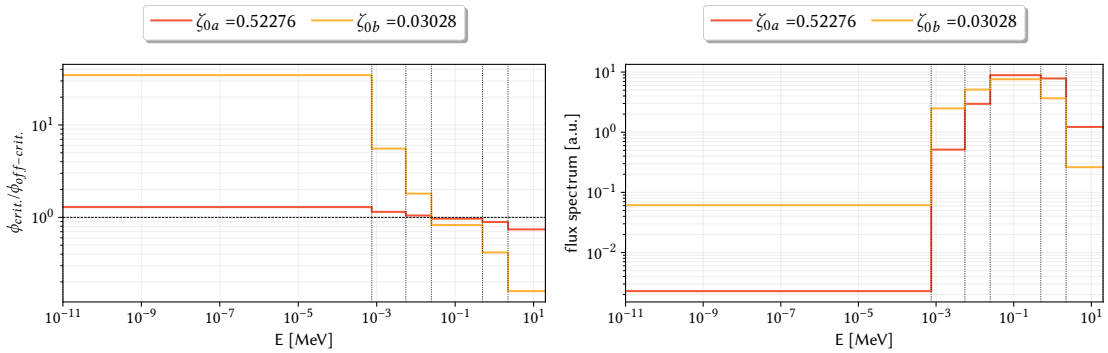

Figure 5.16: *Ratio between the critical and the sub-critical energy spectra for the two possible critical configurations (left) and the critical energy spectra (right) for a lattice of MOx and liquid lead.*

5.8 Determination of neutron absorbers for reactivity control

The last application presented in this section concerns another classical problem in reactor physics, namely the evaluation of the absorber density required for a control rod device in order to achieve criticality. Assuming that the control rods are located in some specific volumes, $\mathcal{X}_{CR} = [x_i, x_{i+1}], \ldots, [x_j, x_{j+1}]$, the eigenproblem can be cast as

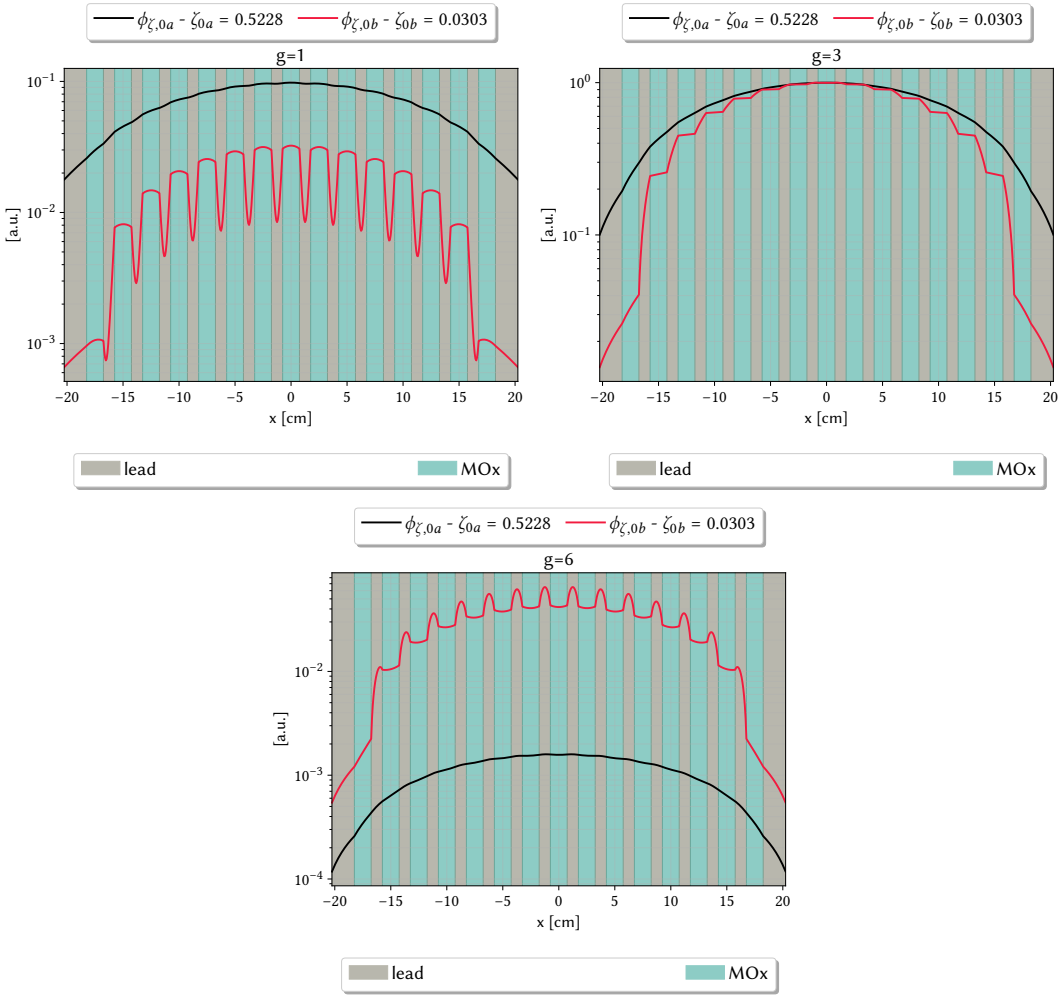

Figure 5.17: *Group-wise fluxes for the two critical configurations for the MOx-lead lattice.*

follows,

$$\begin{cases} \mu\dfrac{\partial\phi(x,E,\mu)}{\partial x} + \dfrac{1}{\zeta}N_{CR}\sigma_{t,CR}(E)\phi(x,E,\mu) = \\ \dfrac{1}{\zeta}\displaystyle\int_0^\infty dE'\int_{-1}^{1} d\mu' N_{CR}\sigma_{s,CR}(E')f_{s,CR}(E'\longrightarrow E,\mu')\phi(x,E',\mu') \qquad x\in\mathcal{X}_{CR}, \\ \\ \mu\dfrac{\partial\phi(x,E,\mu)}{\partial x} + \Sigma_t(x,E)\phi(x,E,\mu) = \\ \displaystyle\int_0^\infty dE'\int_{-1}^{1} d\mu'\Sigma_s(x,E')f_s(x,E'\longrightarrow E,\mu')\phi(x,E',\mu') + \qquad x\notin\mathcal{X}_{CR}, \\ \displaystyle\int_0^\infty dE'\int_{-1}^{1} d\mu'\,\nu_m(x,E')\Sigma_{f,m}(x,E')\frac{\chi(x,E)}{2}\phi(x,E',\mu') \end{cases} \tag{5.20}$$

where N_{CR} indicates the atomic density of the control rod.

In the following, the critical absorber density (or volume) is searched for different control rod arrangements and initial off-criticality levels, dealing with a thermal system similar to the one discussed in section 5.5.4. Since the control rods are usually sized when most of the core characteristics like the moderation ratio and the fuel enrichment have been selected, the initial configuration will be assumed to be super-critical. This is the only reasonable situation that could be considered, as, in the case of sub-criticality, it may not be possible to achieve a steady state configuration in general, unless to consider unphysical, negative density corrections.

All the problems treated in the following have been solved using the P_1 model and collapsing the group constants on the CASMO-3 grid. The determination of the whole ζ eigenvalue spectrum reveals that only one density allows to achieve criticality for an initially super-critical, provided that the reactivity excess is not too large. Figure fig. 5.18 reports the three-group fundamental k mode for the super-critical configuration ($k_{\text{eff}} = 1.11155$) and the fundamental ζ mode which corresponds to the critical flux when the two sheets of absorber are localised near the centre of the core. With respect to the boron dilution in water, this reactivity control system introduces a larger distortion in the energy spectrum, especially in the thermal group. The ES associated to this critical configuration amounts to 0.8, while $1/\zeta\text{eff} = 18.93716$.

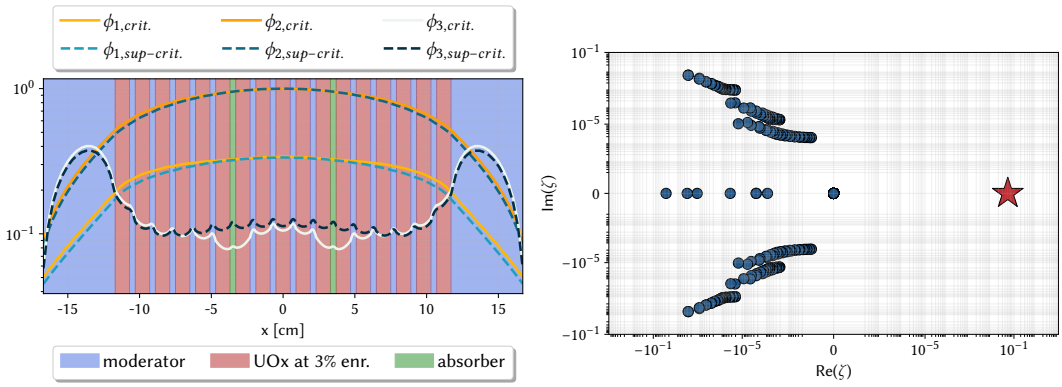

Figure 5.18: *Three-group critical and off-critical fluxes (right) and eigenvalue spectrum (left) for the case considering the control rods near the center of the lattice.*

When the control devices are placed in the periphery of the core, see fig. 5.19, the spatial decoupling of the system is reduced, ES=1.12759. However, due to the proximity with the boundaries, also the effectiveness of the control devices is reduced, i.e. their worth reduces when they are located far from the centre of the cor. Hence, the same static reactivity ($\rho = 10035$ pcm) should be compensated with a larger absorber concentration, $1/\zeta\text{eff} = 37.18518$. Also in this case, there is only one solution to the design problem, i.e. only one real and positive value of ζ can be found.

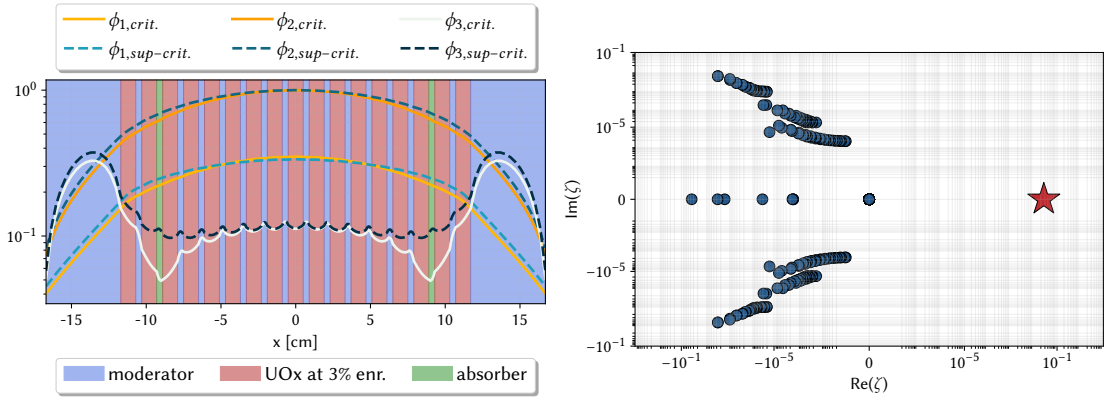

Figure 5.19: *Three-group critical and off-critical fluxes (right) and eigenvalue spectrum (left) for the case considering the control rods near the reflector.*

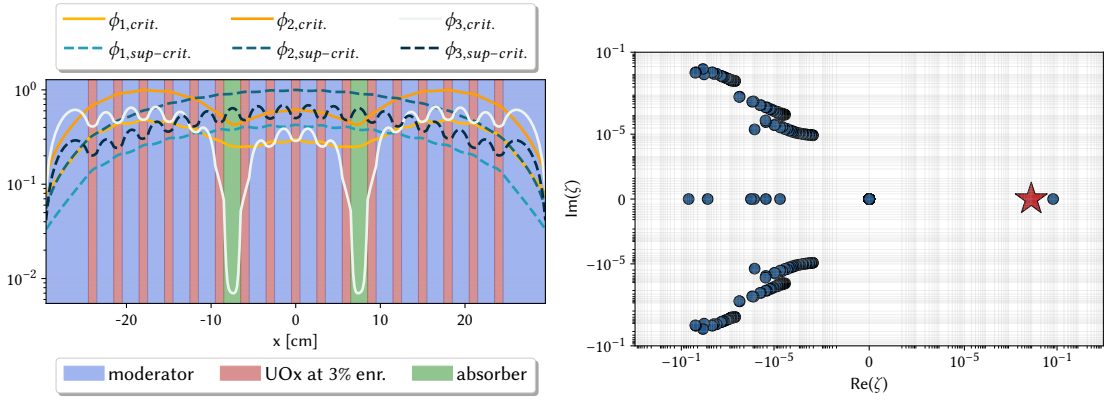

Figure 5.20: *Three-group critical and off-critical fluxes (right) and eigenvalue spectrum (left) for the case considering the control rods near the center of the lattice.*

Figures 5.20-5.21 refer to a different initial configuration, featured by a larger moderation ratio and, thus, by a larger departure from criticality (k_{eff} = 1.39879, ρ = 28509 pcm). When the control rods are positioned at the core centre, the ζ spectrum (see right of fig. 5.20) exhibits two real and positive eigenvalues, associated to the fundamental and to the first-order harmonic. As for some cases discussed previously, the fundamental eigenvalue is smaller than the first-order one. The appearance of a higher-order real and positive eigenvalue is probably related to the larger departure from criticality with respect to the previous case. Following this intuition, the same problem is addressed placing the control rods in peripheral position. In this case, there is no solution to the problem, i.e. it is not possible to determine a correction factor for the control devices such that they are able to remove the excess of reactivity. As visible in fig. 5.21, no fundamental eigenvalue, represented with a star marker throughout the thesis, appears in the spectrum. Therefore, the appearance of higher-order eigenvalues could be related

to the offset to criticality, although a deeper investigation would be required.

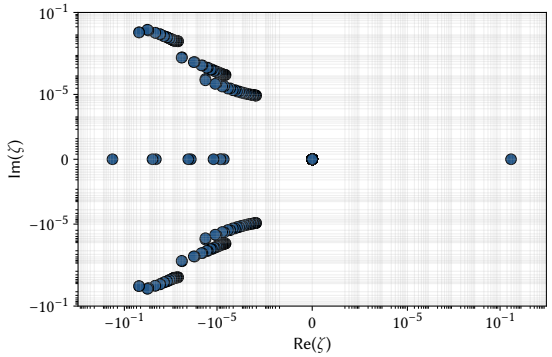

Figure 5.21: *Three-group critical and off-critical fluxes (right) and eigenvalue spectrum (left) for the case considering the control rods near the reflector.*

Concerning the spatial profile displayed in fig. 5.20, it is easy to notice the strong flux depression in correspondence of the control sheets, which is caused by the spatial self-shielding effects induced by the adjusted absorber density. The overall effect of these flux spikes is an increase of the core spatial decoupling, ES=0.04787. The significant self-shielding effect raises again the issue of the few-group constant generation: in practical applications, the ζ method should be applied during the group constants generation process, to avoid the under-/over-estimation of the self-shielding effects.

It is interesting to notice how, focusing only on the neutronic aspects of the core design, the location of the control rods should require a compromise between the core stability and their worth. An analogous discussion applies also to the number of control rods in relation to the core decoupling and to the offset from criticality, although this aspect has not been taken into account in this section. In light of these considerations and of the results of this section, the proposed eigenvalue formulation seems to well suit the needs of the design process, providing an efficient computational framework. As a matter of fact, the existence of only one physical solution, due to the absence of competing phenomena, would allow to compute only a few dominant eigenpairs instead of the full spectrum, which could be a considerable reduction of the computational time in practical applications.

5.9 Conclusions

In this chapter, it has been shown how the eigenvalue formulations to the neutron transport equation could be traced back to a generalised eigenvalue formulation, called ζ. This eigenvalue can be introduced in order to filter specific regions of the phase space. In particular, bearing in mind the possible practical constraints arising during the core-design process, the ζ eigenproblem has been cast in a form that extends the

applicability of the density eigenvalue δ to specific nuclides and regions of the phase space.

This novel approach has been applied to a wide range of different classical yet realistic problems in reactor physics, considering the main types of materials encountered in the design of a reactor core, e.g., the fuel, the coolant, the moderator and the localised absorbers. These applications provided remarkable results. First, the ζ eigenvalue yields equivalent results to the iterative method commonly applied in such framework, but with a strong reduction of the computational effort. More importantly, the existence of one or more design solutions seems related to the presence, in the ζ spectrum, of one or more real and positive eigenvalues associated to positive eigenfunctions. This is a remarkable feature, which should facilitate to rigorously assess whether criticality can be attained or not acting on the selected nuclides, even in case of complex systems. Moreover, the knowledge of all the possible criticality arrangements of a system is of the utmost importance for the safety studies involving the re-criticality phenomena. This study of the ζ eigenvalue spectrum suggests that, in some situations, featured by the absence of competing interaction phenomena, there may exist only one positive solution, associated to an eigenvalue separation which is large enough to ensure an efficient numerical convergence on the dominant one.

Due to its novelty, there are many open questions that should be addressed in future activities. First of all, the ζ spectrum should be studied more thoroughly, starting from a more rigorous physico-mathematical framework and taking into account the impact of the different spatial, angular and energy approximations of the neutron transport equation. Moreover, the physico-mathematical meaning of the higher-order ζ harmonics should be investigated as well. A better comprehension of the ζ superior modes could disclose the possibility to apply perturbation methods, like the Generalised Perturbation Theory, which could be very useful for design-purpose calculations. Then, the action of the eigenvalue on more specific portions of the phase space should be studied, involving for example only some reaction channel, e.g. the capture, and a reduced energy range, e.g. the thermal region. Finally, some research efforts should be devoted to incorporate the ζ calculation in the cross sections collapsing and homogenisation process, in order to properly account for the self-shielding effects.

References

Allibert, M., D. Gérardin, D. Heuer, E. Huffer, A. Laureau, E. Merle, S. Beils, A. Cammi, B. Carluec, S. Delpech, A. Gerber, E. Girardi, J. Krepel, D. Lathouwers, D. Lecarpentier, S. Lorenzi, L. Luzzi, M. Ricotti, and V. Tiberi (2017). *SAMOFAR European Project D1.1 Description of initial reference design and identification of safety aspects*. Technical report 661891 (cited on page 170).

Beckner, W. D. and R. A. Rydin (1975). "A higher order relationship between static power tilts and eigenvalue separation in nuclear reactors". In: *Nuclear Science and Engineering* 56, pages 131–141 (cited on page 156).

Cacuci, D. G. (2010). "Handbook of Nuclear Engineering: Vol. 1: Nuclear Engineering Fundamentals; Vol. 2: Reactor Design; Vol. 3: Reactor Analysis; Vol. 4: Reactors of Generations III and IV; Vol. 5: Fuel Cycles, Decommissioning, Waste Disposal and Safeguards". Volume 1. Springer Science & Business Media (cited on page 162).

Gandini, A. (1978). "Higher order time-dependent generalized perturbation theory". In: *Nuclear Science and Engineering* 67, pages 91–106 (cited on pages 164, 166).

— (1987). In: *Advances in Nuclear Science and Technology. Advances in Nuclear Science and Technology, vol 19.* Edited by Lewins J. and Becker M. Boston: Springer (cited on page 164).

Gandini, A. (1981). "On the Standard Perturbation Theory". In: *Nuclear Science and Engineering* 79.4, pages 426–430 (cited on page 164).

Quarteroni, A., R. Sacco, and F. Saleri (2010). "Numerical mathematics". Volume 37. Springer Science & Business Media (cited on page 159).

Saad, Y. (1992). "Numerical methods for large eigenvalue problems". Manchester University Press (cited on page 158).

Shirakata, K., T. Sanda, and F. Nakashima (1999). "Spatial neutronic decoupling of large fast breeder reactor cores: Application to nuclear core design method". In: *Nuclear science and engineering* 131.2, pages 187–198 (cited on page 167).

Vitali, V. (2020). "Monte Carlo analysis of heterogeneity and core decoupling effects on reactor kinetics: Application to the EOLE critical facility". PhD thesis. Université Paris-Saclay (cited on page 156).

Weinberg, A. M. and E. P. Wigner (1958). "The Physical Theory of Neutron Chain Reactors". University of Chicago Press, Chicago (cited on page 156).

Chapter 6

A non-intrusive, computationally efficient modelling framework for the safety analysis of complex systems

Frustra fit per plura quod potest fieri per pauciora
(It is inconvenient to do with more actions something you can do with fewer)

Summa Totius Logicae, William of Ockham

6.1 Introduction

The last decades have witnessed a sharp increase both in the computational power (Moore, 1998) and in the development of high-fidelity models, enabling to tackle most of the real-life physico-engineering problems, e.g., the design of a safety-critical system, with sophisticated computer codes. However, the more complex the problem, the larger the computational resources required to accomplish the task: on one side, a computer model may be particularly expensive to solve because of several numerical complexities, e.g. non-linearities; on the other, a huge number of code runs could be required in case a large input parameter space needs to be explored, due to the *curse of dimensionality* (Bellman, 1957).

These issues have to be often faced, for instance, when dealing with design- (Jameson and Vassberg, 2001; Dur, Coskun, et al., 2011; Ballarin, Manzoni, et al., 2014) and safety-oriented (Parihar, Vergara, and Clutter, 2011; Fu, Yan, et al., 2016; Bagheri, Alamdari, and Davoudi, 2016; Seike, Kawabata, and Hasegawa, 2017) Computational Fluid-Dynamics (CFD) simulations, which are featured by several geometrical, material and model parameters. The same complexities can be found as well in the different disciplines of nuclear engineering, e.g., neutronics, thermo-hydraulics and thermo-mechanics.

Some strategies to minimise the computational resources consumption exploit *ad hoc* features of the problem under examination, e.g., geometrical symmetries (Tommasi, Maillot, and Rimpault, 2016). These approaches can be very effective, but are strongly case-dependent. More general strategies rely on *reduced order models* (ROMs) (Pedroni and Zio, 2017; Pedroni, 2022).

The basic idea of this kind of approach is to generate a simpler but more computationally efficient model that mimics, in some way, either the reality, reproducing the experimental data, or a physico-mathematical-computational model, reproducing its output, at the price of some controllable approximations (Benner, Gugercin, and Willcox, 2015).

When the surrogate is built as a cheaper alternative to the reference model, it is often addressed with the term *meta-model*, since it aims at reproducing the responses of the original model as well as the latter tries to imitate the reality. In this respect, the definition of Science given by Popper and Barthley III, 1988,

> *"Science may be described as the art of systematic over-simplification — the art of discerning what we may with advantage omit",*

perfectly describes the "art" of meta-modelling: in some specific situations, it is convenient and possible to simplify a complex model that represents the real world, still retaining its most important features in order to map exhaustively its behaviour in a very broad range of conditions. In other words, we omit some physical details in favour of information concerning the overall system behaviour, which is the fundamental information that cannot be disregarded.

Meta-modelling is particularly relevant in the frame of the safety analysis of complex systems described by complex models. In this case, a thorough quantitative risk assessment would require an analysis of the system behaviour in different operational and off-operational conditions, often as a function of different input parameters.

Reduced order models can be roughly divided in physics-driven and data-driven methods. The first ones yield an approximated model by manipulating directly the high-fidelity model (Lorenzi, Cammi, et al., 2016; 2017). Acting on the original equations allows to minimise possible biases in the model response and even to give an *a priori* estimate of the ROM error bounds (Rahman, San, and Rasheed, 2018). However, on top of the manifest difficulty in accessing the high-fidelity model equations in most of the commercial codes, these modifications would require a new code verification and validation (V&V) phase, which is a critical aspect when dealing with codes used for the

design verification of nuclear installations.

On the contrary, the second class of methods considers the code as a black-box, which is seen as a set of input and output data that are used to train the empirical regression model. Due to the data labelling, this class of methods is known as *supervised machine learning* (Russell, 2010), which includes, for instance, various regression models like Artificial Neural Networks (ANNs) (Demazière, Mylonakis, et al., 2021) and Support Vector Machines (SVMs) (Cortes and Vapnik, 1995). The data-driven nature of such methods makes them non-intrusive and application-independent, hence they can be employed effectively even with commercial, validated codes (Casenave, Gariah, et al., 2020).

However, this class of methods also brings some drawbacks. First, the fact that they need data to learn makes their performances sensitive to the training data selection. In order to realise an accurate yet flexible model, a trade-off between the model variance and the model accuracy, known as *model bias*, i.e. the error between the meta-model and the reference model, is needed. In case a few data were available, the meta-model would operate in an *under-fitting* regime, i.e. it would be simpler and more flexible (low variance) but very inaccurate (high bias). On the contrary, if many training evaluations were available, the model would be very accurate but also very complex and over-specialised on the training the data. This situation, featured by a low bias and a high variance, is known as *over-fitting* (Ghojogh and Crowley, 2019). The other main drawback is the fact that the lack of important training data can seriously limit the ROM prediction capability. As it is brilliantly summarised in Lassila, Manzoni, et al., 2014,

"If it is not in the snapshots, it is not in the ROM".

Finally, it is very difficult to obtain an *a priori* error prediction (Rahman, San, and Rasheed, 2018).

Nevertheless, the advantages of these methods are so attractive with respect to their shortcomings that they are becoming very popular. Audouze, De Vuyst, and Nair, 2013 were among the first ones to present a non-intrusive reduced order model (NIROM) for the solution of parametrised partial differential equations, but, to the best of our knowledge, the first NIROM application to the Navier-Stokes equations is due to Xiao, Fang, et al., 2015, who proposed a method relying on Taylor expansion and another one based on sparse grid collocation. Since then, many approaches have been proposed to perform non-intrusive model reduction, especially for CFD applications (Kumar, Raisee, and Lacor, 2016; Demo, Tezzele, and Rozza, 2019).

Most of these NIROMs, including the ones presented in this chapter, share some common features. First, they are composed by an offline, computationally intensive phase and by an online, fast-running stage. In the offline phase, the (expensive) FOM is run possibly a small number of times (e.g., few hundreds) to gather the input-output data realisation for the ROM training, while in the online phase the trained ROM can be used to approximate the FOM solution in correspondence of new input parameter values. Second, the different ROMs typically rely on is the reduction of the data dimensionality,

which allows to decouple them into a set of parameter-dependent coefficients and a set of spatial and dynamic modes (Marrel, Pérot, and Mottet, 2014; Nanty, Helbert, et al., 2017; Wu, Kozlowski, et al., 2018; Wu, Kozlowski, and Meidani, 2018; Roma, Di Maio, et al., 2021). The most popular technique to extract the modes and the coefficients from functional (spatial- or time-dependent) data is the Proper Orthogonal Decomposition (POD) (Volkwein, 2011), which has proven to be very efficient for the dimensionality reduction of physical fields(Lorenzi, Cammi, et al., 2016).

On the other hand, the major differences in the NIROMs recently proposed are due to the way the POD parameter-dependent coefficients are evaluated on new parameters which does not belong to the training dataset. In Kumar, Raisee, and Lacor, 2016, a regression-based polynomial chaos expansion is employed to estimate the POD coefficients for an uncertainty quantification study in a CFD framework, while in Guo and Hesthaven, 2019 a Gaussian process regression model is applied. Another approach is presented by Demo, Tezzele, and Rozza, 2019, where the POD coefficients are interpolated over new parameters through the adoption of the active subspaces technique. Another popular option to perform such interpolation is the use of SVM with a kernel constituted by radial basis functions (RBF) (Schaback, 1995), which have been proved to be very effective for non-linear, high-dimensionality interpolation in a broad range of applications (Xiao, Fang, et al., 2017; Dutta, Farthing, et al., 2021; Iuliano and Quagliarella, 2013; Chen, Hesthaven, et al., 2018). Due to its advantages, the SVM-RBF model is adopted to interpolate the POD coefficients on new parameters in this work.

The purpose of this chapter is to present a non-intrusive POD-RBF model and its advantages for obtaining an efficient model reduction in three different applications. The first involves the stability analysis of a large thermal reactor, while the second deals with the neutronic transient analysis of the ALFRED lead fast reactor design. Finally, the third application regards the safety analysis of gaseous releases in congested, industrial plants. This last application aims at demonstrating the NIROM applicability to a broad variety of different problems, proving its versatility. In the following, an overview of the POD-RBF model is presented, focusing on its structure and on its algorithms. Then, the various applications of the model are illustrated and discussed.

Some parts of this chapter have been already published in two conference proceedings, while another part has been submitted as peer-reviewed article for publication in the Journal of Computational Physics,

- N. Abrate, S. Dulla, N. Pedroni, *"A non-intrusive reduced order model for Light Water Reactor core stability analysis"*, Proceedings of the ESREL-PSAM 2020 conference, Venice (Italy), 2020

- N. Abrate, A. Moscatello, G. Ledda, N. Pedroni, F. Carbone, M. Maffia, A. Carpignano, *"A novel approach combining bootstrapped non-intrusive reduced order models and unscented transform for the robust and efficient CFD analysis of accidental gas releases in congested plants"*, submitted to Journal of Computational Physics, 2022

- N. Abrate, S. Dulla, N. Pedroni, "A non-intrusive reduced order model for neutronic transient analyses of the ALFRED reactor", Proceedings of the M&C conference 2021, Raleigh, NC, U.S.A., 2021

6.1.1 A non-intrusive POD-RBF model

Basically all the physico-mathematical problems that may be posed in the field of physics and engineering can be compactly represented as the action of a certain model $\mathcal{M}$ on a P-dimensional input vector parameter $\vec{p}$,

$$\vec{y} = \mathcal{M}(\vec{p}), \tag{6.1}$$

where $\vec{y}$ is the m-dimensional output response, named *snapshot*. The model $\mathcal{M}$ hides both the model variables (e.g., space, time, energy...) and the different modelling and numerical approximations and complexities. Hence, it may be though as a black-box taking a certain input from the outside and responding with a certain output. Incidentally, this is exactly the way any computer code aiming at solving any practical problem works. Therefore, in the following the notions of *physico-mathematical model* and *computer model* are assumed to be interchangeable.

6.1.1.1 Reduced order model overview: offline and online phases

The reduced order models presented in this chapter aim at approximating (with a reduced computational burden) the response $\vec{y}$ of a general physico-mathematical model $\mathcal{M}$ depending on a certain vector input parameter $\vec{p}$. As previously mentioned, this is achieved with a data-driven approach. First, according to a suitable sampling strategy, the FOM is sampled to gather the high-fidelity responses, whose dimensionality is reduced via POD. The POD coefficients, representing the solutions in a reduced order space, are then used to train the RBF network. Afterwards, the ROM is validated on some untrained parameter values, in order to verify that the approximation error of the ROM is acceptable for the intended application. Finally, the bootstrap method may be applied to estimate and, potentially, to propagate the ROM approximation error induced by the training samples choice. This procedure is performed by constructing a set of different ROMs, each trained with datasets sampled with replacement from the original training set.

Once this computationally expensive phase is completed, the ROM can be used as a fast-running tool to approximate the FOM responses on new parameter values. If the ROM response is employed as input for another model $\mathcal{M}'$, an estimate of the ROM approximation error can be obtained via the unscented transform (UT). This method estimates the uncertainty in the response of $\mathcal{M}'$ by means of a limited number of model evaluations. These steps are summarised in algorithm 1 and in figs. 6.1 and 6.2.

In spite of the large availability of codes and libraries for the fast deployment of reduced-order modelling applications, especially open-source, all the steps constituting these algorithms have been implemented *ex novo* in an in-house Python package

called ROMpy (Reduced-Order Modelling in Python). The reason for having taken this additional effort is two-fold: first, it allows to obtain a higher level of comprehension of the model than with a *plug-and-play* code, and, second, it makes easier the algorithm development in case some code modifications were needed. In this respect, the package collects all the *ad hoc* functionalities needed to gather the input-output data from the different external codes for the training and validation stages.

Algorithm 1: POD-RBF with uncertainty estimation

Offline procedures

1. define the p-dimensional parameter space $\mathbb{R}^p$;
2. select a parameter space sampling strategy (i.e. sparse grids, random sampling...);
3. generate full-order model snapshots $\vec{y}_i \in \mathbb{R}^m$ for each parameter sample $\vec{p}_i$;
4. divide the data into the training and the validation sets;
5. reduce dataset dimensionality, using POD (see Algorithm 2);
6. train the RBF net with the POD coefficients $\vec{a}_i \in \mathbb{R}^n$ (see Algorithm 3);
7. apply the bootstrap method (see Algorithm 5) to generate a set of ROMs;
8. compute the error distribution of the ROMs on the validation set;
9. validate the ROM on the validation set. If the average error between validation data and the set of bootstrapped ROMs is not acceptable, go back to step 3, adding more training points;

Online procedure

1. interpolate with RBF the POD coefficients over a new point (i.e. not used during training) $\vec{p}_j$ in $\mathbb{R}^p$;
2. back-project the POD coefficients $\vec{a}_j \in \mathbb{R}^n$ to get the approximated snapshot in the original space, $\vec{y}_j \in \mathbb{R}^m$.
3. if the ROM response is used as input for another model, apply the UT (algorithm 6) to estimate the confidence interval.

6.1.1.2 Model sampling and reduction

The performances of data-driven models are strongly dependent on the quality of the training data. Therefore, independently on the reduced order modelling approach,

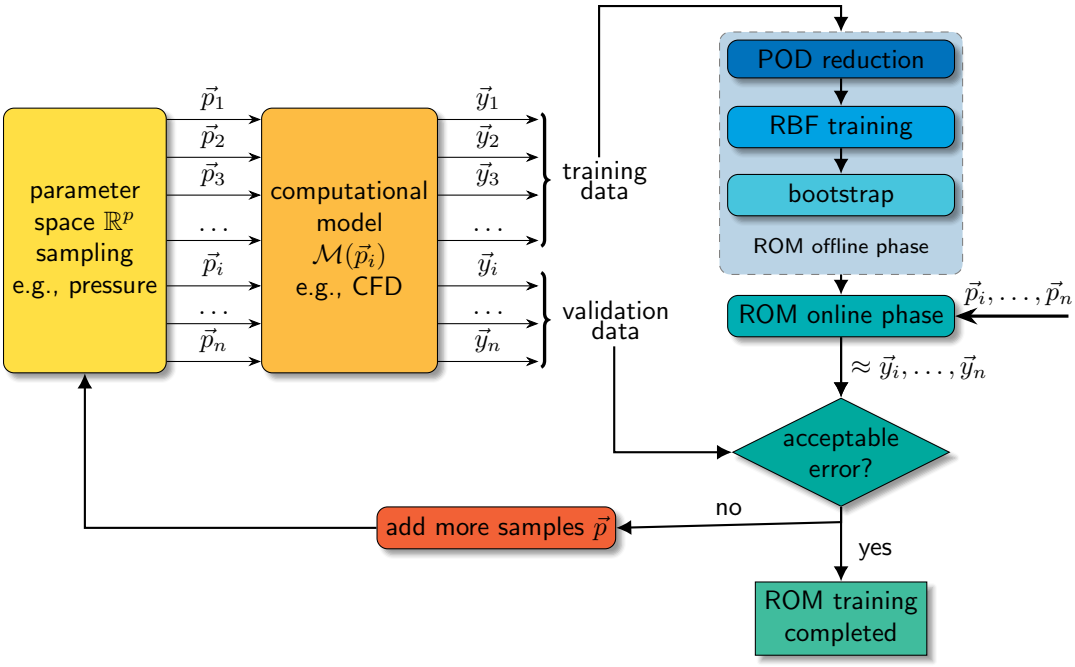

Figure 6.1: *Offline phase procedure workflow.*

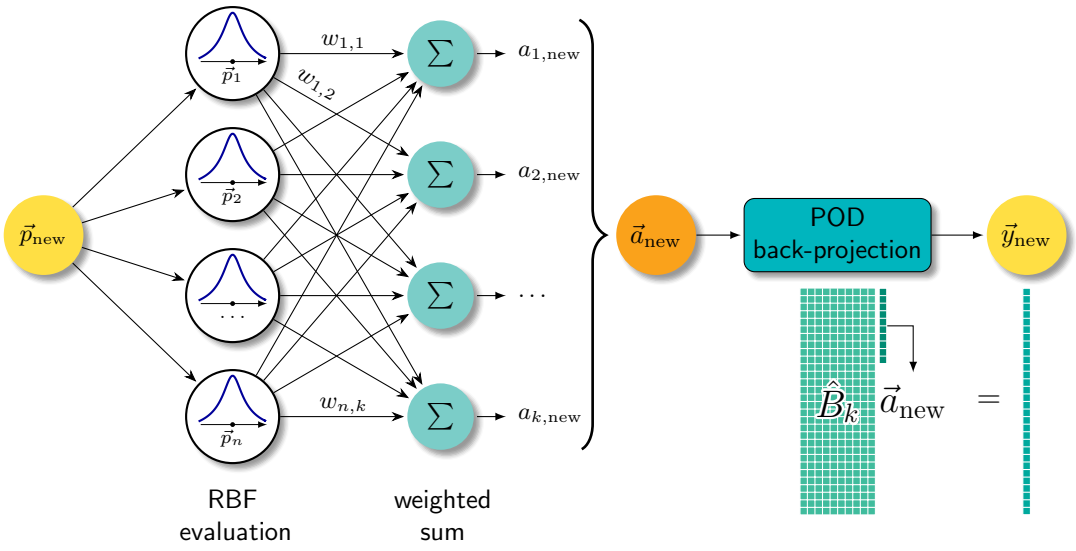

Figure 6.2: *Online phase procedure workflow when a new parameter value $\vec{p}_{\text{new}}$ is provided to the ROM. The set of weights $w_{i,j}$ is computed in the training phase, see algorithm 3.*

one of the most important steps is sampling the FOM.

Among the deterministic sampling techniques, the Smolyak sparse grid (Smolyak, 1963) approach is one of the most popular ones in this framework, due to its nice features. First, it allows an anisotropic sampling for multi-dimensional parameter spaces. Second, different levels of nested nodes can be obtained with a proper choice of the quadrature rule. The use of nested levels allows to efficiently train the ROM, allowing an *a posteriori* refinement of the parameter samples. In case of a high-dimensional parameter space, the Smolyak grid can be also coupled with an adaptive simulation strategy, as in Alsayyari, Perkó, et al., 2019; 2021. Since this chapter aims to present and test the non-intrusive ROM presented above for different applications, more detailed discussions concerning the sampling phase will be given for each case.

After the FOM sampling, the data are reduced by means of the POD. The core idea of the POD method, described in algorithm 2 and in fig. 6.3, is to express the original data as an expansion of basis functions, known as POD modes, extracted with a singular value (eigenvalue) decomposition of the FOM snapshot matrix (correlation matrix). The main advantage of this technique is that the first modes retain most of the FOM dataset information, which means that, usually, truncating the POD expansion implies a limited loss of information. This evidence is justified by the fact that the POD basis is optimal in a least-square sense (Volkwein, 2011).

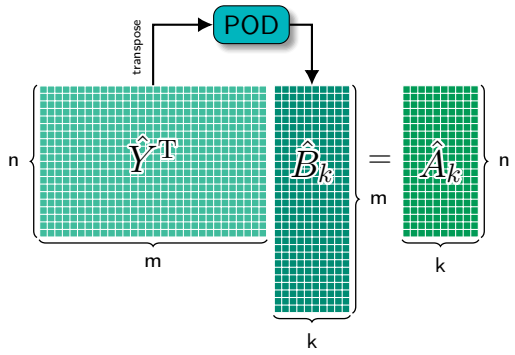

Figure 6.3: *POD-driven dimensionality reduction for the snapshot matrix containing the training CFD solutions.*

The usual figure of merit employed to assess the number of POD basis functions needed to achieve a certain accuracy is the POD energy $\mathcal{E}_k$, i.e. the ratio of the sum of the first k squared singular values to the sum of all the squared singular values. The calculation of this quantity is simple and cheap, but often not enough in order to fully characterise the POD expansion accuracy. Therefore, in this paper, the root mean squared error between the FOM output and the ROM estimates will be evaluated as well to have an additional figure of merit.

Algorithm 2: Proper Orthogonal Decomposition algorithm

Input

1. snapshot matrix $\hat{Y} = [\vec{y}_1, \vec{y}_2, \dots, \vec{y}_n]$, with $\vec{y}_i \in \mathbb{R}^m$;
2. snapshot matrix rank r;
3. truncation error ε;

Output

1. POD basis $\hat{B}_k = [\vec{b}_1, \vec{b}_2, \dots, \vec{b}_k]$, with $\vec{b}_i \in \mathbb{R}^m$;
2. POD eigenvalues $\lambda_i, \forall i = 1, \dots, k$;
3. POD energy $\mathcal{E}_k$;
4. POD coefficients $\hat{A}_k = [\vec{a}_1, \vec{a}_2, \dots, \vec{a}_k]$, with $\vec{a}_i \in \mathbb{R}^n$;

try:
  $[\hat{\Psi}, \hat{\Sigma}, \hat{\Phi}] = \texttt{svd}(\hat{Y})$ # *Singular Value Decomposition*
  for $i = 1, \dots, r$ **do**
    $\vec{b}_i = \vec{\psi}_i$ # $\vec{\psi}_i$ *is the* $\hat{\Psi}$ *i-th column*
    $\lambda_i = \sigma_i^2$ # σ_i *is the i-th diagonal entry of* $\hat{\Sigma}$
  end
except *Memory Error*:
  if $n > m$ **then**
    $[\hat{\Psi}, \hat{\Lambda}] = \texttt{eig}(\hat{Y}\hat{Y}^{\mathrm{T}})$ # *Eigenvalue Decomposition*
    for $i = 1, \dots, r$ **do**
      $\vec{b}_i = \vec{\psi}_i$ # $\vec{\psi}_i$ *is the i-th column of* $\hat{\Psi}$
      $\lambda_i = \hat{\Lambda}_{i,i}$ # $\hat{\Lambda}_{i,i}$ *is the i-th diagonal entry of* $\hat{\Lambda}$
    end
  else
    $[\hat{\Phi}, \hat{\Lambda}] = \texttt{eig}(\hat{Y}^{\mathrm{T}}\hat{Y})$ # *Eigenvalue Decomposition*
    for $i = 1, \dots, r$ **do**
      $\vec{b}_i = \frac{\hat{Y}\vec{\phi}_i}{\sqrt{\lambda_i}}$ # $\vec{\psi}_i$ *is the i-th column of* $\hat{\Psi}$
      $\lambda_i = \hat{\Lambda}_{i,i}$ # $\hat{\Lambda}_{i,i}$ *is the i-th diagonal entry of* $\hat{\Lambda}$
    end
  end
end
choose k such that $1 - \mathcal{E}_k < \varepsilon$
$\hat{A}_k = \hat{Y}^{\mathrm{T}}\hat{B}_k$ # *compute reduced order coefficients*

6.1.1.3 Model training and tuning

Once the reduction step is completed, the parameter-dependent POD coefficients are employed to train a network of RBFs, which can be then adopted in the online phase to interpolate the FOM solution on new parameter values.

Among the different types of radial basis functions, in this chapter it has been chosen to rely mostly on the inverse multi-quadrics formulated by Hardy, 1971 and on the Gaussian distribution. The value of these functions depend on two parameters. The first one is the L_2 distance between the centers, i.e. the training parameter values $\vec{p}_i$, and the collocation points, i.e. the new parameter $\vec{p}_j$, while the second one is the so-called hyperparameter σ, which is a free parameter determining the shape of the RBFs. The choice of this parameter is a very delicate aspect of the training phase, as it strongly affects both the interpolation accuracy and its numerical stability. Usually, the choice of this parameter is performed in order to minimise the interpolation error on some test points, which do not belong to the training set.

This The main drawback of this approach, however, is the need to partition the high-fidelity solutions in three subsets, namely the training, the test and the validation set, in order to train, tune and validate the model, respectively. Due to the large computational cost usually associated to the high-fidelity simulations, this approach is too computationally expensive.

Algorithm 3: Radial Basis Function training algorithm.

Input

1. data reduced via POD, $\hat{A}_k \in \mathbb{R}^{n \times k}$;
2. parameter matrix $\hat{P} = [\vec{p}_1, \vec{p}_2, \dots, \vec{p}_n]$, with $\vec{p}_i \in \mathbb{R}^p$;
3. RBF type f (e.g. $f = 1/\sqrt{||\vec{p}_1 - \vec{p}_j||_2 + \sigma^2}$);
4. hyperparameter σ via Algorithm 4 or Hardy's formula Hardy, 1971;

Output

training matrix $\hat{W} \in \mathbb{R}^{n \times k}$

 # loop over each column of $\hat{A}_k$, $\vec{a}_i \in \mathbb{R}^n$

for $i = 1, \dots, k$ **do**

  choose hyperparameter σ_i (optimal selection with algorithm 4)

  # compute distance matrix $\hat{D} = [\vec{d}_1, \dots, \vec{d}_n] \in \mathbb{R}^{n \times n}$

  for $j = 1, \dots, n$ **do**

    $\vec{d}_j = [f(||\vec{p}_1 - \vec{p}_j||_2, \sigma_i), \dots, f(||\vec{p}_n - \vec{p}_j||_2, \sigma_i)]$

  end

  $\vec{w}_i = \hat{D}^{-1}\vec{a}_i$ *#* $\vec{w}_i$ *is the i-th column of* $\hat{W}$

end

Algorithm 4: Optimal hyperparameter selection.

Input

1. data reduced via POD, $\hat{A}_k \in \mathbb{R}^{n \times k}$;
2. parameter matrix $\hat{P} = [\vec{p}_1, \vec{p}_2, \dots, \vec{p}_n]$, with $\vec{p}_i \in \mathbb{R}^p$;
3. RBF type f (e.g. $f = 1/\sqrt{\|\vec{p}_1 - \vec{p}_j\|_2 + \sigma^2}$);
4. initial hyperparameter guess $\sigma_0 = \dfrac{0.815}{n} \displaystyle\sum_{i=1}^{n} \|\vec{p}_i - \vec{p}_\ell\|_2$, where ℓ is the closest point to i in the parameter space Hardy, 1971.

Output

1. Optimal hyperparameter σ_{opt}

Optimise σ **minimising** RMSE

Select σ # *e.g. via conjugate gradient method*
Compute $\hat{D}$ and $\vec{w}_i$ as in algorithm 3
use Rippa's algorithm Rippa, 2011 and LOOCV
$[\hat{L}, \hat{U}]$ = lu($\hat{D}$) # *Compute LU decomposition*
for *j=1, ..., n* **do**
  $\vec{x} = \hat{U}^{-1}\hat{L}^{-1}\vec{e}_j$ # $\vec{e}_j$ *is the j-th column of the identity matrix*
  $\delta_j = \|\dfrac{w_{i,j}}{x_j}\|$ # *compute interpolation error with j-th components of* $\vec{x}$ *and* $\vec{w}_i$
end
RMSE = $\sqrt{\dfrac{1}{n}\displaystyle\sum_{j=1}^{n}\delta_j^2}$

end

Among the many possible approaches suggested in the literature, the Leave-One-Out-Cross-Validation (LOOCV) technique is followed, due to its generality. The LOOCV consists in training the meta-model with each of the N sets obtained taking N-1 samples and using the left one as a test point. In this framework, the best hyperparameter is the one minimizing the root-mean square error (RMSE) computed from the N trained models. In order to reduce the computational cost related to the LOOCV optimisation, the formula developed by Rippa, 2011 is used to evaluate the cost function, i.e. the RMSE, in combination with the conjugate gradient optimisation algorithm. The shape optimisation is initialised using the empirical formula for σ given by Hardy, 1971.

The RBF training phase is summarised in algorithm 3, while the hyperparameter optimisation is presented in algorithm 4.

6.1.1.4 Model validation and error estimation by a bootstrap-based ensemble of ROMs

When the training phase is completed, the model needs a validation on new parameter values to verify its accuracy and consistency with respect to the FOM solution. An extensive validation would require lots of FOM evaluations, jeopardising the overall computational efficiency of the meta-model. A common strategy to overcome this issue consists in being satisfied with the selection of a few, significant new parameter values not too close to the training points. This is the most popular approach in the literature when the NIROMs do not allow an *a priori* estimation of their confidence interval (Rahman, San, and Rasheed, 2018; Xiao, Fang, et al., 2017).

In this thesis the same approach is pursued, albeit trying to complement this limited validation with a statistical sensitivity study concerning the training set. As a matter of fact, the ROM responses are biased by the selection of the training points, whatever is the sampling strategy of the parameter space. Therefore, as a complement of the validation phase, the bootstrap method is applied for a full exploitation of the available training set, maximising the amount of information extracted. The idea of this non-parametric statistical method, presented in algorithm 5 and sketched in fig. 6.4, consists in training a large number of ROMs using different training sets, obtained by resampling with replacement the original training set. In this way, it is possible to build an ensemble of meta-models, which can be used to construct a distribution of output responses: in the end, this can be employed to estimate the error distribution for each validation point (Zio, 2006; Secchi, Zio, and Di Maio, 2008; Zio, Apostolakis, and Pedroni, 2010; Pedroni, Zio, and Apostolakis, 2010; Marelli and Sudret, 2018).

The training phase of the NIROM is usually much cheaper than the offline phase, yet it may be still quite time consuming if the number of training parameters and/or the number of reduced order coefficients are large, because of the RBF hyperparameter optimisation process. However, since each model reboot is independent, the bootstrap procedure can be massively parallelised.

Due to the features of the POD-RBF ROM approach, some precautions are needed. First of all, since the RBF kernel becomes singular if the same training data is repeated, each time that a training case is resampled, it is deliberately ignored, thus the resampled set is always poorer than the original one. Then, due to the interpolatory nature of the RBF approach, some care should be devoted when the meta-model is tested on the validation set, because one or more validation samples could fall outside the sampled parameter space, i.e. the convex hull obtained from the sampled points. In these situations, the RBF net extrapolates rather than interpolating. In order to better understand the model behaviour in such cases, the bootstrap is applied, in the following, either in extrapolation or in interpolation mode. In the first mode, each validation point is accepted and evaluated by the ROM, which thus could extrapolate parameter values falling outside the training points, while, in the second mode, the validation points

Algorithm 5: Bootstrap method

Input

1. number of reboots N_r;
2. training parameter values $\hat{P} = [\vec{p}_1, \vec{p}_2, \dots, \vec{p}_n]$;
3. training snapshots $\hat{Y} = [\vec{y}_1, \vec{y}_2, \dots, \vec{y}_n]$;

Output

Ensemble of ROMs, $\mathcal{R}_1, \dots, \mathcal{R}_{N_r}$

 # this can be done in parallel

for *i=1, ..., N_r* **do**
  for *j=1, ..., N* **do**
    Sample one parameter point $\vec{p}_j$ from $[\vec{p}_1, \vec{p}_2, \dots, \vec{p}_n]$ with replacement;
    if $\vec{p}_j$ exists **then**
      Discard $\vec{p}_j$ to avoid singular RBF kernel;
  end
  Reduce dataset with Algorithm 2;
  Train and tune the RBF network with Algorithms 3, 4;
end

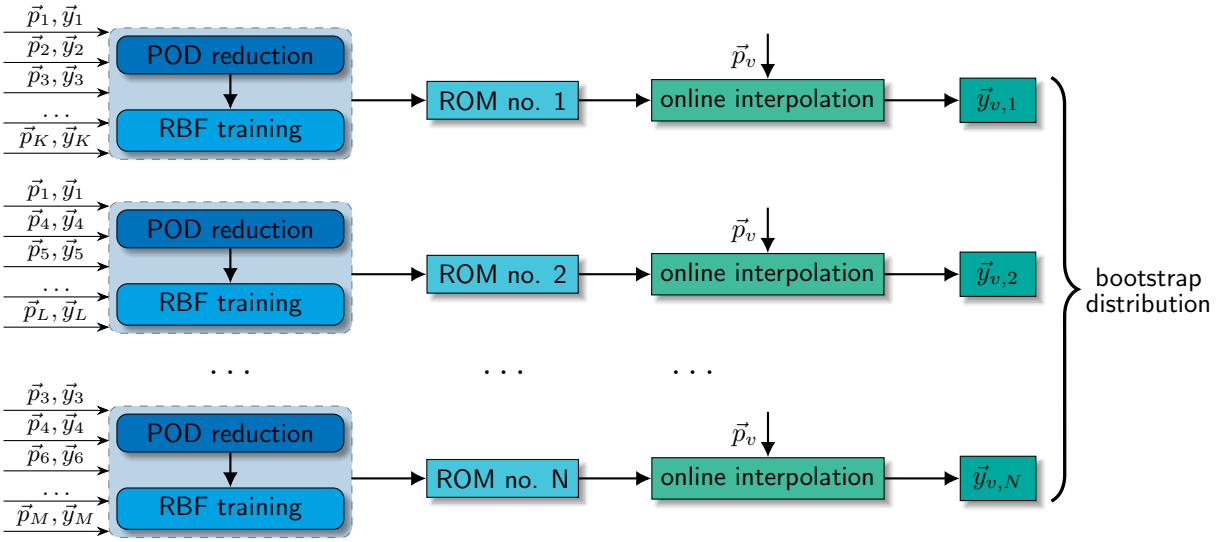

Figure 6.4: *Sketch of the generation of the ROM distribution, and, consequently, of the output spatial fields via bootstrapping.*

falling outside the training range are discarded. In this last case, no extrapolation occurs for parameter values drawn outside the parameter "box".

6.1.1.5 Unscented Transform and POD for uncertainty propagation and confidence interval estimation

As mentioned in the previous subsection, bootstrapping the ROM generates an ensemble of meta-models. If the ROM response is the final goal of its application, confidence intervals can be extracted directly from the ensemble distributions. However, when the ROM response $\vec{y}_{ROM}$ is an input for another model $\mathcal{M}'$, this operation may not be trivial, especially when $\vec{y}_{ROM}$ is a spatio-temporal field. In this case, the uncertainty in the ROM responses should be propagated through $\mathcal{M}'$ in order to obtain a confidence interval for the final output of the calculation chain. To avoid many queries of the model, it is proposed to approximate the confidence interval with the so-called Unscented Transform (UT) method (Julier and Uhlmann, 1997).

This method, which is an extension of the Kalman filter (Kalman, 1960) to non-linear models, approximates the original m-dimensional statistical distribution with a set of $2m + 1$ specific samples, identified as *sigma points*, that are then transformed using the non-linear model, i.e. $\mathcal{M}'$ in this case. The transformed sigma points can be used to estimate the mean and the variance of the non-linear model due to the uncertain input.

Since the input distribution dimension is proportional to its number of degrees of freedom, the choice of the sigma points may not be trivial. To overcome this issue, the

Algorithm 6: Unscented Transform and POD for uncertainty propagation

Input

ensemble of ROM responses $\hat{Y}_{\mathcal{R}} = [\vec{y}_{\mathcal{R},1}, \dots, \vec{y}_{\mathcal{R},N_r}]$ (spatial fields) for a certain parameter value $\vec{p}_{\text{new}}$;

Output

mean $\mathrm{E}[\vec{z}]$ and covariance $\mathrm{cov}[\vec{z}]$ estimates for the response z of the model $\mathcal{M}'$;

 # choose sigma points

Compute reduced order coefficients $\vec{a} \in \mathbb{R}^k$ via POD (Algorithm 2) of $\hat{Y}_{\mathcal{R}}$;

Compute mean $\vec{\mu} = \mathrm{E}[\vec{a}]$ and covariance $\hat{C} = \mathrm{cov}[\vec{a}]$;

Compute Cholesky or SVD decomposition to obtain $\hat{L}\hat{L}^{\mathsf{T}} = k\hat{C}$;

Apply the scaling factor $s = k + \lambda$, $\hat{S} = \sqrt{s}\sqrt{\hat{C}}$; *# λ is a free parameter (here λ=0)*

Determine weights as $w_i = 1/2s$, $i = 1, \dots, k$ and $w_0 = \lambda/s$ (associated to $\vec{\mu}$);

 # this can be performed in parallel

for *i=1, ..., k* **do**

$\vec{\sigma}_{UT,i} = \vec{\mu} - \hat{S}_i$ *# $\hat{S}_i$ is the i-th column of the $\hat{S}$ matrix*

$\vec{z}_i = \mathcal{M}'(\vec{\sigma}_{UT,i})$ *# apply non-linear model*

$\vec{\sigma}_{UT,i+k} = \vec{\mu} + \hat{S}_i$

$\vec{z}_{i+k} = \mathcal{M}'(\vec{\sigma}_{UT,i+k})$ *# apply non-linear model*

end

compute $\mathrm{E}_w[\vec{z}] = \sum_{i=0}^{2k+1} w_i \vec{z}_i$ and $\mathrm{cov}_w[\vec{z}] = \sum_{i=0}^{2k+1} w_i (\vec{z}_i - \mathrm{E}_w[\vec{z}])(\vec{z}_i - \mathrm{E}_w[\vec{z}])^{\mathrm{T}}$;

POD algorithm could be applied to reduce the dimensionality of the ROM ensemble, similarly to what is done in Foad, Yamamoto, and Endo, 2020. The UT-POD procedure is presented in algorithm 6, while a conceptual scheme is presented in fig. 6.5.

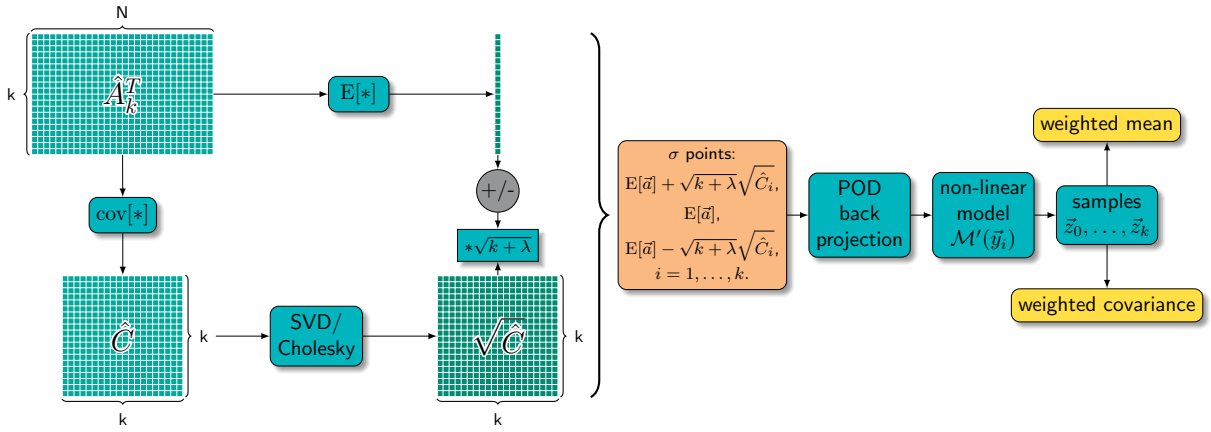

Figure 6.5: *Sketch of the POD-UT approach for uncertainty quantification.*

In the following sections, the non-intrusive POD-RBF modelling framework discussed so far is adapted and tested on three different industrial applications, with the purpose of highlighting its capabilities and its potential issues. Therefore, considering also the overall aim of the thesis, it is important to remark here that the attention will be focused more on the methodology and modelling aspects rather than on the application of the NIROM itself. This choice is also related to the fact that each real-life study case is properly simplified in order to make the problem more suitable for the NIROM development, still trying to retain its most important features in view of the potential full-scale industrial use of the NIROM.

6.2 A non-intrusive reduced order model for the stability analysis of large thermal reactors

6.2.1 Introduction

6.2.1.1 Stability issues in Gen-III+ reactors

Due to the more and more strict constraints on safety, sustainability and capital cost, the Gen-III+ Light Water Reactors (LWRs) are endowed with new design features which aims at extending the life of the system, reducing the radioactive waste and increasing the safety level of the plant.

This is the case, for example, of the European Pressurised Reactor, which is currently under operation in China and under construction in France (Flamanville) and United Kingdom (Hinkley Point). Among the new design features, the most relevant ones are, from a neutronic perspective:

- the possibility to use MOx fuel assemblies (FAs), obtained by the spent fuel reprocessing. These FAs can introduce some significant distortions in the energy spectrum of the reactor with respect to the traditional, UOx-based FAs;
- an increase in the core size, in order to extend its burn-up and, thus, the lifetime of the plant;
- the adoption of a heavy reflector, made of stainless steel, for the reduction of the core leakages. Compared to traditional reflectors, made of water and structural materials, the heavy reflector tends to absorb more thermal neutrons, reflecting the epithermal ones towards the core. This aspect constitutes an advantage both on the radiological risk, that is reduced, and on the neutron economy, that improves.

In spite of these advantages, the larger core optical size and the heavy reflector increase the overall spatial decoupling of the system, which thus becomes more sensitive to localised perturbations than compact, leakage-dominated cores. The combination of different perturbations, which may be either of operational nature, like the FAs bowing, or of fabrication nature, like the fuel tolerances, can induce local inhomogeneities in the moderation process. As a consequence, when these disturbances do not mutually compensate, some localised perturbations in the flux, known as *flux tilts*, can arise. According to the standard safety practices for PWRs (NRC, 2016), the Quadrant Power Tilt Ratio (QPTR), which is a figure of merit defined as the ratio between the peak ex-core detector output and the average of the ex-core detector outputs, should be smaller than 1.02. If this limit is exceeded, a set of specific actions, starting with the thermal power reduction, should be followed in order to bring the core back to a safe operational state.

6.2.1.2 Computational analysis to the aid of core monitoring

The effect of the tilt on the overall power distribution, which has to be carefully monitored in order to keep the reactor operation into its safety margins, is proportional to the spatial decoupling of the system. Therefore, in spite of their advantages, the adoption of a heavy reflector and of a larger core size amplify the tilt detrimental effect on the core neutronic stability. This unpleasant design feature makes the operation of the EPR more delicate, since the detection of flux and power tilts is practically quite difficult, especially during the cold start-up. In this phase, the tilts can be particularly dangerous, since the thermal feedback is not effective in damping their effects, and the fission chambers used to map the flux distribution in the core are less precise, because of the lower flux with respect to the nominal one. Therefore, the ex-core measurements should be complemented by accurate calculations.

Due to these considerations, in order to complement the experimental monitoring and to help its interpretation, the use of a computationally efficient simulation framework is of paramount importance. Unfortunately, the larger spatial decoupling of these systems have detrimental effects not only on their operation, but also on the efficiency of the numerical techniques used to simulate them. Most of the legacy codes used in the LWRs industry heavily rely on the so-called *power iteration method*, described in chapter 2, whose convergence rate depends on the dominance ratio of the system, i.e. the ratio between the fundamental and the first-order eigenvalue of the multiplication eigenvalue problem.

Since this parameter is inversely proportional to the decoupling degree of the reactor, the determination of the fundamental eigenpair of the system is extremely inefficient.

As mentioned in chapter 2, among the different proposals to enhance the numerical convergence of the eigenvalue solvers, one of the best options consists in adopting a method belonging to the class of Krylov-Arnoldi methods (Saad, 1992). In virtue of its non-intrusiveness, these methods can be wrapped around an existing code, minimising the implementation effort and making its validation easier.

However, even in the case a Krylov-Arnoldi method was implemented in the legacy codes, the number of parameters influencing the flux distribution would require a too vast number of calculations.

The usual way to reduce the number of expensive calculations in reactor physics is to rely on perturbation methods, like the Generalised Perturbation Theory (GPT) (Gandini, 1978). As pointed out in chapter 5, this approach yields an approximation of the perturbed eigenpair, exploiting the knowledge of the perturbation and of some of the higher-order flux harmonics. In this respect, this method would take full advantage of computationally efficient methods like the Krylov-Arnoldi, which are sufficiently robust to yield the leading higher-order harmonics even for system featured by a low dominance ratio.

Although the GPT is a well-established technique, available in most legacy codes, its range of application is not rigorously defined. The fact that this approach suffers

from some convergence flaws can be proven quite easily considering a homogeneous slab, modelled with the two-group diffusion equation, and assuming that the fission operator is perturbed by means of a perturbation δ in the number of neutrons emitted per fission,

$$\nu' = \nu + \delta\nu = (1 + \delta)\nu. \tag{6.2}$$

Since this perturbation does not affect neither the cross sections nor the diffusion coefficient, the perturbed eigenvalue λ', i.e. the inverse of k'_{eff}, can be evaluated analytically,

$$\lambda' = \frac{(1 + L_1^2B^2)(1 + L_2^2B^2)}{k'_\infty} = \frac{\Sigma_1\Sigma_2(1 + L_1^2B^2)(1 + L_2^2B^2)}{\nu\Sigma_{f,2}\Sigma_{1\to2}(1 + \delta)} = \frac{\lambda}{1 + \delta}, \tag{6.3}$$

where λ is the reference, unperturbed eigenvalue and λ' is the eigenvalue of the perturbed system. In this specific case, the GPT coincides with the Taylor expansion with respect to δ,

$$\lambda' = \lambda \sum_{n=0}^{\infty} (-1)^n \delta^n, \tag{6.4}$$

which converges if and only if $|\delta| < 1$. Therefore, when the perturbation intensity is beyond a certain threshold, the GPT series is not convergent.

Since it is extremely difficult to rigorously assess the application ranges of this approach for realistic configurations, its use for this kind of analysis may not be sufficiently robust and reliable to perform the core qualification,

In light of these limitations concerning the code computational performances and considering that modifying the legacy codes is not viable as a short term solution due to complexity of their qualification, a possible approach to tackle these issues is to resort to non-intrusive surrogate models.

In the following section, the physico-mathematical formulation of the full-order problem is presented. Then, a NIROM for this application is proposed and its training is carried out for a realistic yet simplified study case, represented by the 2D UAM benchmark reactor. Finally, the accuracy of this model is discussed and some concluding remarks and future perspectives are given.

6.2.1.3 Physico-mathematical statement of the problem

The characterisation of the tilt behaviour according to the different types of localised perturbations occurring during the nominal core operation can occur estimating the flux and the associated thermal power distributions, which can be obtained by solving the steady state neutron balance equation.

Since the analysis should involve the full-core, it is not practical nor useful to use a detailed transport model. As it is usually done in this case, a low-transport model is often sufficient to convey a sufficient amount of information regarding the state of the core, provided that a set of homogenised and collapsed cross sections representative of the system under investigation is available. The generation of the few-group data is

usually accomplished using a high-fidelity transport calculation on a simplified reactor configuration, e.g., a set of representative fuel assemblies. The usual definition of collapsed cross section yields

$$\Sigma_{y,g}(\vec{r},\vec{p}) = \frac{\int_{E_{g-1}}^{E_g} dE\ \Sigma_y(E,\vec{p})\phi(E,\vec{p})}{\int_{E_{g-1}}^{E_g} dE\phi(E,\vec{p})}, \tag{6.5}$$

where the terms have their usual meaning (as detailed in chapter 4) and $\vec{p}$ represents a general localised perturbation that can affect the nominal local conditions.

More specifically, for the EPR case, the localised perturbations indicated by $\vec{p}$ can be assumed to belong to two main families, namely fabrication tolerances and operational disturbances. In the first group, the main fabrication uncertainties can be due to

1. the fuel pellet density, which has an impact on the fission rate
2. the fuel pellet diameter, which influences both the fission rate and the moderation ratio
3. the cladding thickness, which has an impact on the parasitic capture and on the moderation ratio
4. the enrichment, which affects the fission rate.

Concerning the operational disturbances, it is possible to identify

1. the pump uncertainty, which affects the local water density and, thus, the local moderation
2. the assembly bowing, which alters the flow cross section in the sub-channel and, thus, the local moderation ratio
3. the change in the fuel density, which depends on two competing phenomena, i.e. the fuel densification and the fuel swelling (Cacuci, 2010). The first mechanism, due to the coalescence of the micro-pores in the fuel structure under irradiation, tends to increase the density of the fuel, while the second one, caused by the accumulation of the gaseous fission products, tends to decrease the fuel density because of the pellet ballooning.

These random, localised disturbances introduce some competing phenomena in the neutron balance. Because of the large spatial decoupling of the system, which is a consequence of the short diffusion length of the neutrons, the information of these disturbances is not propagated at the full-core level, but affects the local flux behaviour, inducing the tilt. Since these phenomena occurs at the fuel assembly level, but different

assemblies can be affected, the proper characterisation of these disturbances should be carried out considering them since the few-group data generation process.

Once the set of nominal and perturbed few-group constants has been produced, the full-core flux and power distributions can be finally estimated with a few-group diffusion model. Due to the thermal spectrum of the system, a two-group approach can be adopted for this purpose. Consistently with the system features, it is possible to neglect the up-scattering and to consider that all neutrons coming from fissions are emitted in the fast group,

$$\begin{cases} -\nabla \cdot D_1(\vec{r},\vec{p})\nabla\phi_1(\vec{r},\vec{p}) + \Sigma_{r,1}(\vec{r},\vec{p})\phi_1(\vec{r},\vec{p}) = \dfrac{1}{k_{\text{eff}}}\left[\nu\Sigma_{f,1}(\vec{r},\vec{p})\phi_1(\vec{r},\vec{p}) + \nu\Sigma_{f,2}(\vec{r},\vec{p})\phi_2(\vec{r},\vec{p})\right] \\ \\ -\nabla \cdot D_2(\vec{r},\vec{p})\nabla\phi_1(\vec{r}) + \Sigma_{r,1}(\vec{r},\vec{p})\phi_1(\vec{r}) - \Sigma_{s,1\to 2}(\vec{r},\vec{p})\phi_1(\vec{r}) = 0, \end{cases} \tag{6.6}$$

where the terms have their usual meaning, as detailed in chapter 4.

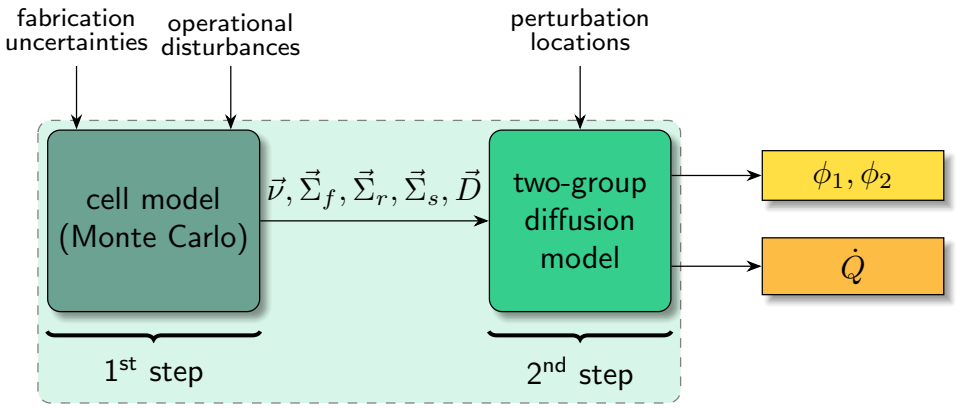

Figure 6.6: *Two-step calculation path followed for the full-core neutronic simulation.*

The two-step nature of the full-core diffusion calculation, depicted in fig. 6.6, poses a question concerning the development of a reduced order simulation framework. One possibility is to consider this calculation chain as a single model $\mathcal{M}$, sketched as the dashed box in the figure, which takes as input parameters the perturbation intensities and their location in the core and outputs the flux and power distributions at the full-core level. Considering the approach as monolithic, the resulting ROM would have the advantage of avoiding the evaluation of the set of few-group data, establishing a direct relationship between input and output. However, due to the large number of input parameters, especially concerning the number and the location of the perturbations, the training phase would be very computationally demanding.

An alternative strategy to this monolithic approach is to consider a reduced order model consisting in two steps, each one approximating the two steps of the FOM. This

two-step ROM would allow to decouple the training phase, taking advantage of the features of the two models, although at the price of the propagation of the modelling errors from the cell ROM to the full-core ROM.

In order to develop an *ad hoc* ROM for the tilt characterisation, a simplified yet still realistic problem is considered, based on the Uncertainty Analysis in Modelling (UAM) benchmark for the Gen-III+ systems (Ivanov, Avramova, et al., 2007), which is sketched in fig. 6.7. This specific 2D model is featured by 529 squared fuel assemblies with a pitch of 21.42 cm, and includes the different regions of the core, like the heavy reflector and the borated water surrounding the core.

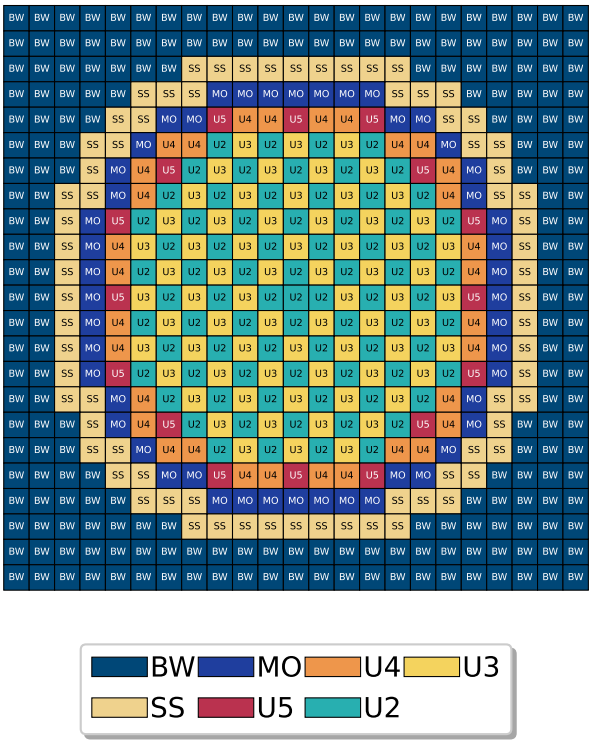

Figure 6.7: *Sketch of the UAM benchmark. BW: borated water; MO: Mixed Oxides of U and Pu; U4: 2.1 % enriched UOx; U3: 3.2 % enriched UOx with burnable poison rods of $UO_2 - Gd_2O_3$; SS: stainless steel; U5: 3.2 % enriched UOx with burnable poison rods of $UO_2 - Gd_2O_3$; U2: 2.1 % enriched UOx;*

Figure 6.8 shows the detailed geometry for the fuel assemblies (FAs) constituting the core. For each kind of FAs, a set of energy collapsed and spatial homogenised cross sections and diffusion coefficients are computed with the Serpent code.

Because of the large number of FAs, the input parameter space of this problem is huge and very complex, since, in principle, different disturbances can affect different FAs at the same time, with different probabilities. Since the aim of this section is to provide a "proof of concept" for the development of a non-intrusive ROM to characterise

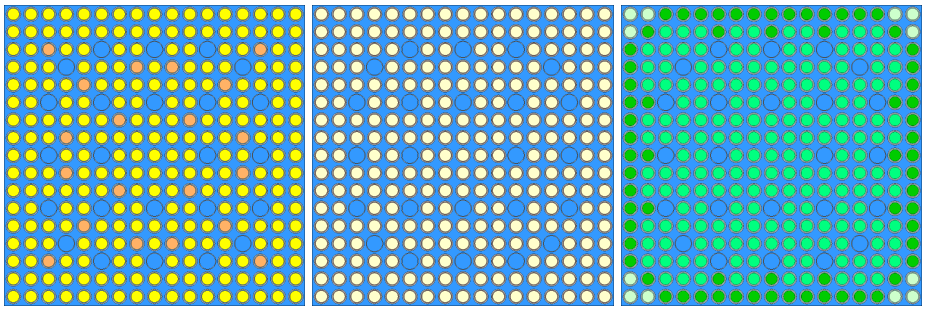

Figure 6.8: *Pin cells of the UAM benchmark: UOx with 3.2% enrichment and Gd rods in orange (left), UOx with 2.1% enrichment (centre) and MOx with 9.8% (emerald green), 6.5% (pine green) and 3.7% (mint green) Pu enriched rods (right) .*

the tilt effects on the core operation, the parameter space variability is properly reduced to limit the computational effort for the model training, still maintaining an adequate level of generality. Therefore, to reduce the number of scenarios, a simplifying assumption concerning the operational and fabrication disturbances is introduced: only two of them are considered in the following.

The first disturbance is assumed to be the fuel diameter pellet. Since it affects both the fission and the moderation, which depends on the ratio between the fuel and the coolant volume in the elementary cell, this parameter is a good representative for the group of disturbances of fabrication uncertainties. As such, it is assumed that this parameter is normally distributed, following the specifications in Ivanov, Avramova, et al., 2007, i.e. a nominal value of 0.41625 cm and a standard deviation equal to $0.0004\bar{3}$. The second disturbance is assumed to be a variation of the water density, which can be assumed originating either from the FAs bowing or from the pump operational uncertainty, as done in Sargeni, Burn, and Bruna, 2016. The nominal coolant density is 0.700758 g cm^{-3} and its standard deviation is assumed to be 0.02102274 g cm^{-3}. Due to the difficulty in evaluating the probability of this water density variations, it is assumed that this parameter has a uniform distribution between ±3% of the nominal value, following again Sargeni, Burn, and Bruna, 2016. The Probability Density Functions (PDFs) for both the parameters is reported in fig. 6.9.

As briefly discussed above, if the ROM was designed to be "monolithic", the training process would be very expensive, since the input parameter space is very large and the cost of each calculation would include both the cell calculation, which is the most expensive in this specific case, and the full-core simulation. On the contrary, if a two-step approach was employed, it could be possible to split the training phase in two stages, each benefiting of the specific features of each model. The choice of tailoring the ROM according to the peculiarities of the FOM follows a popular principle suggested by Vapnik, who gave fundamental contributions to the development of the Support Vector Machine method (Cortes and Vapnik, 1995):

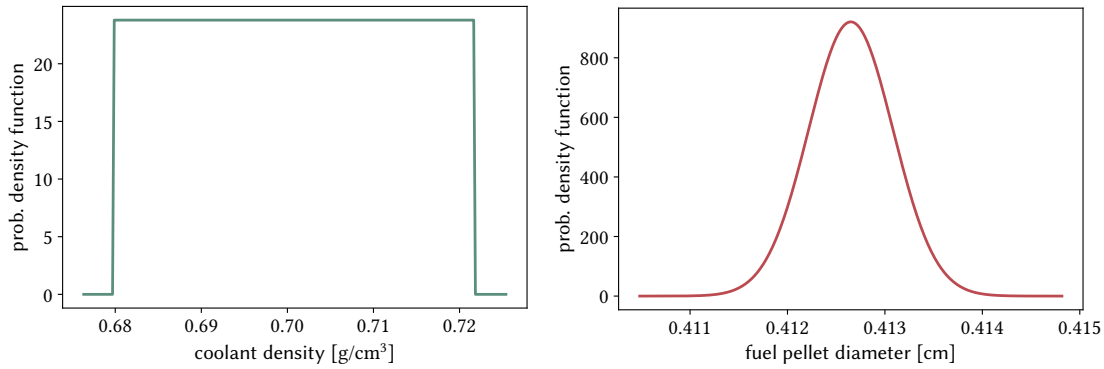

Figure 6.9: *Distributions considered for the uncertainties in the physical input parameters for the lattice calculation.*

> *When solving a problem of interest, do not solve a more general problem as an intermediate step.*

Since, in this case, the cell calculation performed with Monte Carlo is the most computationally expensive, this strategy allows to simplify the input parameter space, decoupling the aspect of the perturbation location in the reactor, which is the most challenging aspect of the problem, and the intensity of the perturbations, which are more relevant for the generation of the few-group constants. Of course, the response of the full-core diffusion model would depend both on the kind of perturbation, through the few-group parameters, and on the location of the perturbations, but each set of perturbed cross sections and diffusion coefficients would be generated with a small effort by the cell ROM.

In the following section, the cell and the full-core ROMs are presented and their performances in terms of accuracy and computational efficiency are discussed.

6.2.2 Non-intrusive model reduction for the cell calculations

Since each of the two input parameters for the cell calculations follows a statistical rule, the polynomial chaos expansion is selected to generate the surrogate model for the generation of the few-group data. This approach and the motivations behind this choice are described in section 6.2.2.1.

6.2.2.1 The Polynomial Chaos Expansion method

The Polynomial Chaos Expansion (PCE) is a very popular technique for Uncertainty Quantification (UQ) and Sensitivity Analysis (SA) that was first suggested by Wiener, 1938 and then extended and rigorously formalised by Xiu and Karniadakis, 2002. After this seminal work, this technique has been extensively tested for several applications, proving its flexibility in a wide range of applications., including reactor physics.

To the author's knowledge, the first application in this field traces back to M. M. R. Williams, 2007, who discussed the application of PCE for the solution of the neutron diffusion equation in presence of spatially random cross sections. Then, this technique has been applied to approach several problems, especially concerning the propagation of the uncertainties through neutron transport (Gilli, Lathouwers, et al., 2013) and multiphysics calculations (Santanoceto, Tiberga, et al., 2021).

The basic idea of the PCE approach, which belongs to the class of spectral methods (Canuto, Hussaini, et al., 2007), is to express a stochastic model $\mathcal{M}$ in terms of an expansion of orthogonal polynomials Ψ,

$$\mathcal{M}(\vec{s}, t, \vec{p}) = \vec{y} = \sum_{k=0}^{\infty} \vec{a}_k(\vec{s}, t)\Psi_k(\vec{p}) \approx \sum_{k=0}^{K} \vec{a}_k(\vec{s}, t)\Psi_k(\vec{p}), \tag{6.7}$$

where $\vec{s}$ is the vector of the state variables (e.g., spatial coordinates and energy), t is the time, $\vec{p}$ is the vector of stochastic parameters (in this case, the pellet diameter and the water density) and a_k is the k-th expansion coefficient, which is obtained by means of a projection, weighted on the random variable distribution $w(\vec{p})$, of the model on the k-th basis function, namely

$$\vec{a}_k(\vec{s}, t) = \int_{-\infty}^{+\infty} d\vec{p}\mathcal{M}(\vec{s}, t, \vec{p})\Psi_k(\vec{p})w(\vec{p}). \tag{6.8}$$

The choice of the orthogonal polynomial basis is determined by the distribution of the random variables.

If the vector of random input parameters was constituted by independent random variables, the multivariate polynomial basis would be defined as

$$\Psi_k(\vec{p}) = \prod_{i=1}^{d} \psi_i(p_i), \tag{6.9}$$

where d is the number of independent random variables.

The calculation of the projection coefficients, whose number depends both on the desired polynomial order K and on the number of independent random variable d, can be carried out following different strategies.

Concerning non-intrusive procedures, which allow to treat the model $\mathcal{M}$ as a black-box, it is possible to identify two general procedures (Kaintura, Dhaene, and Spina, 2018), namely:

- *the pseudo-spectral approach*, which consists in approximating (6.8) through a quadrature rule,

$$\vec{a}_k(\vec{s}, t) = \int_{-\infty}^{+\infty} d\vec{p}\mathcal{M}(\vec{s}, t, \vec{p})\Psi_k(\vec{p})w(\vec{p}) \approx \sum_{i=1}^{I} \mathcal{M}(\vec{s}, t, \vec{p}_i)\Psi_k(\vec{p}_i)w(\vec{p}_i); \tag{6.10}$$

- *the least-square regression approach*, which consists in approximating the PCE coefficients $\vec{a}_k$ through a least-square fit.

One of the advantages of the first approach is that, in many situations, a limited number of points is sufficient to provide a good estimate of eq. (6.8). For example, in a few dimensional problem, the Gauss quadrature would allow to integrate exactly all the polynomials with a degree $2n-1$ or less with n model evaluations. On the contrary, the accuracy of the regression approach would depend on the choice of the model samples, thus it would be more difficult to assess its adequateness. As expressed in eq. (6.9), when the input vector $\vec{p} \in \mathbb{R}^d$ is constituted by independent random variables, the multivariate polynomials would be expressed as a product of univariate polynomials, meaning that the number of their coefficients and, thus, the number of integral evaluations, would grow exponentially with the number of dimensions, due to the so-called *curse of dimensionality* (Bellman, 1957). In this respect, the least-square regression could be more convenient than the pseudo-spectral method.

However, the use of sparse grids could mitigate this issue, making the adoption of the quadrature suitable also for relatively large values of d. The first application of these sparse grids is due to Smolyak, 1963, who observed that it is possible to get good estimates of integrals and interpolations on a high-dimensional cube, i.e. a hypercube, by selecting only the most important elements of the tensorial grid obtained combining each parameter. In this way, the growth rate of the points becomes polynomial instead of exponential. An intuitive explanation of the effectiveness of the sparse grids despite their limited number of points compared to the full tensor grid is that high-dimensional spaces does not behave as intuitively as 2D and 3D Euclidean spaces. Particularly, comparing the volume of a hyper-sphere with radius r with the one of a hyper-cube with edge $2r$ (Izenman, 2008), it is possible to find out that the volume of the sphere is negligible with respect to the one of the cube, which is simply $(2r)^d$,

$$\lim_{d\to\infty} \frac{V_{hypersphere}}{V_{hypercube}} = \frac{\pi^{d/2}}{\Gamma(d/2)d2^{d-1}} \to 0, \tag{6.11}$$

where Γ is the Gamma function. Since the hypersphere is inscribed inside the hypercube, this behaviour suggests that most of the volume of the hypercube is distributed in its corners, justifying the use of sparse grids. Moreover, since the distance between one corner and the centre of the hypercube is $r\sqrt{d}$, the volume of the hypercube tends to spread away from the centre as the space dimension gets higher and higher.

An advantage of using sparse grids is that, for some specific quadrature rules, they allow to realise nested levels of points, i.e. the higher-order levels contain all the preceding lower-order ones. Despite these rules do not achieve the same accuracy as the Gauss-Legendre quadrature, they allow to perform an adaptive quadrature, which can be improved with more points when needed.

Figure 6.10 shows the sparse grids constructed to get the model evaluations needed for the quadrature. On the left, it is possible to see the first four levels of quadrature

points, sampled with a combination of the Clenshaw-Curtis rule, appropriate for the uniform PDF related to the water density, and of the Genz-Keister rule, appropriate for the normal PDF associated to the pellet density. On the right, the 4^{th} level of the grid is showed distinguishing between positive and negative weights. In both figures, the size of the points is proportional to the absolute value of their weights. Because of this representation, it is not easy to notice the nodes beyond the dashed lines, which are located at $\pm 3\sigma_{p_D}$, where σ_{p_D} indicates the standard deviation of the normal distribution for the pellet diameter. The low values of these weights is due to the fact that the region inside the dashed lines covers up to 99.7% of the data, meaning that the values falling outside this range are extremely unlikely.

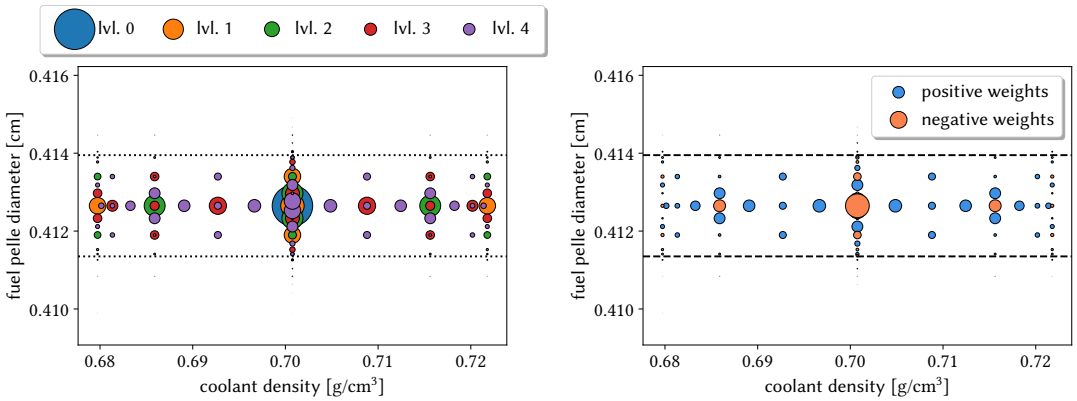

Figure 6.10: *Quadrature weights used in the pseudo-spectral projection. The size of the dots is proportional to their weight, while the dashed, horizontal lines cover the 99.7% of the area, i.e. they are located at $\pm 3\sigma_{p_D}$, where σ_{p_D} is the standard deviation of the pellet diameter.*

To better appreciate all the points in the sparse grid, fig. 6.11 reports both these points and a set of 161 points generated with Sobol's rule for the validation of the PCE model. In this case, the size of the nodes is not proportional to the weights, in order to appreciate also the points falling outside the range $p_D \leqslant \pm 3\sigma_{p_D}$. Sobol's rule generates a low-discrepancy, quasi-random sequence of points that obey to the statistical rules of each random variable. This sampling rule has been chosen because, although no validation point falls outside the region delimited horizontally by the two dashed lines, the points cover more uniformly the parameter space in the region with largest probability, allowing to check the performances of the PCE model more thoroughly.

6.2.2.2 Two-group constants generation

As specified previously in the chapter, the full order model for the cell calculation is represented by the Serpent 2 Monte Carlo code. As discussed in chapter 4, the choice of the regions to perform the spatial homogenisation is of paramount importance in order

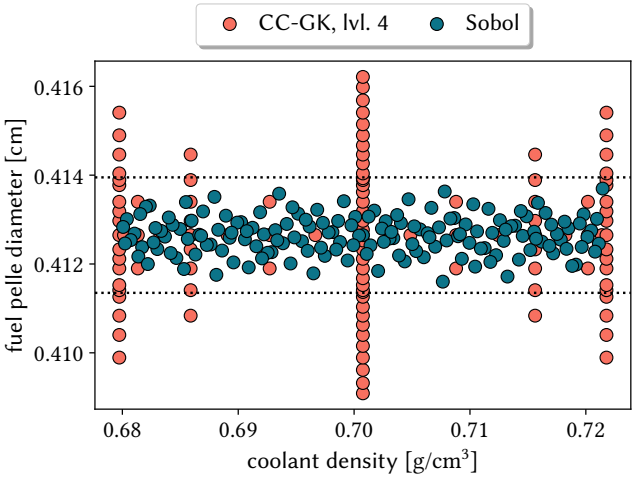

Figure 6.11: *Quadrature points used to construct the pseudo-spectral PCE model and 160 quasi-random testing points generated using Sobol's rule. The dashed, horizontal lines cover the 99.7% of the area, i.e. they are located at* $\pm 3\sigma_{p_D}$*, where* σ_{p_D} *is the standard deviation of the pellet diameter.*

to get accurate data for the full-core calculation.

Usually, the homogenisation is carried out at the assembly level, since it provides a sufficient spatial detail to represent the core behaviour. In particular, exploiting the low diffusion length of neutrons in a thermal system, a simplified system made of one or more types of FAs is considered for the homogenisation procedure, imposing reflective boundary conditions and then applying some leakage-correction model to take into account the effects of the flux gradients near the boundaries (Rahnema and Nichita, 1997). Although this approach is very popular, it is not suitable to get the constants for the inactive regions like the reflector or the borated water surrounding it. In order to get the effective constants for these regions, several strategies are possible, namely

- performing a full-core simulation;
- generating the constants for the inactive regions running a source-driven calculation using the energy spectrum featuring the fuel lattice;
- considering a simplified system composed by an active region and the other inactive regions.

The first strategy would definitively be the most accurate one, but also the most computationally expensive, especially for the Gen-III+ systems, which are featured by a large dominance ratio. In this case, the higher accuracy of this approach would not be worth the price of the large number of inactive neutron histories needed for a good fission source convergence (De Mulatier, Dumonteil, et al., 2015), especially since more than one calculation would be required for the PCE model training.

The second strategy is much more affordable to generate the cross sections for the inactive regions with a sufficient accuracy. However, since the aim of the Serpent model is to evaluate the two-group constants for different input perturbations affecting the FAs, this approach would not be viable. As a matter of fact, the most sensitive regions to localised perturbations are the outer ones, close to the reflector, where the flux is maximum. Therefore, in order to take into account the spectral and spatial effects induced by the reflector on these assemblies, the cell model should include the fuel and the reflector as well, as proposed in the third strategy.

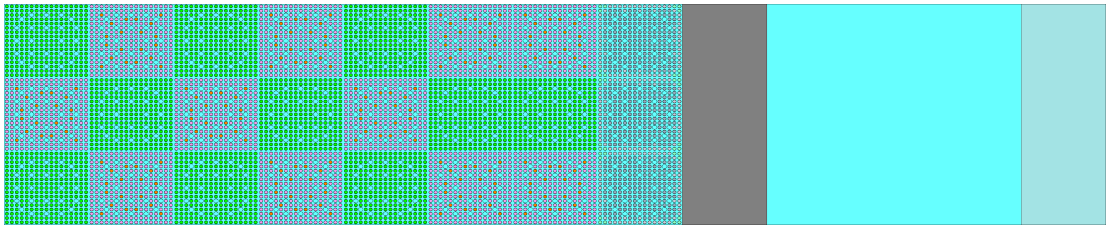

Figure 6.12: *Sketch of the 2D system used to generate the two-group constants with Serpent 2. From left to right, it is possible to see the fuel assemblies, the heavy stainless-steel reflector (grey), the water baffle (cyan) and the external boron layer (cerulean) used to simulate the vacuum boundary conditions.*

Figure 6.12 represents the simplified reactor model used to generate the group constants, which is a portion of the full-core model in fig. 6.7 with reflective boundary conditions. This choice allows to consider all the most relevant FAs and inactive regions featuring the system reducing as much as possible the core dimension and, thus, its dominance ratio. Since Serpent does not allow to specify different boundary conditions for different surfaces, an additional layer of assemblies filled with water with a higher boron concentration has been added at the boundary, in such a way that the flux practically vanishes in that region, decoupling the system from its "mirrored" version on the right side. Figure 6.13 shows the ratio between the energy flux spectrum evaluated with the simplified and the one computed with the full-core models. Except for the borated water region, which is a region featured by a low neutron importance, the spectrum of the simplified model is very close to the one evaluated with the full-core calculation, justifying the adoption of such approach to generate the few-group constants.

A delicate aspect concerning the model reduction in a Monte Carlo simulation framework that should be carefully taken into account is the fact that each output is affected by statistical uncertainty. Usually, model reduction is applied to deterministic models, so the possibility to have uncertain outputs is often not considered. The PCE model is designed to deal with uncertain output responses, but, in this case, it is not possible to associate the output samples from the sample average normal distribution to an input parameter. Some techniques could be used to overcome this issue, e.g., bootstrapping.

However, since the aim of this work is to develop a computationally efficient model

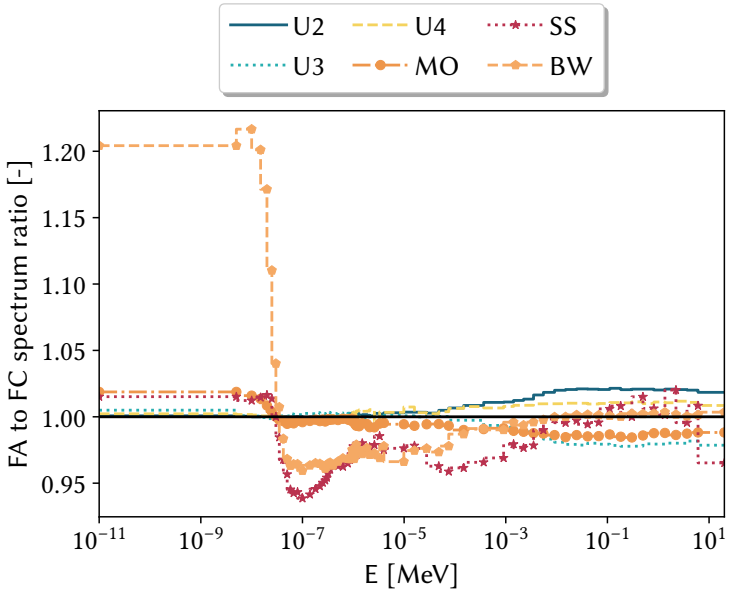

Figure 6.13: *Ratio between the flux energy spectrum computed with the simplified geometry and the spectrum evaluated with the full-core model.*

that could be applied to a general industrial code, this specific aspect will not be taken into account, as, in general, the cross section and diffusion coefficient generation is carried out using deterministic cell codes. Thus, each Monte Carlo calculation is carried out minimising the statistical uncertainty of the outputs to an acceptable level, so that their impact on the quality of the results is negligible for this specific application.

Figure fig. 6.14 shows the convergence trends for the Shannon entropy and the k_{eff} as a function of the number of neutron cycles for different combinations of active and inactive cycles, which are delimited by the vertical lines in the graph, using 10^6 neutrons per cycle. The convergence behaviour of these parameters and the statistical error of the group-constants of interest have been considered acceptable with 200 inactive cycles and 300 active cycles, so each simulation used to train the PCE model relied on these neutron population settings. As a further confirmation, it has been then verified that the output variations due to the physical parameter perturbations are not covered by the statistical noise in the results.

With these settings, each Serpent simulation requires, on average, about 3 hours with 16 CPUs (2x Intel Xeon Scalable Processors Gold 6130 2.10 GHz).

6.2.2.3 Model training and validation

The PCE model construction discussed in this section is carried out exploiting the open source Python library *chaospy* (Feinberg and Langtangen, 2015), which offers a

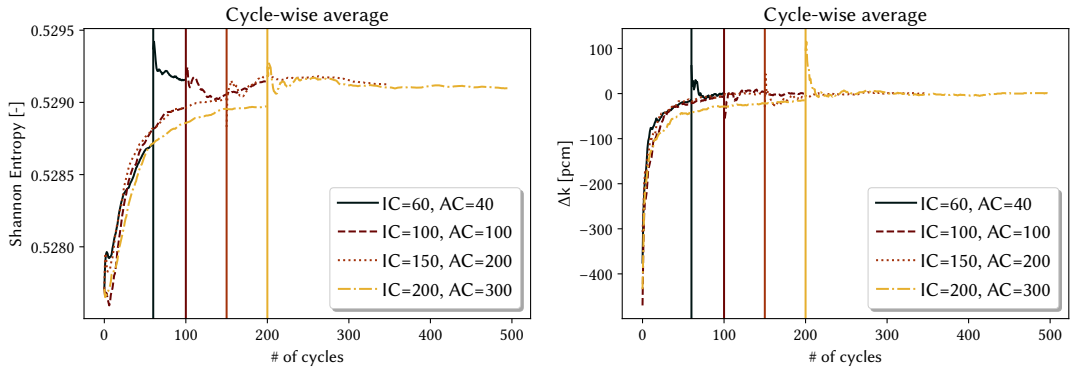

Figure 6.14: *Convergence trend for the Shannon entropy.*

complete pipeline for the ROM training. Among the wide selection of sampling techniques and PCE-based methods, the deterministic sampling approach based on the Smolyak sparse grids is chosen and, as discussed previously, the Pseudo-Spectral (PS) projection is selected to evaluate the coefficients of the chaos polynomial. In parallel with the data generation for the training phase, about 160 model evaluations are performed using a low-discrepancy sequence generated with the Sobol rule.

The number of the PCE coefficients scales as the number of input random variables times the order of the polynomial. Therefore, the calculation of these coefficients through the quadrature rule requires a larger and larger number of points for an accurate evaluation of the coefficients. While the Gaussian quadrature allows to integrate exactly one-dimensional polynomials up to degree $2n - 1$ using n model evaluations, the Clenshaw-Curtis rule (Clenshaw and Curtis, 1960) allows an exact integration with n nodes only up to order $n - 1$. Since in eq. (6.10) the basis functions Ψ_k are polynomials of order m and the model $\mathcal{M}$ is assumed to be smooth enough to be represented by an m^{th} order polynomial, the evaluation of the integral would require $2m + 1$ nodes. Concerning the Genz-Keister (Genz and Keister, 1996) rule, the information concerning the exactness order is not available in the literature. Therefore, although the accuracy of the PCE model should increase as the expansion order increase, a compromise between the integration accuracy and the model expansion order should be accepted in practice for a fixed number of model evaluations, especially for high-dimensional problems.

Exploiting the fact that both rules allow to obtain nested sparse grids, the PCE model training is progressive, increasing, when needed, the accuracy level of the grid albeit minimising the number of new model evaluations. Excluding the 0^{th} order PCE, the first four levels of the sparse grid are employed to generate the PCE models ranging from 1^{st} to 4^{th} order.

Figure 6.15 shows the percentage Root-Mean Square Error (RMSE) computed between the PCE model evaluations and the validation set for different orders of the polynomials. The trend of the RMSE clearly shows the need for a compromise needed between the polynomial order and the accuracy required to evaluate its coefficients. From

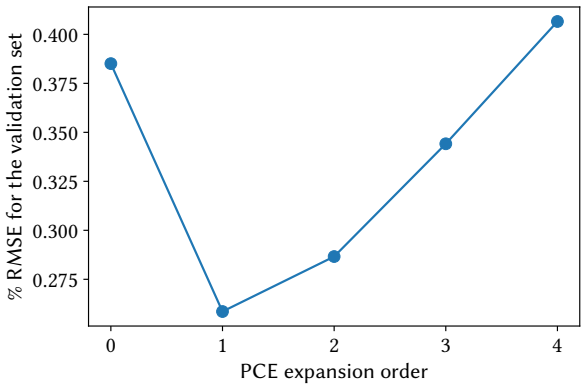

Figure 6.15: *RMSE between the PCE models evaluations and the validation set, sketched in fig. 6.11.*

another perspective, the curve is a clear example of the Occam's Razor principle (Bargagli Stoffi, Cevolani, and Gnecco, 2022), according to which simpler models should be preferred to complex ones when all the other conditions are equal (in this case, the validation set). Since this is one of the golden rules in the reduced-order modelling framework to resolve the *dilemma* between low-variance, highly specialised, biased models and high-variance, low-biased models (Geman, Bienenstock, and Doursat, 1992), the first-order PCE model is selected as a surrogate for the cell calculations performed with Serpent.

Figures 6.16 and 6.17 seem to further justify this choice. Despite a slight statistical noise affecting some of the parameters, the linear PCE seems the most adequate in representing the full-order model response, especially the dependence to the pellet diameter random variable. As it can be clearly seen in fig. 6.17, the quadratic PCE fails to represent the data falling outside the range $\pm 2\sigma_{p_D}$, represented by the dashed vertical lines.

In light of these considerations, one could argue that the adoption of a PCE reduced-order modelling framework could have been avoided using a much simpler model, e.g., a linear regression. However, it is important to remark that, in a general problem, one does not know *a priori* the general behaviour of a model with respect to a set of input parameters, especially when their number is large and they follow some statistical distributions. Despite this is a simplified problem, the objective of this work is to provide a computationally efficient framework that could be extended to more complex problems. Thus, the fact that the PCE allows to obtain a linear model should be interpreted as a positive feature of this approach.

Moreover, since the dependence between the input parameters and the few-group constants is, in general, non-linear, the linear relationship between input and output is probably a consequence of the small input variations ($\approx$ 0.1 % for the pellet diameter,

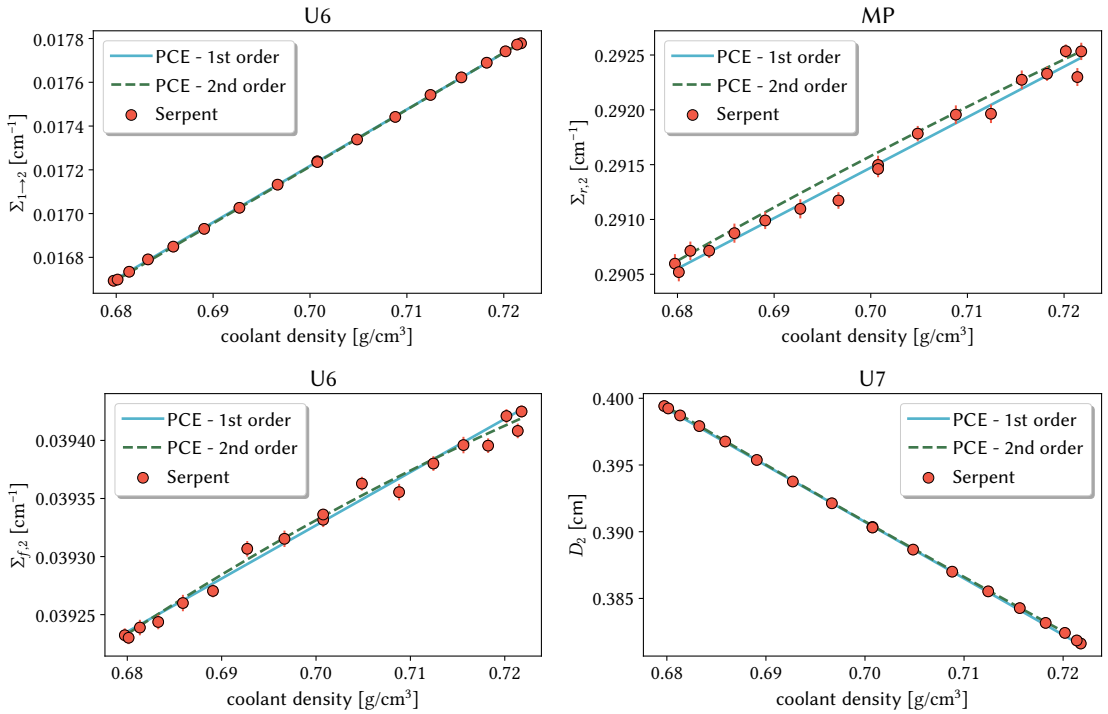

Figure 6.16: *PCE fitting and full-order model evaluations as a function of the coolant density for different FAs. The pellet diameter is considered at its nominal value, 0.41265 cm. U6 indicates the 2.1% enriched UOx FAs, U7 indicates the 3.2% enriched UOx FAs and MP indicates the MOx FAs.*

≈ 3% for the coolant density), thus the linearity may not hold anymore if the uncertainty range should become larger. With respect to other simplified models, e.g., the perturbation analysis, the PCE model could be naturally extended to a non-linear case, for example if the few-group data dependencies on the burn-up and the temperature were accounted for. Nevertheless, this extension will not be addressed in this chapter, leaving it as a future development for this activity.

Concerning the validation phase, the quadrature nodes that are not employed in the model training, i.e. the evaluation of the polynomial coefficients through integration, are added to the validation set. The main advantage of this choice is the fact that, contrarily to the points generated with the Sobol rule, these nodes cover also the most unlikely parameter region, improving the reliability of the evaluation of the modelling error.

The overall quality of the PCE model is acceptable for the intended application, as it can be noticed by inspection of fig. 6.18, which shows the % relative error between the PCE and the Serpent output for some selected responses of the validation simulations. Most of the points are featured by an error which is by far lower than 0.1 %, as displayed by the error distributions in fig. 6.19, where the dashed, vertical lines indicate the values

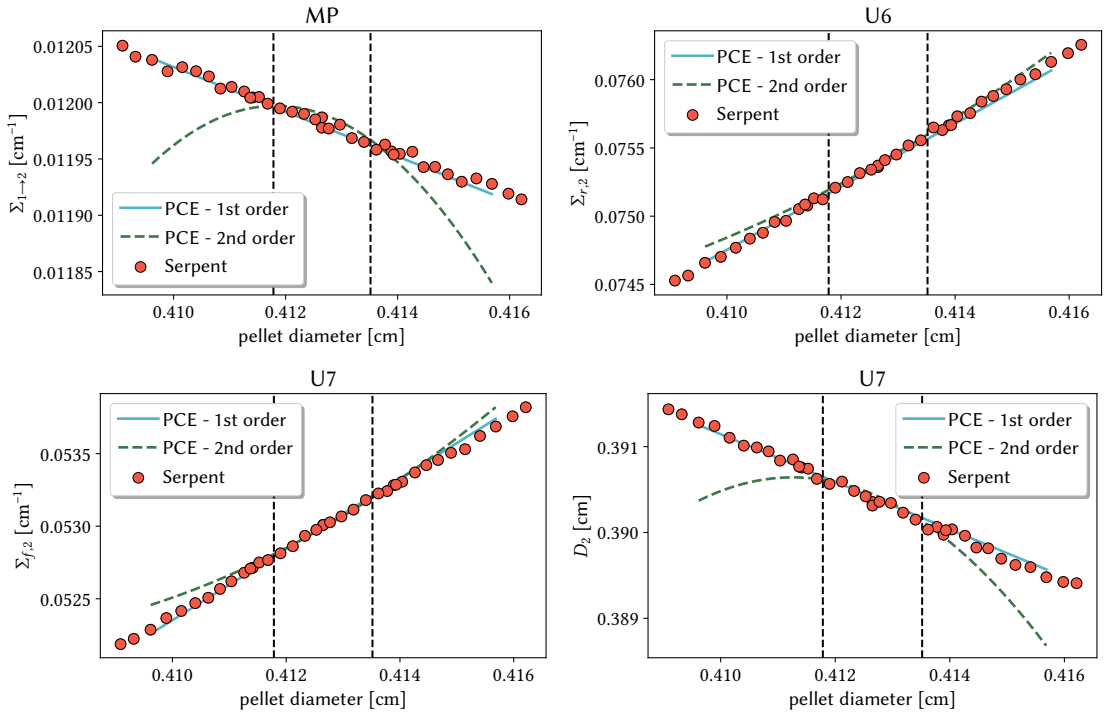

Figure 6.17: *PCE fitting and full-order model evaluations as a function of the pellet diameter for different FAs. The coolant density is assumed to be at its nominal value,* 0.700758 g cm^{-3}. *U6 indicates the 2.1% enriched UOx FAs, U7 indicates the 3.2% enriched UOx FAs and MP indicates the MOx FAs.*

±0.05%. In general, the points featured by the largest error are the ones falling outside the range $\pm 2\sigma_{p_D}$.

One of the advantages of the PCE approach is that its coefficients can be used to have a direct evaluation of the first-order Sobol's indices for each output response, defined as

$$S_i = \frac{\sigma_i^2}{\sigma^2[R]}, \tag{6.12}$$

where σ_i^2 is the variance obtained varying only the i-th parameter and $\sigma^2[R]$ is the total variance of the output response R. In general, the indices are normalised. In this particular case, they obey to the following relationship,

$$S_\rho + S_{p_D} + S_{\rho,p_D} = 1, \tag{6.13}$$

where S_ρ is the index associated to the coolant density, S_{p_D} is related to the pellet diameter and S_{ρ,p_D} is the index accounting for the mutual interaction of the two parameters. These figures of merit are fundamental in the framework of the Global Sensitivity Analysis (GSA) (Sudret, 2008), which estimates the relative importance of the various input parameters, and their correlation, in the determination of the output variance.

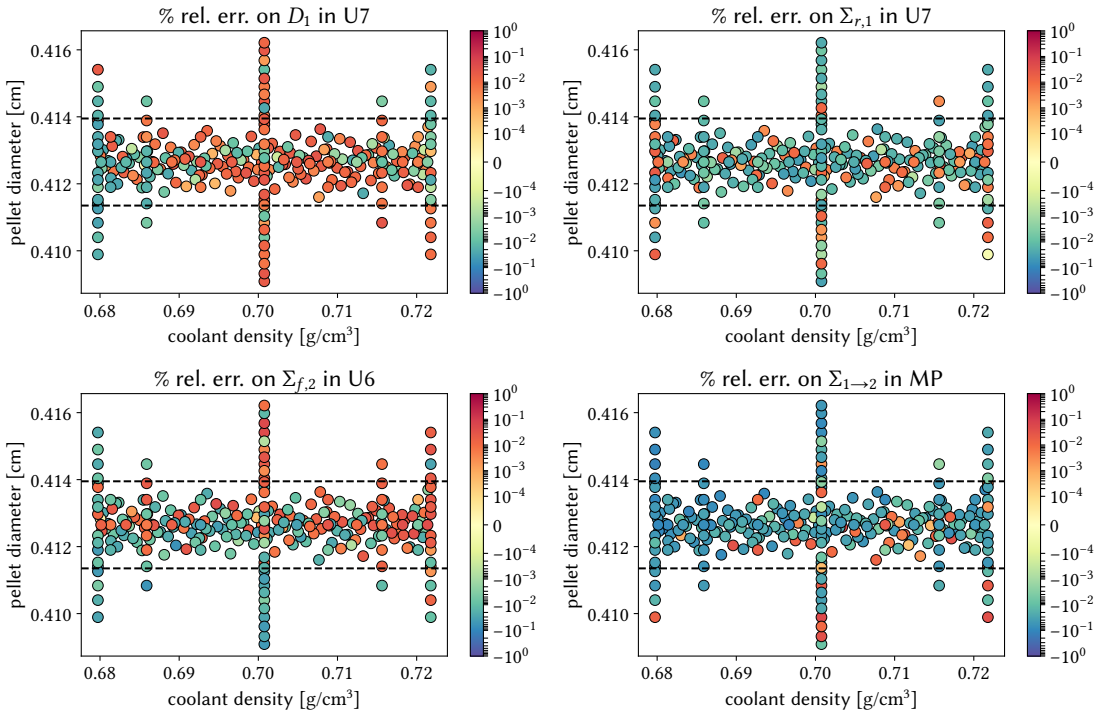

Figure 6.18: *% relative error between PCE and Serpent output for some selected responses. U6 indicates the 2.1% enriched UOx FAs, U7 indicates the 3.2% enriched UOx FAs and MP indicates the MOx FAs.*

In this case, it is interesting to notice that, except for the diffusion coefficients, the most important uncertain parameter is the coolant density. In addition to its largest relative variation, this parameter is tightly related to the moderation, which strongly alters the flux energy spectrum at the cell level. The overall low sensitivity of the two-group data to the fuel pellet diameter can be explained by its small relative variation with respect to the coolant density. The fact that the diffusion coefficient is more sensitive to the fission cross sections can be explained by a competing phenomena involving the moderation and the spatial self-shielding featuring the fuel pins (M. L. Williams, 2011). For a given coolant density, perturbing the pellet diameter alters the coolant-to-fuel volume ratio inside the cell, which has a non-negligible impact on the mean free path of the particles inside the system and, thus, on their diffusion coefficient. Since the neutron penetration inside the fuel mostly occurs in the outer region, due to the self-shielding, slightly changing the pellet diameter does not significantly impact the fission rate.

Finally, it can be appreciated that the mutual interaction of the two input variables has a negligible impact on the variance of the output responses: the largest index associated to the input parameter correlation is about 0.03 % and, as such, it could be appreciated in the figure.

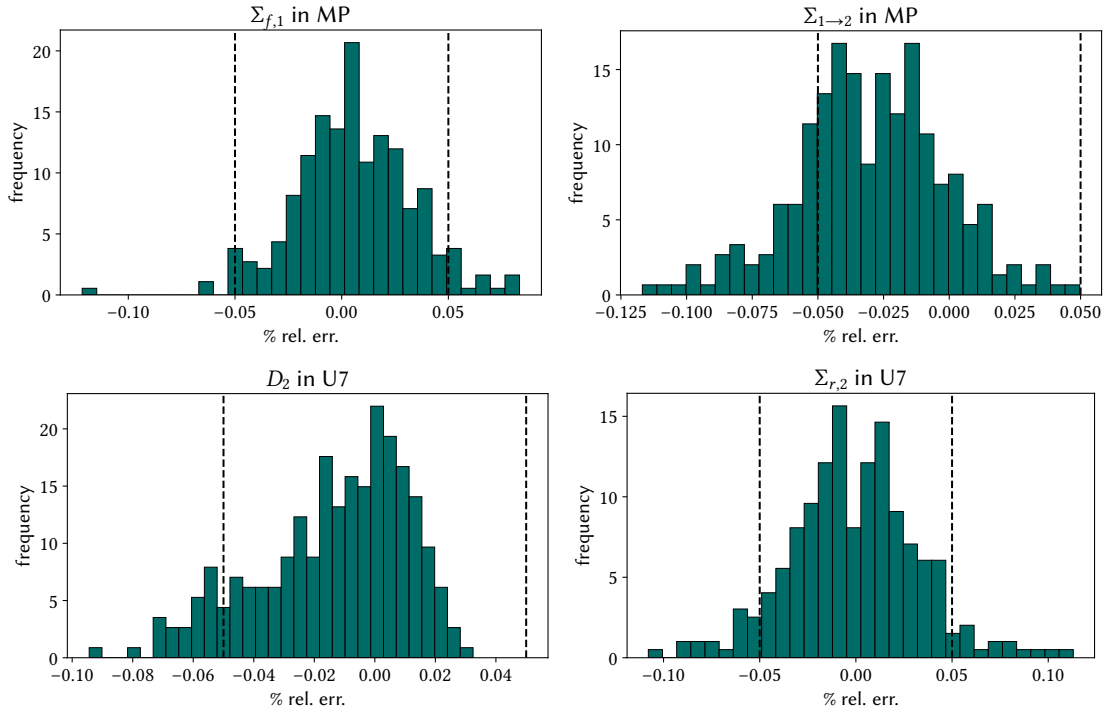

Figure 6.19: *Distribution of the % relative error between PCE and Serpent output for some selected responses. U6 indicates the 2.1% enriched UOx FAs, U7 indicates the 3.2% enriched UOx FAs and MP indicates the MOx FAs.*

6.2.3 Non-intrusive model reduction for the full-core calculations

In this section, the main aspects concerning the training and the validation of the full-core NIROM are discussed, focusing on the peculiarities of the problem under examination.

6.2.3.1 High-fidelity model of the UAM benchmark

Concerning the high-fidelity full-core model of the UAM benchmark, the finite element code FreeFEM++ (Hecht, 2012) has been selected for the solution of the two-group diffusion equation. Despite finite volumes and coarse-mesh methods are usually preferred for the numerical approximation of the neutron diffusion operator, this tool has been selected for several reasons, namely:

- it is open-source;
- it is optimised to handle strongly heterogeneous geometries like the one of the UAM benchmark;

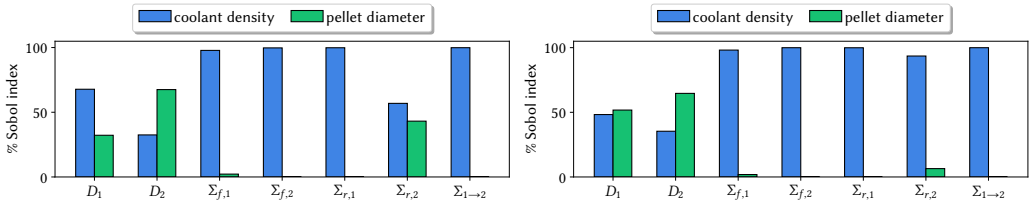

(a) *Sobol indices for the perturbed MOx FA.* (b) *Sobol indices for the perturbed UOx FA enriched at 3.2%.*

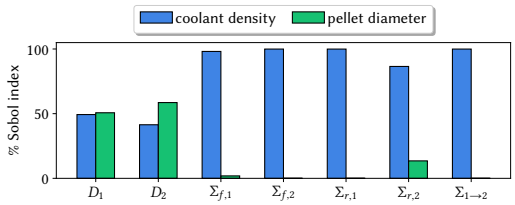

(c) *Sobol indices for the perturbed UOx FA enriched at 2.1%.*

Figure 6.20: *First-order Sobol indexes for each output model response.*

- both the computational mesh generation and the manipulation of the input and output fields are very fast and easy;
- it offers a wide number of wrappers to other computationally efficient libraries, like PETSc (Balay, Abhyankar, et al., 2020) and SLEPc (Hernandez, Roman, and Vidal, 2005), which are very efficient for the solution of eigenvalue problems, as pointed out in chapter 2.

On the right of fig. 6.21, the UAM benchmark sketch with the indication of the numbers used to indicate the various FAs is reported, while on the left the adapted computational mesh employed for the generation of the training and validation solutions is provided. The number of elements for this mesh was selected according to the results of a grid independence study, reported in fig. 6.22.

Using this mesh, composed by 632 430 elements, each finite element simulation requires about 3-5 minutes, according to the machine architecture, using 12 CPUs to parallelise the solution of the eigenvalue problem.

6.2.3.2 Definition of *ad hoc* sampling strategies

The selection of an adequate sampling strategy is of paramount importance for training an efficient and robust meta-model. To the author's knowledge, a specific sampling strategy adequate to handle the special feature of this application, i.e. the spatial dependence of the perturbations, does not exist in the literature. Therefore, since extending the usual sampling strategies for an input parameter space made of scalar quantities to

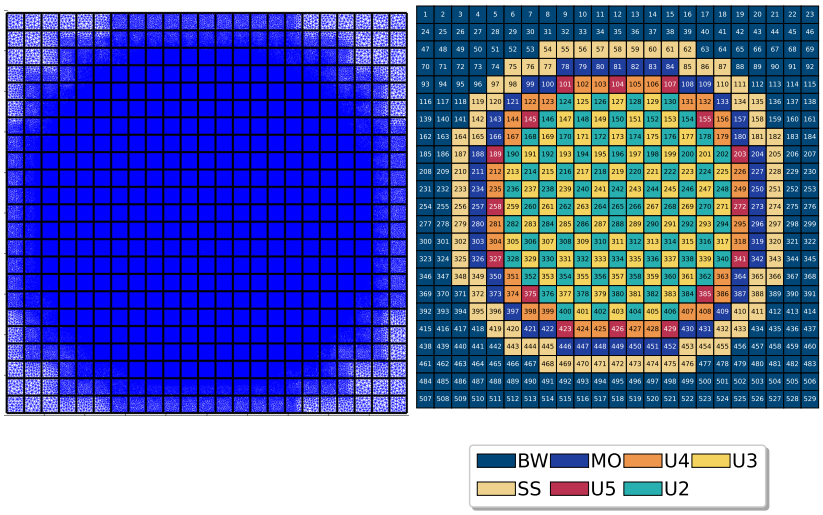

Figure 6.21: *Finite element mesh adopted for the full-core diffusion calculation (left) and sketch of the UAM core with the FA numbers (right).*

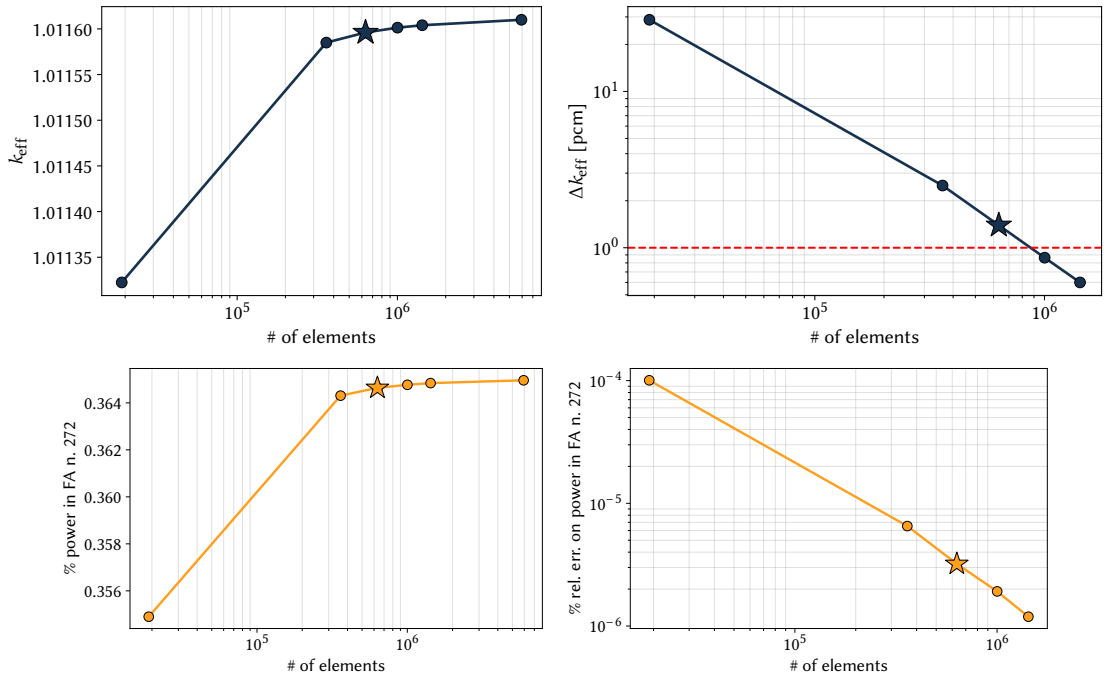

Figure 6.22: *On the left, spatial convergence trend for k_{eff} (top) and the total fission power in the FA number 272 (bottom). On the right, the relative error with respect to a reference calculation with $\approx 5.9 \times 10^6$ elements for k_{eff} (top) and the total fission power in the FA number 272 (bottom).*

this specific case is not straightforward, an *ad hoc* procedure is proposed in the following, trying to exploit the physical features of the problem.

The first aspect that is exploited in the definition of the sampling procedure is the fact that, from the point of view of the power production by fission, not all the neutrons diffusing in the reactor are equal: some of them are more important than others in contributing to the fission chain reaction. Therefore, it would be advisable to introduce the perturbations in the FA to which the fission source is more sensitive.

The concept of neutron importance Ψ, first introduced by (Usachev, 1956), is tightly related to the adjoint equation and its solution $\phi^\dagger$, which has been interpreted historically as a measure of the importance of one single neutron in contributing to the response of a certain detector or, for a critical system, to the fission reaction. Although the interpretation $\Psi = \phi^\dagger$ is the most popular one, it is possible to define also other importance functions in the frame of neutron transport (Tal, Israeli, et al., 2019). For example, in the framework of the Generalised Contributon Theory (M. Williams, 1991), the importance function can be defined as the product between the adjoint and the direct fluxes, namely

$$\Psi = \phi\phi^\dagger, \tag{6.14}$$

or as the product between the adjoint flux and the neutron density, namely

$$\Psi = \frac{\phi}{\mathrm{v}}\phi^\dagger. \tag{6.15}$$

Figure 6.23 reports the assembly-wise spatial distributions in each energy group for the direct and adjoint fluxes and for the neutron density, computed ensuring criticality through a proper normalisation of the fission operator by k_{eff}. Since the factor $1/\mathrm{v}_g$, $g = 1{,}2$ is spatially uniform, the spatial distribution of the direct flux and of the neutron density does not change, but, since $\mathrm{v}_1 >> \mathrm{v}_2$, the ratio between the thermal and the fast densities is reversed: the flux, i.e. the neutron track length per unit volume, is larger in the fast group, but the density, i.e. the number of particles per unit volume, is larger in the thermal group. Since the thermal adjoint in figs. 6.23e and 6.23f is larger than the fast one, the resulting importance function would be very different according to its definition.

The three assembly-wise importance function definitions can be appreciated in fig. 6.24. In all cases, the most important FAs are the peripheral ones featured by 2.1% enriched UOx, without Gd, where the flux achieves its peak. However, the importance of the other FAs strongly depends on the kind of definition employed. The one coinciding with the adjoint, obtained summing the group-wise adjoint fluxes, is more spatially uniform than the other ones. Thus, according to this definition, the neutrons generated in the inner FAs have roughly the same importance in sustaining the fission reaction. If the adjoint is weighted with the direct flux, the spatial heterogeneity effects increases, due to the sensitivity of the thermal flux to the FA composition. This effect is exacerbated when the adjoint is weighted with the neutron density, due to the largest weight associated to the thermal density.

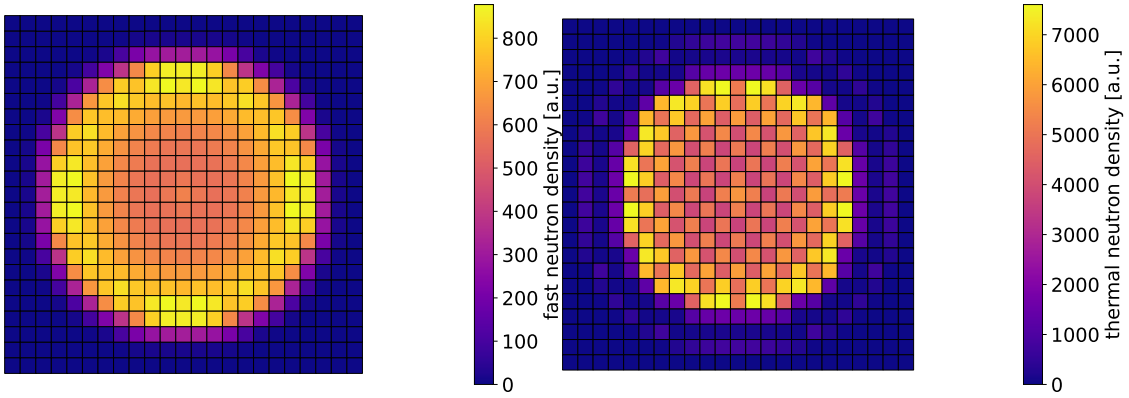

(a) *Fast neutron density.* (b) *Thermal neutron density.*

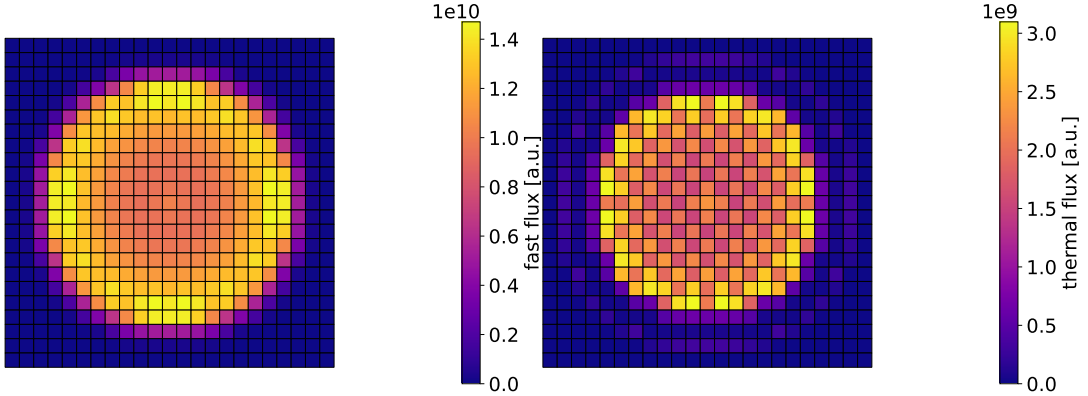

(c) *Fast neutron flux distribution.* (d) *Thermal neutron flux distribution.*

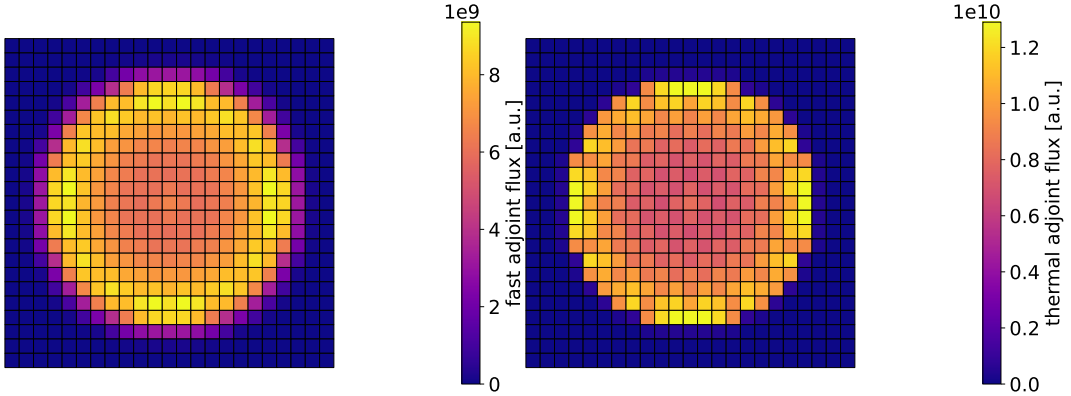

(e) *Fast neutron adjoint flux distribution.* (f) *Thermal neutron adjoint flux distribution.*

Figure 6.23

Since the last formulation is constructed weighting the adjoint on the actual number of particles inside each FAs, this definition is considered to be the best candidate for the definition of the probability density function for sampling the location of the perturbed FAs. The assembly-wise distribution of the resulting PDF is reported in 6.25,

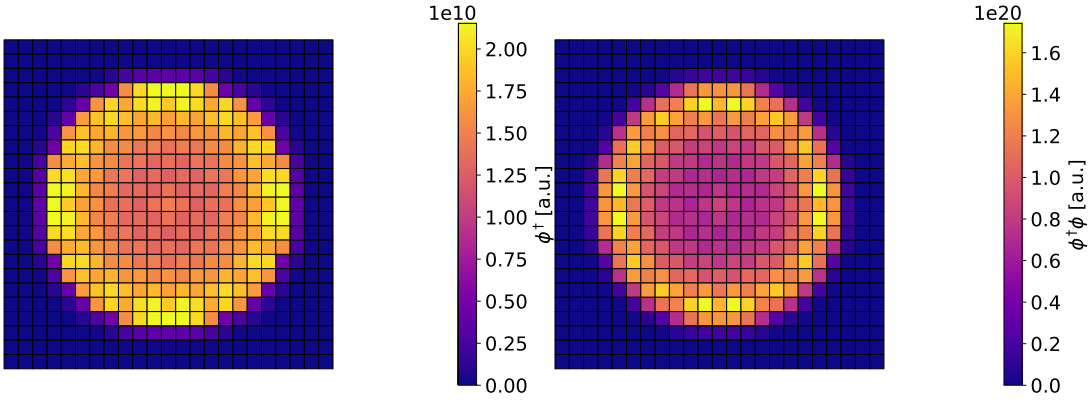

(a) *Importance function* Ψ *defined as* $\phi^\dagger$.

(b) *Importance function* Ψ *defined as* $\phi^\dagger\phi$.

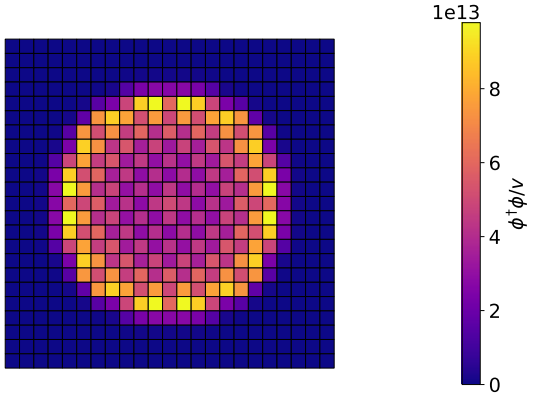

(c) *Importance function* Ψ *defined as* $\phi^\dagger \frac{\phi}{v}$.

Figure 6.24

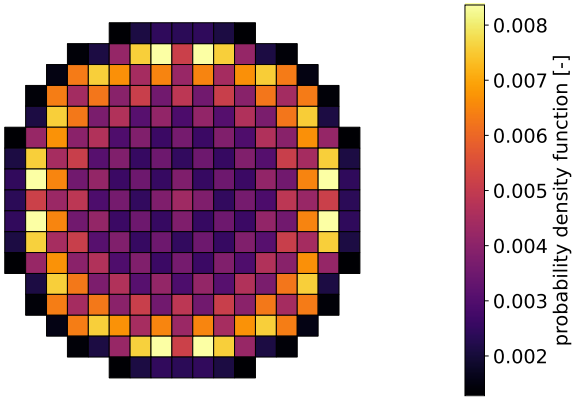

Figure 6.25: *Probability density function to sample the location of the perturbed FA.*

The other physical feature that could be exploited is the symmetry of the core, which could be used to increase the number of training data at basically no cost by means of

proper rotations of the solution. In this way, each FreeFEM++ calculation provides four solutions, one for each multiple of the rotation angle $\theta = \frac{\pi}{2} + k\frac{\pi}{2}$, with $k = 0, 1, 2, 3$. An example of this rotation procedure is visible in fig. 6.26. In order to emphasise the visualisation of the perturbation clusters, each one is represented by a single colour, although the FAs are featured by different few-group constants according to their type.

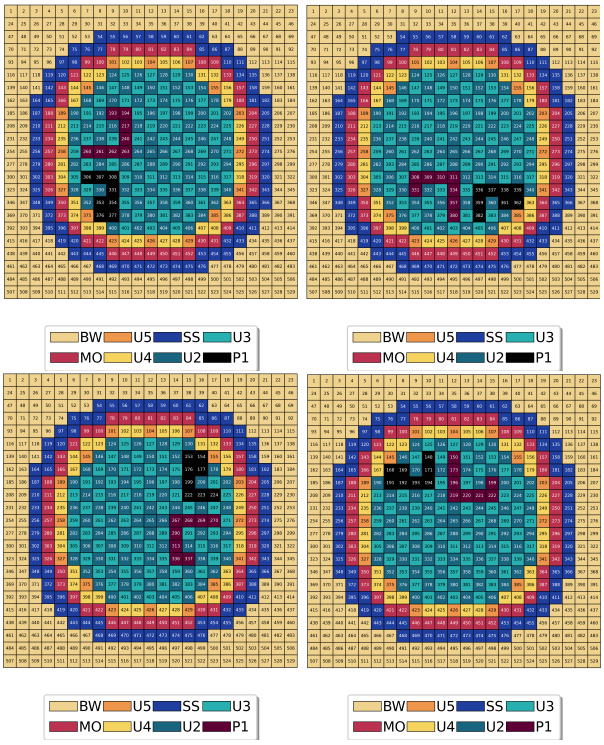

Figure 6.26: *Rotated perturbed configurations. The starting configuration (upper left) is progressively rotated with multiple of $\pi/2$ counter-clockwise.*

To induce the perturbation clusters visible in fig. 6.26, only the initial FA is sampled according to the importance PDF. Then, a FA among the north, east, south and west ones is selected randomly, and the procedure is iterated until the maximum number of perturbed FAs per each perturbation cluster is achieved. In this way, a kind of perturbation random walk is defined. Figure 6.27 provides a support to visualise the sampling strategy used to define the block of perturbed FAs. First, the number of perturbed FA is sampled from a uniform distribution defined among 6 and 10, included. Then, the initial FA, 103 in the figure, is sampled according to the PDF in fig. 6.25. Afterwards, the FA 126 is sampled among the equally probable FAs surrounding the FA 103. The red arrow indicate the direction of the disturbance random walk, while the white arrows indicate the other possible, non-sampled directions. The sampling process goes on until the number of perturbed FAs is achieved, verifying that each new configuration is not

contained in the previous samples. This check is more and more expensive as the number of samples grows, but it is necessary to avoid the generation of duplicate training data, which, in addition to the obvious waste of computational resources, would make the RBF kernel singular.

Each perturbation cluster is featured by the same perturbation intensities, which are sampled according to the joint PDF obtained combining the PDFs showed in fig. 6.9. The presence of blocks of FAs with the same perturbation is particularly reasonable because of the fact that a change in the coolant conditions would affect also the adjacent FAs, due to the cross flow phenomena. The same assumption is made for the fuel pellet diameter uncertainties, in order to reduce the number of possible combinations. For each perturbation, the corresponding set of two-group constants are generated using the PCE model, described in section 6.2.2.1.

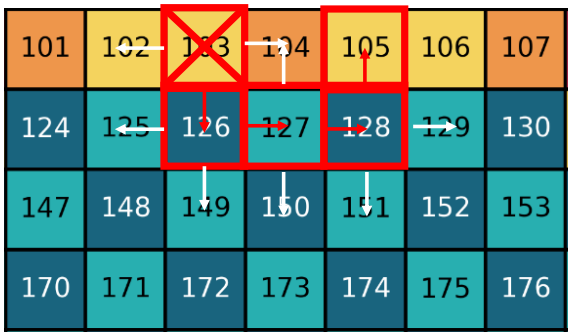

Figure 6.27: *Example of a perturbation random walk. The white arrows indicate the FAs that could be extracted, while the red arrows indicate the selected FAs. The red X indicates the starting FA.*

In spite of this simplifying assumption, the number of possible scenarios is still dramatic. First, the PDF for the extraction of the first FA is strictly positive for each FA, meaning that potentially every FA could be selected as the origin of the perturbation. Then, even though only some surrounding FAs can be selected to define the perturbation cluster, the total number of perturbed FAs can vary in the range 6-10, increasing the number of potential scenarios. As a further complication, more than one perturbation clusters may appear, each one featured by different values of coolant density and pellet diameter, which are random parameters themselves.

Due to the huge parameter space, two alternative strategies are proposed and tested in the following, in combination to the algorithm described above for the generation of the perturbation random walks:

1. a *full random sampling*, which consists in sampling both the spatial features of the perturbation and the perturbation intensities;

2. a *hybrid sampling*, which consists in using a random sampling for the spatial features of the perturbations and a deterministic rule, i.e. the Smolyak sparse grid,

for the intensity of the perturbations.

The advantages and disadvantages of these methods will be discussed later in more detail, but it is important to observe here their fundamental features.

The brute-force random sampling is simpler and more *naive* than the hybrid one, but it can be conveniently used to split the dataset into a training and a validation sets. Moreover, combined with the importance sampling, this approach could be still effective in providing a uniform mapping of the parameter space. Thus, this technique is used to generate a set of around 1125 scenarios (4500 effective scenarios, considering the solution rotations), each featured by a random number of batches, a random number of FAs per batch and a random perturbation intensity, i.e. the values of coolant density and pellet diameter, per batch.

The hybrid sampling is more involved, but it allows a better control of the random physical parameters, enabling also to perform an adaptive training with the nested sparse grids. This feature would be very important, because it would allow to progressively take into account the super-position of different perturbations at the same time. An inspection of fig. 6.10 would be useful to notice that the lower-order levels of the grid are constructed by varying only one parameter and leaving the other unperturbed, meaning that, to have simultaneous perturbations, the level of the grid should be larger than 2. For larger number of parameters, this value would increase.

Notwithstanding its nice features, some precautions are needed to reduce the effects of the curse of dimensionality: since each perturbed batch is featured by an independent perturbation intensity, the number of configurations would scale exponentially with the number of deterministic points used to map the perturbation intensity. For example, if the second level of the Smolyak sparse grid was used to map the pellet diameter and the coolant density, 17 points would be generated, as in fig. 6.10. Since each perturbation batch would be featured by 17 values of the physical parameters, the number of configurations would scale as 17^b, where b is the number of batches considered.

Table 6.1: *Example of sampling scaling when the second level of the Smolyak sparse grid is defined for each batch independently or considering as input parameters all the density-diameter couples per each batch.*

n. batches	batch-wise sampling	global sampling
1	17	17
2	289	49
3	4913	97
4	83521	161

To avoid this behaviour, it is possible to profit by the polynomial scaling of the Smolyak algorithm, considering a higher-dimensional input space composed by $2b$ parameters, where 2 refers to the density and to the diameter inputs. In this way, only

an optimal subset of the possible 17^b combinations would be selected by the Smolyak algorithm. Table 6.1 provides the number of samples obtained following the batch-wise and the global sampling. As expected, the batch-wise sampling strategy is not affordable, while the other sampling strategy allows to achieve a massive reduction in the number of samples. On top of that, it is important to notice that each Smolyak level contains the 0^{th} level, i.e. the reference, unperturbed input. Therefore, excluding these points, the actual number of points is expected to be even lower. Even though, the number of training simulations required to map the core with four batches would be still very large, as 161 simulations are required for a single perturbation configuration. Because of this reason, the hybrid sampling is adopted in the following to analyse a simpler problem, featured by only one batch of perturbed FAs in each configuration, leaving the number of FAs and their location as free, independent parameters. For this problem, 32 independent spatial arrangements are considered, for a total of 1024 cases, considering the rotations and the 16 Smolyak points required per each arrangement.

6.2.3.3 Evaluation of the distance between the input parameters

Figure 6.28 and fig. 6.29 shows some examples of physical perturbations affecting the core, which is supposed to have a uniform density spatial distribution, being at the uniform temperature of 570 K, i.e. at hot zero power.

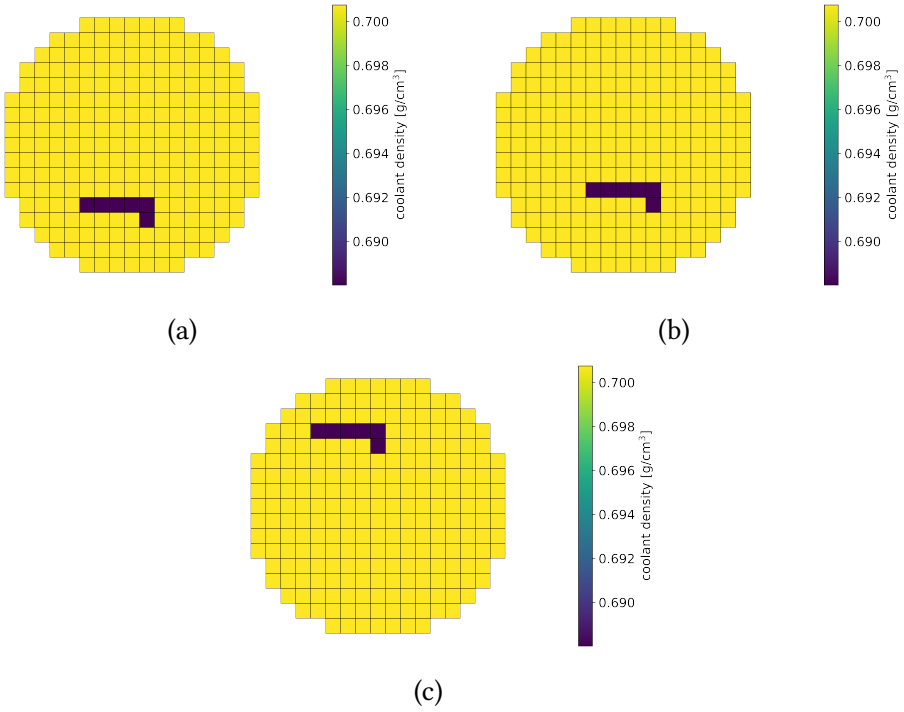

Figure 6.28: *Some configurations for a single perturbation in the coolant density distribution in the active FAs.*

The fact that the input parameters (coolant density and pellet diameter) are not scalar quantities but assembly-wise distributions poses the question of taking the spatial aspect into account during the RBF weights assignment. By inspection of the figures it appears manifest that, due to the linearity of the diffusion equation, the perturbations in figs. 6.28a and 6.29a will induce a neutron flux and fission power distributions quite close to the one induced by the perturbations in figs. 6.28b and 6.29b, respectively, being the perturbation intensity in each batch of FAs equal. On the contrary, it is reasonable to expect that the perturbation in figs. 6.28c and 6.29c would provide substantially different flux and power profiles, due to the location of the L-shape perturbation, which is placed in the northern part of the core instead of the southern one.

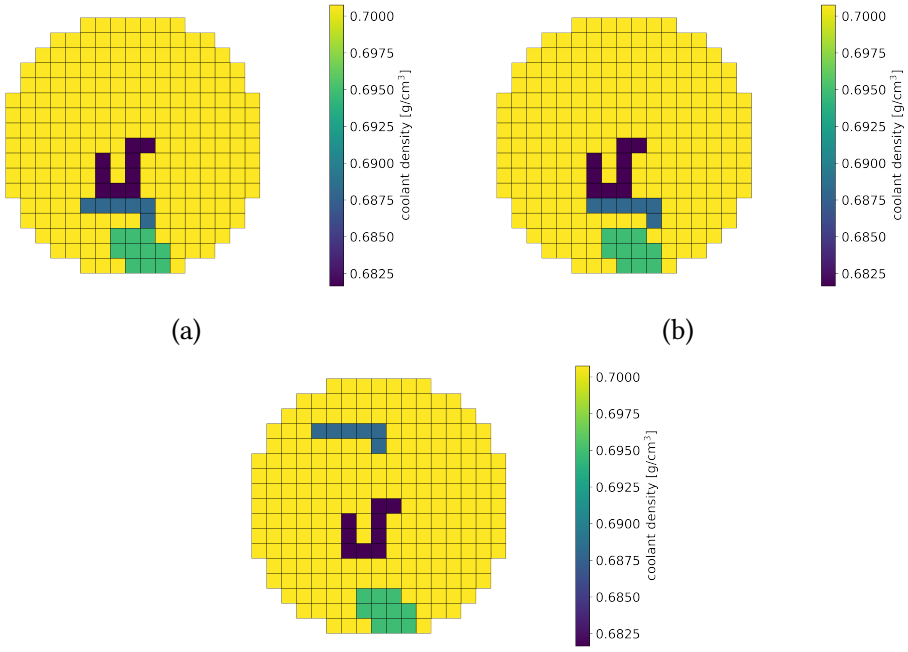

Figure 6.29: *Some configurations for multiple perturbations in the coolant density distribution in the active FAs.*

However, the resulting RBF weights do not follow this physical expectation when the usual L_2 norm is adopted to evaluate the distance $||\vec{p}_i - \vec{p}_j||_2$ between the various input parameter distributions. In particular, the Euclidean distance between fig. 6.28a and fig. 6.28c turns out to be equal to the one between fig. 6.28a and fig. 6.28b, 0.0442. Despite it contradicts the physical expectations, this result is fully consistent with the mathematical expression of the L_2 norm,

$$||\vec{p}_i - \vec{p}_j||_2 = \sqrt{\sum_{k=0}^{K} (\vec{p}_{ik} - \vec{p}_{jk})^2}. \tag{6.16}$$

Since the only non-zero differences would be found for the locations of the perturbed FAs, and both the perturbation intensity and the number of perturbed FAs are the same, also the resulting distance between the two input parameters would be the same. In case the perturbation intensity and the number of perturbed FAs were different, which is likely considering the dimensions of the input parameter space, the distance would certainly change, but it would not still be very sensitive to the spatial distribution of the input. For instance, the Euclidean distance between fig. 6.29a and fig. 6.29c would be around 0.0254, while the one between fig. 6.29a and fig. 6.29b would be around 0.0442, which are quite similar despite the spatial distributions are noticeably different.

Among the huge number of different metrics available in the literature, the so-called IMage Euclidean distance (IMED) (Wang, Zhang, and Feng, 2005) seems the most adequate to tackle this issue, due to its robustness to small perturbations and to its simplicity. Contrarily to the traditional L_2 norm, this metric accounts for the relative position of the different pixels composing an image thanks to a proper weighting matrix $\hat{G}$, which has to be positive definite,

$$||\vec{p}_i - \vec{p}_j||_{IMED} = \sqrt{(\vec{p}_i - \vec{p}_j)^\intercal \hat{G} (\vec{p}_i - \vec{p}_j)}. \tag{6.17}$$

Given an image defined in $\mathbb{R}^{N \times M}$, the g_{nm} element of the weighting matrix $\hat{G}$ is defined as

$$g_{nm} = h(||P_n - P_m||), \tag{6.18}$$

where $\mathrm{P_n}$ and $\mathrm{P_m}$ are the n-th and m-th coordinates of the pixel composing the image and h is a continuous function that should be monotonically decreasing when its argument $||\mathrm{P_n} - \mathrm{P_m}||$ increases. As in the reference paper, in this work the h function is chosen to be a Gaussian distribution, namely

$$g_{nm} = \frac{1}{2\pi\sigma^2} \exp\left(-\frac{||\mathrm{P_n} - \mathrm{P_m}||}{2\sigma^2} \right). \tag{6.19}$$

Although the IMED has been developed for image recognition algorithms, it can be easily extended to other multi-dimensional objects for which the relative position in space is important, considering the intensity of the field instead of the pixel colour. In this specific application, each input parameter can be cast as an object belonging to $\mathbb{R}^{X_N \times Y_M}$, where X_N and Y_M are the number of spatial points along the x and y coordinates, respectively. The application of the IMED to one-dimensional fields is trivial, since it would be sufficient to consider $Y_M = 1$, while the application to three dimensional fields, e.g., $\vec{p}(x, y, z)$, which is interesting for 3D full-core analyses, would require an extension of the IMED algorithm to three-dimensional images. This generalisation is not addressed in this work, but it is left as a future development to extend the applicability of this ROM framework to 3D full-core systems.

The IMED distance between the configuration in fig. 6.28a and the one in fig. 6.28c yields 0.027, while the one between fig. 6.28a and fig. 6.28b amounts to 0.009, proving

the higher sensitivity to the perturbation spatial pattern. The better performance of this metric can be verified also comparing the other perturbations depicted in fig. 6.29. The distance between fig. 6.29a and fig. 6.29c yields 0.0267, while the one between fig. 6.29a and fig. 6.29b yields, as expected, a lower value, 0.018.

The main disadvantage of the IMED algorithm is its higher computational cost compared to the traditional L_2 norm, since the distance evaluation requires to perform a vector-matrix-vector product, and the RBF approach requires to compute the distance between each pair of training data. However, exploiting the linearity of the algorithm, it is possible to apply a linear transformation to each input that allows to reduce the number of matrix-vector products. Exploiting a factorisation of the $\hat{G}$ matrix (Wang, Zhang, and Feng, 2005), the IMED turns out to be the classical Euclidean between two transformed variables $\vec{r}_i$ and $\vec{r}_j$, i.e.

$$\begin{aligned} ||\vec{p}_i - \vec{p}_j||_{IMED} &= \sqrt{(\vec{p}_i - \vec{p}_j)^\intercal \hat{G} (\vec{p}_i - \vec{p}_j)} = \sqrt{(\vec{p}_i - \vec{p}_j)^\intercal \hat{H}^\intercal \hat{H} (\vec{p}_i - \vec{p}_j)} = \\ &= \sqrt{(\vec{r}_i - \vec{r}_j)^\intercal (\vec{r}_i - \vec{r}_j)}, \end{aligned} \tag{6.20}$$

where $\hat{H}$ can be obtained either from SVD or from the eigenvalue decomposition of the weighting matrix $\hat{G}$.

Thanks to this property, the IMED can be naturally embedded non-intrusively in the ROM framework, just applying the linear transformation to each input before passing them to the POD-RBF algorithm. Figure 6.30 shows the smoothing effect obtained applying the $\hat{H}$ matrix to the input coolant density field.

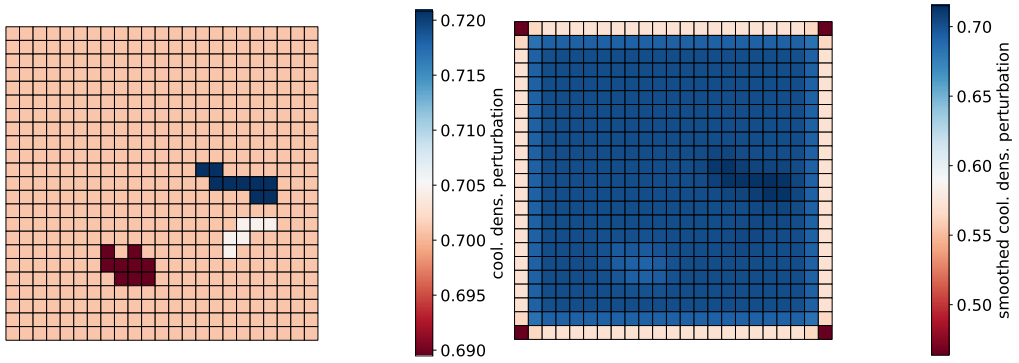

Figure 6.30: *Original (left) and smoothed (right) perturbed coolant density distributions.*

If the input parameters considered to train the ROM were the actual inputs for the diffusion model, i.e. the few-group constants, the smoothing effect would be more relevant for the thermal properties, featured by a stronger spatial variation, as visible in fig. 6.31. Concerning this case, it is possible to notice the appearance of an unphysical "stripe" in the thermal diffusion coefficient distribution. These values are not physical perturbations, but are a consequence of the fact that, to apply the IMED to the few-group data, each group-wise data is stacked in a vector of length $n_{data} N_x N_y$, where n_{data}

is the number of data and N_x and N_y are the number of assemblies in the x and y directions. Since each "image" is stacked one below the other to form a unique "image" for the IMED application, the linear transform $\hat{H}$ smooths the passage from one figure to the other. This aspect does not influence at all the distance between the parameters in this application, since each perturbation is applied only in the active region, where this effect does not occur. In view of other applications where this issue may be relevant, it could be possible to avoid it adding some dummy values between each data, which could be interpreted as adding some blank space between each figure.

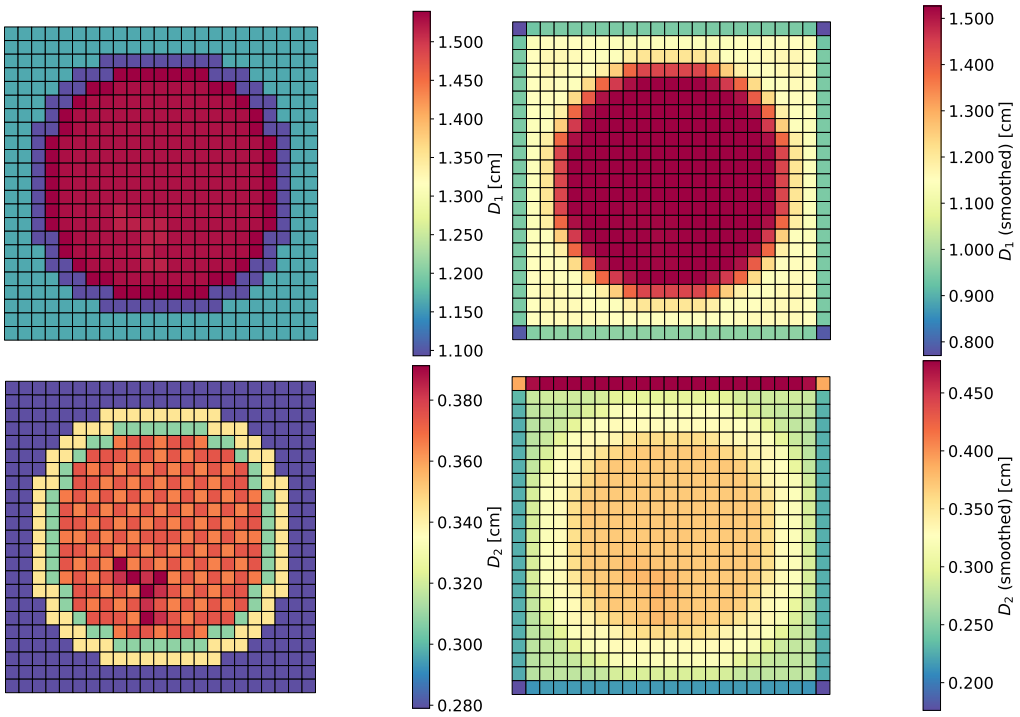

Figure 6.31: *Original (left) and smoothed (right) fast (top) and thermal (bottom) diffusion coefficient.*

Another challenging aspect of this application is the large dimension of the input data. In this case, which is featured by a low number of energy groups, $n_{data} = 7$, i.e. the two-group diffusion coefficients, production cross sections, removal cross sections and the slowing down cross section, while N_x and N_y are both equal to 23, for a total of 3703 values. Since the computational cost of the distance matrix evaluation is $\mathcal{O}(n^2)$, where n is the number of training snapshots, and this operation has to be performed several times in the RBF training process (see algorithm 3), the total cost would be prohibitive.

This issue can be effectively mitigated using the POD algorithm to reduce the input dimensionality, exploiting its redundancies. Since the POD is linear, the overall IMED

does not change if the reduction is applied to the smoothed input data, making the combination of these two methods straightforward. In fig. 6.32 it is possible to appreciate the first three POD modes of the thermal fission production cross section $\nu\Sigma_{f,2}$. Concerning the criterion adopted to select the number of POD modes, a very strict truncation error (10^{-12}) is considered, in order to ensure a sufficiently accurate data representation in the reduced-order space and, thus, a precise evaluation of the distance between the various input perturbations.

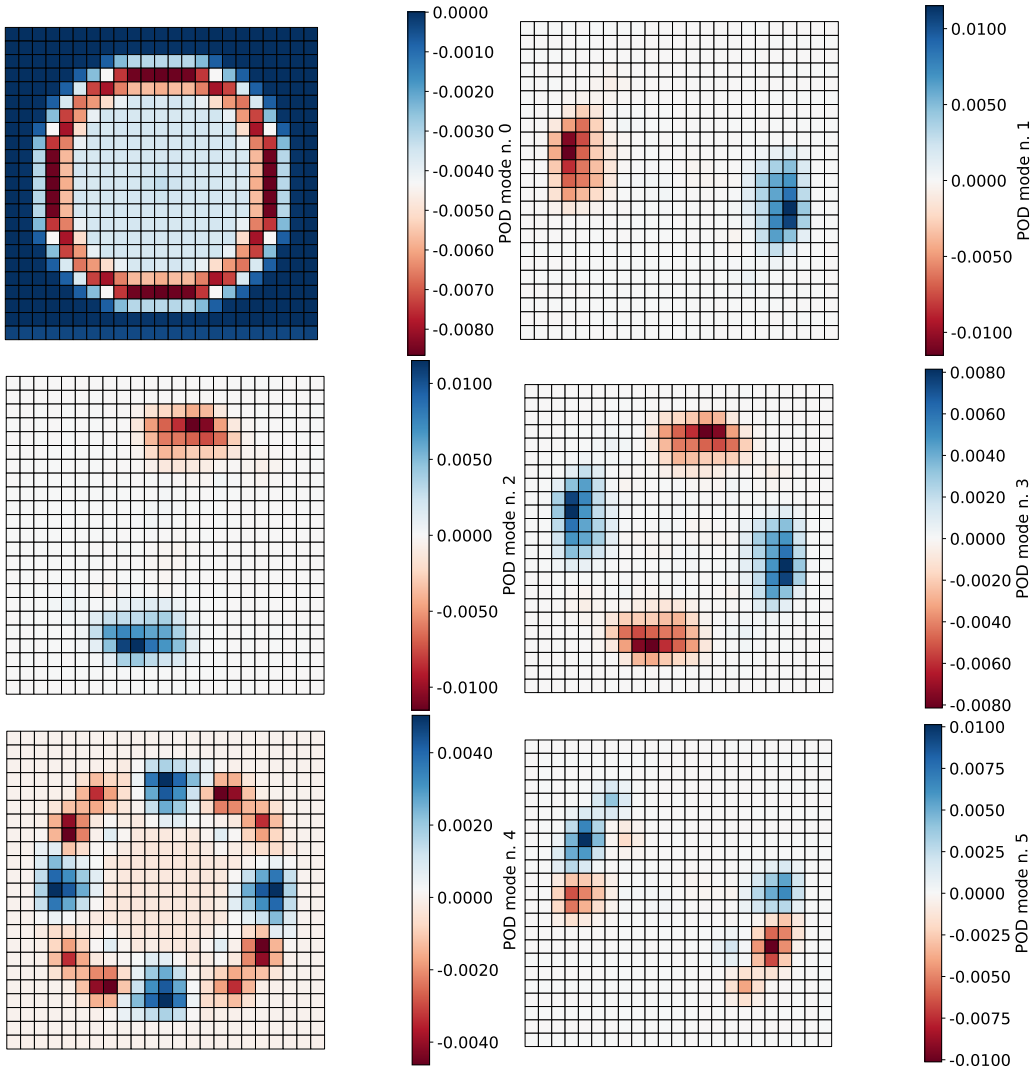

Figure 6.32: *POD modes for thermal fission production cross section, with increasing spatial frequency moving from top to bottom and from left to right.*

6.2.3.4 Model training and validation

In this section, the full-core model results are presented and discussed, considering as output response the assembly-wise power distribution, which is the physical parameter adopted to assess the core conformity in presence of localised perturbations.

fig. 6.33 presents the first six modes obtained by applying the POD reduction to the power training snapshots. Contrarily to the POD application to the input data, in this case it is possible to use a much looser tolerance, around $5 \cdot 10^{-6}$, which guarantees an energy of the POD basis larger than 99.999%. It is interesting to notice that the spatial shapes of these modes are very similar to the ones of the higher k-eigenmodes.

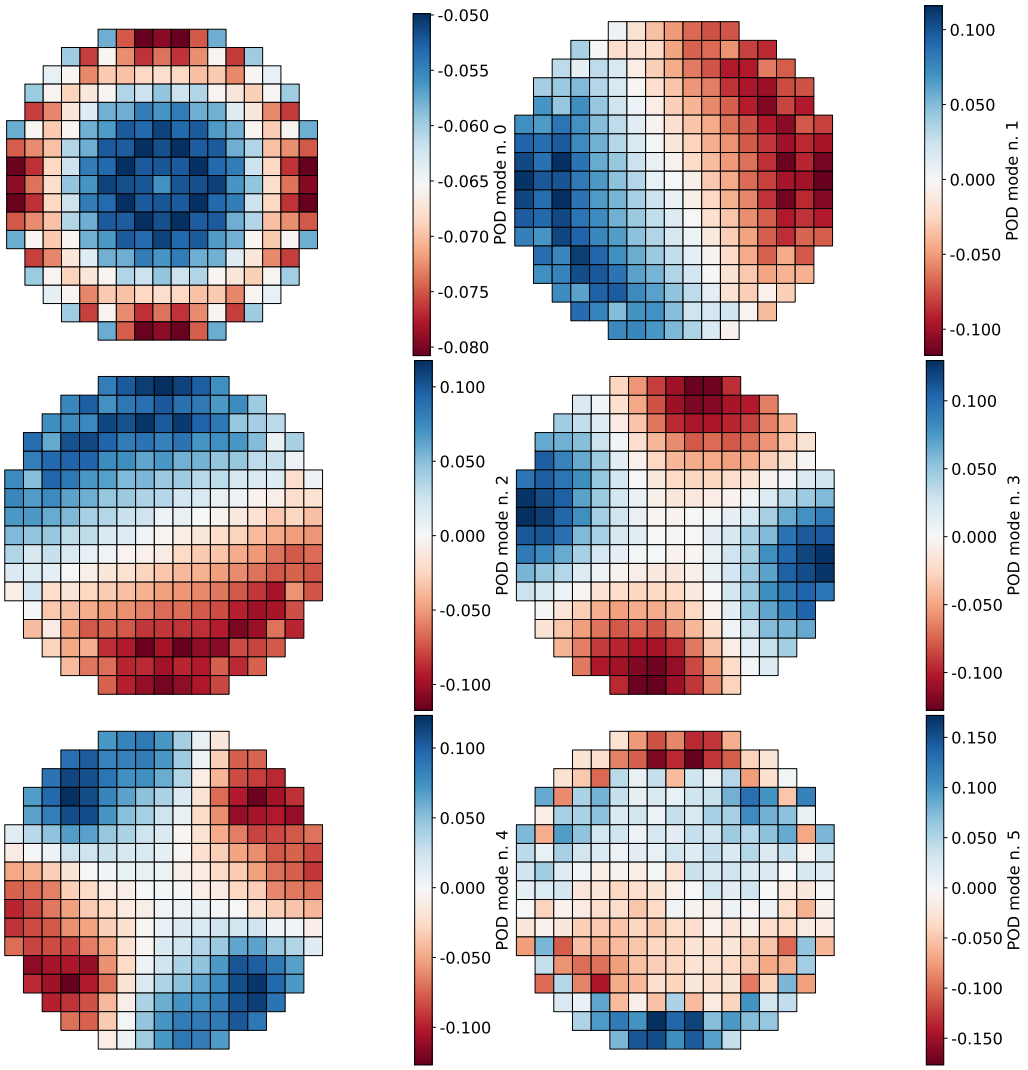

Figure 6.33: *POD modes for fission power distribution.*

The POD reduction is very important to minimise the computational cost associated

to the model training, as one RBF net is trained per each POD coefficient (see algorithm 3), including the RBF shape parameter optimisation with the LOOCV technique (see algorithm 4). Also in presence of a significant dimensionality reduction, the computational time of the RBF evaluation strongly depends on the number of training snapshots n, as the RBF weights have to be determined by inverting the distance matrix $\hat{D} \in \mathbb{R}^{n \times n}$. This is a well-known limit of non-parametric techniques like RBF-SVM (Russell, 2010), together with the possible over-fitting behaviour. Since the datasets used to map the input parameter space of the problem are very large, in the following the model sensitivity to the number of training samples will be assessed taking into account both the accuracy of the model and its computational efficiency.

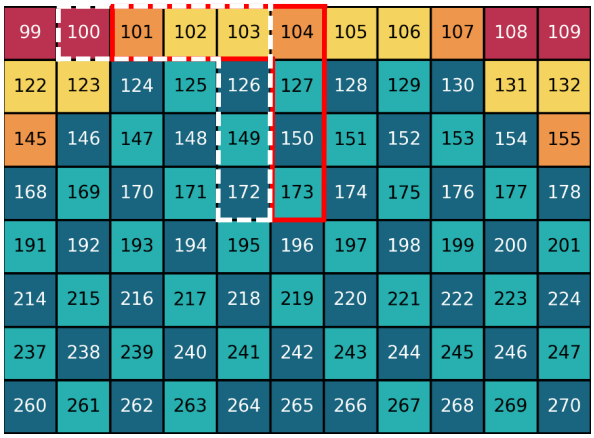

Figure 6.34: *Example of perturbation arrangements which are spatially similar but involve different kinds of FAs.*

Before moving on with this evaluation, it is of paramount importance to discuss the input-output association logic. Due to the two-step structure of the high-fidelity model depicted in fig. 6.6 and since the ROM is non-intrusive, one could be led to assume that the best labelling strategy for the supervised learning model would be to assign the spatial distributions of the coolant density and of the pellet diameter as input to the ROM. This choice could appear completely legitimate, since, from a physical point of view, the reactor responds with a certain power distribution to a certain perturbation arrangement. However, from the point of view of the model, the same relative density variation affects in a different way each type of FAs in a certain perturbation batch, meaning that the full-core diffusion model would "see" different cross sections and diffusion coefficients in each perturbation batch. This has an non-negligible impact on the effective distance between the training configurations, as visible from fig. 6.34. The two perturbation batches shown are very similar from a topological point of view, but involve different families of FAs. Therefore, if the ROM input were the density and the diameter distributions, the two configurations would turn out to be much closer than they actually would if the two-group data were considered. Figure 6.35 reports the

PDF and the Cumulative Distribion Function (CDF) of the percentage relative error on the assembly-wise power $\dot{Q}_i$ between the FOM and the ROM for 2000 validation cases generated with the full-random sampling approach, namely

$$\epsilon_{\dot{Q}}\% = \sum_{i=1}^{N_{FAs}} \left\| \frac{\dot{Q}_{i,FOM} - \dot{Q}_{i,ROM}}{\dot{Q}_{i,FOM}} \right\|_2 100. \tag{6.21}$$

On the left, the physical perturbations are used as input parameters for the model, while, on the right, the input parameters are the actual two-group constants. At a first glance, it may seem that there is no striking difference between the two cases, but looking at the frequency axis it is easy to notice how the right graph is featured by peak around 1% and by a strong reduction of the frequency for the error around 6-10 %.

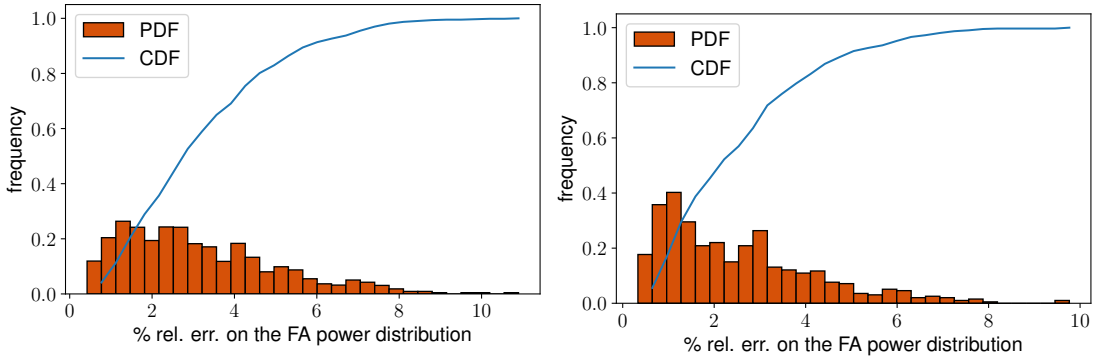

Figure 6.35: *Percentage relative error distribution on the validation samples for the full-random sampling case considering four perturbation batches in the core. On the left, the model is trained considering the coolant density and the pellet diameter as input, on the right the model is trained using the actual few-group data.*

Therefore, these results confirm that, for a proper evaluation of the input parameter distance, which is fundamental to assign the correct weights to the RBF, it is necessary to assign the actual input data of the FOM to each snapshot.

Figure 6.36 reports the PDF and CDF of the percentage relative error computed as in (6.21) for 3000 validation cases generated with the full-random sampling approach using 500, 1000 and 1500 training snapshots. Although the number of samples doubles and then triplicates, the shape of the error distribution for the 3000 validation snapshots does not seem to change significantly, apart from an increase in the frequency of the error values around 1%. On one side, this is an excellent feature of the model, since it suggests that a good trade-off between accuracy and complexity has been achieved and that the model is rather insensitive to the addition of new samples. On the other, the fact that the error seems to decrease slowly would suggest that reducing the validation error to an arbitrary value would require a huge number of snapshots.

Finally, it is worth mentioning the behaviour of the other figure of merit, i.e. the computational efficiency of the model. Table 6.2 proves that both the ROM training

Table 6.2: *Computational performances of the ROM trained with different dataset sizes.*

n. snapshots	ROM training time [s]	ROM execution time [s]	Normalised memory consumption [-]
500	90	0.035	1
1000	369	0.136	4
1500	860	0.30	9

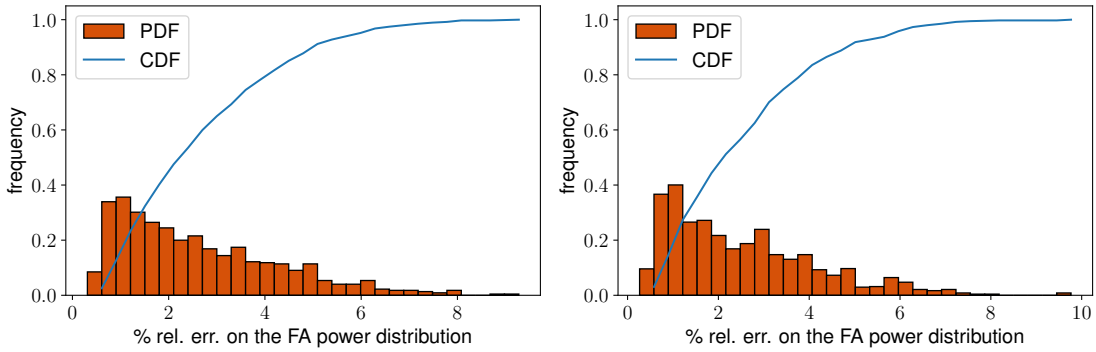

(a) *500 training samples.*

(b) *1000 training samples.*

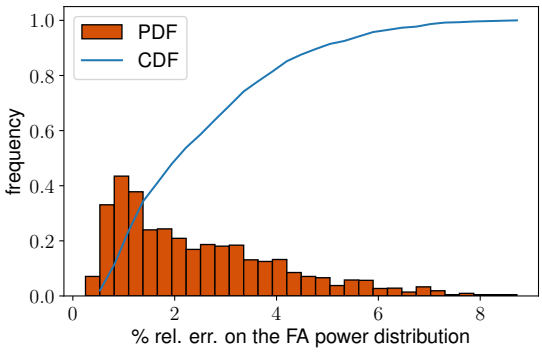

(c) *1500 training samples.*

Figure 6.36: *Percentage relative error distribution on 3000 validation samples obtained with the full-random sampling algorithm considering four perturbation batches in the core.*

and the ROM execution times increase dramatically with the number of snapshots n, as well as the memory resources. Therefore, considering also the behaviour of the error distribution, it is not probably worth to further increase the number of the random training samples.

The final goal of the full-core NIROM described in this section is the accurate and fast estimation of the assembly-wise power to study the appearance of the power tilt instability. Hence, in order to complete the evaluation of the ROM performances, it is

important to examine more in detail the spatial distribution of the modelling error. Figure 6.37 reports the perturbation effect on the thermal diffusion coefficient distribution and the relative error between FOM and ROM for a training case. Since the ROM is built in order to reproduce the training data with a very large accuracy, it interesting to notice that the overall error spatial behaviour is rather uniform, except some local maxima where it can reach values even larger than 1 %. Nevertheless, this accuracy is sufficient to provide an adequate estimate on the quadrant-wise power, which is used in the tilt evaluation (NRC, 2016). The quadrant power is obtained summing the assembly-wise power in each of the four quadrants, obtained dividing the core FAs with the lines $x = 0$ and $y = 0$, assuming that the origin of the reference cartesian frame is located in the central FA, the number 265 (section 6.2.3.1).

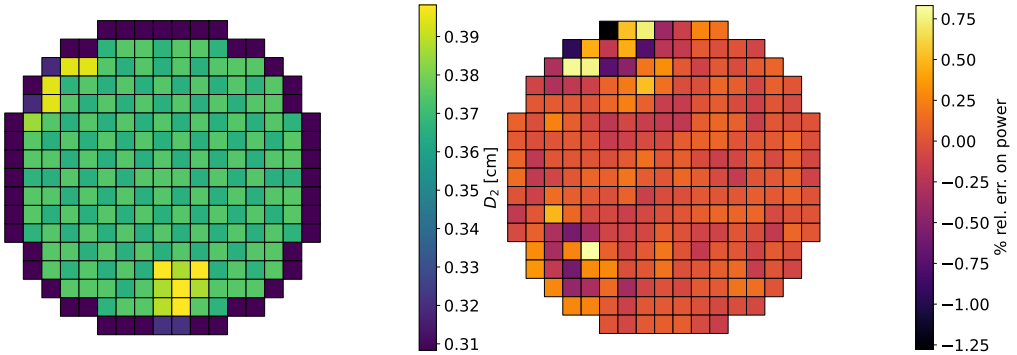

Figure 6.37: *Input disturbance on the thermal diffusion coefficient (left) and relative relative error on the assembly-wise power (right) for a training case.*

Concerning the validation cases, fig. 6.38 and fig. 6.39 show the maps of the largest and lowest power relative errors, respectively. In the first figure, it is possible to appreciate the perturbation effect of the thermal diffusion coefficient and, consequently, on the power distribution, which is clearly skewed towards the left part of the core, due to the increased leakages in the opposite direction. The ROM provides a very good reconstruction of the power, yielding a value of the largest relative error in line with the one characterising the training case in fig. 6.37, despite some in this case the local spatial distortions are more evident. On the contrary, fig. 6.39, which is featured by the largest relative error ϵ%, shows *ictu oculi* that the ROM completely fails in reproducing the power shape. Despite most of the validation points have an error which is less than 5%, the lack of accuracy featuring this case is unacceptable for the intended purpose of the model.

Given that decreasing the modelling error to an acceptable level would require a huge increase in the number of training snapshots, and that a larger dataset could bring the model to the over-fitting condition, a different strategy should be pursued to achieve the goal of the accuracy.

In this respect, it is convenient to recall the so-called *divide et impera* (divide and

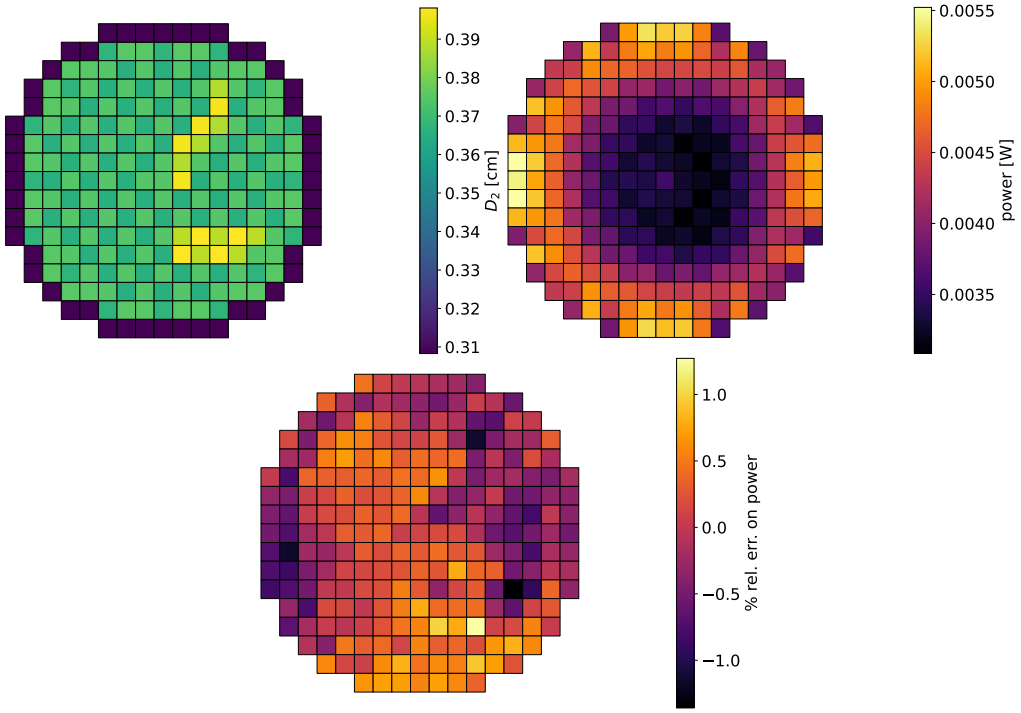

Figure 6.38: *Input disturbance on the thermal diffusion coefficient (top left), power distribution computed by the FOM (top right) and relative relative error on the assembly-wise power (bottom) for the validation case featured by the lowest error.*

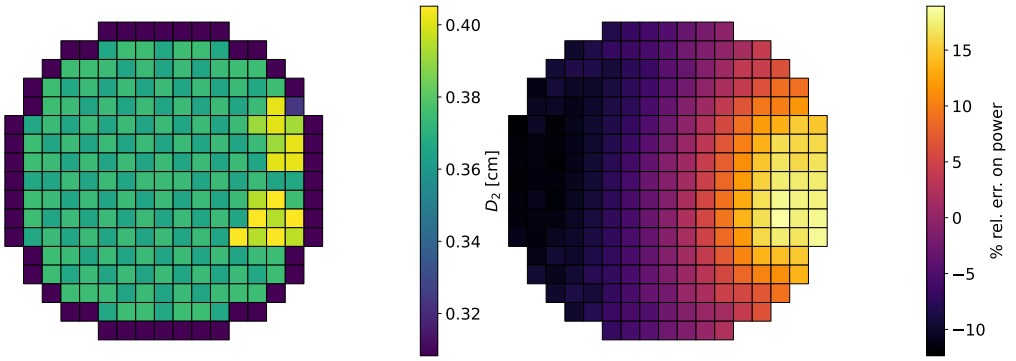

Figure 6.39: *Input disturbance on the thermal diffusion coefficient (left) and relative relative error on the assembly-wise power (right) for the validation case featured by the largest error.*

conquer) approach (Knuth, 1998), which is a general principle adopted in problem solving. According to this principle, an effective solution strategy consists in dividing recursively the original, complex problem into smaller and smaller sub-problems until a sub-problem that could actually be solved is obtained. Then, one can move backwards

solving the each sub-problem from the bottom to the top.

In a similar way, smaller, very specialised ROMs could be built for modelling specific situations, e.g., the core behaviour when only one perturbation batch can appear. This approach would require to train of a potentially large number of models, but it would offer the advantage of reducing dramatically the parameter space dimension, which could enable the adoption of smart sampling strategies and it could allow to increase the overall accuracy of the model, due to the lower input variability.

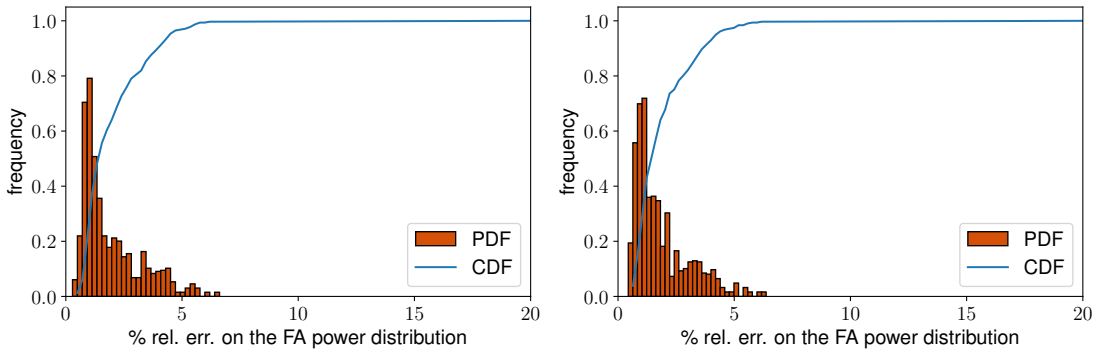

(a) *512 training samples, composed by 32 differ-*

ent arrangements with 16 different input pertur-

bations each.

(b) *768 training samples, composed by 48 different arrangements with 16 different input perturbations each.*

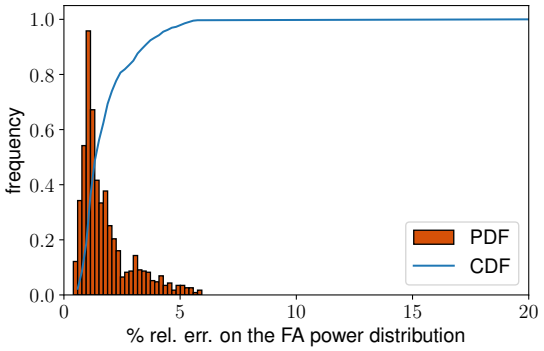

(c) *1024 training samples, composed by 64 different arrangements with 16 different input perturbations each.*

Figure 6.40: *Percentage relative error distribution on 1252 validation samples obtained with the full-random sampling algorithm considering one perturbation batch in the core.*

In the following, the results obtained with a meta-model designed to deal with a single perturbation batch appearing in the full-core are presented. Due to the reduced spatial variability, the hybrid sampling technique described in section 6.2.3.2 is employed to map more rigorously the parameter dependence. Concerning the validation samples, the subset of the 3000 cases featured by one perturbation cluster is selected,

for a total of 1252 cases.

As expected, the specialised ROM is featured by a lower error than the general one, as visible from fig. 6.40. The training process has been accomplished using 32, 48 and 64 different spatial configurations, combined with the 16 Smolyak points. Despite the lower number of validation samples, the error distribution is clearly peaked towards 1%, with no case going beyond 6%. The superior accuracy of this model can be appreciated looking at the maps for the relative error on the assembly-wise power, reported in fig. 6.41. The training case is featured by a lower error compared to the one for the general ROM, as well as the validation cases featured by the lowest and the largest errors. Compared to the spatial profile depicted in figs. 6.38 and 6.39, the error seems also more spatially uniform, which means that the local deformation of the power distribution due to the modelling approximation is less important.

6.2.4 Conclusions and future developments

In this section, the POD-RBF model has been applied to reduce the computational cost associated to the full-core diffusion calculations needed to assess the core behaviour in presence of local disturbances.

Due to the two-step nature of the full-core calculations, which require a set of few-group homogenised constants, a two-step meta-model has been proposed, combining the polynomial chaos expansion method for the estimation of the multi-group data and the POD-RBF model for the estimation of the assembly-wise power distribution obtained in response to a localised perturbations, which are assumed to be variations in the coolant density and in the fuel pellet diameter.

The first-order polynomial chaos expansion is sufficient to reproduce within an acceptable accuracy the cross sections behaviour as a function of the two input perturbations, with only a few full-order model evaluations. However, it must be acknowledged that, in presence of larger variations, probably more training points would be required to match the target accuracy.

Concerning the full-core calculations, some precautions are needed to handle the spatial arrangement of the perturbations. First of all, an algorithm for the definition of the perturbation and its constraints, e.g., the perturbation shape, is envisaged. Then, two different sampling techniques are devised to produce the training dataset. The first one draws the first perturbed FA according to an importance probability density function based on the neutron importance, and then randomly selects the surrounding FAs, assigning a random value to the physical perturbation as well. The second sampling technique works in the same way, but the perturbation intensity is sampled according to a deterministic rule.

The last precaution regards the distance evaluation among the input parameters: due to the spatial arrangement of the disturbance, the classical euclidean distance between the various input parameter is not adequate to distinguish similar perturbations,

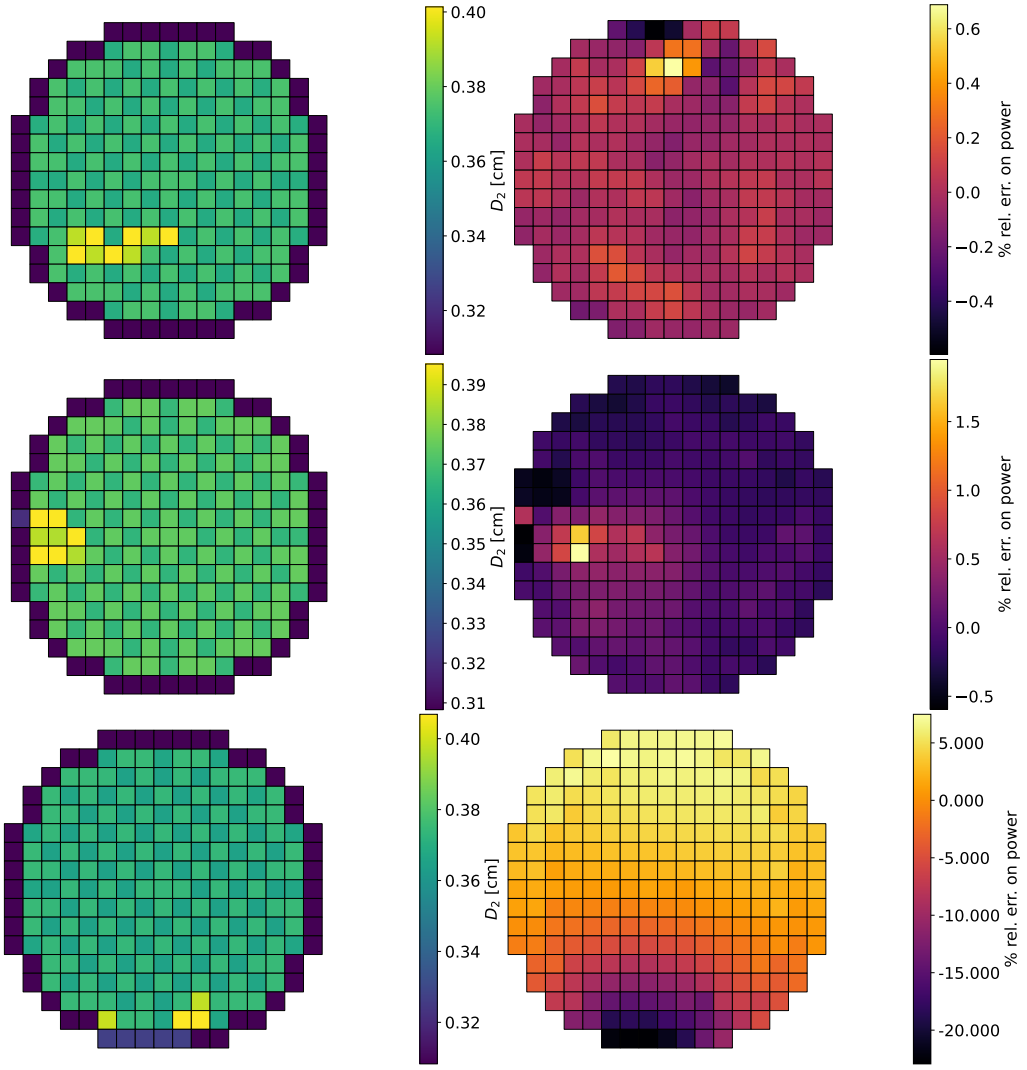

Figure 6.41: *Input disturbance on the thermal diffusion coefficient (left) and relative relative error on the assembly-wise power (right) for a training case (top), for the best validation case (centre) and for the worst validation case (bottom).*

engendering the learing capabilities of the model. Thus an alternative algorithm for image recognition is selected, to guarantee a consistent evaluation of the training samples distance with respect to a new parameter point.

When it is assumed that more perturbations can occur in the core, the parameter space of the problem becomes huge. However, according to the results obtained, it seems that the random sampling technique is adequate to provide good results. Nevertheless, it seems difficult to strongly reduce the error, due to the large variability in the input space.

If a simpler problem is addressed, assuming that only one batch of perturbed FA can

occur, the overall accuracy of the model improves a lot, also thanks to the adoption of the hybrid sampling process. This observation suggests that more specialised meta-models could be the most efficient solution to the problem.

As a future development, hybrid techniques based on data- and physics-driven should be investigated. For example, it would be interesting to use the legacy Generalised Perturbation Theory technique to provide a set of sensitivity coefficients to drive the sampling phase towards the most relevant perturbations.

6.3 Application to the neutronic transient analysis of the ALFRED reactor

6.3.1 Introduction

Due to their physico-engineering peculiarities, the deployment of the Gen-IV Lead Fast Reactor demands the adoption of high fidelity computational techniques for both design and licensing purposes. Its fast neutron spectrum and the strong coupling between neutronics, thermo-hydraulics and thermo-mechanics requests the adoption of very accurate models, which are often very computationally expensive: on top of this multiphysics aspect, these systems are featured by the usual complexity characterising the nuclear reactors, i.e. their multi-scale nature. Even with the computational resources at disposal nowadays, the full-core analyses that are required for the design verification and for the safety evaluations cannot be carried out in a reasonable time, especially when operational and off-operational transients are analysed.

Since the very beginning of the nuclear industry, most of the issues due to the multi-scale modelling have been overcome reducing the complexities of the physics introducing some approximations in the high-fidelity models. Concerning neutronics, for instance, the usual approach to treat the multiple spatial and energy scales consists, as discussed in chapter 4, in solving the steady-state neutron transport equation over a fine energy group structure over some specific volumes of the core, e.g. at the pin lattice level, in order to generate the spatially homogenised multi-group constants. Exploiting the equivalence principle described by eq. (4.1), and accepting some distortions in the physics, the set of few-group cross sections is then used as input data for a low-order transport model at the full-core scale, which can provide, within a reasonable time, the macroscopic quantities needed for design and licensing purposes.

Due to the presence of different time scales between neutronics, heat transfer and fuel depletion, also the time variable needs some special handling. If the objective of the analysis is to perform an accurate analysis of an operational transient involving the core, a common method to manage the different time scales is the *quasi-static* (QS) approach (Henry, 1958). The key idea of this method is to exploit the fact that, physically, the changes in the neutron population amplitude are much faster than the changes in the neutron spatial and energy shape, meaning that it is possible to separate the two time scales over a certain time window, whose width depends on the current state of the system, e.g., its reactivity. From the mathematical and numerical point of view, this method takes advantage of the fact that the faster time scales is governed by an ordinary differential equation, which is usually cheap to solve, while the slower time scale is determined by a partial differential equation in the phase space, whose solution is much more expensive. On the other hand, if the transient analysis involves the primary and secondary systems, which are featured by much longer time scales, the QS method would be too expensive to run. In this case, the core time-dependent behaviour is often approximated with the Point Kinetics (PK) approach, which brutally neglects

all the spatial and energy effects occurring in the core, treating it like a point object. Despite its wide adoption in safety parametric analyses, the adoption of PK may lead to very inaccurate results, especially if the transient regards some design-basis accidents like a reactivity insertion accident. In this case, one possible initiating event could be the ejection of a control rod, which would heavily modify the shape of the neutron flux, jeopardising the PK method.

In this context, disposing of a fast running tool able to accurately simulate the behaviour of the core would be extremely useful to enhance the accuracy of the safety evaluations. Hence, the aim of this chapter is to apply the POD-RBF model to mimic the output responses of a neutronic transient model, in order to show the potentialities of the POD-RBF ROM also in a time-dependent framework. In particular, the application of the NIROM will regard the neutronic transient analysis of the ALFRED (Advanced Lead Fast REactor Demonstrator) core design, i.e. the European LFR concept (Grasso, Petrovich, et al., 2014).

6.3.2 Statement of the problem

The application case presented in the following regards the accidental insertion of one of the 12 control rods (CRs) in the core, starting from an initial close-to-critical configuration. The starting configuration is obtained by inserting all the control rods at a height equal to 45 cm with respect to the active zone bottom plane, i.e. the plane delimiting the beige and the blue regions appearing in the right sketch of fig. 6.43. On the left of the figure, it is possible to observe the radial section of the ALFRED core and, on top of it, it can be notice a white X that indicates the CR that triggers the transient.

The CR is assumed to follow the motion law described in fig. 6.42, i.e. its constant insertion speed is assumed to change at a certain time instant $t = \Delta t_1$. The insertion heights are assumed to be z_1=57 cm and z_2 =67 cm, both measured from the bottom plane of the active zone, while the time intervals Δz_1 and Δz_2 are considered as the unknown, free parameters featuring the problem, but assuming that t_2 is always less or equal to 20 s.

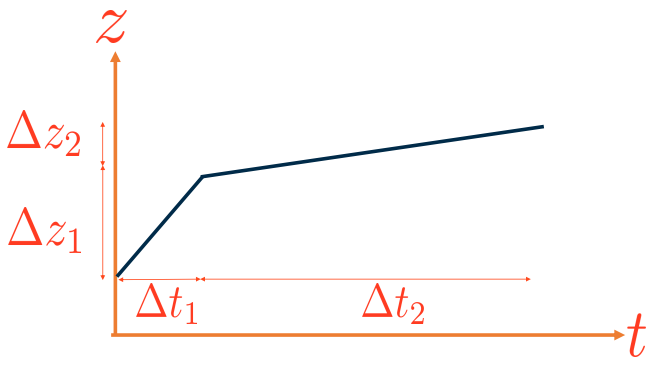

Figure 6.42: *Motion diagram of the moving control rod.*

The reasons behind the selection of this off-operational scenario are summarised in the following,

- the asymmetry introduced by the CR movement highlights the drawbacks of the PK method, which would fail in capturing the spatial effects induced by the CR motion. Hence, an accurate modelling would require the adoption of more sophisticated models, e.g. the QS approach;
- the insertion of the control rod in a close-to-critical configuration is expected to bring the reactor in a sub-critical state. From the computational point of view, treating a sub-critical transient is much simpler than studying a super-critical transient without the effect of the thermal feedback.

Concerning the computational model for the problem, the neutronic module of the FRENETIC code, briefly described in chapter 4, is adopted to simulate the CR accidental insertion, exploiting the Improved Quasi-Static (IQS) method (Caron, 2017).

In order to be as much general as possible, a 3D full-core model of the reactor is employed in FRENETIC. The version of the ALFRED design considered in this work is the one produced in the LEADER project. The multi-group constants needed by the nodal diffusion module of FRENETIC are generated with Serpent 2. To perform this task, a 3D full-core Monte Carlo model of ALFRED at the beginning-of-life condition has been developed, subdividing the core regions according to the sketches in fig. 6.43: each type of sub-assembly (SA) is subdivided axially in a certain number of regions, which are indicated by different colours in the right graph. For each region, Serpent 2 produces a set of group constants, collapsing them over the six-group energy grid presented in 6.3 and using the ENDF-B/VIII.0 nuclear data library. A more detailed rationale behind the selection of this group structure and of the spatial region subdivision adopted for the homogenisation can be found in (Nallo, Abrate, et al., 2020; Massone, Abrate, et al., 2022).

Table 6.3: *Six-group energy grid adopted to perform the macroscopic cross sections energy collapsing (Nallo, Abrate, et al., 2020).*

Energy [MeV]	$2.000 \cdot 10^{1}$	$1.353 \cdot 10^{0}$	$1.832 \cdot 10^{-1}$	$6.738 \cdot 10^{-2}$	$9.119 \cdot 10^{-3}$	$2 \cdot 10^{-5}$	10^{-11}

Adopting these effective group constants, FRENETIC yields a k_{eff} equal to 1.00045, which is in excellent agreement with the one computed by Serpent 2, 1.00008(24), considering the various approximations featuring the nodal diffusion approach.

6.3.3 The time-dependent POD-RBF model

In this section, the main modifications needed to adapt the POD-RBF model described in section 6.6.1 to consider a time-dependent output are briefly described.

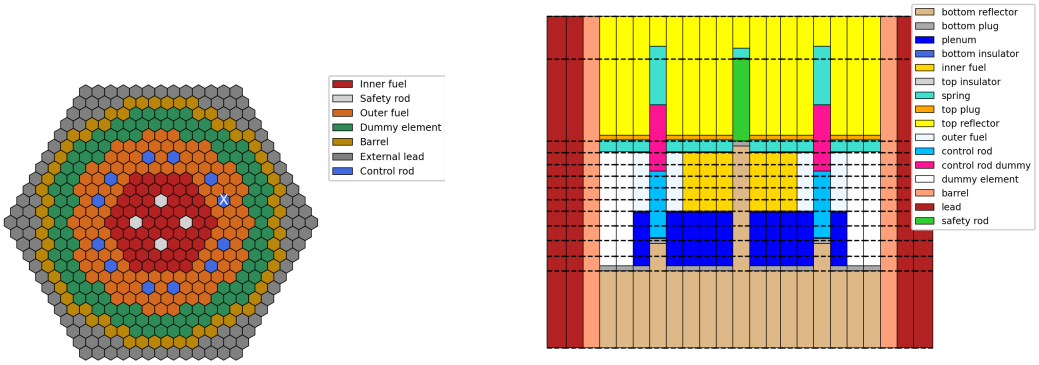

Figure 6.43: *Radial section (left) and axial regions (right) of ALFRED 3D model employed in the study. The X symbol identifies the control rod inserted during the transient.*

The general idea of the method is to approximate a certain physical field, which is the output of the reference model, by means of an expansion like the following one,

$$\mathcal{M}(\vec{r}, \vec{p}_j) = \vec{y}_j \approx \sum_{i=1}^{I} a_i(\vec{p}_j)\psi_i(\vec{r}, \vec{p}_j) \tag{6.22}$$

where I is the POD basis dimension, ψ_i is the i-th POD basis function and a_i is the i-th POD coefficient estimated with the RBF interpolation, assuming that $\vec{p}_j$ does not belong to the training dataset. The coefficient represents the i-th component of the solution on the reduced space, and depends on a certain input parameter $\vec{p}$.

If the model $\mathcal{M}$ depends also on time, a natural way to treat this additional complexity would be to decouple the space and the time dependencies, and then to treat each of them using the POD-RBF approach. In other words, the output response $\vec{y}_j(t)$ obtained applying $\mathcal{M}$ to an input $\vec{p}_j$ is decomposed with algorithm 2 into a set of time coefficients $a_i(\vec{p}_j, t)$ and spatial basis functions $\psi_i(\vec{r}, \vec{p}_j)$.

Since the POD is applied to each model realisation $\vec{y}_j(t)$, both a and ψ depend on the input parameter $\vec{p}_j$, so for a training dataset composed by n snapshots, a set of n pairs of coefficients and basis function would be obtained,

$$\vec{y}_j \longrightarrow \{\vec{a}(\vec{p}_j, t), \vec{\Psi}(\vec{r}, \vec{p}_j)\} \; j = 1, \dots, n, \tag{6.23}$$

where $\vec{a} \in \mathbb{R}^I$ is the column vector composed by a_i for $i = 1, \dots, I$ and $\vec{\Psi} \in \mathbb{R}^{IM}$ is the column vector obtained stacking each basis function $\vec{\psi} \in \mathbb{R}^M$. These column vectors can be interpreted, respectively, as time and spatial snapshots of the original model $\mathcal{M}$, and can be paired with the corresponding input parameters $\vec{p}$ to build a POD-RBF model for time and a POD-RBF model for space. Hence, applying the POD decomposition and using the RBF formalism presented in algorithm 3, the time and space snapshots for a

new parameter $\vec{y}_n$, not included in the training set, can be expressed as follows,

$$\begin{aligned}\vec{a}(t,\vec{p}_n) &= \sum_{m=1}^{M}\alpha_m(\vec{p}_n)\vec{u}_m(t) = \sum_{m=1}^{M}\left[\sum_{l=1}^{L} f_\alpha(\|\vec{p}_l-\vec{p}_{\text{new}}\|,\sigma_{\alpha,l})\vec{w}_{\alpha,l,m}\right]\vec{u}_m(t)\\ \hat{\Psi}(\vec{r},\vec{p}_n) &= \sum_{k=1}^{K}\beta_k(\vec{p}_n)\vec{v}_k(\vec{r}) = \sum_{k=1}^{K}\left[\sum_{l=1}^{L} f_\beta(\|\vec{p}_l-\vec{p}_{\text{new}}\|,\sigma_\beta)\vec{w}_{\beta,l,k}\right]\vec{v}_k(\vec{r}).\end{aligned} \tag{6.24}$$

Exploiting the last equation, the output $\vec{y}_n(t)$ can be finally retrieved,

$$\begin{aligned}\vec{y}(\vec{r},\vec{p}_n,t) &\approx \sum_{i=1}^{I} a_i(\vec{p}_j,t)\psi_i(\vec{r},\vec{p}_j) =\\ &\approx \sum_{i=1}^{I}\left\{\sum_{m=1}^{M}\left[\sum_{l=1}^{L} f_\alpha(\|\vec{p}_l-\vec{p}_{\text{new}}\|,\sigma_{\alpha,l})\vec{w}_{\alpha,l,m}\right]\vec{u}_{m,i}(t)\ *\right.\\ &\left.*\ \sum_{k=1}^{K}\left[\sum_{l=1}^{L} f_\beta(\|\vec{p}_l-\vec{p}_{\text{new}}\|,\sigma_\beta)\vec{w}_{\beta,l,k}\right]\vec{v}_{k,i}(\vec{r})\right\}.\end{aligned} \tag{6.25}$$

6.3.4 Model training and validation

6.3.4.1 High fidelity simulations

The coarse mesh nodal diffusion module currently available in FRENETIC allows to compute the neutron flux and the associated reaction rates at the assembly level and for each node employed in the axial discretisation. The black dashed lines on top of the right sketch in fig. 6.43 indicate the core axial subdivisions considered by FRENETIC. Since each volume defined between two planes must be homogeneous, the consistency of the six-group data computed by Serpent with the regions of FRENETIC is ensured by performing a post-homogenisation that exploits the group-wise flux averaged on the cell volumes, provided by Serpent, namely

$$\overline{\Sigma}_{x,g,i} = \frac{\sum_{r=1}^{R}\overline{\Sigma}_{x,g,r}\overline{\phi}_{x,g,i}V_i}{\sum_{r=1}^{R}\overline{\phi}_{x,g,i}V_i}. \tag{6.26}$$

Concerning the solution of the time-dependent neutron diffusion and delayed neutron precursors equations, FRENETIC offers a wide variety of methods, from the point kinetics approach to the predictor-corrector quasi-static method, which is endowed with an adaptive time step selection algorithm for the solution of the shape and of the amplitude equations.

Despite the manifest computational efficiency of this approach (Caron, 2017), this algorithm asks the code to solve for the flux shape only at some specific time instants,

meaning that the shape is not computed and, thus, printed on a regular time grid. Moreover, the time-step selection algorithm behaves differently according to the transient evolution, meaning that each set of parametric snapshot, depending on $\vec{p}$, a different number of time snapshots is produced. However, the POD algorithm deals with rectangular matrices, i.e. each parameter evaluation must produce the same number of time snapshots.

Since the aim of this section is to assess the capabilities of the POD-RBF algorithm to handle time-dependent problems, this issue is tackled by simply forcing FRENETIC to solve for the flux shape every 0.5 s. Each transient simulation is solved up to 35 s, in order to allow the system to properly relax also in case the control rod insertion ends at $t_2 = 20$ s. Hence, each parametric snapshot is composed by 71time snapshots. On average, the solution of a transient simulation requires about three hours on a commercial laptop.

In analogy with section 6.2.2, also in this application the output response of the model will be the power distribution, $\dot{Q}(x, y, z, t, \vec{p}_i)$, where $\vec{p}_i$ is the input parameter vector defined as (t_1, t_2). The rationale behind such choice is two-fold. First, it is a safety-critical parameter. Second, it allows to easily evaluate the total power $\dot{Q}_T(t)$, which can be used to assess the impact of the ROM approximation errors on a macroscopic integral parameter.

6.3.4.2 Model reduction and training

In order to efficiently draw the points needed for the training simulations the Smolyak sparse grid algorithm is used again to perform the training sample selection. Contrarily to the application discussed in section 6.2.2, here the grid is based on the Chebyshev polynomials extrema, which have the property of being a nested set. Thus, also in this case it is possible to train the model with the lowest grid level and the iterating *a posteriori*, recycling the training samples of the previous levels. To generate the samples, it is assumed that both time intervals, defined as $\Delta t_1 = t_1 - 0$ and $\Delta t_2 = t_2 - t_1$, range from 0.5 to 10 s. Figure 6.44 shows the two-dimensional sparse grid constructed to sample the training points up to the 5–th approximation level.

After the sampling, the POD-RBF parametrised non-intrusive ROM is trained using the first four levels of the Smolyak sparse grid, for a total of 65 model evaluations. Then, the model validation is performed with an additional set of independent 100 simulations. Among these, 80 are taken from the points of the 5–th level of the Smolyak grid, removing the training points, while 20 are sampled randomly, extracting 5 points per each quadrant.

As already specified, each simulation contains 71 time snapshots spanning uniformly the interval $t \in [0, 35]$ s, and each snapshot is defined over the 171 fuel assemblies, each divided in 10 axial nodes uniformly distributed along the active height, for a total of 121410 degrees of freedom.

Thanks to the strong redundancy in the data, the dimensionality reduction allows

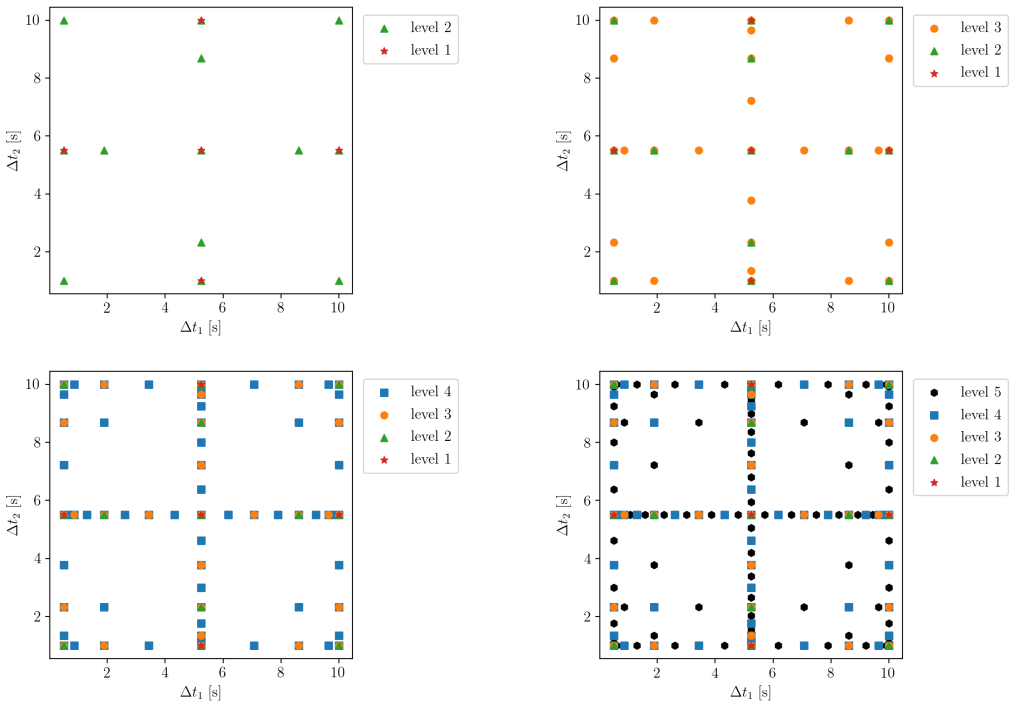

Figure 6.44: *The first levels of the Smolyak sparse grid used to generate the training samples.*

to use only 30 out of 71 POD pairs $\{a_k, \psi_k\}$, allowing to spare a significant amount of computational time in the NIROM training, at the price of a negligible loss of information, due to the POD basis truncation. With these settings, the ROM composed by the two POD-RBF models requires a few seconds to provide the approximated FRENETIC solution on a new parameter point.

fig. 6.45 shows the relative error featuring each validation sample, defined as the L_2 norm between the time-dependent power distribution estimated by the ROM and the one computed by FRENETIC. By inspection of the figure, it is easy to notice that, as one could reasonably expect, increasing the number of points makes the error decrease. The stars appearing in the graph indicate the training points, while the squares indicate the random samples generated for validation purposes. Using 65 training points, the maximum error falls below 4%. Considering that this is the global error for the time-dependent spatial distribution of the power, this value is judged acceptable for the intended application, i.e. a fast estimate of the power evolution in case of accidental control rod insertion in the core. Of course, an even larger number of training points could be employed, maybe selecting only the ones in the regions featured by the maximum error.

In the following, a detailed comparison between the ROM and the FRENETIC evaluations is carried out, focusing on validation cases featured by the largest and lowest

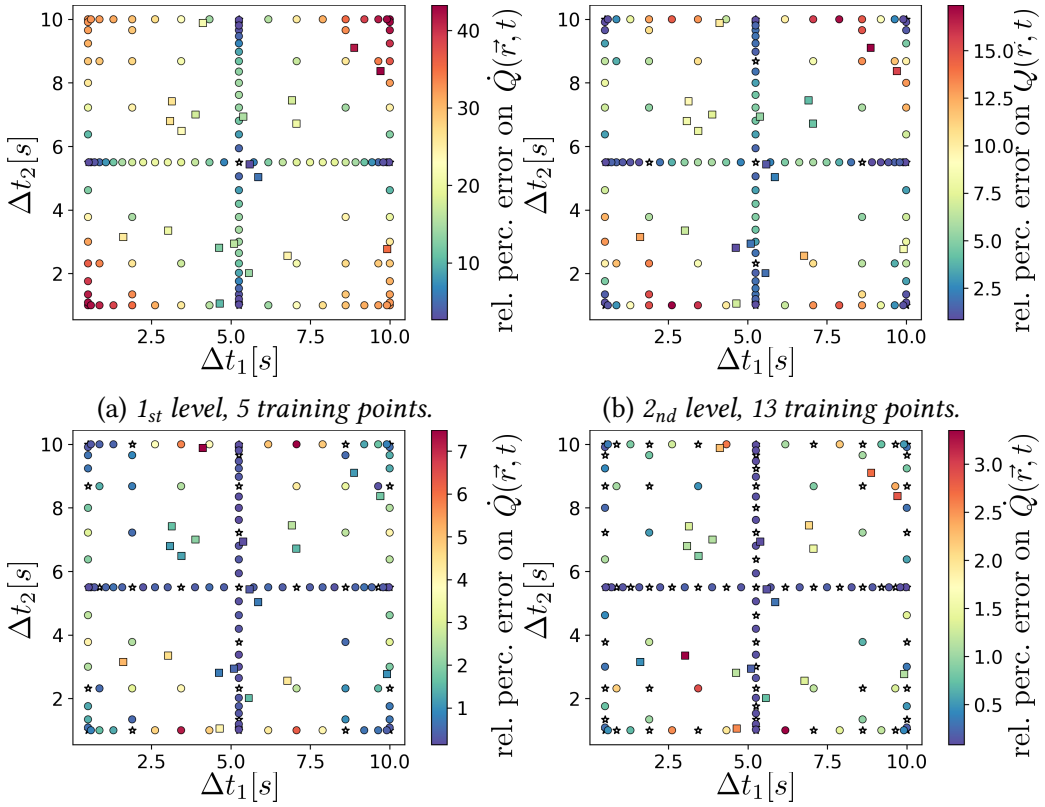

(a) *1_{st} level, 5 training points.*

(b) *2_{nd} level, 13 training points.*

(c) *3_{rd} level, 29 training points.*

(d) *4_{th} level, 65 training points.*

Figure 6.45: *% relative error on the power distribution time snapshots with a progressively increasing number of training points.*

error with respect to the FRENETIC solutions. The first comparison focuses on the axial power profiles, which are visible in fig. 6.46. In this figure, it is possible to notice that, in the worst case, the discrepancy on the local power can be significant, suggesting that the ROM, trained with only 65 points, is not adequate to perform local analyses, for example concerning the hot spot analyses.

Similar considerations could be made for the assembly-wise relative error on the power, which is depicted in fig. 6.47. In this case, it can be observed *ictu oculi* that the larger local distortion of the spatial distributions occurs around the CR that is inserted. A part from this zone, the overall error distribution seems quite uniform.

Finally, the upper part of fig. 6.48 shows the comparison between the total power evolution during the whole transient, computed by the ROM and by the improved quasi-static method available in FRENETIC, respectively. In spite of the non negligible local errors affecting the worst validation case, the agreement between the total power profiles is very good, and seems adequate to perform parametric safety analyses. The lower part of the figure shows a comparison between the total power evolution computed by

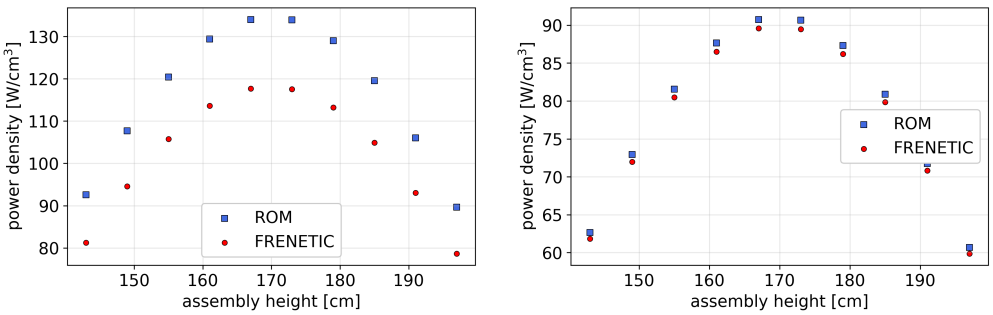

Figure 6.46: *Power density axial profile. The one on the left refers to worst case at the time instant with the largest error in the FA featured by the largest error, while the one of the right refers to the best case at the time instant with the largest error in the FA featured by the largest error.*

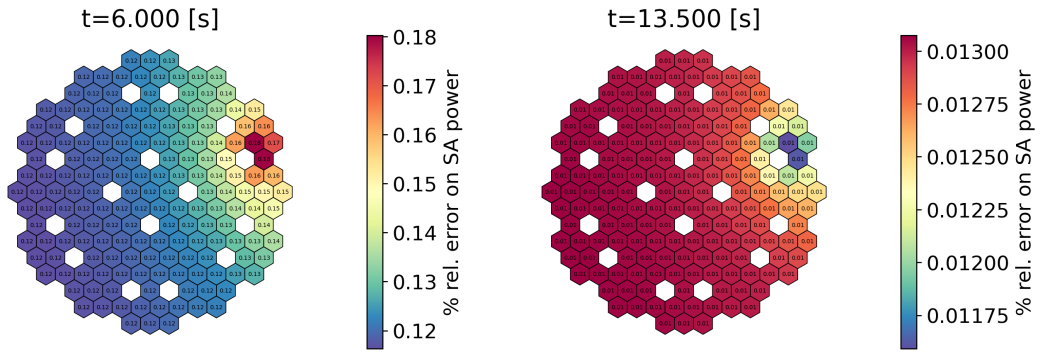

Figure 6.47: *Relative % error on the assembly-integrated power at the time instants featured the largest error for the worst (left) and best (right) validation cases.*

ROM and FRENETIC and the one evaluated with the point kinetics approach, for the worst validation case. This figure clearly shows that the ROM can be a far more accurate alternative to low-order methods commonly used in the safety studies. On top of that, after the training phase, the ROM power profile can be obtained in a fraction of the time needed by PK.

6.3.5 Conclusions and future perspectives

In this section, the POD-RBF model presented in section 6.6.1 has been extended to treat also time-dependent models, proposing an algorithm that suitably combines the algorithms already implemented in the ROMpy package.

The case study regarded the accidental insertion of a control rod in a close-to-critical initial configuration of the ALFRED core design, considering as free parameters the insertion times of the rod, which have the effect of changing the insertion speed of the

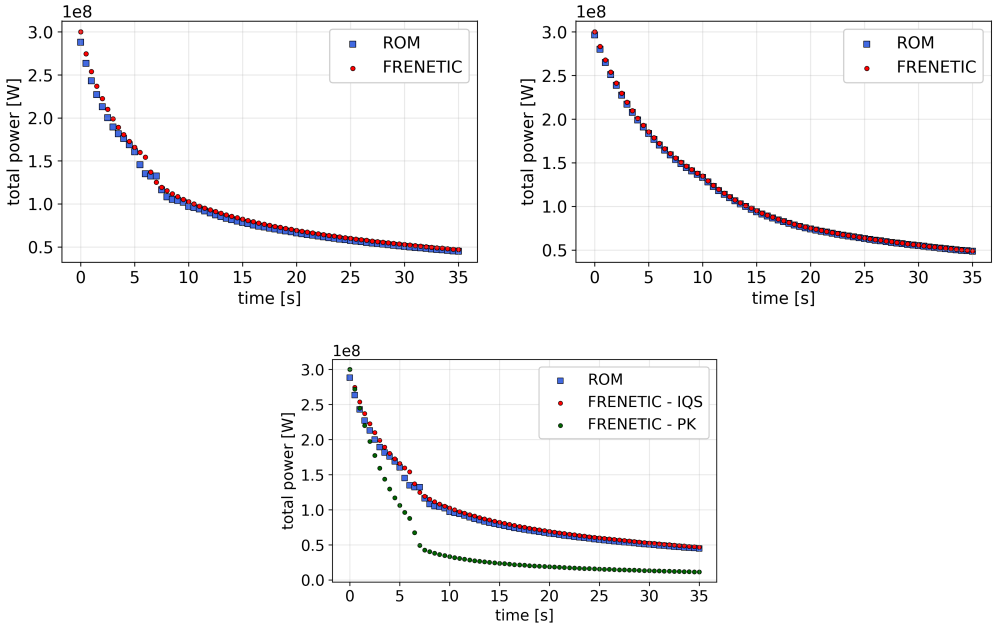

Figure 6.48: *Total power evolution for the worst (top left) and best (top right) cases and comparison between ROM, point kinetics and the quasi-static method (bottom).*

CR.

The full-core snapshots, representing the power density of the system, are generated with the FRENETIC nodal diffusion code. In spite of the relatively low number of samples, the ROM shows a good accuracy (the global error is below 4%) with respect to the full-order model for the validation points considered, on both the local and global spatial scales and for the whole transient duration. From the computational burden point of view, excluding the off-line training phase, which is though affordable with a laptop compute due to the fairly low number of training points, the ROM outperforms FRENETIC, providing the full-core power density time snapshots in less than a dozen of seconds, with respect to the 3 hours required by the code.

As a future development, efforts will be devoted to improve the training parameters sampling, trying to reduce the number of samples needed to match the target accuracy. Since the Smolyak grid based on the Chebyshev polynomials is more dense at the corners, the sampling performances could be improved a lot considering alternative point distributions, like the evenly-space Clenshaw-Curtis points. Finally, the ROM will be improved to fully exploit the time adaptive features of the predictor-corrector algorithm, thus considering only the snapshots that are more significant for the reactor dynamics, in contrast to the uniform time binning employed in this work.

6.4 A bootstrapped meta-model combined with the unscented transform for the CFD analysis of accidental gas releases in congested plants

In this section, the POD-RBF approach is adopted to reduce the computational burden associated to the QRA-oriented, Computational Fluid-Dynamics (CFD) modelling of accidental high-pressure gaseous release in congested industrial plants. This application is certainly an outlier in the context of a PhD thesis concerning the development of methods for the safety of nuclear fission reactors, but it is reported here to show that there is a broad variety of industrial applications related to the safety assessment that could be efficiently approached with the non-intrusive reduced order model presented in this chapter. The results presented and discussed in the following have been obtained in the frame of a collaboration with the SEADOG research group at Politecnico di Torino. In particular, all the CFD simulations mentioned in the following for the ROM training and validation have been carried out by former students Federica Carbone and Manuela Maffia during their Master's thesis projects and by Dr. Gianmario Ledda and Alberto Moscatello, who is currenlty a PhD student in Politecnico di Torino. Finally, it is acknowledged the overall supervision of Prof. Andrea Carpignano and Dr. Raffaella Gerboni.

Actually, a thorough QRA for congested industrial plants would be computationally prohibitive, due to the large number of accidental sequences to be simulated, each one characterised by uncertain parameters to be thoroughly explored and propagated, and to the complexity of each CFD simulation, which has to model a complex physical phenomenon in a complex geometry.

Within this framework, a computationally efficient approach, named Source Box Accident Model (SBAM) (Moscatello, Uggenti, et al., 2021) has been recently proposed to overcome the issue of computational cost. It consists in splitting the accident evolution in two steps: i) the *release* phase, which concerns a small volume around the break, named Source Box (SB), where the compressibility effects are relevant and ii) the *dispersion* phase, where the flow can be considered incompressible and buoyancy forces are relevant. In this last step, where the SB flow profiles and gas concentrations are taken as input, the analysis is extended to the full spatial scale of the plant (e.g. an offshore platform, see figure 6.50 later), in order to evaluate some safety-critical parameters, e.g., the flammable volume. This two-step approach allows to fairly reduce the computational burden with respect to a monolithic CFD simulation, as different numerical settings, e.g., the computational mesh, can be tailored according to the physical phenomena involved. Decoupling the two physical stages implies that also the parameter space can be partitioned. For example, the break size and release pressure are relevant in the gas release, while the wind direction is not. This means that it is possible to compute the concentration and flow fields for several SB characterised by different combinations of parameters and use them in the dispersion scenarios, whenever they are needed.

This procedure would lend itself to the generation of a SB library as a ready-to-use input to the dispersion simulation, which is strongly case-dependent. Relying on data libraries is a common approach in the framework of the risk analysis, but in this case it would jeopardise the advantages of using a CFD approach. For example, the risk analyst would not be free to select the flow field profiles for an arbitrary set of parameters, losing the CFD flexibility. Moreover, a thorough evaluation of the different SB scenarios would be still quite computationally expensive.

Therefore, the aim of this study is to assess the NIROM effectiveness in reducing the computational cost associated to the SB simulations (i.e., to the generation of the spatial SB flow profiles). A successful model reduction of the release phase would represent the first step for a computationally smart strategy for safety-oriented, CFD-based analyses. Thanks to its non-intrusiveness, this approach could be applied to any validated code for the QRA of different industrial congested systems, like the forthcoming nuclear fusion plants and hydrogen installations. In the following, study case concerns the accidental release of CH_4 on an oil&gas off-shore platform, simulated using the ANSYS Fluent code.

Since the objective of the NIROM application is to approximate the behaviour of a Source-Box (SB) and to provide a set of flow fields for a subsequent (dispersion) simulation, it is of paramount importance to quantify the ROM approximation error and propagate it on the dispersion simulation output. In the works mentioned in section 6.6.1, except for (Xiao, 2019), a little effort was devoted to this perspective. Therefore, in this work a novel combination of the POD-RBF model with two statistical approaches is proposed, namely the bootstrap method (Efron, 1981; Kohavi, 1995) and the unscented transform (Julier and Uhlmann, 1997), for an estimation of confidence intervals on the final output (i.e. the irreversible injuries area). The techniques to estimate the error bounds are quite general and could be applied to other NIROMs.

From the methodological viewpoint, the novel contribution of this application is twofold:

1. the bootstrap method is combined for the first time (to the best of the authors' knowledge) with a (fast-running) POD-based NIROM to obtain an empirical (bootstrapped) distribution of a functional output, which allows building confidence in the ROM estimates (i.e., in the gas flow spatial fields);

2. the unscented transform is employed to propagate - with a relatively small number of long-running CFD simulation - the uncertainties in the spatial fields onto the final simulation output (i.e., released pollutant mass).

From the application viewpoint, the efficient combination of statistical techniques mentioned above is employed for the first time in the quantitative analysis of a congested oil&gas off-shore platform. As a final remark, it is worth to acknowledge that the aim of this work is not carrying out a complete, full-scale QRA of an energy plant, but rather developing a versatile tool that can support it, in an efficient and computationally tractable fashion.

6.4.0.1 Two-step CFD modeling for the accidental gas release in a congested environment

In this case, the computational model is the CFD approach to study the accidental gas releases in industrial, congested plants. In order to focus on the peculiarities featuring this case study and the implications to realise a ROM simulation framework, this method will be briefly discussed in the following.

High-pressure gas releases, i.e. from 10 bar onward, in large, open environments (e.g. 30x20x5 m platform deck, see figure 6.50) always lead to a complex multi-scale and multi-physics phenomenon. In such cases, an under-expanded jet is generated near the release point (Franquet, Perrier, et al., 2015), i.e. a supersonic highly compressible flow (Ma >0.3, where Ma is the Mach number) (Munson, Young, et al., 2010, chapter 9), characterised by a strong discontinuity in the flow-field quantities. Such discontinuities are located at a specific distance from the release point, where a Mach disk appears: this is a normal shock where steep variation of velocity, density, temperature and pressure is expected. In this region, near the release point, the flow is dominated by inertial effects, and buoyancy forces are negligible. If the high-pressure release occurs in a large environment, there is enough space for the gas to slow down from supersonic to subsonic velocity. Hence, far from the release point, the flow reaches a subsonic condition (Ma <0.3). At this point, the flow can be considered incompressible and it is no more inertia-dominated, i.e. buoyancy forces can be relevant.

These two phases can be named *release* (compressible, inertia-dominated) and *dispersion* (incompressible, subsonic). In (Moscatello, Uggenti, et al., 2021) it is demonstrated that splitting the entire phenomenon in this two pieces has some advantages from a modelling point of view, especially if the CFD simulation is QRA-oriented. This is the basis of the Source Box Accident Model (SBAM), in which the release phase is simulated in a small domain, the SB, sized in a proper way to contain all the compressibility effects, and the dispersion in the environment under analysis, e.g., an off-shore oil&gas platform. The coupling of the two simulations is realised imposing the velocity flow field ($\vec{v}(x, y, z)$) and gas concentration distributions on the SB faces ($C_{gas}(x, y, z)$) as boundary conditions in the dispersion simulation.

This last step, as sketched in fig. 6.49, allows to evaluate the mass and volume of the gas cloud resulting from the dispersion. Thanks to these results, some safety related quantities can be evaluated. In the case considered in this paper, which concerns a CH_4 release, the interests safety parameters are:

- the total dispersed CH_4 mass [kg]
- the CH_4 mass in the flammable cloud [kg]
- the flammable cloud volume [m^3]
- the Irreversible Injuries (II) volume [m^3]
- the Irreversible Injuries Area (IIA) at 1.5 m height [m^3]

Apart from the first parameter, the other ones are related to the flammability which is defined by the LFL (Low Flammability Limit) and the UFL (Upper Flammability Limit). For CH_4, these quantities are equal to 5 % and 15 % by volume of air, respectively. The CH_4 mass in the flammable cloud is a relevant parameter as it is a measure of the potential energy released in the accident. The flammable cloud volume (which can be defined also the High Lethality zone) represents the region in which the gas concentration is between the LFL and UFL and a gas ignition can occur causing serious damage to the equipment and deaths. The II volume and area are the one with a gas concentration above the 0.5·LFL, and in which some damages to equipment and people are expected. Since these scalar quantities are relevant for the QRA, they will be considered as the final output of the whole calculation chain. Nevertheless, in order to avoid any loss of generality, they will be indicated as $\vec{z}$, in order to remark that the methodology presented in the paper can be applied to spatial and/or dynamic distributions as well.

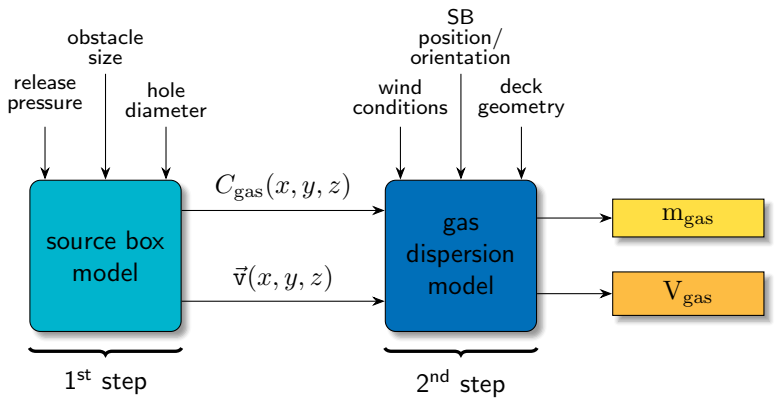

Figure 6.49: *Sketch of the SBAM approach.*

This computational strategy allows to simplify the simulation of this complex, multi-physics phenomena, allowing to save considerably computational time when several scenarios are needed for a QRA. This is possible because each SB simulation available can be employed for several dispersion scenarios. As it will be explained later, the SB simulation can be performed by the ROM model, dramatically reducing the computational cost. In addition, the SB and the dispersion simulations are affected by different set of parameters. The first one is affected mainly by the gas properties, its pressure, the piping break size and the shape and orientation of the obstacles near the break, while the second depends on the congested plant configuration, the release position and direction and the wind velocity magnitude and direction. This suggested the development of a surrogate model to mimic the SB behavior, thus reducing dramatically the computational cost associated to SBAM.

This paper aims at proving the effectiveness of the NIROM approach to maximise

the computational gain of this decoupled simulation approach. As this is a proof-of-concept, the pressure will be considered as the only SB varying parameter. It could be argued that the choice of only one out of all the possible varying parameters may jeopardise the considerations drawn throughout the paper about the accuracy, the robustness and the reliability of the proposed method. The gas release pressure, however, is the most relevant parameter from both the physical and the computational point of view, ranging continuously from 10 to 80 bar (Vivalda, Gerboni, and Carpignano, 2018), which is a very large interval from the fluid-dynamics perspective. On the contrary, the break size and the SB obstacle dimensions usually assume only few discrete values in the QRA framework, thus limiting the interest for such parameters from a ROM perspective. Moreover, the focus of our analysis is more related to prove the methodology proposed to quantify and propagate the NIROM uncertainty rather than focusing on the parameter space sampling.

6.4.1 Study case: accidental gas release in a congested environment

In this section the results of the NIROM application to the QRA-oriented, SBAM approach are presented and discussed, with a specific focus on the peculiarities featuring this case study.

6.4.1.1 Numerical setup of the case study

The considered case study is a high pressure methane release in an offshore platform deck under wind conditions. The domain is visible in fig. 6.50 and its dimensions are 30x20x5 m. The release position is indicated by the blue box in fig. 6.50. The possible release pressure (p_{rel}) range is 10-80 bar while the release diameter is fixed to 1 cm. The wind velocity is assumed equal to 6 m/s and the direction is along the x-axis as well as the release direction.

The SB is dimensioned as a cube whose length (L_{SB}) is such that all the compressibility effects are exhausted in its volume (Moscatello, Uggenti, et al., 2021). Inside the cube, an obstacle is present to have an impinging jet. To ensure a robust coupling with the dispersion model, a fixed reference coordinate system and a fixed denomination for the SB faces, visible in fig. 6.51 (left), is employed. Within this reference frame, the release point is always positioned at the centre of the back face and the release direction is always parallel to x-axis in the SB. Moreover, since two symmetry planes can be defined, the simulation is carried out only on one quarter of the cube, using the denomination in fig. 6.51 (right). The obstacle inside the SB is featured by a diameter equal to 20 cm and a distance of 30 cm.

The SB dimensions, in principle, would change according to the release pressure. The different size of the SB, however, can be an issue when the interesting profiles are

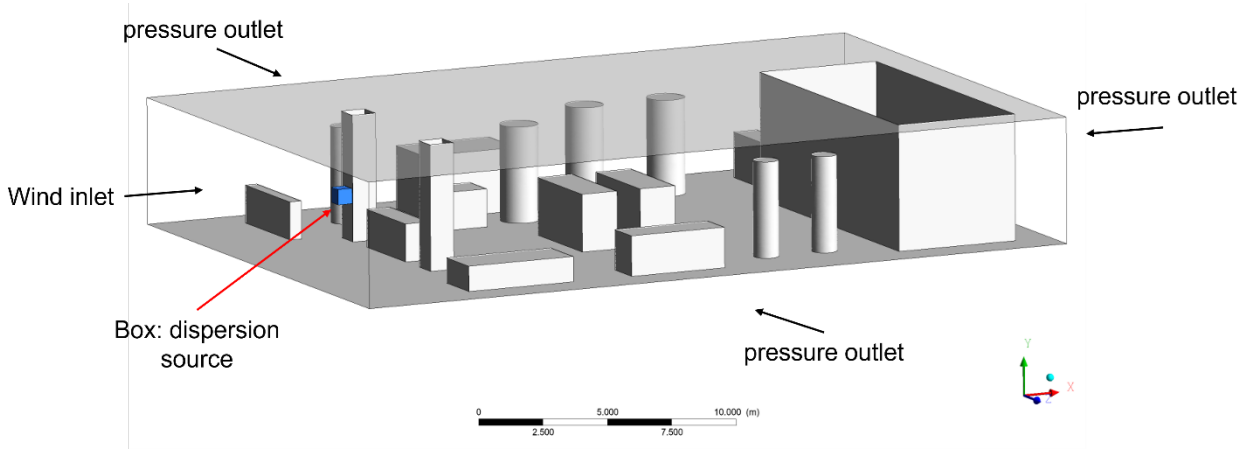

Figure 6.50: *CAD of the case study domain with the representation of the source box.*

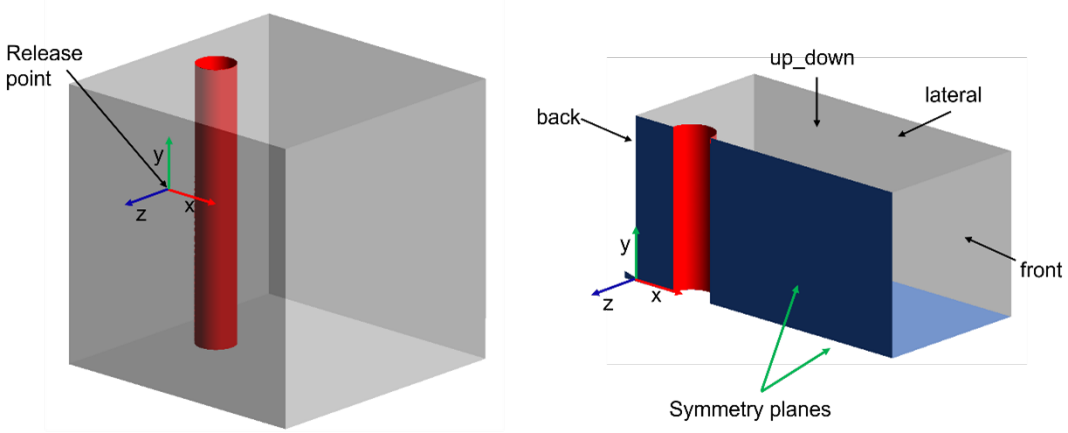

Figure 6.51: *Source Box with reference coordinate frame and face names.*

extracted and used to train a NIROM. At first, the SB is sized following the procedure explained in Moscatello, Uggenti, et al., 2021, considering p_{rel}=80 bar (the largest possible). The resulting characteristic length of the SB is L_{SB}=0.6 m. A non-uniform tetrahedral mesh is realised in ANSYS meshing. The simulation is performed in steady-state using a k-ω SST formulation of the RANS equations. The mixture CH_4-Air is employed in the Fluent setup and the "Species Transport" model without chemical reaction is used. The CH_4 mole fraction is imposed equal to 1 at the domain inlet and a mass flow inlet is set considering a chock mass flow rate due to the pressure release condition. A pressure outlet set at atmospheric pressure is imposed on all the external SB surfaces called *back*, *up_down*, *front* and *lateral* to reproduce the open environment around. A wall with no-slip condition is imposed on the obstacle surface and a symmetry condition is imposed on the symmetry planes.

In principle, the SB size scales as the square root of the release pressure. However,

in order to ensure that the snapshots have the same dimensionality for the POD application, each calculation has been run using the same SB dimensions, selected for the maximum pressure. Then, the different velocity profile components (along x, y and z directions) and CH_4 mass fraction profiles on the faces delimiting the SB (back, lateral, front, up-down) are exported from Fluent on the same cartesian mesh. These profiles are used as boundary conditions in the dispersion simulation. Each dispersion simulation requires about 4 hours on a Precision Dell Tower 7820 with a Intel Xeon Gold 6136 CPU (3.00GHz) and 64 RAM.

The dispersion simulation is performed in steady-state with a k-ω standard formulation of the RANS equation. A wind with intensity of 6 m/s and direction along x is modelled on the face indicated in fig. 6.50. On the other lateral faces of the domain, a pressure outlet with ambient pressure is imposed. The blue box represents the dispersion source: on its faces, the velocity and the CH_4 mass fraction profiles obtained by the SB simulations are loaded as boundary conditions. All the other platform surfaces are modelled as walls with no slip condition.

6.4.1.2 Sampling strategy and CFD dimensionality reduction

Despite in this application the parameter space is one-dimensional, its variation is remarkable from both the physical and the numerical point of view. Increasing the pressure requires more computational resources, as the formation of vortexes is enhanced. Therefore, the sampling strategy should be carefully selected to adequately cover the release pressure range (10-80 bar), which is expected to induce very large variations in the resulting flow fields. The parameter values for the CFD snapshot generation are chosen according to the Newton-Cotes rule (Quarteroni, Sacco, and Saleri, 2010).

It is important to remark that to carry out SB simulations at high pressure, the mass flow inlet boundary conditions must be used instead of imposing directly the pressure. Hence, mass flows are evaluated consistently with the needed release pressures considering the chocked flow conditions. Since the pressure is the reference engineering parameter for QRA, the mass flow is sampled, but the corresponding value of the pressure is considered as the free parameter $\vec{p}$, exploiting the fact that the CFD model is considered as a black-box. Contrarily to the applications dealing with the Gen-III+ PWR stability, where great differences can be found considering the physical perturbations instead of the perturbed few-group data, here there is a unique relationship between pressure and mass flow inlet, due to the sonic flow regime, allowing thus to use the pressure.

Figure 6.52 provides a sketch of the mass flow and pressure samples. As a starting point, an initial level is generated dividing the range to have intervals of about 10 bar each (red dots). Then, the range is partitioned to have intervals of approximately 5 bar each, so that the previous level is included (light blue squares). Finally, the intervals width is halved again, in order each simulation to span 2.5 bar.

Concerning the dimensionality reduction, a sensitivity study on the approximation

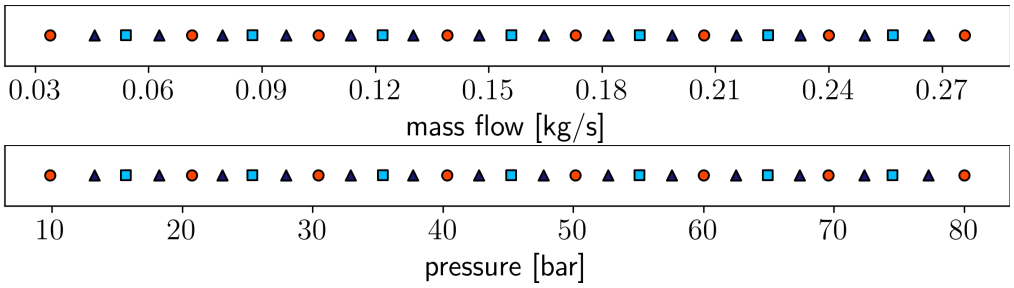

Figure 6.52: *High-fidelity model samples generated with the Newton-Cotes rule. The orange circles are the first level, the light blue squares are the second level and the dark blue triangles are the third level.*

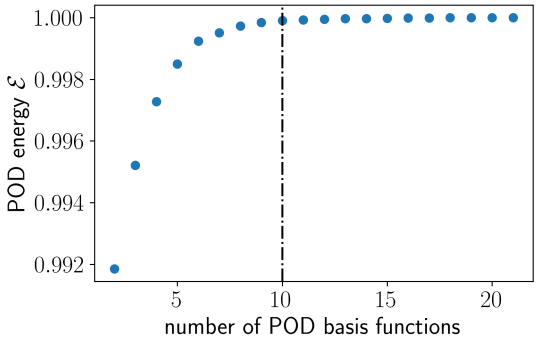

Figure 6.53: *POD basis energy, computed as in Algorithm 2.*

error induced by the POD expansion truncation shows that a relatively small number of basis functions is sufficient to adequately represent the original gas concentration and flow field, catching the 99.99 % of the POD energy $\mathcal{E}$, whose convergence trend is provided in fig. 6.53. Figure 6.54 shows the Root-Mean-Square Error (RMSE) between the CFD snapshots and its POD representation (left) and the RMSE between the CFD snapshot and its ROM approximation (right) as a function of different truncation orders, for different values of the training pressures. The RMSE on the left is useful to highlight that the truncation error approaches zero as the number of basis functions increases, as reasonably expected looking at the trend in fig. 6.53. On the contrary, the second one shows that, after a certain expansion order, the error stabilises on a certain value. This behaviour is explained by the fact that, in addition to the vanishing truncation error, the NIROM snapshot is also affected by the interpolation error due to the RBF interpolation. This trend has an important implication related to the NIROM approximation capabilities, i.e. the truncation error is negligible with respect to the interpolation error, provided that a sufficient number of basis functions is employed to represent the original dataset.

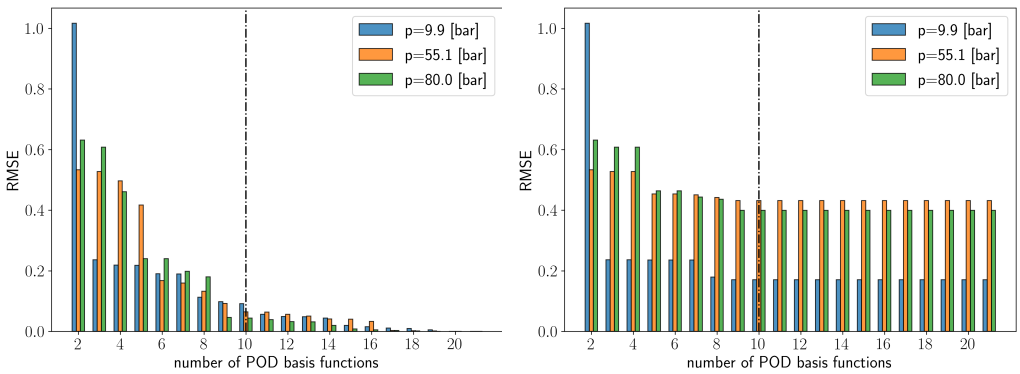

Figure 6.54: *Root-Mean Squared-Error between the original snapshot and its truncated POD representation (left) and Root-Mean-Squared Error between the original snapshot and the ROM reconstruction (right) for some training pressures.*

Hereafter, all the POD expansions are truncated at least at the 10^{th} term, unless differently specified, as indicated by the dashed black line in figs. 6.53 and 6.54.

6.4.1.3 Model training

Exploiting the fact that the samples are nested, the NIROM is initially trained with the first level of points and validated with the points belonging to the second level.

Figures 6.55 and 6.58 provide an overview of the percentage relative error between NIROM and CFD CH_4 and velocity profiles for each face of the SB (see fig. 6.51). The black stars are the training points belonging to the first level, while the coloured dots represent the validation points. The size of these points is proportional to the magnitude of the error. By inspection of these figures, it is possible to notice the presence of significant errors on the back face, where the profiles are featured by some oscillations due to the gas entrainment with the air. Despite their magnitude, these errors do not affect the overall quality of the NIROM approximations, because the back plane, which is tangent to the source point, has a negligible contribution to the overall mass flowing out of the sourcebox. In spite their lower physical importance for the dispersion phase, the contributions for this face dominates the overall error behaviour, making the L_2 norm on the whole snapshot unreliable. To overcome this issue, the face-wise errors are weighted with the mass fraction flowing from each face,

$$\varepsilon = \sum_{i=1}^{faces} \frac{||\vec{y}_{\text{CFD,i}} - \vec{y}_{\text{ROM,i}}||}{||\vec{y}_{\text{CFD,i}}||} w_i, \tag{6.27}$$

where the weights are defined as

$$w_i = \frac{\dot{m}_i}{\dot{m}_{tot}}. \tag{6.28}$$

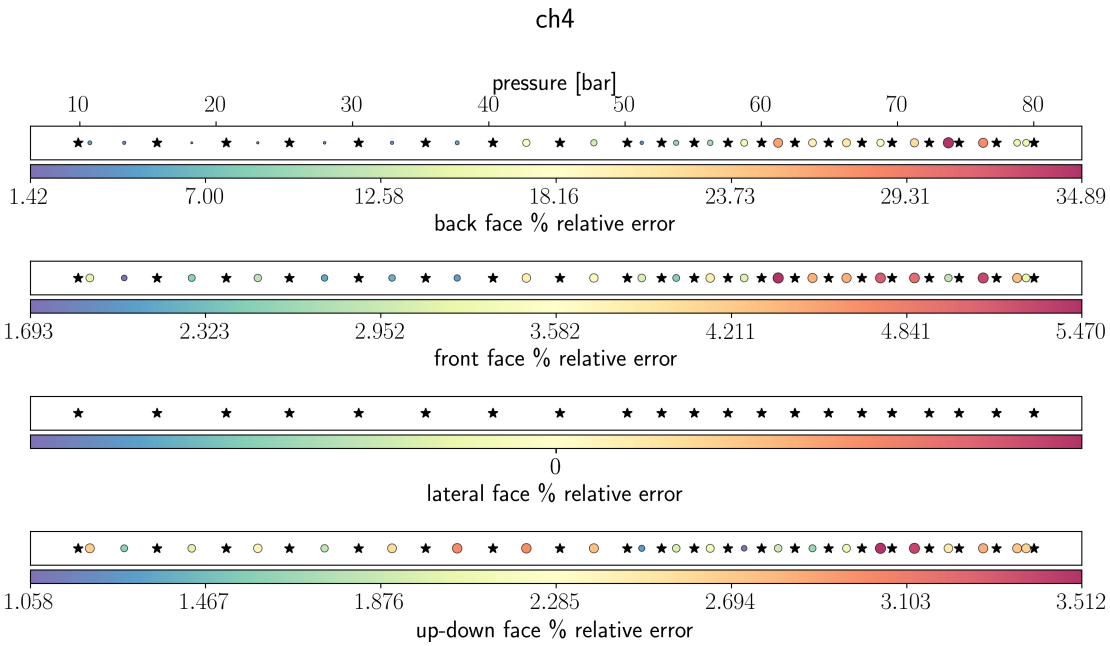

Figure 6.55: *Face-wise relative L_2 error for the CH_4 concentration.*

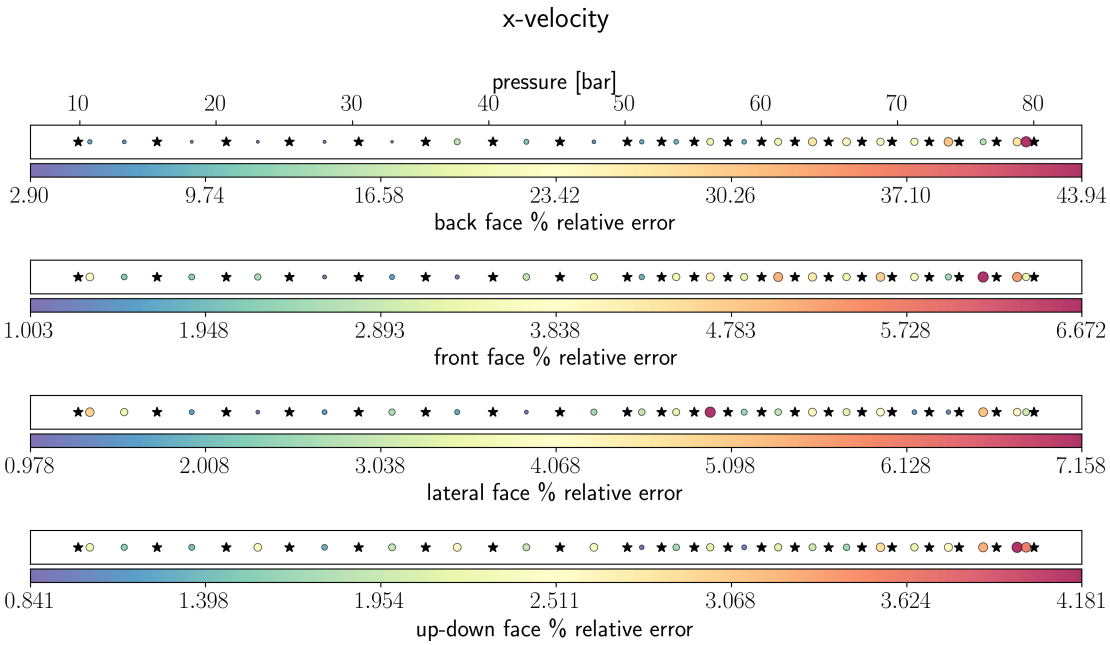

Figure 6.56: *Face-wise relative L_2 error for the x-component of the velocity.*

Concerning the CH_4 concentration profile, it is important to notice here that the error on the lateral face cannot be measured since no gas reaches this face.

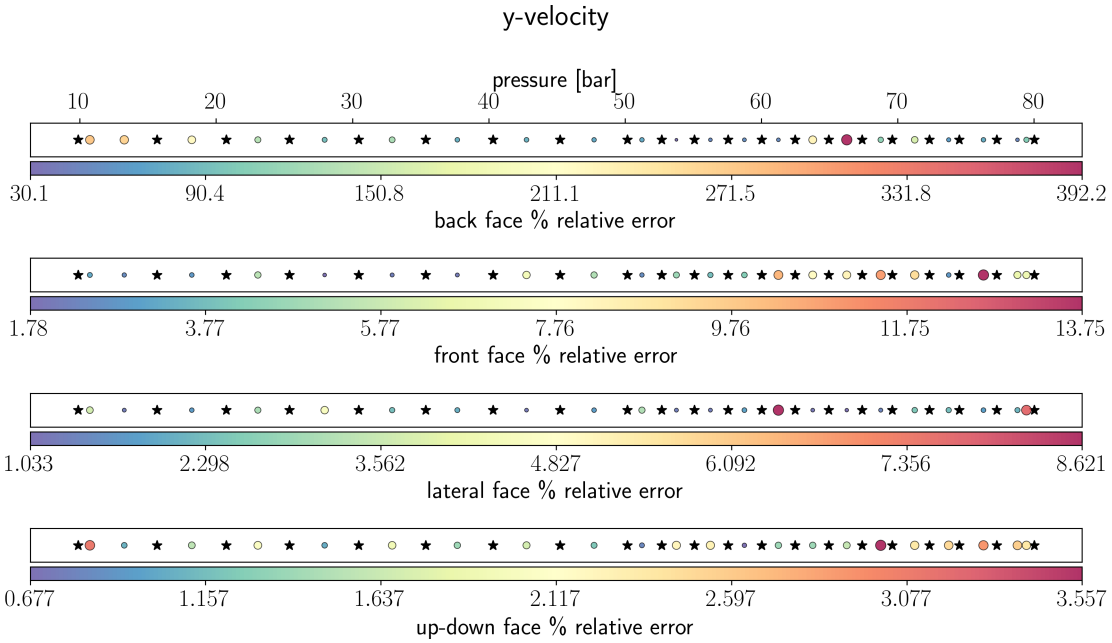

Figure 6.57: *Face-wise relative L_2 error for the y-component of the velocity.*

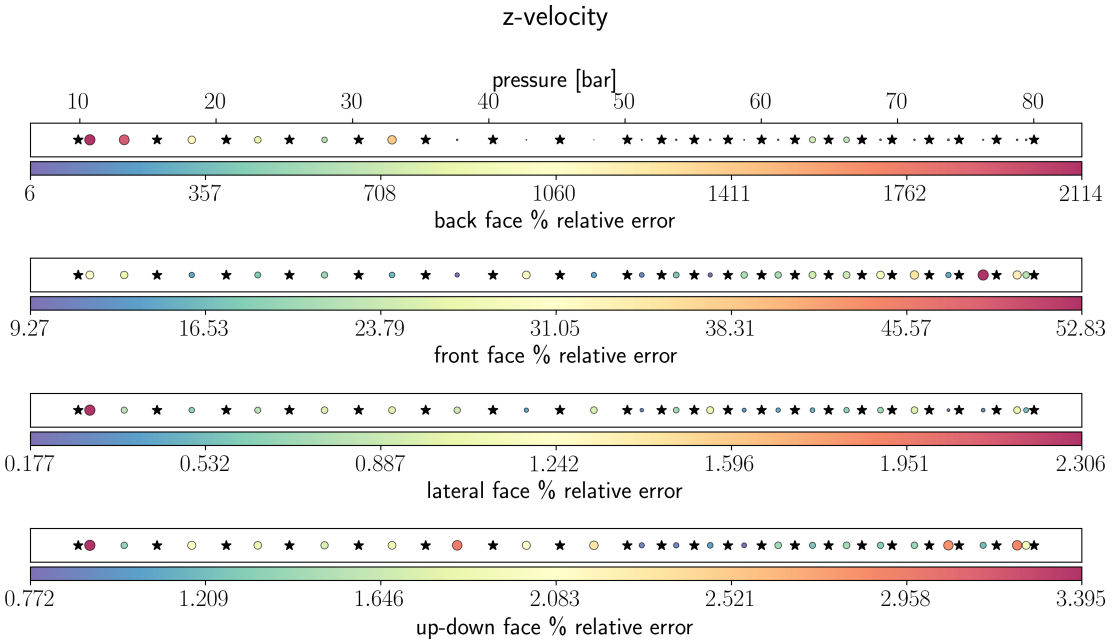

Figure 6.58: *Face-wise relative L_2 error for the z-component of the velocity.*

Exploiting the estimator given by eq. (6.27), it is possible to combine the relative errors for the different profiles on each face to get a more realistic, meaningful and physically reliable overview of the NIROM accuracy with respect to the reference solution.

The values of this estimator is reported in fig. 6.59. The graph on the top represents the

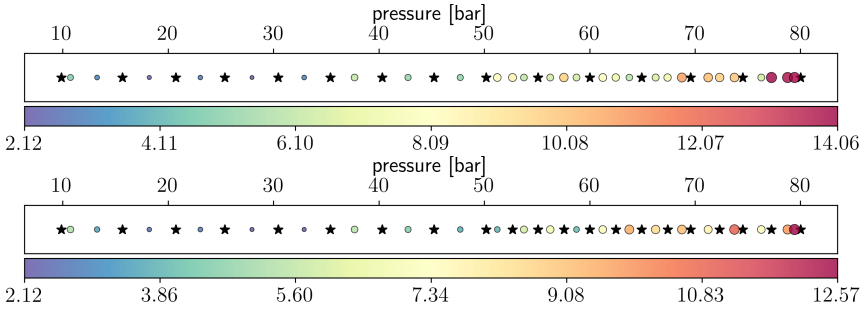

Figure 6.59: *Weighted percentage relative error between NIROM and CFD using two different sets of training points.*

weighted relative error obtained using the first level of the sampled points as training and the other levels as validation, while the graph on the bottom provides the same estimator using the first level and some points of the second for training and the remaining points for validation. As it can be noticed, more training points were taken above 50 bar, in order to reduce the relative error in this region. If the parameter space would be high-dimensional, a more rigorous adaptive selection technique could be employed to spare some computational time, as in Alsayyari, Perkó, et al., 2021.

An example of the ROM surrogate ability to mimic the response of the SBAM model is visible in figs. 6.60 to 6.62, where it is possible to see the CH_4 mass fraction on the front face, the x-component of the velocity on the front face and the y-component of the velocity on the *up_down* face, respectively. Each figure provides the reference profile, computed with CFD, the NIROM surrogate profile and the difference between the two. By direct inspection, it is possible to conclude that the NIROM is able to reproduce fairly well the main spatial features of the flow field, with negligible errors except for a few, small regions on some faces, where oscillations around zero due to the entrainment with air may occur, as already discussed for the back one.

In light of these considerations, the orders of magnitude of the errors reported in fig. 6.59 are judged sufficiently low for the purpose of QRA. In what follows, the analysis is thus focused on another source of (model) uncertainty in the ROM estimation, i.e. the error variability due to the training point selection.

6.4.1.4 ROM error estimation by bootstrap

The error distribution for each validation case is constructed rebooting the NIROM 500 times, by sampling with replacement the initial set of 21 training points.

As mentioned in section 6.1.1.4, some care should be used during the evaluation of the bootstrapped error distribution, checking whether the validation case falls in the training range or not. In the following, only the interpolation situation is examined,

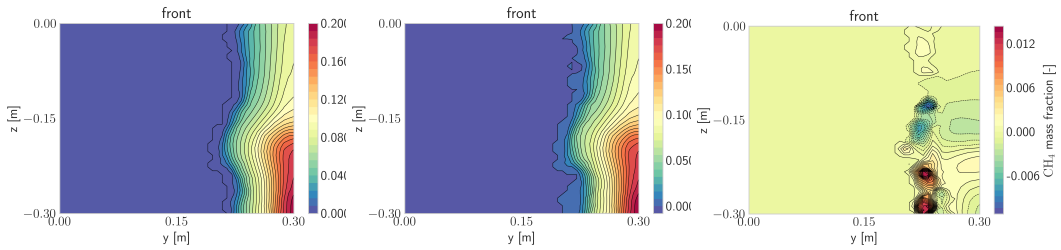

Figure 6.60: *CH_4 mass fractions for CFD (left) and NIROM (centre) and their difference (right) on the front face for the validation case with p=51.237 bar.*

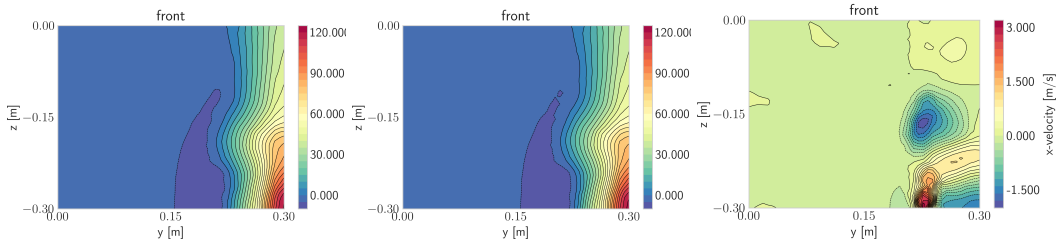

Figure 6.61: *x-component of the velocity field for CFD (left) and NIROM (centre) and their difference (right) on the front face for the validation case with p=51.237 bar.*

since the NIROMs, due to their data-driven nature, are usually employed as interpolating tools. It should be remarked here that, with respect to the deterministic rule used to generate the training and validation samples for our application, there is no guarantee that the bootstrap random resampling covers uniformly the parameter space, therefore this approach should yield, in this particular case, conservative confidence intervals.

Figures 6.63 and 6.64 show the sample distributions of the weighted percentage relative error and RMSE for the validation cases featured by the minimum and maximum pressure, respectively, i.e. 10.374 and 79.442 bar. These graphs are quite informative about the method robustness: the distributions for both the cases are highly skewed towards lower bounds of the error, suggesting that the NIROM is weakly sensitive to the selection of the finite-sized set of training points.

Figure 6.65 provides the distributions for the validation case p_{rel}=51.237 bar, which is featured by the largest variance and mean error. Due to its larger sensitivity to the training sample choice with respect to the others, this case is identified as the worst one, therefore it will be used in the following section to propagate the ROM approximation error through the dispersion calculation chain by means of the UT.

6.4.1.5 Uncertainty propagation to the dispersion simulation

Propagating the bootstrap-evaluated uncertainty characterising the profiles computed by the NIROM onto the output of the successive CFD dispersion simulation is

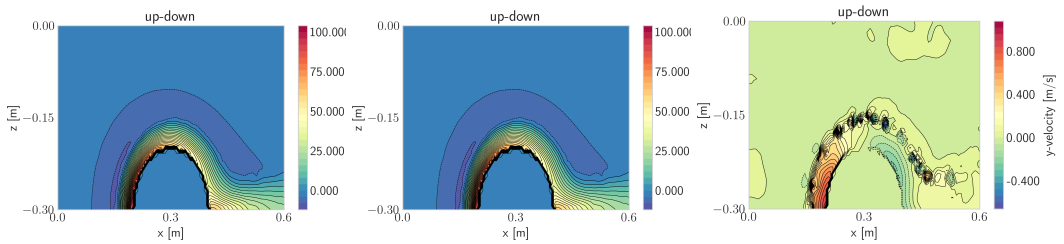

Figure 6.62: *y-component of the velocity field for CFD (left) and NIROM (centre) and their difference (right) on the up-down face for the validation case with p=51.237 bar.*

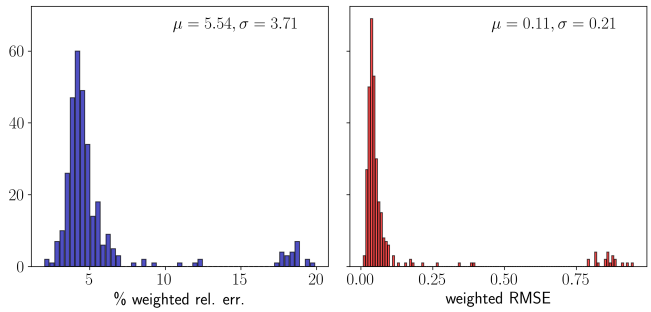

Figure 6.63: *Weighted relative percentage error (left) and weighted RMSE (right) computed for the validation case p_{rel}=10.739 bar.*

certainly not a trivial task. In addition to the large dimensionality of the uncertain input (each snapshot contains $> 6 \cdot 10^6$ elements), the bootstrapped profiles are not associated to real, physical parameters, but only to the set of training points. Thus, the empirical nature of this distribution makes difficult to adopt a smart sampling strategy. A possible option could be using a brute force technique, evaluating the dispersion model with each bootstrapped ROM response. However, despite the dispersion simulations are faster than the SB calculations (~10 hours against ~25), this would not be practically feasible.

To overcome these issues, the procedure illustrated in algorithm 6 is employed. The POD technique helps reducing the dimensionality of the SB gas flow profiles, providing a set of t scalar coefficients for each profile, while the UT allows to select only the most relevant coefficients for the final uncertainty estimation. Consistently with the POD reduction for the training phase, also in this case the POD is truncated at the 10^{th} order, yielding $k = 2t = 20$ sigma points. For each of this point, a dispersion calculation is performed. In particular, the scenario with the largest variance and mean error (p_{rel}=51.237 bar) is investigated. In the following, some safety-critical output parameters estimated by a dispersion calculation are analysed, comparing the results obtained using the high-fidelity, CFD profiles in one case and the approximate, ROM profiles in the other one. Figure 6.66 shows the irreversible injuries volumes obtained using respectively the CFD

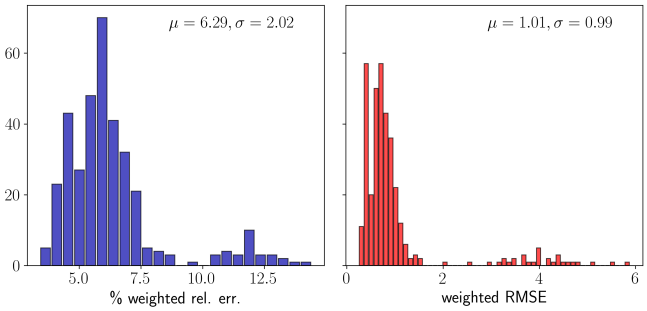

Figure 6.64: *Weighted relative percentage error (left) and weighted RMSE (right) computed for the validation case p_{rel}=79.442 bar.*

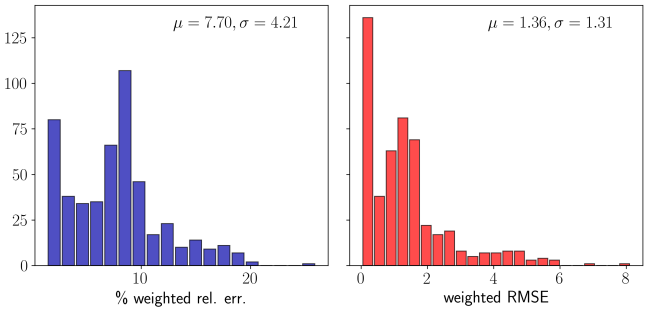

Figure 6.65: *Weighted relative percentage error (left) and weighted RMSE (right) computed for the validation case p_{rel}=51.237 bar.*

SB profiles and the NIROM SB profiles are represented. At a first look, no relevant differences can be appreciated in the two pictures. In both cases the gas cloud tends to split in two portions along the vertical direction, and the same platform components are invested by the gas. Some small discrepancies are highlighted by the red circles and it is difficult to observe any other difference in the shape of the two clouds. In fact, in the case of the CFD profile, an II volume equal to 22.2 m^3 is obtained, while in the NIROM case the II volume is 22.4 m^3, confirming that the difference is negligible (~ 0.9%). This qualitative comparison can be helpful in verifying if there are some relevant differences in the dangerous cloud shape: however, a more detailed analysis needs to be carried out by comparing some safety related quantities. For the purposes of a QRA, the evaluation of the mass and volumes involved in the accident is fundamental for the estimation of the energy that can be released in case of fire or explosion. In addition, a QRA requires to estimate the dangerous zones extension in terms of volumes and areas. For these reasons, the total CH_4 dispersed mass, the CH_4 mass in the flammable cloud, the flammable cloud volume, the II volume and the flammable area at 1.5 m are evaluated. Table 6.4 provides the main output quantities computed within the dispersion calculation using

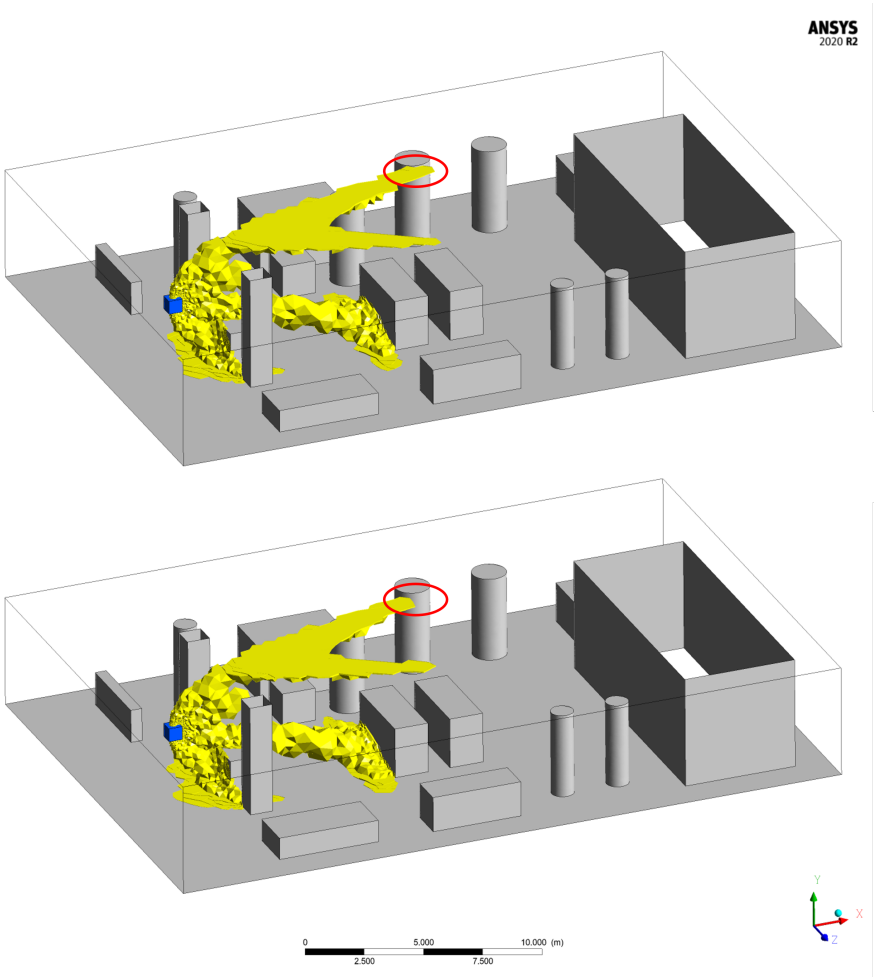

Figure 6.66: *Irreversible Injuries volume obtained using the CFD SB profiles (top) and of the NIROM SB profiles (bottom)*

the original CFD profiles, provided by the SB simulation, and the surrogate profiles computed with the NIROM. The results in the NIROM column, i.e. the mean and the standard deviation of each response, are obtained from the 20 dispersion calculations, exploiting the UT. The results obtained using the NIROM SB profiles are surprisingly similar to the CFD related ones. The relative difference in the mean values is always below 7%, and this is a remarkable result if we consider the dramatic computational cost reduction. In fact, to obtain the CFD SB profiles, almost 24 h are employed, while the ROM profiles are obtained in few seconds. Moreover, from a safety point of view an overestimation of the accident consequences is desirable to avoid risk underestimations. If the upper bound of the ROM-related results are considered, the CH_4 mass in the flammable cloud and the related parameters are overestimated, while the total CH_4 mass and the flammable volume are slightly underestimated (~ 3%).

Table 6.4: *Dispersion calculation outputs computed with the original profiles computed with the CFD approach and the surrogate profiles computed with the NIROM approach. The results of the last column are provided with an uncertainty, put in parentheses, given in terms of 1 standard deviation.*

	CFD profile	ROM profile
Total dispersed CH_4 mass [kg]	5.959	5.6(2)
CH_4 mass in the flammable cloud [kg]	0.066	0.064(4)
Flammable cloud volume [m^3]	1.925	1.8(1)
Irreversible injuries volume [m^3]	22	23(1)
Irreversible injuries area at 1.5 m height [m^2]	4.20	4.5(3)

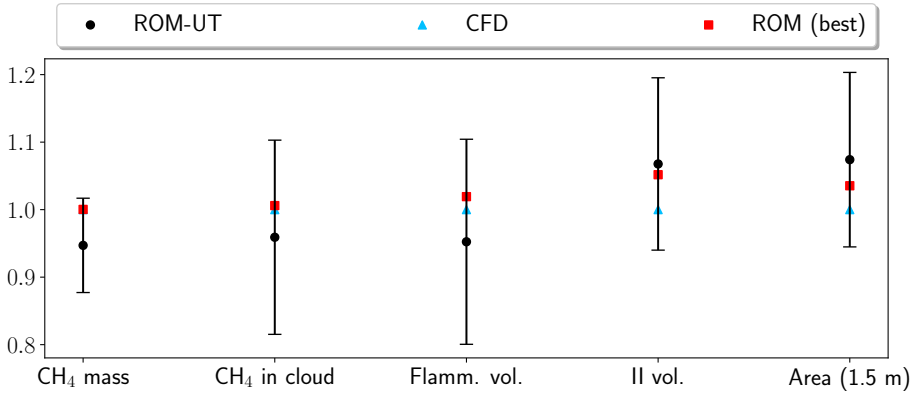

Figure 6.67: *Expected value and standard deviation for some safety-relevant quantities, i.e., the total dispersed mass of CH_4, the mass of CH_4 in the cloud, the flammable volume, the irreversible injuries volume and the irreversible injuries area at 1.5 m. Each data is normalised with respect to the CFD case.*

6.4.2 Conclusions and future perspectives

In this section the POD-RBF framework was applied for the non-intrusive reduced order modelling of QRA-oriented CFD simulations. This class of NIROMs has been recently applied in many research fields, yet most of the applications do not show satisfactory assessment and propagation of the ROM approximation errors, in particular in the presence of functional (e.g., time- and/or space-dependent) outputs.

In this respect, since the final aim of this application is the adoption of these surrogate models to minimise the computational effort associated to QRA studies (where it is of paramount importance to endow the simulation model responses with confidence intervals), a methodology for the assessment of the ROM uncertainty in the estimation of functional (in this case, space-dependent) safety-critical quantities is proposed. To test this methodology and prove its effectiveness, the ROM is applied to the case of high pressure, accidental gas release in an off-shore oil&gas plant, where the critical output

variables of interest are the flammable gas volume, which is related to the irreversible injuries area.

First, the NIROM is trained exploiting a set of nested parameter samples in order to adaptively refine it with a reduced computational burden. The validation error, computed as a weighted sum of the sourcebox face-wise errors, is considered sufficiently low (<15%) using the first level of training cases plus additional cases above 50 bar.

Then, to estimate the model response variability to the training samples, the bootstrap method is employed to obtain the statistical distributions from the ensemble of ROM responses. Since, in this case study, the ROM response is used as input for the CFD dispersion simulation, a quantitative assessment of the impact of the ROM approximation error is mandatory.

The propagation of the uncertainty from the ROM response distribution to the dispersion model output is achieved combining the POD and the UT techniques. The first is employed to reduce the input data dimensionality, while the second is adopted to select the input data for the dispersion calculations and finally to estimate the dispersion output confidence intervals. The main quantities of interest in such calculations, pertinent to the QRA analysis, are in very good agreement with the same results obtained using the profiles computed by CFD, with a relative error between the two approaches below 10% and a reduction of the computational time of about three orders of magnitude, suggesting that the POD-RBF NIROM is adequate to obtain fast yet very accurate results. It should be remarked that a QRA study has an intrinsically high level of uncertainty, which makes the additional 10% introduced by the ROM model acceptable.

A future development of this activity could be to increase the number of training points considering also other input parameters affecting the SB, namely the break size and the obstacle features. Since these parameters have a strong influence on the SB dimension, a more sophisticated strategy should be devised in order to handle the snapshots defined on a different spatial domain. Moreover, adaptive sparse sampling techniques should be employed in order to progressively refine the parameter space where the error is not acceptable.

In parallel to these activities, a surrogate model for the dispersion phase should be trained as well, in view of a coupling with the source-box ROM, allowing to realise a real-time simulation framework, featured by the capability of providing confidence intervals on the main results thanks to the combination of bootstrapping and UT.

References

Alsayyari, F., Z. Perkó, D. Lathouwers, and J. L. Kloosterman (2019). "A nonintrusive reduced order modelling approach using Proper Orthogonal Decomposition and locally adaptive sparse grids". In: *Journal of Computational Physics* 399, page 108912 (cited on page 188).

Alsayyari, F., Z. Perkó, M. Tiberga, J. L. Kloosterman, and D. Lathouwers (2021). "A fully adaptive nonintrusive reduced-order modelling approach for parametrized time-dependent problems". In: *Computer Methods in Applied Mechanics and Engineering* 373.January, page 113483 (cited on pages 188, 262).

Audouze, C., F. De Vuyst, and P. B. Nair (2013). "Nonintrusive reduced-order modeling of parametrized time-dependent partial differential equations". In: *Numerical Methods for Partial Differential Equations* 29.5, pages 1587–1628 (cited on page 183).

Bagheri, M., A. Alamdari, and M. Davoudi (2016). "Quantitative risk assessment of sour gas transmission pipelines using CFD". In: *Journal of Natural Gas Science and Engineering* 31, pages 108–118 (cited on page 182).

Balay, S., S. Abhyankar, M. F. Adams, J. Brown, P. Brune, K. Buschelman, L. Dalcin, A. Dener, V. Eijkhout, W. D. Gropp, D. Karpeyev, D. Kaushikand, M. G. Knepley, D. A. Mayand, L. C. McInnes, R. T. Mills, T. Munson, K. Rupp, P. Sanan, B. F. Smith, S. Zampini, and H. Zhang (2020). *PETSc Users Manual*. Technical report ANL-95/11 - Revision 3.13. Argonne National Laboratory, Cass Ave, Lemont, IL (U.S.A.) (cited on page 217).

Ballarin, F., A. Manzoni, G. Rozza, and S. Salsa (2014). "Shape Optimization by Free-Form Deformation: Existence Results and Numerical Solution for Stokes Flows". In: *Journal of scientific computing* 60 (3), pages 537–563 (cited on page 182).

Bargagli Stoffi, F. J., G. Cevolani, and G. Gnecco (2022). "Simple Models in Complex Worlds: Occam's Razor and Statistical Learning Theory". In: *Minds and Machines* 32.1, pages 13–42 (cited on page 212).

Bellman, R. (1957). "Dynamic Programming". Rand Corporation research study. Princeton University Press (cited on pages 181, 206).

Benner, P., S. Gugercin, and K. Willcox (2015). "A Survey of Projection-Based Model Reduction Methods for Parametric Dynamical Systems". In: *SIAM Review* 57.4, pages 483–531 (cited on page 182).

Cacuci, D. G. (2010). "Handbook of Nuclear Engineering: Vol. 1: Nuclear Engineering Fundamentals; Vol. 2: Reactor Design; Vol. 3: Reactor Analysis; Vol. 4: Reactors of Generations III and IV; Vol. 5: Fuel Cycles, Decommissioning, Waste Disposal and Safeguards". Volume 1. Springer Science & Business Media (cited on page 200).

Canuto, C., M. Y. Hussaini, A. Quarteroni, and T. A. Zang (2007). "Spectral methods: evolution to complex geometries and applications to fluid dynamics". Springer Science & Business Media (cited on page 205).

Caron, D. (2017). "Neutronics methods for the multiphysics analysis of nuclear fission systems". PhD thesis. Politecnico di Torino (cited on pages 243, 245).

Casenave, F., A. Gariah, C. Rey, and F. Feyel (2020). "A nonintrusive reduced order model for nonlinear transient thermal problems with nonparametrized variability". In: *Advanced Modeling and Simulation in Engineering Sciences* 7.1 (cited on page 183).

Chen, W., J. S. Hesthaven, B. Junqiang, Y. Qiu, Z. Yang, and Y. Tihao (2018). "Greedy Nonintrusive Reduced Order Model for Fluid Dynamics". In: *AIAA Journal* 56.12, pages 4927–4943 (cited on page 184).

Clenshaw, C. W. and A. R. Curtis (1960). "A method for numerical integration on an automatic computer". In: *Numerische Mathematik* 2.1, pages 197–205 (cited on page 211).

Cortes, C. and V. Vapnik (1995). "Support-vector networks". In: *Machine learning* 20.3, pages 273–297 (cited on pages 183, 203).

De Mulatier, C., E. Dumonteil, A. Rosso, and A. Zoia (2015). "The critical catastrophe revisited". In: *Journal of Statistical Mechanics: Theory and Experiment* 2015.8, P08021 (cited on page 208).

Demazière, C., A. Mylonakis, P. Vinai, A. Durrant, F. D. S. Ribeiro, J. Wingate, G. Leontidis, and S. Kollias (2021). "Neutron noise-based anomaly classification and localization using machine learning". In: *EPJ Web of Conferences*. Volume 247. EDP Sciences, page 21004 (cited on page 183).

Demo, N., M. Tezzele, and G. Rozza (2019). "A non-intrusive approach for the reconstruction of POD modal coefficients through active subspaces". In: *Comptes Rendus - Mecanique* 347.11, pages 873–881 (cited on pages 183–184).

Dur, O., S. T. Coskun, K. O. Coskun, D. H. Frakes, L. B. Kara, and K. Pekkan (2011). "Computer-Aided Patient-Specific Coronary Artery Graft Design Improvements Using CFD Coupled Shape Optimizer". In: *Cardiovascular Engineering and Technology* 2, pages 35–47 (cited on page 182).

Dutta, S., M. W. Farthing, E. Perracchione, G. Savant, and M. Putti (2021). "A greedy non-intrusive reduced order model for shallow water equations". In: *Journal of Computational Physics* 439, page 110378 (cited on page 184).

Efron, B. (1981). "Nonparametric Estimates of Standard Error: The Jackknife, the Bootstrap and Other Methods". In: *Biometrika* 68.3, pages 589–599 (cited on page 252).

Feinberg, J. and H. P. Langtangen (2015). "Chaospy: An open source tool for designing methods of uncertainty quantification". In: *Journal of Computational Science* 11, pages 46–57 (cited on page 210).

Foad, B., A. Yamamoto, and T. Endo (2020). "Efficient uncertainty quantification for PWR during LOCA using unscented transform with singular value decomposition". In: *Annals of Nuclear Energy* 141, page 107341 (cited on page 196).

Franquet, E., V. Perrier, S. Gibout, and P. Bruel (2015). "Free underexpanded jets in a quiescent medium: A review". In: *Progress in Aerospace Sciences* 77, pages 25–53 (cited on page 253).

Fu, S., X. Yan, D. Zhang, C. Li, and E. Zio (2016). "Framework for the quantitative assessment of the risk of leakage from LNG-fueled vessels by an event tree-CFD". In: *Journal of Loss Prevention in the Process Industries* 43.2016, pages 42–52 (cited on page 182).

Gandini, A. (1978). "Higher order time-dependent generalized perturbation theory". In: *Nuclear Science and Engineering* 67, pages 91–106 (cited on page 198).

Geman, S., E. Bienenstock, and R. Doursat (1992). "Neural networks and the bias/variance dilemma". In: *Neural computation* 4.1, pages 1–58 (cited on page 212).

Genz, A. and B. D. Keister (1996). "Fully symmetric interpolatory rules for multiple integrals over infinite regions with Gaussian weight". In: *Journal of Computational and Applied Mathematics* 71.2, pages 299–309 (cited on page 211).

Ghojogh, B. and M. Crowley (2019). "The theory behind overfitting, cross validation, regularization, bagging, and boosting: tutorial". In: *arXiv preprint arXiv:1905.12787* (cited on page 183).

Gilli, L., D. Lathouwers, J. Kloosterman, T. van der Hagen, A. Koning, and D. Rochman (2013). "Uncertainty quantification for criticality problems using non-intrusive and adaptive Polynomial Chaos techniques". In: *Annals of Nuclear Energy* 56, pages 71–80 (cited on page 205).

Grasso, G., C. Petrovich, D. Mattioli, C. Artioli, P. Sciora, D. Gugiu, G. Bandini, E. Bubelis, and K. Mikityuk (2014). "The core design of ALFRED, a demonstrator for the European lead-cooled reactors". In: *Nuclear Engineering and Design* 278, pages 287–301 (cited on page 242).

Guo, M. and J. S. Hesthaven (2019). "Data-driven reduced order modeling for time-dependent problems". In: *Computer Methods in Applied Mechanics and Engineering* 345, pages 75–99 (cited on page 184).

Hardy, R. L. (1971). "Multiquadric equations of topography and other irregular surfaces". In: *Journal of Geophysical Research (1896-1977)* 76.8, pages 1905–1915 (cited on pages 190–191).

Hecht, F. (2012). "New development in FreeFem++". In: *Journal of numerical mathematics* 20.3-4, pages 251–266 (cited on page 216).

Henry, A. F. (1958). "The Application of Reactor Kinetics to the Analysis of Experiments". In: *Nuclear Science and Engineering* 3, pages 52–70 (cited on page 241).

Hernandez, V., J. E. Roman, and V. Vidal (2005). "SLEPc: a scalable and flexible toolkit for the solution of eigenvalue problems". In: *ACM Transactions on Mathematical Software* 31, pages 351–362 (cited on page 217).

Iuliano, E. and D. Quagliarella (2013). "Aerodynamic shape optimization via non-intrusive POD-based surrogate modelling". In: *2013 IEEE Congress on Evolutionary Computation*, pages 1467–1474 (cited on page 184).

Ivanov, K., M. Avramova, I. A. Kodeli, and E. Sartori (2007). "Benchmark for uncertainty analysis in modeling (UAM) for design, operation and safety analysis of LWRs". Citeseer (cited on pages 202–203).

Izenman, A. J. (2008). "Modern multivariate statistical techniques". In: *Regression, classification and manifold learning* 10, pages 978– (cited on page 206).

Jameson, A. and J. Vassberg (2001). "Computational fluid dynamics for aerodynamic design - Its current and future impact". In: *39th Aerospace Sciences Meeting and Exhibit* (cited on page 182).

Julier, S. J. and J. K. Uhlmann (1997). "New extension of the Kalman filter to nonlinear systems". In: *Signal Processing, Sensor Fusion, and Target Recognition VI*. Edited by I. Kadar. Volume 3068. International Society for Optics and Photonics. SPIE, pages 182–193 (cited on pages 194, 252).

Kaintura, A., T. Dhaene, and D. Spina (2018). "Review of polynomial chaos-based methods for uncertainty quantification in modern integrated circuits". In: *Electronics* 7.3, page 30 (cited on page 205).

Kalman, R. E. (Mar. 1960). "A New Approach to Linear Filtering and Prediction Problems". In: *Journal of Basic Engineering* 82.1, pages 35–45 (cited on page 194).

Knuth, D. E. (1998). "The Art of Computer Programming Volumes 1-3". Addison-Wesley Longman Publishing Co., Inc. (cited on page 236).

Kohavi, R. (1995). "A Study of Cross-Validation and Bootstrap for Accuracy Estimation and Model Selection". In: *Proceedings of the 14th International Joint Conference on Artificial Intelligence - Volume 2*. IJCAI'95. Montreal, Quebec, Canada: Morgan Kaufmann Publishers Inc., pages 1137–1143 (cited on page 252).

Kumar, D., M. Raisee, and C. Lacor (2016). "An efficient non-intrusive reduced basis model for high dimensional stochastic problems in CFD". In: *Computers and Fluids* 138, pages 67–82 (cited on pages 183–184).

Lassila, T., A. Manzoni, A. Quarteroni, and G. Rozza (2014). "Model Order Reduction in Fluid Dynamics: Challenges and Perspectives". In: *Reduced Order Methods for Modeling and Computational Reduction. MS&A - Modeling, Simulation and Applications*. Edited by Quarteroni A., Rozza G. Volume 9. Cham: Springer. Chapter 10 (cited on page 183).

Lorenzi, S., A. Cammi, L. Luzzi, and G. Rozza (2016). "POD-Galerkin method for finite volume approximation of Navier–Stokes and RANS equations". In: *Computer Methods in Applied Mechanics and Engineering* 311, pages 151–179 (cited on pages 182, 184).

— (2017). "A reduced order model for investigating the dynamics of the Gen-IV LFR coolant pool". In: *Applied Mathematical Modelling* 46, pages 263–284 (cited on page 182).

Marelli, S. and B. Sudret (2018). "An active-learning algorithm that combines sparse polynomial chaos expansions and bootstrap for structural reliability analysis". In: *Structural Safety* 75, pages 67–74 (cited on page 192).

Marrel, A., N. Pérot, and C. Mottet (2014). "Development of a surrogate model and sensitivity analysis for spatio-temporal numerical simulators". In: *Stochastic Environmental Research and Risk Assessment* 29, pages 959–974 (cited on page 184).

Massone, M., N. Abrate, G. F. Nallo, D. Valerio, S. Dulla, and P. Ravetto (2022). "Code-to-code SIMMER/FRENETIC comparison for the neutronic simulation of lead-cooled fast reactors". In: *Annals of Nuclear Energy* 174, page 109124 (cited on page 243).

Moore, G. E. (1998). "Cramming More Components Onto Integrated Circuits". In: *Proceedings of the IEEE* 86, pages 82–85 (cited on page 181).

Moscatello, A., A. C. Uggenti, R. Gerboni, and A. Carpignano (2021). "A novel approach to high-pressure gas releases simulations". In: *Journal of Loss Prevention in the Process Industries* 72, page 104531 (cited on pages 251, 253, 255–256).

Munson, B., D. Young, T. Okiishi, W. Huebsch, and A. Rothmayer (2010). "Fluid Mechanics". Wiley (cited on page 253).

Nallo, G. F., N. Abrate, S. Dulla, P. Ravetto, and D. Valerio (2020). "Neutronic benchmark of the FRENETIC code for the multiphysics analysis of lead fast reactors". In: *The European Physical Journal Plus* 135, page 238 (cited on page 243).

Nanty, S., C. Helbert, A. Marrel, N. Pérot, and C. Prieur (2017). "Uncertainty quantification for functional dependent random variables". In: *Computational Statistics* 32, pages 559–583 (cited on page 184).

NRC (2016). *Standard Technical Specifications, Westinghouse Advanced Passive 1000 (AP1000) Plants, Volume 1: Specifications*. Technical report NUREG-2194. Office of New Reactors, U.S. Nuclear Regulatory Commission, Washington, DC (U.S.A.) (cited on pages 197, 235).

Parihar, A., C. Vergara, and J. K. Clutter (2011). "Methodology for consequence analysis of LNG releases at deepwater port facilities". In: *Safety Science* 49.5, pages 686–694 (cited on page 182).

Pedroni, N. (2022). "Computational methods for the robust optimization of the design of a dynamic aerospace system in the presence of aleatory and epistemic uncertainties". In: *Mechanical Systems and Signal Processing* 164, page 108206 (cited on page 182).

Pedroni, N. and E. Zio (2017). "An Adaptive Metamodel-Based Subset Importance Sampling approach for the assessment of the functional failure probability of a thermal-hydraulic passive system". In: *Applied Mathematical Modelling* 48, pages 269–288 (cited on page 182).

Pedroni, N., E. Zio, and G. Apostolakis (2010). "Comparison of bootstrapped artificial neural networks and quadratic response surfaces for the estimation of the functional failure probability of a thermal-hydraulic passive system". In: *Reliability Engineering and System Safety* 95.4, pages 386–395 (cited on page 192).

Popper, K. R. and W. Barthley III (1988). "The Open universe: an argument for indeterminism from the postscript to the logic of scientific discovery". Routledge, London, U.K. (cited on page 182).

Quarteroni, A., R. Sacco, and F. Saleri (2010). "Numerical mathematics". Volume 37. Springer Science & Business Media (cited on page 257).

Rahman, S. M., O. San, and A. Rasheed (2018). "A Hybrid Approach for Model Order Reduction of Barotropic Quasi-Geostrophic Turbulence". In: *Fluids* 3.4 (cited on pages 182–183, 192).

Rahnema, F. and E. M. Nichita (1997). "Leakage corrected spatial (assembly) homogenization technique". In: *Annals of Nuclear Energy* 24.6, pages 477–488 (cited on page 208).

Rippa, S. (2011). "An algorithm for selecting a good value for the parameter c in radial basis function interpolation". In: *Advances in Computational Mathematics* 34.1, pages 105–126 (cited on page 191).

Roma, G., F. Di Maio, A. Bersano, N. Pedroni, C. Bertani, F. Mascari, and E. Zio (2021). "A Bayesian framework of inverse uncertainty quantification with principal component analysis and Kriging for the reliability analysis of passive safety systems". In: *Nuclear Engineering and Design* 379, page 111230 (cited on page 184).

Russell, S. J. (2010). "Artificial intelligence a modern approach". Pearson Education, Inc. (cited on pages 183, 232).

Saad, Y. (1992). "Numerical methods for large eigenvalue problems". Manchester University Press (cited on page 198).

Santanoceto, M., M. Tiberga, Z. Perkó, S. Dulla, and D. Lathouwers (2021). "Preliminary uncertainty and sensitivity analysis of the Molten Salt Fast Reactor steady-state using a Polynomial Chaos Expansion method". In: *Annals of Nuclear Energy* 159, page 108311 (cited on page 205).

Sargeni, A., K. Burn, and G. Bruna (2016). "The impact of heavy reflectors on power distribution perturbations in large PWR reactor cores". In: *Annals of Nuclear Energy* 94, pages 566–575 (cited on page 203).

Schaback, R. (1995). "Error estimates and condition numbers for radial basis function interpolation". In: *Advances in Computational Mathematics* 3.3, pages 251–264 (cited on page 184).

Secchi, P., E. Zio, and F. Di Maio (2008). "Quantifying uncertainties in the estimation of safety parameters by using bootstrapped artificial neural networks". In: *Annals of Nuclear Energy* 35.12, pages 2338–2350 (cited on page 192).

Seike, M., N. Kawabata, and M. Hasegawa (2017). "Quantitative assessment method for road tunnel fire safety: Development of an evacuation simulation method using CFD-derived smoke behavior". In: *Safety Science* 94, pages 116–127 (cited on page 182).

Smolyak, S. A. (1963). "Quadrature and interpolation formulas for tensor products of certain classes of functions". In: *Dokl. Akad. Nauk SSSR* 148.5, pages 1042–1045 (cited on pages 188, 206).

Sudret, B. (2008). "Global sensitivity analysis using polynomial chaos expansions". In: *Reliability engineering & system safety* 93.7, pages 964–979 (cited on page 214).

Tal, O., E. Israeli, P. Ravetto, and E. Gilad (2019). "The adjoint problem as physical heuristic for loading pattern optimization". In: *Annals of Nuclear Energy* 134, pages 226–234 (cited on page 219).

Tommasi, J., M. Maillot, and G. Rimpault (2016). "Calculation of higher-order fluxes in symmetric cores—I: theory". In: *Nuclear Science and Engineering* 184, pages 174–189 (cited on page 182).

Usachev, L. N. (1956). "Equation for the importance of neutrons, reactor kinetics and the theory of perturbations". In: *Proc. Int. Conf. on the Peaceful Uses of Atomic Energy, Geneva, Switzerland, Aug. 8-12, 1955*. Volume 5, pages 503–510 (cited on page 219).

Vivalda, C., R. Gerboni, and A. Carpignano (2018). "A practical approach to risk-based gas monitoring system design for oil and gas offshore platforms". In: *Proceedings of the 14th Probabilistic Safety Assessment and Management Conference* (cited on page 255).

Volkwein, S. (2011). "Model reduction using proper orthogonal decomposition". In: *Lecture notes, Institute of Mathematics and Scientific Computing, University of Graz. see http://www. uni-graz. at/imawww/volkwein/POD. pdf* 1025 (cited on pages 184, 188).

Wang, L., Y. Zhang, and J. Feng (2005). "On the Euclidean distance of images". In: *IEEE transactions on pattern analysis and machine intelligence* 27.8, pages 1334–1339 (cited on pages 227–228).

Wiener, N. (1938). "The homogeneous chaos". In: *American Journal of Mathematics* 60.4, pages 897–936 (cited on page 204).

Williams, M. M. R. (2007). "Polynomial Chaos Functions and Neutron Diffusion". In: *Nuclear Science and Engineering* 155.1, pages 109–118 (cited on page 205).

Williams, M. L. (2011). "Resonance self-shielding methodologies in SCALE 6". In: *Nuclear Technology* 174.2, pages 149–168 (cited on page 215).

Williams, M. (1991). "Generalized contributon response theory". In: *Nuclear Science and Engineering* 108.4, pages 355–383 (cited on page 219).

Wu, X., T. Kozlowski, and H. Meidani (2018). "Kriging-based inverse uncertainty quantification of nuclear fuel performance code BISON fission gas release model using time series measurement data". In: *Reliability Engineering & System Safety* 169, pages 422–436 (cited on page 184).

Wu, X., T. Kozlowski, H. Meidani, and K. Shirvan (2018). "Inverse uncertainty quantification using the modular Bayesian approach based on Gaussian process, Part 1: Theory". In: *Nuclear Engineering and Design* 335, pages 339–355 (cited on page 184).

Xiao, D. (2019). "Error estimation of the parametric non-intrusive reduced order model using machine learning". In: *Computer Methods in Applied Mechanics and Engineering* 355, pages 513–534 (cited on page 252).

Xiao, D., F. Fang, A. Buchan, C. Pain, I. Navon, and A. Muggeridge (2015). "Non-intrusive reduced order modelling of the Navier–Stokes equations". In: *Computer Methods in Applied Mechanics and Engineering* 293, pages 522–541 (cited on page 183).

Xiao, D., F. Fang, C. C. Pain, and I. M. Navon (2017). "A parameterized non-intrusive reduced order model and error analysis for general time-dependent nonlinear partial differential equations and its applications". In: *Computer Methods in Applied Mechanics and Engineering* 317, pages 868–889 (cited on pages 184, 192).

Xiu, D. and G. E. Karniadakis (2002). "The Wiener–Askey polynomial chaos for stochastic differential equations". In: *SIAM journal on scientific computing* 24.2, pages 619–644 (cited on page 204).

Zio, E. (2006). "A study of the bootstrap method for estimating the accuracy of artificial neural networks in predicting nuclear transient processes". In: *IEEE Transactions on Nuclear Science* 53.3, pages 1460–1478 (cited on page 192).

Zio, E., G. Apostolakis, and N. Pedroni (2010). "Quantitative functional failure analysis of a thermal–hydraulic passive system by means of bootstrapped Artificial Neural Networks". In: *Annals of Nuclear Energy* 37.5, pages 639–649 (cited on page 192).

Chapter 7

Generalized Perturbation Techniques for Uncertainty Quantification in Lead-Cooled Fast Reactors

> You just don't get it, do you, Jean-Luc? The trial never ends. [...]
> For that one fraction of a second, you were open to options you had never considered. That is the exploration that awaits you. Not mapping stars and studying nebulae, but charting the unknowable possibilities of existence.
>
> Q, Star Trek: The Next Generation

7.1 Introduction

Almost 2500 years ago, the greek philosopher and poet Xenophanes already pointed out, with some remarkable lines, that our knowledge of the world is imperfect and inevitably based on hypotheses and guesses. The fragment 18 of his production quotes

> *The Gods did not reveal, in the beginning, all things to mortal,*
> *but as time goes by, by seeking, they can know things better,* [1]

[1] (Popper, 1998)

while the fragment 34 reads

But as for certain truth, no man has known it,
Nor will he know it; neither of the gods,
Nor yet of all the things of which I speak.
And even if by chance he were to utter
The perfect truth, he would himself not know it;
For all is but a woven web of guesses.[1]

In spite of the complex, cutting-edge physico-mathematical models and computational tools we dispose today, these ancient words are still echoing today and will probably echo forever. Our knowledge of the nature may improve through experiments and observations of the reality, but we will never be able to tear "the web of Maya" (Schopenhauer, 1859). Apart from the philosophical implications of this fact, the intrinsic uncertainty characterising our models has important consequences in practical life, especially when it amounts to design and operate an engineering system. Therefore, estimating the uncertainty and all its components is a key issue in order to prove the system effectiveness and to ensure its safe and reliable operation, especially if it is a nuclear installation.

Among the different approaches adopted nowadays to perform the safety studies of nuclear power plants, the so-called Best Estimate Plus Uncertainty (BEPU) methodology is becoming more and more popular. The purpose of this approach is the qualification of the results provided by reference computational models through an estimate of their uncertainty (D'Auria, Camargo, and Mazzantini, 2012), which may be epistemic, i.e. connected to the physico-mathematical model and its approximations (e.g., continuous-energy vs. multi-group, transport vs. diffusion, ...), or aleatory (Hüllermeier and Waegeman, 2019), i.e. related to the intrinsic randomness in the phenomena observed (e.g., the interaction of radiation with matter).

Among the various sources of uncertainties, the one affecting the raw nuclear data evaluations, i.e. cross sections, fission yields and energy-angular distributions, is certainly one of the most relevant, being a superposition of both aleatoric and epistemic contributions. In particular, the uncertainty in the continuous-energy nuclear data has a direct impact on the homogenised and collapsed multi-group constants, which are computed to carry out the neutronic analyses at the full-core level. As mentioned previously (e.g., in chapter 4), the legacy methodology to produce the multi-group constant consist in using high-fidelity computational tools that take into account all the energy and angular details on a local scale, e.g., at the pin-cell or at the assembly levels, with the aim of providing an accurate local evaluation for the flux. This information is then adopted to generate the effective cross sections and diffusion coefficient through the energy collapsing and spatial homogenisation procedure, described by (4.1). As mentioned in chapter 4, this process is carried out using either deterministic codes like the ECCO-ERANOS system (Rimpault, Plisson, et al., 2002) or Monte Carlo codes like Serpent 2 (Leppänen, Pusa, and Fridman, 2016). With respect to the deterministic approach,

the stochastic codes allow to achieve a significant reduction of both modelling and numerical errors, due to their continuous treatment of the phase space, but at the price of a statistical uncertainty, inherent to the Monte Carlo method.

Independently on the approach pursued in the multi-group constants generation, the uncertainty vector in the nuclear data, indicated with p, on the output vector response r of interest is often estimated with the so-called sandwich rule Cacuci, 2003,

$$\mathrm{var}[r] = \vec{S}_p^{\,r} \mathrm{cov}[p] \vec{S}_p^{\,r^T}, \tag{7.1}$$

where var$[r]$ is the variance of the response, $\vec{S}_p^{\,r}$ is the relative sensitivity of r with respect to a variation in the input p, and cov$[p]$ is the relative covariance matrix associated to p. This formula only yields a first-order estimate of the variance, but this is usually enough to propagate the uncertainty in reactor physics, where it is often combined with the Generalized Perturbation Theory (GPT). This technique, which is a reduced-order model exploiting the forward and adjoint neutron models, was originally conceived by L.N. Usachev (Usachev, 1964) and later developed and generalised by A. Gandini and M. Salvatores (Gandini, Salvatores, and Bono, 1968; Gandini and Salvatores, 1970). Among its various applications, GPT is applied to get a first-order estimate of the sensitivities of some output responses to a large number of input parameters in a computationally efficient manner, although the information conveyed is limited to the variance of the response.

When a richer information is needed, e.g. the full statistical distribution of the response or its moments, the Uncertainty Quantification (UQ) study can be performed, for instance, with a brute-force sampling technique. Among the various methods available in the literature, the so-called Total Monte Carlo (TMC) method (Rochman, A. J. Koning, et al., 2011) is the reference tool for UQ, since it does not suffer from the curse of dimensionality (Bellman, 1957). Nevertheless, being based on the Monte Carlo method, it is featured by a slow convergence, scaling as $1/\sqrt{N}$, where N is the number of samples. Hence, since this approach is often computationally not affordable, some cheaper approximations of TMC have been conceived, like the fast TMC ("Uncertainty Propagation with Fast Monte Carlo Techniques" 2014) and the GRS method (W. Zwermann, B. Krzykacz-Hausmann, et al., 2012). Despite their are much more computationally efficient than TMC, these methods provide only the response variance, similarly to GPT.

A promising alternative to these methods is represented by the eXtended Generalised Perturbation Theory (XGPT), which is a projection technique recently developed and implemented in Serpent 2 (Aufiero, Martin, and Fratoni, 2016; Leppänen, Pusa, et al., 2015). Likewise GPT, also this method yields a first-order approximation of the response variance, but, exploiting its features, it can be profitably used to get also a first-order approximation for the response distributions, acting as a reduced-order version of TMC. This useful feature makes XGPT a fast and accurate method to estimate the statistical distributions of the output responses of the model. Having this information, although with a first-order accuracy, may be extremely relevant when it is necessary

to propagate the resulting uncertainty of the response through a calculation chain, e.g. from the multi-group data to the output of the full-core analysis.

An example of this situation regards the safety-oriented design of the Gen-IV fast systems, which have an inherent multiphysics behaviour. This peculiarity, in addition to the presence of uncommon nuclides with respect to commercial reactors, demands the adoption of state-of-the-art methodologies to actually propagate the uncertainty from the raw nuclear data to the final output of the whole multiphysics calculation chain. The propagation of the input uncertainties through computationally expensive models is nowadays performed with efficient methods, like the Polynomial Chaos Expansion, presented in chapter 6. However, to unleash the full potential of PCE, the distributions for the model input parameters is required, even in an approximated form. In this perspective, the XGPT approach may be very useful to perform a consistent UQ study bridging the raw nuclear data to the final output of the multiphysics full-core calculations.

The aim of this chapter is to study the effectiveness of XGPT in delivering estimates of the response distributions of the output quantities, focusing on some selected multi-group constants. The first part of the chapter presents a preliminary UQ study concerning the ALFRED (Advanced Lead Fast Reactor European Demonstrator) reactor design (Grasso, Petrovich, et al., 2014), with the legacy GPT technique. Then, two of the most important nuclides are selected to assess the uncertainties computed with the GPT and XGPT methods available in Serpent 2, focusing on the influence of the various tuning parameters, e.g. the energy grid structure. Finally, the statistical distributions for some model responses are calculated with XGPT and some conclusions on the potentialities of this approach are given.

Most of the content of this chapter has been published as a peer-reviewed journal article on the special issue of Annals of Nuclear Energy dedicated to the memory of Massimo Salvatores,

- N. Abrate, S. Dulla, P. Ravetto, *"Generalized perturbation techniques for uncertainty quantification in lead-cooled fast reactors"*, Annals of Nuclear Energy, **164**, 2021

7.2 Generalized perturbation methods for uncertainty quantification

GPT is a well-established tool in reactor analysis, hence it a standard routine available in the majority of the neutronic deterministic codes (Rimpault, Plisson, et al., 2002). Due to the fact that these codes approximate the energy variable with the multi-group approximation, both the sensitivity coefficients provided by GPT and the covariance matrix used in eq. (7.1) are multi-group quantities. This aspect has induced the nuclear data evaluators to develop computational tools, like the NJOY processing code (MacFarlane, Muir, et al., 2018), to score the covariance matrices over relatively coarse

energy structures, which contains no more than $\approx 10^3$ groups. Notwithstanding this approximation, the application of GPT has been successful for sensitivity and uncertainty analyses in reactor physics and engineering applications since the 70's. Being very popular, GPT has been recently coded in the continuous-energy Monte Carlo codes MCNP (Pelowitz, Goorley, et al., 2013) and Serpent 2. However, in spite of the discretisation-free nature of the Monte Carlo method, also in this case GPT is forced to score the sensitivities on a multi-group structure, since decreasing the tally bin width has a detrimental effect on the statistical uncertainty.

The XGPT method has been developed aiming at overcoming this limitation of the Monte Carlo version of GPT (Aufiero, Martin, and Fratoni, 2016). The key idea of this technique is to evaluate the sensitivity coefficients by means of energy-integrated projections on basis functions generated from the covariance matrices. Thanks to the integration over the energy, the XGPT coefficients are less prone to the statistical error, enabling potentially to evaluate continuous-energy sensitivities.

Moreover, XGPT also offers the possibility to adopt high-resolution covariance matrices, scored on a very fine energy grid. Nevertheless, since legacy codes are multi-group, it is currently not possible to get continuous-energy matrices from the Evaluated Nuclear Data Files (ENDF) tapes. The only relevant exception, to the authors' knowledge, is the T6 package (A. Koning and Rochman, 2012; A. Koning, Rochman, et al., 2019; A. Koning, 2020), which allows to extract the sample covariance matrices from a set of continuous-energy perturbed ENDF tapes produced by the code itself.

Figure 7.1 shows the correlation matrices for Pu-239 and U-238 data, generated from the ENDF/B-VIII.0 library (Brown, Chadwick, et al., 2018) and scored on different energy grids with the ERRORR module of NJOY (MacFarlane, Muir, et al., 2018). By inspection of the figures, it is possible to notice that the rôle of the energy grids choice is much more evident for Pu-239 than for U-238, as it will be discussed in more detail later.

7.2.1 Evaluation of sensitivity coefficients

Given a certain physical system, the first-order relative sensitivity of a certain response R of the system to a certain physical parameter P is defined as:

$$S_P^R = \frac{\partial R/R}{\partial P/P} = \frac{P}{R}\frac{\partial R}{\partial P}. \tag{7.2}$$

Hereafter, the parameter P is always assumed to be the microscopic cross section of a specific nuclide j for a certain reaction y, i.e. $\sigma_{y,j}(E)$, while the response is assumed to be the linear reaction rate ratio defining the macroscopic cross section for reaction x, which is homogenised over the volume V and collapsed over the energy group g,

$$R_g^x = \frac{\int_V d\vec{r} \int_{E_{g-1}}^{E_g} dE\, \Sigma_x(\vec{r},E)\Phi(\vec{r},E)}{\int_V d\vec{r} \int_{E_{g-1}}^{E_g} dE\, \Phi(\vec{r},E)} = \frac{\langle \Sigma_x \rangle \Phi_g}{\langle 1 \rangle \Phi_g} = \frac{R_{1,g}^x[\Sigma_x,\Phi]}{R_{2,g}^x[\Phi]}, \tag{7.3}$$

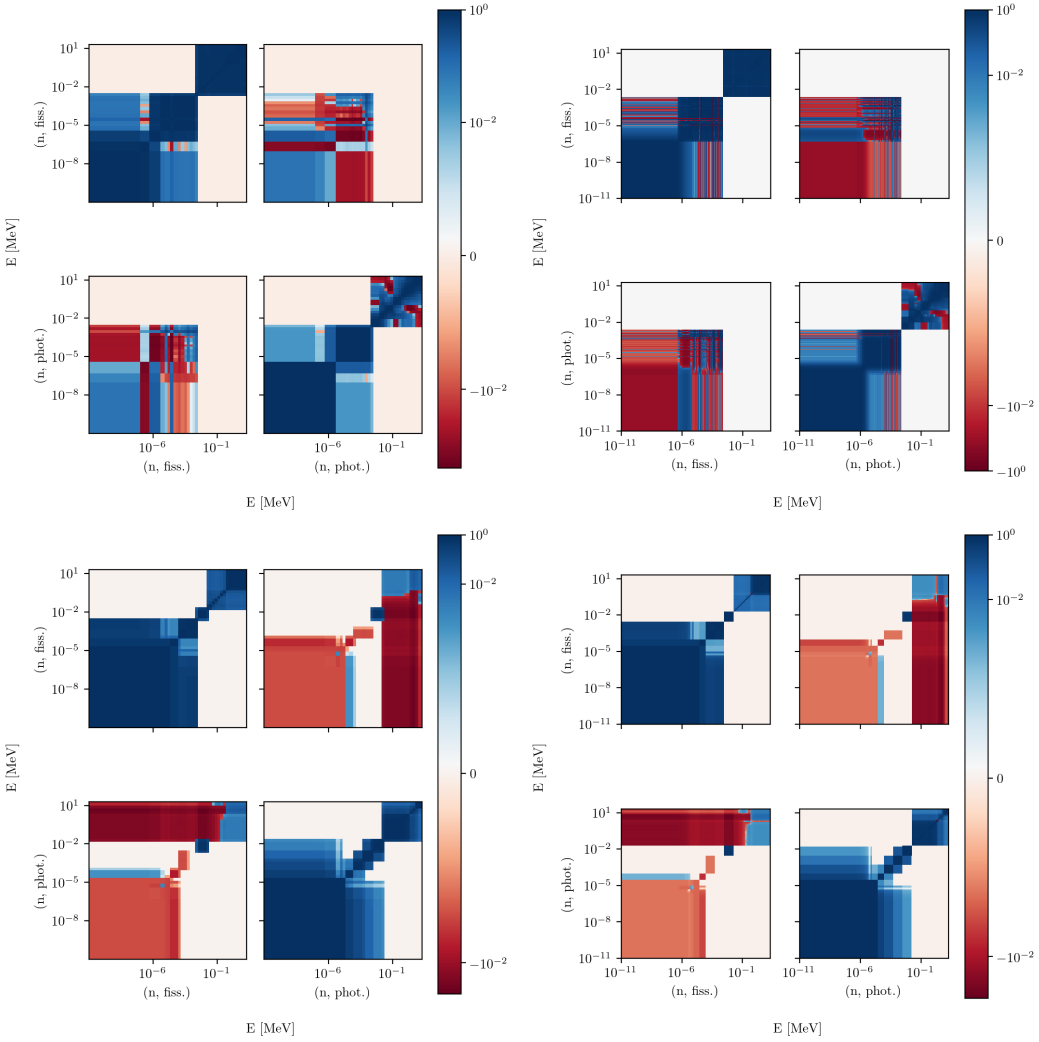

Figure 7.1: *Correlation matrices for Pu-239 (top) and U-238 (bottom) data evaluated on ECCO-33 groups (left) and using 1500 groups (right).*

where the notation adopted underlines the fact that the response of interest is the ratio of two functionals, $R^x_{1,g}$ and $R^x_{2,g}$. As a consequence, eq. (7.2) can be manipulated in order to get:

$$S_P^{R^g_x} = P\frac{R^x_{2,g}}{R^x_{1,g}}\frac{\partial}{\partial P}\left(\frac{R^x_{1,g}}{R^x_{2,g}}\right) = \frac{P}{R^x_{1,g}}\frac{\partial R^x_{1,g}}{\partial P} - \frac{P}{R^x_{2,g}}\frac{\partial R^x_{2,g}}{\partial P} = S_P^{R^x_{1,g}} - S_P^{R^x_{2,g}}. \tag{7.4}$$

The term $S_P^{R^x_{1,g}}$ can be written as the sum of two first-order functional derivatives, as:

$$S_P^{R^x_{1,g}} = \frac{P}{R^x_{1,g}}\frac{\langle \delta\Sigma_x \rangle \Phi_g}{\delta P} + \frac{P}{R^x_{1,g}}\frac{\langle \Sigma_x \rangle \delta\Phi_g}{\delta P} = S^{R^x_{1,g}}_{P,dir} + S^{R^x_{1,g}}_{P,ind} \tag{7.5}$$

that are often referred to as the *direct* and the *indirect* terms, respectively. The direct term expresses the change of the macroscopic cross section due to P, while the indirect term provides the flux change due to P. From now on, the variation symbol δ will be used in substitution of the continuous derivative.

From version 2.1.31 onward, Serpent 2 is able to compute automatically both $S^{R^x_{1,g}}_{P,dir}$ and $S^{R^x_{1,g}}_{P,ind}$ only in case the GPT routine is adopted. When the XGPT mode is employed, *ad hoc* detectors must be set for the direct term estimation.

The explicit tally definitions required to estimate the direct sensitivities presented in this work can be obtained noticing that, for a heterogeneous system like the ALFRED core design, Σ_x can be defined as

$$\Sigma_x(\vec{r}, E) = \sum_{i=0}^{I} N_i(\vec{r})\sigma_{x,i}(E), \tag{7.6}$$

where N_i is the atomic density of the i-th nuclide species. Since the analysis carried out in the following regards only the fissile isotopes, the atomic density spatial distribution turns out to be a piece-wise constant,

$$N_i(\vec{r}) = \begin{cases} N_i & \forall \vec{r} \in D_1 \cup D_2 \cup ... \cup D_F \\ 0 & \text{otherwise,} \end{cases} \tag{7.7}$$

where D_k indicates the k-th fuel pellet volume.

Equations (7.6) and (7.7) allow to evaluate the direct term explicitly for the case $P = \sigma_{y,j}(E)$:

$$\begin{aligned} S^{R^x_{1,g}}_{P,dir}(E) &= \frac{\sigma_{y,j}(E)}{R^x_{1,g}} \frac{\langle \delta\Sigma_x \rangle \Phi_g}{\delta\sigma_{y,j}(E)} \\ &= \frac{\sigma_{y,j}(E)}{R^x_{1,g}} \frac{1}{\delta\sigma_{y,j}(E)} \int_V d\vec{r} \int_{E_{g-1}}^{E_g} dE\ \delta\Sigma_x(\vec{r}, E)\Phi(\vec{r}, E) \\ &= \frac{\sigma_{y,j}(E)}{R^x_{1,g}} \frac{1}{\delta\sigma_{y,j}(E)} \int_V d\vec{r} \int_{E_{g-1}}^{E_g} dE\ \sum_{i=0}^{I} N_i(\vec{r})\delta\sigma_{i,x}(E)\Phi(\vec{r}, E) \\ &= \frac{\sigma_{y,j}(E)}{R^x_{1,g}} \sum_{i=0}^{I} \int_V d\vec{r} N_i(\vec{r}) \int_{E_{g-1}}^{E_g} dE\ \Phi(\vec{r}, E) \frac{\delta\sigma_{i,x}(E)}{\delta\sigma_{y,j}(E)}, \end{aligned} \tag{7.8}$$

The direct sensitivity coefficient vanishes if reactions x and y are independent or if the nuclide species i and j are not the same, therefore the previous equation can be simplified as follows,

$$S^{R^x_{1,g}}_{P,dir}(E) = \frac{N_j\sigma_{y,j}(E)}{R^x_{1,g}} \int_{V_F} d\vec{r}\Phi(\vec{r}, E)\delta_{xy}, \tag{7.9}$$

where δ_{xy} behaves as the standard Kronecker operator and V_F indicates the total fuel volume inside the volume V considered for the homogenisation. As previously mentioned, the major difference between GPT and XGPT lies in the way the sensitivity defined in eq. (7.4) is computed. GPT scores group-wise sensitivities,

$$S^{R_g^x}_{P,h} = \int_{E_h}^{E_{h+1}} dE\, S^{R_g^x}_P(E), \quad \forall\, h = 1, \dots, H, \tag{7.10}$$

while XGPT scores the projections of the sensitivity coefficient $S^{R_g^x}_P(E)$ on continuous-energy basis functions $b_k(E)$ generated from the covariance matrices,

$$\begin{aligned} S^{R_g^x}_{P,k} &= \int_{E_{\min}}^{E_{\max}} dE\, S^{R_g^x}_P(E) b_k(E) \\ &= \int_{E_{\min}}^{E_{\max}} dE \left(S^{R^x_{1,g}}_{P,dir}(E) + S^{R^x_{1,g}}_{P,ind}(E) - S^{R^x_{2,g}}_{P}(E) \right) b_k(E), \end{aligned} \tag{7.11}$$

where the integration covers the interval between the minimum and maximum energies considered for the intended calculation. Since the direct effect for a collapsed cross section is influenced only by perturbations occurring within its energy limits, it can be written in XGPT fashion as:

$$\begin{aligned} S^{R^x_{1,g}}_{P,dir,k} &= \int_{E_g}^{E_{g+1}} dE\, S^{R^x_{1,g}}_{P,dir}(E) b_k(E) \\ &= \frac{1}{R^x_{1,g}} \int_{E_g}^{E_{g+1}} dE\, N_j \sigma_{j,x}(E) b_k(E) \int_{V_F} d\vec{r}\, \Phi(\vec{r}, E) \\ &= \frac{1}{\langle \Sigma_x \rangle \Phi_g} \int_{E_g}^{E_{g+1}} dE\, \Sigma_{j,x}(E) b_k(E) \int_{V_F} d\vec{r}\, \Phi(\vec{r}, E). \end{aligned} \tag{7.12}$$

The denominator of eq. (7.12) can be evaluated by the definition of a suitable tally, but the direct score of the scalar product over the basis functions cannot be carried out in Serpent. Thus, the integration is performed *a posteriori*, estimating the reaction rate over the whole volume of interest and over the same energy grid employed to define the basis functions. This procedure allows to approximate the integral as follows:

$$\int_{E_g}^{E_{g+1}} dE\, \Sigma_{j,x}(E) \Psi(E) b_k(E) \cong \sum_{h=1}^{H} \Sigma_{j,x,h} \Psi_h b_{k,h} \Delta E_h, \tag{7.13}$$

where Ψ is the flux integrated over the fuel volume. All the sensitivity and tally results presented throughout this chapter have been processed exploiting the excellent open-source *serpentTools* package (Johnson, Kotlyar, et al., 2020) and some in-house Python scripts.

Despite the projection requires an *ad hoc* implementation in the Monte Carlo code, it is remarkable to observe that this process could be carried out as an *a posteriori* step

to obtain approximated projections using group-wise sensitivities evaluated on a sufficiently fine energy grid:

$$S^{R_x^g}_{P,b_k} = \int_{E_{\min}}^{E_{\max}} dE\, S^{R_x^g}_{P}(E) b_k(E) \cong \sum_{h=1}^{H} S^{R_x^g}_{P,h} b_{k,h} \Delta E_h. \tag{7.14}$$

This approach would be non-intrusive and could potentially disclose the possibility of using also deterministic codes to get approximated response distributions.

7.2.2 Determination of the basis functions

The basis functions required to perform the scalar product of the sensitivity coefficients can be extracted from the covariance matrix by means of the Proper Orthogonal Decomposition (POD) algorithm (Volkwein, 2011), described in detail in algorithm 2 and sketched in fig. 6.3.

If a set of perturbed cross sections was available, the POD could be carried out with the Singular Value Decomposition (SVD) of the snapshot matrix, i.e. the matrix obtained by arranging the perturbed data along each column. The perturbed data can be obtained, for instance, exploiting the open-source SANDY code (Fiorito, Žerovnik, et al., 2017) or already mentioned T6 package A. Koning, 2020, which permits to apply continuous-energy perturbations to the ENDF tapes and, consequently, to obtain continuous-energy sample covariance matrices. A more detailed description of this approach can be found in Aufiero, Martin, and Fratoni, 2016 and Abrate, Aufiero, et al., 2019. In case ENDF-6 files storing the group-wise covariance matrix was available, the POD could be carried out applying the SVD to the covariance matrix itself. In the following, this approach will be followed, in order to avoid the introduction of statistical errors and biases related to the sample covariance matrix evaluation, in spite of its limited energy resolution.

The POD computed via SVD allows to factorise the relative covariance matrix $\mathrm{cov}[p] \in \mathbb{R}^{m\times m}$ as

$$\mathrm{cov}[p] = \hat{B}\hat{\Sigma}\hat{A}^{\mathsf{T}}, \tag{7.15}$$

where $\hat{B} \in \mathbb{R}^{m\times m}$ is the column-wise set of $\mathrm{cov}[p]$ left eigenvectors, $[\vec{b}_1, \vec{b}_2, \dots, \vec{b}_m]$, $\hat{\Sigma} \in \mathbb{R}^{m\times m}$ contains $\mathrm{cov}[p]$ singular values and $\hat{A} \in \mathbb{R}^{m\times m}$ is the column-wise set of $\mathrm{cov}[p]$ right eigenvectors. In this case $\hat{A} = \hat{B}$, since $\mathrm{cov}[p]$ is square and symmetric.

Since the singular values σ_i of $\mathrm{cov}[p]$ are a monotonically decreasing sequence ($\sigma_1 > \sigma_2 > \dots > \sigma_m$) that usually decays very quickly, the dimensionality reduction can be very effective. Since each eigenvalue is proportional to the information content carried by the corresponding basis function, the original matrix $\mathrm{cov}[p]$ can be approximated using a limited number t of eigenvectors. As mentioned in chapter 6, the value of t is often

selected in order to reach a certain value of the POD energy, defined as

$$\mathcal{E}(t) = \frac{\sum_{k=1}^{t} \sigma_k^2}{\sum_{k=1}^{r} \sigma_k^2}. \tag{7.16}$$

The POD energy is equal to 1 when $t = m$, so the tolerance is checked against $1 - \mathcal{E}$.

7.2.3 XGPT uncertainty quantification

Once the projected sensitivities $S^r_{p,b_k}\ \forall\ k = 1, ..., t$ are available, the response variance may be computed either thanks to the sandwich formula, or thanks to the XGPT model, which can provide a first-order approximation to the response distribution. In the first case, the uncertainty is estimated starting from the continuous version of the sandwich formula Aufiero, Martin, and Fratoni, 2016,

$$\begin{aligned}
\mathrm{var}[r] &= \int_{E_{\min}}^{E_{\max}} dE \int_{E_{\min}}^{E_{\max}} dE'\, S^r_p(E)\mathrm{cov}[p](E,E')S^r_p(E') \\
&= \int_{E_{\min}}^{E_{\max}} dE \int_{E_{\min}}^{E_{\max}} dE'\, S^r_p(E)\hat{B}(E)\hat{\Sigma}\hat{B}(E')^{\intercal} S^r_p(E') \\
&= \left(\int_{E_{\min}}^{E_{\max}} dE\ \hat{B}(E)^{\intercal} S^r_p(E)\right)^{\intercal} \hat{\Sigma} \left(\int_{E_{\min}}^{E_{\max}} dE\ \hat{B}(E)^{\intercal} S^r_p(E)\right) \\
&= \vec{S}^{r\intercal}_{p,b}\ \hat{\Sigma}\ \vec{S}^{r}_{p,b},
\end{aligned} \tag{7.17}$$

where $\vec{S}^r_{p,b}$ is the column vector obtained stacking the projected sensitivities S^r_{p,b_k}. Since $\hat{\Sigma}$ is a diagonal matrix whose entries are filled with the singular values of cov$[p]$, eq. (7.17) turns out to be a weighted sum of contributions that are smaller and smaller.

With the same quantities, a first-order model can be devised to approximate the full-order model output response. Starting from eq. (7.2) and assuming a linear variation, the model yields:

$$\begin{aligned}
\frac{R_i - R_0}{R_0} &= \vec{S}^{R\intercal}_P \frac{\vec{P}_i - \vec{P}_0}{\vec{P}_0} = \vec{S}^{R\intercal}_P \vec{X}_i = \vec{S}^{R\intercal}_P \hat{I}\vec{X}_i = \\
&= \vec{S}^{R\intercal}_P \hat{B}_t\hat{B}^{\intercal}_t\vec{X}_i = (\hat{B}^{\intercal}_t\vec{S}^{R}_P)^{\intercal}\hat{B}^{\intercal}_t\vec{X}_i = \vec{S}^{R\intercal}_{P,b}\vec{\alpha}_i\ ,
\end{aligned} \tag{7.18}$$

where $\hat{B}_t$ is the truncated POD basis $\hat{B}$ and $\vec{\alpha}_i$ is the i–th response projection in the reduced space. Rearranging the terms, eq. (7.18) finally yields

$$R_i = R_0\left(1 + \sum_{k=1}^{t} \alpha_{ik} S^R_{P,b_k}\right). \tag{7.19}$$

Exploiting eq. (7.19), the output response to an input perturbation $\vec{P}_i$ can be estimated consistently with respect to the continuous-energy Monte Carlo approach, disclosing the possibility to carry out a first-order uncertainty propagation from the raw nuclear data to the output homogenised coarse-group constants.

It is important to notice that, due to the way the basis functions are extracted, eq. (7.19) may yield different approximations to the output distribution. If the basis functions were computed directly via SVD of the covariance matrix, they would not contain any information on the input parameter distribution. In this case, eq. (7.19) behaves as a linear model that approximates the output distribution of an input parameter that is implicitly assumed to be normally distributed. This implies that also the output distribution will be normal as well.

On the contrary, if the basis functions were obtained via POD of the snapshot matrix, the basis functions would convey a richer statistical information, since they would contain also an information related to the distribution of the samples. In this last case, the model would behave as a linearisation of the TMC approach.

7.3 Application to the ALFRED reactor model

The methodology previously described is now applied to the same Monte Carlo model of the ALFRED reactor design discussed in chapter 6. The geometry and material specifications are taken from Grasso, Petrovich, et al., 2014 for the Lead-Cooled Fast Reactor design, developed within the European project LEADER. The core is assumed to be in the Beginning of Life (BoL) configuration, with all the safety and control rods withdrawn.

For the sake of clarity, fig. 7.2 reports the zones defined for the spatial homogenisation of the multi-group. On the left, the different types of assemblies are sketched, while on the right their axial discretisation is provided. and thermal power distribution Nallo, Abrate, et al., 2020. The reference thermodynamic condition considered in this chapter to account for the Doppler effect is a uniform temperature equal to 1073 K for the whole system. All the Monte Carlo simulations have been performed with the ENDF/B-VIII.0 nuclear data library.

Table 7.1: *Six-group energy grid adopted to perform the macroscopic cross section energy collapsing Nallo, Abrate, et al., 2020.*

Group	Upper boundary [MeV]	Lower boundary [MeV]
1	$2.000 \cdot 10^{1}$	$1.353 \cdot 10^{0}$
2	$1.353 \cdot 10^{0}$	$1.832 \cdot 10^{-1}$
3	$1.832 \cdot 10^{-1}$	$6.738 \cdot 10^{-2}$
4	$6.738 \cdot 10^{-2}$	$9.119 \cdot 10^{-3}$
5	$9.119 \cdot 10^{-3}$	$2.000 \cdot 10^{-5}$
6	$2.000 \cdot 10^{-5}$	$1.000 \cdot 10^{-11}$

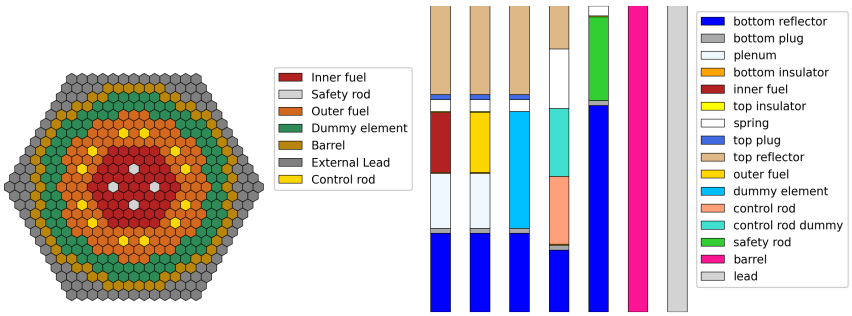

Figure 7.2: *Radial section (left) and axial regions (right) of ALFRED 3D model, as in Nallo, Abrate, et al., 2020.*

7.3.1 Uncertainty quantification with GPT

In this section, the results of a UQ study carried out with the GPT technique Valtavirta, 2018 are shown and discussed. Among the various responses produced by Serpent 2, in the following the attention will be focused on the effective multiplication factor k_{eff} and on the six-group fission and capture cross sections, $\Sigma_{f,g}$ and $\Sigma_{c,g}$, homogenised over the inner and outer fuel regions of ALFRED. Concerning the perturbations used to evaluate the sensitivity coefficients with GPT, the total fission (σ_f or MT18 according to ENDF-6 format Herman, Trkov, et al., 2010) and the radiative capture (σ_γ or MT102) microscopic cross sections characterising the main fissile nuclides in the fuel oxide are considered. The nuclides and their atomic densities are reported in table 7.2.

Table 7.2: *Nuclides considered for the GPT UQ study.*

Nuclide	Inner fuel mass fraction %	Outer fuel mass fraction %
U-234	$2.07419 \cdot 10^{-3}$	$1.91216 \cdot 10^{-3}$
U-235	$2.79419 \cdot 10^{-1}$	$2.57515 \cdot 10^{-1}$
U-236	$6.91511 \cdot 10^{-3}$	$6.37300 \cdot 10^{-3}$
U-238	$6.88468 \cdot 10^{+1}$	$6.34847 \cdot 10^{+1}$
Pu-238	$4.41008 \cdot 10^{-1}$	$5.64897 \cdot 10^{-1}$
Pu-239	$1.07564 \cdot 10^{+1}$	$1.37778 \cdot 10^{+1}$
Pu-240	$5.10655 \cdot 10^{+0}$	$6.53959 \cdot 10^{+0}$
Pu-241	$1.15483 \cdot 10^{+0}$	$1.47901 \cdot 10^{+0}$
Pu-242	$1.45497 \cdot 10^{+0}$	$1.86386 \cdot 10^{+0}$
Am-241	$2.47320 \cdot 10^{-1}$	$3.16741 \cdot 10^{-1}$

Figure 7.3 shows the typical behaviour of the six-group macroscopic cross section relative sensitivity, scored on the ECCO 33-group structure for Pu-239 in response to a

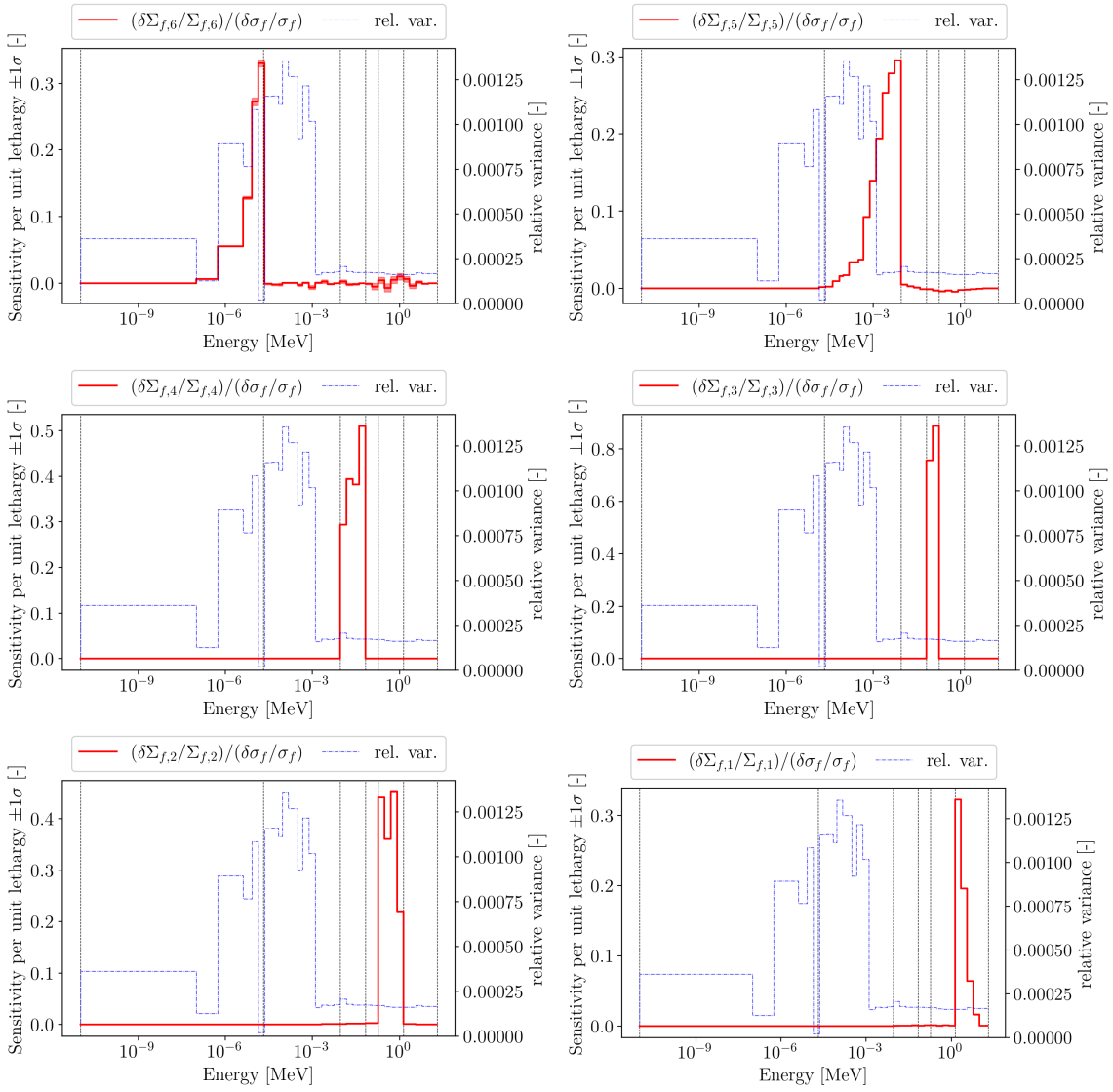

Figure 7.3: *Sensitivity coefficients with respect to the total fission microscopic cross section (MT18) of Pu-239 for $\Sigma_{f,g}$, scored on ECCO 33-group structure with GPT.*

perturbation in the MT18 reaction. As one might expect on a physical ground, the sensitivity per unit lethargy is very large for the sub-groups belonging to the coarse group where the cross section is collapsed, while it is negligible for the other sub-groups, except of the thermal region. In these cases, it can be noticed that both $\Sigma_{f,5}$ and $\Sigma_{f,6}$ are sensitive to perturbations occurring in the sub-groups at higher energies, outside the coarse groups within the thermal range.

The trend of the sensitivity energy profiles can be justified considering the different rôle played by the direct and indirect terms appearing in eq. (7.5). In the fast and

intermediate groups the overall sensitivity behaviour is dominated by the direct sensitivity, while in the lowest-energy groups the contribution of the indirect sensitivity from higher energies gets more relevant. These graphs also display the relative variance obtained from the 33-group covariance matrix, which is a useful information to notice that there, in some cases, the lowest uncertainty is in correspondence of the the largest sensitivity to the nuclear data.

It should be highlighted that, in spite of its limitations, GPT still is the best technique to carry out sensitivity analysis, thanks to the fact that the energy-dependent sensitivities have a straightforward physical interpretation. On the contrary, the same statement does not apply to the energy-integrated projected sensitivities provided by XGPT.

The sensitivity coefficients have been calculated with 10^9 active neutron histories (10^6 neutrons per generation, 10^3 generations divided in 25 batches), starting from an already converged fission source, initialised with $5{\cdot}10^8$ inactive histories. The number of neutron latent generations used for the adjoint estimator is 10, which seems an adequate number according to the convergence trends depicted in fig. 7.4. This graph provides the uncertainties of $\Sigma_{c,1}$ and k_{eff} computed with the sensitivity coefficients estimated considering different numbers of latent generations.

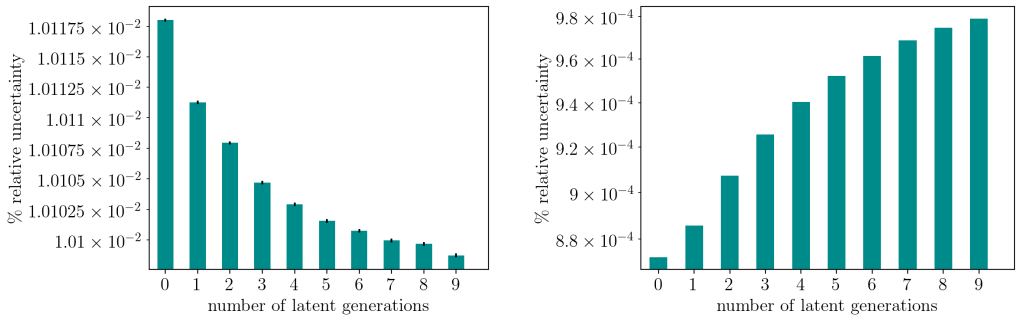

Figure 7.4: *Latent generation convergence trend for $\Sigma_{c,1}$ (left) and k_{eff} (right). In the right plot the error bars are very small and, thus, not visible.*

Figures 7.5 and 7.6 provide the contribution of each actinide present in the inner and outer fuel compositions to the percentage uncertainty affecting both $\Sigma_{f,g}$ and $\Sigma_{c,g}$, due the uncertainties in the MT18 and MT102 reactions. As it could be expected, the major contributions are due to Pu-239 and U-238, i.e. the most abundant fissile and fissionable nuclides, respectively. By inspection of these graphs it can be also concluded that, in spite of slightly different compositions and flux spectra, the uncertainties in the two fuel regions are very similar.

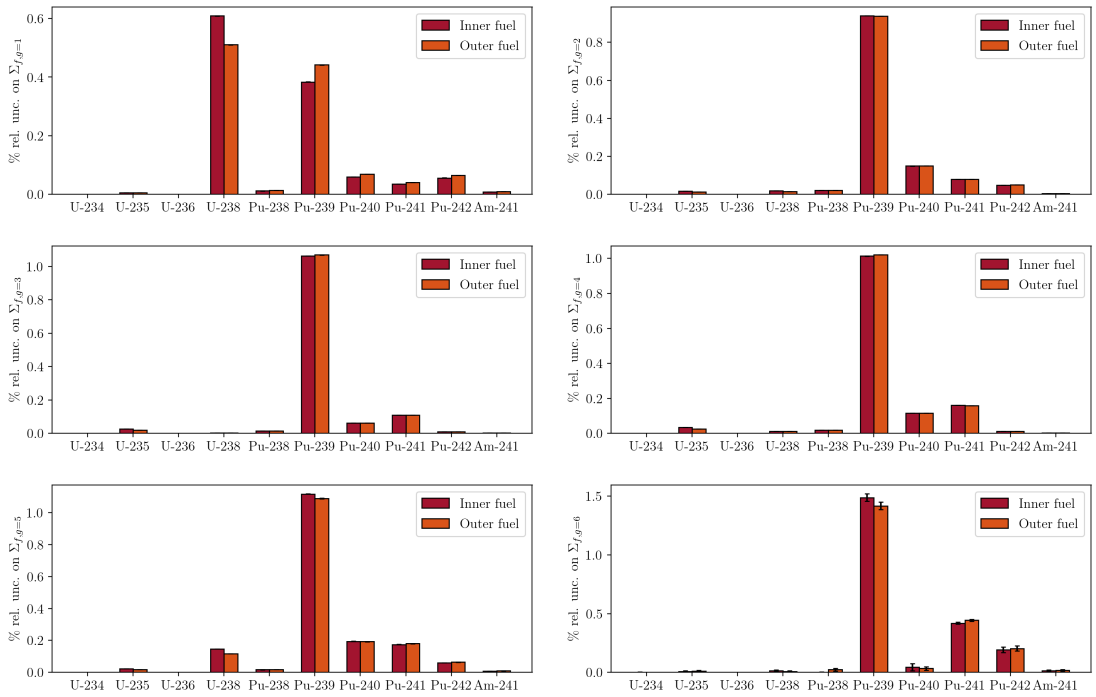

Figure 7.5: *Nuclide contributions to the total % uncertainty on $\Sigma_{f,g}$ homogenised over the inner and outer fuel regions. The first group (the fastest) is on top-left, the sixth is on bottom-right.*

7.3.2 Comparison between XGPT and GPT results

In this section the uncertainty estimated with the GPT and XGPT methods is compared, with the goal of highlighting better their different characteristics in the Monte Carlo framework. The assessment is carried out focusing on the impact of two specific isotopes, namely Pu-239 and U-238, on k_{eff} and on the six-group capture and fission cross sections homogenised over the inner fuel region of the ALFRED reactor. The motivation for the selection of these isotopes is two-fold:

1. they are the most relevant from the uncertainty point of view, as concluded in section 7.3.1;

2. their covariance matrices have different features that evidence the impact of the POD-SVD truncation error on the final calculation results. To the authors' knowledge, this is the first application of XGPT for the propagation of the nuclear data uncertainty throughout the overall homogenisation and collapsing procedure.

To quantify the impact of the energy group structures on the final uncertainties, the XGPT evaluations are performed considering two sets of covariances. The first one is scored on the ECCO 33-group grid, i.e. the same adopted for the GPT calculation,

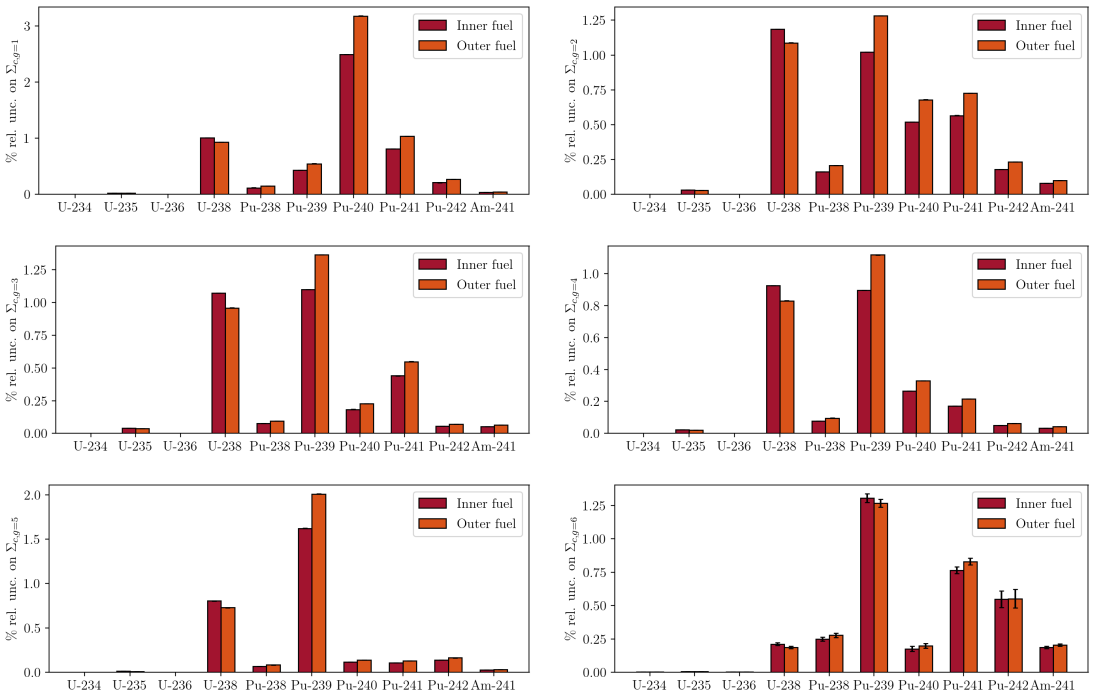

Figure 7.6: *Nuclide contributions to the total % uncertainty on $\Sigma_{c,g}$ homogenised over the inner and outer fuel regions. The first group (the fastest) is on top-left, the sixth is on bottom-right.*

while the second one is processed on a fine-group structure consisting of 1500 groups. It is worth mentioning that the ERRORR module of NJOY, used to process the ENDF-6 files, currently has some limitations that restrict the maximum number of groups to a value which is around 1550. As a consequence, this 1500-group grid has been obtained starting from the ECCO 1968-group and distributing the groups to obtain a consistent coverage of the energy range, also considering the flux spectra of the fuel regions and of the radial and axial reflectors, depicted in fig. 7.7. Since statistics in the lower and upper energy range limits is very poor, as a consequence of the fast spectrum of LFRs, most of the bins have been located in the epithermal region. The details of the fine-group structure can be retrieved from table 7.3, while fig. 7.8 shows a graphical sketch of the 6, 33 and 1500-group grids adopted.

The direct observation of fig. 7.9 shows the typical decay of the singular values of the covariance matrices scored on the 33-group and the 1500-group structures. In the first case, a similar number of basis functions, 56 and 65, is sufficient to approximate the Pu-239 and U-238 covariances, respectively, within the prescribed tolerance ($1 - \mathcal{E} \leq 10^{-8}$). However, when the covariances are scored on 1500 groups, 191 and 1446 basis functions are required to approximate the U-238 and Pu-239 matrices, respectively, within the selected tolerance. The significant difference between the amount of basis functions

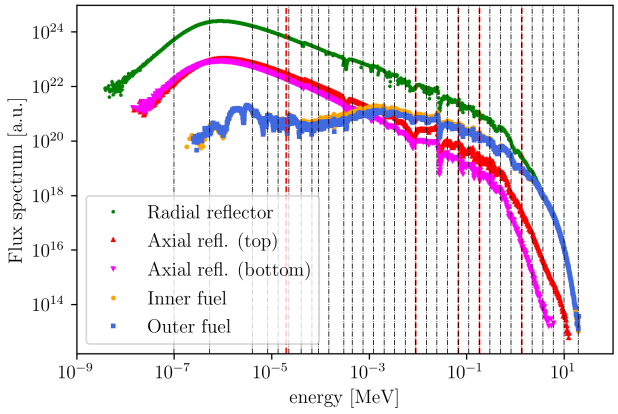

Figure 7.7: *Inner fuel, outer fuel and radial reflector (dummy element) flux spectra. The red dashed line represent the six-energy groups while the black dashed-dotted lines identify the ECCO 33-group grid.*

Table 7.3: *Energy groups specifications to construct the 1500-group grid employed for the calculations.*

Region	Lower boundary [MeV]	Upper boundary [MeV]	Points in lethargy
Thermal 1	10^{-11}	10^{-7}	1
Thermal 2	10^{-7}	10^{-5}	20
Epithermal	10^{-5}	10^{1}	1472
Fast	10^{1}	$2 \cdot 10^{1}$	10

required by the covariance of each isotope in the two cases can be appreciated observing the associated correlation matrices reported in fig. 7.1. In the U-238 case, the 1500-group description does not add significant improvements to the correlation matrices appearance, while the higher resolution in the fast and intermediate regions is patent for the Pu-239 case.

Figure 7.10 provides the impact of the covariance truncation error on the final uncertainty estimated with eq. (7.17). Even in the worst case scenario, represented by the Pu-239 MT18 uncertainty on $\Sigma_{f,2}$, around 200 basis functions seem adequate to yield a truncation error that is far below the statistical one. This behaviour justifies the adoption of the POD reduction technique, showing that an acceptable accuracy can be achieved with tolerances that are even larger than the one initially selected.

Of course, for reasons pertaining to linear algebra, the number of energy points used to evaluate the sensitivity energy profiles should match the rank of the covariance matrix in eq. (7.1). Thus, if a continuous-energy (i.e. an ultra-fine group) covariance was available, the sensitivities should be evaluated on the same group structure. It is clear that this calculation would not be practically feasible, neither by a deterministic

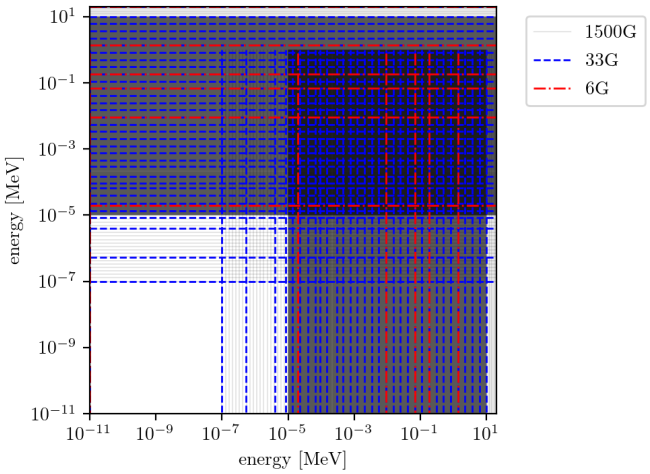

Figure 7.8: *Energy group structures employed for the sensitivity and uncertainty analyses.*

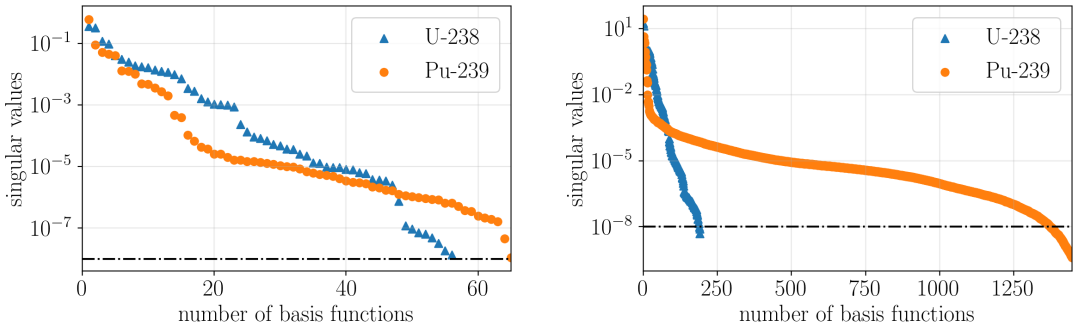

Figure 7.9: *POD eigenvalues decay for the covariance matrices of Pu-239 and U-238 evaluated on ECCO 33-group (left) and on the 1500-group energy structures (right). The dashed-dotted black line represents the tolerance level.*

nor by a stochastic code, because of the too demanding computational resources. On the contrary, if eq. (7.17) was employed, a reduced number of energy-integrated projected sensitivities would be required, since the dimension of the POD basis, t, is generally much smaller than the rank m of the covariance, because of the rapid singular values decay. This fact has a very important implication, i.e. there is no limit to the energy detail considered in the evaluation of the sensitivity, making this technique suitable for stochastic methods or asymptotic theory (Dulla and Ravetto, 2020).

Tables 7.4 and 7.7 report the percentage uncertainty for the group-wise capture and fission homogenised cross sections induced by the uncertainty of U-238 and Pu-239

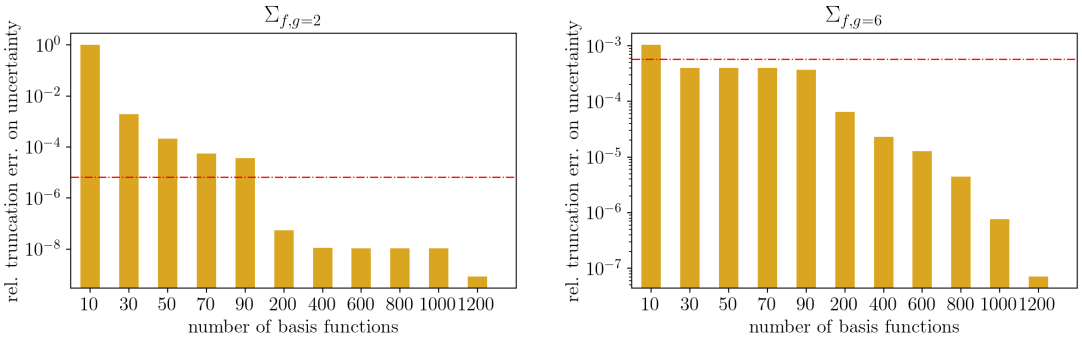

Figure 7.10: *POD truncation error on the relative Σ_f uncertainty due to Pu-239 MT18. The statistical error is represented by the dashed-dotted red line.*

MT18 and MT102. For all the results in the tables, the statistical uncertainty associated to the sensitivity coefficients is propagated through eq. (7.17) using the classical linear uncertainty propagation and neglecting the cross-correlation among the terms. Tables 7.4 and 7.5 show the uncertainties evaluated with GPT and XGPT, respectively, scoring the sensitivity and the covariance on the 33-group grid. It can be concluded that

Table 7.4: *Percentage uncertainties evaluated scoring both the GPT sensitivities and the covariances on the 33-group structure.*

g	U-238				Pu-239			
	σ_f (MT18)		σ_c (MT102)		σ_f (MT18)		σ_c (MT102)	
	Σ_f	Σ_c	Σ_f	Σ_c	Σ_f	Σ_c	Σ_f	Σ_c
1	0.60903(39)	0.00460(24)	0.00225(42)	1.00988(81)	0.38327(79)	0.0220(14)	0.00270(95)	0.42913(68)
2	0.01813(13)	0.000161(94)	0.00414(18)	1.18629(27)	0.93934(38)	0.00658(29)	0.00659(43)	1.02227(29)
3	0.003286(33)	0.00024(13)	0.00240(20)	1.07346(27)	1.06370(41)	0.00557(36)	0.00242(35)	1.10009(38)
4	0.001834(20)	0.00097(17)	0.01290(17)	0.92626(34)	1.01347(39)	0.02507(42)	0.01231(38)	0.89525(54)
5	0.00557(33)	0.00246(39)	0.14641(67)	0.80428(92)	1.1121(16)	0.15478(96)	0.3103(18)	1.6214(22)
6	0.0055(42)	0.0055(43)	0.0149(67)	0.2118(99)	1.279(28)	0.103(17)	0.740(43)	1.297(33)

the general agreement between the methods is acceptable within the statistical confidence interval, with some relevant exceptions, e.g. for the U-238 MT102 uncertainty on Σ_c.

These discrepancies can be explained recalling eq. (7.13), where the evaluation of the direct projected sensitivity is performed introducing an approximation. When both the direct sensitivities and the basis functions are evaluated on the 1500-group grid, the integration error is sufficiently reduced so that the overall agreement is good, at least in the statistical sense (see table 7.6). Clearly, if the direct sensitivity was computed directly by Serpent 2 during the transport process, the two methods would produce a set of statistically equivalent results, since they share the same energy grid. It should be noticed that columns Σ_c for MT18 and Σ_f for MT102 are identical in tables 7.5 and 7.6

Table 7.5: *Percentage uncertainties evaluated scoring both the XGPT sensitivities and the covariances on the 33-group structure.*

g	U-238				Pu-239			
	σ_f (MT18)		σ_c (MT102)		σ_f (MT18)		σ_c (MT102)	
	Σ_f	Σ_c	Σ_f	Σ_c	Σ_f	Σ_c	Σ_f	Σ_c
1	0.83637(95)	0.00433(41)	0.00288(38)	2.1566(17)	0.7045(10)	0.0203(13)	0.00299(82)	1.0935(13)
2	0.003942(86)	0.00015(11)	0.00348(10)	0.87510(67)	0.68924(63)	0.00687(27)	0.00654(35)	0.87966(48)
3	0.002744(17)	0.00011(13)	0.00243(21)	1.6049(12)	1.2850(11)	0.00553(42)	0.00257(37)	1.7165(12)
4	0.0013672(59)	0.00094(16)	0.01136(20)	1.14865(41)	0.82977(69)	0.02489(43)	0.01207(34)	1.07996(65)
5	0.00725(22)	0.00246(37)	0.14365(66)	0.52445(91)	1.4452(28)	0.13179(90)	0.2971(20)	0.9774(20)
6	0.0064(82)	0.0117(77)	0.015(11)	0.156(11)	0.393(28)	0.097(21)	0.555(32)	0.441(32)

for both species, since the direct effect is exactly zero.

Table 7.6: *Percentage uncertainties evaluated with XGPT scoring the indirect sensitivities on the 33-group structure and the direct effect (including the basis functions) on the 1500-group structure.*

g	U-238				Pu-239			
	σ_f (MT18)		σ_c (MT102)		σ_f (MT18)		σ_c (MT102)	
	Σ_f	Σ_c	Σ_f	Σ_c	Σ_f	Σ_c	Σ_f	Σ_c
1	0.60075(62)	0.00433(41)	0.00288(38)	0.65441(87)	0.38291(79)	0.0203(13)	0.00299(82)	0.3229(10)
2	0.026123(90)	0.00015(11)	0.00348(10)	0.79698(47)	0.67001(51)	0.00687(27)	0.00654(35)	0.54147(31)
3	0.004379(12)	0.00011(13)	0.00243(21)	1.47092(83)	1.6264(10)	0.00553(42)	0.00257(37)	1.62678(95)
4	0.0016899(69)	0.00094(16)	0.01136(20)	1.15964(35)	1.01185(74)	0.02489(43)	0.01207(34)	1.05397(60)
5	0.00508(28)	0.00246(37)	0.14365(66)	0.63134(82)	1.5018(22)	0.13179(90)	0.2971(20)	1.0821(20)
6	0.0064(82)	0.0117(77)	0.015(11)	0.396(12)	1.191(38)	0.097(21)	0.555(32)	1.069(37)

Table 7.7 presents the uncertainties provided by the XGPT approach scoring both direct and indirect sensitivities on the 1500-group grid. Since this is the finest group-structure adopted in the calculations, these values should be considered as the reference. Their agreement with the GPT results is very good, except for the impact of Pu-239 MT18 on $\Sigma_{f,6}$ and $\Sigma_{c,6}$, where GPT gives underestimated results. This difference is remarkable, and can be justified by the adoption of a larger number of low-energy groups in the 1500-group grid (XGPT) with respect to the ECCO 33-group grid (GPT), as it can be noticed in fig. 7.8.

On the contrary, by inspection of table 7.8 it can be concluded that the total uncertainty on k_{eff} coming from MT18 and MT102 and computed with GPT and XGPT using the two grids yield very similar results. This accordance is a consequence of two aspects. First, the direct contributions, which can induce large discrepancies between the two methods, are missing. Second, the effective multiplication factor is an integral parameter, thus it is less sensitive to the group-structure adopted in the calculation.

The results presented in this section allow to draw two important observations:

1. from the methodological point of view, XGPT is proved to yield a higher energy

Table 7.7: *Percentage uncertainties evaluated scoring both the XGPT sensitivities and the covariances on the 1500-group structure.*

g	U-238				Pu-239			
	σ_f (MT18)		σ_c (MT102)		σ_f (MT18)		σ_c (MT102)	
	Σ_f	Σ_c	Σ_f	Σ_c	Σ_f	Σ_c	Σ_f	Σ_c
1	0.61121(54)	0.00494(17)	0.00230(40)	0.95971(69)	0.38295(86)	0.0216(13)	0.00399(80)	0.42283(95)
2	0.01783(10)	0.000224(70)	0.00440(13)	1.18858(63)	0.94018(65)	0.00666(26)	0.00682(38)	1.02393(41)
3	0.003328(27)	0.000057(30)	0.00251(23)	1.07471(59)	1.06230(74)	0.00533(41)	0.00228(39)	1.09587(82)
4	0.001930(16)	0.00098(14)	0.01188(18)	0.91814(43)	1.00993(71)	0.02518(43)	0.01190(38)	0.89899(61)
5	0.00609(26)	0.00276(26)	0.14526(72)	0.80626(88)	1.0021(19)	0.14730(95)	0.2197(17)	1.6575(20)
6	0.0059(68)	0.0040(36)	0.0126(48)	0.202(16)	2.121(57)	0.075(27)	0.646(47)	1.240(47)

Table 7.8: k_{eff} *relative uncertainty in pcm.*

Nuclide	GPT 33	XGPT 33	XGPT 1500
U-238	101.55(11)	99.66(11)	101.53(12)
Pu-239	259.61(23)	259.63(23)	259.18(34)

resolution compared to the stochastic version of GPT. The superior accuracy is particularly evident when the responses are not integrated on the whole energy axis;

2. from the physical point of view, an appropriate number of low-energy groups is mandatory even in the case of a fast spectrum system analysis.

7.3.3 Multi-group constant distributions

The first-order model expressed by eq. (7.19) is now employed as a surrogate of the original model, i.e. the Serpent code, to sample the group-wise fission and capture cross sections in the inner fuel region. Figure 7.11 provides the average and perturbed fission and capture cross sections for Pu-239. The perturbations are obtained by sampling according to the 1500-group covariance matrix. Figure 7.12 shows the best-estimate homogenised and collapsed cross sections and their uncertainties. The purpose of these graphs is to help the visualisation of how the uncertainty in the raw nuclear data is propagated to the multi-group cross sections through the homogenisation and collapsing procedure. Since the perturbations in the basic nuclear data have been sampled assuming a multi-variate normal distribution, which is a standard assumption in the absence of information on the underlying distribution of the data, also the final output are normally distributed, due to the linearity of the model. The distributions can be observed by inspection of fig. 7.13. For sake of conciseness, only the group with the largest uncertainty is shown for both responses. The standard deviations featuring the distributions in fig. 7.13 are fully consistent with the ones reported in table 7.7.

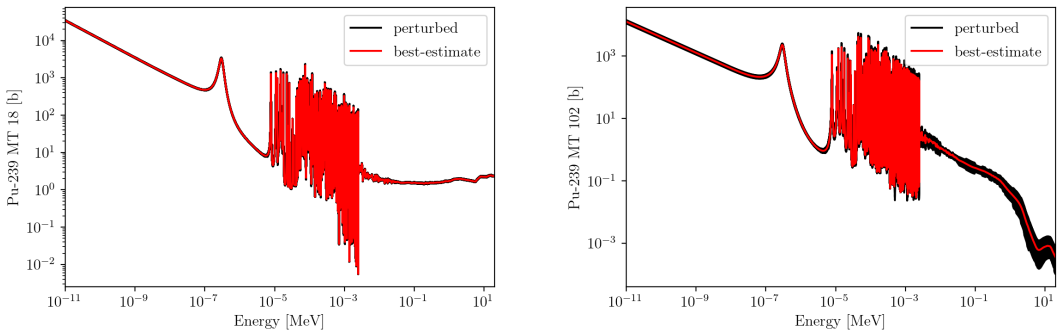

Figure 7.11: *Best-estimate and set of perturbed MT18 (left) and MT102 (right) cross sections for Pu-239. The black band is obtained by superposition of 100 perturbed values.*

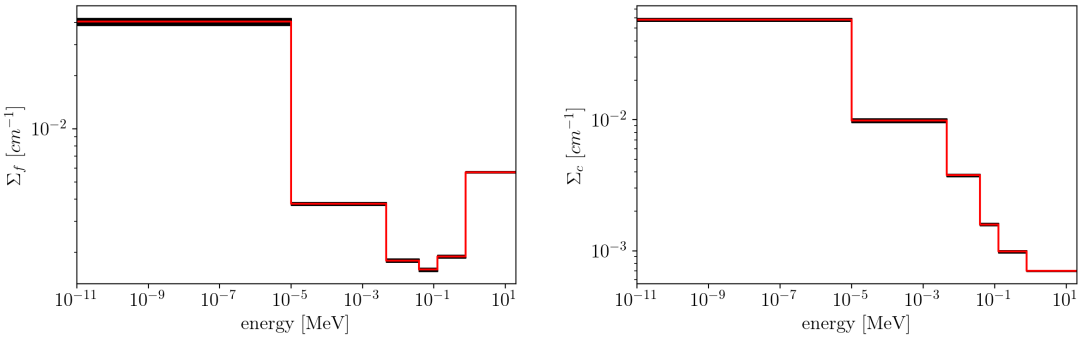

Figure 7.12: *Best-estimate (red) and 2-σ uncertainty (black) on 6-group values of fission (left) and capture (right) cross sections for Pu-239.*

Finally, fig. 7.14 reports the correlation matrices of the input raw nuclear data, processed on the 1500-group grid, and of the effective cross sections computed by Serpent 2 on the 6-group grid. The output correlation matrix has been estimated with 10^5 samples, generated with eq. (7.19).

7.4 Conclusions

In this chapter, the GPT and XGPT methods, both implemented in the Serpent 2 Monte Carlo code, are compared within the framework of uncertainty and sensitivity analysis. In particular, the comparison has been carried out focusing on the uncertainty propagation from the raw nuclear data to the energy collapsed and spatially homogenised cross sections for the ALFRED reactor design.

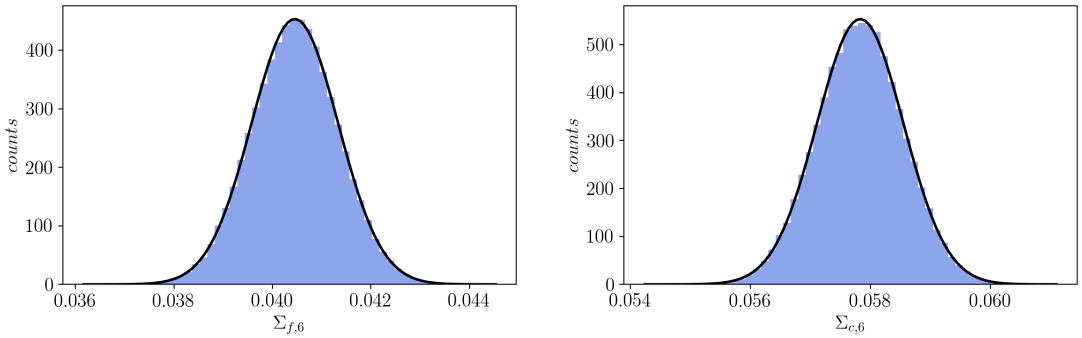

Figure 7.13: *Sample distributions for $\Sigma_{f,6}$ (left) and $\Sigma_{c,6}$ (right) due to the uncertainty in Pu-239 MT18 and MT102. The histograms have been constructed with 10^5 samples. The superimposed black line follows the Gaussian function.*

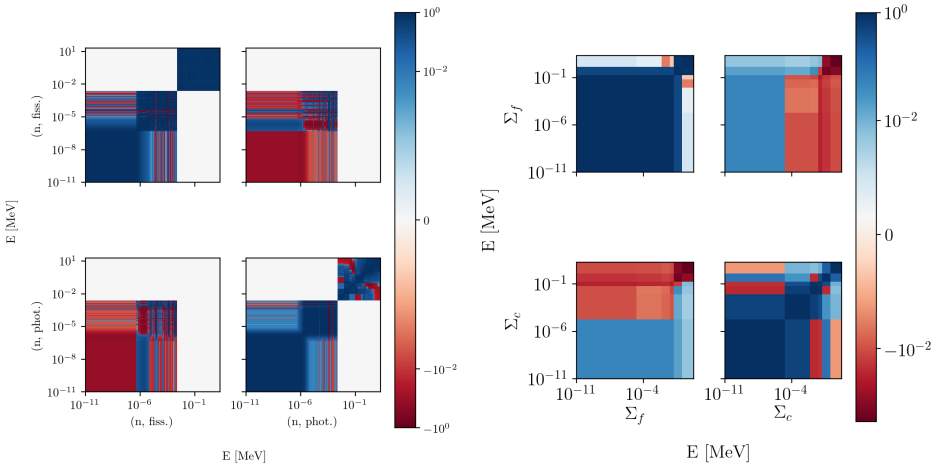

Figure 7.14: *Structure of the correlation matrices for the Pu-239 raw nuclear data scored on the 1500-group grid (left) and for the collapsed and homogenised cross section of the inner fuel region (right). The energy range is the same for all graphs.*

In the first part of the chapter, the features of each method are presented and discussed, outlining the calculation steps needed to estimate the direct sensitivity contributions in the case of a linear reaction rate response. Both GPT and XGPT allow to obtain a first-order estimates of the sensitivity coefficients, which are then inserted in the sandwich rule to estimate the response variance. The most relevant difference between the two methods lies within the energy treatment: XGPT is an inherently continuous-energy approach, whilst GPT requires the multi-group approximation.

Then, an uncertainty quantification study is carried out exploiting the GPT approach, focusing on all the heavy nuclides constituting the MOx fuel whose adoption is foreseen in the ALFRED reactor core. This assessment has shown that the two most

abundant nuclides, i.e. Pu-239 and U-238, are also the top contributors to the overall uncertainty on the few-group cross sections Σ_f and Σ_c for both the fuel regions considered in the homogenisation process, i.e. the inner and outer fuel assemblies.

The second part of the paper compares the uncertainties on Σ_f, Σ_c and k_{eff} calculated previously with GPT to the ones estimated with XGPT, focusing on the impact of the different energy grids where the sensitivities are scored. The major outcome of this comparison is that a more accurate energy resolution can be obtained with the XGPT method, making it the preferable choice among the perturbation techniques for uncertainty and sensitivity analyses in a Monte Carlo framework, thanks to its continuous-energy feature. However, according to the specific system (e.g., a thermal reactor) and to its output responses of interest, the use of a coarse-group GPT approach could be sufficiently accurate if only a rough estimate of the uncertainty is required or if the energy effects are less relevant. Different systems and responses should be analysed in the future to draw some more general conclusions.

Moreover, this analysis has also proved that an adequate number of low-energy groups is mandatory also if the system under analysis is featured by a fast spectrum. Finally, the output correlation matrix for the output responses Σ_f and Σ_c is compared to the correlation matrix of the input Pu-239 nuclear data, showing the covariance propagation from the raw nuclear data to the final output response of interest.

As a further development to this activity, it would be extremely useful to evaluate the impact of adopting continuous-energy covariances, extracted from the random evaluations produced by the T6 package, instead of fine-group covariances on the final output of XGPT calculations. Such an analysis would shed some light on the influence of the input parameter distributions on the final output and could highlight the importance for point-wise covariances with respect to fine-group ones.

Data availability

In the spirit of open-science, the complete datasets and scripts employed to pre- and post-process the Serpent calculations presented in this chapter are available in the open access Zenodo repository 10.5281/zenodo.4540785.

References

Abrate, N., M. Aufiero, S. Dulla, and L. Fiorito (2019). "Nuclear Data Uncertainty Quantification in Molten Salt Reactors with XGPT". In: *Proceedings of the ANS International Conference M&C2019*. Portland, OR (cited on page 285).

Aufiero, M., M. Martin, and M. Fratoni (2016). In: *Annals of Nuclear Energy* 96, pages 295–306 (cited on pages 279, 281, 285–286).

Bellman, R. (1957). "Dynamic Programming". Rand Corporation research study. Princeton University Press (cited on page 279).

Brown, D., M. Chadwick, R. Capote, A. Kahler, A. Trkov, M. Herman, A. Sonzogni, Y. Danon, A. Carlson, M. Dunn, D. Smith, G. Hale, G. Arbanas, R. Arcilla, C. Bates, B. Beck, B. Becker, F. Brown, R. Casperson, J. Conlin, D. Cullen, M.-A. Descalle, R. Firestone, T. Gaines, K. Guber, A. Hawari, J. Holmes, T. Johnson, T. Kawano, B. Kiedrowski, A. Koning, S. Kopecky, L. Leal, J. Lestone, C. Lubitz, J. Márquez Damián, C. Mattoon, E. McCutchan, S. Mughabghab, P. Navratil, D. Neudecker, G. Nobre, G. Noguere, M. Paris, M. Pigni, A. Plompen, B. Pritychenko, V. Pronyaev, D. Roubtsov, D. Rochman, P. Romano, P. Schillebeeckx, S. Simakov, M. Sin, I. Sirakov, B. Sleaford, V. Sobes, E. Soukhovitskii, I. Stetcu, P. Talou, I. Thompson, S. van der Marck, L. Welser-Sherrill, D. Wiarda, M. White, J. Wormald, R. Wright, M. Zerkle, G. Žerovnik, and Y. Zhu (2018). "ENDF/B-VIII.0: The 8th Major Release of the Nuclear Reaction Data Library with CIELO-project Cross Sections, New Standards and Thermal Scattering Data". In: *Nuclear Data Sheets* 148. Special Issue on Nuclear Reaction Data, pages 1–142 (cited on page 281).

Cacuci, D. G. (2003). "Sensitivity & Uncertainty Analysis, Volume I: Theory". Chapman & Hall/CRC, New York, page 285 (cited on page 279).

D'Auria, F., C. Camargo, and O. Mazzantini (2012). "The Best Estimate Plus Uncertainty (BEPU) approach in licensing of current nuclear reactors". In: *Nuclear Engineering and Design* 248, pages 317–328 (cited on page 278).

Dulla, S. and P. Ravetto (2020). "A re-visitation of space asymptotic theory in neutron transport". In: *European Physical Journal Plus* 135, page 347 (cited on page 294).

Fiorito, L., G. Žerovnik, A. Stankovskiy, G. V. den Eynde, and P. E. Labeau (2017). In: *Annals of Nuclear Energy* 101, pages 359–366 (cited on page 285).

Gandini, A. and M. Salvatores (1970). "Effects of Plutonium-239 Alpha Uncertainties on some Significant Integral Quantities of Fast Reactors". In: *Nuclear Science and Engineering* 41.3, pages 452–455 (cited on page 279).

Gandini, A., M. Salvatores, and I. D. Bono (1968). "Sensitivity Study of Fast Reactors Using Generalized Perturbation Techniques". In: *Fast Reactor Physics Vol. I. Proceedings of a Symposium on Fast Reactor Physics and Related Safety Problems* (cited on page 279).

Grasso, G., C. Petrovich, D. Mattioli, C. Artioli, P. Sciora, D. Gugiu, G. Bandini, E. Bubelis, and K. Mikityuk (2014). "The core design of ALFRED, a demonstrator for the European lead-cooled reactors". In: *Nuclear Engineering and Design* 278, pages 287–301 (cited on pages 280, 287).

Herman, M., A. Trkov, et al. (2010). Technical report BNL-90365-2009 Rev.1 (cited on page 288).

Hüllermeier, E. and W. Waegeman (2019). "Aleatoric and Epistemic Uncertainty in Machine Learning: a Tutorial Introduction". In: *CoRR* (cited on page 278).

Johnson, A. E., D. Kotlyar, S. Terlizzi, and G. Ridley (2020). "serpentTools: A Python Package for Expediting Analysis with Serpent". In: *Nuclear Science and Engineering* 194.11, pages 1016–1024 (cited on page 284).

Koning, A. (2020). Technical report (cited on pages 281, 285).

Koning, A. and D. Rochman (Dec. 2012). "Modern Nuclear Data Evaluation with the TALYS Code System". In: *Nuclear Data Sheets* 113.12 (cited on page 281).

Koning, A., D. Rochman, J.-C. Sublet, N. Dzysiuk, M. Fleming, and S. van der Marck (2019). "TENDL: Complete Nuclear Data Library for Innovative Nuclear Science and Technology". In: *Nuclear Data Sheets* 155. Special Issue on Nuclear Reaction Data, pages 1–55 (cited on page 281).

Leppänen, J., M. Pusa, T. Viitanen, V. Valtavirta, and T. Kaltiaisenaho (2015). "The Serpent Monte Carlo code: Status, development and applications in 2013". In: *Annals of Nuclear Energy* 82, pages 142–150 (cited on page 279).

Leppänen, J., M. Pusa, and E. Fridman (2016). In: *Annals of Nuclear Energy* 96, pages 126–136 (cited on page 278).

MacFarlane, R. E., D. W. Muir, R. M. Boicourt, A. C. Kahler, J. L. Conlin, and W. Haeck (2018). Technical report (cited on pages 280–281).

Nallo, G. F., N. Abrate, S. Dulla, P. Ravetto, and D. Valerio (2020). "Neutronic benchmark of the FRENETIC code for the multiphysics analysis of lead fast reactors". In: *The European Physical Journal Plus* 135, page 238 (cited on pages 287–288).

Pelowitz, D., T. Goorley, M. James, T. Booth, F. Brown, J. Bull, L. Cox, J. Durkee, J. Elson, M. Fensin, R. Forster, J. Hendricks, H. Hughes, R. Johns, B. Kiedrowski, R. Martz, S. Mashnik, G. Mckinney, R. Prael, and T. Zukaitis (May 2013). (Cited on page 281).

Popper, K. (1998). "The world of Parmenides: essays on the Presocratic enlightenment". Routledge, London (cited on page 277).

Rimpault, G., D. Plisson, J. Tommasi, R. Jacqmin, D. Verrier, and D. Biron (2002). "The ERANOS Code and Data System for Fast Reactor Neutronic Analyses". In: *Proceedings of the PHYSOR conference 2002* (cited on pages 278, 280).

Rochman, D., A. J. Koning, S. C. Van Der Marck, A. Hogenbirk, and C. M. Sciolla (2011). "Nuclear data uncertainty propagation: Perturbation vs. Monte Carlo". In: *Annals of Nuclear Energy* 38.5, pages 942–952 (cited on page 279).

Schopenhauer, A. (1859). "The world as will and representation" (cited on page 278).

"Uncertainty Propagation with Fast Monte Carlo Techniques" (2014). In: *Nuclear Data Sheets* 118, pages 367–369 (cited on page 279).

Usachev, L. (1964). "Perturbation theory for the breeding ratio and for other number ratios pertaining to various reactor processes". In: *Journal of Nuclear Energy. Parts A/B. Reactor Science and Technology* 18.10, pages 571–583 (cited on page 279).

Valtavirta, V. (2018). *Nuclear data uncertainty propagation to Serpent generated group and time constants*. Technical report VTT-R-04681-18. VTT research center, Finland (cited on page 288).

Volkwein, S. (2011). "Model reduction using proper orthogonal decomposition". In: *Lecture notes, Institute of Mathematics and Scientific Computing, University of Graz. see http://www. uni-graz. at/imawww/volkwein/POD. pdf* 1025 (cited on page 285).

W. Zwermann, B. Krzykacz-Hausmann, L. Gallner, M. Klein, A. Pautz, and K. Velkov (2012). "Aleatoric and epistemic uncertainties in sampling based nuclear data uncertainty and sensitivity analyses". In: Proc. of the International Topical Meeting on Advances in Reactor Physics (PHYSOR '12), Knoxville, TN, USA, April 15–20, 2012 (cited on page 279).

Chapter 8

Conclusions and future perspectives

There must be some kind of way outta here.
[...]
There's too much confusion
I can't get no relief
[...]
So let us stop talkin' falsely now
The hour's getting late

All along the watchtower
Jimi Hendrix (Bob Dylan)

8.1 Summary

The main purpose of the thesis is developing new methods for the safety and stability analyses of nuclear reactors, without loosing sight of the industrial requirements and needs concerning the adoption of qualified codes.

The first part of the thesis is focused on the analysis and development of new methods in the frame of reactor physics and their application to simplified systems, with the aim of grasping better their physico-mathematical features without loosing track of the real-life applications. In the first chapter, the classical P_N and S_N approximations are presented, in order to approach numerically the solution of the eigenvalue problems arising in neutron transport. After addressing some old-fashioned but still relevant questions concerning the angular parity order, the equivalence between odd and even angular orders and the possibility to accelerate numerically the angular convergence of these methods, some numerical benchmarks are carried out to check the

implementation of these methods in an in-house Python package, called TEST.

Then, the classical eigenvalue formulations to the neutron transport equation, i.e. the multiplication eigenvalue, the collision eigenvalue, the time eigenvalue and the density eigenvalue, are presented and discussed, focusing on their physico-mathematical peculiarities and analysing their eigenvalue spectra.

Exploiting the results of the eigenvalue formulation analysis, a possible application of the eigenfunctions associated to the various formulations are proposed as alternative weighting functions for the group collapsing procedure. The behaviour of the different weighting functions is assessed by comparing the main integral parameters obtained by multi- and few-group calculations.

Then, a generalisation of the standard eigenvalue formulations is proposed, with the final aim of deriving a new eigenvalue problem which allows to act on specific portions of the phase space and nuclides, for design-oriented applications. After discussing the main physico-mathematical aspects of this formulation, relevant engineering problems, like the determination of the critical boron concentration, are evaluated using this new approach.

In the remaining chapters, more realistic systems are analysed, focusing on 2D and 3D models of some Gen-III+ and Gen-IV reactor concepts. This last part of the work mainly aims at proposing computationally efficient methods for the safety analyses of the neutronic behaviour of the core, trying to reduce as much as possible any intervention in the code. This goal is accomplished by means of Non-Intrusive Reduced-Order Modelling (NIROM) techniques, which permit a fair reduction of the computational time without any code modifications at the price of small approximations.

A non-intrusive reduced-order model based on a combination of Proper Orthogonal Decomposition and Radial Basis Function techniques is presented as an efficient way of reducing the computational cost of the original, high-fidelity models. Then, this model is applied to three different industrial application, with the goal of proving the NIROM effectiveness.

The first application deals with the spatial stability stability of the Gen-III+ core, and aims at developing an efficient NIROM to perform a sensitivity analysis of the flux and power tilt behaviour at the full-core level with respect to a random, localised perturbations.

The second application concerns the parametric safety analysis of accidental transient scenarios in LFR, which require accurate evaluations of the safety-critical parameters in different operational and accidental conditions.

In order to show that the methods proposed have a wide applicability range also outside the nuclear field, the last application presents another variation of the NIROM approach, which is applied to model accidental high-pressure gas releases in industrial, congested environments.

Finally, the last chapter focuses on the nuclear data uncertainty quantification, which is a relevant topic in the safety analysis of nuclear system. More specifically, this chapter is devoted to perform an assessment of the main techniques used in the Monte Carlo

framework to carry out the sensitivity and uncertainty analysis, focusing on the propagation of the uncertainty from the raw nuclear data to some relevant neutronic output quantities, focusing on the lead-cooled fast reactor ALFRED design.

8.2 Conclusions and future perspective

The thesis has been organised in two parts, one more theoretical and devoted to the development of reactor physics methods, and one more practical, focused on industrial applications.

In the following, the main outcomes and contributions of this work are summarised:

- In chapter 2, the numerical framework based on the P_N and S_N multi-group models is presented, with the goal of solving the eigenvalue problem formulations arising in neuron transport. After proving the equivalence between the odd P_N equation and the succeeding even order P_{N+1}, the numerical implementation of the in-house TEST is verified with several benchmark values taken from the available literature on the topic. Then, the impact of the boundary conditions and of the parity order on the angular convergence of the fundamental eigenvalues was assessed. In this case, it was interesting to show that, with a proper selection of the boundary conditions, it is possible to realise even and odd sequences that converge to the asymptotic value from two opposite directions. This interesting feature is thus exploited to study the possibility to accelerate the eigenvalue sequences, which suffers from the energy and spatial modelling error, to the asymptotic values. In this case, the Wynn-ε scheme is employed, showing its applications to estimate the numerical errors.

- In chapter 3, the different eigenvalue formulations to the neutron transport equation available in the literature, i.e. the time, the multiplication, the collision and the density eigenvalues, and a newly introduced capture eigenvalue, introduced here for the first time, have been presented, discussing thoroughly both their advantages and their disadvantages. The attention has been focused mainly on the behaviour of the different eigenvalue spectra according to the spatial, angular and energetic models employed and to the spatial heterogeneity. The analysis of the spectrum, led using the TEST code, has been extremely useful to highlight the tight connection between the spectra and the approximation used to solve the neutron transport equation and to draw some important, practical conclusions to drive the eigenvalue solver towards the fundamental eigenpair according to the spectral formulation employed. Finally, a possible application of the spectrum as a concise figure of merit for the optimal selection of the group boundaries has been suggested as a future perspective.

- In chapter 4, one of the current open issues in reactor physics, i.e. the cross section group-collapsing, has been addressed from the point of view of the weighting

spectrum used to perform the integration over the energy range. In particular, the use of the fundamental eigenfunctions associated to the different eigenvalue formulations arising in neutron transport is investigated as an alternative to the usual choice of considering the k-eigenvalue spectrum. Due to the problem complexity and to the large number of parameters affecting the group constant generation, the analysis was carried out performing some numerical experiments for a simplified system, i.e. a homogeneous slab, for which the calculation of the various eigenfunctions is possible using the TEST code. The choice of neglecting any heterogeneity effect allowed to focus on the energy effects related to the system spectrum, to the choice of the weighting function and to the energy group structure used for the cross sections and diffusion coefficient condensation.

The analysis showed that it is actually very difficult to foresee the performances of each weighting eigenfunction only relying on physical considerations, because of the appearance of numerical error compensations in the condensation scheme that depend on the type of the reactivity insertion, on the few-group grid, on the type of the eigenfunction and, of course, on the system energy spectrum.

Nevertheless, it is possible to conclude that, in most of the cases, the k eigenfunction, which is the one traditionally employed in the group constant generation process, is certainly the one yielding the worst results, especially when the system is far from criticality. In this respect, the best option for the condensation procedure seems to be γ energy spectrum. Actually, other eigenfunctions like the ω and the θ ones may provide slightly more accurate results than the ones produced with the γ condensation, but the evaluation of these eigenfunctions is always much more computationally expensive. On top of that, the performances of γ can found a justification on a physical ground, since, among the static eigenvalue formulations presented in the thesis, it is the one which distorts the less the energy spectrum of the system.

From this perspective, the low relative error obtained with the θ collapsing may be explained by the fact that both the nature of the perturbation and the θ eigenvalue definition involve the capture cross section. In order to shed some light on this aspect, the reactivity should be driven by the change of other parameters, for example the fission cross section or the density of the system, which are strongly related to k and δ, respectively.

In order to draw some more general conclusions, other numerical experiments should be envisaged in the future. In addition to the analysis of the influence of the kind of perturbation triggering the reactivity insertion, the spatial and energy effects related to the presence of heterogeneities in the system should be definitively taken into account. Finally, the thermal feedback should be introduced, especially for the analysis of heavily off-criticality.

- In chapter 5, it has been shown how the eigenvalue formulations to the neutron

transport equation could be traced back to a generalised eigenvalue formulation, called ζ. This eigenvalue can be introduced in order to filter specific regions of the phase space. In particular, bearing in mind the possible practical constraints arising during the core-design process, the ζ eigenproblem has been cast in a form that extends the applicability of the density eigenvalue δ to specific nuclides and regions of the phase space.

This novel approach has been applied to a wide range of different classical yet realistic problems in reactor physics, considering the main types of materials encountered in the design of a reactor core, e.g., the fuel, the coolant, the moderator and the localised absorbers. These applications provided remarkable results. First, the ζ eigenvalue yields equivalent results to the iterative method commonly applied in such framework, but with a strong reduction of the computational effort. More importantly, the existence of one or more design solutions seems related to the presence, in the ζ spectrum, of one or more real and positive eigenvalues associated to positive eigenfunctions. This is a remarkable feature, which should facilitate to rigorously assess whether criticality can be attained or not acting on the selected nuclides, even in case of complex systems. Moreover, the knowledge of all the possible criticality arrangements of a system is of the utmost importance for the safety studies involving the re-criticality phenomena. This study of the ζ eigenvalue spectrum suggests that, in some situations, featured by the absence of competing interaction phenomena, there may exist only one positive solution, associated to an eigenvalue separation which is large enough to ensure an efficient numerical convergence on the dominant one.

Due to its novelty, there are many open questions that should be addressed in future activities. First of all, the ζ spectrum should be studied more thoroughly, starting from a more rigorous physico-mathematical framework and taking into account the impact of the different spatial, angular and energy approximations of the neutron transport equation. Moreover, the physico-mathematical meaning of the higher-order ζ harmonics should be investigated as well. A better comprehension of the ζ superior modes could disclose the possibility to apply perturbation methods, like the Generalised Perturbation Theory, which could be very useful for design-purpose calculations. Then, the action of the eigenvalue on more specific portions of the phase space should be studied, involving for example only some reaction channel, e.g. the capture, and a reduced energy range, e.g. the thermal region. Finally, some research efforts should be devoted to incorporate the ζ calculation in the cross sections collapsing and homogenisation process, in order to properly account for the self-shielding effects.

- In chapter 6, a non-intrusive reduced order model has been introduced for the efficient computational analysis of complex problems. This chapter presents three different applications of this methodology.

The first deals with the stability analysis of Gen-III+ systems, which require full-core diffusion calculations to assess the core behaviour in presence of local disturbances. Due to the two-step nature of the full-core calculations, which require a set of few-group homogenised constants, a two-step meta-model has been proposed, combining the polynomial chaos expansion method for the estimation of the multi-group data and the POD-RBF model for the estimation of the assembly-wise power distribution obtained in response to a localised perturbations, which are assumed to be variations in the coolant density and in the fuel pellet diameter.

The first-order polynomial chaos expansion is sufficient to reproduce within an acceptable accuracy the cross sections behaviour as a function of the two input perturbations, with only a few full-order model evaluations. However, it must be acknowledged that, in presence of larger variations, probably more training points would be required to match the target accuracy.

Concerning the full-core calculations, some precautions are needed to handle the spatial arrangement of the perturbations. First of all, an algorithm for the definition of the perturbation and its constraints, e.g., the perturbation shape, is envisaged. Then, two different sampling techniques are devised to produce the training dataset. The first one draws the first perturbed FA according to an importance probability density function based on the neutron importance, and then randomly selects the surrounding FAs, assigning a random value to the physical perturbation as well. The second sampling technique works in the same way, but the perturbation intensity is sampled according to a deterministic rule.

The last precaution regards the distance evaluation among the input parameters: due to the spatial arrangement of the disturbance, the classical euclidean distance between the various input parameter is not adequate to distinguish similar perturbations, engendering the learing capabilities of the model. Thus an alternative algorithm for image recognition is selected, to guarantee a consistent evaluation of the training samples distance with respect to a new parameter point.

When it is assumed that more perturbations can occur in the core, the parameter space of the problem becomes huge. However, according to the results obtained, it seems that the random sampling technique is adequate to provide good results. Nevertheless, it seems difficult to strongly reduce the error, due to the large variability in the input space.

If a simpler problem is addressed, assuming that only one batch of perturbed FA can occur, the overall accuracy of the model improves a lot, also thanks to the adoption of the hybrid sampling process. This observation suggests that more specialised meta-models could be the most efficient solution to the problem.

As a future development, hybrid techniques based on data- and physics-driven should be investigated. For example, it would be interesting to use the legacy Generalised Perturbation Theory technique to provide a set of sensitivity coefficients

to drive the sampling phase towards the most relevant perturbations.

Concerning the second application, the model has been extended to treat also time-dependent models, proposing an algorithm that suitably combines the algorithms already implemented in the ROMpy package.

The case study regarded the accidental insertion of a control rod in a close-to-critical initial configuration of the ALFRED core design, considering as free parameters the insertion times of the rod, which have the effect of changing the insertion speed of the CR.

The full-core snapshots, representing the power density of the system, are generated with the FRENETIC nodal diffusion code. In spite of the relatively low number of samples, the ROM shows a good accuracy (the global error is below 4%) with respect to the full-order model for the validation points considered, on both the local and global spatial scales and for the whole transient duration. From the computational burden point of view, excluding the off-line training phase, which is though affordable with a laptop compute due to the fairly low number of training points, the ROM outperforms FRENETIC, providing the full-core power density time snapshots in less than a dozen of seconds, with respect to the 3 hours required by the code.

As a future development, efforts will be devoted to improve the training parameters sampling, trying to reduce the number of samples needed to match the target accuracy. Since the Smolyak grid based on the Chebyshev polynomials is more dense at the corners, the sampling performances could be improved a lot considering alternative point distributions, like the evenly-space Clenshaw-Curtis points. Finally, the ROM will be improved to fully exploit the time adaptive features of the predictor-corrector algorithm, thus considering only the snapshots that are more significant for the reactor dynamics, in contrast to the uniform time binning employed in this work.

The last application regarded the reduced-order modelling of QRA-oriented CFD simulations. This class of NIROMs has been recently applied in many research fields, yet most of the applications do not show satisfactory assessment and propagation of the ROM approximation errors, in particular in the presence of functional (e.g., time- and/or space-dependent) outputs.

In this respect, since the final aim of this application is the adoption of these surrogate models to minimise the computational effort associated to QRA studies (where it is of paramount importance to endow the simulation model responses with confidence intervals), a methodology for the assessment of the ROM uncertainty in the estimation of functional (in this case, space-dependent) safety-critical quantities is proposed. To test this methodology and prove its effectiveness, the ROM is applied to the case of high pressure, accidental gas release in an off-shore oil&gas plant, where the critical output variables of interest are the flammable gas

volume, which is related to the irreversible injuries area.

First, the NIROM is trained exploiting a set of nested parameter samples in order to adaptively refine it with a reduced computational burden. The validation error, computed as a weighted sum of the sourcebox face-wise errors, is considered sufficiently low (<15%) using the first level of training cases plus additional cases above 50 bar.

Then, to estimate the model response variability to the training samples, the bootstrap method is employed to obtain the statistical distributions from the ensemble of ROM responses. Since, in this case study, the ROM response is used as input for the CFD dispersion simulation, a quantitative assessment of the impact of the ROM approximation error is mandatory.

The propagation of the uncertainty from the ROM response distribution to the dispersion model output is achieved combining the POD and the UT techniques. The first is employed to reduce the input data dimensionality, while the second is adopted to select the input data for the dispersion calculations and finally to estimate the dispersion output confidence intervals. The main quantities of interest in such calculations, pertinent to the QRA analysis, are in very good agreement with the same results obtained using the profiles computed by CFD, with a relative error between the two approaches below 10% and a reduction of the computational time of about three orders of magnitude, suggesting that the POD-RBF NIROM is adequate to obtain fast yet very accurate results. It should be remarked that a QRA study has an intrinsically high level of uncertainty, which makes the additional 10% introduced by the ROM model acceptable.

A future development of this activity could be to increase the number of training points considering also other input parameters affecting the SB, namely the break size and the obstacle features. Since these parameters have a strong influence on the SB dimension, a more sophisticated strategy should be devised in order to handle the snapshots defined on a different spatial domain. Moreover, adaptive sparse sampling techniques should be employed in order to progressively refine the parameter space where the error is not acceptable.

In parallel to these activities, a surrogate model for the dispersion phase should be trained as well, in view of a coupling with the source-box ROM, allowing to realise a real-time simulation framework, featured by the capability of providing confidence intervals on the main results thanks to the combination of bootstrapping and UT.

- In chapter chapter 7, the GPT and XGPT methods, both implemented in the Serpent 2 Monte Carlo code, are compared within the framework of uncertainty and sensitivity analysis. In particular, the comparison has been carried out focusing on the uncertainty propagation from the raw nuclear data to the energy collapsed and spatially homogenised cross sections for the ALFRED reactor design.

In the first part of the chapter, the features of each method are presented and discussed, outlining the calculation steps needed to estimate the direct sensitivity contributions in the case of a linear reaction rate response. Both GPT and XGPT allow to obtain a first-order estimates of the sensitivity coefficients, which are then inserted in the sandwich rule to estimate the response variance. The most relevant difference between the two methods lies within the energy treatment: XGPT is an inherently continuous-energy approach, whilst GPT requires the multi-group approximation.

Then, an uncertainty quantification study is carried out exploiting the GPT approach, focusing on all the heavy nuclides constituting the MOx fuel whose adoption is foreseen in the ALFRED reactor core. This assessment has shown that the two most abundant nuclides, i.e. Pu-239 and U-238, are also the top contributors to the overall uncertainty on the few-group cross sections Σ_f and Σ_c for both the fuel regions considered in the homogenisation process, i.e. the inner and outer fuel assemblies.

The second part of the paper compares the uncertainties on Σ_f, Σ_c and k_{eff} calculated previously with GPT to the ones estimated with XGPT, focusing on the impact of the different energy grids where the sensitivities are scored. The major outcome of this comparison is that a more accurate energy resolution can be obtained with the XGPT method, making it the preferable choice among the perturbation techniques for uncertainty and sensitivity analyses in a Monte Carlo framework, thanks to its continuous-energy feature. However, according to the specific system (e.g., a thermal reactor) and to its output responses of interest, the use of a coarse-group GPT approach could be sufficiently accurate if only a rough estimate of the uncertainty is required or if the energy effects are less relevant. Different systems and responses should be analysed in the future to draw some more general conclusions.

Moreover, this analysis has also proved that an adequate number of low-energy groups is mandatory also if the system under analysis is featured by a fast spectrum. Finally, the output correlation matrix for the output responses Σ_f and Σ_c is compared to the correlation matrix of the input Pu-239 nuclear data, showing the covariance propagation from the raw nuclear data to the final output response of interest.

As a further development to this activity, it would be extremely useful to evaluate the impact of adopting continuous-energy covariances, extracted from the random evaluations produced by the T6 package, instead of fine-group covariances on the final output of XGPT calculations. Such an analysis would shed some light on the influence of the input parameter distributions on the final output and could highlight the importance for point-wise covariances with respect to fine-group ones.

This Ph.D. thesis has been typeset by means of the TEX-system facilities. The typesetting engine was pdfLATEX. The document class was `toptesi`, by Claudio Beccari, with option `tipotesi=scudo`. This class is available in every up-to-date and complete TEX-system installation.